GEOMORPHOMETRY 2020

Conference Proceedings

edited by

Massimiliano Alvioli
Ivan Marchesini
Laura Melelli
Peter Guth

Proceedings of
GEOMORPHOMETRY 2020 Conference

Massimiliano Alvioli, Ivan Marchesini, Laura Melelli & Peter Guth

Italian National Research Council
Research Institute for Geo-Hydrological Protection
University of Perugia Department of Physics and Geology
International Society for Geomorphometry Society

Book DOI: 10.30437/GEOMORPHOMETRY2020
ISBN: 978 88 8080 282 2

URL: http://www.irpi.cnr.it/conference/geomorphometry-2020

Perugia 2020
Italy

Please cite this book as:
Massimiliano Alvioli, Ivan Marchesini, Laura Melelli, and Peter Guth (2020) Proceedings of the Geomorphometry 2020 Conference, Perugia, Italy, CNR Edizioni, 266 p., doi: 10.30437/GEOMORPHOMETRY2020.

Volume a cura di
Massimiliano Alvioli, Ivan Marchesini, Laura Melelli, Peter Guth

P.le Aldo Moro 7 - Roma
www.edizioni.cnr.it

Preface

Geomorphometry is the science of quantitative land surface analysis. It gathers various mathematical, statistical and image processing techniques to quantify morphological, hydrological, ecological and other aspects of a land surface. Common synonyms for geomorphometry are geomorphological analysis, terrain morphometry or terrain analysis and land surface analysis. The typical input to geomorphometric analysis is a square-grid representation of the land surface: a digital elevation (or land surface) model.

The first Geomorphometry conference dates back to 2009 and it took place in Zürich, Switzerland. Subsequent events were in Redlands (California), Nánjīng (China), Poznan (Poland) and Boulder (Colorado), at about two years intervals. The International Society for Geomorphometry (ISG) and the Organizing Committee scheduled the sixth Geomorphometry conference in Perugia, Italy, June 2020. Worldwide safety measures dictated the event could not be held in presence, and we excluded the possibility to hold the conference remotely. Thus, we postponed the event by one year - it will be organized in June 2021, in Perugia, hosted by the Research Institute for Geo-Hydrological Protection of the Italian National Research Council (CNR IRPI) and the Department of Physics and Geology of the University of Perugia.

One of the reasons why we postponed the conference, instead of canceling, was the encouraging number of submitted abstracts. Abstracts are actually short papers consisting of four pages, including figures and references, and they were peer-reviewed by the Scientific Committee of the conference. This book is a collection of the contributions revised by the authors after peer review. We grouped them in seven classes, as follows:

- Data and methods (13 abstracts)
- Geoheritage (6 abstracts)
- Glacial processes (4 abstracts)
- LIDAR and high resolution data (8 abstracts)
- Morphotectonics (8 abstracts)
- Natural hazards (12 abstracts)
- Soil erosion and fluvial processes (16 abstracts)

Proceedings of the Geomorphometry 2020 Conference
DOI: 10.30437/GEOMORPHOMETRY2020

The 67 abstracts represent 80% of the initial contributions. The remaining ones were either not accepted after peer review or withdrawn by their Authors. Most of the contributions contain original material, and an extended version of a subset of them will be included in a special issue of a regular journal publication.

Three keynote speakers were scheduled for the conference: Marco Cavalli, Igor V. Florinsky and Michael Hutchinson. Prof. Hutchinson is the recipient of the ISG's Lifetime Achievement Award.

Marco Cavalli is researcher at CNR IRPI Padova since 2009. His research interests mainly focus on the development and application of geomorphometric approaches to LiDAR data and high-resolution Digital Terrain Models with specific attention to geomorphic processes and sediment dynamics in mountain catchments. His main works concerned the development of indices of surface roughness and sediment connectivity along with the use of DEM differencing techniques to assess geomorphic changes.

Igor V. Florinsky is a Principal Research Scientist at the Institute of Mathematical Problems of Biology, Keldysh Institute of Applied Mathematics at the Russian Academy of Sciences. He is the author or editor of over 150 publications including 4 books and 60 papers in peer-reviewed journals. His research interests include theory, methods, and applications of digital terrain modeling and geomorphometry, as well as the influence of geological environment on humans, society, and civilization.

Michael Hutchinson is recognized internationally for his contributions to the theory and practice of spatial and temporal analysis of environmental data. His methods for modelling of climate and terrain, as implemented in the ANUDEM, ANUSPLIN and ANUCLIM computer packages, are widely used to support hydrological and ecological modelling and the assessment of the impacts of climate change. His Australia-wide terrain and climate models have underpinned much of the natural resource and environmental analysis carried out by Australian Universities and Natural Resource Agencies over the last 30 years.

Patron

IAG - International Association of Geomorphologists

AIGeO – Associazione Italiana di Geografia Fisica e Geomorfologia

Supporting Organizations

Research Institute for Geo-Hysrological Protection, Italy

Department of Physics and Geology, University of Perugia, Italy

T4E Technology four Elements

Proceedings of the Geomorphometry 2020 Conference
DOI: 10.30437/GEOMORPHOMETRY2020

Conference Scientific Committee:

Alexander Brenning Friedrich Schiller University
A-Xing Zhu University of Wisconsin
Carlos Grohman University of Sao Paolo
Hannes I. Reuter ISRIC - World Soil Information
Helena Mitasova North Carolina State University
Ian Evans Durham University
Jaroslav Hofierka University of Presov
John Gallant CSIRO
John Lindsay University of Guelph
Lucian Dragut West University of Timisoara
Massimiliano Alvioli CNR IRPI Perugia
Mihai Niculita University Al. I. Cuza
Peter L. Guth US Naval Academy
Qiming Zhou Hong Kong Baptist University
Qin Cheng-Zhi Chinese Academy of Sciences
Robert A. MacMillan LandMapper Environmental Solutions Inc.
Samantha Arundel USGS
Steve Kopp ESRI
Tomislav Hengl OpenGeoHub Foundation

Conference Organizing Committee:

Massimiliano Alvioli CNR IRPI Perugia
Ivan Marchesini CNR IRPI Perugia
Laura Melelli University of Perugia
Peter L. Guth US Naval Academy
Scott Peckham University of Colorado and rivix.com

Contents

Section 1: Data & Methods

Proceedings of Geomorphometry 2020
DOI: 10.30437/GEOMORPHOMETRY2020

Proceedings of Geomorphometry 2020
DOI: 10.30437/GEOMORPHOMETRY2020

Section 7: Soil Erosion & Fluvial Processes

Proceedings of Geomorphometry 2020
DOI: 10.30437/GEOMORPHOMETRY2020

GEOMORPHOMETRY 2020 PERUGIA, ITALY JUNE 22 - 26 2020

Comparative study of delineation of urban areas using imperviousness products and open data

Massimiliano Alvioli
Istituto di Ricerca per la Protezione Idrogeologica
Consiglio Nazionale delle Ricerche
via Madonna Alta 126, I-06128 Perugia, Italy
massimiliano.alvioli@irpi.cnr.it

Abstract—**City boundaries are not self-manifest, and typically do not coincide with administrative boundaries. A sound delineation of cities, more generally of urban areas, is a non-trivial task. A delineation method should comply with a well-defined metric, in order to reduce subjectivity, to favour reproducibility, and to allow assimilation with other methods. In fact, many existing city delineation methods rely heavily on numerical parameters such as population density thresholds. Here, we present city delineation for the whole of Italy performed with two different methods. On the one hand, we consider delineation based on terrain imperviousness, as a proxy for the existence of continued human presence, which is an inherently parametric method. On the other hand, we adopt a strictly data-driven method known as "natural cities", based on head-tail breaks of areas extracted from road junctions. We compare results from the two methods by considering numerical figures from the two delineated set of cities. We further propose an additional metric for assessing the results, namely a scaling relation between area and population of individual cities in the two sets. We show that the two results are similar in terms of number and total areal extent of cities, while area-population relations highlights substantial differences which can be ascribed to the parametric character of delineation from imperviousness.**

I. INTRODUCTION

The size, shape and geographical location of cities is relevant to many studies including demographic and social issues, labor trends, natural hazards, urban planning, to mention some. To date, little consensus exists on where city boundaries are located, and how the criteria to delineate them should be formalized. A recent review [1] compiled a survey of 32,231 studies of urban agglomerations, with a wide range of variability regarding the definition of city itself. United Nations [2] acknowledges, "no standardized international criteria exist for determining the boundaries of a city and often multiple boundary definitions are available for any given city". Urban areas exist in three nested levels, in the definition of United Nations: City Proper, Urban Agglomeration and Metropolitan Area, in order of increasing sizes with respect to both planimetric area and population, but these definitions are not standard.

Delineation of cities has been performed in the relevant literature using a number of different methods, relying on very heterogeneous data sources. Batty [3] distinguished city delineation methods by three different criteria: (a) population and/or urbanization density, (b) interactions, described by different kinds of networks, either physical or non-physical, and (c) geographical proximity and/or contiguity.

In this work, we applied two specific methods, falling in the categories (a) and (c) above, respectively. The first method makes use of artificial surfaces obtained from satellite data, inferring that sealed (or impervious) surfaces are a proxy for continued human presence, *i.e.* urbanization. The second method [4] uses street nodes to build geographically contiguous areas, which we consider as part of cities based on a head-tail break rule applied to their planimetric size. The first method is intrinsically parametric, while the second is parameter-free.

We investigated the outcome of the two methods within the framework of area-population scaling relations. Scaling relations among a number of different urban indicators exist [5, 6] and many authors used them and critically analyzed them [7, 8]. A scaling relation for planimetric area, A, as a function population, P, of a set of cities has the following form:

$$A = \beta\, e^{\alpha}. \qquad (1)$$

It implies that a city twice as large of another city, in terms of population P, is expected to cover a planimetric area $A_2 = 2\, A_1$, with A_1 and A_2 the area of the smaller and larger city, respectively. Different urban indicators exhibit scaling with respect to city size, taken as the population, with different values of the exponent. If a scaling relations as in Eq. (1) is in effect, the value scaling exponent α being larger, smaller or consistent with unity has different implications. A value $\alpha < 1$ signals a diseconomy of scale, while $\alpha > 1$ signals an economy of scale. A value of α

Massimiliano Alvioli (2020) Comparative study of delineation of urban areas using imperviousness products and open data:

in Massimiliano Alvioli, Ivan Marchesini, Laura Melelli & Peter Guth, eds., Proceedings of the Geomorphometry 2020 Conference, doi:10.30437/GEOMORPHOMETRY2020_1.

consistent with unity would correspond to constant returns to scale.

Figure 1 shows, for illustrative purposes, a log-log plot of area-population (*A*-*P*) relations for world's cities. In the figure, we used data from http://www.demographia.com, which lists a data set of 1,750 cities compiled a few years ago. We used this data source to show *A*-*P* relations with data collected in a homogeneous way. We show data separately for five European countries, along with the whole data set. The straight lines in Fig. 1 are linear regressions of the log A versus the log P. In fact, taking the log of Eq. (1) one obtains a linear relation between the logarithms A and P as follows:

$$\log A = \beta' + \alpha \log P, \qquad (2)$$

with $\beta' = \log \beta$. Figure 1 shows that different countries may have substantially different scaling exponents, as far as *A*-*P* scaling relations are concerned. In this work, we focused on two independent ways of delineating cities and, thus, of obtaining area and population, in the case of Italy.

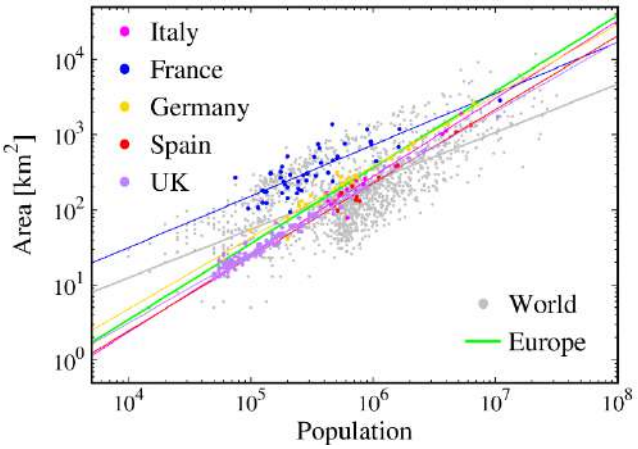

Figure 1. Area-population relations of a few European countries and corresponding linear fits as in Eq. (2); "Europe" refers to the five countries shown in this Figure; "World" refers to the whole set of 1,750 cities. The table below lists the coefficient of the fits, Eq. (2) (*after Ref. [4]*).

Country	α	R^2	**# cities**
Italy	1.03	0.91	14
France	0.68	0.66	47
Germany	0.95	0.95	25
Spain	0.98	0.94	12
United Kingdom	0.94	0.97	138
Europe	1.01	0.78	236
World	0.64	0.50	1,750
World – Ref. [5]	0.56-1.04	-	-

II. METHODS

In the following, we describe in detail the two methods we used in this work to delineate cities in Italy, in two separate paragraphs. The outcome of both methods is a set of polygons, representing urban areas in Italy. We will compare them in the framework of area-population scaling relations, Eqs. (1) and (2).

A. City delineation from imperviouness

Imperviouness is a measure of the degree (percentage) of soil sealing. Impervious surfaces are both built-up and non-built-up, and include a variety of objects that we identify with human locations or activities [9]. Artificial surfaces can be detected using remote sensing [10], and assuming that any impervious (or sealed) surface is part of an urban system [11]. Separate clusters of impervious terrain can be identified with individual cities.

The Copernicus programme makes available imperviousness data as raster layers [9] with a resolution of 20 m. Each grid cell in the raster is a percent value, which introduces the need for a parameter: one can introduce a percent threshold over which one can flag a grid cell as an urban area. In this work, we considered any non-zero value as indicator of an urban area. Next, we need to cluster grid cells, in order to obtain individual cities. This step introduces the additional difficulty of delineating boundaries between areas who might actually have relations, either spatial or regarding human activities, which highlights that cities are difficult to delineate, and also difficult to study in isolation [12]. We overcome the difficulty by introducing an additional parameter. We selected disjoint clusters resulting from generating a buffer with negative radius (GIS raster reduction operation) around the original cells with non-zero imperviousness, and then a positive buffer (GIS grow operation). The radius of the two operations was arbitrarily set to five grid cells, which is the additional parameter.

B. Delineation of "natural cities"

The original algorithm of "natural cities" [14] implements city delineation starting from a collection of point-like populated sites, and performs an iterative clustering of sites within a given radius. The requirement for a radius was dropped by an improvement in Ref. [15], who applied the algorithm selecting streets nodes as starting points and using the head-tail rule to select polygons corresponding to urban areas. The polygons occurring in the generalized algorithm were subsequently singled out by using either city blocks as clustering domains [15], triangulated irregular network (TIN) [16], or Thiessen polygons [17].

In this work, and in Ref. [4], we used street nodes obtained from the OpenStreetMap vector layer as a starting point, and generated a TIN network separately for the peninsular Italy and the major islands, Sicily and Sardinia. Application of the head-tail break rule consisted in considering the planimetric area

distribution of the triangles. A head-tail break rule applies because an unbalanced ratio exists within the three sub regions of Italy for the number of triangles with planimetric area above and below the average value. Numerical figures for the number above/number below average were as follows: 0.11 for peninsular Italy, 0.14 for Sicily, and 0.21 for Sardinia. Jiang and Liu found for comparable

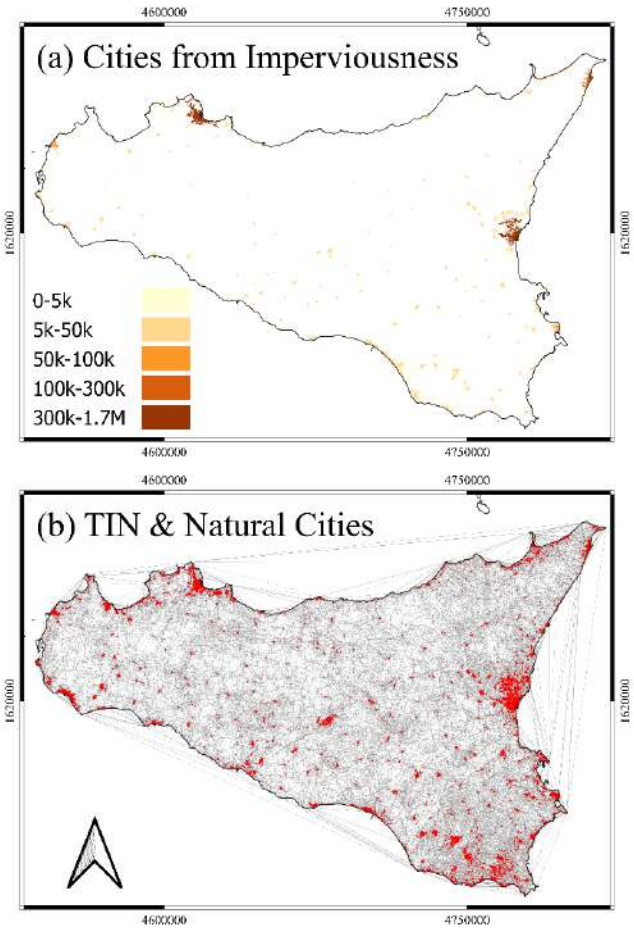

Figure 2. Sample of city delineation in Italy: we show a subset of the results, in Sicily, obtained from the two methods used in this work. (a) Results from the method based on imperviousness; the scale indicates number of citizens. (b) Results from the method of natural cities; grey lines show the TIN network generating natural cities (*after Ref. [4]*). Maps are in LAEA projection, EPSG:3035

quantities in France, Germany and UK the values of 0.05, 0.14 and 0.09 for the ratio, respectively [15].

We discarded all of the TIN polygons with area above average, along with all of the polygons with area below average, which were adjacent to a polygon with large area, as in Ref. [15]. This last step is a replacement for utilizing a clustering radius to single out cities in this work, at variance with Ref. [14].

III. Results and Conclusions

Figure 2 shows results of city delineation, limited to the subset in Sicily (one of the 20 Italian administrative Regions).

Note that Fig. 2 (a) also reports the population of each delineated city. Population data at municipality level is available from the Italian Institute for statistics (ISTAT, http://www.istat.it). We calculated population at city level by distributing the population, known at municipality level, on a grid aligned with the imperviousness layer.

Delineation of cities based on the imperviousness layer and on the natural cities method produces different numbers of agglomerations, listed in the following Table.

Imperviousness	**Number of cities**	**Max. area [km^2]**	**Mean area [km^2]**
Peninsular	54,379	443,602	0.232
Sicily	9,808	53,002	0.080
Sardinia	2,467	45,023	0.204
Italy	66,654	443,602	0.201
Natural cities (*after Ref. [4]*)	**Number of cities**	**Max. area [km^2]**	**Mean area [km^2]**
Peninsular	77,103	1,311,601	0.244
Sicily	6,190	112,829	0.189
Sardinia	5,979	86,762	0.182
Italy	89,272	1,311,601	0.224

Figure 3 shows *A*-*P* relations calculated from the two methods, in a log-log scale as in Fig. 1. In both Fig. 3 (a), corresponding to the imperviousness method, and Fig. 3 (b), for natural cities, we show separately the (*P*, *A*) data points for peninsular Italy, Sicily and Sardinia. The straight lines, instead, are linear fit of the merged data sets. Both boxes also contain the linear fit for European cities (green curve), also shown in Fig. 1.

One can immediately appreciate that the two methods provide substantially different results, as far as the distribution of data points is concerned. In the case of Fig. 3 (a), corresponding to cities in Fig. 2 (a), data not only have a lower limit for the area, 400 m^2, dictated by the resolution of the imperviousness layer, they also show peculiar patterns, which are specific of the three distinct sub sets and can hardly be explained with simple arguments. On the other hand, in the case of Fig. 3 (b), corresponding to cities in Fig. 2 (b), data nicely distribute on the (P, A) plane, hinting to a linear correlation [4]. In this case, some patterns seem to emerge as well; however, they mostly emerge as collinear structures to the overall linear fit. Moreover, they seem

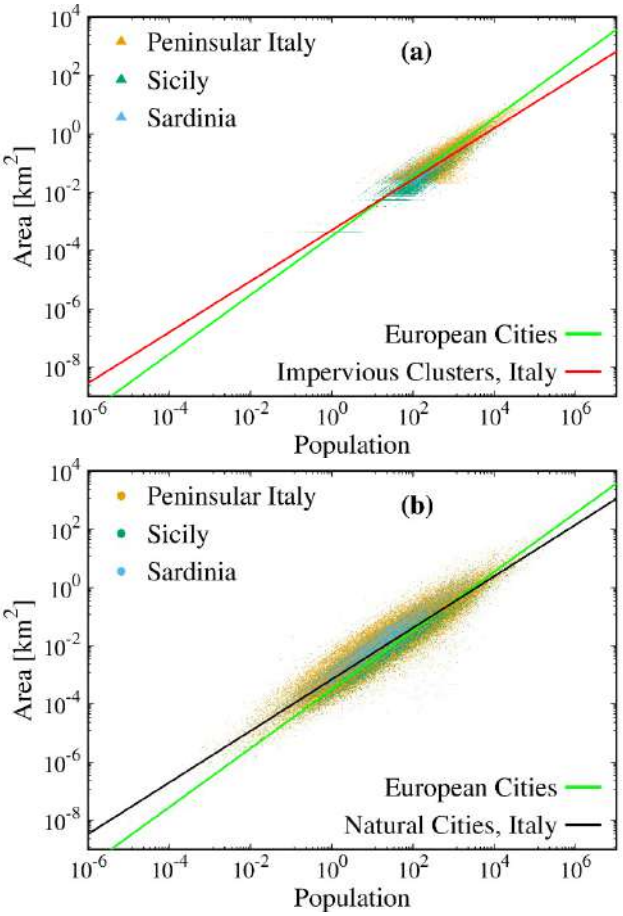

Figure 3. *A-P* relations from the two different approximations to delineate cities considered in this work, compared to results for municipalities (black and red curves). (a): cities delineated as disjoint clusters in the imperviousness layer; (b) natural cities (*after Ref. [4]*). A comparison of the geographical distributions of the two results, for Sicily, is in Fig. 2. Data points consist of three subsets, but the linear fits correspond to the aggregate data set. Green curve: fit to (P, A) data of European cities, from an independent data source, as in Fig. 1.

to exist only in the Sicily and Sardinia sub sets, suggesting some bias might occur for delineation of natural cities in smaller areas.

In conclusion, we gave proof that a data-driven method for delineating cities such as natural cities, adopted in this work and in Ref. [4], represents an objective method for city delineation. The method provides advantages with respect to the delineation of cities by means of imperviousness products, as far as area-population scaling relations are concerned.

REFERENCES

[1] Fang, C., D. Yu, 2017. "Urban agglomeration: An evolving concept of an emerging phenomenon". Landscape and Urban Planning 162, 126–136. DOI: 10.1016/j.landurbplan.2017.02.014

[2] United Nations, 2018. "The world's cities in 2018". Department of Economic and Social Affairs, Population Division. Data booklet, ST/ESA/ SER.A/417

[3] Batty, M., 2018. "Inventing future cities". The MIT Press, Cambridge, MA, USA. 304 pp. ISBN: 9780262038959

[4] Alvioli, M., 2020. "Administrative boundaries and urban areas in Italy: a perspective from scaling laws". Landscape and Urban Planning (*in press*)

[5] Bettencourt, L., 2013. "The origins of scaling in cities". Science 340, 1438-1441. DOI: 10.1126/science.1235823

[6] Barthelemy, M. et al., 2013. "Self-organization versus top-down planning in the evolution of a city". Scientific Reports 3, 2153. DOI:10.1038/srep02153

[7] Arcaute, E. et al., 2015. "Constructing cities, deconstructing scaling laws". Journal of the Royal Society Interface. DOI: 10.1098/rsif.2014.0745

[8] Cottineau, C. et al., 2017. "Diverse cities or the systematic paradox of urban scaling laws". Computers, Environment and Urban Systems 63, 80-94. DOI:10.1016/j.compenvurbsys.2016.04.006

[9] Steidl, M. et al., 2016. "Copernicus Land Monitoring Service - High Resolution Layer Imperviousness". Technical Report version 1 of 985 2018-12-21. European Environment Agency. https://land.copernicus.eu

[10] Lu, D. et al., 2014. "Methods to extract impervious surface areas from satellite images". International Journal of Digital Earth 7, 93-112. DOI: 10.1080/17538947.2013.866173

[11] Ma, D.et al., 2018. "Why topology matters in predicting human activities". Environment and Planning B: Urban Analytics and City Science 0, 1-17. DOI: 10.1177/2399808318792268

[12] Thomas, I. et al., 2018. City delineation in European applications of LUTI models: review and tests. Transport Reviews 38, 6-32. DOI: 10.1080/01441647.2017.1295112

[13] Bettencourt, L., G. West, 2010. "A unified theory of urban living". Nature 467, 897 912-913. DOI: 10.1038/467912a

[14] Rozenfeld, H.D. et al., 2009. "The Area and Population of Cities: New Insights from a Different Perspective on Cities". Working Paper 15409. National Bureau of Economic Research. DOI: 10.3386/w15409

[15] Jiang, B., X. Liu, 2012. "Scaling of geographic space from the perspective of city and field blocks and using volunteered geographic information". International Journal of Geographical Information Science 26, 215-229. DOI: 10.1080/13658816.2011.575074

[16] Jiang, B., Y. Miao, 2015. "The evolution of natural cities from the perspective of location-based social media". The Professional Geographer 67, 295-306. DOI: 10.1080/00330124.2014.968886

[17] Jiang, B., 2018. "A topological representation for taking cities as a coherent whole". Geographical Analysis 50, 298-313. DOI: 10.1111/gean.12145

GEOMORPHOMETRY 2020 PERUGIA, ITALY JUNE 22 - 26 2020

An optimization of triangular network and its use in DEM generalization for the land surface segmentation

Richard Feciskanin[§], Jozef Minár
Faculty of Natural Sciences
Comenius University in Bratislava
Ilkovičova 6, 842 15 Bratislava, Slovakia
[§] richard.feciskanin@uniba.sk

Abstract—**Appropriate generalization of digital elevation model (DEM) is important for the land surface segmentation. We tested some methods of generalization based on irregular triangular networks. Based on the theory of an optimal triangle for (land) surface representation, suitable methods simplifying triangle networks have been identified. The *quadric error metrics simplification* algorithm was used to generalize surface models. It belongs to the decimation algorithms developed in computer graphics, however the use of it for land surface modeling is rare. Suitability of the method for the land surface segmentation was evaluated for a variety of models created at different generalization levels. Numerical expression of the concentration of the third-order parameter values (curvature changes) around zero (K_0) was used as an indicator of the suitability. The hypothesis that the affinity of higher-order variables to a constant value should be significantly higher for real land surfaces with elementary forms than for mathematical surfaces was confirmed. The resulting K_0 values are significantly lower in the artificial surface than in the real surface model, however only to a threshold limit of generalization.**

I. Introduction

The question of scale and resolution is very important in geomorphological mapping. One of the major issues of quantitative modeling and analysis of the land surface is filtering to denoise, generalize, and decompose DEMs into components of different spatial scales [1]. When a coarser analytical scale is required, the original finer-resolution DEM needs to be generalized or simplified to reduce data redundancy [2].

A resampling method is one of the most widely used methods for DEM generalization, which requires averaging the neighboring cells of a high-resolution, square-grid DEM into a series of lower-resolution data sets. This method will inevitably have a peak-clipping and valley-filling smoothing effect [3]. Other groups of grid-based DEM generalization methods include wavelet transform, morphology-based, and drainage-constrained methods, each of them with its own difficulties [4].

The polynomial least squares fitting method with a changing calculation window size was used to generalize gridded data for hierarchical land surface segmentation in [5]. In this paper, we present the use of generalized triangular irregular networks (TIN) with different level of details for the same purpose. TIN allows to simplify the detailed model so that the resulting model retains as much information about the shape of the modeled surface as possible. The spatial structure of the TIN can represents the modeled surface very efficiently and yet accurately when designed with respect to the shape of the modeled surface.

Generalization algorithms developed for land surface modeling are mostly used to create a TIN model from a regular grid. These include traditional, still popular: The Fowler and Little algorithm [6], the Very important points algorithm [7], the Drop heuristic method [8]. Similarly, other algorithms presented in [9-12, 4] use various techniques to find the most appropriate (important) points for describing the land surface.

Generalization algorithms based on TIN are more widespread outside the land surface modeling domain. They are especially widespread in the computer graphics. In contrast to the algorithms mentioned above, they primarily focus on the overall shape fidelity of the simplified model. [13] evaluated simplification methods in computer graphics as mature almost two decades ago. Unlike grid-based method, TIN-based methods from computer graphics are exceptionally used in the land surface modeling.

II. Methods

A. Optimal triangle

When optimizing the triangle network, we start from the theoretical assumption of an optimal triangle. [14] defines an optimal triangle whose plane has the same normal as the land surface at its centroid. A simpler but sufficiently precise description of this relationship will allow the replacement of part of the land surface with an osculating paraboloid with a vertex on land surface at the triangle centroid: Then it follows from the

Richard Feciskanin and Jozef Minar (2020) An optimization of triangular network and its use in DEM generalization for the land surface segmentation: in Massimiliano Alvioli, Ivan Marchesini, Laura Melelli & Peter Guth, eds., Proceedings of the Geomorphometry 2020 Conference, doi:10.30437/GEOMORPHOMETRY2020_2.

above condition that the plane of the optimal triangle is parallel to the tangent plane of the surface (osculating paraboloid) at the triangle centroid (Fig. 1). The intersection of the triangle plane and the paraboloid is the same as Dupin indicatrix [15]. Consequently, the optimal triangle is one whose centroid lies in the center of the intersection conic. This can only be achieved in the case of an ellipse. The intersection is a circumscribed ellipse of a triangle centered in its centroid, known as the circumscribed Steiner ellipse. From the all circumscribed ellipses of the triangle, Steiner ellipse has the smallest area. It confirms the desirability of the approach. In places where Dupin indicatrix is not an ellipse, the condition cannot be fulfilled without deviation.

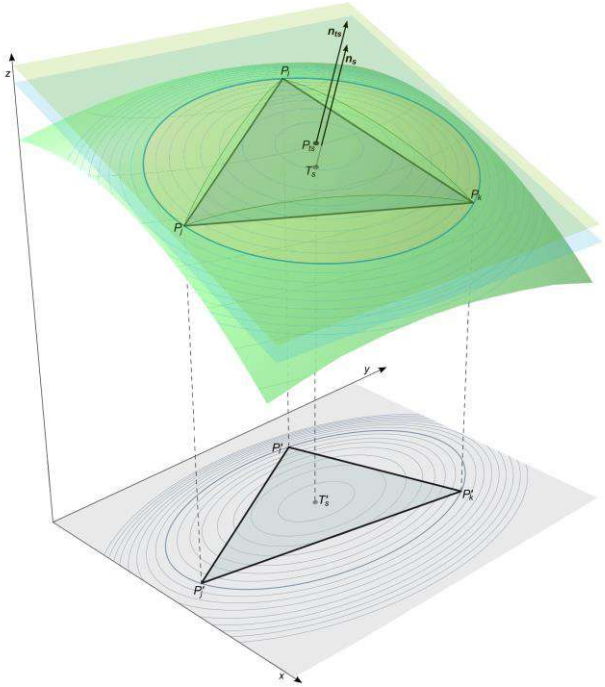

Figure 1. Optimal triangle representing land surface. The plane of the triangle $P_iP_jP_k$ is parallel to tangential plane of the land surface in the point P_{ts} at the triangle centroid T_s. n_s, n_{ts} – triangle normal and normal to surface at P_{ts} are identical. Isolines of height difference between the plane of the triangle and the land surface are shown.

[16] came to the same relationship, he defined the optimum ratio of triangle (ρ) replacing the quadratic surface as:

$$\rho = \sqrt{\frac{\lambda_2}{\lambda_1}} \qquad (1)$$

where λ_1 and λ_2 are eigenvalues of Hessian of elevation function $z = f(x, y)$. [17] defines a triangle aspect ratio as the ratio of the principal axes of the ellipse with the smallest area that passes through the triangle vertices. Although not explicitly stated, the authors deal with the circumscribed Steiner ellipse.

B. Simplification algorithms

We have identified simplification methods whose optimization conditions are in accordance with the above characteristics. These are the *quadric error metrics simplification* (*QEMS*) method presented in [18] and the *memoryless simplification* (*MS*) method introduced in [19]. Both methods were developed primarily for computer graphics, however they are also suitable for use in terrain modeling. [4] directly mention the *QEMS* method as a method for terrain simplifying, although they do not use it.

Both methods belong to the category of decimation methods. They use edge contraction to simplify the model's geometry. When contracting an edge, its two end points V_0 and V_1 are merged into a new vertex V. Condition for placing a new vertex is crucial. The final model consists of vertices that are not in the original data set. It allows to better maintain the local shape and has the ability to minimize the impact of random errors in the input data. The order of edges in edge list for contracting is determined by weighting of edge contraction. The contraction is repeated until the target condition is reached – most often the number of elements in the model.

The *QEMS* algorithm determines the edge contraction weight based on the value of the sum of the quadratic distance of the new vertex V from the individual planes of the triangles with the original merged vertices V_0 and V_1. New vertex location is in the smallest quadratic distance from the planes of triangles with the vertices V_0 and V_1. An example of one contraction step is shown in Fig. 2. In the *MS* method, the algorithm uses the sum of tetrahedron volumes that arise from the surrounding triangles by shifting the original vertices V_0 and V_1 to a new vertex V and an additional condition of preserving the volume.

Figure 2. Edge contraction and new vertex localization in *quadric error metrics simplification* in 2D.

[17] showed that the aspect ratio, which is based on minimizing the quadric error, corresponds to the optimum ratio (1). Eigenvalues λ_1 and λ_2 are the extremes of principal normal curvature κ_1 and κ_2 and thus $\lambda_1 = \kappa_1$, $\lambda_2 = \kappa_2$. Extremal curvatures κ_1 and κ_2 correspond to the principal axes of Dupin indicatrix [17]. [20] presents that objective function for a new vertex localization

in *MS* bears a great deal of similarity to the quadratic form in the *QEMS* algorithm. The difference is only the weight of the triangle, they use squared value and absolute value of triangle area, respectively. This confirms that the above approach and so these methods use the same characteristics of the optimal triangle. The *QEMS* method we used to generalize the surface models.

C. Testing triangle networks

Third-order morphometric variables were used to describe the suitability of a triangular network for land surface segmentation. Third-order variables may be used for confirmation of land surface affinity to constant values of second-order variables, that is a precondition of existence elementary forms suitable for geomorphological mapping [21]. A quantile-based measure of kurtosis (K_0) presented in [21] was used as a numerical expression of concentration of data around zero

$$K_0 = \frac{\tilde{x}_{95} - \tilde{x}_5}{\tilde{x}_{0+5} - \tilde{x}_{0-5}} \qquad (2)$$

where $\tilde{x}_{95}$ and $\tilde{x}_5$ are percentiles representing the spread of the set disregarding extreme values and $\tilde{x}_{0+5}$ and $\tilde{x}_{0-5}$ represent the fifth percentiles on the right and on the left from the zero value. The values of slope line (s) and contour line (c) changes of profile curvature $(k_n)_s$ and tangential curvature $(k_n)_c$ denoted $(k_n)_{ss}$, $(k_n)_{sc}$, $(k_n)_{cc}$, $(k_n)_{cs}$ were used.

We have determined the partial derivatives up to the third order for each vertex (except borders) and triangle centroids of the optimized triangular network based on the fourth order polynomial least square fitting. The input to the least square fitting were 3-ring neighborhood vertices. We calculated the summary characteristic K_0 from the determined $(k_n)_{ss}$, $(k_n)_{sc}$, $(k_n)_{cc}$, $(k_n)_{cs}$ values. This calculation was performed repeatedly for generalized models at different degrees of generalization.

[21] presents the hypothesis: The affinity of higher-order variables to a constant value should be significantly higher for real land surfaces with elementary forms or other structures than for mathematical surfaces. To confirm this, the same calculation of K_0 was made on generalized models of the artificial surface.

III. RESULTS AND DISCUSSION

The basic DEM of the surveyed area was created from a photogrammetric mapping in the form of a grid of 166×163 (27058) cells with a resolution of 2 meters. It represents an area located on the west of Bratislava, Slovakia, around the hill of Slovinec. The artificial surface model was calculated for 241×241 (58081) points based on a mathematical formula (trigonometric polynomial) with a fictitious 5 meters resolution.

The nodes of the regular grids form the vertices of the initial triangular networks. Initial TIN was generalized to more than 100 levels up to last 30 (40 in artificial surface) triangular faces. The selected generalization levels of the models are shown in fig. 3 and 4. The ability of the algorithm to capture the most important surface shapes with a very small number of elements is evident.

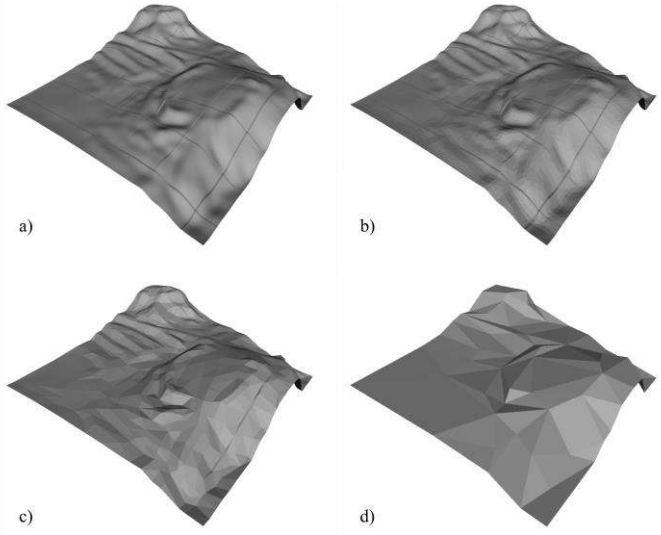

Figure 3. Examples of generalized models of Slovinec: a) initial model (53460 triangles), b) 5000 triangles, c) 1000 triangles d) 100 triangles.

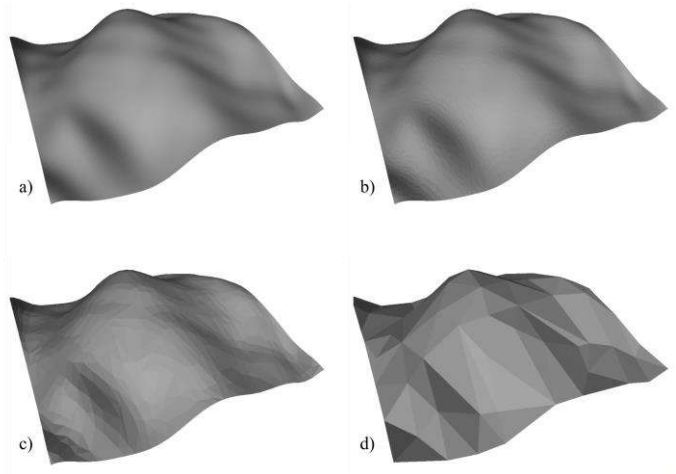

Figure 4. Examples of generalized artificial surface models: a) initial model (115200 triangles), b) 5000 triangles, c) 1000 triangles d) 100 triangles.

The calculated values of K_0 from the set of changes of curvature $(k_n)_{ss}$, $(k_n)_{sc}$, $(k_n)_{cc}$, $(k_n)_{cs}$ in each model are shown in fig. 5.

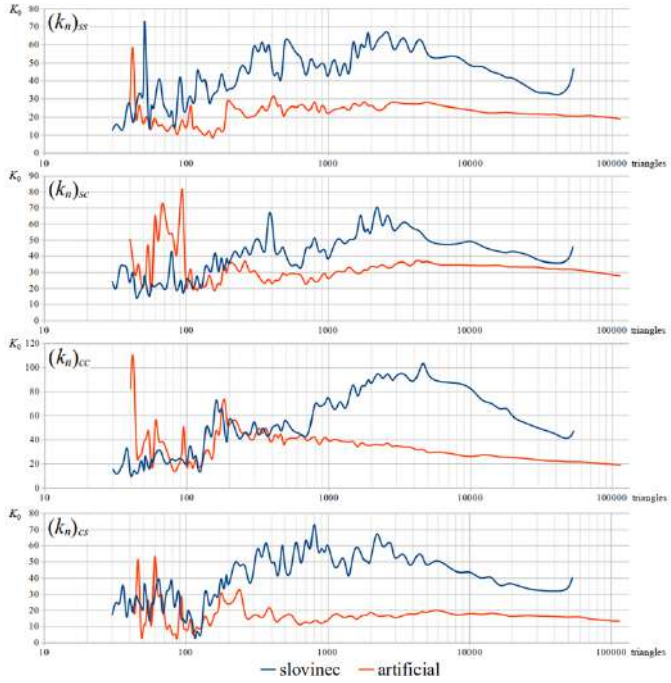

Figure 5. Values of K_0 for each types of curvature changes in the whole range of generalization.

The artificial surface has much lower values of K_0 up to generalization 100 – 200 triangles excluding $(k_n)_{cc}$ (~700 triangles). It points to existence of elementary forms with affinity to constant value of $(k_n)_s$ and $(k_n)_c$ and/or their parent variables – slope, aspect and altitude. Generalizations with < 200 triangles make artificial and natural surface equal in light of K_0. Instability of moment based K_0 (strong dependence on random values) for small datasets can be one reason. An artificial facets (surface of particular big triangles) is another possible reason of convergence and extremums of both (artificial and natural) K_0 curves.

IV. Conclusions

The optimization of triangular network by *QEMS* method (used nearly exclusively in computer graphics till now) can be effectively used for generalization of DEM. K_0 index can be suitable for determination of generalization levels optimal for land surface segmentation only to a certain level of generalization, given by approach of K_0 curves of artificial and natural surface.

Acknowledgment

This work was supported by the Slovak Research and Development Agency under contract APVV-15-0054.

References

[1] Florinsky, I. V. & Pankratov, A. N., 2016. "A universal spectral analytical method for digital terrain modeling". Int. J. Geogr. Inf. Sci. 30, pp. 2506–2528.

[2] Zhou, Q. & Chen, Y., 2011. "Generalization of DEM for terrain analysis using a compound method". ISPRS J. Photogramm. Remote Sens. 66, pp. 38–45.

[3] Chen, Y., Wilson, J. P., Zhu, Q. & Zhou, Q., 2012. "Comparison of drainage-constrained methods for DEM generalization". Comput. Geosci. 48, pp. 41–49.

[4] Wu, Q., Chen, Y., Wilson, J. P., Liu, X. & Li, H., 2019. "An effective parallelization algorithm for DEM generalization based on CUDA". Environ. Model. Softw. 114, 64–74.

[5] Minár, J., Minár, J. Jr. & Evans, I.S., 2015. "Towards exactness in geomorphometry". In Geomorphometry 2015 Conference Proceedings, Edited by: Jasiewicz, J., Zwoliński, Z., Mitasova, H. and T. Hengl, Adam Mickiewicz University in Poznań, Poland.

[6] Fowler, R. J. & Little, J. J., 1979. "Automatic extraction of Irregular Network digital terrain models". ACM Comput Graphics 13, pp. 199–207.

[7] Chen, Z.-T. & Guevara, J. A., 1987. "Systematic selection of very important points (VIP) from digital terrain model for constructing triangular irregular network". Auto Carto 8. pp. 50–56.

[8] Lee, J., 1989. "A drop heuristic conversion method for extracting irregular networks for digital elevation models". Proceedings of GIS & LIS'89. pp. 30–39.

[9] Fei, L. & He, J., 2009. "A three-dimensional Douglas-Peucker algorithm and its application to automated generalization of DEMs". Int. J. Geogr. Inf. Sci. 23, pp. 703–718.

[10] Chen, Y. & Zhou, Q., 2013. "A scale-adaptive DEM for multi-scale terrain analysis". Int. J. Geogr. Inf. Sci. 27, pp. 1329–1348.

[11] Chen, Y. et al., 2016. "A new DEM generalization method based on watershed and tree structure". PLoS One 11, p. 23.

[12] Sun, W., Wang, H. & Zhao, X., 2018. "A simplification method for grid-based DEM using topological hierarchies". Surv. Rev. 50, pp. 454–467.

[13] Luebke, D. P., 2001. "A developer's survey of polygonal simplification algorithms". IEEE Comput. Graph. Appl. 21, pp. 24–35.

[14] Krcho J., 1999. "Modelling of georelief using DTM - the influence of point configuration of input points field on positional and numeric accuracy". Geogr. časopis. 1999;51(3). pp. 225-260.

[15] Günther, F., Jiang, C. & Pottmann, H., 2020. "Smooth polyhedral surfaces". Adv. Math. 363, p. 31.

[16] Nadler, E., 1986. "Piecewise linear best l_2 approximation on triangles". In: Chui, C.K., Schumaker, L.L. and Ward, J.D. (Eds.), Approximation Theory V, Academic Press, 499–502.

[17] Heckbert, P. S. & Garland, M., 1999. "Optimal triangulation and quadric-based surface simplification". Comput. Geom. Theory Appl. 14, pp. 49–65.

[18] Garland, M. & Heckbert, P. S., 1997. "Surface simplification using quadric error metrics". Proceedings of the 24th Annual Conference on Computer Graphics and Interactive Techniques, SIGGRAPH 1997. pp. 209–216.

[19] Lindstrom, P. & Turk, G., 1998. "Fast and memory efficient polygonal simplification". Proceedings Visualization'98.

[20] Lindstrom, P. & Turk, G., 1999. "Evaluation of memoryless simplification". IEEE Trans. Vis. Comput. Graph. 5 (2), pp. 98–155.

[21] Minár, J. et al. "Third-order geomorphometric variables (derivatives): Definition, computation and utilization of changes of curvatures". Int. J. Geogr. Inf. Sci. 27, pp. 1381–1402.

GEOMORPHOMETRY 2020 PERUGIA, ITALY JUNE 22 - 26 2020

Detection of crevasses using high-resolution digital elevation models: Comparison of geomorphometric modeling and texture analysis

Olga T. Ishalina [a], Dmitrii P. Bliakharskii [a], Igor V. Florinsky [b, §]

[a] Department of Cartography and Geoinformatics
Institute of Earth Sciences, St. Petersburg University
St. Petersburg, 199034, Russia

[b] Institute of Mathematical Problems of Biology
Keldysh Institute of Applied Mathematics, Russian Academy of Sciences
Pushchino, Moscow Region, 142290, Russia

[§] iflor@mail.ru

Abstract—**The Vostok Station is the only Russian inland polar station in Antarctica. It is supplied by sledge and caterpillar-track caravans via a long sledge route. There are a lot of crevasses on the way. In this article, we compare capabilities of two techniques – geomorphometric modeling and texture analysis – to detect open and hidden crevasses using high-resolution digital elevation models (DEMs) derived from images collected by unmanned aerial survey. The first technique is based on the derivation of local morphometric variables. The second one includes estimation of Haralick texture features. The study area was the first 30 km of the sledge route between the Progress and Vostok Stations, East Antarctica. We found that, in terms of crevasse detection, the most informative morphometric variables and texture features are horizontal and minimal curvatures as well as homogeneity and contrast, correspondingly. In most cases, derivation and mapping of morphometric variables allow one to detect crevasses wider than 3 m; narrower crevasses can be detected for lengths from 500 m. Derivation and mapping of Haralick texture features allow one to detect a crevasse regardless of its length if its width is 2-3 pixels. Geomorphometric modeling and Haralick texture analysis can complement each other.**

I. INTRODUCTION

There are five year-round operating Russian polar stations in Antarctica. Four of them – Bellingshausen, Novolazerevskaya, Progress, and Mirny Stations – are located on the coast of the Southern Ocean. The inland Vostok Station is situated at 3,488 m above sea level, at the southern Pole of Cold, near the Southern Pole of Inaccessibility and the South Geomagnetic Pole. Since 2007, the Vostok Station is supplied by sledge and caterpillar-track caravans via a 1430-km sledge route from the Progress Station.

The sledge route is intersected by a large number of crevasses formed due to glacier movements. The width of crevasses can vary from a few millimeters to tens of meters [1]. Crevasses hidden by snow bridges are extremely dangerous for researchers. Monitoring and timely detection of crevasses is important for the safety of participants of sledge and caterpillar-track caravans.

There are two main approaches for rapid detection of hidden crevasses: ground-based and remote sensing ones. The ground-based approach involves studying a glacier with geophysical methods. Ground penetration radars are particularly applied, with antennas usually mounted in front of a vehicle. However, the safety and effectiveness of this approach is questionable [2]. The use of aerial and satellite imagery to detect open crevasses has high potential [1, 3, 4]. In this context, texture analysis of satellite data showed great efficiency. Low resolution of data is the main disadvantage of this approach [5].

In recent years, unmanned aerial systems (UASs) and UAS-derived products – orthomosaics and digital elevation models (DEMs) – have been increasingly used in glaciology [6]. In this article, we compare capabilities of two techniques – geomorphometric modeling and texture analysis – to detect open and hidden crevasses using UAS-derived high-resolution DEMs.

II. STUDY AREA

The study area is located south of the Progress Station, Princess Elizabeth Land, East Antarctica. We consider the first 30 km of the sledge route between the Progress and Vostok Stations (Fig. 1). From north to south, ice sheet elevations increase uniformly from 230 m to 850 m above sea level.

Olga Ishalina, Dmitrii Bliakharskii and Igor Florinsky (2020) Detection of crevasses using high-resolution digital elevation models: Comparison of geomorphometric modeling and texture analysis: in Massimiliano Alvioli, Ivan Marchesini, Laura Melelli & Peter Guth, eds., Proceedings of the Geomorphometry 2020 Conference, doi:10.30437/GEOMORPHOMETRY2020_3.

This area is characterized by a particularly large number of open and hidden crevasses, which makes the sledge route very dangerous. The width of crevasses varies from 0.5 m to 23 m. It was decided to detect crevasses in a buffer zone 1.5 km wide relative to the axis of the sledge route.

III. MATERIALS AND METHODS

An unmanned aerial survey (Fig. 1) was performed within the frameworks of the 62nd Russian Antarctic Expedition (austral summer 2016–2017); for details see [7]. For the study area, we obtained orthomosaics with a resolution of 0.08 m and DEMs with resolutions of 0.25 m, 0.5 m, and 1 m.

A hidden crevasse has a snow bridge, which makes it difficult to detect. However, a snow bridge can sink under gravity and, so, forms some sort of ditch. In fact, hidden crevasses are micro-landforms of the ice sheet topography. They should be manifested in a high-resolution DEM. Thus, to detect hidden crevasses, we previously used local and nonlocal morphometric variables derived from UAS-based DEMs [8].

On the other hand, crevasses can be reflected by changes in surface texture characteristics. Thus, to detect hidden crevasses, DEMs can also be processed by texture analysis techniques, in particular, using Haralick texture features [9]. Such approach was earlier utilized to reveal crevasses from satellite imagery [5].

To compare and validate these two approaches, we decided, first, to detect crevasses in areas where they can be visually recognized on orthomosaics or single images. For this purpose, 15 test crevasses were visually detected (Fig. 1). Length and approximate width of each crevasse were measured (Table 1).

It is not known *a priori* which particular morphometric variable will allow detecting crevasses. Therefore, for a site with two neighboring test crevasses (## 6 and 7), digital models for a set of fourteen local morphometric variables were derived from the DEMs, namely: slope, aspect, horizontal curvature, vertical curvature, mean curvature, Gaussian curvature, minimal curvature, maximal curvature, unsphericity curvature, difference curvature, vertical excess curvature, horizontal excess curvature, ring curvature, and accumulation curvature. For their definitions, formulas, and interpretations, see [10]. Both test crevasses were detected by only two morphometric variables, namely, horizontal and minimal curvatures. These two variables were used to reveal other crevasses at the further stages of the study.

These calculations were initially performed using the 1-m gridded DEM. Then, the DEMs with a resolution of 0.25 m and 0.5 m were tested. However, the experiment showed that these DEMs are marked by a high level of high-frequency noise resulted from photogrammetric processing of aerial images. These DEMs are not suitable for geomorphometric modeling [8].

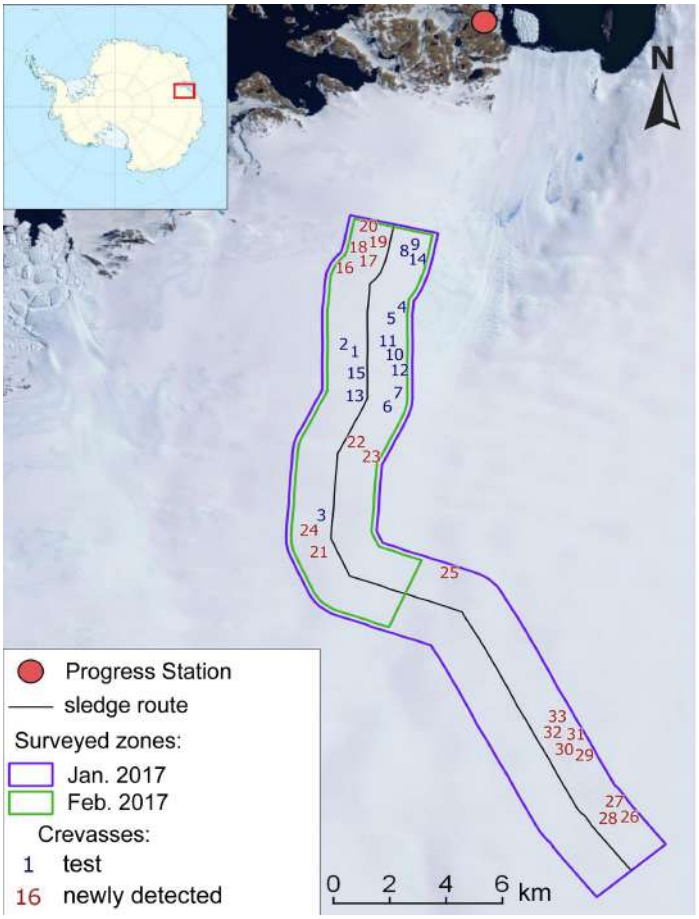

Figure 1. Study area, zones of the UAS surveys, and location of crevasses.

Table 1. Characteristics of test crevasses (Fig. 1)

Crevasse, #	Length, m	Width, m
1	123	1.5
2	77	1.5
3	883	2.0
4	191	3.0
5	170	5.0
6	913	7.0
7	476	8.0
8	117	0.5
9	99	0.6
10	644	5.0
11	247	7.0
12	501	2.0
13	300	3.0
14	155	0.6
15	139	2.0

Next, for the site with test crevasses ## 6 and 7, we derived a set of eleven Haralick texture features from the DEMs, namely: angular second moment (homogeneity), contrast, correlation, variance, inverse difference moment, sum average, sum variance, sum entropy, entropy, difference variance, and difference entropy. For their definitions, formulas, and interpretations, see [9]. In terms of crevasse detection, two Haralick texture features were the most informative, such as, homogeneity and contrast. These features are reciprocal, so only homogeneity was used in the next stages of the study.

To calculate the Haralick texture features, a gray level coincidence matrix (GLCM) is used [9]. GLCM is a table describing how often different combinations of brightness values or gray levels between adjacent pixels occur in an image in a certain direction.

To calculate the Haralick texture features, one should choose the following parameters:

- Size of a moving window.
- Number of gray levels.
- Distance between compared pixels.
- Direction.

The smaller is the size of features under study, the smaller should be a moving window. Elevation is a continuous variable, so elevation values should be re-coded into integer 'gray levels' before calculating the Haralick texture features from DEMs. If the number of gray levels is too small, the elevation range for each level will be too large. As a result, some topographic features will not be described because the corresponding pixels will have the same gray value. So, the number of gray levels should be as large as possible. A DEM has to be splitted into blocks, within which an elevation range does not exceed a certain value. In the calculation, each direction emphasizes topographic features of a certain orientation.

In this study, the size of a moving window was 3×3 pixels because crevasses are described by a small number of pixels. The distance between compared pixels was 1 pixel, that is, the values of neighboring pixels were compared. The number of gray levels was 256. We assumed that there could be different crevasse orientations, so all possible directions were considered. The 1-m gridded DEM was split into blocks so that an elevation range did not exceed 30 m.

Calculation and visualization of both local morphometric variables and Haralick texture features was carried out using QGIS software.

Table 2. Test crevasses detected (+) by different techniques

Crevasse, #	Horizontal curvature	Minimal curvature	Homogeneity
1	+		
2	+	+	+
3	+	+	+
4	+	+	+
5	+	+	+
6			+
7	+	+	+
8			
9			
10	+	+	+
11	+	+	+
12		+	+
13			
14			
15			+

IV. RESULTS AND DISCUSSION

In contrast to local morphometric variables, Haralick texture features are not so sensitive to the high-frequency noise and can be applied to DEMs with resolutions of 0.5 m and 0.25 m. As a result, the homogeneity map derived from the 0.25-m gridded DEM allowed us to reveal crevasses less than 1 m wide.

Figure 2 shows examples of crevasse manifestation on the orthomosaic and maps of elevation, horizontal curvature, and homogeneity. One can see no sign of two crevasses on the orthomosaic and elevation map, some traces of two crevasses on the horizontal curvature map, as well as clear image of two crevasses on the homogeneity map.

To compare capabilities of two techniques, we used the 1-m gridded DEM only. As a measure of technique effectiveness, we estimated the probability of test crevasse detection, that is, the probability is 1 if all 15 test crevasses are recognized by a technique.

Using the geomorphometric modeling, 9 of 15 crevasses were detected. The Haralick texture analysis allowed us to find 10 of 15 crevasses. As expected, all crevasses cannot be revealed by either technique (Table 2).

The probability of crevasse detection by the geomorphometric modeling and the Haralick texture analysis is 0.60 and 0.66, correspondingly. Combination of two techniques leads to the probability of 0.73. Notice that among 15 test crevasses, 3 ones were less than 1 m wide (c.f. Tables 2 and 1). According to the first consequence of the sampling theorem [10], these crevasses cannot be detected using the 1-m gridded DEM: to keep the information on topographic features with typical planar sizes λ in a DEM, one should use the DEM grid size $w \le \lambda/(2n)$, where $n \ge 2$. Excluding these 3 test crevasses, the probability of the geomorphometric and Haralick detection

increases up to 0.75 and 0.83, correspondingly. Combination of both techniques leads to the probability of 0.91. Thus, the two techniques complement each other.

There is a relationship between the possibility of detecting a hidden crevasse and its geometrical characteristics. No crevasses with a width of less than 1 m were detected by both approaches, even if they are clearly visible on the orthomosaic due to the lack of clear subsidence of a snow bridge.

In most cases, mapping of morphometric variables allow one to detect crevasses wider than 3 m; narrower crevasses can be detected only for lengths from 500 m. Derivation and mapping of Haralick texture features allow one to detect a crevasse regardless of its length if its width is 2–3 pixels.

Notice that new hidden crevasses were detected within the study area by the described analysis (Fig. 1; Table 3). Totally, 18 new crevasses with lengths ranging from 80 m to 1 km were found; the average width of crevasses was 10 m.

V. CONCLUSIONS

The results show that the processing of UAS-derived high-resolution DEMs is an effective way to detect open and hidden crevasses. Geomorphometric modeling and Haralick texture analysis can complement each other.

VI. ACKNOWLEDGMENTS

The work is supported by the Russian Foundation for Basic Research and the National Natural Science Foundation of China, grant # 20-51-53016.

REFERENCES

[1] Colgan, W., H. Rajaram, W. Abdalati, C. McCutchan, R. Mottram, M.S. Moussavi, S. Grigsby, 2016. “Glacier crevasses: observations. models and mass balance implications”. Rev. Geophys., 54(1), 119–161.

[2] Popov, S.V. and S.P. Polyakov, 2016. “Georadar location of cracks in the region of the Russian Antarctic stations Progress and Mirny (East Antarctica) in the 2014/15 season”. Earth’s Cryosphere, 20(1), 90–98 [in Russian].

[3] Glasser, N. and T. Scambos, 2008. “A structural glaciological analysis of the 2002 Larsen B ice-shelf collapse”. J. Glaciol., 54(184), 3–16.

[4] Holt, T., N. Glasser, D. Quincey, 2013. “The structural glaciology of southwest Antarctic Peninsula ice shelves (ca. 2010)”. J. Maps, 9(4), 37–41.

[5] Xu, T., W. Yang, Y. Liu, C. Zhou, Z. Wang, 2011. “Crevasse detection in Antarctica using ASTER images”. Lec. Notes Comp. Sci., 6754, 370–379.

[6] Bhardwaj, A., L. Sam, Akanksha, F.J. Martín-Torres, R. Kumar, 2016. “UAVs as remote sensing platform in glaciology: present applications and future prospects”. Remote Sens. Envir., 175, 196–204.

[7] Bliakharskii, D.P., I.V. Florinsky, T.N. Skrypitsyna, 2019. “Modelling glacier topography in Antarctica using unmanned aerial survey: assessment of opportunities”. Int. J. Remote Sens., 40(7), 2517–2541.

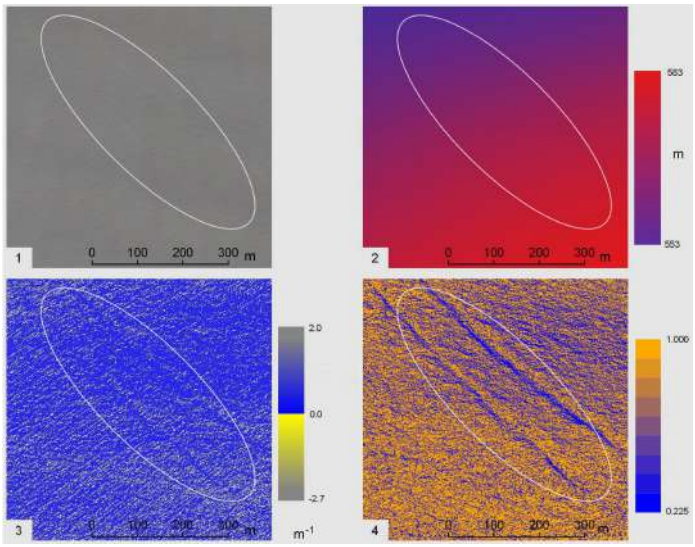

Figure 2. Examples of the crevasse manifestation: 1 – orthomosaic, 2 – elevation, 3 – horizontal curvature, 4 – homogeneity. The white oval shows location of two test crevasses, ## 6 and 7.

Table 3. Characteristics of newly detected hidden crevasses.

Crevasse, #	Length, m	Width, m	Latitude*, °S	Longitude*, °E
16	319	8	69.46525	76.26893
17	185	6	69.46396	76.28075
18	285	7	69.4626	76.27525
19	85	5	69.46041	76.28082
20	120	2	69.46023	76.28308
21	322	12	69.57285	76.25495
22	1115	10	69.53393	76.28528
23	930	15	69.54094	76.31048
24	175	7	69.56875	76.25538
25	640	20	69.57085	76.37607
26	619	11	69.65806	76.55022
27	232	12	69.65868	76.54793
28	190	12	69.66001	76.54977
29	437	13	69.63652	76.46882
30	423	10	69.63779	76.4677
31	812	15	69.63578	76.46726
32	169	10	69.63518	76.47282
33	471	10	69.63314	76.47313

* Coordinates are for crevasse centroids.

[8] Florinsky, I.V. and D.P. Bliakharskii, 2019. “Detection of crevasses by geomorphometric treatment of data from unmanned aerial surveys”. Remote Sens. Lett., 10(4), 323–332.

[9] Haralick, R.M., K. Shanmugam, I. Dinstein, 1973. “Textural features for image classification”. IEEE Trans. Syst. Man Cyber., SMC-3(6), 610–621.

[10] Florinsky, I.V., 2016. Digital Terrain Analysis in Soil Science and Geology. 2nd ed. Amsterdam: Academic Press.

GEOMORPHOMETRY 2020
PERUGIA, ITALY
JUNE 22 - 26 2020

Pit-centric depression removal methods

John B. Lindsay[§]
Department of Geography, Environment, and Geomatics
The University of Guelph
50 Stone Rd. East, Guelph, ON, Canada, N1G 2W1
§ jlindsay@uoguelph.ca

Abstract—**Topographic depressions are problematic for digital elevation model (DEM) based flow-path modelling applications. Two new depression removal methods are presented in this paper, including a depression filling and a depression breaching algorithm. These new methods adopt an approach to depression removal that is in contrast to the simulated landscape flooding approaches that dominate current leading methods. Instead, these methods start by identifying pit cells to each depression, and apply flood-simulation (filling) and least-cost breaching only to a relatively small area of grid cells contained within (filling) or around (breach channels) depressions. Algorithm performance was tested using two large LiDAR DEMs of watersheds in Southwestern Ontario, Canada. Both of the new pit-centric methods were found to be between 5.0 and 10.7 times faster than the widely used algorithms based on simulated landscape flooding. In addition to computational efficiency, other benefits of the new methods are discussed.**

I. Introduction

Topographic depressions are bowl-like features of digital elevation models (DEMs) with undefined flow directions [1]. Depressions are particularly abundant in fine-resolution DEMs [1] and may represent actual landforms or can result from DEM error [2]. Road and rail embankments are a common source of artifact depressions in DEMs, particularly those derived from LiDAR, because of the inability of these data to represent sub-surface drainage infrastructure (e.g. culverts) and flow beneath bridges [3-5]. Depression are particularly problematic for geomorphometric applications involving modelled surface flow paths [6-7], including contributing area mapping, watershed mapping, stream mapping, and the calculation of wetness index, stream power, sediment transport index, and other common terrain attributes.

Numerous depression removal methods have been developed over the past three decades to automatically adjust elevations within depressions to ensure continuously defined flow paths (see [8] for a good review). Three broad approaches exist for depression removal, including filling, which raise elevations within depressions to their outlet heights, breaching, which carves channels from depression interior pit cells to outside points, and hybrid methods [9]. Ongoing development of these methods has been primarily driven by improved algorithm efficiency and reduced modification to the DEM.

While there have been numerous advancements in depression removal methods in recent years, the two most widely implemented removal methods, and therefore, the most commonly used in practice, include the techniques of Planchon and Darboux (P&D) [10] and the priority flood method, first proposed by Soille and Gratin [7] and popularized by Wang and Liu (W&L) [11] and Barnes et al. [8]. Many recent techniques are modifications of these two basic approaches [12-14]. Most of the advanced techniques for depression removal therefore operate by either shedding water from an inundated landscape toward its edges [10], or by progressively flooding the digital landscape from the data edges inward using the priority flood approach [7, 11].

Two novel depression removal techniques are presented in this paper, including a depression filling method and a least-cost depression breaching algorithm. These techniques adopt a pit-centric approach that does not require visiting each cell in the DEM and therefore has potential efficiency advantages over previous alternatives.

II. Methods

Depression removal techniques that are based on the P&D and W&L methods identify depressions as a bi-product of the simulated water shedding or flooding operations. Any DEM grid cells for which the elevation after the operation is higher than the input elevations are contained within depressions. Simulated water shedding and flooding are both relatively costly computational operations and their processing times scale with the total number of DEM grid cells. Because the number of cells contained within topographic depressions is always less (usually significantly so) than the total number of DEM cells, a method that explicitly identifies depressions, without the need for a broader simulation, could potentially be more efficient.

Jenson and Domingue [6] proposed a method (J&D) for depression filling that was based on identifying the pit cells (i.e. interior cells with undefined flow) contained within each depression and then mapping full depression extents.

John Lindsay (2020) Pit-centric depression removal methods:

in Massimiliano Alvioli, Ivan Marchesini, Laura Melelli & Peter Guth, eds., Proceedings of the Geomorphometry 2020 Conference, doi:10.30437/GEOMORPHOMETRY2020_4.

Unfortunately, this early filling technique was computationally inefficient because the method for mapping depression extents relied on identifying each pit cell's watershed, the majority of which lies outside of the feature, and special handling of nested depressions, in the case of features containing multiple pit cells, was required. Rieger [15], Martz and Garbrecht [16, 17], and Lindsay and Dhun (L&D) [6] each proposed a pit-centric (i.e. a method based on identifying depression pit cells first) depression breaching method. The L&D technique was demonstrated to provide a low-impact solution that was particularly well suited to carving through embankments and predicting culvert/bridge locations. However, this method was also very computationally inefficient owing to the need to perform expensive cost-accumulation operations on each pit cell. Furthermore, the performance of the algorithm degrades significantly when larger search distances for breach paths are specified. These computational challenges with least-cost depression breaching were the motivation for Lindsay [18] proposing the 'efficient breaching' (EB) method, based on the W&L priority flood algorithm. While significantly improving computational performance, this method often provides much higher impact than EB and can yield unintuitive breach channels that follow the flood-order of the priority flood operation on which it is based.

The following two sections describe two new pit-centric depression removal methods. Both of the new depression removal methods, *FillDepressions* and *BreachDepressionsLeastCost*, have been implemented as tools within the open-source geospatial analysis software WhiteboxTools (WBT) [19]. Brief descriptions of each method are presented below and the source code of the tools is available for inspection online (https://github.com/jblindsay/whitebox-tools) for further detail.

A. Pit-Centric Filling Algorithm

The pit cells in a DEM can be mapped by identifying interior cells with no lower neighbors, an operation that is readily parallelized. Once pits are located, they are placed into a list and sorted from highest to lowest order based on cell elevations. The highest pit cell is popped from the list and a check is completed to determine whether the pit cell has already been raised in the output raster during a previous iteration. If the pit is unmodified, a region-growing operation is initiated to identify the pour point(s) and the depression interior of the feature to which the pit cell belongs. A priority queue, based on lowest cell heights, is initialized with the pit cell. All undiscovered neighbors are scanned and pushed into the queue if they are higher. Once a previously undiscovered neighboring cell of lower elevation (than the discovering cell's elevation) is located, the discovering cell is flagged as the depression's pour point. This priority-queue region-growing operation is only then terminated once there are no further cells of equal elevation to the outlet cell contained in the queue—this allows for the possibility of multiple pour-point cells. Each cell that was visited during the search for pour point cells are then raised to the pour point elevation. Importantly, this operation does not require visiting any cells contained outside of depressions (except for the single cell used to identify the pour-point cell) and there is no special handling required for nested depression. The region-growing operation raises the interior of topographic depressions to the level of their pour-point cells, leaving behind a flat surface. This flat surface may optionally have a slope applied to enforce flow across the extent of the depression. The flats-correcting algorithm applies another priority-queue based region-growing operation, initiated at outlets and with priority values set by the elevations contained within the original input DEM. This has the impact of forcing flow directions within depressions to follow similar patterns to the pre-flooding land-surface. This same procedure is iterated for each pit cell in the DEM.

The pit-centric depression filling technique identifies pit cells and their corresponding pour-point cells prior to filling. Therefore, it is possible to know a depression's depth in advance. If a depression's depth is greater than a user-specified maximum value, the feature can be left unfilled; this characteristic can be useful when working within closed geological basins. The P&D and W&L methods, in contrast, begin to fill features before their depths are known and can only mimic this property using post-processing.

B. Pit-Centric Least-Cost Breaching Algorithm

This method is inspired by the L&D least-cost breaching method and follows a similar method for identifying least-cost breach channels for each pit cell in the DEM. Here, the notion of cost is the height to which a cell's elevation would need to be lowered to ensure continuous flow from the pit cell along a breach channel. The iterative technique used by L&D for performing the cost-accumulation operation, needed to identify least-cost paths connecting pit cells to downstream cells exterior to depressions, has been replaced with a priority-queue based cost-accumulation operation that offers significant efficiency improvements. This new approach is in effect a region-growing operation that expands outward from each pit cell, from areas of lowest-cost to areas of increased cost, and accumulating the cost of breaching continuously descending channels to each newly discovered cell. The operation ceases once a cell with an elevation lower than the calculated breach channel height is identified. Importantly, this priority-based region-growing operation does not require a constant search window (unlike the L&D method) and will continue only until either a low enough breach channel end-point is located or no suitable target is identified within the constraints of a user-specified maximum breach distance or breach depth. The L&D method, by comparison, uses constant-sized search windows for each least-cost operation regardless of how far a

breach end cell is from the pit, and therefore exhibits a relatively high computational cost. Because the vast majority of pits in a DEM can be resolved after relatively short-running region-growing search operations, this represents a significant speed up for this new breaching method. If any unresolved pits exist after the region-growing operation, because potential candidates for breach end cells exceed the specified maximum distance/depth, pit-centric depression filling may optionally be applied afterwards—thus, this method is a potentially hybrid solution.

C. Study Site and Data

Two test DEMs were used to evaluate the relative performance of the new pit-centric depression removal methods. Catfish Creek and Big Otter Creek are adjacent coastal watersheds draining to Lake Erie in Southwestern Ontario, Canada (Figure 1). The watersheds are dominated by agricultural land-uses, although there are small urbanized areas in each site. The physiography of the watersheds is composed of clay, sand, and till plains with an area of till moraines in the north [20]. Local relief is low, with elevations ranging from approximately 175 m at the outlets to 345 m in the headwater areas. The embankments of several major roads/railways transect both watersheds, which create apparent dams in the DEMs and extensive artificial topographic depressions.

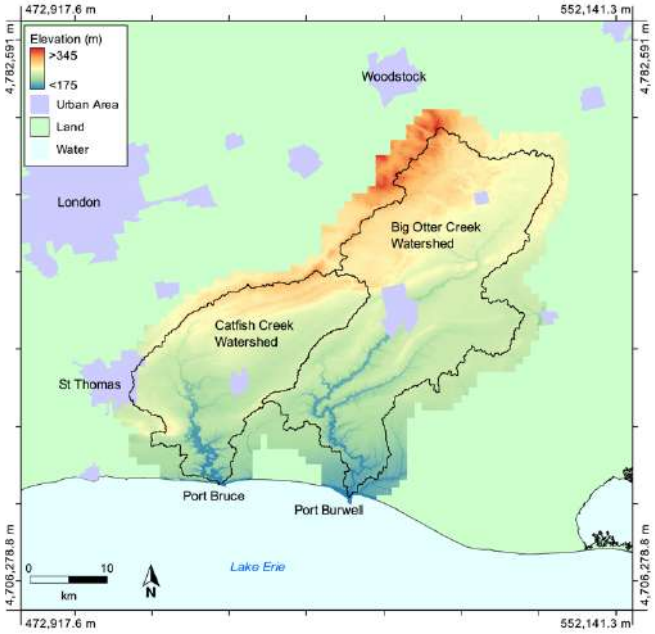

Figure 1. The test DEMs of the Catfish Creek and Big Otter Creek watersheds.

The test DEMs were interpolated using Delaunay triangulation from ground-classified returns of the source Lake Erie Watershed LiDAR point cloud data set. The source data were collected during leaf-off and snow-free conditions in the spring of 2018 by a private contractor commissioned by the Ontario Ministry of Agriculture, Food and Rural Affairs (OMAFRA) and the Ministry of Natural Resources and Forestry (MNRF). The average density of the data set is 8 points·m−2 and the overall vertical accuracy was estimated to be 0.05 m in unforested areas. The LiDAR data were stored in the NAD83 UTM zone 17N (EPSG:2958) coordinate system. Both DEMs were treated using the feature-preserving smoothing method [21], owing to the high degree of surface roughness common with fine-resolution LiDAR data. Table 1 summarizes the salient characteristics of the DEMs. Importantly, both DEMs are large data sets, with greater than one billion grid cells. Therefore, they provide suitable tests for algorithm efficiency and the practicality of the methods.

Table 1. Properties of the test DEMs for Catfish Creek and Big Otter Creek.

DEM Property	Catfish Creek	Big Otter Creek
Area (km^2)	685.0	1201.4
Resolution (m)	1.00	0.75
DEM file size[1] (GB)	4.55	15.29
Total cells in raster	$1.138x10^9$	$3.822x10^9$
Non-NoData cells	$6.850x10^8$	$2.136x10^9$
Pit cells	$1.033x10^6$	$3.745x10^6$
Depressions	$5.054x10^5$	$1.633x10^6$

[1] The input DEMs were stored as 32-bit floating point values, however, the output DEMs were 64-bit floats because fixing flat areas uses very small elevation increments. Thus, output DEM sizes were double the values reported here.

III. Results and Conclusions

The computational performance of the two pit-centric depression removal methods, were compared with other methods that are available in common geospatial analysis software (Table 2). Each of the tests were conducted using a computer system with a 3.0-GHz 8-core Intel processor and 64 GB of 1866-MHz memory. The P&D implementation in WhiteboxTools was used for testing, however, this is the same algorithm that is implemented in the widely used *Fill* tool in ArcGIS. The WhiteboxTools and SAGA GIS (*Fill sinks xxl*) implementations of the W&L depression filling method were both tested and were found to perform similarly. Lindsay's [15] EB method was the only depression breaching algorithm used for comparison. Being based on a priority-flood operation, this breaching method was found to have a broadly similar performance profile to the W&L algorithm. Attempts were made to test the L&D least-cost breaching method [5], however, this tool could not successfully process the large test DEMs.

The pit-centric filling and breaching tools were able to remove depressions in the Catfish Creek test site in less than one minute and the larger Big Otter Creek DEM in less than five minutes.

Both of the tools had similar efficiency, with the breaching solution providing the fastest solution for the Catfish Creek DEM, while pit-centric filling provided the fastest solution for the Big Otter Creek DEM. Notice that the pit-centric breaching tool was run using a maximum breach channel length (2048 cells) that was sufficiently long to ensure complete removal of depressions by breaching, with no subsequent filling required. Both of the new pit-centric methods were between 5.0 and 10.7 times faster than the P&D and the W&L algorithms (Table 1). The J&D method, one of the earliest depression removal techniques and implemented in GRASS GIS's *r.fill.dir* tool, was unsurprisingly the slowest tested method. The J&D Big Otter Creek test appeared suspended until the process was manually terminated after nearly 30 hours of processing. Unexpectedly, the tool did successfully produce a filled DEM after the process was terminated, and therefore, the reported time for this test is suspect.

Table 2. Depression removal algorithm performance. Processing times are in seconds and exclude file input/output. The two pit-centric techniques are compared to various software implementations of the Planchon & Darboux (P&D) filling, Wang & Liu (W&L) filling, Jenson & Domingue (J&D) filling, and Lindsay (2016) efficient breach (EB) methods.

Software / Algorithm	Catfish Creek	Big Otter Creek
WBT / Pit-centric filling	45.89	227.13
WBT / Pit-centric breaching	39.56	269.19
WBT / P&D	341.60	1340.97
WBT / W&L	300.50	1450.42
SAGA / W&L	422.08	1451.67
GRASS / J&D	6975.09	108,202.65
WBT / EB	324.62	1902.28

The pit-centric filling tool provided a very similar depression removal solution to all other filling methods (Figure 2B), although the way that this tool enforces slopes on flats using the pre-fill surface provided an improved flow accumulation pattern in flooded areas (see Figure 3A and Figure 3B). The pit-centric least-cost breaching tool was able to breach through embankments and dams at appropriate locations near stream crossings (Figure 2C), and therefore, was found to provide flow accumulation patterns that simulated flow through culverts (Figure 3C). Breach channels were found to be substantially shallower, shorter, and more appropriately located compared with the EB method. The differences were particularly evident where an embankment raises toward stream-road crossings to accommodate wide-diameter culverts. Under such conditions, EB can breach the road embankment long distances from the actual stream road crossing, while the pit-centric least-cost method typically follows a closer path to the mapped stream network (and presumed culvert location) in these cases.

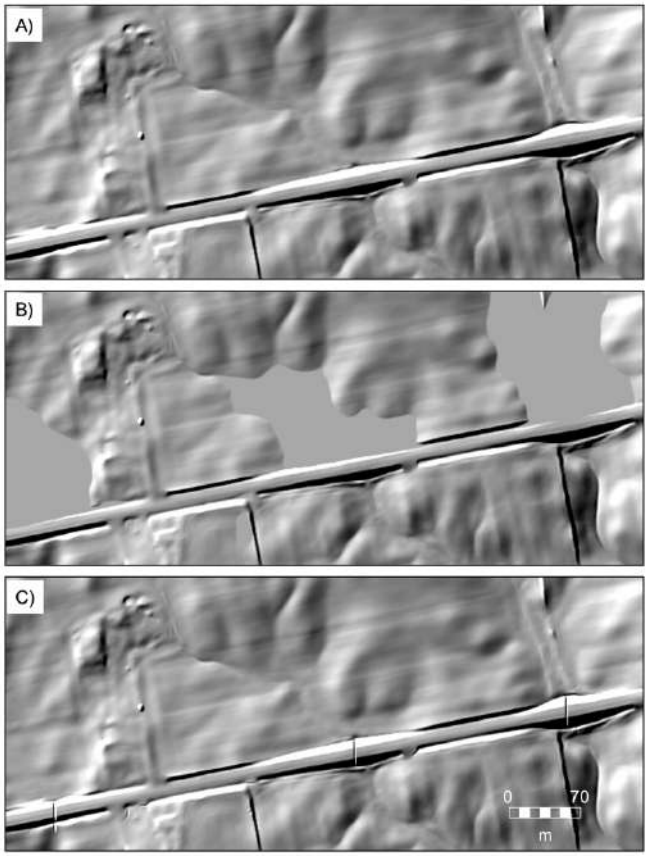

Figure 2. Hillshade images of a road embankment in the Catfish Creek Watershed, derived from A) the raw DEM, B) the pit-centric filled DEM, and C) the pit-centric least-cost breached DEM.

In conclusion, the two pit-centric depression removal methods presented in this paper were found to be significantly more efficient than methods that simulate landscape-wide flooding because they restrict the relatively costly simulation component to fewer grid cells in and around depression features. These methods can be used to resolve flow in multi-billion cell DEM data sets, offering the advantages of more natural flow enforcement on flats and least-cost breach channels, with the additional flexibility provided to users by allowing for maximum depression depth and breach channel length/depth parameters. Both pit-centric filling and breach methods offered very similar computational performance. Therefore, unless an application requires depression extents (i.e. sink mapping), the lower-impact breaching solution (*BreachDepressionsLeastCost*), which was found to resolve flow at stream-road crossings more naturally,

should be preferred by practitioners. Lastly, both algorithms benefited from the parallelization of the pit discovery step, but were sequential for their more computationally expensive simulation steps. Future work may focus on further exploration of parallel version of these workflows.

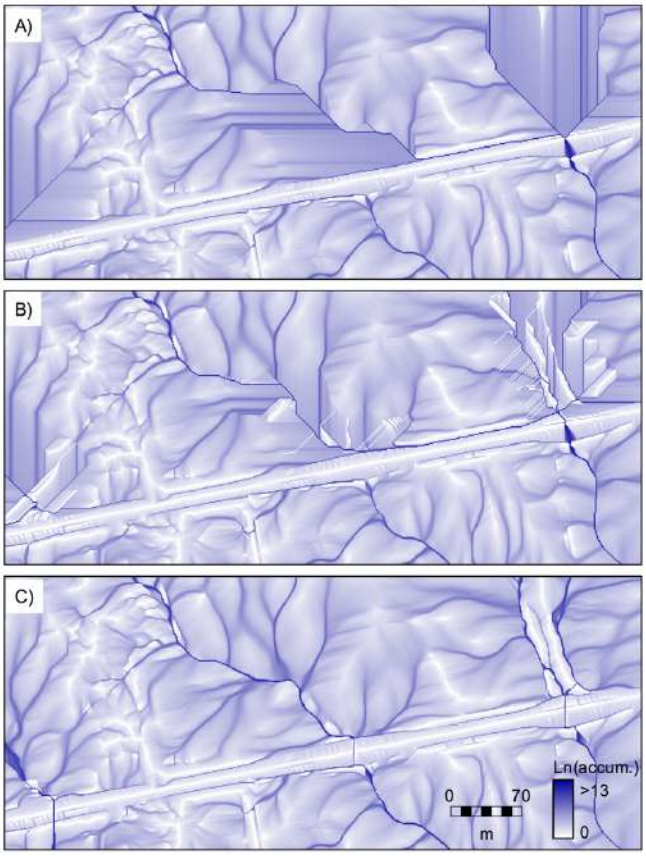

Figure 3. D∞ flow accumulation [22] rasters derived from DEMs treated using the A) Wang & Liu filling, B) pit-centric filling, and C) pit-centric least-cost breaching depression removal methods. The same road embankment found in Figure 2 is mapped here.

REFERENCES

[1] Lindsay, J.B. and Creed, I.F., 2005. "Sensitivity of digital landscapes to artifact depressions in remotely-sensed DEMs." Photogrammetric Engineering & Remote Sensing, 71(9), pp.1029-1036.

[2] Lindsay, J.B. and Creed, I.F., 2006. "Distinguishing actual and artefact depressions in digital elevation data." Computers & Geosciences, 32(8), pp.1192-1204.

[3] Duke, G.D., Kienzle, S.W., Johnson, D.L. and Byrne, J.M., 2003. "Improving overland flow routing by incorporating ancillary road data into digital elevation models." Journal of Spatial Hydrology, 3(2).

[4] Barber, C.P. and Shortridge, A., 2005. "Lidar elevation data for surface hydrologic modeling: Resolution and representation issues." Cartography and Geographic Information Science, 32(4), pp.401-410.

[5] Lindsay, J.B. and Dhun, K., 2015. "Modelling surface drainage patterns in altered landscapes using LiDAR." *International Journal of Geographical Information Science*, *29*(3), pp.397-411.

[6] Jenson, S.K. and Domingue, J.O., 1988. "Extracting topographic structure from digital elevation data for geographic information system analysis." Photogrammetric engineering and remote sensing, 54(11), pp.1593-1600.

[7] Soille, P. and Gratin, C., 1994. "An efficient algorithm for drainage network extraction on DEMs." Journal of Visual Communication and Image Representation, 5(2), pp.181-189.

[8] Barnes, R., Lehman, C. and Mulla, D., 2014. "Priority-flood: An optimal depression-filling and watershed-labeling algorithm for digital elevation models." Computers & Geosciences, 62, pp.117-127.

[9] Lindsay, J.B. and Creed, I.F., 2005. "Removal of artifact depressions from digital elevation models: towards a minimum impact approach." Hydrological Processes, 19(16), pp.3113-3126.

[10] Planchon, O. and Darboux, F., 2002. "A fast, simple and versatile algorithm to fill the depressions of digital elevation models." Catena, 46(2-3), pp.159-176.

[11] Wang, L. and Liu, H., 2006. "An efficient method for identifying and filling surface depressions in digital elevation models for hydrologic analysis and modelling." International Journal of Geographical Information Science, 20(2), pp.193-213.

[12] Wei, H., Zhou, G. and Dong, W., 2019. "A Variant of the Planchon and Darboux Algorithm for Filling Depressions in Raster Digital Elevation Models." ISPRS International Journal of Geo-Information, 8(4), p.164.

[13] Barnes, R., 2016. "Parallel Priority-Flood depression filling for trillion cell digital elevation models on desktops or clusters." Computers & Geosciences, 96, pp.56-68.

[14] Yong-He, L., Wan-Chang, Z. and Jing-Wen, X., 2009. "Another fast and simple DEM depression-filling algorithm based on priority queue structure." Atmospheric and Oceanic Science Letters, 2(4), pp.214-219.

[15] Rieger, W., 1998. "A phenomenon-based approach to upslope contributing area and depression in DEMs." Hydrological Processes, 12(6), pp.857-872.

[16] Martz, L.W. and Garbrecht, J., 1998. "The treatment of flat areas and depressions in automated drainage analysis of raster digital elevation models." Hydrological Processes, 12(6), pp.843-855.

[17] Martz, L.W. and Garbrecht, J., 1999. "An outlet breaching algorithm for the treatment of closed depression in a raster DEM." Computer & Geosciences, 25(7), pp.835-844.

[18] Lindsay, J.B., 2016. "Efficient hybrid breaching‐filling sink removal methods for flow path enforcement in digital elevation models." Hydrological Processes, 30(6), pp.846-857.

[19] Lindsay, J.B., 2019. "WhiteboxTools User Manual, v.1.1.0." Available online at https://jblindsay.github.io/wbt_book/intro.html (accessed Feb. 9, 2020).

[20] Chapman, L.J. and Putnam, D.F., 1973. "Physiography of Southern Ontario". Published for the Ontario Research Foundation by University of Toronto Press.

[21] Lindsay, J.B., Francioni, A. and Cockburn, J.M., 2019. "LiDAR DEM smoothing and the preservation of drainage features." Remote Sensing, 11(16), p.1926.

[22] Tarboton, D.G., 1997. "A new method for the determination of flow directions and upslope areas in grid digital elevation models." Water resources research, 33(2), pp.309-319.

GEOMORPHOMETRY 2020 PERUGIA, ITALY JUNE 22 - 26 2020

A framework for using handheld 3D surface scanners in quantifying the volumetric tufa growth

Ivan Marić[§], Ante Šiljeg, Fran Domazetović, Neven Cukrov
University of Zadar
Department of Geography
Trg kneza Višeslava 9, 23000 Zadar, Hrvatska
[§] imaric1@unizd.hr

Abstract— **The emergence of handheld 3D surface scanners can play an important role in improving the understanding of tufa formation dynamics. For the first time volumetric tufa growth was calculated using *Artec Eva* handheld 3D scanner. Volumetric tufa growth was measured on two limestone plates (PLs) which were installed near the Roški waterfall (National park Krka, Croatia). Tufa volumetric growth was calculated from a 3D models in *Artec Studio 14 Professional*. The applicability of *Artec Eva* in the measurement of small objects (25 cm²) was tested by comparing the volume of PL with a reference "true" value measured with *Artec Space Spider*. The mean volumetric tufa growth for Roški waterfall site was 1490,02 mm³ in six months period. Although initially *Artec Eva* is not intended for measurement of small objects, it can be used if the dimensions of the PLs on which the volumetric growth are slightly bigger. *Artec Eva* overestimated the PL volume by only 904.66 mm³, or 6.38%. This new approach uses handheld 3D surface scanners and high quality 3D models providing the alternative and user-friendly method for studying tufa formation dynamics.**

I. INTRODUCTION

Tufa is localized [13], terrestrial, highly porous, mainly monomineral rock typical for karst areas [1] which is formed in freshwaters [5] of ambient to near ambient temperature [2]. Tufa formation dynamic studies seek to quantify the mechanism of precipitation and growth or erosion rates [18]. Rates can be expressed as the mass accumulated or lost per unit area (eg. mg cm^2 a^{-1}) or height (mm a^{-1}) and volume (mm^3 a^{-1}) formed or eroded at some period. There are very few studies that quantified volumetric (mm^3 a^{-1}) tufa growth over longer time period [3]. Accurate calculation of tufa formation dynamics is important for several reasons. It addesses the fundamental geomorphological question of individual element landscape evolution. Second, recent rates of volumetric tufa growth can be compared to older ones and the determined difference may indicate on the important changes in the tufa environment (eg. achieving sustainable tufa formation condition or otherwise tufa degradation process) [8,9]. Despite the fact that recent advances in geospatial technologies (GST) have revolutionized the ability to quantifying the Earth's surface [16] at different scales [17], until now tufa volumetric growth (mm^3) has not been measured using the handheld 3D surface scanners. Of all modern geospatial sensors, only [10] presented the possibility of using SfM photogrammetry in quantifying the linear tufa growth (mm a^{-1}).

In this research a framework for using the 3D surface scanner *Artec Eva* in the quantification of tufa volumetric growth is presented. *Artec Eva* has been used for volume measurements in various scientific fields, from medicine [4, 6-7, 14] to geomorphometry [19]. Case study was Roški waterfall at National park "Krka" (NPK) in Croatia. Three main objectives of research were: propose a framework process for 3D scanning of small tufa samples, examine the applicability of *Artec Eva* in small object scanning and determine the average tufa volumetric growth for specific location in Roški waterfall.

Roški waterfall is located at National park "Krka" (NPK) in Šibenik-Knin County (Croatia) (Figure 1). It is one of the most famous landmarks of the NPK. According to Köppen's climate classification, this area belongs to Csa type.

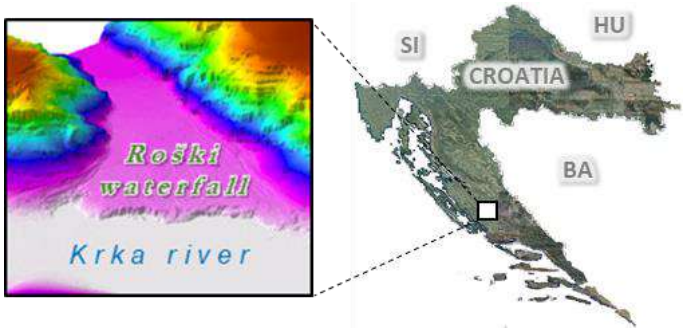

Figure 1. Location of Roški waterfall in Croatia.

Ivan Maric, Ante Siljeg, Fran Domazetovic and Neven Cukrov (2020) A framework for using handheld 3D surface scanners in quantifying the volumetric tufa growth: in Massimiliano Alvioli, Ivan Marchesini, Laura Melelli & Peter Guth, eds., Proceedings of the Geomorphometry 2020 Conference, doi:10.30437/GEOMORPHOMETRY2020_5.

II. METHODS

The volumetric tufa growth was measured using a 3D surface scanner *Artec Eva*. It is a state-of-the-art 3D scanning technique that uses triangulation and structured light while collecting 3D data. It is compact and lightweight 3D scanner [11]. 3D resolution of *Eva* is up to 0.5 mm at a working distance of 40 cm to 1 m, while accuracy of 3D points is up to 0.1 mm [11] although [15] and [12] states an accuracy of 0.05 mm. Results have shown that *Eva* is very reliable instrument for measuring volume [14]. In this study, the applicability of *Eva* in the measurement of small objects was examined using the *Artec Space Spider* measurements (Figure 2). *Space Spider* is newer handheld 3D surface scanner designed for measuring small objects. It has 3D resolution up to 0,1 mm, 3D point accuracy up to 0,05 mm and working distance of 0.2 – 0.3 m.

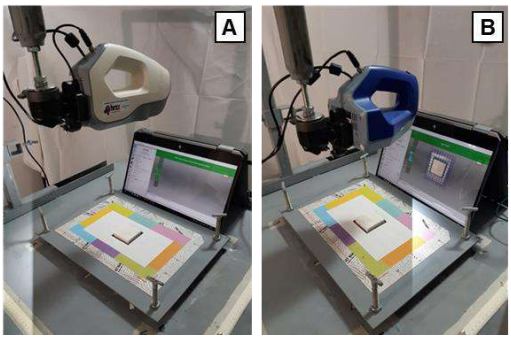

Figure 2. Measurements of the test limestone PL32 using the *Artec Eva* A) and *Artec Space Spider* B) for the testing the applicability of *Artec Eva* in the measurement of small objects

A. Installation of limestone plates (PLs)

Tufa volumetric growth was measured on the upper surface (25 cm²) of two limestone plates (PLs). The PLs were positioned in the immediate surroundings of the Roški waterfall. Specific code was engraved beneath each PLs and unique ID and name were assigned to location (Figure 3). Each PL was measured using *Artec Eva* before being installed in tufa forming watercourse. On July 1st. 2019. PLs were fixed with two stainless steel screws. Before the second measurement, which was done after six months on January 10th, 2020, they were left drying at room temperature for 4 days.

Figure 3. Limestone PLs installed near Roški waterfall.

B. Data processing of scans

Scans of the initial and final PLs were processed in *Artec Studio 14 Professional*. It is an industry-recognized software package designed for advanced 3D scanning and data processing. No scan segmentation occurred during the scanning therefore processing workflow included five steps (Figure 4). First was *crop surroundings.* Using the *rectangular selection* tool, the larger scanned area around the PLs was erased. Next was *global registration*. The position of the scans has been optimized to prepare them for further processing. The algorithm converts all one-frame surfaces into a single coordinate system using information about the shared location of paired surface points. The third was *outliner removal*. This eliminates noise or larger errors on the scans. The fourth was *sharp fusion*. A unique model surface was created with respect to the initial input. The *simplify mesh* function was not used because we wanted to retain a large number of polygons. The final step was *apply texture*. The texture was acquired by integrated 1.3 MPx camera.

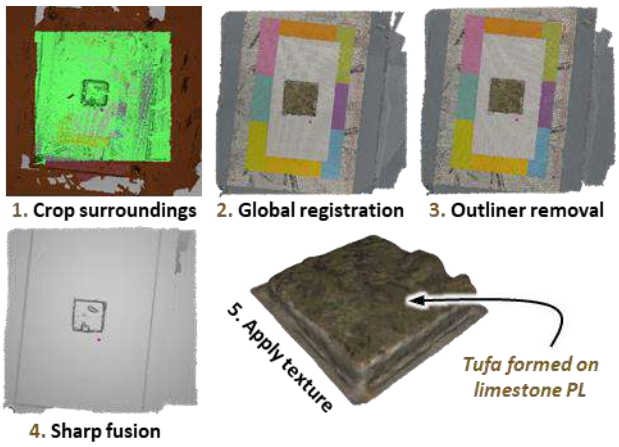

Figure 4. Data processing in *Artec Studio 14 Professional*

C. Calculation of volumetric (mm³) tufa growth

The volume of PLs and tufa was calculated from derived 3D models using the *Measure - Section* tool. Volume was calculated above the specific plane of the local coordinate system (LCS). The initial and final 3D models were positioned in the same LCS using the *Positioning* tool. The volumetric (mm³) tufa growth was calculated as the difference between the B) volume of the final model and the A) volume of the initial PL model (Figure 5).

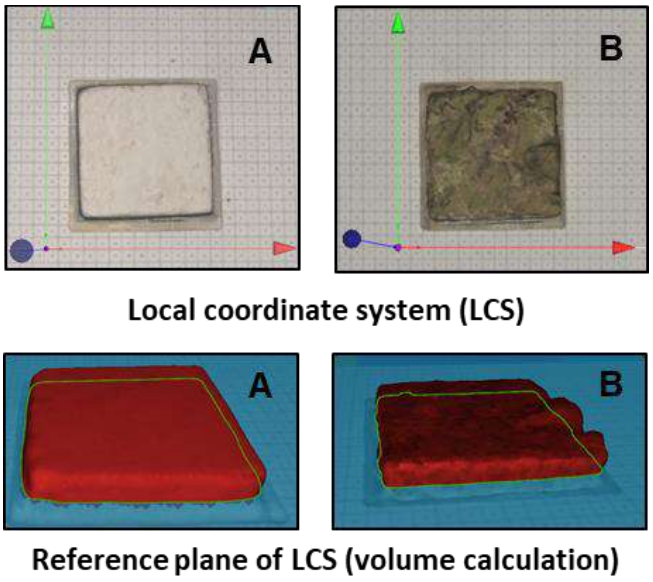

Figure 5. Calculation of tufa volumetric (mm³) growth

D. Comparison of Artec Eva and Space Spider

The applicability of *Eva* in small objects measurement was tested by the comparison of the volume (mm^3) of a specific PL with surface area of 25 cm^2. The volume generated using *Space Spider* was used as the benchmark or reference "true" data. *Eva* and *Space Spider* scans of the specific PL were processed using the above mentioned processing workflow. Two 3D models of the same PL were imported into one *Artec Studio* project (Figure 6).

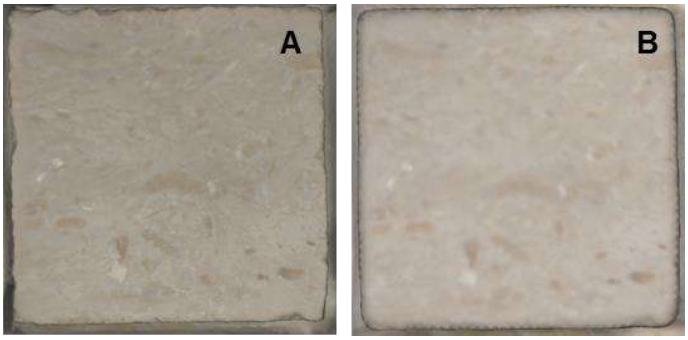

Figure 6. 3D model of PL32 generated with A) *Space Spider* and B) *Eva*

Volume of PLs was calculated from 3D models in *.obj format.* The accuracy of the *Eva* is then expressed the with absolute (AE) and percentage error (PE). AE was calculated as the difference between the "true" (volume generated by *Space Spider*) and the measured value (volume generated by *Eva*). PE is expressed as the percentage difference between the measured and the "true" value by formula:

$$Pe = \frac{|A_E|}{"true"\ value}\ X\ 100 \qquad (1)$$

where A_E is absolute error and "true" value is volume of PL generated using *Space Spider.*

The accuracy of *Artec Eva* is then analysed through the *surface-distance map* from which the RMS (root mean square-the square root of the arithmetic mean of the squared distances) and MAD (mean absolute deviation) were derived. *Surface-distance map* enables comparison of two 3D models and assess the deviation of their forms. Also, it can be used in quality control of the original "true" model with the scanned one.

III. Results and Conclusions

A. Volumetric tufa growth for Roški waterfall site

The PLs were removed from the site on January 10th, 2020, after around six months (193 days) (Figure 7) spent in a watercourse.

Figure 7. Surface of PLs 30 and 43 after 193 days spent in the flow

In total four 3D model of PLs were generated from which two represent initial PL shape and others two shape after six months spent in the flow. Despite the fact that the PL30 and 43 were placed in a flow at a distance smaller than 30 cm, volumetric tufa growth for PL43 was 791,70 mm³ larger than on the PL30. This is due to the characteristics of the PLs micro locations. The PLs are set at a similar slope, but the PL43 is more exposed to water spray zone than the PL30. The mean volumetric tufa growth for location was 1490,02 mm³ (Table 1). The data obtained show that the tufa grew 7,72 mm³ per day.

Table 1. Volumetric (mm³) tufa growth calculated in *Artec Studio*

PL CODE	Volume (mm³)		Volumetric tufa growth (mm³)
	Initial state	Final state	
PL30	14070,08	15164,25	**1094,17**
PL43	15258,66	17144,53	**1885,87**
MEAN			**1490,02**

B. Application of Artec Eve in small object measurement

Surface-distance map is a colored rendering on the particular regions of surfaces. Corresponding values of distances and their distribution can be read from the graduated scale with the histogram (Figure 8). Blue color corresponds to negative distance while red represents positive distance. RMS was 0.259 while MAD was 0.281 mm.

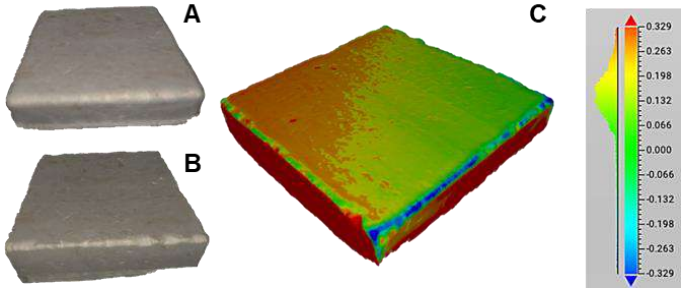

Figure 8. 3D model of PL32 generated with A) *Eva* and B) *Space Spider* with C) *Surface-distance map*

Volume of PL32 measured with *Artec Eva* and *Space Spider* was compared. The AE of measurement with *Artec Eva* was -904,66 mm³. Respectively, *Artec Eva* overestimated the PL volume by only 904.66 mm³, or 6.38% (PE) (Table 2).

Table 2. PL volume (mm³) calculated in *Artec Studio* for *Artec Space Spider* and *Artec Eva*

PLCODE	Volume (mm³)	
	Artec Eva	***Artec Space Spider***
PL32	**15077.14**	**14172.48**

In conclusion, we have demonstrated a framework for using handheld 3D surface scanners in quantifying the volumetric tufa growth. The mean volumetric tufa growth for Roški waterfall was 1490,02 mm³ in six month period. The applicability of *Artec Eva* in measurement of small objects was tested. Although *Eva* is not intended for measuring small objects (eg. surface area of 25 cm²), it can be used to measure volumetric tufa growth if the dimensions of the artificial substrates (PLs) are slightly bigger. In this case, *Artec Eva* overestimated the PL volume by only 904.66 mm³, or 6.38% (PE).

REFERENCES

[1] Capezzuoli E, Gandin A, Pedley M. 2014. Decoding tufa and travertine (fresh water carbonates) in the sedimentary record: the state of the art. Sedimentology 61(1): 1-21.

[2] Carthew KD, Taylor MP, Drysdale RN. 2002. Aquatic insect larval constructions in tropical freshwater limestone deposits (tufa): preservation of depositional environments. General and Applied Entomology: the Journal of the Entomological Society of New South Wales 31: 35 – 41.

[3] Demott LM, Scholz CA, Junium CK. 2019. 8200‐year growth history of a Lahontan‐age lacustrine tufa deposit. Sedimentology 66: 2169–2190.

[4] Ferguson, D. J. (2018). Evaluating the accuracy of facial models obtained from volume wrapping: 2D images on CBCT versus 3D on CBCT. In Seminars in Orthodontics (Vol. 109, p. 110).

[5] Ford, T. D. (1989). Tufa: a freshwater limestone. Geology Today, 5(2), 60-63.

[6] Koban, K. C., Shenck, T. L., Giunta, R. E. (2016). Using mobile 3D scanning systems for objective evaluation of form, volume, and symmetry in plastic surgery: intraoperative scanning and lymphedema assessment. In Proceedings of the 7th International Conference on 3D Body Scanning Technologies.

[7] Koban, K. C., Titze, V., Etzel, L., Frank, K., Schenck, T., & Giunta, R. (2018). Quantitative volumetric analysis of the lower extremity: validation against established tape measurement and water displacement. Handchirurgie, Mikrochirurgie, plastische Chirurgie: Organ der Deutschsprachigen Arbeitsgemeinschaft fur Handchirurgie: Organ der Deutschsprachigen Arbeitsgemeinschaft fur Mikrochirurgie der Peripheren Nerven und Gefasse: Organ der V..., 50(6), 393-399.

[8] Liu L. 2017. Factors Affecting Tufa Degradation in Jiuzhaigou National Nature Reserve, Sichuan, China. Water 9(9): 702.

[9] Liu Z, Sun H, Li H, Wan N. 2011. δ13C, δ18O and deposition rate of tufa in Xiangshui River, SW China: implications for land-cover change caused by climate and human impact during the late Holocene. Geological Society, London, Special Publications 352(1): 85-96.

[10] Marić, I., Šiljeg, A., Cukrov, N., Roland, V., & Goreta, G. (2019, June). 3D image based modelling of small tufa samples using macro lens in digital very close range photogrammetry. In 5th Jubilee International Scientific Conference GEOBALCANICA 2019.

[11] Modabber, A., Peters, F., Kniha, K., Goloborodko, E., Ghassemi, A., Lethaus, B., Möhlhenrich, S. C. (2016): Evaluation of the accuracy of a mobile and a stationary system for three-dimensional facial scanning. Journal of Cranio-Maxillofacial Surgery, 44(10), 1719-1724

[12] Ozsoy, U., Sekerci, R., Ogut, E. (2015): Effect of sitting, standing, and supine body positions on facial soft tissue: detailed 3D analysis. International journal of oral and maxillofacial surgery, 44(10), 1309-1316.

[13] Pevalek, I. (1956). Slap Plive u Jajcu na samrti. Naše starine III, 269-273.

[14] Seminati, E., Talamas, D. C., Young, M., Twiste, M., Dhokia, V., Bilzon, J. L. (2017). Validity and reliability of a novel 3D scanner for assessment of the shape and volume of amputees' residual limb models. PloS one, 12(9), e0184498.

[15] Shah, P. B., Luximon, Y. (2017): Review on 3D scanners for head and face modeling. In International Conference on Digital Human Modeling and Applications in Health, Safety, Ergonomics and Risk Management (pp. 47-56). Springer, Cham.

[16] Smith, M. W., Carrivick, J. L., Quincey, D. J. (2016). Structure from motion photogrammetry in physical geography. *Progress in Physical Geography*, 40(2), 247-275.

[17] Verma, A. K., Bourke, M. C. (2019). A method based on structure-from-motion photogrammetry to generate sub-millimetre-resolution digital elevation models for investigating rock breakdown features. Earth Surface Dynamics, 7(1), 45-66.

[18] Viles, H, Pentecost, A. (2007). Tufa and travertine. In DJ. Nash, SJ. McLaren (Esd.). Geochemical Sediments and Landscapes. (pp. 173-199). Singapore: Blackwell Publishing Ltd.

[19] Wang, P., Jin, X., & Li, S. (2018, July). Application of Handheld 3D Scanner in Quantitative Study of Slope Soil Erosion. In IOP Conference Series: Earth and Environmental Science (Vol. 170, No. 2, p. 022178). IOP Publishing.

GEOMORPHOMETRY 2020 PERUGIA, ITALY JUNE 22 - 26 2020

What does land surface curvature really mean?

Jozef Minár, **Marián Jenčo**
Department of Physical Geography and Geoecology
Comenius University in Bratislava, Slovakia
jozef.minar@uniba.sk

Ian S. Evans
Department of Geography
Durham University, England

Abstract — **The complex development of geomorphometric theory has led to various concepts of land surface curvature (LSC), whose compatibility has not yet been systematically investigated. The definition, terminology and interpretation of LSCs show significant confusion and gaps reflected in various applications in geoscience modelling and prediction. Here we discuss the present situation, specify basic problems, and make initial suggestions for their solution.**

I. INTRODUCTION

Land surface curvatures (LSCs) are an important part of systems of geomorphometric variables [1]. For long, the characterisation of land surface by curvatures of contour line and slope line (i.e. plan and profile) was considered sufficient [2-5]. During the 1990s came an explosion of new definitions of LSCs. The introduction of particular new LSCs (tangential curvature [6], flow line curvature [7], and Laplacian as a 'curvature' [8]) was followed by two attempts to build a system of LSCs. The first system used directional derivatives of slope and aspect to derive all existing and two new curvatures – changes of slope in directions of contour and of slope line [9]. The second system draws from differential geometry of surfaces, and includes four curvatures long known in geometry (maximal, minimal, mean and total) as well as six new curvatures (unsphericity, difference, horizontal and vertical excess, total accumulation and total ring) [10]. This remains the most compact comprehensive system of LSCs and is well represented in three representative books devoted to digital terrain analysis [11-13].

Nevertheless different definitions of LSCs with the same name are frequently used in practice: plan and profile curvature [5], maximum and minimum curvature [14], mean curvature [15], and total curvature [16]. Moreover, further new curvatures or curvature-like variables have appear in the literature: curvedness [17], transverse and profile terrain curvature [18], slope of slope or slope of aspect (e.g. [19]), and a very strange variable simple termed 'curvature' [20]. GIS packages offer dozens of variously termed 'curvatures', frequently without clearly distinguishing between them. All this is a challenge for the geomorphometric community to discuss standardization of formal expression, terminology and labelling, elucidating systemic relationships and improving the interpretation of LSCs. Space here does not permit presentation of our proposals synthesizing contemporary knowledge and some new theoretical concepts into a new system of definition and interpretation of LSCs. Here we focus on the state of the art and outline some questions and principles important for the building of such a system. Discussion of the interpretation of curvatures in terms of attractors of land surface development is an example of a new research problem formulated on the basis of our approach.

II. DEFINITIONS

LSCs sensu stricto are the subject of this paper: they are local field-based geomorphometric variables defined by partial derivatives in the differentially small surrounding of a point [1]. There are other variables termed as 'curvature' that do not meet this requirement (e.g. [18, 20]). Two overlapping approaches to definition and derivation of LSCs exist. The first uses formulae from differential geometry to derive basic geometric curvatures defined by the inverted value of an osculating circle [4, 7, 10, 21]. Curvature of curves and normal curvatures of surface are most frequently used. However, the synthesizing concept of curvature of curves on surfaces, defining their normal and geodesic curvature as well as geodesic torsion (e.g. [22]) has not yet been systematically applied in geomorphometry. The second approach understands LSCs as 2nd directional derivatives of altitude or 1st directional derivatives of slope and aspect [3, 5, 19]. Some authors show the compatibility of both approaches [9, 23] but it is not absolute.

LSCs can be defined exactly by mathematical formulae in general or specific form. The most frequent general expression in Cartesian coordinates [4, 6, 7, 9, 10, 21] permits the simple comparison of particular variables. Specific computational expressions, using coefficients of interpolation polynomials [5, 8, 14, 24], is also frequent. Unifying the expression of all investigated LSCs in the Cartesian coordinate system produces more than 30 different equations, some of which are similar. Deeper understanding of their derivation and interpretation has permitted preparation of a new classification system containing all generally used LSCs, and expressing interrelationships.

Jozef Minar, Marian Jenco, and Ian S. Evans (2020) What does land surface curvature really mean?:

in Massimiliano Alvioli, Ivan Marchesini, Laura Melelli & Peter Guth, eds., Proceedings of the Geomorphometry 2020 Conference, doi:10.30437/GEOMORPHOMETRY2020_6.

Shary [10] proved that three curvatures (mean, unsphericity and difference curvature) can be considered as independent components of LSC; and seven other geometric curvatures are combinations of the three. However, that is only one kind of relationship between LSCs. Some LSCs can be defined as slope (S) dependent transformations (subforms) of others (e.g. the well-known relationship between plan contour (p) and tangential curvature (t): $p = t / \sin S$), and some curvatures are the same as others, but only in specific conditions (we label this 'imitation'). Combination of these various kinds of relationships with classification of the mathematical basis of particular curvatures is at the core of our suggested new system of LSCs.

A very frequent problem of LSC definition concerns signs of the defining equations. At first sight trivial, this problem (what is convex in mathematics, and what on the land surface) has far from trivial consequences. To be mathematically correct we should term hills as concave and dells as convex. Changing the direction of slope gradient permits correct definition (geographically as well as mathematically) of basic LSCs [25]: a problem remains, however, in definition of maximal and minimal curvatures. A simple change of signs is not effective here: maximal curvature in the geographical convention is described by minimal directional derivatives and vice versa. The biggest problem, however, comes from mixing mathematical and geographical conventions, as e.g. in [5] and [8] and subsequently in further GIS packages.

Insufficient understanding of LSC definition is reflected also in the dimensions attributed to particular LSCs. The dimension [m^{-1}] is natural for LSCs defined by radius of an osculating circle, and for second derivatives of altitude. The latter express change of tangent of inclination over unit distance in a given direction. Expression of the plan curvature of a curve in [$rad.m^{-1}$] (the central angle of a 1 m long circular arch of osculating circle, which is equal to the radius of the circle) is also acceptable. However, in many application studies dimensions are undeclared or poorly declared.

III. TERMINOLOGY

Absence of a comprehensive classification system of LSCs has led to vagueness in LSC terminology. The same term frequently has various meanings: e.g. for plan curvature, four GIS packages (ArcGIS, SAGA-GIS, GRASS, MICRODEM) give four different results. On the other hand, the same curvature has been given different names in different papers: e.g. the tangential curvature of [6] and [21] is identical with the horizontal curvature of [10]; the profile curvature of [5] is the same as the longitudinal curvature of [14], and so on. Moreover the majority of terms do not fully express the mathematical basis of the specified curvature. Plan curvature is curvature of a contour line, i.e. in plan projection. However, rotor, flowline or streamline curvature [10, 23, 7] also occur in plan projection ('plan slope line curvature'). But flow or stream lines are generally considered as spatial curves that have three various measures of curvature, and rotor curvature is most frequently understand as curvature of a material rotor. Even less specific is the traditional term profile curvature, as we can draw an infinite number of profiles through every point on the land surface. The worst situation is in many application papers where the bare term 'curvature' is used, or terms such as 'general', 'conventional' or 'standard' curvature which have no specified definition. This generally unsystematic labelling of curvatures provides a terminological chaos.

Systematic terminology and labelling of LSCs should contain mathematical meaning yet express functional hierarchy. On higher (broader) hierarchical level we can preserve traditional terms such as plan and profile curvature, for groups of similar curvature; and to specify a subform of the group we can label curvature by combining terms of differential geometry with basic topographic lines, e.g.: normal contour curvature and geodesic contour curvature as subforms of plan curvature. If no geometric curvature is adequate, direction of directional derivative and name of derived field (eventually also order of derivative) can be used: e.g. (2^{nd}) contour derivative of altitude is another subform of the plan curvature group. This permits systematic symbolisation of subforms, e.g. (if c is contour): $(k_n)_c$ and $(k_g)_c$ for normal and geodesic curvatures of contour; and (if z is altitude) z_{cc} for the next subform of plan curvature – second derivative of altitude in direction of contour.

IV. INTERPRETATION

Interpretation of LSCs is the most important aspect for their practical use. About 30 formally defined LSCs are fruitless if we lack efficient interpretation of each one. In the great majority of application papers, the simplest dynamic interpretation of plan and profile curvature is used: plan curvature determines divergence and convergence, profile determines acceleration and deceleration of mass flows. However, if we have four similar curvatures (subforms), that all produce convergence and divergence, what is the difference between them? Many authors ignore this problem: exceptions are e.g. [10] and [28]. Yet little attention is paid to interpretation of Shary's compound curvatures [10] although rare empirical studies confirm their importance [26, 27]. One exception is [28], showing how profile and tangential curvature interact during soil erosion (in the form of mean curvature). [29] presents an attempt to show the importance of difference curvature for definition of potential energy applicable to mass flow on the land surface. This concept can also influence appraisal of the importance of various kinds of plan and profile curvature. If both are sources of change of energy of gravity flows, the possibility of infinite values leads to physical

nonsense. As the energy of gravity flows is a finite quantity, curvatures reaching infinity for slope extrema (0° or 90°) are not suitable measures for dynamic interpretation.

Reflection of long-term landform evolution is another essential aspect of interpretation. Curvatures are commonly used in mapping individual landforms, land surface segmentation, and classification. However, an a priori concept of the evolutionary interpretation of LSC has hardly ever been used. The germ of such an interpretation can be found in the concept of elementary forms defined by constant values of altitude, slope, aspect and curvatures [30]. If a tendency to such uniformity really exists, it can be reflected by a concentration of values around zero, in the ascending hierarchical order: altitude – slope / aspect – curvatures – changes of curvature [31]. Various lines of theoretical and empirical evidence show that at least linearity (zero plan and profile curvature) is an attractor of landform development in many cases. We should consider the possibility of interpreting zero values of other LSCs as attractors of landscape development.

Shary's system of LSCs provides a general classification of landforms using LSCs [10]. In the space defined by mean, difference and total (Gaussian) curvature projected onto the plane, where unsphericity curvature = 0, Shary defined twelve main types of landforms (Fig. 1)

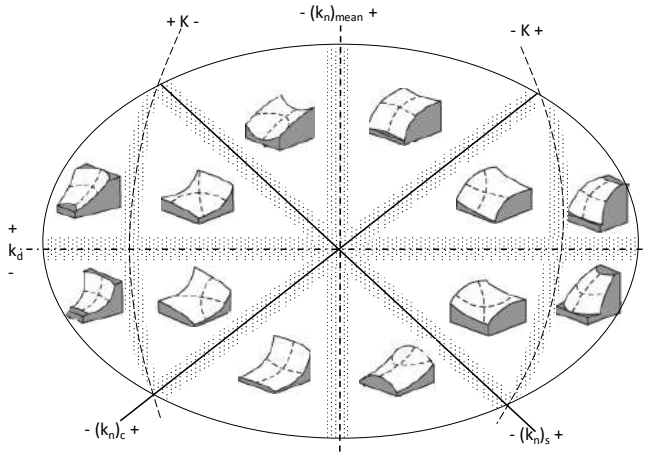

Figure 1. Shary's landform classification. K – total (Gaussian) curvature, $(k_n)_c$ – normal contour (tangential) curvature, $(k_n)_s$ – normal slope line (profile) curvature, k_d – difference curvature. Dotted belts represent the special character of zones along axes – see Fig. 2. Adapted from [32], and modified.

From Shary's statistical hypothesis, there is a 1/12 probability of the random appearance of each landform type in Fig. 1 [10]. As shown in [32], this is generally valid and differences from the statistical hypothesis can be morphogenetically interpreted. However, Shary's assertation that "land form types, for which at least one curvature is zero, are extremely rare; as a rule, they are related to artefacts in elevation matrices" [32, p. 96] is challenged by the elementary forms concept [30]. For this concept, attractors of land surface development are on the axes of the Shary's system (Fig. 2). Cases where a curvature exactly achieves zero value are very exceptional in reality, but we hypothesize a natural tendency to approximate zero values of curvatures: this justifies the importance of classifications containing zero [e.g. 4, 6, 33, 34]. Investigation of any tendency of LSCs to concentrate around zero (as executed e.g. in [31]) results from this theoretical interpretation of LSCs and is an example of using of deeper theoretical knowledge about LSCs in the empiric research.

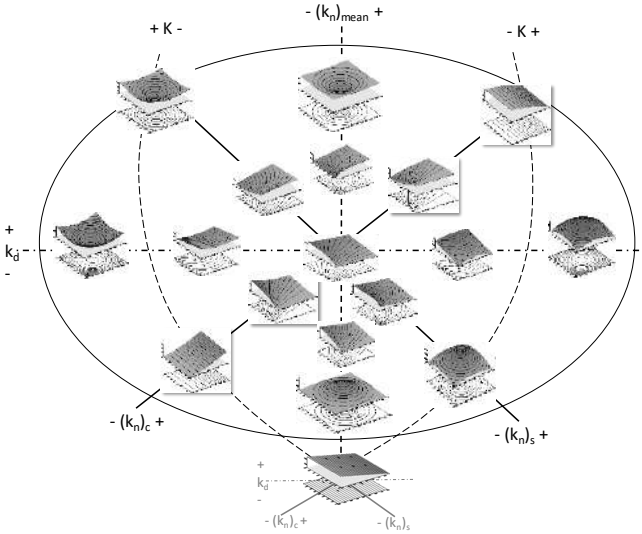

Figure 2. Elementary forms of Minár and Evans [30] positioned in Shary's landform classification. Their position on the axes of Shary's system indicates that zero values of curvatures should be attractors in landform development. Labelling as in Fig. 1.

V. CONCLUSIONS

Ongoing confusions in LSC terminology, definitions and interpretations provide an impetus to prepare a comprehensive system of LSCs, unifying terminology and clearly specifying relationships between various types of LSCs. The system should be built on Shary's system of geometric normal curvatures [10], but must go further. It can help to ensure identification of every LSC used in GIS (with definition equations in general form) and in papers (with standardized terminology and labelling).

The place of any curvature in the system should be conditioned not only by clear mathematical definition and relationships with other LSCs, but also by a clear interpretational potential. To develop physically based interpretation of LSCs as both dynamic (influencing distribution of energy on the land

surface) and as evolutionary (defining a long term disequilibrium or as attractors of land surface development) is the biggest challenge for the future. The result can be substitution of recent experiments with LSCs which lack a basis in sound theory, by theory-driven investigations as is typical for developed sciences.

ACKNOWLEDGMENT

This work was supported by the Slovak Research and Development Agency under contract APVV-15-0054.

REFERENCES

[1] Evans, I. S. and Minár, J. 2011. A classification of geomorphometric variables. *International Geomorphometry 2011*, 105-108. Geomorphometry.org.

[2] Aandahl, A.R., 1948. The characterization of slope positions and their influence on the total nitrogen content of a few virgin soils of Western Iowa. Soil Science Society of America Proceedings 13, 449–454.

[3] Evans, I.S., 1972. General geomorphometry, derivatives of altitude and descriptive statistics, in: Chorley, R.J. (Ed.), Spatial Analysis in Geomorphology. Methuen, London, pp. 17–90.

[4] Krcho, J., 1973. Morphometric analysis of relief on the basis of geometric aspect of field theory. Acta Geographica Universit. Comenianae, Geographico–physica No 1, pp. 7–233.

[5] Zevenbergen, L.W., Thorne, C.R., 1987. Quantitative analysis of land surface topography. Earth Surface Processes and Landforms 12 (1), 47–56.

[6] Krcho, J., 1990. Morfometrická analýza a digitálne modely georeliéfu., [Morphometrical Analysis and Digital Elevation Models]. Veda, Bratislava (in Slovak).

[7] Shary, P.A., 1991. Topographic method of second derivatives. In: Stepanov, I.N. (Ed.), The Geometry of Earth Surface Structures. Poushchino Scientific Center, Poushchino, pp. 28–58 (in Russian).

[8] Moore, I.D., Grayson, R., Ladson, A., 1991. Digital terrain modelling: A review of hydrological, geomorphological, and biological applications. Hydrol. Process. 5 (1), 3–30.

[9] Jenčo, M., 1992. The morphometric analysis of georelief in terms of a theoretical conception of the complex digital model of georelief. Acta Facultatis Rerum Naturalium Universitatis Comenianae, Geographica 33, 133–153.

[10] Shary, P.A., 1995. Land surface in gravity points classification by a complete system of curvatures. Math. Geol. 27 (3), 373–390.

[11] Hengl, T., Reuter, H.I. (Eds.), 2009. Geomorphometry: Concepts, Software, Applications. Developments in Soil Science 33. Elsevier, Amsterdam.

[12] Florinsky I.V., 2016. Digital Terrain Analysis in Soil Science and Geology, second ed. Elsevier, Amsterdam.

[13] Wilson, J.P., 2018. Environmental Applications of Digital Terrain Modelling. Wiley.

[14] Wood, J.D., 1996. The geomorphological characterisation of digital elevation models. PhD Thesis. University of Leicester, UK.

[15] Pirotti, F., Tarolli, P., 2010. Suitability of LiDAR point density and derived landform curvature maps for channel network extraction. Hydrol. Process. 24, 1187–1197.

[16] Gallant, J.C., Wilson, J.P., 2000. Primary Topographic Attributes, in: Wilson, J.P., Gallant, J. (Eds.), Terrain Analysis: Principles and Applications, Wiley, New York, pp. 51–85.

[17] Koenderink, J.J., van Doorn, A.J., 1992. Surface shape and curvature scales. Image and Vision Computing 10 (8), 557–564.

[18] Krebs, P., Stocker, M., Pezzatti, G.B., Conedera, M. 2015. An alternative approach to transverse and profile terrain curvature. Int. J. Geographical Information Science 29 (4), 643–656.

[19] Cheng, G., Liu, L., Jing, N., Chen, L., Xiong, W., 2012. General-purpose optimization methods for parallelization of digital terrain analysis based on cellular automata. Computers & Geosciences 45, 57–67

[20] Evans, J.S., Hudak, A.T., 2007. A multiscale curvature algorithm for classifying discrete return LiDAR in forested environments. IEEE Transactions on Geoscience and Remote Sensing 45 (4), 1029–1038.

[21] Mitasova, H., Hofierka, J., 1993. Interpolation by regularized spline with tension: II Application to terrain modeling and surface geometry analysis. Mathematical Geology, 25, 657–669.

[22] Hyde, S., Andersson, S., Larsson, K., Blum, Z., Landh, T., Lidin, S., Ninham, B.W., 1997. The Language of Shape. The Role of Curvature in Condensed Matter: Physics, Chemistry and Biology. Elsevier Science

[23] Peckham, S.D., 2011. Profile, Plan and Streamline Curvature: A Simple Derivation and Applications, in: Geomorphometry 2011, Redlands, USA, 7–11 September 2011, pp. 27–30.

[24] Evans, I.S., 1980. An integrated system of terrain analysis and slope mapping. Z. Geomorphol. 36, 274–295.

[25] Krcho, J., Benová, A., 2013. Problém správnej a exaktnej definície geometrických foriem georeliéfu vzhľadom na tiažové pole Zeme., [The problem of correct and exact definition of geometrical forms of georelief regarding the Earth's gravitational field]. Geografický časopis 65 (3), 189–216 (in Slovak).

[26] Mitusov, A., Mitusova, O.E., Wendt, J., Dreibrodt, S., Bork, H.–R., 2014. Correlation of colluvial deposits with the modern land surface and the problem of slope profile description. Geomorphology 220, 30–40.

[27] Mitusov, A.V., Burian, L., Khrisanov, V.R., 2017. Distribution of local landforms at head and end points of gullies on different grid spacing. Catena 159, 159–170.

[28] Mitas, L. and H. Mitasova, 1998. Distributed soil erosion simulation for effective erosion prevention. Water Resources Research, 34 (3): 505-516.

[29] Minár, J., Bandura, P., Holec, J., Popov, A., Gallay, M., Hofierka, J., Kaňuk, J., Drăguţ, L., Evans, I.S., 2018. Physically-based land surface segmentation: Theoretical background and outline of interpretations. PeerJ Preprints 6:e27075v1.

[30] Minár, J. and I.S. Evans, 2008. Elementary forms for land surface segmentation: The theoretical basis of terrain analysis and geomorphological mapping. Geomorphology, 95: 236-259.

[31] Minár, J., Jenčo, M., Evans, I.S., Minár Jr., J., Kadlec, M., Krcho, J., Pacina, J., Burian, L., Benová, A., 2013. Third–order geomorphometric variables (derivatives): definition, computation and utilization of changes of curvatures. Int. J. Geographical Information Science 27 (7), 1381–1402.

[32] Shary, P.A., Sharaya, L.S., Mitusov, A.V., 2005. The problem of scale–specific and scale–free approaches in geomorphometry. Geografia Fisica e Dinamica Quaternaria 28 (1), 81–101.

[33] Richter, H., 1962. Eine neue Methode der grossmassstäbigen Kartierung des Reliefs. Petermanns Geogr. Mitteilungen (Gotha) 106, 309–312.

[34] Dikau, R., 1989. The application of a digital relief model to landform analysis in geomorphology. In: Raper, J. (Ed.), Three-dimensional Applications in Geographical Information Systems. Taylor & Francis, London, pp. 51–77.

GEOMORPHOMETRY 2020 PERUGIA, ITALY JUNE 22 - 26 2020

Burial mound detection using geomorphometry and statistical methods: pixels versus objects

Mihai Niculiță[§]
Department of Geography
Alexandru Ioan Cuza University of Iași
Caro II 20A, 700505 Iași, Romania
[§] mihai.niculita@uaic.ro

Abstract—**Burial mound detection on high resolution data is a practical aspect of geomorphometry that has recently been in the focus of various researchers. Considering two of the best rated approaches in the literature, one based on a pixel approach and the other based on an object approach, a comparison was performed between the results of the two applied for a study area in North-Eastern Romania. The conclusion is that classification is slightly better in the case of the object-based approach in terms of confusion matrix, and much better in terms of false positive results, that need to be checked in order to separate the true positive cases. The object-based approach performs much better due to the reduction of feature space and the ability of the Random Forest algorithm to identify the geomorphometric signature of the burial mounds.**

I. Introduction

In a previous research [1] burial mounds were detected using a three stages approach: a system of surface specific points, a segmentation approach and Random Forest classification using geomorphometric variables and shape descriptors. The proposed method obtained the second-best results in the literature regarding the confusion matrix [2]. The method that is rated as the first [3] used a multi-scale geomorphometric variable and Random Forest classifier trained on that variable to classify pixels as burial mound or not burial mound. Beside the fact that is pixel based, this methodology was not tested enough to convince that actually is the best: there was no exterior validation and the confusion matrix was computed based on pixels which gives biased measures since the classes are very imbalanced. We believe that actually if applied to a wide area, the number of false positives will be quite high, since any dominant position revealed by this index will be identified.

Classification problems assessed from a statistical point of view were shown to have multiple pitfalls [4], while multiple approaches for dealing with this were proposed [5-7]. While these results are not in the geoscience field, their conclusion is transferable since the machine learning methods are not different. Beside the normalization, multicollinearity and outlier removal, very often variable selection is an important approach. Cross-validation and bootstrapping are good methods for testing the improvement on the model for every variable, but biased results can be obtained if this is performed over the training data, the use of external data being proposed as an alternative approach [5,4]. Very few classifications from geosciences validate both internally and externally, regression or classification predictive models.

If for regression approaches the prediction power is assessed using various approaches (RMSE or AUROC), in classification problems the overall measures of confusion matrix like accuracy or even sensitivity can be inflated, if large number of false positives are present. It was shown that for Random Forest (RF) even importance measures are biased [8], situation that was found also in the object-based burial mound delineation previously [1].

In the present research I have considered the study case presented in [1], with two study areas of the same size and in proximity of each other (the two study areas are available in high-resolution images at https://doi.org/10.6084/m9.figshare.11798517.v2 and https://doi.org/10.6084/m9.figshare.11798613.v2), reflecting similar physiographic condition and archaeologic setting. The results obtained in [1] with geomorphometric objects segmented from local convexity and filtered by peak and seed presence are compared with a pixel-based approach implemented in this study.

While the final objective of the research is to find which method is better at identifying burial mounds from a certain area based on their geomorphometric signature, there are some details that need to be clarified in the case of pixel-based approach. The object-based approach has the advantage that the result is an object that can be easily assessed as burial mound or not based on a validation dataset of existing burial mounds, or if a user will browse the predicted objects. For the pixel-based approach since the number of predicted pixels is large, two approaches can be used: a quadtree search through which pixels clusters of predicted burial mound class are evaluated or the browsing of the spatial clusters of pixels with the burial mound class predicted. The

Mihai Niculita (2020) Burial mound detection using geomorphometry and statistical methods: pixels versus objects:
in Massimiliano Alvioli, Ivan Marchesini, Laura Melelli & Peter Guth, eds., Proceedings of the Geomorphometry 2020 Conference, doi:10.30437/GEOMORPHOMETRY2020_7.

quadtree approach is too expensive in terms of time, so the spatial clusters approach chosen as the best way to validate.

II. METHODS

Iterative tuning of the RF parameters and variables was performed in R software [9]. Rather than starting with parameter tuning, which is inexpensive from a computational point of view, training dataset setting selection was performed first. Then, variable selection was performed, and finally RF parameter tuning was realized.

In the literature, the training and validation can be performed both internally (intra-domain) and externally (extra-domain) [10], by using various proportions of class membership and training/validation ratios. In the present study latin hypercube sampling [11,12] was used to select the training dataset with the clhs package [13]. 75% percent of the burial mound (BM) pixels from the northern study area were used for training with a various number of non-burial mound (NBM) pixels: 13302, 43302 and 93302 (Figure 1) to model the class imbalance. Since if the number of burial pixels is decreased under 75% the fitted models performance degrades too much, values under this threshold were not considered. The 28 geomorphometric variables used by [1] (listed in Table S1 from the supplementary files) were used for selection based on the results of the prediction confusion matrix on the southern study area (external validation). The variables were evaluated both as single predictors (to assess the best performing variable), but also by bootstrapping to select the best prediction set of variables.

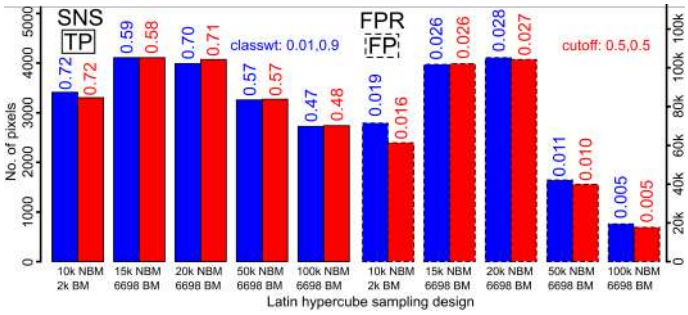

Figure 1. True positives and false positives and their confusion matrix measures for various settings of the latin hypercube sampling (SNS is sensitivity, FPR is false positive rate) and RF imbalance (blue is imbalanced, red is not).

For the selection of spatial clusters of predicted burial mounds, first single predicted burial mound pixels were excluded, then the prediction raster was converted to a polygon vector.

III. RESULTS AND DISCUSSIONS

The pixel-based approach is performing worse than the object-based approach both in terms of true positives (sensitivity) and false positives (false positive rate) for any setting of variables (Figures 1 and 2, Table 1). The main issue in the pixel-based approach scenario is related to the large number of false positives (Figures 3 and 4). Only by increasing this number to approx. 75% of the pixel candidates, the sensitivity (SNS) reach a reasonable value, similar with the object-based approach. But these results might be misleading, since the true validation should be done on how these predicted pixels characterize the burial mound sites.

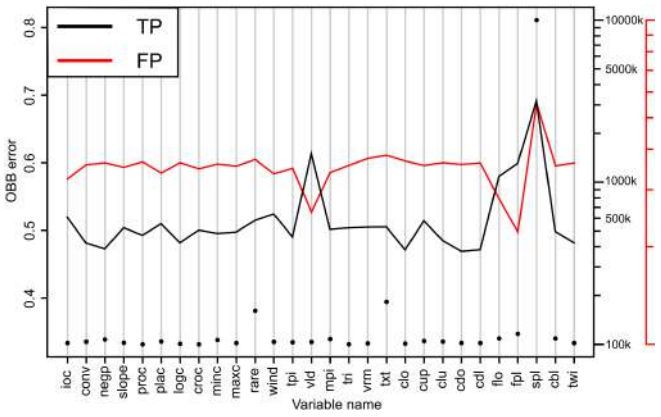

Figure 2. The OBB error (black points), true (TP) and false (FP) positive pixels (lines) for single RF models fitted with a single geomorphometric variable (the codes correspond to the Table S1 supplementary files of [1]).

TABLE I. CONFUSION MATRIX AND ITS MEASURES FOR THE OBJECT-BASED APPROACH OF [1] FOR THE SOUTHERN STUDY AREA (FIRST ROW) AND THE PIXEL-BASED APPROACH (SECOND ROW)

RF parameters	OBB error	TP	FP	SNS	FPR
1000 segments from which 75% burial mounds, 100 ntree, 5 mtry, 1 nodesize	3.1	25	46	0.93	0.004
15000 pixels from which 6698 burial mounds, 100 ntree, 3 mtry, 1 nodesize	0.08	4109	101763	0.72	0.026

If the validation is performed in a small area where the burial mound density is high, very high SNS and FPR could be achieved, which is what [3] have done. But the validation needs to be achieved globally, for the training dataset (the northern study area – intra-domain) and for the validation dataset (the southern study area – extra-domain). A first approach could be the evaluation of how many pixels predicted as burial mounds were identified for every delineated burial mound. This analysis show that the

majority of the burial mounds, both for the northern and the southern study areas have predicted burial mound pixels for over than 50% of their surface.

The second approach is to check if the predicted burial mound pixels are spatially clustered, so that the high number of false positive pixels can reach a reasonable amount, that allow the manual checking by an expert, in order to find all the burial mound sites.

Unfortunately, this result is not possible to be applied. If the spatial clusters are allowed to have more than 20 pixels, which is the smallest number of pixels that fit a delineated burial mound, five burial mounds for the northern study area will be missed. These results are showing that some burial mounds overlay only a small number of pixels predicted as burial mounds.

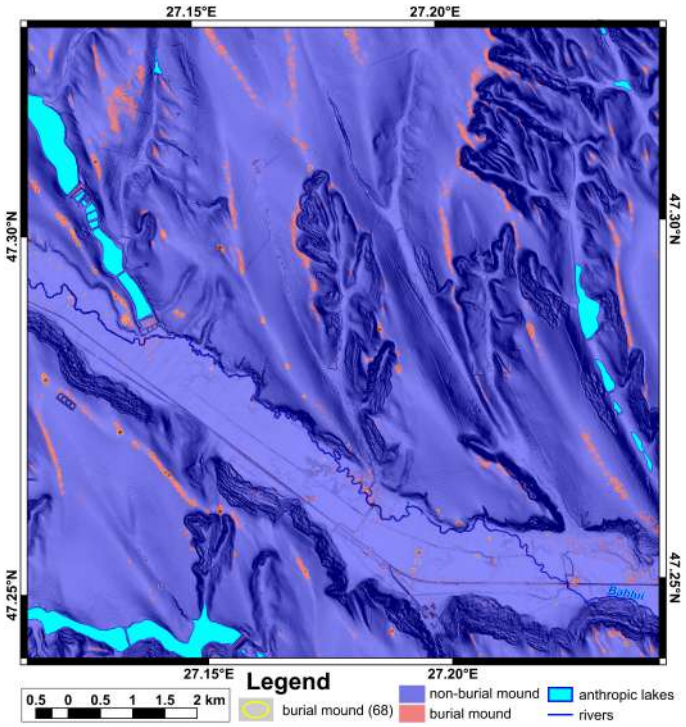

Figure 3. The results of the pixel-based approach for the northern study area (a high-resolution version is available at https://doi.org/10.6084/m9.figshare.11853564.v1).

For the southern study area, the results are better, all the 29 burial mounds having more than 20 pixels predicted. But, the number of these spatial clusters is still higher than the false positives obtained through the object-based approach.

For the northern study area 8592 clusters are obtained, while for the southern study area 9838 are obtained. The object-based approach of [1] obtained only 52 and 46 respectively.

Another observation is that sometimes the spatial clusters are very big or too small, situation that can hinder the manual or the semi-automatic verification of the predicted burial mound potential areas (Fig. 5).

IV. Conclusions

In conclusion, I have shown that the object-based approach performs better than the pixel-based approach, both in terms of confusion matrix measures and in practical validation. The explanation of the superiority of the object-based approach is given by its power of feature space reduction, spatial aggregation and the usability of shape descriptors in the RF model. In this way the RF algorithm is able to find the geomorphometric signature of the burial-mound segments.

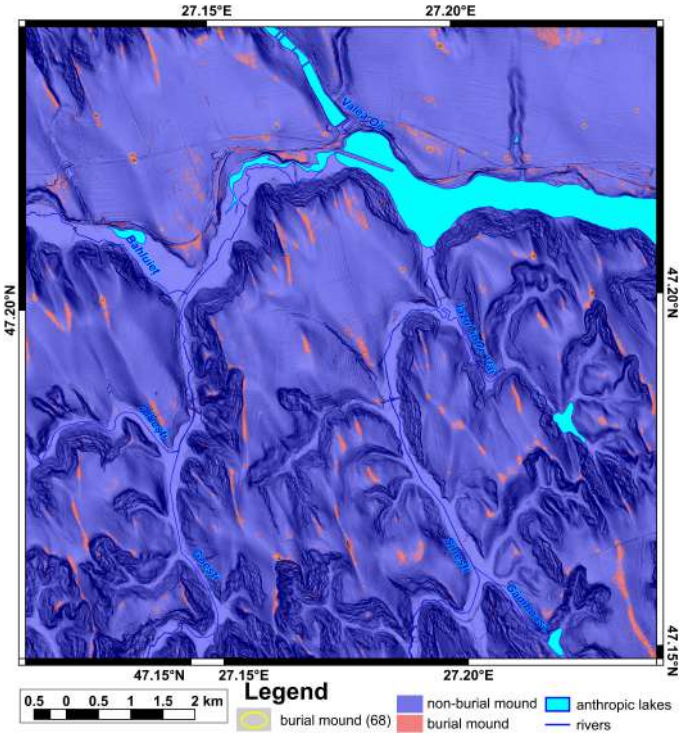

Figure 4. The results of the pixel-based approach for the southern study area (a high-resolution version is available at https://doi.org/10.6084/m9.figshare.11853570).

Because the classification problem is an imbalanced one, a certain amount of false positive cases is found, that need to be

checked by an operator, in order to identify the burial mound sites. In the case of object-based approach the number of false positive segments is low enough to allow this check, while for the pixel-based approach the number is not reasonable enough.

ACKNOWLEDGMENTS

This work was supported by a grant of the "Alexandru Ioan Cuza" University of Iași, within the Research Grants program, Grant UAIC, code GI-UAIC-2017-07. I am grateful to Prut-Bârlad Water Administration who provided me the LIDAR data.

REFERENCES

[1] Niculiță, M. 2020. "Geomorphometric Methods for Burial Mound Recognition and Extraction from High Resolution LiDAR DEMs". Sensors 20(4), 1192.

[2] Trier, Ø. D., Cowley, D. C., Waldeland, A. U. 2018. "Using deep neural networks on airborne laser scanning data: Results from a case study of semi-automatic mapping of archaeological topography on Arran, Scotland". Archaeological Prospection 26 (2), 165-175.

[3] Guyot, A., Hubert-Moy, L., Lorho, T. 2018. "Detecting Neolithic Burial Mounds from LiDAR-Derived Elevation Data Using a Multi-Scale Approach and Machine Learning Techniques". Remote Sensing 10 (2), 225.

[4] Simon, R., Radmacher, M.D., Dobbin, K., McShane, L. M. 2003. "Pitfalls in the use of DNA microarray data for diagnostic and prognostic classification". J Natl Cancer Inst 95 (1), 14-18.

[5] Ambroise, C., McLachlan, G. J. 2002. "Selection bias in gene extraction on the basis of microarray gene-expression data". Proc Natl Acad Sci U S A 99 (10), 6562-6566.

[6] Diaz-Uriarte, R., Alvarez de Andres, S. 2006. "Gene selection and classification of microarray data using random forest". BMC Bioinformatics 7 3.

[7] Blanquero, R., Carrizosa, E., Jiménez-Cordero, A., Martín-Barragán, B. 2019. "Variable selection in classification for multivariate functional data". Information Sciences 481, 445-462.

[8] Strobl, C., Boulesteix, A. L., Zeileis, A., Hothorn, T. 2007. "Bias in random forest variable importance measures: illustrations, sources and a solution". BMC Bioinformatics 8, 25.

[9] R Team 2019. "R: A language and environment for statistical computing". version 3.6.2 edn. R Foundation for Statistical Computing, Vienna, Austria.

[10] Brenning, A. 2005. "Spatial prediction models for landslide hazards: review, comparison and evaluation". Natural Hazards and Earth System Science 5 (6), 853-862.

[11] Minasny, B., McBratney, A. B. 2006. "A conditioned Latin hypercube method for sampling in the presence of ancillary information". Computers & Geosciences 32 (9), 1378-1388.

[12] Roudier, P., Beaudette, D. E., Hewitt, A. E. 2012. "A conditioned Latin hypercube sampling algorithm incorporating operational constraints". In: Minasny B, Malone BP, McBratney AB (eds) Digital Soil Assessments and Beyond: Proceedings of the 5th Global Workshop on Digital Soil Mapping, Sydney, Australia, 2012, CRC Press, pp 1-6.

[13] Roudier, P., Brugnard, C., Beaudette, D., Louis, B. 2019. "clhs: Conditioned Latin Hypercube Sampling". version 0.7-2 edn. R package.

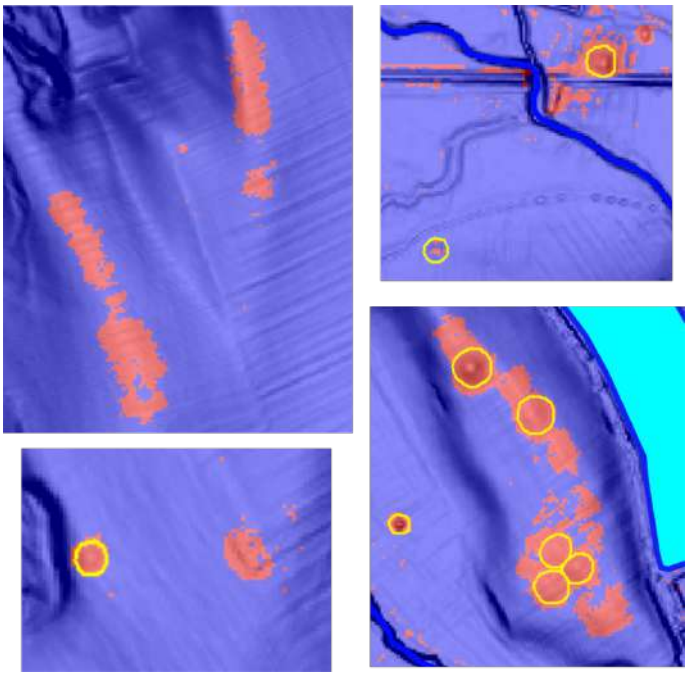

Figure 5. The results of the pixel-based approach for several situations: top left – false positive pixels with clear spatial clusters; top right – true positive pixels with spatial clustered and non-clustered false positives; bottom left – spatial cluster of true positive pixels for a well delineated burial mound and a false positive spatial cluster; bottom right – true positive and false positive spatial clusters of pixels in an area with high burial mound density (the legend is similar with Fig. 3).

GEOMORPHOMETRY 2020 PERUGIA, ITALY JUNE 22 - 26 2020

Generalization of DEM looking for hierarchic levels of landforms in the land surface segmentation process.

Anton Popov, Jozef Minár
Department of Physical Geography and Geoecology,
Comenius University in Bratislava, Slovakia
popov3@uniba.sk
Michal Gallay
Institute of Geography
Pavol Jozef Šafárik University in Košice, Slovakia

Abstract— **High-resolution digital elevation models (DEMs) need to be generalized before a land surface segmentation is applied. A measure of the quality of segmentation can reflect the usefulness of the generalization. We developed a method to evaluate a quality of results of multiresolution segmentation (MRS). The method was implemented in geographic object-based image analysis (GEOBIA). We tested a dependence of local variance (LV) on a number of resultant objects, generalization level and coincidence of segmentation with real landforms. The last was tested using a hypothesis, that an index of concentration of values of curvature change around zero (K_0) reflects an optimal DEM generalization. Estimation of scale parameter by ESP 2 tool and DEM generalization using polynomial approximation in increasing window, was used. Altitude, slope, aspect, profile and plan curvatures were used as the input variables. Results from the two areas with a different type of land surface show a clear dependence of local variance on generalization level, and partially confirm the suitability of the K_0 index for determination of optimal generalization.**

I. INTRODUCTION

High-Resolution DEMs enabled detection of landforms of different orders: From the simplest forms (elementary forms) to complex forms (landforms, land systems) [1]. However, such DEMs contain noise and elevation uncertainty leading to incorrectness in landform delineation. A task of looking for an appropriate measure of generalization that follows a method of landform mapping is crucial in this aspect. The concept of elementary forms, developed for detailed geomorphological mapping [1], is used in our study.

II. THEORETICAL BACKGROUND

Generalization

In general, elementary forms can be defined as "landform elements with a constant value of altitude or two or more readily interpretable morphometric variables, bounded by lines of discontinuity" [1]. Later, in ref. [2] was proposed a quantile – based index of concentration of derivatives of altitude around zero (K_0) as a measure of the affinity of real land surface to set of elementary forms:

$$K_0 = \frac{\tilde{x}_{95} - \tilde{x}_5}{\tilde{x}_{0+5} - \tilde{x}_{0-5}}$$

where $\tilde{x}_{95}$ and $\tilde{x}_5$ are percentiles representing the spread of the set without extreme values and $\tilde{x}_{0+5}$ and $\tilde{x}_{0-5}$ represent the fifth percentiles on the right and on the left from the zero value [2].

If the affinity to constant value of various geomorphometric variables exists, K_0 index should rise with variable (derivative) order. For the first, second and third derivative of altitude in the direction of slope line, the K_0 index increases up to the third-order much more for real surface than for various mathematical models. Thus it confirms the affinity of altitude, slope and profile curvature to constant values [2].

The computation of change of curvature is the first step to K_0 determination. Upgrading the least squares method applied on a polynomial function [3], dynamic last squares method (DLS) was suggested by [4] for the third-order geomorphometic variables computation. To achieve an optimal relation between method and data error, flexible window size and polynomial order were used. Generalization of the land surface is a side effect of such computation [4]. The method allows generalize a DEM in two ways: extending either number of computational points (window size), or by increment of polynomial order. In both cases it is supposed to detect a nested hierarchy of elementary forms by peak values of concentration around zero (K_0) index.

Segmentation

One of the most popular approaches of a land surface segmentation is Object-Based Image Analysis (OBIA). OBIA targets on the maximization of internal homogeneity within an image object and external contrast, which are fundamental properties of elementary forms. Average heterogeneity of segments within a scene defines the local variance (LV). LV is calculated as the average standard deviation of all input variables for all objects. LV depends on (fig. 2): i) Number of objects (1),

Anton Popov, Jozef Minír, Michal Gallay (2020) Generalization of DEM looking for hierarchic levels of landforms in the land surface segmentation process.:
in Massimiliano Alvioli, Ivan Marchesini, Laura Melelli & Peter Guth, eds., Proceedings of the Geomorphometry 2020 Conference, doi:10.30437/GEOMORPHOMETRY2020_8.

consequently, LV increase with the number of delimitated objects; ii) Window size (WS) (2), a measure of generalization, that increases with WS; iii) Coincidence of segmentation with real landforms (3), that is investigated in this work.

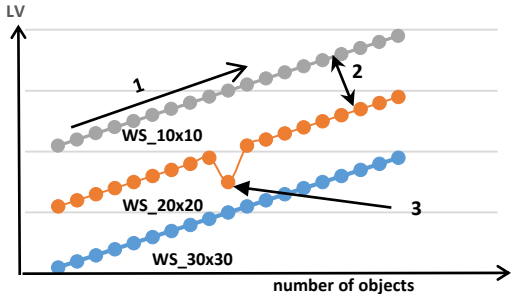

Figure 2. Schematic interpretation of Local Variance. From Upper line to the bottom 10x10, 20x20,30x30 cells window sizes (WS)

Estimation of Scale parameter (ESP) tool was proposed in [7] to substitute the frequently used method of trial and error for determination of optimal SP.

III. MATERIAL AND METHODS

The first test area with hilly topography, Slovinec (9.36 ha), is located on the boundary of the Carpathians and the Vienna basin (fig. 3A). The DEM of Slovinec was derived by digital aerial photogrammetry with pixel size 2x2 meters. The second area, Silica (222.7 ha), comprises karst plateaus with sinkholes and uvala (fig. 3B). The DEM of the area was generated from airborne laser scanning (ALS) data with original 1x1 m cell size, resampled to 2x2 m cell size [10].

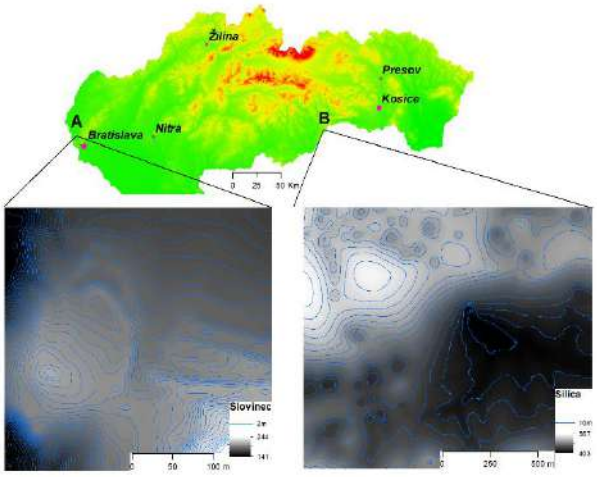

Figure 3. Locations of the test areas in the Slovakia. A– Slovinec, B – Silica

We tested whether generalizations with maximal K_0 values of change of profile curvature (G_{nn}), generally lead to optimal land surface segmentation in areas of interest. It was decided to use fix polynomial function of 4th order with changing window size to find optimal generalization levels for elementary forms mapping.

We suppose that LV can be used as a measure of the quality of segmentation processes over various generalization levels of DEM and so confirm or refuse K_0 index utility for DEM generalization. To achieve this goal, the influence of DEM generalization and number of land surface segments on LV was investigated first.

IV. RESULTS

Graphs of dependence K_0 on window size (Fig. 4) show distinct local maxima (green) that should identify generalization levels the most suitable for the segmentation.

Beside local maximums of K_0 values we also tested local minimums values to compare results and to test a hypothesis of K_0 as the generalization criterion. For Silica was chosen one absolute maximum (window size 43) and two minimums (window size 5 and 145). For the Slovinec area we chose most distinct local maximums (window size 5, 61, 91) and local minimum values according to their affiliation to the maximums, i.e. (window size 27 most distinct to WS 5 max, 43 to 61, 107 to 91 and127 as the absolute minimum).

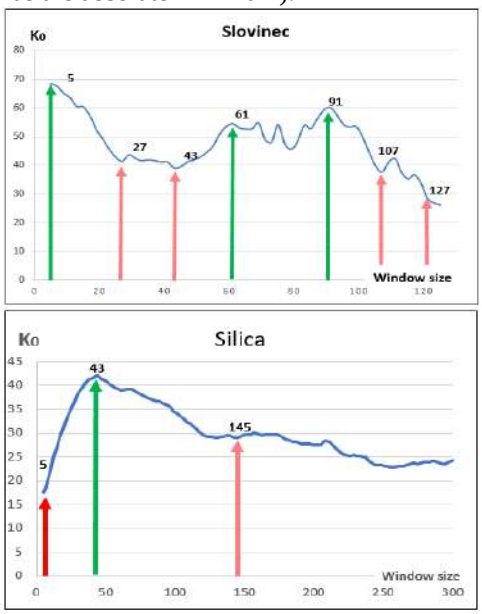

Figure 4. Dependence of K_0 of G_{nn} on the window size for areas of interest. Green arrows pointed to local maximums, red ones – local minimums of K_0 values.

For each area and generalization level (represented by the window size) was undertaken a multiresolution segmentation using ESP2 tool with step sizes 1 to 20, and calculated average segment area (ASA, hectares) for each segmentation. To avoid distortions of results, repeating values were eliminated. 54 of such segmentations was done for the Slovinec territory (fig. 5, A).

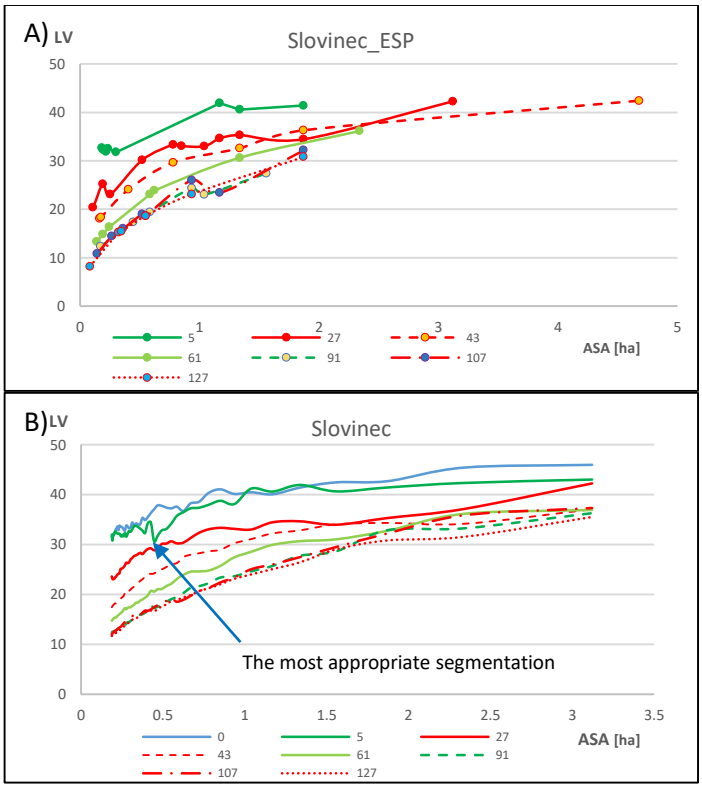

Figure 5. Dependence of local variance (LV) on average segment area (ASA, ha), for different window sizes; A) using ESP2 tool, B) with constant increment of object number. Green – local maximums, red – local minimums of $G_{nn} - K_0$ values. Slovinec territory.

The graph shows clear decrease of LV with increment of the generalization level. However, dependence of LV on ASA for high generalization levels (WS 91, 107,127) is (mainly for range 0.1 – 1 ha) practically same. It can be explained by an "overgeneralization" in these cases. Another multiresolution segmentation was done without ESP2 tool to trace a behavior of LV with constant increment of object number (fig. 5, B). At WS 5 it is clearly seen an abrupt decline of LV that after the hypothesis points to the best segmentation.

In the Silica area the same procedure was done. Graph of dependence LV on ASA (fig. 6) do not shows general decrease of LV with generalization levels. LV values for WS 43 sharply increase from ASA 0.41 to 1.51, then stabilize at the values of LV 30 – 36 and last two levels (WS 5 and 145) are parallel. It can be an evidence of absence of a hierarchic levels of elementary forms in this size diapason.

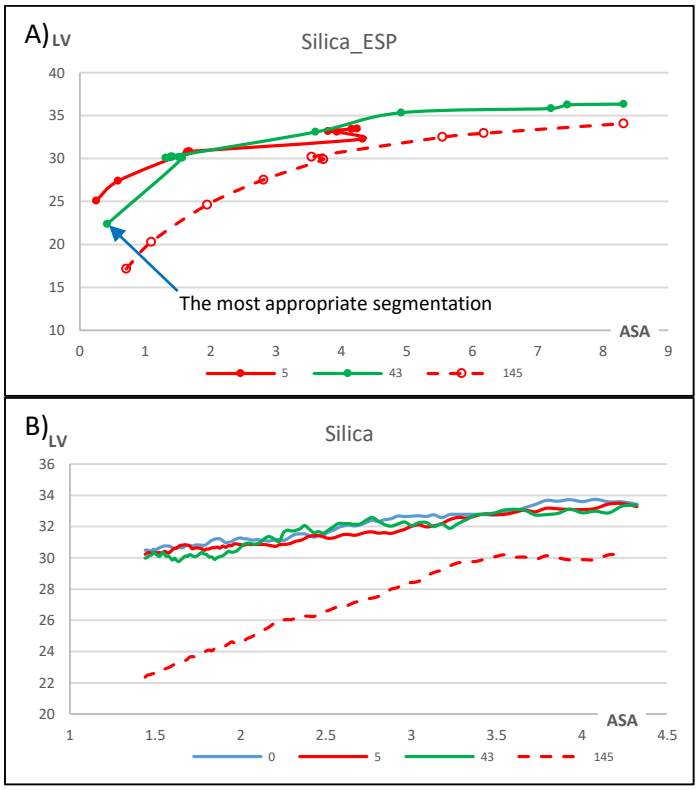

Figure 6. Dependence of local variance (LV) on average segment area (ASA, ha), for different window sizes; A) using ESP2 tool, B) with constant increment of object number. Green – local maximums, red – local minimums of $G_{nn} - K_0$ values. Silica territory.

The best results of segmentation on WS 43 are for ASA = 0.25 ha, that could be considered as a partial confirmation of $G_{nn} - K_0$ hypothesis. The rest of the data does not show any meaningful results. The LV dependence on the number of objects (fig. 6, B) also shows decreasing trend of LV with generalization levels. WS 43 has no clear decline of LV in comparison with the original data and WS 5, while WS 145 is distributed aside of the rest of the data, which could point to catch bigger landforms by this generalization level.

V. DISCUSSION AND CONCLUSIONS

The results partially confirm the suitability of K_0 index for the Slovinec area. However, the algorithm does not work perfectly for all of the generalization levels, as was shown at the area of Silica. It can probably point to overmuch simplification of theoretical assumption. Suitability of generalization level with a maximal value of K_0 index for elementary land surface segmentation results from the following assumption: Elementary forms with affinity to the constant value of normal change of gradient change (G_{nn}) and its parents' variable (normal gradient change - G_n and slope gradient G) make the significant part of the area. It is probably not true for the Silica territory. One of the most appropriate ways to find optimal generalization for land surface segmentation is to use a more complex criterion (criteria) for selecting a suitable window size or polynomial order in the framework of approximation by DLS method. The new index should include optimization of the generalization not only in the slope gradient (normal) direction, but also in the orthogonal (tangential) direction, as these are the directions used to define slope aspect, plan and tangential curvatures. A substitution of used DEM generalization by more sophisticated method, e.g. by the widely used wavelet transform [11] can also leads to a progress.

In conclusion, the hypothesis about suitability of the DEM generalization using minimization of concentration of change of gradient change (G_{nn}) around zero (K_0 coefficient minimization) [3] was partially confirmed. The method developed for evaluation of resultant quality of GEOBIA land surface segmentation shows potential to become widely applicable for finding appropriate level of DEM generalization in the task of detection hierarchy of real landforms. The method can be not only instrumental to distinguish the most suitable generalization of a DEM but it can also serve as a general tool for evaluation of effectiveness in using various input variables or variants of the segmentation procedure.

VI. ACKNOWLEDGMENTS

This work was supported by the Slovak Research and Development Agency under contract APVV-15-0054 and by Grant for young scientists of Comenius University UK/413/2019.

REFERENCES

[1] Minár, Jozef and Ian S. Evans. 2008. "Elementary Forms for Land Surface Segmentation: The Theoretical Basis of Terrain Analysis and Geomorphological Mapping." Geomorphology 95(3–4):236–59.

[2] Minár, Jozef et al. 2013. "Third-Order Geomorphometric Variables (Derivatives): Definition, Computation and Utilization of Changes of Curvatures." International Journal of Geographical Information Science 27(7):1381–1402.

[3] Florinsky, I.V., 2009. Computation of the third-order partial derivatives and derivation function from a digital elevation model. International Journal of Geographical Information Science, 23 (2), 213–231.

[4] Minar, J., J. Minár Jr. and I.S. Evans, 2015. "Towards exactness in geomorphometry". In Geomorphometry 2015 Conference Proceedings, Edited by: Jasiewicz, J., Zwoliński, Z., Mitasova, H. and T. Hengl, Adam Mickiewicz University in Poznań, Poland.

[4] Blaschke, T., Strobl, J. 2001. What's wrong with pixels? Some recent developments interfacing remote sensing and GIS. GIS–Zeitschrift für Geoinformationssysteme, vol 14, 6, pp. 12–17.

[5] Hay, G. J., Castilla, G. 2008. Geographic Object-Based Image Analysis (GEOBIA): A new name for a new discipline. In: Blaschke, T., Lang, S., Hay, G. J. (eds.), Object-Based Image Analysis: Spatial Concepts for Knowledge-Driven Remote Sensing Applications, Berlin, Springer, pp. 75–89.

[6] Blaschke, T., Hay, G. J., Kelly, M., Lang, S., Hofmann, P., Addink, E., Queiroz Feitosa, R., Van Der Meer, F., Van Der Werff, H., Van Coillie F., Tiede, D. 2014. Geographic Object-Based Image Analysis - Towards a new paradigm. ISPRS Journal of Photogrammetry and Remote Sensing, vol. 87, 100, pp. 180–191.

[7] Drăguţ, Lucian, Dirk Tiede, and Shaun R. Levick. 2010. "ESP: A Tool to Estimate Scale Parameter for Multiresolution Image Segmentation of Remotely Sensed Data." International Journal of Geographical Information Science 24(6):859–71.

[8] Woodcock, Curtis E. and Strahler Alan H. 1987. "The Factor of Scale in Remote-Sensing." Remote Sensing of Environment 21(3):311–32.

[9] Drăguţ, L., O. Csillik, C. Eisank, and D. Tiede. 2014. "Automated Parameterisation for Multi-Scale Image Segmentation on Multiple Layers." ISPRS Journal of Photogrammetry and Remote Sensing 88:119–27.

[10] Hofierka J., Gallay M., Bandura P., and Šašak J.. 2018. "Identification of Karst Sinkholes in a Forested Karst Landscape Using Airborne Laser Scanning Data and Water Flow Analysis." Geomorphology 308:265–77.

[11] Kalbermatten, M., Van De Ville D., Turberg P.,Tuia D.,Joost S. 2012. "Multiscale Analysis of Geomorphological and Geological Features in High Resolution Digital Elevation Models Using the Wavelet Transform." Geomorphology 138(1):352–63.

GEOMORPHOMETRY 2020 PERUGIA, ITALY JUNE 22 - 26 2020

A case-based classification strategy of automatically selecting terrain covariates for modeling geographic variable–environment relationship

Cheng-Zhi Qin[§], Peng Liang
State Key Laboratory of Resources and Environmental Information System, Institute of Geographic Sciences and Natural Resources Research, CAS
Beijing, China
[§] qincz@lreis.ac.cn

A-Xing Zhu
Jiangsu Center for Collaborative Innovation in Geographical Information Resource Development and Application and School of Geography
Nanjing Normal University
Nanjing, China

Department of Geography
University of Wisconsin-Madison
Madison, Wisconsin, USA

Abstract—**It is valuable for modelers (especially those non-experts) in real applications to automatically select a proper set of terrain covariates for modeling the relationship between a geographic variable (phenomenon) and its environment, which is the basis for many predictive mapping of geographic variables (such as soil properties, landslide susceptibility, and species habitat suitability). For this aim, in this study we propose a case-based classification strategy which is designed based on two considerations. The first is that the cases created from existing predictive mapping applications with terrain covariates determined by experts would contain the implicit and non-systematic knowledge on selecting covariates according to specific application contexts. The second is that a binary classifier for each of terrain covariate candidates can be trained by the cases collected in advance and then be applied to a new application for automatically determining if the corresponding covariate should be selected or not for the new application. The proposed strategy can relieve users' burden on using traditional statistical methods of selecting terrain covariates for mapping in a study area, i.e., collecting a large number of samples in the study area in advance, and preparing dataset of all terrain covariate candidates of the study area. Two methods based on the proposed strategy were implemented, i.e., the random forests (RF) method, and the logistic regression (LR) method. With the application domain of digital soil mapping (DSM), we built a case base containing 191 DSM cases which totally use 38 terrain covariates, and then conducted a leave-one-out experiment for evaluation. Experimental results show that RF with the proposed strategy performed better.**

I. INTRODUCTION

Spatial distribution of geographical variables (phenomena; such as soil properties, landslide susceptibility, and species habitat suitability) is estimated increasingly by predictive mapping through modeling the relationship between geographical variables and environmental covariates [1]. Among those environmental covariates, terrain covariates are those mostly used (even exclusively used) [2,3], due to not only the substantial relationship between geographical variables and terrain [1] but also the high availability of digital elevation model (DEM) data for deriving diverse terrain covariates [4].

Selection of a proper set of terrain covariates is crucial for building a reliable model for depicting a geographic variate–environment relationship. Ignorance of important terrain covariate(s) will obviously impact the reliability of the built model of the relationship. Besides, inclusion of unnecessary terrain covariates may introduce errors to the model result.

For modelers of predictive mapping (especially those non-experts), it is still a challenge to select a proper set of terrain covariates for real applications. The selection of proper terrain

Cheng-Zhi Qin, Peng Liang,A-Xing Zhu (2020) A case-based classification strategy of automatically selecting terrain covariates for building geographic variable-environment relationship: in Massimiliano Alvioli, Ivan Marchesini, Laura Melelli & Peter Guth, eds., Proceedings of the Geomorphometry 2020 Conference, doi:10.30437/GEOMORPHOMETRY2020_9.

covariates highly depends on the domain knowledge related to the application context (such as the target of predictive mapping, geographic characteristics of study area, and data resolution), while nowadays so many topographic attributes are candidates of terrain covariates [2,4]. Such application context knowledge, although crucial in modeling, is often implicit, non-systematic, and hard to be presented in a clear form (such as rules) for modelers [4,5].

Currently there still has no effective method of automatically selecting a proper set of terrain covariates for predictive mapping, so to lower the burden of modelers. Some statistical methods have been designed to select terrain covariates for predictive mapping [6-9]. However, they need modelers to collect a large number of samples in the application area in advance, and to prepare dataset of all candidates of terrain covariates of the area. Then it could be tested if each individual of terrain covariate candidates is statistically related to the geographical variable of predictive mapping. Such requirements of using these statistical methods are heavy burden on modelers and often unpractical in real applications. Thus the statistical methods are with limited applicability and also hard to be automated.

In this study we propose a case-based classification strategy of automatically selecting terrain covariates for modeling geographic phenomenon–environment relationship. Two methods are designed based on the proposed strategy and evaluated based on an experiment of selecting terrain covariates for digital soil mapping (DSM).

II. METHODS

The case-based classification strategy is proposed based on two considerations. The first is that the cases created from existing applications with terrain covariates determined by experts would contain the application context knowledge on selecting terrain covariates. Artificial intelligent domain provides "case" as a suitable way to formalizing the prior and non-systematic knowledge [10]. Case-based method has been primarily explored in digital terrain analysis [5] and showed promising performance in using application context knowledge to support automatic modeling. The second consideration is that a binary classifier for each individual of terrain covariate candidates can be trained by the collected cases in advance and then be applied to a new application. Then it could be automatically determined if the corresponding covariate should be selected for the new application [11]. Unlike those existing statistical methods of selecting terrain covariates, the proposed strategy need neither collecting a large number of samples in the study area of the new application, nor preparing the dataset of all candidates of terrain covariates in the study area. Both the training process and applying process of the proposed strategy can be automated, once the case base was built. Therefore, the proposed strategy should be reasonable and practical for automatically selecting a proper set of terrain covariates for predictive mapping.

A. Case formalization

Similar to the normal design of cases, a case which records an existing applications with terrain covariates determined by experts is designed as two parts, i.e., the problem part, and the solution part. The problem part of a case describes the application context information of the case. In this study, the target of predictive mapping, geographic characteristics of application area, and data resolution are recorded in the case problem part. Specifically, the geographic characteristics of application area are described by two factors (i.e., the area size, and the terrain complexity of the application area) and further formalized as four quantitative attributes (i.e., the size of application area, the total relief, the standard deviation of elevation, and the mean slope of the application area) [5,11].

In this study, the solution part of a case records those terrain covariates adopted by the corresponding application case.

According to above-designed case formalization, a case base could be built through collecting and formalizing existing applications with terrain covariates determined by experts. These existing applications could be collected from scientific publications and open technical reports of real applications of predictive mapping.

B. Binary classification methods

Above-built case base can be used to train a binary classifier for each terrain covariate appearing in the solution part of cases in the case base. The input features of the classifiers are attribute values of the case problem part. The output of each classifier is a Boolean value, that is, whether the corresponding terrain covariate should be selected for modeling the geographical variate–environment relationship under the input features (i.e., the application context of the case). Then, such classifiers trained for each terrain covariates can be used to automatically select terrain covariates for a new application case, according to the problem part of the new case.

In current study we consider two popular binary classification methods, i.e., the random forests (RF) method, and the logistic regression (LR) method. RF [12] is a typical ensemble machine learning method widely used for classification. Its advantages include noise resistance, working well on imbalanced data, and free of variable distribution [12]. It has been proposed for the case-based strategy of automatically selecting of terrain covariates [11].

LR is a generalized linear model for classification, which can produce the probability of classification and require no assumption on the data distribution. LR could be potentially available for the proposed strategy in this study.

III. EXPERIMENT

Above-presented two methods with the proposed strategy were evaluated through an experiment of selecting terrain covariates for digital soil mapping (DSM). DSM is often conducted by modeling the soil–environment relationship for a study area, in which terrain covariates are mostly used and even exclusively used [3]. While results from RF with the proposed strategy was recently published in Ref. [11], this study focuses on comparison between RF and LR with the proposed strategy.

A. Case base of DSM

In this experiment we adopted a DSM case base built in Ref. [11]. The DSM case base contains 191 cases spread around the world (Figure 1), which were collected from the scientific papers published in DSM-related journals in recent years. A total of 38 terrain covariates appear in the case base. Details of the case base are referred to Ref. [11].

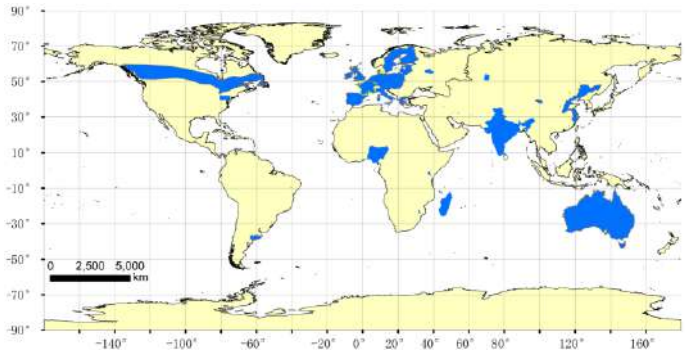

Figure 1. Map of DSM cases.

B. Experimental design

A leave-one-out experiment was designed to evaluate the performance of the two methods with the proposed strategy.

A so-called Novice method was also test as a reference method for comparison with the proposed methods. The Novice method simulates a normal way of selecting covariates by novices, that is, adopting those terrain covariates which were most frequently appeared in the case base, according to the count of covariates adopted in the original solution (i.e., the solution part) of an evaluation case [11].

Three quantitative evaluation indices widely used for classification accuracy evaluation were calculated for the results from the tested methods when applying to a new application case (i.e., evaluation case) in the leave-one-out experiment.

$$recall = \frac{TP}{TP + FN} \quad (1)$$

$$precision = \frac{TP}{TP + FP} \quad (2)$$

$$F1\text{-}score = \frac{2 * (precision * recall)}{precision + recall} \quad (3)$$

where *TP*, *FN*, and *FP* mean True Positives, False Negatives, and False Positives, respectively. The *recall* index is the ratio of covariates selected correctly by the method under test to those covariates adopted in the original solution of the evaluation case. The *precision* index is the ratio of covariates correctly selected by the method under test to those covariates selected out by the method. The *F1-score* ranges from 0 (the worst performance) to 1 (the best performance).

Mean and standard deviation (Std.) of these three evaluation indices were calculated for comparing the performance of the methods under test.

C. Experimental results

Table 1 shows that RF with the proposed strategy performed best. RF correctly selected most of covariates for evaluation cases, and meanwhile selected less covariates which were not in the original solution of evaluation cases. Although LR with the proposed strategy performed better than the Novice method according to the *precision* index, LR performed worst according to the *recall* index and *F1-score* index. By comparison, LR often selected less covariates for evaluation cases, which resulted in lower values of *recall* index. Note that the imbalance among frequency of individual covariates appeared in the case base plays a challenge on the classification methods, RF showed its advantage of working well on imbalance data, while LR performed poorly on current limited case base with imbalance data.

TABLE I. MEAN AND STANDARD DEVIATION (STD.) OF THE EVALUATION INDICES FROM THE METHODS UNDER TEST.

Method	Evaluation Index	Mean	Std.
RF with the proposed strategy	*recall*	**0.644**	0.380
	precision	**0.704**	0.391
	F1-score	**0.624**	0.362
LR with the proposed strategy	*recall*	0.414	0.350
	precision	0.546	0.407
	F1-score	0.332	0.275
Novice	*recall, precision, F1-score*	0.474	0.321

IV. CONCLUSIONS

In this study we propose a case-based classification strategy of automatically selecting terrain covariates for modeling geographic phenomenon–environment relationship. Two methods (i.e., RF, and LR) based on the proposed strategy were

implemented and compared. A leave-one-out experiment based on a DSM case base shows that RF with the proposed strategy performed best.

REFERENCES

[1] Zhu, A-X., G. Lu, J. Liu, C.-Z. Qin, C. Zhou, 2018. "Spatial prediction based on Third Law of Geography". Ann. GIS 24, 225–240.

[2] Hengl, T., and H.I. Reuter (Eds), 2008. "Geomorphometry: Concepts, Software, Application". Developments in Soil Science - Volume 33, Elsevier, 765 p.

[3] McBratney, A., M. Mendonça Santos, B. Minasny, 2003. "On digital soil mapping". Geoderma 117, 3–52.

[4] Wilson, J.P. (Eds), 2018. Environmental Applications of Digital Terrain Modeling. Hoboken, NJ: Wiley Blackwell.

[5] Qin, C.-Z., X.-W. Wu, J.-C. Jiang, A-X. Zhu, 2016. "Case-based knowledge formalization and reasoning method for digital terrain analysis – application to extracting drainage networks". Hydrol. Earth Syst. Sci. 20, 3379–3392.

[6] Lagacherie, P., A.-R. Sneep, C. Gomez, S. Bacha, G. Coulouma, M.H. Hamrouni, I. Mekki, 2013. "Combining Vis–NIR hyperspectral imagery and legacy measured soil profiles to map subsurface soil properties in a Mediterranean area (Cap-Bon, Tunisia)". Geoderma 209–210, 168–176.

[7] Adhikari, K., A.E. Hartemink, B. Minasny, R.B. Kheir, M.B, Greve, M.H. Greve, 2014. "Digital mapping of soil organic carbon contents and stocks in Denmark". PloS One 9, e105519.

[8] de Carvalho Junior, W., P. Lagacherie, C. da Silva Chagas, B. Calderano Filho, S.B. Bhering, 2014. "A regional-scale assessment of digital mapping of soil attributes in a tropical hillslope environment". Geoderma 232–234, 479–486.

[9] Vaysse, K., and P. Lagacherie, 2015. "Evaluating Digital Soil Mapping approaches for mapping GlobalSoilMap soil properties from legacy data in Languedoc-Roussillon (France)". Geoderma Reg. 4, 20–30.

[10] Kaster, D.S., C.B. Medeiros, H.V. Rocha, 2005. "Supporting modeling and problem solving from precedent experiences: the role of workflows and case-based reasoning". Environ. Model. Softw. 20, 689–704.

[11] Liang, P., C.-Z. Qin, A-X. Zhu, Z.-W. Hou, N.-Q. Fan, Y.-J. Wang, 2020. "A case-based method of selecting covariates for digital soil mapping". Journal of Integrative Agriculture, doi: 10.1016/S2095-3119(19)62857-1.

[12] Breiman, L., 2001. "Random Forests". Mach. Learn. 45, 5–32.

GEOMORPHOMETRY 2020 PERUGIA, ITALY JUNE 22 - 26 2020

Automated extraction of areal extents for GNIS Summit features using the eminence core method

Gaurav Sinha[1], Samantha T. Arundel[2]

[1]Department of Geography
122 Clippinger Labs, Ohio University, Athens, Ohio, USA
sinhag@ohio.edu

[2]U.S. Geological Survey
Center of Excellence for Geospatial Information Science
1400 Independence Rd, Rolla, Missouri USA

Abstract— **An important objective of the U.S. Geological Survey (USGS) is to enhance the Geographic Names Information System (GNIS) by automatically associating boundaries with terrain features that are currently spatially represented as two-dimensional points. In this paper, the discussion focuses on experiments for mapping GNIS *Summit* features using the eminence core region-growing method, which maps the area between a peak and its key col (saddle). A secondary goal of this project is to improve the positional accuracy of GNIS *Summit* features, since those locations were derived long ago and need to be snapped to local morphometric peaks detected from analysis of the highest-resolution digital elevation models (DEMs). The eminence cores delineated for a subset of GNIS *Summit* features were compared visually against basemaps and manually digitized polygons created by USGS staff. The comparisons revealed substantial differences between the computationally derived eminence cores and the manually generated polygons. Results clearly suggest that the default core delineation method tested must be modified to "roll back" or truncate growth of unreasonably large cores to smaller extents that would match people's intuitive expectations. However, these results are far more encouraging than any method tested previously, since this method guarantees a 1-1 correspondence between polygons and GNIS *Summit* features.**

I. INTRODUCTION

An important objective at the U.S. Geological Survey (USGS) is to enhance the Geographic Names Information System (GNIS) by associating boundaries with terrain features that are currently spatially represented simplistically as two-dimensional points [1]. The driving force for this work is the need for more realistic representation of features to answer spatial semantic queries that rely on their areal boundary. There is no standard method for delineating landforms. Three broad approaches that are being tested in parallel at the USGS for landform mapping are object-based image segmentation and analysis, hybrid pixel and object-oriented region-growing methods, and machine learning-based image segmentation and object detection.

The authors initially experimented with well-known pixel-based landscape classification and segmentation methods, defined in [2-5], but none of them can guarantee outcomes where each GNIS feature can be mapped exclusively to one specific polygon. A geographic object-based image analysis (GEOBIA) workflow originally proposed in [6] was tested for mapping areal extensions for GNIS terrain features [1]. Out of 16 terrain feature classes recognized in GNIS, only *Summit* and *Valley* feature class members were found to be spatially correlated with only the high and low elevation GEOBIA terrain classes. The segmented terrain objects did not provide a unique polygon for each feature and the shapes of most polygons did not match common sense expectations of boundaries of individual *Summit* or *Valley* features. Thus, the authors concluded that GEOBIA is probably best for general physiographic characterization of terrain, but not for extracting cognitively plausible areal footprints for individual terrain features.

The current approach is on top-down region-growing methods for mapping landforms. The initial focus is on mapping only GNIS *Summit* features because they are shown on most topographic maps, and several algorithms for mapping areal extents of topographic eminences (in other words, convex-shaped landforms such as *Summit*s) are available for comparison already [7-11]. In this paper, results are reported from the application of the eminence core region-growing method [11], chosen specifically because of its cognitive and technical simplicity, the guarantee of exclusive discrete regions for every feature, and potential to serve as a general purpose and easily customizable method for mapping the wide variety of features classified as *Summit* features in GNIS.

Gaurav Sinha, Samantha Arundel (2020) Automated Extraction of Areal Extents For GNIS Summit Features Using the Eminence-Core Method: in Massimiliano Alvioli, Ivan Marchesini, Laura Melelli & Peter Guth, eds., Proceedings of the Geomorphometry 2020 Conference, doi:10.30437/GEOMORPHOMETRY2020_10.

II. METHODS

A. *Eminence Core Delineation Method*

The eminence core method is a region-growing method proposed originally in [9] and then adapted and extended into a more comprehensive cognitive modeling framework for eminence delineation in [11]. This method must be "seeded" with the location of a known morphometric peak, which can be defined as a local maximum of zero dimension within a defined neighborhood. The method then expands iteratively from the peak to map an eminence core that can be exclusively associated with only one peak. The default conceptualization of the eminence core is the area between the peak and the lowest (base) contour that completely encloses the peak and contains no location higher than the peak [11]. However, a smaller relative drop may also be specified to extract a smaller core. The base contour also supports the peak's key col, which is the lowest saddle between the peak and another higher peak (Figure 1). The difference in elevation between the peak and the key col is the peak's topographic prominence, widely used in the mountaineering community for ranking the attractiveness of peaks for mountain climbing. Prominence is an intuitive and highly effective filtering parameter for selecting topographically salient peaks from the large number of inconsequential peaks that are initially identified from local moving window analysis [11].

In [10], a vector contour-based representation method was used for mapping the core area. The authors prefer a DEM-based region-growing method using a priority queue data structure that ensures O(n) complexity [9]. The core area is mapped through expansion beginning at the peak cell by first adding the immediate eight neighboring cells to the queue, forming the minimal possible core area for a peak. The priority queue automatically sorts cells in descending order of elevation, and then selects the peak cell to promote the next highest cell to the top of the queue. This process is iterated until the cell at the top of the priority queue is at the edge of the study area or higher than the starting peak cell. The selected cells collectively delineate the eminence core area associated with the peak. The lowest elevation cell that reaches the top of the priority queue is the key col cell, which can be used to additionally determine the peak's prominence.

A limitation of this method is that for high-prominence peaks, the key col is at such a large distance that the eminence core grows unreasonably large to enclose cores of all other salient peaks between the prominent peak and its key col [9], [11]. Moreover, in planar areas with few isolated eminences, even a gentle slope can force the core to continue growing until the key col is detected, whereas people would judge the eminence boundary to be far more compact [11]. Two different approaches to solve this problem are presented in the literature [10-11] and may need to be implemented and compared to derive cognitively plausible cores for *Summit* features.

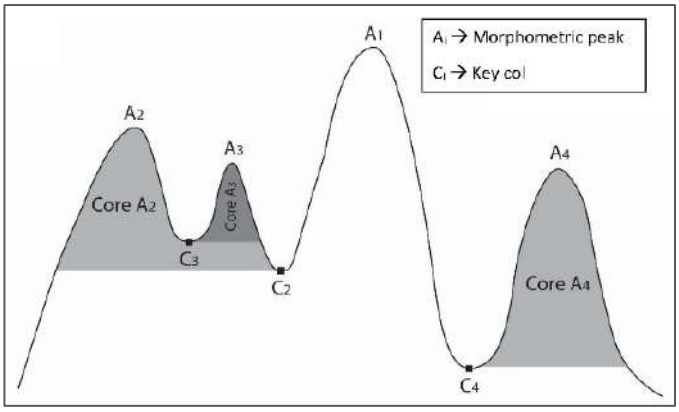

Figure 1. Conceptual diagram for illustrating the core area and key cols ($C_2 – C_4$) of peaks ($A_2 – A_4$). The highest peak A_1's key col is beyond the area shown.

B. *Snapping GNIS Summit features to morphometric peaks*

Because GNIS terrain point locations were collected for the names as opposed to their location, most GNIS *Summit* features do not coincide exactly with the morphometric peaks detected from high-resolution DEM analysis. For implementing the eminence core delineation method for GNIS *Summit* features specifically, it is essential to relocate or "snap" the GNIS *Summit* feature to the correct morphometric peak nearby. Because there are currently about 70,000 *Summit* features in the GNIS database, a separate secondary project was launched for automating as much of this *Summit* feature location enhancement process as possible. This effort presented its own challenges that are now documented in a separate manuscript [12] and not discussed here for lack of space. For this paper, it is pertinent that the experiments detailed below with GNIS *Summit* features successfully snapped to the correct morphometric peak.

III. RESULTS

The cognitive plausibility of the delineated eminence cores was visually assessed using Esri's ArcGIS Pro software, wherein the extracted core polygons were overlaid on a topographic basemap and a terrain hillshade layer in both two-dimensional map views and three-dimensional scenes. Additionally, the authors used 118 manually delineated polygons corresponding to GNIS *Summit* features in the Blue Ridge mountains of the Appalachian mountain range as reference data (Figure 2). These polygons were digitized manually by USGS staff in the National Geospatial Technical Operations Center's US Topo program to capture the extent of feature labels on historical USGS topographic maps. Labels were originally placed on USGS topographic maps to reflect USGS field surveyors' assessment of the approximate extent of the features. While comparing the polygons overlaid on topographic maps, the authors also found the digitized polygons as cognitively plausible representations of the *Summit* features.

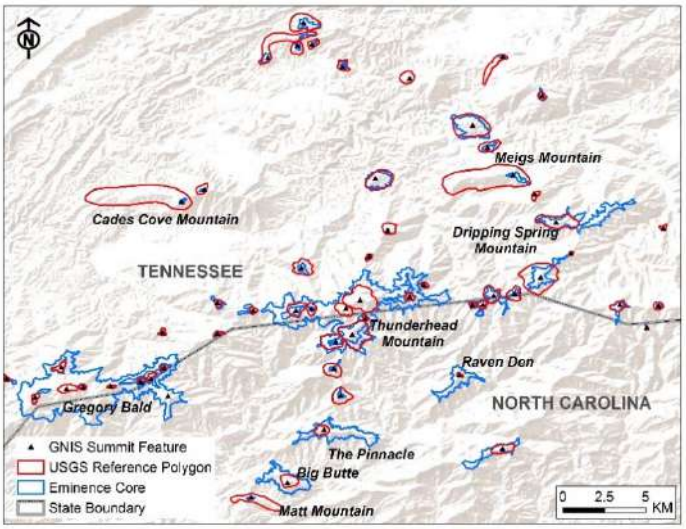

Figure 2. A comparison of a subset of computationally generated eminence cores and manually digitized polygons for GNIS *Summit* features in the Blue Ridge province of the Appalachian mountain range in USA.

A. *Visual comparison of computationally extracted eminence cores and digitized polygons*

The map in Figure 2 shows a part of the Great Smoky mountain range along the Tennessee–North Carolina border. Visual comparison of the computationally extracted eminence cores (blue polygons) and the manually digitized reference polygons (red polygons) offer several insights. It is obvious that both eminence cores and manual polygons comprise a wide range of shapes between compact and elongated (Figure 2). This map clearly establishes that the GNIS *Summit* feature class is a general category that includes a wide variety of topographic eminences. Mapping areal representations of the individual features will clearly reveal hitherto unknown information about the range of shapes and sizes of eminences, not just in the United States, but anywhere in the world.

The overlap patterns between the cores and polygons are also quite revealing. Sometimes, the manual polygon is contained within or is larger than the core, but the reverse is also true for many features. It is only for smaller and compact eminences that the core and reference polygons look similar. However, there are several cases where the two sets of areal representations are substantially different in shape and extent. For example, Cade's Cove Mountain (west), Meigs Mountain (east) and Matt Mountain (south) were digitized as elongated polygons, but the eminence core growth is truncated quite prematurely. The most likely explanation is that the digitized polygons for these *Summit* features represent larger eminences containing multiple topographic peaks, as shown on the historical USGS topographic map.

Conversely, there are several cases of extremely large and extended cores, which result when the key col is distant from the summit point. In these cases, the core is too large and can contain smaller cores of other nearby *Summit* features. These cores must be shrunk or "rolled back" to match the boundaries of those eminences based on people's common-sense expectations of acceptable feature extents. Two examples are Thunderbird Mountain (center) and Gregory Bald (southwest) in the map in Figure 2. These are *Summit* features with high prominence due to distant key cols, which means their cores will be large and contain the cores of subsidiary peaks. The USGS staff did not interpret these major *Summit* features to have such extremely large extents, since the polygons they delineated were much smaller.

B. *Geometric comparison of computationally extracted eminence cores and digitized polygons*

Results from the analysis of eminence cores and manually derived polygons are presented in Table 1. The *geodesic area* and *geodesic perimeter* were calculated for both sets of polygons. The *percentage difference* was also calculated. The summary statistics in Table 1 clearly show that the range and variance of area and perimeter measures are substantially higher for the automatically extracted eminence cores. The last column reveals that the difference in percentage in size between the computationally extracted cores and manually digitized polygons is extremely high. This clearly supports the visual assessment that there are many cores that are quite large and are the reason for the extreme percentage change values.

Property	Statistic	Automated Core	Manual Polygon	Percent Difference
Area (m^2)	***Min***	603	11,281	1.4
	Max	17,276,850	9,795,338	74,863
	Mean	1,397,879	1,001,331	1,893
	Std. Dev	3,600,661	1,636,711	3,246
Perimeter (m)	***Min***	142	401	0.3
	Max	101,708	18,192	1,733
	Mean	9,233	3,497	123
	Std. Dev	17,406	3,246	253

Table 1. Statistical summary of geometric measures for computationally and manually generated areal representations of GNIS *Summit* features

Figure 3 shows summary statistics for *Coefficient of Areal Correspondence (CAC)* index, which is a ratio of the overlapping area to the sum of all areas occupied by individual features measured [13]. CAC ranges from a minimum of zero (no overlap) to a maximum value of 1 (perfect overlap between the two sets of features). The mean of the CAC values for the 118 pairs of cores and manual polygons is quite low, underscoring again that there is a substantial difference between the two sets of representations.

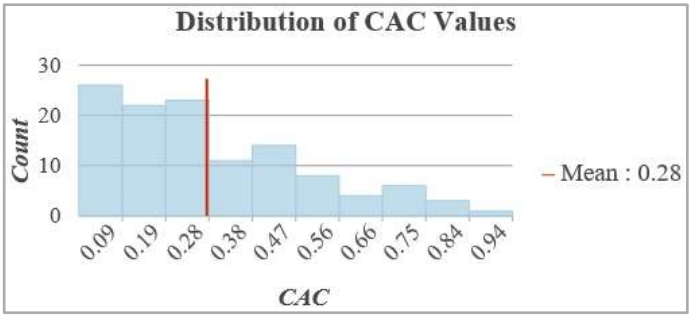

Figure 3. Histogram of Coefficient of Areal Correlation (CAC) values obtained from overlay of manually generated polygons and computationally extracted eminence cores.

IV. DISCUSSION AND CONCLUSION

In this paper, the focus was on testing the eminence core region-growing method's feasibility for creating areal representations of GNIS *Summit* features. Validation of automatically generated eminence cores against manually digitized polygons provided useful insights for advancing this project. The most encouraging finding is that this method of delineating boundaries generates a cognitively plausible solution because there is a clear 1-1 correspondence between features and the delineated areas. This approach is far more encouraging than the GEOBIA workflow tested earlier [1].

However, the default key-col-based delineation produced larger than acceptable polygons for major *Summit* features, suggesting the need for a more complex set of criteria for deciding how to terminate eminence core region growth. The smaller and compact cores correspond well to manually digitized polygons, but there are many extremely large cores that need to be truncated to match people's common-sense assumptions of eminence extents. It is quite difficult to delineate complex eminences with multiple peaks. In [10], a morphological variance reduction method was suggested, whereas in [11] the suggested method is to "roll back" the core based on continually measuring the average boundary slope threshold criterion until it exceeds a threshold. Both approaches need to be tested and compared further.

There is no prescriptive method for mapping the boundaries of topographic eminences. The eminence core approach is easy to implement and was tested first because of expediency, but this does not mean that alternative conceptualizations for mapping the areal extent of eminences will not be supported in this project. As shown in [11], instead of relying on the key col contour, other core mapping techniques (for example, maximum relative drop or minimum elevation threshold, fiat cols, salient apexes, slope inflection points, and landcover change line) may provide more satisfying results.

Whereas it may be sufficient to modify and use the default eminence core method for meeting the short-term mapping goals of the USGS, the alternative methods may be more cognitively appealing in other mapping projects, such as those at other national mapping agencies, mapping of extents of sacred landforms by indigenous communities, and perspective-driven landform visualizations. Thus, the authors hope that this research will lead to a more holistic and comprehensive framework that can support multiple methods and provide guidelines for dynamically extracting context-specific and cognitively appealing boundaries for topographic eminences.

Any use of trade, firm, or product names is for descriptive purposes only and does not imply endorsement by the U. S. Government.

REFERENCES

[1] Arundel, S. T., Sinha, G., 2019. Validating the use of object-based image analysis to map commonly recognized landform features in the United States. *Cartography and Geographic Information Science*, 46(5), 441–455.

[2] Wood, J., 1996. The Geomorphological Characterisation of Digital Elevation Models. Unpublished PhD Dissertation, Leicester University.

[3] Deng, Y., and Wilson, J. P., 2008. Multi-scale and multi-criteria mapping of mountain peaks as fuzzy entities. *International Journal of Geographic Information Science*, 22, 205–218.

[4] Fisher, P., Wood, J., and Cheng, T., 2004. Where Is Helvellyn? Fuzziness of Multi-scale Landscape Morphometry. *Transactions of the Institute of British Geographers*, 29, 106–128.

[5] Jasiewicz, J., and Stepinski, T. F., 2013. Geomorphons — a pattern recognition approach to classification and mapping of landforms. *Geomorphology* 182: 147–156.

[6] Drăguț, L., and Eisank, C., 2012. Automated object-based classification of topography from SRTM data. *Geomorphology*, 141–142, 21–33.

[7] Graff, L., and Usery, E. L., 1993. Automated Classification of Terrain Features in Digital Elevation Models. *Photogrammetric Engineering & Remote Sensing* 59: 1409-1417.

[8] MacMillan, R. A., Pettapiece, W. W., Nolan, S. C., and Goddard, T.W., 2000. A Generic Procedure for Automatically Segmenting Landforms into Landform Elements Using DEMs, Heuristic Rules and Fuzzy Logic. *Fuzzy Sets and Systems* 113/1: 81-109.

[9] Wood, J., 2004. A New Method for the Identification of Peaks and Summits in Surface Models. *Proceedings of GIScience 2004*.

[10] Chaudhry, O. Z., and Mackaness, W. A., 2008. Creating Mountains out of Mole Hills: Automatic Identification of Hills and Ranges Using Morphometric Analysis. *Transactions in GIS*, 12(5): 567-589.

[11] Sinha, G., 2008. Delineation, Characterization, and Classification of Topographic Eminences. *Unpublished PhD Dissertation*, Department of Geography, University at Buffalo, NY.

[12] Arundel, S. T., Sinha, G., and Chan, A., 2020. Automated location correction and spot height generation for named summits in the coterminous United States. *International Journal of Digital Earth. Accepted*.

[13] Taylor, P. J., 1977. *Quantitative methods in geography: An introduction to spatial analysis*. Areal association, Houghton Mifflin, Boston, p. 396.

GEOMORPHOMETRY 2020 PERUGIA, ITALY JUNE 22 - 26 2020

Geomorphometric feature selection based on intrinsic dimension estimation

Sebastiano Trevisani
Università IUAV di Venezia
(Venice, Italy)
strevisani@iuav.it

Abstract— **The use of geomorphometric variables or, from a machine learning perspective, geomorphometric features, sometimes coupled with other remote sensing derived variables, is often adopted for the spatial prediction of geoenvironmental properties of interest (e.g. soil and geo-engineering mapping). In other circumstances, geomorphometric features are analyzed for unsupervised approaches in the context of landscape classification and pattern recognition. The detection of the relevant features and the distinction between redundant and irrelevant features is crucial both for improving prediction accuracy as well as for reducing computational cost. Moreover, the detection of relevant features improves the interpretation of studied processes. In this short paper, the potentialities of a new feature selection algorithm are evaluated in a supervised learning problem, tested on ad-hoc designed synthetic dataset. The feature selection algorithm adopted is a Sequential Forward Selection filter, based on a fractal measure of Intrinsic Dimension, relying on a generalization of the Morisita index. The synthetic data set, built from real topography, is characterized by challenging characteristics as for example a strong linear correlation between relevant features. The tests performed on the data set show that the algorithm correctly individuates the relevant features and the irrelevant ones. Moreover, the impact of subsampling on the feature selection algorithm has been tested, showing a stable response up to roughly the 10% of the original data set. The results of this preliminary study suggest that the algorithm is promising in the geomorphometric context and that it is worth to investigate further its applicability in geomorphometry.**

I. INTRODUCTION

The use of geomorphometric variables or, from a machine learning perspective, geomorphometric features (the two terms are used interchangeably in the text), sometimes coupled with other remote sensing derived variables, can be adopted for the spatial prediction of geoenvironmental properties of interest, for example in soil and geo-engineering mapping [1-3]. In other circumstances, geomorphometric features are analyzed via unsupervised approaches for landscape classification and pattern recognition (e.g., [4]). The detection of relevant and non-redundant geomorphometric features in these prediction tasks is crucial both for improving prediction accuracy as well as for reducing computational cost. Moreover, the selection of relevant features improves the interpretation of studied processes, shedding light on main influencing factors and/or processes. Feature selection and reduction are crucial when dealing with geomorphometric analysis. In fact, the quantitative analysis of digital elevation models (e.g., [5-6]) can generate high-dimensional datasets, i.e., characterized by a high number of geomorphometric features. This is partially related to the high number of morphometric variables and local statistical metrics (e.g., [7]) that can be computed. Another reason is related to the spatial-scale dependency of geomorphometric variables and of the related calculation parameters. First, the various geomorphometric variables can be computed from different resolutions and smoothing of the input topography. Second, many geomorphometric variables and local statistical metrics have calculation parameters related to the spatial scale (e.g., the radius of a local search window) or to spatial directionality.

Consequently, given the potentially high number of input geomorphometric features in unsupervised and supervised learning tasks, the discrimination between relevant/irrelevant features (in supervised setting) and of the redundant/non-redundant features is of fundamental importance. The nonlinearity and the complexity of the potential interactions between geomorphometric features make difficult the application of standard parametric data reduction approaches, based for example on principal component analysis or on the linear correlation between variables.

In this context, the recently developed fractal-based estimator of Intrinsic Dimension (ID, [8]), relying on a generalization of Morisita Index [9], is particularly promising. The authors of the new ID estimator developed a set of ID-based algorithms for feature selection both in unsupervised [10] as well as in supervised learning settings [11]. These tools are implemented in R programming environment [12] with a specific package; the algorithms have been designed taking into consideration computational efficiency and ease of use.

Sebastiano Trevisani (2020) Geomorphometric features selection based on intrinsic dimension estimation:

in Massimiliano Alvioli, Ivan Marchesini, Laura Melelli & Peter Guth, eds., Proceedings of the Geomorphometry 2020 Conference, doi:10.30437/GEOMORPHOMETRY2020_11.

This short paper is part of a broader ongoing research exploring the application of these algorithms in geomorphometry both in unsupervised as well as supervised learning settings. The focus of this presentation is on the applicability of the approach in a supervised setting; in particular, the capabilities of the algorithm are tested considering an exemplary and demanding (from the predictive viewpoint) data set, built from real topography.

II. INTRINSIC DIMENSION AND FEATURE SELECTION

ID is strictly related to fractal dimension [8] and is an interesting parameter both for the analysis of spatial point patterns [13-14] as well as in the analysis of multidimensional data [10-11]. In the latter context, it is particularly useful because it allows to detect if the data lie on a lower-dimensional manifold in data space; when data lie on manifolds the ID dimension (not necessarily integer) is lower than the data dimension, i.e. the number of features. The example of the "Swiss roll" [10] distribution is emblematic (figure 1); even if the dataset has 3 variables, the true ID is 2, because the data lie on a 2D surface. The Morisita-based ID estimator is capable of estimating the ID from a multidimensional data set very efficiently and has been proven to be applicable in a wide set of settings, considering noise and under-sampling [8-10-11].

The estimation of ID is at the base of feature selection/reduction algorithms both in unsupervised (e.g., unsupervised clustering) as well as supervised (e.g., regression) settings. The key idea of these algorithms is based on the analysis of the impact of the single features on the ID estimation. For example, in an unsupervised setting, redundant features have a slight impact on ID estimated values. In a supervised setting, the input features can have different characteristics from the perspective of ID and in relation to the predictive capability of the output variable. Concerning ID, some of the input features can be redundant (e.g., strongly correlated) and hence leading to a lower ID respect the number of input features. Some other input features can be irrelevant, i.e., bring no information on output feature, and then contribute to the increase of the ID of the dataset. With real datasets based on geomorphometric features, redundant input features can be irrelevant as well as relevant The supervised feature selection algorithm of Golay et al. [11] is a Sequential Forward Selection filter, using the ID measure for discriminating relevant versus irrelevant features. The algorithm evaluates iteratively, for different subsets of input features, the index of dissimilarity (Diss), according to the equation:

$$Diss(F,Y) = ID(F,Y) - ID(F) \quad (1)$$

where F is a subset of the input features and Y is the output feature. When F is composed exclusively by all relevant features, the dissimilarity index should be theoretically zero. Differently, the irrelevant features have no impact in reducing the dissimilarity.

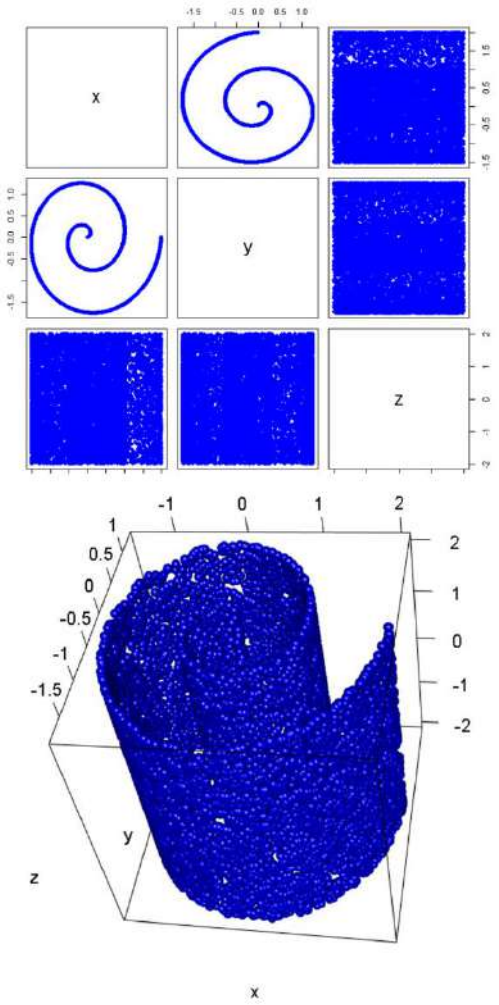

Figure 1. 2D and 3D scatterplots of the "Swiss roll" synthetic dataset. The ID is 2, because data lie on a 2D surface.

III. THE EXPERIMENTAL DESIGN

For testing the supervised feature selection algorithm, a synthetic data set has been built, based on real topography, from which 9 input features and one output feature have been derived. The DTM considered, derived from airborne Lidar technology, is representative of an alpine area with complex morphology (fig. 2, [15]) and has a grid of 350x350 pixels, with a resolution of 20 m. A synthetic dataset has been considered, given the necessity to know exactly the true relationship between input and output features, and test the impact of subsampling on the algorithm performance. The use of real topography and not of a pure

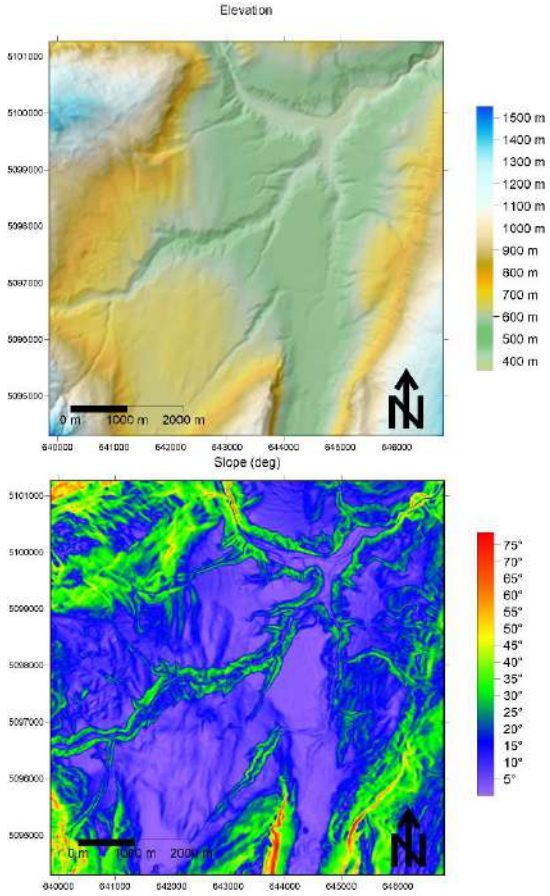

Figure 2. The DTM (Trentino, NE Italy) and the calculated slope. Slope (in the dataset expressed as percent rise) represents the output feature.

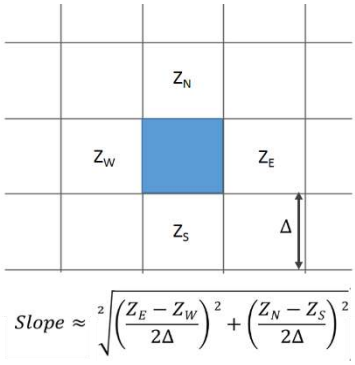

Figure 3. Simplified equation for computing the slope.

synthetic dataset generated from theoretical random distributions (e.g., [11]), is dictated by the need of testing spatial-statistical distributions representing real morphology, even if limited to an alpine setting. Another target of the built dataset is to analyze complex and non-linear relationships between input and output features, including potential redundancy between relevant features. This aspect is particularly relevant in geomorphometry, because of linear correlations between potentially relevant features can be present (e.g., linear correlation between roughness and slope, [4]). Moreover, it may happen that the set of relevant features have a predictive power only if used jointly and, conversely, the predictive capability of a single relevant feature can be marginal. From this viewpoint, topographic slope is a simple and convenient geomorphometric feature for building a synthetic data set for testing purposes. The slope (i.e., output feature) has been computed according to the simple equation reported in figure 3. Consequently, the relevant features are the elevations of the four nodes, here named as features Zn, Ze, Zs and Zw. The formulation of slope permits to model a complex non-linear relationship, with high redundancy between relevant features, and in which the features are relevant only if used in combination. Then, four irrelevant and non-redundant features (named x1, x2, x3 and x4) have been generated via random shuffling of the elevation and consequently are characterized by the same statistical distribution of relevant features. Finally, a redundant (with x4) and irrelevant feature, named y1, has been generated considering the square of x4 plus a Gaussian random noise of zero mean and a standard deviation of 0.1 m. For the dataset, considering all features the ID is 5.62; excluding the output feature the ID is 5.2. It is worth noting, that a feature selection approach based on the analysis of the linear correlation between input features would induce to do not consider some of the relevant features.

IV. Preliminary Results and Future Developments

The tests performed on the synthetic data set are highly positive: the algorithm correctly detects relevant input features and the irrelevant ones. The ID of the set of relevant features with and without the output feature is respectively 1.85 and 1.44; the ID of the set of irrelevant features with and without the output feature is respectively 4.71 and 3.74. The computational parameter to be set in the algorithm is the range of variation of the parameter L^{-1}, controlling the size of the moving windows inherent to Morisita index calculation [8-9]. L is the length of the side of the search windows in the data space, being all features normalized in the 0-1 interval. In this study, after different trials and following the approach suggested in [8], the integer values of L^{-1} were set to {10,11,…, 50}. The output is easily interpretable from the diagnostic curve (figure 4) reporting the impact of the single input features on the variation of the dissimilarity index. Only the features reducing the Dissimilarity index are relevant for the supervised learning.

From the perspective of computational time the algorithm (the non-parallelized version has been tested) is quite fast; the application on the whole dataset required 5.3 minutes with a ten years old Processor Intel® Core™2 Quad Q8300 2.5 GHz and 12 Gb of ram.

A first test on the sensitivity of the algorithm to sampling density has been conducted. The impact of under-sampling has been explored by means of random sub-sampling (100 times) the original distribution with different levels of sub-sampling. Up to an under-sampling of 90 % (only 10% of the values retained), the algorithm is stable in terms of features selection, even if the diagnostic curve is characterized by a high variance.

The results are promising even if more tests should be conducted to fully evaluate potentialities and limitations of the approach in geomorphometry [16]. The capability to handle complex non-linear relationships, the robustness to under-sampling and the straightforwardness of the approach are appealing characteristics. A critical point, to be further investigated, is the sensitivity of the algorithm to the L^{-1} parameter in presence of features with statistical distributions characterized by high kurtosis and/or skewness. It is worth noting that this kind of approach is particularly interesting also in the context or remote sensing imagery.

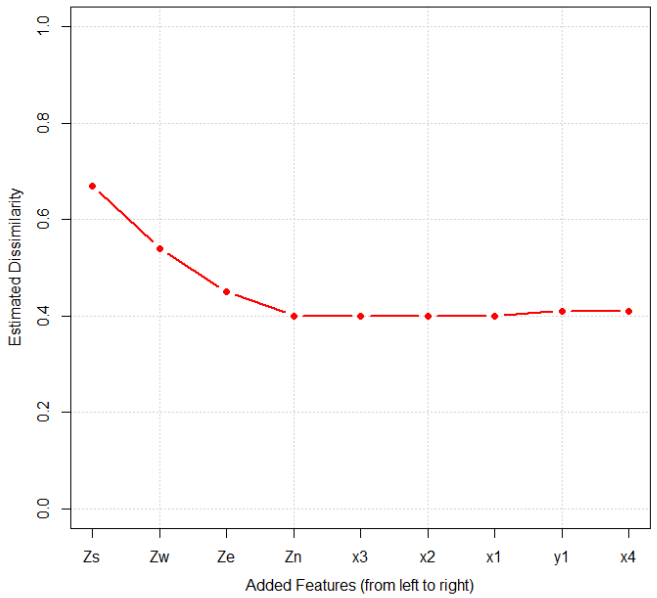

Figure 4. Results of the ID-based supervised feature selection approach applied to the whole data set. The features located on the right of Zn do not reduce the dissimilarity and are considered irrelevant.

REFERENCES

[1] Florinsky, I.V. 2016, "Digital Terrain Analysis in Soil Science and Geology: Second Edition" in Digital Terrain Analysis in Soil Science and Geology: Second Edition, pp. 1-486.

[2] Florinsky, I.V., Eilers, R.G., Manning, G.R. & Fuller, L.G. 2002, "Prediction of soil properties by digital terrain modelling", Environmental Modelling and Software, vol. 17, no. 3, pp. 295-311.

[3] Trevisani, S., Cavalli, M., Golay, J. & Pereira, P. 2019, "Editorial to the topical collection "Learning from spatial data: unveiling the geo-environment through quantitative approaches"", Environmental Earth Sciences, vol. 78, no. 5.

[4] Trevisani, S., Cavalli, M. & Marchi, L. 2012, "Surface texture analysis of a high-resolution DTM: Interpreting an alpine basin", Geomorphology, vol. 161-162, pp. 26-39.

[5] Florinsky, I.V. 2017, "An illustrated introduction to general geomorphometry", Progress in Physical Geography, vol. 41, no. 6, pp. 723-752.

[6] Pike, R.J., Evans, I.S. & Hengl, T. 2009, Geomorphometry: A brief guide.

[7] Trevisani, S. & Rocca, M. 2015, "MAD: Robust image texture analysis for applications in high resolution geomorphometry", Computers and Geosciences, vol. 81, pp. 78-92.

[8] Golay, J. & Kanevski, M. 2015, "A new estimator of intrinsic dimension based on the multipoint Morisita index", Pattern Recognition, vol. 48, no. 12, pp. 4070-4081.

[9] Morisita, M. 1962, "Iσ-Index, a measure of dispersion of individuals", Researches on Population Ecology, vol. 4, no. 1, pp. 1-7.

[10] Golay, J. & Kanevski, M. 2017, "Unsupervised feature selection based on the Morisita estimator of intrinsic dimension", Knowledge-Based Systems, vol. 135, pp. 125-134.

[11] Golay, J., Leuenberger, M. & Kanevski, M. 2017, "Feature selection for regression problems based on the Morisita estimator of intrinsic dimension", Pattern Recognition, vol. 70, pp. 126-138.

[12] R Development Core Team (2009) R: A language and environment for statistical computing. R Foundation for Statistical Computing, Vienna, Austria

[13] Golay, J., Kanevski, M., Vega Orozco, C.D. & Leuenberger, M. 2014, "The multipoint Morisita index for the analysis of spatial patterns", Physica A: Statistical Mechanics and its Applications, vol. 406, pp. 191-202.

[14] Kanevski, M. & Pereira, M.G. 2017, "Local fractality: The case of forest fires in Portugal", Physica A: Statistical Mechanics and its Applications, vol. 479, pp. 400-410.

[15] Florinsky, I.V., Skrypitsyna, T.N., Trevisani, S. & Romaikin, S.V. 2019, "Statistical and visual quality assessment of nearly-global and continental digital elevation models of Trentino, Italy", Remote Sensing Letters, vol. 10, no. 8, pp. 726-735.

[16] Trevisani S., 2019. "Unsupervised geomorphometric feature selection based on intrinsic dimension estimation".Geophysical Research Abstracts. Vol. 21, EGU2019-7318, 2019.

GEOMORPHOMETRY 2020 PERUGIA, ITALY JUNE 22 - 26 2020

Classification of Terrain Concave and Convex Landform Units by using TIN

Guanghui Hu, Wen Dai, Liyang Xiong, Guoan Tang
Key Laboratory of Virtual Geographic Environment, Ministry of Education
Nanjing Normal University
No.1 Wenyuan Road, Nanjing City, Jiangsu Province, China
huguanghui0503@qq.com

Abstract— **The concave and convex landform units are significant components of terrain surface. However, the properties of two landform units are traditionally calculated from the Grid-DEM, which is usually the secondary product of TIN-DEM. Therefore, the use of TIN can reduce the uncertainty caused by this conversion. In this study, we proposed a qualitative method based on TIN DEM data to classify terrain concave and convex landform units. By judging the property of each node and then setting the Voronoi region in a TIN, the concave and convex areas will be determined. The proposed method was used and validated in a mathematical Gaussian surface and two small catchments in this study. Results show that the proposed method has a high correctness for classification of concave and convex landform units. And our method is also suitable for the constrained and non-constrained TIN. In addition, the proposed method should be an extension in digital terrain analysis based on TIN.**

I. INTRODUCTION

The terrain surface of concavity and convexity are fundamental concepts in geomorphology. Generally speaking, the concave and convex landform units control the direction of flow, the transport of materials, and the deposition of soil [1] [2]. The calculation of concavity and convexity is traditionally based on Grid-DEM by using terrain curvature. Nowadays, the production modes of Grid-DEM have been rapidly developed, such as the point clouds method [3]. Obtaining point clouds from Lidar or UAVs becomes more and more convenient. The triangulated irregular network (TIN) usually becomes the bridge from point clouds to Grid-DEM [4]. However, this conversion has uncertain problem of interpolation method, which may lead to unforeseeable errors in application [5]. On the other hand, the simplification of many high resolution (5m or higher) Grid-DEM is necessary for the coarser analytical scale [6], especially the classification of concavity and convexity. There are many studies on extracting terrain feature information from Grid- DEM to reconstruct TIN [7], which is helpful for large scale research. To reduce the uncertainty from point clouds to Grid-DEM and improve the generalization in scale transformation, a group of new methods based on TIN should be explored.

Currently, the terrain analysis methods based on TIN have been discussed for decades. Several terrain derivatives (like slope and aspect), flow direction algorithms, visibility analysis, and dynamic hydrology models can be well calculated based on TIN [8] [9] [10]. In addition, the extraction of morphological information from TIN has been exploring as well. Falcideeno and Spagunolo (1991) pointed out that the morphological type of an edge can be determined by its adjacent two triangles [11]. However, they then decided the morphological type of a triangle by its labeled edges, which was inappropriate in some special cases (like the boundary of TIN). Van Kreveld (1996) defined the plane and profile curvature for each node in a TIN, and proposed the Voronoi diagram which can be used as terrain partition [12]. Nevertheless, this method is unable to effectively classify terrain concave and convex landform units. In fact, the mentioned methods did not make use of the positional relationship between a node and its adjacent nodes. The relationship should be explored and used in the classification of terrain concave and convex landform units. In this study, we firstly give a concave or convex label to each node of a TIN by taking the relationship between a node and its adjacent nodes into account. Then, the Voronoi diagram is applied to these labeled nodes to divide the terrain surface.

II. DATA AND METHODOLOGY

A. Data

In this work, three study areas are selected to validate the proposed method: a simulated mathematical Gaussian surface and two small catchments. The Gaussian Surface is defined by the formula [13] as follows:

$$z = 100A[1-(\frac{x}{m})^2]e^{-(\frac{x}{m})^2-(\frac{y}{n}+1)^2} - 100Ce^{-(\frac{x}{m}+1)^2-(\frac{y}{n})^2} - 100B[0.2(\frac{x}{m})-(\frac{x}{m})^3-(\frac{y}{n})^5]e^{-(\frac{x}{m})^2-(\frac{y}{n})^2} \quad (1)$$

Guanghui Hu, Wen Dai, Liyang Xiong and Guoan Tang (2020) Classification of Terrain Concave and Convex Landform Units by using TIN: in Massimiliano Alvioli, Ivan Marchesini, Laura Melelli & Peter Guth, eds., Proceedings of the Geomorphometry 2020 Conference, doi:10.30437/GEOMORPHOMETRY2020_12.

where *A*, *B*, and *C* are terrain relief parameters; and m and n are range control parameters. These parameters are set as $A = 3$, $B = 10$, $C = 1/3$, $m = 500$, $n = 500$ with 5 m of resolution (Figure 1(a)). The first small catchment is Qiaogou (37°34′11″ N, 110°16′53″ E) with 0.45 km^2 area (Figure 1(b)). The point clouds data generated by UAVs is used to construct TIN to validate our method on the non-constrained TIN. Then, the second larger catchment Liujiagou (Figure 1(c)) (37°36′48″ N, 110°17′20″ E) is 6.9 km^2 with a loess-hill landform. Grid-DEM data with 5 m resolution in this area will be convert into TIN with different *z-tolerance*, and the vertices of stream lines will be participated in the construction of TIN [14]. The two catchments are located in the north of Suide County, Shaanxi Province, China.

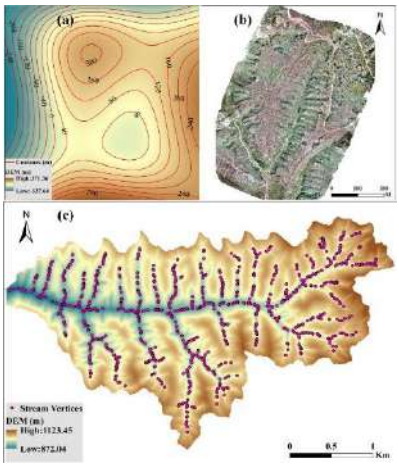

Figure 1. Study areas. (a) Gaussian surface, (b) image of Qiaogou from the UAVs and (c) small catchment Liujiawan with the stream lines vertices.

B. Method

A TIN is consisted of nodes, edges and triangles. Except the nodes on the boundary of the TIN, there are at least three nodes around a center node. These around nodes are called adjacent nodes of the center node. For each center node, its convexity or concavity is certain. As we all know, three points in space can form a plane. The positional relationship between a center node and a plane is above, below, or within (e.g. the center node is above a plane). Without loss of generality, the case of a center node with four adjacent nodes was selected as an example to represent all situations. The four space points can generate four different planes at most. Considering all the cases, the positional relationships between the center node and the four space planes can be summarized in Table 1 and Figure 2.

There is a special case in Figure 2(g), the center node is a saddle point in theory. However, we still regard it as a concave node. Then, we can set a series of simple judgment principles for a center node with more adjacent nodes.

(1) If the number of "below" is greater than or equal to the number of "above", the center node is a concave node.

(2) If the number of "below" is less the number of "above", the center node is a convex node.

(3) If the center node is in all the planes, it is a flat node.

Finally, each labeled node can generate a Voronoi region with the same label.

Table 1 Positional relationship between center node and four planes (e.g. the center node is above the Plane BCE).

Positional Relationship	Plane BCE	Plane BCD	Plane BDE	Plane CDE	Center Node Property
(a)	Below	Below	Below	Below	Concavity
(b)	In	Below	Below	Below	Concavity
(c)	In	In	Below	Below	Concavity
(d)	Above	Above	Above	Above	Convexity
(e)	In	Above	Above	Above	Convexity
(f)	In	In	Above	Above	Convexity
(g)	Below	Below	Above	Above	Saddle
(h)	In	In	In	In	Flat

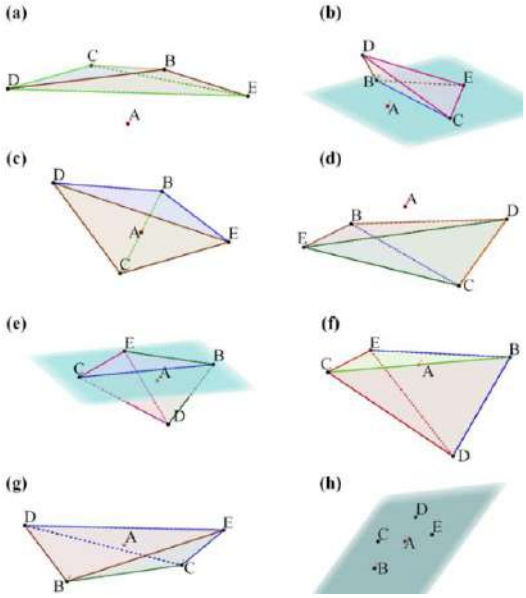

Figure 2. Eight cases for positional relationship between the center node and four adjacent nodes. Each case corresponds with a column in the table 1.

III. Results and Conclusion

A. Comparison with the surface curvature

To assess the accuracy of our method, we set the surface curvature results as the reference data [15]. If the surface

curvature value of a grid is less than or equal to zero, this grid set as concave, otherwise as convex. The *z-tolerance* is 0 m in the conversion from Grid-DEM to TIN, which means all the grid points are participated in building of TIN (The surface curvature and Grid-DEM to TIN tools can be found in ArcMap 10.2). The Gaussian surface results are displayed with contours (Figure 3(a) and (b)). The result of our method is the same as the surface curvature result in the majority area of the Gaussian surface. And some differences mainly belong to the saddle region, which may come from the conversion of Grid-DEM to TIN. In addition, the comparison results in real landform of Liujiawan are also displayed (Figure 4 (a) and (b)). Obviously, both results are almost the same. The comparisons between results of surface curvature and our method on Gaussian surface and real landform show that our method can provide a credible enough classification of terrain concave or convex landform unit. The correctness of our method can be validated to some extent.

B. Classificaton for contrained and non-contrained TIN

TINs can be divided into constrained and non-constrained TIN. In this section, we explore the classification capacity of our method on both two types of TINs.

The TINs are firstly generated from the Grid-DEM data in Liujiawan by *z-tolerance* method, and then constrained by the stream vertexes. With the *z-tolerance* increasing, the terrain will be generalized and the analytical scale will be coarser. In the small catchment Liujiawan, we select 5 m, and 15 m as two *z-tolerances* parameters. Although the terrain information was sharply reduced, the streamlines vertices still control the valley areas. The results are displayed in Figure 5 and overlaid with hill shading as well. Under such scale, the positive terrain can be regarded as convex terrain, while negative terrain is concave terrain. Our method can provide a reasonable concave and convex classification of terrain on the constrained TIN.

On the other hand, the non-constrained TIN is produced from the points clouds data in Qiaogou. The classification result is displayed in Figure 6. Due to the point clouds data is relatively density, the micro terrain information can be well described, such as the agricultural terraces, the steep scarp in the bottom of the valley, the artificial path, the ridges, and the rills on the hill slope. Meanwhile, the concavity and convexity classification of these terrain elements by our method is good enough to a certain extent.

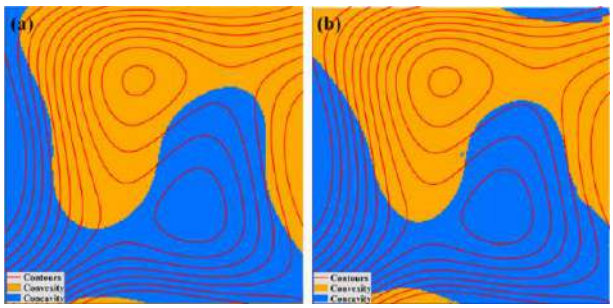

Figure 3. Results in Gaussian surface. (a) Classification by surface curvature based on Grid-DEM. (b) Classification by our method based on TIN with 0 m *z-tolerance*.

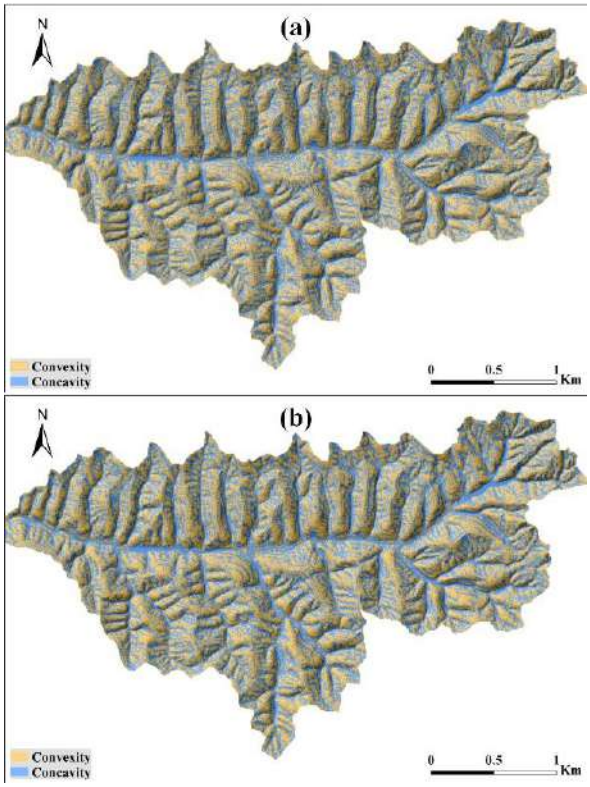

Figure 4. Results in Liujiawan. (a) Classification by surface curvature based on Grid-DEM. (b) Classification by our method based on TIN with 0 m *z-tolerance*.

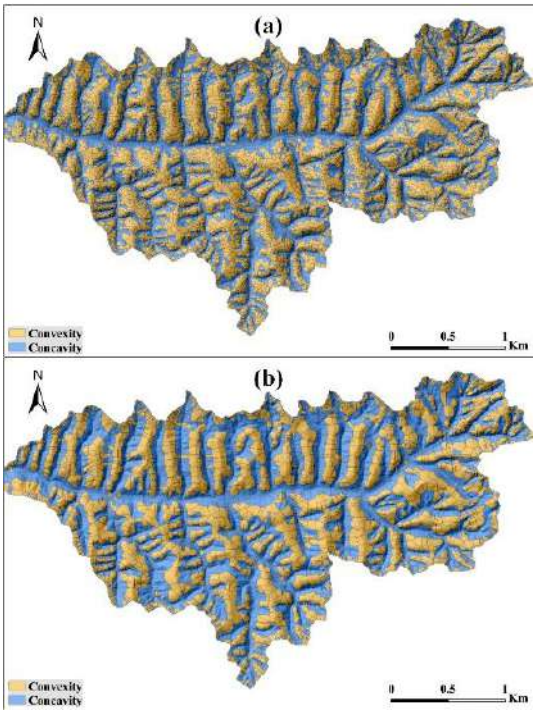

Figure 5. Results of constrained TINs that from Grid-DEM with different z-tolerance. (a) TIN with 5 m *z-tolerance*. (b) TIN with 15 m *z-tolerance*.

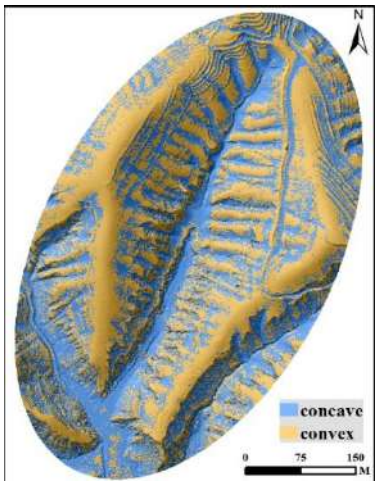

Figure 6. Result of non-constrained TIN that generated from point cloud.

Conclusion and Future Work

In this study, we proposed a qualitative method to classify the terrain concave and convex landform unit. By judging the positional relationship between the center node and its adjacent nodes, the property of the center node was determined. Then the terrain was divided by the Voronoi region of each node. The results obtained from our method were compared with the surface curvature method, which shows the correctness of our method. Our method also displays the ability of processing the constrained and non-constrained TINs.

Comparing with the kinds of curvature calculation methods based on Grid-DEM, our method is still inadequate. The future work is to explore the quantitative calculation method of concavity and convexity based on TIN.

REFERENCES

[1] Xiong, L.Y., Jiang, R., Lu, Q.H., Li, F.Y., Tang G., 2019. "Improved Priority-Flood method for depression filling by redundant calculation optimization in local micro-relief areas." Transactions in GIS, 23(2), 259-274.

[2] Li, Z.L., Zhu, Q., Gold, C., 2005. "Digital terrain modeling Principles and methodology". CRC Press

[3] Wilson, J.P., 2018. "Environmental Applications of Digital Terrain Modelling", SN:9781118936214, doi:10.1002/9781118938188

[4] Nelson, A., Reuter, H.I., Gessler, P., 2009. "DEM production methods and sources". In In: T. Hengl & H.I. Reuter (eds) Geomorphometry: Concepts, Software, Applications, Amsterdam, Netherlands: Elsevier.

[5] Guo, Q., Li, W., Yu, H., Alvarez, O., 2010. "Effects of topographic variability and lidar sampling density on several DEM interpolation methods". Photogrammetric Engineering & Remote Sensing, 76(6), 701-712.

[6] Ai, T., Li, J., 2010. "A DEM generalization by minor valley branch detection and grid filling". ISPRS Journal of Photogrammetry and Remote Sensing, 65 (2), 198–207.

[7] Li, Z., Zhu, Q., Gold, C.M., 2005. "Digital Terrain Modeling: Principles and Methodology". DBLP.

[8] Nelson, E.J.; Jones, N.L., Miller, A.W., 1994. "Algorithm for Precise Drainage‐Basin Delineation". Journal of Hydraulic Engineering, 20 (3), 298-312.

[9] Floriani, L., Magillo, P., 2003. "Algorithms for Visibility Computation on Terrains: A Survey". Environment and Planning B: Planning and Design, 30(5), 709–728.

[10] Tucker, G.E., Lancaster, S.T., Gasparini, N.M., Bras, R.L., Rybarczyk S.M., 2001. "An object-oriented framework for distributed hydrologic and geomorphic modeling using triangulated irregular networks". Computers & Geosciences, 27 (8), 959-973.

[11] Falcideeno, B., Spagnuolo, M., 1991. "A new method for the characterization of topographic surfaces". International Journal of Geographical Information System, 5 (4), 397-412.

[12] Van Kreveld, M., 1997. "Digital elevation models and TIN algorithms". In: van Kreveld M., Nievergelt J., Roos T., Widmayer P. (eds) Algorithmic Foundations of Geographic Information Systems. 37-78. CISM School 1996. Lecture Notes in Computer Science, vol 1340. Springer, Berlin, Heidelberg.

[13] Zhou, Q., Liu, X., 2004. "Analysis of errors of derived slope and aspect related to DEM data properties". Computers & Geosciences, 30(4), 369-378.

[14] Zhou, Q., Chen, Y., 2011. "Generalization of DEM for terrain analysis using a compound method". ISPRS Journal of Photogrammetry and Remote Sensing, 66 (1), 38-45.

[15] Moore, I. D., Grayson, R. B., Landson, A. R., 1991. "Digital Terrain Modelling: A Review of Hydrological, Geomorphological, and Biological Applications". Hydrological Processes 5: 3–30.

GEOMORPHOMETRY 2020 PERUGIA, ITALY JUNE 22 - 26 2020

Geomorphic systems, sediment connectivity and geomorphodiversity: relations within a small mountain catchment in the Lepontine Alps

Irene Maria Bollati[1,§], Marco Cavalli[2]
[1]Earth Science Department "Ardito Desio", Università degli Studi di Milano, Milano, Italy
[2]Research Institute for Geo-Hydrological Protection, Padova, Italy
[§] irene.bollati@unimi.it

Abstract—**Mountain regions are characterized by a spatial geomorphic heterogeneity that confers to the environment a significant geomorphodiversity, functioning as a substrate for biodiversity. It is hence important to understand the geomorphic dynamics and its evolution in space and time. A different spatial scale approach was developed to evaluate the relationship existing among geomorphological processes, sediment connectivity and geomorphodiversity. The study areas are the Veglia-Devero Natural Park (Lepontine Alps) and a small mountain catchment (Buscagna catchment) where the analysis was carried out at a highest detail. At the natural park scale, a preliminary geomorphological map was realized and then the index of Geomorphodiversity was computed highlighting the differentiation between the two sides of the Buscagna glacial valley. In the Buscagna catchment where also the index of Connectivity was calculated, the integrated analysis of the two indices allowed to identifying different *geomorpho-connectivity sectors*, testifying the role of geomorphic processes in regulating sediment fluxes and, consequently, controlling landscape units.**

I. INTRODUCTION

Geomorphic systems may present an extremely variable behavior in narrow spaces, especially in mountain environments. This variability can be regarded as *geomorphodiversity* intended as "geodiversity with respect to geomorphology" [1] so that the geomorphological richness of territories could be compared "taking into account the scale of investigation, the purpose of the research and the level of scientific quality" [2]. Geomorphodiversity is usually quantified counting different geomorphic elements included within cells of a certain size (*direct methods*; e.g. [3]) or inferring it indirectly from relief morphometric features (*indirect methods*; e.g. [4; 5]). Geomorphodiversity, hence, mirrors the variability of geomorphic systems dynamic behavior in relation to topographic features. At the core of this dynamic, there are the erosion-transport-sedimentation patterns along channel networks and on the hillslopes, linking sources-to-sinks. In some cases, especially in mountain areas, the continuity of sediment fluxes is regulated by intrinsic (geology, morphometric features of slopes) and extrinsic factors (meteorological events, human interventions). All these aspects are related to the *sediment connectivity*, i.e. the degree of linkage (lateral, longitudinal and vertical) that controls sediment fluxes throughout landscape [6]. Sediment connectivity is an emerging property of a geomorphic system (i.e. coupling relationship between elementary units: landforms, slope units, subcatchments) and reflects the potential of water/sediment to move through the system [7]. According to [8; 9; 10], it is possible also to distinguish between i) *structural connectivity* that describes the spatial contiguity of landscape units and ii) *functional connectivity* that is process based. In this last case, considering geomorphic systems and the related sediment connectivity [11] as a functional component of ecosystems, the influence on soil development, and consequently on vegetation, could be highly relevant [12]. Vegetation could interfere with geomorphic dynamics, being a regulating agent, but also suffering from the impact of geomorphic processes [13]. The main aim of this work is the assessment, through specific indices, of the relationship among geomorphological systems, sediment connectivity and geomorphodiversity in a small mountain catchment. At this scope, the geomorphodiversity assessment was primarily focused, at a wider scale, on the Veglia Devero Natural Park (VDNP, Lepontine Alps). According to the obtained results, the Buscagna stream catchment (12 km^2), was selected to perform a sediment connectivity evaluation. The outcomes of this analysis will be hence discussed in the perspectives of a holistic approach including other components of the landscape.

II. STUDY AREA & PRELIMINARY CONSIDERATIONS

The Buscagna stream catchment is SW-NE elongated and ranges in altitude from 1650 m a.s.l. (Devero plain) to 3237 m a.s.l. (Boccareccio Peak). In the catchment the following lithologies, belonging to the upper and lower Pennidic Nappes,

Irene Maria Bollati and Marco Cavalli (2020) Geomorphic systems, sediment connectivity and geomorphodiversity: relations within a small mountain catchment in the Lepontine Alps: in Massimiliano Alvioli, Ivan Marchesini, Laura Melelli & Peter Guth, eds., Proceedings of the Geomorphometry 2020 Conference, doi:10.30437/GEOMORPHOMETRY2020_14.

outcrop (e.g. [14; 15]): i) orthogneisses with locally intercalated amphibolites, micaschists and paragneiss (Monte Leone Unit); ii) ultramafites rocks, mainly serpentinites (Ultramafic Cervandone-Geisspfad Complex) iii) calcschists and marbles. The i) and ii) type of rocks outcrop on the northwestern side of the Buscagna Stream catchment, while the iii) rocks outcrop on the southeastern side of the catchment.

Concerning geomorphological features, the Buscagna valley is a glacio-structural valley set along the contact between gneisses and calcschists and intensely shaped by glaciers. The landscape reflects the geological and geomorphological dichotomy between the slopes. The northwestern slope, constituted mainly by gneisses, is characterized by a high relief energy, and it is affected by cryoclastism and gravity-related processes like rockfalls and debris-flows. Composite cones (sensu [16]), fed by different processes (water-related, mass wasting and snow avalanches) are recurrent. Calcschists and marbles cropping out along the southeastern slope and at the valley head are more suitable to erosion, soluble and affected by hypogean and epygean karst processes. Pleistocene glacial landforms and deposits are very widespread and are constituted by abundant glacial debris (moraines and erratics), transversal and lateral glacial steps, hanging glacial valley and basins. In the NW-lateral hanging basins Holocenic glaciers, nowadays almost extinct, were present. At higher altitudes, the more recent glacial deposits have been undergoing reworking by paraglacial-type dynamics (sensu [17]). Snow avalanches are also important modeling agent.

III. METHODS

A. Geomorphodiversity Index Calculation

The geomorphological map of the VDNP (Fig, 1a) represented the input data for the calculation of the *Geomorphodiversity Index* (*GmI*). The map was elaborated reorganizing the available data concerning geology and geomorphology, along with an orthophotos interpretation. The methodology proposed by the ISPRA-AIGeo Commission on Geomorphological Mapping was adopted [18]. Hence, lithologies were grouped according to the behavior towards geomorphic processes and landforms were classified according to the genetic processes.

To produce a thematic map on geomorphodiversity of the VDNP, a direct method based on the geomorphological map was selected [19] and using *ArcGIS* functionalities. The area was divided into cells of 500 x 500 m. This size was decided after comparative tests on a random portion of the study area, varying the cells and comparing it with the average size of the landforms represented in the geomorphological map (0.08 km^2). The *GmI* was then calculated for each cell by summing the number of different landforms within each cell and dissolving them according to the landform type (a partial mirror of the genetic process). This was intended to consider landforms only once inside each cell. The final result includes polygons, lines and points for which *sub-GmIs* were created during the procedure. The *Union* tool allowed obtaining the final value for the *GmI* for each cell. The values were finally classified according to the quantile method.

B. Connectivity Index Calculation

Sediment connectivity Index (*IC*), proposed by [6] (https://github.com/HydrogeomorphologyTool), is a topographic based approach and it is mainly addressed to assess the lateral connectivity. The *IC* calculation (1) considers the: i) *Upslope Component* (D_{up}), i.e. the potential for downward routing of the sediment produced upslope (2); ii) *Downslope Component* (D_{dn}), that takes into account the flow path length that a particle has to travel to arrive to the nearest target or sink (3).

$$\textit{Index of Connectivity}\ (IC) = log10\left(\frac{Dup}{Ddn}\right) \quad (1)$$

$$\textit{Upslope Component}\ (Dup) = \overline{\mathrm{WS}}\ \sqrt{A} \quad (2)$$

$$\textit{Downslope Component}\ (Ddn) = \sum_i \frac{di}{WiSi} \quad (3)$$

In the formulas: i) *W* is the average weighting factor, i.e. *Surface Roughness* calculated according to [20]; ii) *S* is the *Average Slope Gradient*; iii) *A* is the *Upslope Contributing Area*; iv) *d* is the length of the flow path according to the steepest downslope direction. In the *Ddn*, the calculation is performed for each *i*-th cell. To perform this analysis, a high-resolution DTM is required [7; 20]. The DTM used for this research is a LiDAR-based DTM with a 5 m resolution (source Geoportale Regione Piemonte; http://www.geoportale.piemonte.it/cms/). Considering DTM resolution, the moving window size for roughness calculation was set at 3x3. The input DTM was hydrologically corrected using the *Pit remove* tool of the *TauDEM 5.3.7* (http://www.engineering.usu.edu/dtarb/taudem) whereas the catchment and the channel network were defined using the *Watershed delineator* of *ArcSwat 2012.10_2_19* (https://swat.tamu.edu/software/arcswat/).

IV. RESULTS AND DISCUSSIONS

Geomorphodiversity Index map

The VDNP is characterized by a variable geomorphodiversity, with local hot spots (red), and other areas more characterized by diffuse low geodiversity (green) (Fig. 1b). Considering the Buscagna Stream catchment, the glacio-structural valley is, in fact, evidently asymmetric due to the different susceptibility of gneisses and calcschists to geomorphic processes, also due to the regional dipping of the surfaces (Fig. 1a).

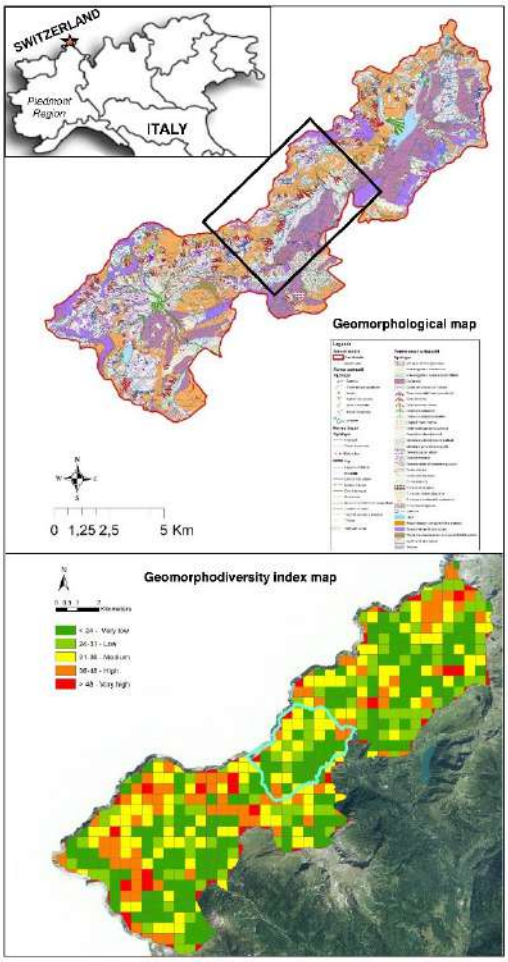

Figure 1. Geomorphological map (a) and Geomorphodiversity Index map (b).

This asymmetry is mirrored in the *GmI* map where:

i) the prevalence of green on the southeastern side of the valley, where calcschists outcrop continuously, could be attributed to the low diversification of landforms and to the large width of landforms due to water-related processes (V-shaped valleys, karst features), glacier action undergoing a structural control;

ii) the medium to high geomorphodiversity values are associated to the highest elevation areas of the northwestern slope (Cervandone, Cornera and Boccareccio Peak slopes) and the related hanging glacial basin (glacial, crionival, gravity- and water-related landforms, more heterogeneous lithology, and local structural influence).

In this method of *GmI* calculation, the role of geomorphological mapping at multi-catchment scale (Fig. 1a) is crucial. According to the results, the Buscagna stream catchment was then selected to perform a more in-detail analysis, applying the *IC*.

Connectivity Index maps

The *IC* maps result different if the outlet (Fig. 2a) or the main streams (Fig. 2b) and the channels (Fig. 2c) were selected as a target of the analysis [11]. Using the outlet as a target (Fig. 2a), a relationship between connectivity patterns and geomorphodiversity can be highlighted. In the Buscagna catchment, in fact, it is possible to appreciate quite clearly the differentiation among the two sides of the valley:

i) low *IC* values (green colour) characterize the calcschists slope. A structural controlled hydrographic pattern mainly constituted by V-shaped valleys, trenches and fractures that interrupt a wide rocky surface shaped by ancient glaciers (C; Fig. 2a);

ii) high *IC* values (red colour) characterize the high relief gneiss slope, especially in correspondence to debris flow and snow avalanche channels re-elaborating glacial and slope debris (B). These higher IC conditions are interrupted by glacial hollows (A1 and A2; Fig. 2a) and steps, acting as sinks (A1) or as a sudden change in longitudinal connectivity (A2) [7; 11].

Considering the main streams (Fig. 2b) and the channels as target (Fig. 2c), the hydrographic pattern role is even more delineated. It is well evident in Fig. 2a how the glacial tributary basins progressively lose the differentiation, well evident in Fig. 2a, between slopes characterized by high connectivity and bottom of the basins (A) where the debris effectively accumulates, correctly characterized by low *IC* values.

Summarizing, as already shown by other Authors in other study cases [7; 11], at least 5 typologies of *geomorpho-connectivity sectors* could be identified:

A1, A2 – Hanging glacial basins: the glacial originated hollows act as temporary sediment traps, and are characterized by a great quantity of debris of glacial and gravity origin, and are surrounded by talus slope deposits. The frontal moraine, in the Cornera basin (A1) in particular, remains hanging on the glacial step that separates the Cornera basin from the valley bottom. The moraine is undergoing dismantling, releasing slowly debris along a high connectivity area and feeding the B1 composite cone.

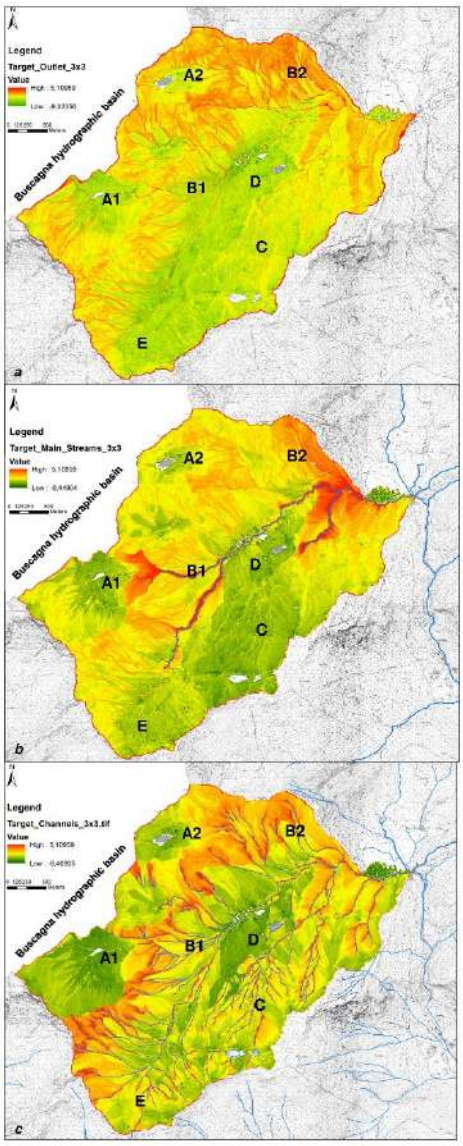

Figure 2. Connectivity Index maps: targeting outlet (a) and targeting channel network (b, c). Capital letters indicates the geomorpho-connectivity sectors discussed along the text.

B1, B2 – Polygenic cones and relative feeding areas: they are generated by the combination of different processes related to water-gravity-snow. Debris flow channels represent an effective way for debris transport. In some cases, snow avalanches can play a role in connectivity since on the one hand, they contribute to the transport of rocky and woody debris, and on the other hand, they can also partially damming the channels as occurred close to the Buscagna outlet during the 2018 (B2). They are especially highlighted considering as a target the main streams (Fig. 2b) or, even more, channels (Fig. 2c).

C – Karst-suitable rocky surfaces shaped by glaciers: the drainage of the debris occurs along small V-shaped valleys, often controlled by the structural pattern. More relevant in this case could be the assessment of the vertical connectivity.

D – Pleistocene glacial deposits: these areas are characterized by widespread, coarse and thick glacial debris. This debris is stocked as relatively high moraines to which the hydrographic network has to adapt.

E - Karst-suitable block fields: in the head of the valley, marble outcrops have been quite completely dissected by gelifraction in coarse blocks, between which fine matrix is often absent. The rocks are karst-susceptible and in this case, the connectivity features described for C and D may combine.

According to the presented results, the comparison with a geomorphological map revealed to be fundamental both in geomorphodiversity and sediment connectivity analyses, as already shown, for the second case, by [7].

V. Conclusions

In the present research, the *GmI* was expected to provide information at VDNP scale (500 X 500 m cell size) and, according to the results of the *GmI*, the *IC* (5 X 5 m cell size) was derived in small mountain catchment where the relationship between sediment connectivity, geomorphology and geomorphodiversity was investigated.

IC confirms to be very suitable for small mountain catchments characterized by a local diversification of geomorphic processes and a complex topography. Using as a target the outlet or the main streams or, even more, the channel network, provide a different detail on processes. Moreover, for this reason, the coupling with a geomorphological map is essential.

Considering the fallouts of geomorphic processes and sediment connectivity on the other components of the ecosystem, a holistic approach is the focus of the in progress investigations. In particular, as already suggested by [21; 9], further elaborations are aimed at comparing these results with geopedological and dendrogeomorphological outcomes.

References

[1] Panizza, M., 2009. "The geomorphodiversity of the Dolomites (Italy): a key of geoheritage assessment" Geoheritage 1, 33-42.

[2] Zwoliński, Z., A., Najwer, M., Giardino, 2018. “Methods for assessing geodiversity”. In: Geoheritage, pp. 27-52.

[3] Pereira, D.I., P., Pereira, J., Brilha, L. Santos, 2013. "Geodiversity assessment of Paraná State (Brazil): an innovative approach". Env. Manage. 52(3), 541-552.

[4] Zwoliński, Z., 2009. "The routine of landform geodiversity map design for the Polish Carpathian Mts." Land. Anal. 11, 77-85.

[5] Melelli, L., F., Vergari, L., Liucci, M., Del Monte, 2017. "Geomorphodiversity index: Quantifying the diversity of landforms and physical landscape" Sci. Tot. Env. 584, 701-714.

[6] Cavalli, M., S., Trevisani, F., Comiti, L., Marchi, 2013. "Geomorphometric assessment of spatial sediment connectivity in small Alpine catchments" Geomorphology 188, 31-41.

[7] Cavalli, M., T., Heckmann, L., Marchi, 2019. "Sediment connectivity in proglacial areas" In Geomorphology of Proglacial Systems (pp. 271-287). Springer, Cham.

[8] Heckmann, T., Cavalli, M., Cerdan, O., Foerster, S., Javaux, M., Lode, E., Smetanova, A., Vericat, D, Brardinoni, F., 2018. "Indices of sediment connectivity: opportunities, challenges and limitations". Earth Sci. Rev. 187, 77-108.

[9] Cavalli, M., Vericat, D., Pereira, P., 2019. "Mapping water and sediment connectivity". Sci. Tot. Env. 660, 899-912.

[10] Zingaro, M., A., Refice, E., Giachetta, A., D'Addabbo, F., Lovergine, V., De Pasquale, G., Pepe, P., Brandolini, A. Cevasco, D., Capolongo, 2019. "Sediment mobility and connectivity in a catchment: A new mapping approach" Sci. Tot. Env. 672, 763-775.

[11] Messenzehl, K., T., Hoffmann, R., Dikau, 2014. "Sediment connectivity in the high-alpine valley of Val Müschauns, Swiss National Park—linking geomorphic field mapping with geomorphometric modelling" Geomorphology 221, 215-229.

[12] Seijmonsbergen, A.C., J.A.M., Van den Ancker, P.D., Jungerius, S.J., Norder, 2019. "Can geodiversity help to save the soil archives?" In: Van Mourik, J.J. and Van Der Meer, J.M. (Eds). Reading the soil archives – unravelling the geoecological code of paleosols and sediment cores. Developments in Quaternary Science 18, pp. 275–298.

[13] Bollati, I., B.C., Lenz, A., Golzio, A. Masseroli, 2018. "Tree rings as ecological indicator of geomorphic activity in geoheritage studies" Ecol Ind, 93, 899-916.

[14] Bigioggero, B., A., Colombo, A., Cavallo, B., Aldighieri, A., Tunesi, 2007. "Geological-structural sketch-map of the Ossola-Simplon area". Snam Rete Gas Ed. (1 map; 1: 50.000 scale)"

[15] Steck, A., 2008. "Tectonics of the Simplon massif and Lepontine gneiss dome: deformation structures due to collision between the underthrusting European plate and the Adriatic indenter". Swiss J. Geosc. 101(2), 515-546.

[16] Baroni, C., R., Gentili, S., Armiraglio, 2013. "Vegetation analysis on composite debris cones". In Dating Torrential Processes on Fans and Cones pp. 187-201.

[17] Ballantyne, C.K., 2002. "Paraglacial geomorphology". Quat. Sci. Rev. 21(18-19), 1935-2017.

[18] ISPRA, 2018. "Carta Geomorfologica d'Italia alla scala 1:50.000 - Aggiornamento ed integrazioni delle linee guida della Carta Geomorfologica d'Italia alla scala 1:50.000", Fascicolo I, Quaderni, serie III, Volume 13, pp. 93.

[19] Bollati I., M., Paleari, E., Zanoletti, M., Pelfini, 2017. "Indexing Geomorphodiversity in the Veglia-Devero Natural Park (Western Italian Alps)", In "Innovative technologies for monitoring past and present geomorpholigical processes", VIIth Young Geomorphologists' Day, Napoli, 15-16 giugno, 2017

[20] Cavalli, M., L. Marchi, 2008. "Characterisation of the surface morphology of an alpine alluvial fan using airborne LiDAR" Nat. Haz. Earth Sys. Sci. 8(2), 323-333.

[21] Savi, S., M., Schneuwly - Bollschweiler, B., Bommer - Denns, M., Stoffel, F., Schlunegger, 2013. "Geomorphic coupling between hillslopes and channels in the Swiss Alps". Earth Surf. Process. Landform 38(9), 959-969.

GEOMORPHOMETRY 2020 PERUGIA, ITALY JUNE 22 - 26 2020

Flow Connectivity Patterns in Complex Anthropized Landscape: Application in Cinque Terre Terraced Site

Lorenzo Borselli*§, Devis Bartolini**, Paolo Corradeghini ***, Alessandro Lenzi**, Paolo Petri**
*Universidad Autónoma de San Luis Potosí, Instituto de Geología, San Luis Potosí, México
**Logica del Territorio Soc. Coop. a r.l., La Spezia (Italy)
***3DMetrica, Lerici (La Spezia, Italy)
§ lborselli@gmail.com

Abstract— **In a study area with a complex dry stone walls terracing system located in the Cinque Terre National Park (Italy), a very high resolution map of the surface connectivity of the flows was generated. A 0.06m resolution DTM produced with aerial photogrammetric techniques by means of UAV allowed to obtain connectivity index (IC) maps that relate the surface flow lines, the IC index and the main instability and collapse processes in the terrace system. The proposed methodology can be integrated with another proposed method for the verification of local stability of dry stone walls. The methodologies are proposed as a new tool for future restoration projects of dry stone wall terraced systems.**

I. INTRODUCTION

In the last 15 years the connectivity paradigm has assumed an increasingly important importance in the scientific literature relating to various processes such as: geomorphological processes of erosion and mass movements; studies relating to geomorphological hazard assessment; evaluation of soil erosion rates; identification of areas most sensitive to soil degradation phenomena, identification of areas with the greatest risk of flow of surface contaminants or nutrients (etc.) [2,3,4,5,7,8,10,13],. The quantitative evaluation of surface connectivity, to be related to other specific indicators of the processes mentioned above, is one of the major developments in geomorphology and environmental science studies in recent years.

The surface connectivity flow, which transport mass and energy through the surface runoff between two specific points located on the surface, has been modeled in the last 15 years by different authors both theoretically and practically [2,4,5].

One of the most used methods is the so-called Connectivity Index (IC) [1]. The IC index was subsequently adopted by several authors [1,6,9,10,11,12] for a large variety of applications. The IC index has also been proposed with a large number of variants.

The IC Index is a parameter that can be calculated in a distributed way across the territory through standard GIS tools once a digital terrain model, with adequate resolution, and a land use map are available. The connectivity index is a geomorphometric parameter that integrates local characteristics of land use or hydraulic impedance produced by the roughness of the ground, depending on which variant is used to calculate it [1].

The results of the study are related to the application of the connectivity theory proposed by [1] in a context of high territorial anthropization such as the drywall systems of the Cinque Terre National Park (Italy). Our study was applied to a digital terrain model (DTM) with high spatial resolution (0.06 m) of a 1 ha area together with a detailed land use classification made on orthorectified Ortho-photo, both obtained by UAV. The study area was chosen given that in the area there are a multiplicity of soil degradation processes linked to the partial abandonment of the drywall system that occurred from the second half of the twentieth century.

The first objective was to test the validity of the calculation methods of the IC index considering the peculiarities of the study area such as: the presence of sub-vertical walls of the dry walls and other characteristics of strong local anthropization. The second objective of the study was to obtain for a highly degraded area, such as the study area, new indications on the design criteria for drywall restoration interventions that consider the dynamics of the degradation processes underway. The tool to reach the second goal was to obtain a map of surface connectivity, a map of the surface drainage lines obtained with very high resolution DTM and a detailed geomorphological map.

II. METHODS

A. Study Area

The selected study area is located within the Cinque Terre national park (La Spezia; Italy) with the coordinates 44 ° 06'34.19 "N, 9 ° 43'49.10" E (Figure 1). The area has an extension of about 1 hectare, between an altitude of 140 m and 180m. The area is characterized by a complex system of terraces that interrupt an average slope of 36 °. The dry-stone walls have an average height of 2m, and are spaced at an average distance of about 6 meters.

Lorenzo Borselli, Devis Bartolini, Paolo Corradeghini, Alessandro Lenzi and Paolo Petri (2020)
Flow Connectivity Patterns in Complex Anthropized Landscape: Application in Cinque Terre Terraced Site:
in Massimiliano Alvioli, Ivan Marchesini, Laura Melelli & Peter Guth, eds., Proceedings of the Geomorphometry 2020 Conference, doi:10.30437/GEOMORPHOMETRY2020_15.

The average slope between one wall and the next is around 8-10 ° (Figure 2). Land use is characterized by bare soil meadows and vineyards. Some of the areas have undergone restoration by the Manarola Foundation with the aim of restoring the portions of the collapsed walls (Figure 3).

Figure 1. Ubication of Study Site, inside Cinque Terre National Park (La Spezia, Italy).

Figure 2. Manarola (Cinque Terre National Parck, La spezia, IT) study site (2017-2018)

B. High Resolution Digital Terrain Model by UAV Aero-photogrammetric Technique.

The high resolution (0.06m) digital terrain model of the entire study area was obtained with aero-photogrammetric technique by UAV. At the time of the investigations, the following cartographic and technical data were available: Regional Technical Map, in scale 1: 5.000, of the Liguria Region; LIDAR data with 1x1m mesh deriving from a survey campaign carried out by the Ministry of the Environment. The UAV vehicle allowed for a complete aero-photogrammetric survey through the acquisition of digital images. Preliminary to the acquisition of the images from the UAV, the high precision measurement of the coordinates of ground control points was carried out by means of a satellite antenna (nRTK survey).

Figure 3. High resolution Ortophoto. Manarola (Cinque Terre National Park, La spezia, IT) study site (2017-2018)

Subsequently, images and measurements were processed within specific software (Agisoft Metashape Professional). Then we proceeded with the elaboration of three-dimensional, oriented and georeferenced points clouds of high information density and their treatment within data processing software (Cloud Compare). At the end the extraction was carried out, from the three-dimensional data returned by ortho-mosaics and digital elevation models with high resolution (0.06 m). The UAV flight was carried out with a flight height of at least 70 m AGL (Above Ground Level). The aerial photographs were taken with the camera in the nadiral position (the optical axis exiting the lens has an inclination of 90 ° with respect to the horizontal) and camera inclined by 45 ° with respect to the horizontal, in consideration of the average slope of the terraced slope. The average overlap between the images was 80%.

C. Index of Connectivity (IC) Map

The connectivity map by means of the IC index was obtained following the original method proposed by [1] through the following equation:

$$IC = \log_{10}\left(\frac{D_{up}}{D_{dn}}\right) = \log_{10}\left(\frac{\overline{W}\times\overline{S}\times\sqrt{A}}{\sum\frac{d}{W\times S}}\right) \quad (1)$$

where The numerator (D_{up}) represents the feature uphill from a selected benchmark point and evaluates the capacity of water and sediment to descend towards the benchmark point (Borselli et al., 2008). $\overline{W}$ = average value of the weighting coefficient related to land cover/use; $\overline{S}$ = average slope of the area that contributes to the reference point (m/m); A = contribution area (m^2).
The denominator (D_{dn}) measures how the features downhill from the benchmark point allow the water and sediment to reach the sink; the elements of the calculation are similar to the D_{up} element, where the distance (d) to the sink (expressed in m) replaces the contribution area (A) (expressed in m^2).The weight factors W used in the eq. (19 are the same originally implemented by [1] for different land use.The map of IC index was obtained considering a minimum contribution area of 5 m^2 in order to produce basic drainage flow line. The basic algorithm used for determine flow direction has been the D8 algorithm [14] implemented in ArcGIS Module TAUDEM [15].

III. RESULTS AND CONCLUSIONS

The most important results of the study are a series of maps, with an extreme spatial resolution, which represent the distribution of connectivity in relation to the main instability phenomena detected in the drywall system (figure 4). The obtained maps relate the main flow lines that interconnect different terraces through two, or more, points in correspondence with collapsed terraces. The collapse of the terraces and the subsequent deterioration upon the establishment of a continuous flow line associated with accelerated erosion phenomena is a fairly common phenomenon in the Cinque Terre area. The phenomenon can considerably aggravate the degradation of the territory and produce more important threats during extreme hydrological events.

A system of flow lines, with high connectivity, which connects two or more terraces, through the collapse areas (figure 5), represents an extremely risky condition which can produce an acceleration of instability and a high production of sediments towards the urbanized downstream areas. In figure 4 the higher IC index value pixels are related to sites with flow lines interconnecting more than one terraces. Instead the lower IC values, that in some case are present in between two contiguous dry-stone walls, are related to recent human artifact as the temporary accumulation of stones and soil due to restoration work in progress.

In general, a rapid local Increase of IC values are always related to a sharp increase of sediment mobility and thus soil degradation associated to dry-stone walls collapse.

Figure 6 shows how even a high-resolution digital terrain model, such as a DTM lidar (1x1m), is unable to effectively reproduce the complex morphology of a terraced system. Instead, a high-resolution DEM, such as that obtained on the study site, is required to correctly represent the distribution of the actual slopes that are used for a multiplicity of applications. In particular, it is effective for studying the stability of single or multiple dry-stone walls using advanced calculation methods [16]. Lower resolution DTMs (for example 1X1m) are not suitable in this terraced system to reproduce sufficiently reliable connectivity maps.

The methodology developed with the application of the connectivity theory [1] to terraced systems together with the new method of verification of local stability of dry walls [16] is proposed here as a new and fundamental tool for the design of restoration interventions in terraced system of the Cinque Terre, with the aim of also mitigating the adverse effects during extreme hydrological events.

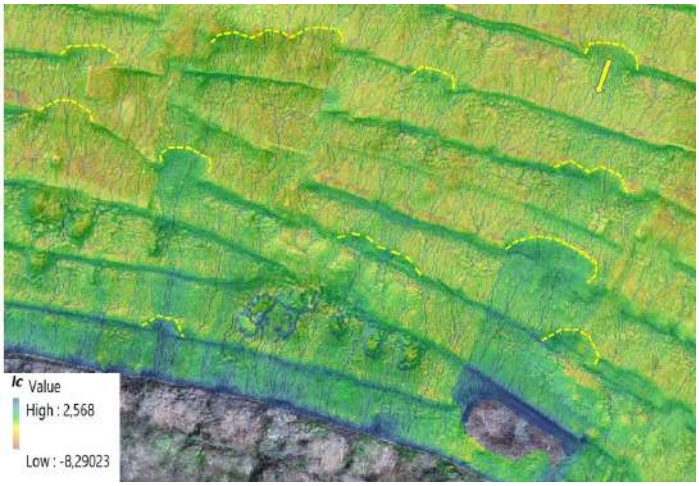

Figure 4..flow Connectivity map by IC index distribution in apportion of study site 30X30m. The grey zone is characterized by dense mediterranean shrub vegetation that do not allow the obtainment of reliable DTM. The yellow lines represent the upper limit of main phenomenon of collapsed dry stone walls. The yellow arrow is positioned in correspondence of site depicted in figure 5

Figure 5 Collapsed Dry stone wall with concentrated runoff pathway across a terraced vineyard in the study site. (Photo P. Petri 2017)

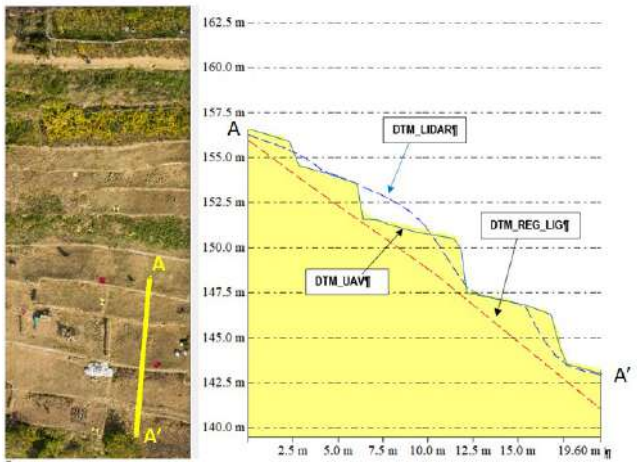

Figure 6 Comparison of three type of topographic profiles obtained from DTM region Liguria (scale 1:5.000 resolution 5x5); DTM form Lidar 1x1m (Ministero Ambiente), DTM obtained by aero-photogrammetric survey by UAV at resolution 0.06x0.06 m.

REFERENCES

[1] Borselli, L., Cassi, P., Torri, D., 2008. Prolegomena to sediment and flow connectivity in the landscape: A GIS and field numerical assessment. CATENA 75, 268–277. https://doi.org/10.1016/j.catena.2008.07.006

[2] Barneveld, R.J., van der Zee, S.E.A.T.M., Greipsland, I., Kværnø, S.H., Stolte, J., 2019. Prioritising areas for soil conservation measures in small agricultural catchments in Norway, using a connectivity index. Geoderma 340, 325–336. https://doi.org/10.1016/j.geoderma.2019.01.017

[3] Bracken, L.J., Croke, J., 2007. The concept of hydrological connectivity and its contribution to understanding runoff-dominated geomorphic systems. Hydrol. Process. 21, 1749–1763. https://doi.org/10.1002/hyp.6313

[4] Bracken, L.J., Turnbull, L., Wainwright, J., Bogaart, P., 2015. Sediment connectivity: a framework for understanding sediment transfer at multiple scales. Earth Surf. Process. Landforms 40, 177–188. https://doi.org/10.1002/esp.3635

[5] Bracken, L.J., Wainwright, J., Ali, G.A., Tetzlaff, D., Smith, M.W., Reaney, S.M., Roy, A.G., 2013. Concepts of hydrological connectivity: Research approaches, pathways and future agendas. Earth-Science Rev. 119, 17–34. https://doi.org/10.1016/j.earscirev.2013.02.001

[6] Cavalli, M., Trevisani, S., Comiti, F., Marchi, L., 2013. Geomorphometric assessment of spatial sediment connectivity in small Alpine catchments. Geomorphology 188, 31–41. https://doi.org/10.1016/j.geomorph.2012.05.007

[7] Chartin, C., Evrard, O., Onda, Y., Patin, J., Lefèvre, I., Ottlé, C., Ayrault, S., Lepage, H., Bonté, P., 2013. Tracking the early dispersion of contaminated sediment along rivers draining the Fukushima radioactive pollution plume. Anthropocene 1, 23–34. https://doi.org/10.1016/j.ancene.2013.07.001

[8] Heckmann, T., Cavalli, M., Cerdan, O., Foerster, S., Javaux, M., Lode, E., Smetanová, A., Vericat, D., Brardinoni, F., 2018. Indices of sediment connectivity: opportunities, challenges and limitations. Earth-Science Rev. 187, 77–108. https://doi.org/10.1016/j.earscirev.2018.08.004

[9] López-Vicente, M., Álvarez, S., 2018. Influence of DEM resolution on modelling hydrological connectivity in a complex agricultural catchment with woody crops. Earth Surf. Process. Landforms 43, 1403–1415. https://doi.org/10.1002/esp.4321

[10] López-Vicente, M., Ben-Salem, N., 2019. Computing structural and functional flow and sediment connectivity with a new aggregated index: A case study in a large Mediterranean catchment. Sci. Total Environ. 651, 179–191. https://doi.org/10.1016/J.SCITOTENV.2018.09.170

[11] Ortíz-Rodríguez, A.J., Borselli, L., Sarocchi, D., 2017. Flow connectivity in active volcanic areas: Use of index of connectivity in the assessment of lateral flow contribution to main streams. Catena 157, 90–111. https://doi.org/10.1016/j.catena.2017.05.009

[12] Ortíz-Rodríguez, A.J., Muñoz-Robles, C., Borselli, L., 2019. Changes in connectivity and hydrological efficiency following wildland fires in Sierra Madre Oriental, Mexico. Sci. Total Environ. 655, 112–128. https://doi.org/10.1016/j.scitotenv.2018.11.236

[13] Turnbull, L., Hütt, M.-T., Loannides, A.A., Kininmonth, S., Poeppl, R., Tockner, K., Bracken, L.J., Keesstra, S., Liu, L., Masselink, R., Parson, A.J., Ioannides, A.A., Kininmonth, S., Poeppl, R., Tockner, K., Bracken, L.J., Keesstra, S., Liu, L., Masselink, R., Parsons, A.J., Loannides, A.A., Kininmonth, S., Poeppl, R., Tockner, K., Bracken, L.J., Keesstra, S., Liu, L., Masselink, R., Parson, A.J., Ioannides, A.A., Kininmonth, S., Poeppl, R., Tockner, K., Bracken, L.J., Keesstra, S., Liu, L., Masselink, R., Parsons, A.J., Loannides, A.A., Kininmonth, S., Poeppl, R., Tockner, K., Bracken, L.J., Keesstra, S., Liu, L., Masselink, R., Parson, A.J., Ioannides, A.A., Kininmonth, S., Poeppl, R., Tockner, K., Bracken, L.J., Keesstra, S., Liu, L., Masselink, R., Parsons, A.J., 2018. Connectivity and complex systems: learning from a multi-disciplinary perspective. Appl. Netw. Sci. 3, 11. https://doi.org/10.1007/s41109-018-0067-2

[14] Tarboton, D. G. (1997). A new method for the determination of flow directions and upslope areas in grid digital elevation models. Water resources research, 33(2), 309-319.

[15] Tarboton, D. G., & Mohammed, I. N. (2013). TauDEM 5.1 quick start guide to using the TauDEM ArcGIS toolbox. Utah State University (USU), United State.

[16] Borselli L, Petri P. (2020). Muri a secco: verifiche di stabilità con software SSAP 5.0 e criterio GHB(GSI) per le strutture in roccia. Researchgate. https://doi.org/10.13140/RG.2.2.21048.90886/1

GEOMORPHOMETRY 2020 PERUGIA, ITALY JUNE 22 - 26 2020

Photogrammetric reconstruction of the Roman fish tank of Portus Julius (Pozzuoli Gulf, Italy): a contribution to the underwater geoarchaeological study of the area.

Claudia Caporizzo [1§], Pietro P.C. Aucelli [1], Gaia Mattei [1], Aldo Cinque [2], Salvatore Troisi [1], Francesco Peluso [1], Michele Stefanile [3], Gerardo Pappone [1]

[1]Dipartimento di Scienze e Tecnologie, Università degli Studi di Napoli Parthenope, Centro Direzionale Is C4, 80121 Napoli, Italy

[2]Dipartimento di Scienze della Terra, dell'Ambiente e delle Risorse, Università degli Studi di Napoli Federico II, Largo San Marcellino, 10, 80138 Napoli, Italy

[3]Dipartimento Asia Africa e Mediterraneo, Università degli Studi di Napoli L'Orientale, Piazza S. Domenico Maggiore, 12, 80134 Napoli, Italy

[§] claudia.caporizzo@uniparthenope.it

Abstract— **This research aims at the 3D reconstruction of a Roman fish tank (*piscina*) located inside the archaeological area of Portus Julius (Gulf of Pozzuoli, Naples) and it is part of a wider research finalized to reconstruct the amount of the vertical ground movements (VGM) occurred during historical times in the Gulf of Pozzuoli. The ancient *piscina* is related to the second life stage of the harbor that, after its construction in 37 BC, during the year 12 BC switched its usage from a military to a commercial one. The photogrammetric survey of the fish tank, curved directly into the embankment of the entry channel of the port, has been carried out in order to better characterize its morphological features, since it represents an important time reference for the area.**

I. INTRODUCTION

The Gulf of Pozzuoli, located in the wide Campi Flegrei Caldera, offers the possibility to collect important information about the modification the coastal landscape and the relative sea level (RSL) changes related to vertical ground movements (VGM) occurred in historical times. In fact, along the littoral, there are several archaeological remains (maritime villae, harbor facility etc.) scattered along the coast and testifying the ancient occupation of the sector. Nowadays the main part of the ancient coastal strip, including all the buildings and maritime structures, is submerged due to overall subsidence started at the end of the Roman period [1].

A multidisciplinary approach made of direct and indirect techniques turns out to be really useful for the study of submerged landscapes, since indirect surveys as the photogrammetric one can provide really accurate morphometric characterization of the underwater features, usually not easily accessible.

The goal of this study is to provide a detailed 3D reconstruction of the nowadays submerged fish tank of the Roman harbor of Portus Julius.

The study site is located inside the Underwater Archaeological Park of Baia, famous all over the world since in historical time the area was affected by sudden VGM that led to the submersion of the entire coastal sector. This intense overall subsidence resulted in a perfect preservation status of the structures still clearly recognizable.

In 37 BC, the area enclosed between the Lucrino and the Averno Lakes was chosen by Agrippa for the construction of the new military harbour system of Portus Julius.

The military purpose of the system ended in the 12 BC, with the conversion of the harbor in a commercial base together with the relocation of the military port in the nearby Misenum, Indeed, Portus Julius was rethought and restructured, with the transformation and the adaptation of military environments into warehouses. [2, 3, 4].

The fish tank here surveyed can be considered as a good evidence of the renovation occurred after 12 BC. This fish tank is particularly interesting because it represents one of the few examples of fish tanks related to commercial activities and not to private maritime villas.

Considering the importance of this feature, together with a direct survey aimed to determine the submersion of its structural element, a photogrammetric survey of the fish tank has been realized. The photogrammetric reconstruction was crucial both for the evaluation of the elements related to the study of the past RSL

Claudia Caporizzo, Pietro P.C. Aucelli, Gaia Mattei, Aldo Cinque, Salvatore Troisi, FrancescoPeluso, Michele Stefanile, and GerardoPappone (2020)

Photogrammetric reconstruction of the Roman fish tank of Portus Julius (Pozzuoli Gulf, Italy): a contribution to the underwater geoarchaeological study of the area:

in Massimiliano Alvioli, Ivan Marchesini, Laura Melelli & Peter Guth, eds., Proceedings of the Geomorphometry 2020 Conference, doi:10.30437/GEOMORPHOMETRY2020_16.

and for the documentation of this singular fish tank built for commercial use, with a great cultural value.

II. METHODS

The fish tank here studied, due to its strategic position, represented the key element of our geoarchaeological interpretations in terms of ground movements occurred during the Roman times. The sluice gate of this fish tank was built directly by cutting the channel embankment. This led to the assumption that it was therefore built in the second construction phase of the Portus Julius, according to Benini and Giacobelli [5]. Therefore, in this area, an underwater photogrammetric survey (Fig.1) has been carried out both to obtain a detailed morphometric analysis of this functional element and to preserve a 3D documentation of this important and unique historical testimony, also considering the extreme fragility of this underwater landscape.

The photogrammetric survey was planned by using a photogrammetric system (Fig. 1a and b) consisting of two high-resolution cameras, having the optical axis vertical.

The stereoscopic base and the submersion of the system were chosen in relation to the bathymetry of the study area and to the resolution of the three-dimensional model of submerged findings (Fig. 1a). With our setting for the cameras, ensuring a minimum overlap of 80% for the images during the survey. Taking into account the characteristics of the video cameras, to ensure a transversal overlap of at least 80%, the stereoscopic base was chosen equal to 30 centimeters. The depth of the photogrammetric system was modified during the survey to guarantee both an adequate completeness of the three-dimensional model and its resolution (see Fig. 1c).

As shown in Figure 1a, the camera system was towed by a rope connected to an emerged float and moved by a diver. This system provides two basic positions, namely position A at -1 meter and position B at -2 meters below sea surface.

The photogrammetric 3D model of the surveyed fish tank was obtained in three two steps [6]:

- The videos at 30 fps recorded by the two Xiaomi cameras (previously calibrated in an underwater environment close to the study area to achieve the inner orientation parameters were synchronized by the use of the trigger system and the images were extracted using a frame every 6th frame. More than one thousand 1920x1080 images were thus obtained;

- The alignment procedure of the images and the dense point cloud extraction was performed by Agisoft Metashape software. The 3D model was not georeferenced because it was not possible to determine the coordinates of the control points, but some linear measurements made by the diver directly on the underwater structure made it possible to scale the dense point cloud.

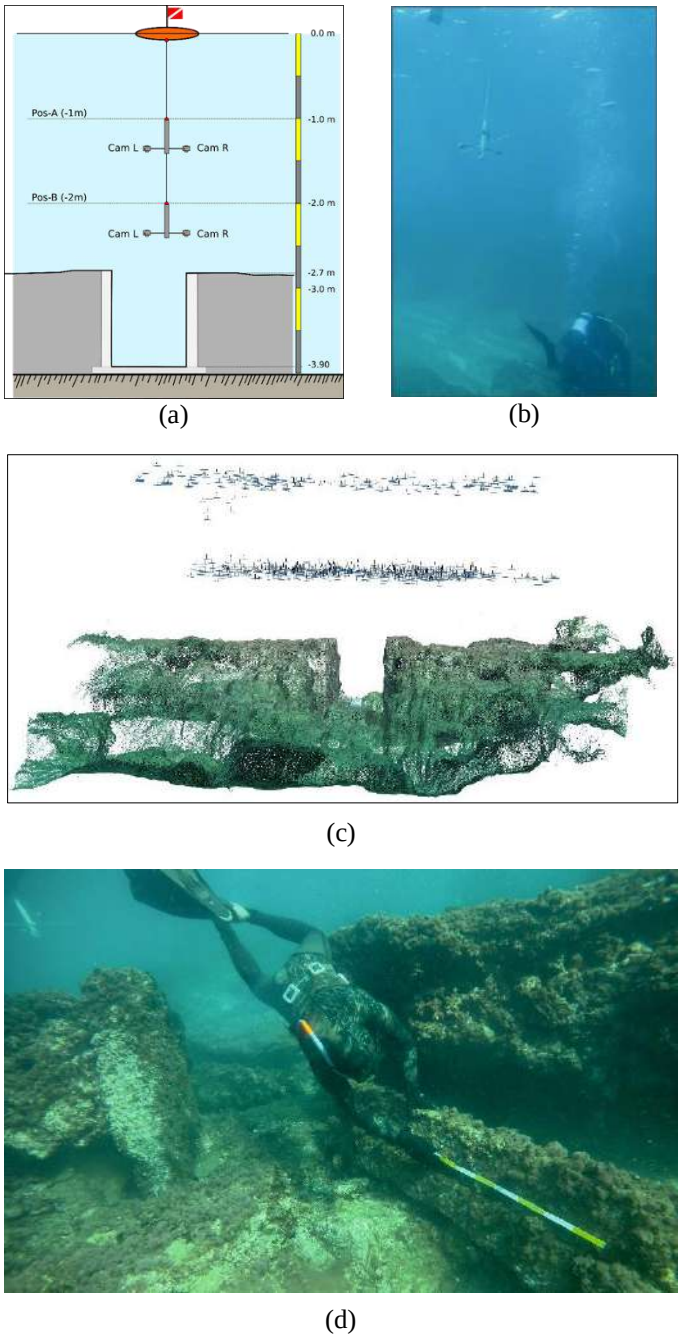

Figure 1. (a) Reconstruction of the photogrammetric system used during the survey; (b) Photogrammetric system used during the survey; (c) Positon of the photogrammetric cameras during the survey; (d) Direct measurement of a linear constrain by a diver.

The buddle adjustment procedure has been performed by using two linear constraints measured directly by a diver and two more distances, used as check in different zones of the sensed fish tank [7, 8, 9] (Fig. 1d). The procedure of alignment produced a difference of less than 2 cm in each of two distances used as check.

III. RESULTS AND CONCLUSIONS

The triangular fish tanks of Portus Julius, with a size of 20x22x16 m, is entirely made of tuff and it appears to be carved directly into the embankment of the entry channel (Fig. 2).

During the direct survey the main constructional element of the *piscina* were measured to evaluate the amount of their submersion. In particular, the measurements concerned the sluice gate of the tank still *in situ* (*cataracta*, i.e. closing gate located at the access of the channels of the tanks into the basin or at communication passage between each tank) [10, 11, 12, 13, 14].

The top of the sluice was built 0.2 m (functional clearance, fc) above the mean high water (MHW), so correcting the submersion measurement with respect to this value and the reference water level (RWL) of the sea level marker, in this case equal to the half of the difference between the MHW and the mean low water (MLW), a RSL of -3.10 m MSL for the 12 BC was calculated [14, 15, 16].

All the measurements and considerations derived from the direct survey have been supported by correlations made on the base of the analysis of the 3D photogrammetric reconstruction (Fig. 2a, b and c).

Nowadays the digital photogrammetric techniques have reached really high levels due to the new technologies. These methods of analysis are becoming more and more common and accessible to a growing number of people due to the low cost of their realization.

The use of the photogrammetry falls into different categories, even in areas of complex approach as in this case of a 3D underwater reconstruction of an element of archaeological interest.

Considering this research carried out on the Roman fish tank of Portus Julius, the results achieved have a meaningful scientific value related to the possibility of carrying out precise measurements of the three-dimensionally reconstructed object. On the other hand, the realization of the 3D model offers a virtual access opportunity to the element located in a submerged environment, normally only open to a specialized public.

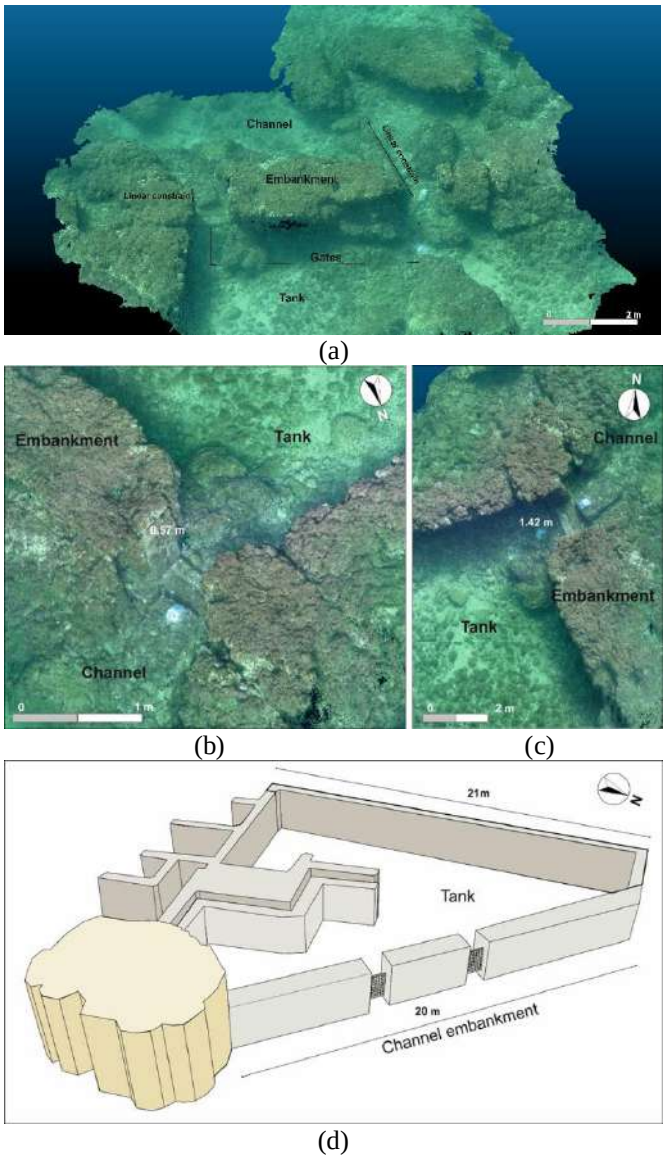

Figure 2. (a) Photogrammetric Point cloud; (b) Zoom of the 3D reconstruction of the well preserved gate; (c) Zoom of the 3D reconstruction of two perimeter walls of the fish tank; (d) 3D sketch of the surveyed fish tank.

REFERENCES

[1] Morhange, C.; Marriner, N.; Laborel, J.; Todesco, M.; Oberlin, C. Rapid sea-level movements and non-eruptive crustal deformation in the phlegrean Fields caldera, Italy. Geology 2006, 34, pp. 93-96.

[2] Benini, A.; Giacobelli, M. Peschiera o Pescheria? Curiosità flegree. Atti del III Convegno di Archeologia Subacquea, Manfredonia, Italy, 4-6 ottobre 2007; Insulae Diomedeae - 24.

[3] Miniero, P. Baia sommersa e portus Iulius. Il rilievo con strumentazione integrata Multibeam. In Ricoveri per navi militari nei porti del Mediterraneo antico e medievale; Blackman, D. J., Lentini, M. C., Bari, Italy, 2010; pp. 101-108.

[4] Gianfrotta, P.A. Ricerche nell'area sommersa del "Portus Iulius" (1988-'90 e successive): un riepilogo. In ATTA 22, 2012; pp. 1-20.

[5] Benini, A.; Giacobelli, M. Peschiera o Pescheria? Curiosità flegree. Atti del III Convegno di Archeologia Subacquea, Manfredonia, Italy, 4-6 ottobre 2007; Insulae Diomedeae - 24.

[6] Mattei, G.; Troisi, S.; Aucelli, P.P.C.; Pappone, G.; Peluso, F.; Stefanile, M. Multiscale reconstruction of natural and archaeological underwater landscape by optical and acoustic sensors. In 2018 IEEE International Workshop on Metrology for the Sea; Learning to Measure Sea Health Parameters (MetroSea), 2019b; pp. 46-49.

[7] Marre, G.; Holon, F.; Luque, S.; Boissery, P.; Deter, J. Monitoring Marine Habitats With Photogrammetry: A Cost-Effective, Accurate, Precise and High-Resolution Reconstruction Method. Front. Mar. Sci. 2019; 6:276. doi: 10.3389/fmars.2019.00276

[8] Neyer, F.; Nocerino, E.; Gruen, A. IMAGE QUALITY IMPROVEMENTS IN LOW-COST UNDERWATER PHOTOGRAMMETRY, Int. Arch. Photogramm. Remote Sens. Spatial Inf. Sci., XLII-2/W10, 135–142, https://doi.org/10.5194/isprs-archives-XLII-2-W10-135-2019, 2019.

[9] Pierre Drap (2012). Underwater Photogrammetry for Archaeology, Special Applications of Photogrammetry. Dr. Daniel Carneiro Da Silva (Ed.), ISBN: 978-953-51-0548-0, InTech, Available from: http://www.intechopen.com/books/special-applications-of-photogrammetry/underwater-photogrammetry-forarchaeology

[10] Leoni, G.; Dai Pra, G. Variazioni del livello del mare nel tardo olocene, ultimi 2500 anni, lungo la costa del Lazio in base ad indicatori geo-archeologici: interazioni fra neotettonica, eustatismo e clima. ENEA, Unità comunicazione e informazione, 1997.

[11] Lambeck, K.; Anzidei, M.; Antonioli, F.; Benini, A.; Esposito, E. Sea level in Roman time in the central Mediterranean and implications for recent change. EPSL 2004, 224, pp. 563–575.

[12] Auriemma, R.; Solinas, E. Archaeological remains as sea level change markers: a review. Quat. Int. 2009, 206 (1), pp. 134-146.

[13] Evelpidou, N.; Pirazzoli, P.A.; Saliegec, J.F. Submerged notches and doline sediments evidence for Holocene subsidence. Cont. Shelf Res. 2011., 31, pp. 1273-1281.

[14] Lambeck, K.; Anzidei, M.; Antonioli, F.; Benini, A.; Verrubbi, V. Tyrrhenian sea level at 2000 BP: evidence from Roman age fish tanks and their geological calibration. Rend. Lincei-Sci. Fis. 2018, 29, pp. 69-80.

[15] Shennan, I.; Long, A. J.; Horton, B. P. Handbook of sea-level research. Oxford: John Wiley & Sons, New York, U.S.A., 2015.

[16] Vacchi, M.; Marriner, N.; Morhange, C.; Spada, G.; Fontana, A.; Rovere, A. Multiproxy assessment of Holocene relative sea-level changes in the western Mediterranean: Sea-level variability and improvements in the definition of the isostatic signal. Earth-Sci. Rev. 2016, 155, pp. 172-197.

GEOMORPHOMETRY 2020 PERUGIA, ITALY JUNE 22 - 26 2020

Changes of selected topographic parameters of Krakow Old Town (Poland) during the last millennium as a result of the deposition of cultural sediments

Adam Łajczak[§], Roksana Zarychta[§], Grzegorz Wałek[§§]
[§]Institute of Geography, Pedagogical University of Krakow
Podchorążych 2, 30-084 Kraków, Poland
[§]alajczak@o2.pl; roksana.zarychta@up.krakow.pl
[§§]Institute of Geography and Environmental Sciences, Jan Kochanowski University in Kielce
Uniwersytecka 7, 25-406, Kielce, Poland
grzegorz.walek@ujk.edu.pl

Abstract—**Investigations of changes in land topography over the last millennium were carried out within the boundaries of Krakow Old Town and were estimated from archaeological and geoengineering data. With the application of DEM, four topographic parameters were calculated (altitude, local relative height, slope and aspect) in two time situations: the present-day and before the rapid development of the town. Based on the parameters, changes in the land morphometry of the study area were analysed in detail and were compared with the thickness of cultural deposits (varying from 1 m to 15 m). There is a dominating trend of land flattening in the study area.**

I. INTRODUCTION

The central parts of towns with a long history distinguish themselves when compared to younger peripheral urban areas in terms of their considerably transformed topography. This is mainly due to the large-scale deposition of cultural sediments, sometimes with a contribution from sedimentation influenced by natural processes [1, 2]. Such changes lead to the building up of the area concerned and usually to its flattening [3]. Simultaneously, processes of land lowering occur on a local scale due to earthworks, mining works or river-control works [4]. Unlike the present situation, the estimation of the morphometry of the former relief of towns (i.e. before the beginning of rapid changes in the topography of urbanised areas) requires knowledge of the spatial differentiation of the thickness of the layer of cultural deposits and the thickness of the loss of the bedrock layer and/or unconsolidated sediments. Vertical changes in the topography of urban areas may be estimated based on archaeological or geoengineering investigations, and, in shorter time intervals, based on comparative analysis of maps [1, 3, 5, 6]. With the application of DEM generated on the basis of LiDAR data, different topographic parameters may be calculated such as altitude, local relative height, slope and aspect. Based on the reconstructed topographic surface before the accumulation of cultural deposits, and on the investigation results which meet strict archaeological and/or geoengineering criteria, it is possible to prepare a DEM and calculate the above-mentioned parameters which describe the former topography. A comparison of the results obtained makes it possible to evaluate changes in the topography of urban areas, which have mainly occurred due to the deposition of cultural sediments.

Studies discussing changes in urban geomorphometry, e.g. [6-10], focus on spatial variability in the thickness of the layers of cultural sediments. They give little attention to how other features of urban topography resulting from this process have changed from their pre-urban status. This study, on the other hand, takes into account changes in slope and aspect within the city's historic centre.

The analysis was carried out within the boundaries of Krakow Old Town, Poland. Based on topographic parameters, the changes in land topography of this area were compared with the thickness of the cultural layer which occurred during the last millennium.

II. DATA USED AND METHODS

The original topography of the area studied was reconstructed based on published contour-line maps of different scales. These maps were prepared from the results of archaeological investigations. The roof of the in situ fossil soil overbuilt by cultural deposits is assumed to be the former level

Adam Lajczak, Roksana Zarychta and Grzegorz Walek (2020) Changes of selected topographic parameters of Cracow Old Town (Poland) during the last millennium as a result of deposition of cultural sediments: in Massimiliano Alvioli, Ivan Marchesini, Laura Melelli & Peter Guth, eds., Proceedings of the Geomorphometry 2020 Conference, doi:10.30437/GEOMORPHOMETRY2020_17.

of the ground surface. Another source of information in the assessment of the original topography of the study area is found in published maps that are based on the results of geoengineering investigations. The maps also show the altitude of the deposits [m a.s.l.] lying under the cultural layer. From the above-mentioned data, a DEM was generated which showed the topography of the study area as it was about 1000 years ago. Using LiDAR data, a DEM was prepared which showed the present topography of the area studied.

To show the present and the former topography of the area studied, the following parameters were calculated: altitude, local relative height, slope, aspect. QGIS, SAGA GIS and GRASS GIS were used for spatial analyses. The values of the parameters were shown graphically for the whole study area which made it possible to evaluate the changes in topography between the initial and modern situations of any part of the area. The location of the parts of the study area analysed is facilitated by a square grid with sides of 150 m placed on the background of the borders of the individual landforms analysed. Based on the altitude [m a.s.l.] calculated as a mean value for each square of the grid at both moments in time analysed, the changes in each square of the grid were determined at a local scale Δh [m]. Changes in the slopes of the study area were estimated based on a comparison of the percentage [%] of parts of the area studied showing selected slopes [°] in both time periods analysed. In a similar way, changes in aspect in the study area were also estimated.

The thickness of the layer of cultural deposits was estimated from the topographic surfaces generated – both initial and modern. The differentiation of deposit thickness was shown as a contour line map which contained the boundaries of the landforms analysed.

III. RESULTS AND CONCLUSIONS

In the boundaries of Krakow Old Town (9 km^2), four types of landform occur: (1) the Holocene plain of the Vistula river which occupies most of the study area, (2) the channels of the Vistula river and its tributaries, (3) a fragment of the Pleistocene terrace which rises 7-10 m above the Holocene plain, (4) isolated limestone hills of steep, locally rocky slopes elevated up to 40 m above the Holocene plain. A fragment of the Pleistocene terrace is connected as a spur with the centrally located Wawel Hill. In the past, the Vistula channel was meandering and adjacent to wetlands (including oxbow lakes and peripheral depressions – backswamps filled with peat). The latter landforms occurred in a large area around Wawel Hill and at the foot of the spur escarpment of the Pleistocene terrace [11]. The original topography of the study area (before the beginning of settlement in Krakow) was dominated by areas at an altitude of 195-200 m a.s.l. Convex landforms (limestone hills, sandbars in the area of the Vistula floodplain) showed clear limits which separated them from the concave landforms. Local height differences at the hill margins often exceeded 10 m reaching even 40 m. In the case of sandbars within the Vistula floodplain, these locally exceeded 5 m [Fig. 1]. The mean depth of the Vistula channel was 2 m (maximum 4 m) and it was accompanied by a low levee. Most of the study area showed a slope <=2° (Vistula floodplain, hilltop of the Middle Pleistocene terrace, fragments of the hilltops of limestone hills). Larger inclinations (2-5°) occurred in the case of sandbar slopes, long sections of the escarpment of the Middle Pleistocene terrace and at the foot of the limestone hills. A slope in the range 5-10° occurred within the escarpment of the Middle Pleistocene terrace directly above the Vistula backswamps and slopes of the limestone hills. The highest limestone hills (especially their slopes adjacent to the Vistula), showed even steeper slopes (10-20°, locally >20°). A vast area of the inclination <=2° was classified as without aspect. The fragments of land with N, E, S and W aspects had similar total areas at that point in time.

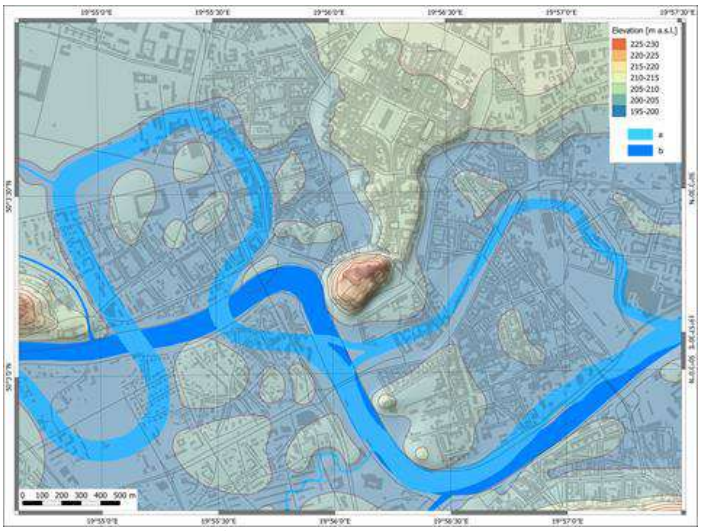

Figure 1. Hypsometry of the study area ca. 1000 AD. River channels: a – ca. 1000 AD, b – today.

The layer of cultural deposits accumulated during the last millennium covered almost the whole of the study area, except for local quarries within the slopes of the limestone hills, and the Vistula channel, which was deepened by about 4 m due to river-control works [12]. The mean thickness of this layer is 3.4 m, but it shows considerable spatial variation from 1-2 m in most of the area studied to 5-8 m within the palaeochannels and in the area of the former backswamps, and even to 15 m on the slopes

of Wawel Hill where the Royal Castle and Cathedral are located [Fig. 2, Photo. 1].

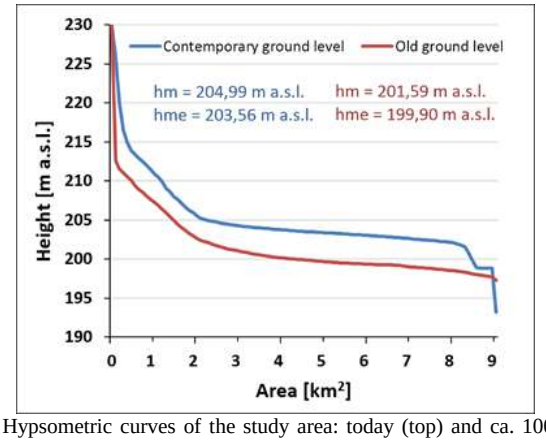

Figure 2. Hypsometric curves of the study area: today (top) and ca. 1000 AD (bottom).

Photo 1. Cultural deposits exposed in the Underground Museum of the Old Town in Krakow (Phot. R. Zarychta).

At present, almost the whole area of the Vistula floodplain is located at an altitude 200-205 ma a.s.l., therefore concave landforms such as palaeochannels, oxbow lakes and backswamps, as well as low convex landforms (sandbars and the lowest limestone hill) became hidden under deposits (partly fluvial ones) [Fig. 3]. At a height exceeding 205 m a.s.l., there is the foot of the escarpments of the Middle Pleistocene terrace, whereas the foot of the highest limestone hills reaches 210 m a.s.l. Some anthropogenic landforms, such as railway embankments, flood control embankments next to the Vistula channel, bridge abutments, and observation hillocks, developed within the Vistula floodplain and these usually exceed 5 m (up to 205 m a.s.l. or higher). During construction works, several metre-deep concave landforms were produced, later occupied by buildings. Local depressions commonly occur within the Vistula floodplain in the area covered by buildings from the 19th century and the beginning of the 20th century. These include back-yards located 1-2 m lower than the neighbouring streets. On the Vistula floodplain and on the Middle Pleistocene terrace, up to 3 m deep local depressions representing the former topography occur around old churches and synagogues [Photo. 2]. At present the hilltop of the spur of the Middle Pleistocene terrace is located above the altitude of 210 m a.s.l. The W-E profile of this landform no longer shows a table-like shape, as its escarpment and foot were overbuilt by cultural deposits, (its southern part providing an exception). The height of limestone hills has not changed, however cultural deposits were accumulated at their foot and on their slopes (e.g. SE slope of Wawel Hill) which resulted in a decrease in local height differences around these hills. Despite the changes in modern relief discussed, the slopes within most of the study area are still <=2°. Within the Vistula floodplain, there are small areas showing slopes of up to 20° or more (convex and concave anthropogenic landforms – especially linear ones). Slopes of the highest limestone hills still reach the value of 20°, and its N and W slopes exceed 20°. At present, areas of zero-aspect still predominate (slope <=2°). Lower located areas contain numerous anthropogenic forms of varying aspect.

Figure 3. Hypsometry of the study area today. River channels: a – ca. 1000 AD, b – today.

Photo 2. Narrow depression around the walls of an old church representing the former ground level (Phot. R. Zarychta).

The overlaying of the area of Krakow Old Town by anthropogenic deposits (more often in the case of concave landforms than convex ones), and also the development of high convex anthropogenic landforms, caused an uneven increase in altitude values (1-15 m) and an increase in the variation of local height differences. This resulted in an increase in slope and differentiation into greater variety at a local scale. In the study area, the area with a slope <=2° decreased by 6%, whereas the areas with slope 5-10° and >20° doubled. Areas without an aspect decreased, whereas the areas with S, W and E aspects increased [Fig. 4]. In the whole study area, a trend to area flattening occurred as a result of the deposition of anthropogenic sediments, however at a local scale, there was a trend to an increase in undulation that is visible.

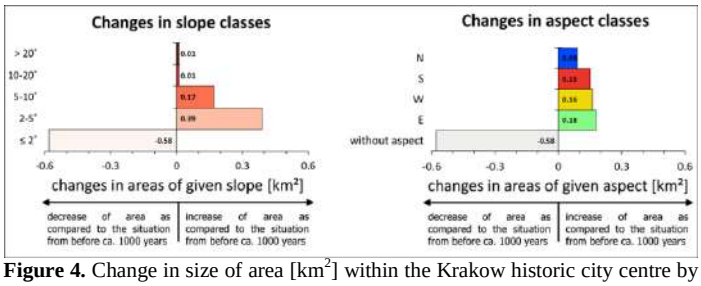

Figure 4. Change in size of area [km^2] within the Krakow historic city centre by slope range [°] and aspect during the last millennium.

Source of Figs. 1-4: [13].

REFERENCES

[1] Carver, M.O.H, 1983. "Forty French Towns: An essay on archaeological site evaluation and historical aims". Oxford Journal of Archaeology 2(3), 339-378.

[2] Brandolini, P., Faccini, F., Paliaga, G., Piana, P., 2017. "Urban geomorphology in coastal environment: man-made morphological changes in a seaside tourist resort (Rapallo, eastern Liguria, Italy)". Quaestiones Geographicae 36(3), 97-110.

[3] Luberti, G.M., 2018. "Computation of modern anthropogenic-deposit thickness in urban areas: A case study in Rome, Italy". The Antropocene Review 5(1), 2-27.

[4] Zarychta R., 2019. "The post-mining landscape of the Liban quarry in Cracow". Polish Geological Review 67(12), 1002-1011.

[5] Dall`Aglio, P.L., De Donatis, M., Franceschelli, C., Guerra, C., Guerra, V., Nesci, O., Piacentini, D., Savelli, D., 2017. "Geomorphological and anthropic control of the development of some Adriatic historical towns (Italy) since the Roman age". Quaestiones Geographicae 36(3), 111-123.

[6] Pröschel B., Lehmkuhl F., 2019. "Paleotopography and anthropogenic deposition thickness of the city of Aachen, Germany". Journal of Maps 15(2), 269-277.

[7] Kaniecki, A., 2013. "The impact of anthropopression on environmental changes in the Warta river valley in Poznań". Landform Analysis 24, 23-34.

[8] Molewski, P., Juśkiewicz, W. 2014. "An attempt to reconstruct the primary relief of the Old Town of Toruń and its close suburbs on the basis of the geological and historical geoinformation". Landform Analysis 25, 115-124.

[9] Tran Thi Van, Dinh Thi Kim Phuong, Phan Y Van, Ha Duong Xuan Bao, 2015. "Mapping changes of surface topography under urbanization process in Ho Chi Minh City, Vietnam, using satellite imagery". [In:] Conference Proceedings Paper – Remote Sensing: of 1st International Electronic Confrence on Remote Sensing 22 June – 5 July 2015, 1-7.

[10] Weifeng Qiao, Yahua Wang, Qingping Ji, Yi Hu, Dazhuan Ge, Min Cao, 2019. "Analysis of the evolution of urban three-dimensional morphology: the case of Nanjing city, China". Journal of Maps 15(1), 30-38.

[11] Łajczak A., Zarychta R., 2020. "Reconstruction of the morphology and hydrography of the center of Krakow before the mid-13th century". Geographia Polonica 93(1), 25-50.

[12] Łajczak A., 1995. "The Impact of River Regulation, 1850-1990, on the Channel and Floodplain of the Upper Vistula River, Southern Poland". [In:] E.J. Hickin (ed.) River Geomorphology. International Association of Geomorphologists, Publ. No 2, J. Wiley & Sons Ltd, Chichester, 209-233.

[13] Łajczak A., Zarychta R., Wałek G. "Changes in topography of Krakow centre during the last millennium, Poland". Journal of Maps (after review).

Necropolis of Palazzone in Perugia: integrated geomatic techniques for a geomorphological analysis

Fabio Radicioni[§], Aurelio Stoppini, Grazia Tosi, Laura Marconi
Dep. of Engineering (DI), University of Perugia
Via G. Duranti 93, 06125 Perugia, Italy
[§] fabio.radicioni@unipg.it

Abstract—**In the geomorphological research field there has been an increasing diffusion of Geomatics in recent times: the introduction of new tools and methodologies has made possible to characterize and reconstruct Earth's surface in 3 dimensions at high resolution, allowing a much better description of the geometries. Geomatics is an applied science that deals with acquiring, modeling, analyzing, processing, archiving and providing geographic and spatial data information with an integrated approach. In particular, among the geomatic techniques that can be profitably utilized in Geomorphometry, there are LiDAR and photogrammetry. These technologies allow to generate high-resolution point clouds representing the soil surface geometry in greater detail than the classic survey techniques, allowing detailed analysis at a few centimeter scale. In this paper we present an application of geomatic methodologies to the case of the Necropolis of Palazzone, an Etruscan funeral site near Perugia, in central Italy: an excellent example of a site combining archaeological and geological interests, being a so called "*archeogeosite*". The geomatic models represent the basis for a sedimentary and geomorphological study of the cavities, a 3D analysis of the lithostratigraphic units aiming to a paleogeographic reconstruction of the Perugia hill. To measure and georeference the cavities and the ground surface of the site, the project has seen a synergistic use of different methodologies in order to obtain a 3D model on which carry out investigations both on the geomorphological and archaeological aspects.**

I. Introduction

Geomatics has progressively affirmed in the geomorphological field thanks to the development of new technologies. This survey science makes it possible to obtain accurate information regarding the environment, creating three-dimensional models that allow geomorphologists to study the shaping processes of the Earth's surface with resolutions not possible in the past [2,5,6]. An example of correct integration between the two sciences is the so-called "archeogeosite", an archaeological site where geological and geomorphological evolutionary conditions are determinant for the knowledge and correct interpretation of the site itself [8].

The Necropolis of Palazzone represents one of the most significant funerary sites of the Etruscan era in central Italy, with almost two hundred tombs excavated in the ground, dating from the fifth century B.C. to the Hellenistic age. Located on the south-east area of the Perugia hill of Perugia, the Necropolis is characterized by a sloping area of about 4 hectares [4]. Despite the obvious archeological importance, the site is penalized from a touristic point of view, being located in a peripheral area of Perugia town where there are no cultural itineraries and penalized by the presence of the above freeway and the adjacent railway. The project "*SILENE: a Lidar System for the Exploration of the NEcropolis of Palazzone - Remote Sensing and Geology for the enhancement of archaeological sites*" fits into this context, with the aim to increase the scientific value and tourist attraction of the site, applying geomatic techniques and using geological data. This project, promoted by the Geology and Engineering Departments of Perugia University, wants to produce an original geomorphological study of the cavities, defining their geometry and position (relative and absolute) creating a unique three-dimensional model in order to geologically correlate the cavities by placing them in the overall paleogeographic reconstruction of the Perugia hill [1].

II. Geomatic Survey

Due to the underground nature of the tombs (with narrow entrances and poor lighting), located on a slope with altimetric irregularities and partially covered by vegetation (olive trees, shrubs, bushes), the 3D survey of the Necropolis was performed with the integrated and synergistic use of a series of the most advanced and effective methodologies of Geomatics [3,7,9]. The geomatic survey workflow has included the following steps:

1. Creation of a 3D network by means of GNSS and Total Station, to georeference the subsequent surveys in a well-defined global datum (ETRF2000);
2. Generation of 3D point clouds of the cavities by Terrestrial Laser Scanning (TLS or T-LiDAR);
3. Total station survey of TLS targets from network points;

Fabio Radicioni, Aurelio Stoppini, Grazia Tosi and Laura Marconi (2020) Necropolis of Palazzone in Perugia: integrated geomatic techniques for a geomorphological analysis: in Massimiliano Alvioli, Ivan Marchesini, Laura Melelli & Peter Guth, eds., Proceedings of the Geomorphometry 2020 Conference, doi:10.30437/GEOMORPHOMETRY2020_18.

4. Terrestrial digital photogrammetry as additional/alternative technique for the main cavity (Volumni's Hypogeum);
5. UAV digital photogrammetry for creating a DSM of the external ground surface;
6. GNSS NRTK survey for georeferencing the photo targets of the DSM and checking its accuracy;
7. Data post-processing and creation of the final products.

In total, 19 tombs of the Necropolis were surveyed, with a precision and a detail level that could not be reached with conventional survey methods.

A. GNSS and Total Station survey

The GNSS technique has been used for two purposes:

- to establish a reference network of the area, expressed in the global datum ETRF2000, for georeferencing the TLS and photogrammetric surveys;
- to check the accuracy of the DSM from UAV survey, through a large number of surface points measured directly.

The GNSS positioning was performed in real time (RTK base-rover and NRTK supported by the GPSUMBRIA permanent network), obtaining a <2 cm position accuracy. Two Topcon GR-5 GPS-GLONASS receivers were used. The overall scheme of the reference network is shown in Figure 1.

By means of a total station (Leica TS06), the reference network was completed connecting the GNSS points outside the tombs with 5 subnets (fig. 1), outside and inside the tombs. Finally, a large number of targets were measured with the total station from the network vertices. The targets, consisting of square plates with a black/white checkerboard pattern, are necessary for the point clouds georeferencing.

B. TLS survey

The detailed survey of the cavities was carried out using the TLS (Terrestrial LiDAR) technique. The laser scanning is one of the most powerful and productive geomatic survey systems, allowing to perform a real 3D scan of the object, thanks to its ability to measure a great number of points in short times (almost one million points per second in the present case). The result of TLS measures is a point cloud, in this case with superimposed RGB colors, deriving from an integrated camera.

A CAM2 FARO FOCUS 3D X130 instrument was used for scanning the 19 tombs, for a total of over 60 scans (900 million points) with an average resolution of about 12 mm at 10 meters distance and an acquisition time of 5-10 minutes for each scan. For describing the geometry of the cavities correctly, it is necessary to scan the object from multiple points of view in order to have overlapping areas. The clouds must be oriented to each other (relative orientation) through a 3D rototranslation maintaining a fixed reference cloud. This process requires common points between adjacent scans: a minimum of 4 targets (see above) and a set of 6 calibrated spheres, 3 of which have to be common to adjacent scans. This procedure was carried out with the Faro Scene software v. 6.2.

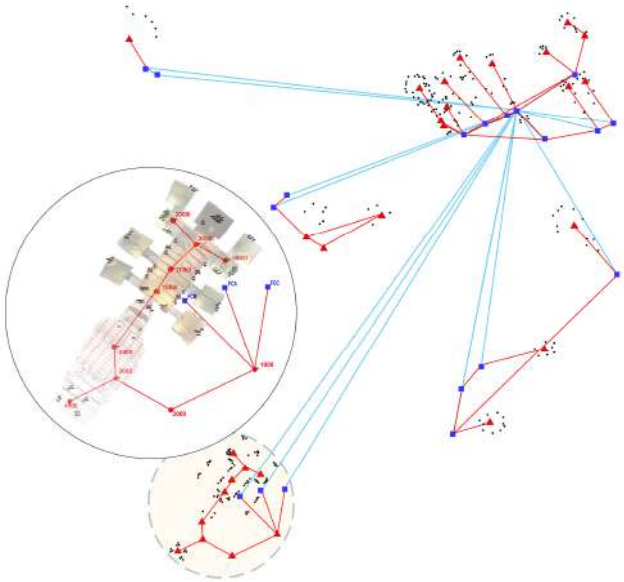

Figure 1. Reference network of Necropolis. On the left-hand side detail of Volumni's network.

The relative orientation generated a unique assembled 3D cloud (Fig. 2), where the density of the points is of the order of 1 cm from each other. The relative orientation was followed by an absolute orientation: an overall georeferencing in the ETRF2000 datum, carried out through the Leica Cyclone software v. 9.1.4. The algorithm is a spatial rototranslation on the 3D target coordinates in the assigned datum, determined by the reference network operations. The georeference residuals on targets are shown in table 1: the mean RMS value is about 5 mm.

C. Terrestrial digital photogrammetry

For the Volumni's Hypogeum (the major tomb) a 3D model was also created using high resolution digital terrestrial images. The shape and position of the object are reconstructed through photogrammetry identifying common points from multiple distinct images of the same object, through automated processes of SfM (Structure from Motion). The images, taken by a Nikon D800E camera (sensor size 24x36 mm and 36.3 megapixels resolution) were processed with the Agisoft Photoscan software v. 1.2. The result of the photogrammetric survey is also a point cloud, similar to the TLS one. It was then possible to obtain a continuous surface model by connecting the cloud points with a triangular mesh network (TIN). Both on the cloud and on the TIN surface it is possible to apply textures extracted from the digital photographs, creating a 3D photorealistic model.

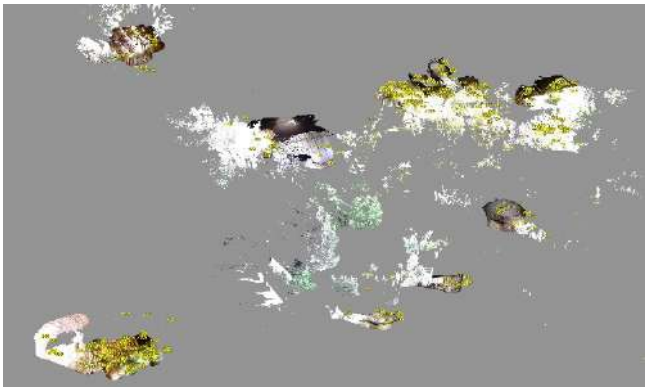

Figure 2. Final point cloud of the underground cavities resulting from the assembly of the single scans.

Target	Weight	RMS (m)	(E,N,H) residuals (m)
226	1	0.005	(0.003,0.003,-0.002)
254	1	0.003	(-0.003,0.000,-0.001)
224	1	0.005	(0.002,-0.004,0.001)
223	1	0.004	(-0.004,-0.001,0.001)
221	1	0.008	(0.001,-0.008,0.000)
225	1	0.009	(0.001,-0.009,0.001)
245	1	0.003	(-0.003,0.000,0.000)
201	1	0.004	(0.001,0.004,0.001)
203	1	0.005	(0.000,0.005,0.000)
246	1	0.003	(-0.003,0.000,0.001)
222	1	0.006	(0.003,0.005,-0.002)
200	1	0.005	(0.002,0.004,0.001)

Table 1. Resulting errors for 3D point cloud georeferencing.

D. UAV survey

A photogrammetric survey was performed with digital photographs acquired by drone (UAV) to define the geometry of the ground surface in the Necropolis area and connect it to the 3D model of the underground spaces. In order to obtain accurate results from a metric point of view, consolidated photogrammetric criteria were applied for all phases of the process (e.g. the guidelines described in [10]).

A SeeFly EBee fixed-wing drone with internal camera Canon S110 (12 MP) and GNSS receiver was used. The flight was designed to obtain a GSD (Ground Sampling Distance) of 4 cm: considering the focal length (5.4 mm), the sensor size (1/1.7″) and resolution (4000x3000 pixel) a height above ground of about 110 meters is necessary. In total, 140 frames were acquired. A set of 25 targets with checkerboard pattern (A3 size) were placed on the ground before the flight as GCP (Ground Control Points), and determined in ETRF2000 by GNSS, to georeference the survey. From the photogrammetric processing through bundle adjustment (Pix4D software), 3D digital models of the ground surface (DSM and DTM) and a digital color orthophoto of the Necropolis area were obtained. The point cloud obtained from the drone flight was then assembled to the TLS cloud, obtaining a unique 3D model of the area and the underground cavities (Fig. 3).

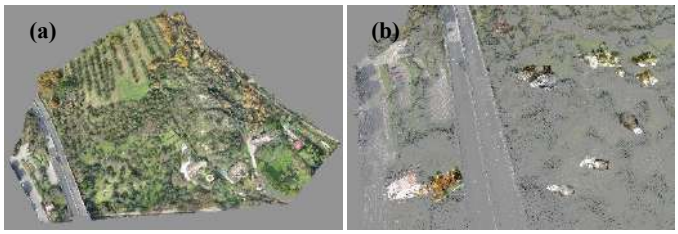

Figure 3. DSM generated by UAV survey (a) and assembled 3D model including outside and underground (b).

The accuracy of the DSM was verified performing a metric comparison between the DSM heights and those directly measured on the ground by GNSS; the Leica Cyclone software was used for this purpose. The measured GNSS points do not coincide with the DSM square grid (approximately 20 x 20 cm). For each GNSS point, the 4 surrounding points of the DSM grid were interpolated with an inverse distance algorithm, verifying the absence of significant altitude differences (> 5 cm).

A first statistical analysis of the differences shows a mean value of -0,07 m and a median of -0,06 m. Figure 5 shows the difference distribution. The few centimeters systematism is included in the altimetric accuracy of the UAV photogrammetric survey (estimated at ± 10 cm). The maximum positive and negative deviations are limited to a very low percentage of the points and are attributable to the DSM distortions caused by the presence of vegetation.

E. Geological and Geomatic data integration

As well as defining the relative and absolute geometry of the Necropolis, the geomatic survey products (3D point cloud and DSM/DTM) has allowed to reconstruct the landform units that characterize the area for a better understanding of the paleogeographic environment in which the sediments had formed. The tombs are located at different levels within the deposits belonging to Perugia hill structure, so their bare earth walls can be considered as parts of 3D geological sections, allowing to observe and describe the hill sediments from various angles (because they are oriented differently). The cavities point clouds integrated by the digital images made the “geological reading” and the paleoenvironmental interpretation easier than by simply observing surface outcrops, often hidden by vegetation or debris coverings.

The analyzed area spans from an altitude of about 210 m (Hypogeum of Volumni) to 238 m a.s.l. The analysis carried out

highlighted that two lithostratigraphic units can be individuated: the Volumni Unit (Vol) and the Palazzone Unit (Plz); in both depositional units there is evidence of a fluvial-type (braided) depositional paleo-environment [8]. The geological and geomorphological structure of the area will be discussed more in detail in the full version of the paper.

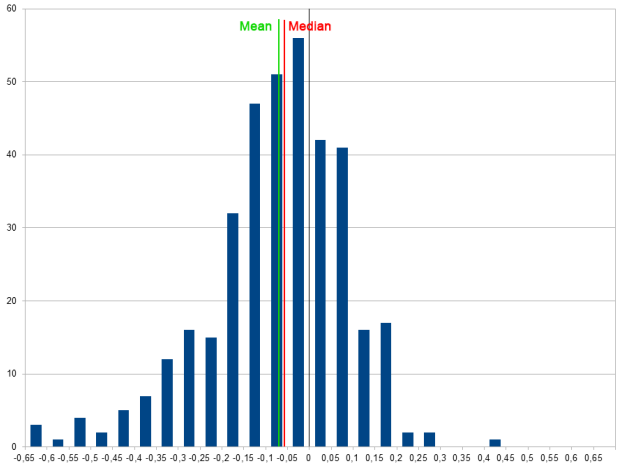

Figure 5. Statistical distribution of the differences between GNSS measures and photogrammetric DTM. Absolute frequency vs. differences in meters.

III. FINAL RESULTS AND PRODUCTS

For all the surveyed tombs, a series of detailed CAD drawings were also obtained (plans, sections, internal elevations) from the 3D models, available for technical or archaeological studies. For some cavities, 3D continuous surface models with triangular meshes (TIN), created with a specific 3D modeling software (3DReshaper), allow for a more realistic and homogeneous details visualization. These models were used to create virtual tours, uploaded in the project website http://www.silenepg.it, contributing to increase the site museum visit experience.

IV. CONCLUSIONS

Geomatics plays a leading role in many applied sciences such as Geomorphometry, thanks to the ability to acquire spatial information. The integrated use of different geomatic techniques makes it possible to perform an accurate 3D survey of the outside and the underground spaces, with an accuracy of a few centimeters order. The geomatic techniques are typically non-invasive and preserve the historical and archaeological sites. They allow to obtain a very detailed documentation, both from the archaeological and the geological points of view, producing traditional drawings beside innovative digital media (3D mesh, virtual tours) increasing the tourist attraction of the site. All these data, complementary to each other, form the basis for a digital archive available at any time.

Using the geomatic techniques, it was possible to obtain a detailed geomorphological analysis allowing to recognize the lithostratigraphic units and to put them in relation with the Perugia hill structure.

This work demonstrates how the integration of different methodologies is necessary to obtain a complete model on which accurate investigations at multiple levels can be carried out.

REFERENCES

[1] Blersch D., Balzani M., Tampone G., 2006. "The Volumnis' Hypogeum in Perugia, Italy. Application of 3D survey and modelling in archaeological sites for the analysis of deviances and deformations". From Space to Place: Proceedings of the 2nd International Conference on Remote Sensing in Archaeology, Campana S., Forte M., Archeopress, Oxford, 389-394.

[2] Borgogno Mondino E., Giardino M., Perotti L., 2006. "Geomatica e geomorfologia: nuove tecnologie per lo studio dell'evoluzione e della dinamica del rilievo alpino". SLM, 26, 2-9.

[3] Brigante R., Dominici D., Fastellini G., Radicioni F., Stoppini A., 2009. "Confronto e integrazione fra tecniche geomatiche per la documentazione e il monitoraggio dei beni culturali". Atti della XIII Conferenza Nazionale ASITA, Bari, Dicembre 2009, 537-542.

[4] Cenciaioli L., 2011. "L'Ipogeo dei Volumni. 170 anni dalla scoperta". Atti del convegno (Perugia, 10-11 giugno 2010), Editore Effe.

[5] Christopher Crosby, 2006. "A geoinformatics approach to LiDAR data distribution and processing with applications to geomorphology". Arizona State University.

[6] Church M., 2010. "The trajectory of geomorphology". Progress in Physical Geography, 34(3), 265–286.

[7] Ercoli M., Brigante R., Radicioni F., Pauselli C., Mazzocca M., Centi G., Stoppini A., 2016. "Inside the polygonal walls of Amelia (Central Italy): A multidisciplinary data integration, encompassing geodetic monitoring and geophysical prospections". Journal of Applied Geophysics, 127, 31-44.

[8] Melelli L., Bizzarri R., Baldanza A., Gregori L., 2016. "The Etruscan "Volumni Hypogeum" Archeo-Geosite: New Sedimentological and Geomorphological Insights on the Tombal Complex". Geoheritage, 8 (4), 301-314.

[9] Radicioni F., Matracchi P., Brigante R., Brozzi A., Cecconi M., Stoppini A., Tosi G., 2017. "The Tempio della Consolazione in Todi: Integrated geomatic techniques for a monument description including structural damage evolution in time". The International Archives of the Photogrammetry, Remote Sensing and Spatial Information Sciences, XLII-5/W1, 433-440.

[10] James M.R., Chandler J.H., Eltner A., Fraser C., Miller P.E., Mills J.P., Noble T., Robson S., Lane S.N., 2019. "Guidelines on the use of structure-from-motion photogrammetry in geomorphic research". Earth Surface Processes and Landforms, 44 (10), 2081-2084.

GEOMORPHOMETRY 2020 PERUGIA, ITALY JUNE 22 - 26 2020

Combined approach for terraced slopes micromorphological analysis through field survey and 3D models: the Stonewallsforlife project

Emanuele Raso[1], Paolo Ardissone, Leandro Bornaz, Andrea Mandarino, Andrea Vigo, Ugo Miretti, Rocco Lagioia, Alba Bernini, Marco Firpo

[1] Università degli Studi di Napoli Federico II
Complesso Universitario di Monte Sant'Angelo, Via Cinthia – 80126, Napoli, Italy
emanuele.raso@unina.it

Abstract—**The analysis of terraced slopes has implications in many different research areas, since this topic is influenced by natural, socioeconomic and cultural dynamics. The ancient technique of dry-stone walling has provided an effective contrast to concentrated erosion and shallow landslide triggering and run out, and in the meanwhile has created a strong cultural identity between the populations involved in this practice. To this aim STONEWALLSFORLIFE (S4L), a LIFE project financed by the European Commission in which the Cinque Terre National Park is involved as coordinating beneficiary, wants to demonstrate how an old technology - drystone walls - can be effectively used to improve the resilience of the territory to climate change through the adoption of a socially and technically innovative approach. The 6ha pilot site of Manarola, located in the heart of the Cinque Terre National Park (Italy), has been investigated through a traditional geomorphological and geological survey together with an accurate terrain analysis through the use of 3D model extracted by a point cloud generated by laser scanner coupled with GNSS survey, laser scanning and UAV photogrammetry. One of the main goals of the project is therefore to provide a deep and precise morphological assessment of the site pointing out the most vulnerable sectors of the pilot area. The results will be elaborated in order to obtain an exportable method in terms of micromorphological characterization of terraced slopes.**

I. INTRODUCTION

The Cinque Terre National Park is a 38 km^2 wide coastal sector of the eastern Liguria region (northwestern Italy) which embraces five small towns (less than 4000 inhabitants) connected by several coastal trails that represent a worldwide-known tourist destination. Since 1997, this area has been included in the 'World Heritage List' of UNESCO for its high scenic and cultural value, being one of the worldwide referenced 'cultural landscape', while in 1999 it has been declared National Park for its environmental and naturalistic relevance. The most relevant feature of this coastal sector is the terraced landscape, which is characterized by agricultural terraces retained by thousands of kilometers of drystone walls, mainly built for vineyards and olive groves (Brandolini, 2015; Terranova, 1984). As reported by Terranova et al. (2002), it can be assumed that in the nineteenth century terraced slopes covered up to 60% of the whole Cinque Terre territory. The STONEWALLSFORLIFE, a LIFE project financed by the European Commission in which the Cinque Terre National Park is involved as coordinating beneficiary, is aiming to demonstrate how an ancient technology - drystone walls - can be effectively used to improve the resilience of the territory to climate change by adopting a socially and technically innovative approach. The project will showcase its environmental, social and economic benefits, prepare the ground for replication and transfer, and draw on actions and experiences in other territories with different conditions and priorities to develop deep and broad knowledge which can then be applied in accordance with local circumstances.

The pilot site (6 hectares wide) is the so called "Anfiteatro dei Giganti" (literally, Giants' amphitheatre) located just above the hamlet of Manarola (Figure 1): this area includes part of the right and left sides of the Groppo creek catchment, has been affected by a progressive abandonment of terraced areas and nowadays is the heart of this new restoration project.

One of the main goals of the project is to perform a complete geomorphological, geological and morphological characterization of the site, together with an accurate terrain analysis through the use of 3D model extracted by a point cloud generated by laser scanner coupled with GNSS survey and UAV photogrammetry.

Emanuele Raso, Paolo Ardissone, Leandro Bornaz, Andrea Mandarino, Andrea Vigo, Ugo Miretti, Rocco Lagioia, AlbaBernini, and Marco Firpo (2020)

Combined approach for terraced slopes micromorphological analysis through field survey and 3D models: the Stonewallsforlife project:

in Massimiliano Alvioli, Ivan Marchesini, Laura Melelli & Peter Guth, eds., Proceedings of the Geomorphometry 2020 Conference, doi:10.30437/GEOMORPHOMETRY2020_19.

II. METHODS

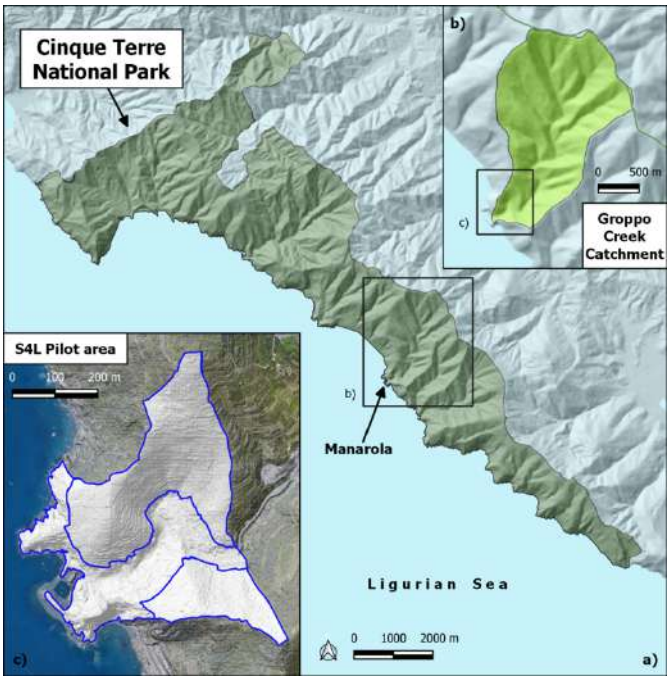

Figure 1. Geographical setting of the Groppo Creek catchment and location of the STONEWALLSFORLIFE Project pilot site.

A. Geological and Geomorphological survey

First, a detailed geological and geomorphological study of the project area through original field surveys and the use of existing IT data was performed: later on, collected data were elaborated in a GIS environment (e.g. high-resolution digital terrain models, vector and raster files available on "Geoportale Regione Liguria", etc.); the main purpose was therefore to obtain:

- A geological-structural model that can provide precise indications on the spatial relationships between discontinuity planes (stratification, substrate fracture planes) and the dry-stone walls structures characterizing the slopes inside the project area.

- Detailed mapping of the main erosional and depositional forms (punctual, linear and areal) inside the study area in order to identify any dangerous factors related to the construction and maintenance of dry-stone walls and terraced strips.

The investigations were conducted in a GIS environment and carried out by means of the free and open source software QGIS and GRASS GIS. The extensive field survey campaign was carried out in January 2020 and was supported by the use of the software QFIELD combined with a common GNSS device. This activity was focused on accessible areas, thus densely-vegetated and impervious plots of land were excluded.

B. Creation of a 3D model from laser scanner and aerial photogrammetry

For the cartographic description of the site, different survey techniques were used: GNSS, Terrestrial Laser Scanner and UAV Photogrammetry.

The first field activity was the materialization and measurement of a benchmarks network: a total of 308 fixed points was measured with GNSS techniques for the calculation of the cartographic parameters and the calculation of the geodetic rules for a correct passage from a local to a global reference system.

Subsequently, following the survey project developed together with the geological managers of the Park, several activities were performed with the double function to check the effective Terrestrial Laser Scans (TLS) coverage and to generate a first 3D model of the areas capable of describing the morphological features of the pilot site, with a good level of detail, and the presence of any obstacles for drone flights (e.g. presence of high vegetation, presence of overhead lines etc.).

2A 2B

Figure 2a High resolution (5cm x 5cm) orthophotos showing the pilot area of Manarola, Cinque Terre National Park; 2b: 3d model of the hamlet of Manarola

Furthermore, a specific 3D flight programmer was used to design flight plans considering the actual 3D shape of the terrain. Flight paths, acquisition points and camera configuration were preset and loaded onto the drone navigator unit, which simultaneously received instructions on speed, route to follow, take-off and landing point.

In this way photogrammetric strips are obtained with always nadiral images, always at constant height above the ground: this aspect is fundamental for obtaining constant resolution data on the surveyed area, since the Cinque Terre territory is characterized by a morphology with strong differences in height. Moreover, the flight routes, programmed following this 3D approach, do not exceed the regulatory limits imposed by ENAC, the Italian Civil Aviation Authority.

III. RESULTS AND CONCLUSIONS

A. Geological and Geomorphological survey

The geological survey was conducted at the scale of 1:2'500, allowing for the investigation of outcrops and structures wider than 2.5 m. The main outcrops of the bedrock were identified and mapped and their principal structural discontinuity planes were measured (bedding or stratification planes, fracture, etc.), in order to obtain a geological-structural model of the substrate. As a result, a set of georeferenced geological data were prepared in order to describe accurately the geological features of the site.

Similarly, the detailed geomorphological survey allowed for the identification and mapping of landforms and deposits at the micro-scale (mainly anthropogenic landforms consisting of dry-stone walls, underground cisterns, drain channels and walkways), and thus for the characterization of past and current geomorphological processes that shaped and are shaping the landscape, respectively.

B. Creation of a 3D model from laser scanner and aerial photogrammetry

About the creation of 3D model (Figure 3) fifty-two 3D flight plans were designed and carried out in order to properly cover the survey area: a total of 7000 images were acquired and processed to generate 3D models using automatic photogrammetry techniques and algorithms. In fact, images were acquired with a aerial photogrammetric logic.

Figure 3. 3D model obtained through the combined use of different survey techniques such as GNSS, Terrestrial Laser Scanner and UAV Photogrammetry

Using the flight plan parameters, it was possible to obtain the approximated position and shooting orientation of the individual frames. These approximate positions have been recomputed for relative orientation which defines the relationship of reciprocal position between images. The relative orientation was calculated considering the geometric behavior of the camera and applying automatic photogrammetric algorithms.

In order to have a good relative orientation, on the acquired images a radiometric recalibration procedure was applied, which had three functions: to highlight morphological details, to eliminate high variation of lights and shadows and to homogenize colors and tones between images and between the different photogrammetric strips.

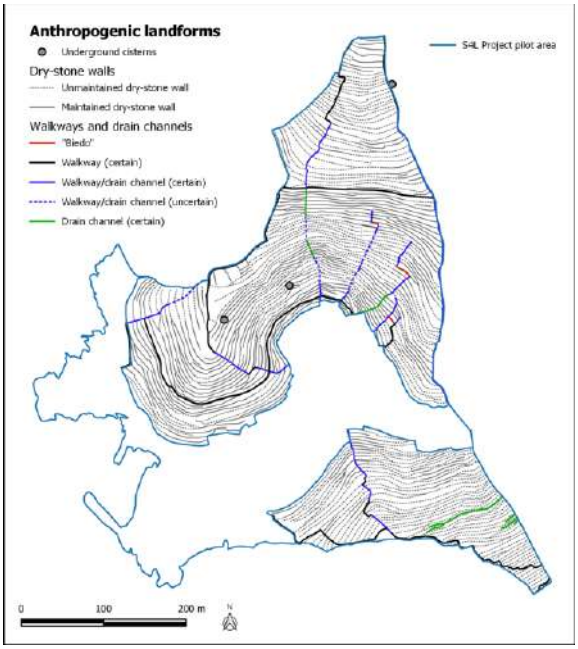

Figure 4. Map showing the anthropogenic landforms of the STONEWALLSFORLIFE Project pilot site.

Through the use of GNSS control points, the absolute orientation of the photogrammetric blocks was defined and globally compensated (bundle adjustment).

Subsequently, 3D models were created, using automatic photogrammetry algorithms, which define the 3D position of points covered by multiple oriented images.

After detailed checking of the image orientations, high-resolution 3D models were generated, keeping under control precision and accuracy. In particular, for the generation of 3D models from images, different algorithms were tested and then used. In fact, these procedures assign different weigh to precision and distribution in the recognition of common points. Three different 3D models were therefore generated, using different algorithms and then merging them together. The integration

between the models generated by the different computational procedures allowed to obtain a better result in terms of accuracy and coverage.

A total of 65 3D models were generated at a constant resolution of 20 cm, and later on they have been classified: the vegetation has been selected and assigned to a specific class (Vegetation), using a semi-automatic procedure: more specifically, it allows to identify and select points that aren't part of the terrain/topographical surface according to a statistical analysis; on a subsequent stage, operators check the results and validate or invalidate it; by re-launching the procedure in different computation sessions, the result has been refined.

Starting from these classified models it was possible to generate global 3D model of the area, contour lines, and DTMs. These data, along with the orthophotos, made it possible to quantitatively investigate the morphometric features of the S4L pilot area and to identify and map the anthropogenic landforms of the whole pilot area, with a high spatial accuracy.

In particular, the geometric features of terraced strips, drain channels and pathways were quantitatively analyzed through common raster and vector geoprocessing tools and terrain analysis tools. Moreover, the dry-stone walls location and total length were pinpointed and measured, respectively.

The outcomes are, thus, based on the analysis of the aforementioned 3D model and DTMs, and on a large photointerpretation activity.

This in-progress research highlighted the great relevance of using the illustrated combined approach for the implementation of a morphologic analysis in such complex areas as the S4L pilot area is.

REFERENCES

[1] Brandolini, P., Cevasco, A., Capolongo, D., Pepe, G., Lovergine, F., & Del Monte, M. (2018). Response of terraced slopes to a very intense rainfall event and relationships with land abandonment: A case study from Cinque Terre (Italy). Land Degradation and Development, 29, 630–642.

[2] Camera, C., Djuma, H., Bruggeman, A., Zoumides, C., Eliades, M., Charamboulos, K., Abate, D., Faka, M., 2018. "Quantifying the effectiveness of mountain terraces on soil erosion protection with sediment traps and dry-stone wall laser scans". Catena 171, 251-264.

[3] Capolupo, A., Kooistra, L., Boccia, L., 2018. "A novel approach for detecting agricultural terraced landscapes from historical and contemporaneous photogrammetric aerial photos". Int J Appl Earth Obs Geoinformation 73, 800-810.

[4] Cevasco, A., Pepe., G., Brandolini., P., 2014. "The influences of geological and land use settings on shallow landslides triggered by an intense rainfall event in a coastal terraced environment". Bull Eng Geol Environ 73, 859–875.

[5] Crosta, G. B., Dal Negro, P., Frattini, P., 2003." Soil slips and debris flows on terraced slopes. Natural Hazards and Earth System Science, 3, 31–42.

[6] Moreno-de-las-Heras, M., Linderberger, F., Latron., J., Lana-Renault, N., Llorens, P., Arnàez, J., Romero-Diaz, A., Gallart, F., 2019. "Hydro-geomorphological consequences of the abandonment of agricultural terraces in theMediterranean region: Key controlling factors and landscape stability patterns". Geomorphology 333, 73-91.

[7] Pepe, G., Mandarino, A., Raso, E., Scarpellini, P., Brandolini, P., Cevasco, A., 2019. Investigation on farmland abandonment of terraced slopes using multitemporal data sources comparison and its implication on hydro-geomorphological processes. Water, 111, 1552.

[8] Pesci, A., Teza, G., Bisson, M., Muccini, F., Stefanelli, P., Anzidei, M., Carluccio, R., Nicolosi, I., Galvani, A., Sepe, V., Carmisciano, C., 2016. "Monitoring of a Coastal Zone by Independent Fast Photogrammetric Surveys: the Case of Monterosso al Mare (Ligurian Sea, Italy)". Journal for Geosciences and Geomatics 4, 73-81.

[9] Pescini, V., Montanari, C.A., Moreno, D.T., 2018. "Multi-proxy record of environmental changes and past land use practices in a Mediterranean landscape: The Punta Mesco cape (Liguria - Italy) between the 15th and 20th century". Quaternary international 463, 376-390.

[10] Raso, E., Cevasco, A., Di Martire, D., Pepe., G., Scarpellini. P., Calcaterra, D., Firpo, M., 2019. "Landslide inventory of the Cinque Terre National Park (Italy) and quantitative interaction with the trail network". Journal of Maps 15, 818-830.

[11] Rodrigo-Comino, J., Seeger, M., Iserloh, T., Senciales-Gonzalez, J.M., Ruiz-Sinoga, J.D., Ries, J.B., 2019. "Rainfall-simulated quantification of initial soil erosion processes in sloping and poorly maintained terraced vineyards - Key issues for sustainable management systems". Science of the total environment 660, 1047-1057.

[12] Spanò, A., Sammartano, G., Calcagno Tunin, F., Ceris, S., Possi, G., 2018. "GIS-based detection of terraced landscape heritage: comparative tests using regional DEMs and UAV data". Applied Geomatics 10, 77-97.

[13] Stavi, I., Gusarov., Y., Halbac-Cotoara-Zamfir, R., 2019. "Collapse and failure of ancient agricultural stone terraces: On-site geomorphic processes, pedogenic mechanisms, and sol quality". Geoderma 344, 144-152.

[14] Terranova, R. (1984). Aspetti geomorfologici e geologico-ambientali delle Cinque Terre: Rapporti con le opere umane (Liguria orientale). Studi e Ricerche di Geografia, 7, 39–90.

[15] Terranova, R., Brandolini, P., Spotorno, M., Rota, M., Montanari, C., Galassi, D., Mus-Amezquita, M. (2002). Patrimoni de marjades a la Mediterrania Occidental. Una proposta de catalogaciò. Commissiò Europea DGX, Programa Raphael, Palma Di Mallorca, Fodesma, pp 243.

[16] Wei, W., Chen, D., Wang, L., Daryanto, S., Chen, L., Yu, Y., Lu, Y., Sun, G., Feng, T. 2016. Global synthesis of the classifications, distributions, benefits and issues of terracing. Earth-Science Reviews 159, 388-403.

GEOMORPHOMETRY 2020
PERUGIA, ITALY
JUNE 22 - 26 2020

Geomorphometry in the deep Norwegian Sea

Margaret F.J. Dolan[§], Lilja Rún Bjarnadóttir, Terje Thorsnes, Markus Diesing, Shyam Chand
Geological Survey of Norway
Postal Box 6315 Torgarden
NO-7491 TrondheimNorway

[§] margaret.dolan@ngu.no

Abstract— **The deep Norwegian Sea spans depths reaching to nearly 6000 m and an area of around 1 000 000 km^2 extending both sides of the rugged mid-Atlantic Ridge. Armed with coarse regional bathymetric and oceanographic datasets the Norwegian national offshore mapping programme, MAREANO, was tasked with mapping 'representative areas' of this vast seabed terrain. Here we introduce the planning process, guided by semi-automatic methods, and present examples from newly acquired ship-borne multibeam bathymetric mapping in this varied deep-sea terrain with a focus on the use of these bathymetry data for onward substrate, geomorphological, and habitat mapping. We discuss the challenges of using these data with existing, lower quality, bathymetry data, as well as highlighting some typical data artefacts which can limit the calculation of meaningful terrain attributes and thereby their use in geological and habitat mapping.**

I. INTRODUCTION

During 2019 new multibeam bathymetry data were acquired in the deep Norwegian Sea by Norway's national offshore mapping programme MAREANO. The survey design was produced to meet management information needs across this vast seabed terrain within budgetary constraints, which precluded full coverage mapping, and comprised a series of boxes, mostly around 35 km x 35 km (Figure 1). These new data provide insights into previously unseen seabed topography and can be set against a backdrop of existing, lower quality multibeam data as well as compiled data from multiple sources (e.g EMODnet bathymetry [1] GEBCO [2]). Connection lines were acquired between all survey boxes to provide an achievable level of continuity in the survey, which will be invaluable for onward use of the data in geological and habitat mapping.

Whilst the multibeam surveys concurrently acquire bathymetry, backscatter and water column data, alongside sediment echosounder data to aid geological interpretation, our focus here is on the bathymetric data. By presenting examples from contrasting types of terrain we examine how these data can be used for far more than just hydrographic purposes and focus on the use of bathymetric data in the development of geological and habitat maps. We discuss the opportunities and challenges associated with fusing these new data with existing, lower resolution data, as well as previewing plans to ground-truth these data in order to provide the additional layers of information MAREANO requires for geological and habitat mapping.

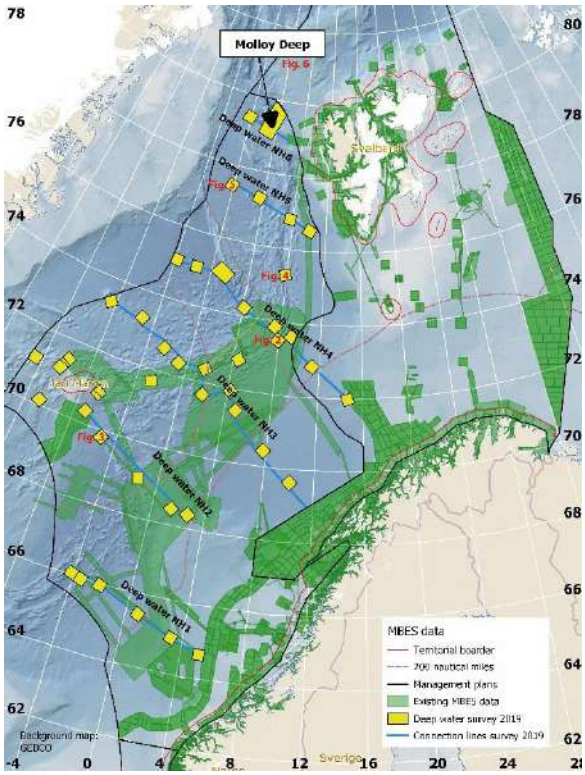

Figure 1. The study area spanning around 1 000 000 km^2 in the in the deep Norwegian Sea. The 2019 deep water multibeam (MBES) survey areas are indicated in yellow with connection lines coloured blue. Existing multibeam data are shown in green. Image: NHS/MAREANO. For details of bathymetric data available for download see https://www.mareano.no/en/maps-and-data/marine-geospatial-data

Margaret Dolan, Lilja Bjarnadottir, Terje Thorsnes, Markus Diesing, and Shyam Chand (2020) Geomorphometry in the deep Norwegian Sea: in Massimiliano Alvioli, Ivan Marchesini, Laura Melelli & Peter Guth, eds., Proceedings of the Geomorphometry 2020 Conference, doi:10.30437/GEOMORPHOMETRY2020_20.

Acoustic mapping of the seabed from surface vessels in the open ocean can present many challenges, not least from the effects of bad weather which often limits survey operations and impacts data quality. These challenges, together with geometric and sensor-related effects linked to the multibeam systems, can generally be overcome to provide processed data and digital terrain models, hereinafter referred to as Digital Bathymetric Models (DBMs), that fall within relatively forgiving deep-water hydrographic standards, but which lead to uncertainty in onward analysis and applied map development for other purposes like geological and habitat mapping. We discuss some methods highlighting these issues including how this uncertainty might best be conveyed to end users alongside the DBM.

II. METHODS

A. Survey planning

Full coverage mapping of the seabed in waters deeper than 200 m is the ambition of Seabed 2030 [3], an initiative to populate global DBMs such as GEBCO with real sounding data. Innovative acquisition methods [e.g. using autonomous vehicles, crowd sourcing from industry and the private sector] are among many approaches to achieving this ambitious goal by 2030, with national mapping programmes such as MAREANO playing an important role towards this global effort. At the national level, however, mapping agencies face the very real task of juggling available funds and management demands for information within shorter timeframes when planning their bathymetric and related surveys. Even in a well-funded programme like MAREANO this can present a challenge. Full coverage multibeam mapping of the deep Norwegian Sea has recently been estimated to require thousands of ship days, at a cost of around 100 million Euro, with significant further costs associated with additional data collection for geological and habitat mapping. Meanwhile government and management agencies require information on this part of the Norwegian seabed within relatively short time scales. When tasked with providing 'representative information' on the seabed of the deep Norwegian Sea MAREANO therefore opted for a compromise solution mapping as many different seabed environments as possible within a suitable timescale (2-3 years).

At a broad scale we can see from regional bathymetry data that the study area comprises continental slope, abyssal plain, marine hills and mountains, concentrated along mid-Atlantic Ridge, as well as the continental shelf near the island of Jan Mayen. Overlying this terrain is a complex pattern of ocean circulation giving rise to different water masses and dynamics occuring in different parts of the area. In order to map representative parts of the seabed we need as complete a picture of the total environment as possible at the survey planning stage. The different environments identified can then be assessed and survey effort balanced against logistical and budgetary contraints. We conducted an unsupervised classification using principal component analysis and k-means clustering of the seabed for the entire deep Norwegian Sea based on the best available bathymetric data (EMODnet bathymetry 2018) and derived terrain attributes plus near-bottom oceanographic attributes (temperature, salinity, current speed). This classification provided an intitial means by which to identify areas of the seabed with similar environmental characteristics. When combined with further knowledge on the geological history and oceanographic characteristics of the area, plus information from previous surveys we were able to prioritise areas to be surveyed.

Based on previous experience in the Barents Sea, MAREANO has found the box-transect to be better matched to management information demands than simple line-transects which provide a very blinkered view of geology and habitats. This box-transect approach was adopted in the deep Norwegian Sea and provides a convenient means by which to map different environments. The size of box was chosen to suit geological and habitat mapping at scales in the range 1:100 000 to 1:250 000, although the achievable map resolution will also be dependent on data quality and available ground-truthing (video and physical samples) from follow-up surveys. We estimate that, even with potential data loss from employing multiple scale terrain analysis methods [4] as required, an area of at least 1000 km^2 will be mapable within each box. This is a reasonable size to get a 'feel' for the geological, habitats and environmental status of the area, as required by MAREANO and is supported by information from connection lines (generally one multibeam swath width [≈ 5.5 x water depth [5]] wide).

B. Data acquisition, processing and analysis

Data were acquired using a Kongsberg Maritime EM304 deep water multibeam echosounder on MV Geograph by DOF Subsea AS under contract to MAREANO through the Norwegian Hydrographic Service (NHS), in partnership with the Geological Survey of Norway (NGU). Multibeam data require cleaning following standard procedures [6] to remove outliers and correct for geometric and motion effects. This work was done by the contractor using industry-standard software with quality control of the bathymetry data undertaken by NHS. Final DBMs were produced by NHS at resolutions from 10-25 m depending on water depth for onward use by MAREANO partners. Supporting information on vertical and horizontal uncertainty were provided by the contractor.

For interpretation and onward analysis, the data were imported to ArcGIS desktop software. Here the data were combined with existing bathymetry data from other sources providing further regional context to the data. We examine methods for data fusion with available existing DBMs such as Petrasova et al. [7] as well

as exploring derivation of terrain attributes both on the regional and high-resolution DBMs [6]. The potential use of the DBMs for geological and habitat mapping including the impact of common data artefacts [8] will be discussed in the context of these methods. We also discuss the use of the data in planning ground-truth surveys, essential to the development of these applied map products. This potentially includes follow-up very high-resolution bathymetric surveys from remotely operated and/or autonomous underwater vehicles [9].

III. RESULTS AND CONCLUSIONS

Selected results will be presented to highlight the invaluable insights into deep-sea topography gained by these data, in additional to discussing the technical challenges associates with their 'jigsaw-puzzle' configuration and varying quality.

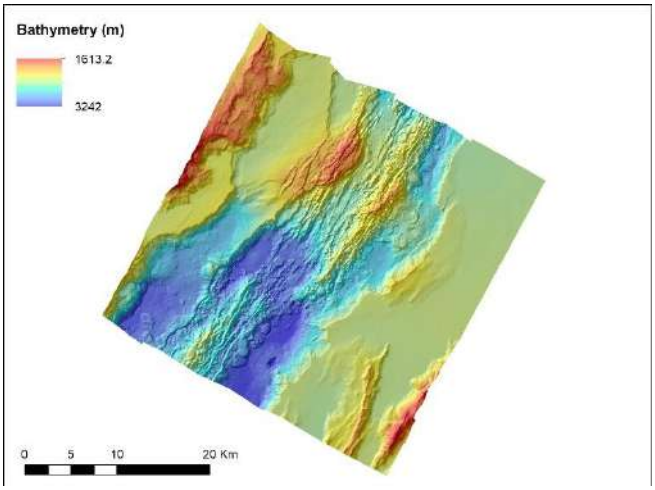

Figure 2 Example colour shaded relief image of topography at the Mid-Atlantic Ridge – see Figure 1 for location

Figure 2 shows an example of the varied topography present at the Mid Atlantic Ridge along transect NH04. We note the contrasting textures of this terrain, likely to have different substrate types and habitats associated with it. This dramatic topography contrasts with the relatively flat abyssal plain that covers large parts of the survey area, yet the new DBMs reveal that in many places, even this flatter part of the seabed is far from devoid of topographic features. An example is shown in Figure 3.

Through MAREANO partnership in EMODnet these new bathymetry data will be incorporated into and help to improve the next revision of EMODnet bathymetry using standardized methods. Nevertheless, within shorter timescales MAREANO scientists require methods to integrate the new DBMs with existing data on a more local scale.

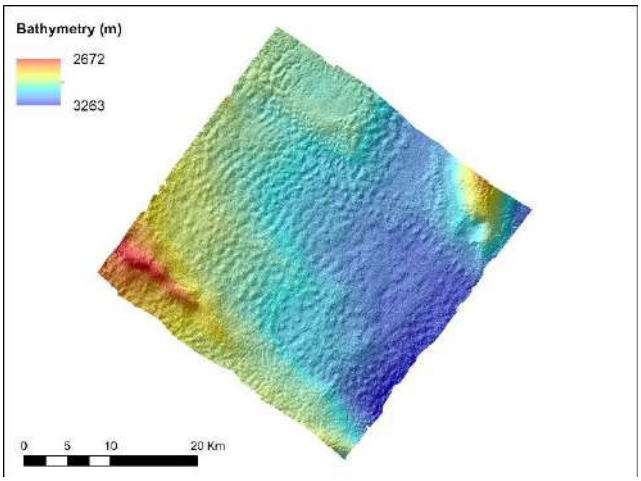

Figure 3 Example colour shaded relief image showing topography on the abyssal plain away from the mid-Atlantic Ridge – see Figure 1 for location

Together with MAREANO partners NHS, NGU are examining methods for data fusion that give the best results for onward use of the data, particularly for the generation of terrain attributes. In Figure 4 we show an example of the new multibeam bathymetry data against a backdrop of existing EMODnet bathymetry data with visible artefacts from multi-source data, most of which is at far lower resolution.

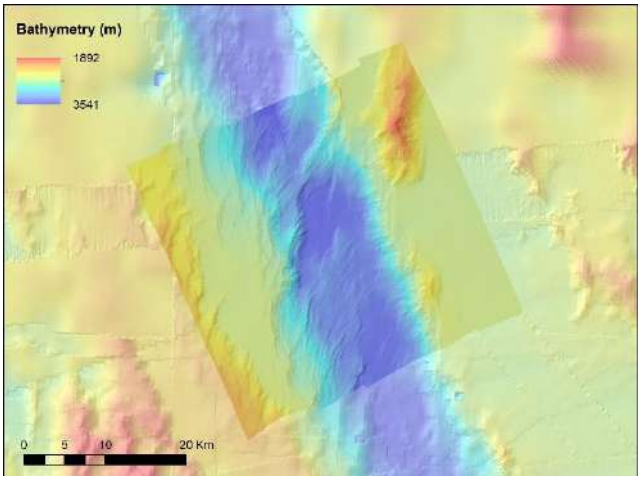

Figure 4 Colour shaded relief image of new multibeam data overlain on existing EMODnet data, compiled from multiple sources. The same colour scale is used for both datasets – see Figure 1 for location.

Despite the invaluable insights into deep sea topography offered by the new DBMs we note that several of the survey areas are plagued by visible artefacts in the data, mostly due to challenging sea conditions. The data are also subject to more systematic vertical and horizontal uncertainty, influenced by

echosounder geometry. An example area affected by such problems is shown in Figure 5 where we highlight the effect of the issue and its consequences for terrain attributes such as slope. Whilst the most rugged terrain in this area is clearly delineated, we also see smaller sized along- and across-track artefacts in the data. These low-level, yet persistent, artefacts can present problems when using the data in onward substrate interpretation and habitat mapping, particularly when terrain attributes such as slope and rugosity are used as predictor variables. Methods to overcome these artefacts include filtering and use of larger neighbourhoods for the generation of terrain attributes, however, the success of these approaches can be limited by the relatively small area covered by the survey blocks.

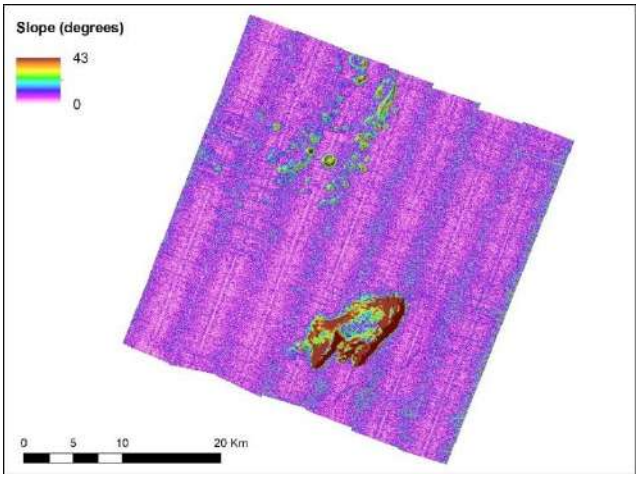

Figure 5 Example of data artefacts visible in many datasets. Here the motion-related artefacts resulting from surveys in poor weather conditions are visible in a slope map derived from the bathymetry data. Slope calculated in ArcGIS using Horn's algorithm [10] using a 3 x 3 pixel neighbourhood on a 25 m DBM i.e. over a distance of 75 m x 75 m.

Finally, we acknowledge that this survey of the deep sea has often documented far more dramatic terrain than is present on land. Depths in the vicinity of the Molloy Deep span more than 4000 m. In the visualization shown in Figure 5 we see how the topography of the Molloy Deep dwarfs the height of Stetind, a notorious anvil-shaped mountain on the Norwegian mainland, which rises to a height of 1392 m. Although such visualisations and vertical exaggeration can help us gain an impression of this dramatic relief in various GIS software we note a general challenge of effectively visualizing negative relief.

Despite any limitations they may have, these new bathymetry data offer an essential baseline for planning follow-up surveys that will provide more information on the geology and habitats present which will be reported by MAREANO in due course. Whilst their extent is relatively small on a global scale these data will help improve regional bathymetric datasets and advance methods for marine geomorphometry in deep sea environments.

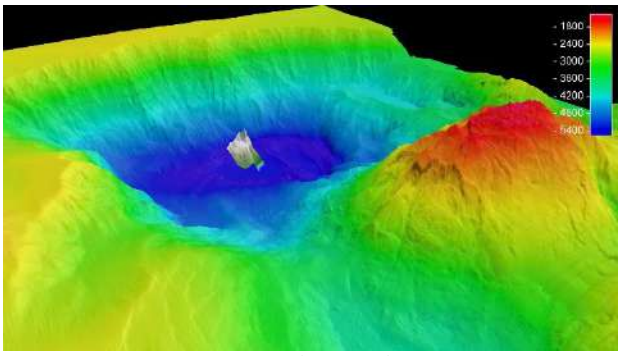

Figure 5. 3D colour shaded relief image of Molloy Deep (5 569 m deep) viewed from the northeast. A terrain model of the mountain Stetind (1 395 m high) has been placed on the bottom of Molloy Deep to illustrate the relative size. DBM resolution 25 m. The colour-scale bar indicates the depths in the Molloy Deep DBM. Image: Kartverket/MAREANO

REFERENCES

[1] EMODnet 2020 https://www.emodnet-bathymetry.eu/ Accessed 13.2.20

[2] GEBCO 2020 https://www.gebco.net/ Accessed 13.2.20

[3] Mayer, L., Jakobsson, M., Allen, G., Dorschel, B., Falconer, R., Ferrini, V., Lamarche, G., Snaith, H. and Weatherall, P., 2018. The Nippon Foundation—GEBCO Seabed 2030 project: The quest to see the world's oceans completely mapped by 2030. Geosciences, 8(2), p.63.

[4] Wilson, M.F.J., O'Connell, B., Brown, C., Guinan, J.C. and Grehan, A.J., 2007. Multiscale terrain analysis of multibeam bathymetry data for habitat mapping on the continental slope. Mar. Geod., 30(1-2), pp.3-35.

[5] Kongsberg Maritime, 2020. EM304 Multibeam echosounder. https://www.kongsberg.com/maritime/products/mapping-systems/mapping-systems/multibeam-echo-sounders/em-304-multibeam-echosounder-max.-8000-m/?OpenDocument=#downloads Downloaded 14.1. 2020.

[6] Lecours, V., Dolan, M.F., Micallef, A. and Lucieer, V.L., 2016. A review of marine geomorphometry, the quantitative study of the seafloor. Hydrol. Earth Syst. Sci., 20(8), p.3207.

[7] Petrasova, A., Mitasova, H., Petras, V. and Jeziorska, J., 2017. Fusion of high-resolution DEMs for water flow modeling. Open Geospat. Data Softw. Stand., 2(1), p.6.

[8] Lecours, V., Devillers, R., Edinger, E.N., Brown, C.J. and Lucieer, V.L., 2017. Influence of artefacts in marine digital terrain models on habitat maps and species distribution models: a multiscale assessment. Remote. Sens. Ecol. Conserv., 3(4), pp.232-246.

[9] Ludvigsen, M., Aasly, K., Ellefmo, S.L., Hilário, A., Ramirez-Llodra, E., Søreide, F.X., Falcon-Suarez, I., Juliani, C.J., Kieswetter, A., Lim, A. and Christian, M., 2016. MarMine cruise report-Arctic Mid-Ocean Ridge 15.08. 2016-05.09. 2016.

[10] Horn, B.K., 1981. Hill shading and the reflectance map. Proc. IEEE, 69(1), pp.14-47.

GEOMORPHOMETRY 2020 PERUGIA, ITALY JUNE 22 - 26 2020

Hypsoclinometric evidence of the degree of modification of mountains by glacial erosion

Ian S. Evans[§], Nicholas J. Cox
Department of Geography
Durham University
Durham DH1 3LE, United Kingdom
[§]i.s.evans@durham.ac.uk

David Milledge
Department of Civil Engineering
Newcastle University
Newcastle, United Kingdom
david.milledge@newcastle.ac.uk

Mihai Niculiță
Department of Geography
Alexandru Ioan Cuza University of Iași
Iași 700505, Romania
mihai.niculita@uaic.ro

Abstract— **Analyses of slope gradient distributions as functions of altitude are described as hypsoclinometry. They show strong distinctions between glaciated and unglaciated mountains, analysing each mountain range as a whole, bounded by low passes. The denser and better-developed the glacial cirques, the greater the proportion of steep slopes among slopes at cirque altitudes, representing cirque headwalls. This is accompanied by increased variability of slope gradient and by consistent directions of vector mean aspects. There may also be a concentration of gentle slopes at cirque floor altitudes. General geomorphometry can thus provide objective measures of the degree of modification by local glaciers.**

I. INTRODUCTION

Hypsometric maxima have been used as evidence of the importance of glaciation in eroding mountain ranges (Egholm et al., 2009). It is inferred that these represent glacial cirque floors: however, summit plateaux and other low-gradient areas also produce maxima in altitude frequency distributions (Crest et al., 2017). Robl et al. (2015) showed that more information can be obtained by combining altitude and slope gradient frequency distributions, an approach labelled hypsoclinometry by Niculiţa and Evans (2018), and Evans (2019). Here we apply this approach to several ranges in British Columbia and make some comparisons with Romania and England. Note that it is important to take a whole mountain range and to focus on altitudes above the lowest closed contour, given by a 'defining pass'. Data on the specific geomorphometry of cirques are used to interpret the results of hypsoclinometry, which is a part of general geomorphometry (Minár et al., 2013).

In British Columbia we used TanDEM-X 0.5 arc-second data gridded at 12.5 m, after digitising lake outlines and replacing lakes with 'missing data' because their radar returns suffered water speckle errors. We compared the well-glaciated Bendor Range with the adjacent, drier, moderately-glaciated Shulaps Range and the lightly-glaciated Mission Ridge. (Later, comparisons will be made with the Ninemile and Clear Ranges, with just a few cirques, and the South Camelsfoot Range that did not suffer local glaciation). The 'glacial signal' comes mainly from the development of glacial cirques (Barr and Spagnolo, 2015; Evans and Cox, 2017; Evans, 2020), hence we relate gradient distributions to altitudes of cirque floors. The Bendor Range has a strong signal for both cirque floors and headwalls; Shulaps shows a signal mainly for headwalls.

II. GRADIENT DISTRIBUTIONS BY ALTITUDE

In the Shulaps Range (122.5° W, 51° N, highest summit 2877 m), only headwalls give a clear 'glacial' signal – mainly above 2456 m (see steeper than 45°, Table I). Floors do not, probably because in general they are only c. 28 % of cirque areas whereas headwalls are 72%. Any low-gradient (see gentler than 20°) signal is blurred by extensive benches just below cirques, on the northeast (Yalakom) slope.

TABLE I. SHULAPS RANGE, B.C.: GRADIENT STATISTICS FOR ALTITUDE BANDS

Altitude (m)	Mean (°)	Median (°)	SD (°)	IQR (°)	<20° %	>45° %	Observations
Above 2610**	28.6	28.8	11.5	14.7	22.8	**7.5** headwalls	53k
2456-*	29.8	29.7	11.4	14.3	**19.1** floors	**8.5**	156k
1957-*	23.9	24.1	10.8	15.8	**36.9**	2.5	1465k
1530-	21.2	20.5	10.7	16.2	48.3	1.5	1946k
Below	25.4	25.0	12.5	16.1	35.7	6.1	1887k

*1957 & 2456 m are 05 and 95 percentiles of lowest altitude per cirque.
**2610 m is the 95 percentile of maximum floor altitude per cirque. k=thousand.

Ian Sylvester Evans, Nicholas J. Cox, Mihai Niculita and David Milledge (2020) Hypsoclinometric evidence of the degree of modification of mountains by glacial erosion: in Massimiliano Alvioli, Ivan Marchesini, Laura Melelli & Peter Guth, eds., Proceedings of the Geomorphometry 2020 Conference, doi:10.30437/GEOMORPHOMETRY2020_21.

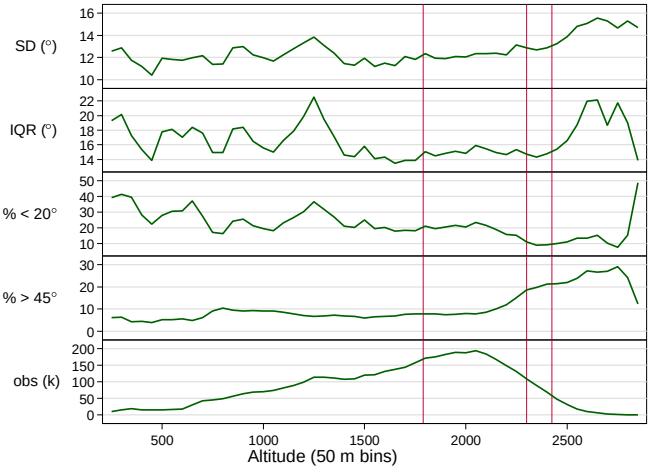

Figure 1. Gradient statistics by altitude (x axis, 25 m bands) for the Bendor Range, British Columbia. Red lines at 1790 and 2300 m are the 05 and 95 percentiles of lowest floor altitude, whereas the right-hand line at 2425 m is the 95 percentile of maximum floor altitude per cirque; obs (k) is the number of observations in thousands.

TABLE II. BENDOR RANGE, B.C.: GRADIENT STATISTICS FOR ALTITUDE BANDS

Altitude (m)	Mean (°)	Median (°)	SD (°)	IQR (°)	<20° %		>45° %		Observations
Above 2425	36.2	35.7	13.8	16.8	11.3		22.6	headwalls	153k
2300-	35.8	35.2	12.8	14.5	9.9	floors	19.4		235k
2080-	31.0	31.4	12.6	15.2	18.9		10.7		708k
1790-	29.6	30.1	12.1	14.9	21.0		7.8		1053k
1600-	29.8	30.4	11.7	13.9	18.8		7.3		538k
1400-	28.8	29.5	11.5	14.7	21.7		6.5		457k
Below	28.2	29.1	12.7	17.9	27.0		8.6		1236k

1790 and 2300 m are 05 and 95 percentiles of lowest altitude per cirque.

2425 m is the 95 percentile of maximum floor altitude per cirque.

k= thousand. (From Evans, 2019.)

The Bendor Range (highest summit 2911 m) shows a strong maximum of high gradients above the mid-altitude of cirque floors (Fig. 1). Low gradients, very variable at lower altitudes, do show a broad maximum from the extensive floors of 222 cirques. This is accompanied by a hypsometric maximum (see obs(k)). Variability, expressed by Standard Deviation and Inter-Quartile Range, is high at cirque floor levels but even higher above these.

Fig. 2 shows that all classes of slopes over 35° in the Bendor Range have a strong maximum towards the top of cirque floor levels. This concentration increases for steeper slopes, especially above 55°. It appears that the sides of glacial troughs, down-valley from cirques, are mainly between 35° and 55°; not as steep as some cirque headwalls.

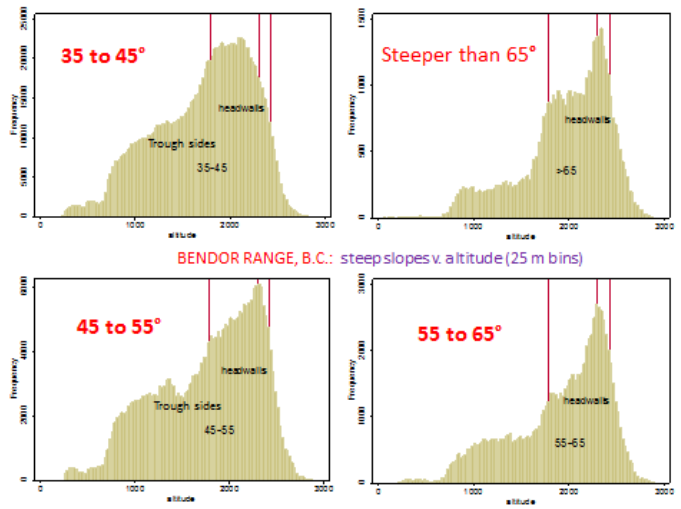

Figure 2. Frequencies of four classes of steep slopes in the Bendor Range, B.C., by 25 m bins of altitude (x axis). Red lines at 1790 and 2300 m are the 05 and 95 percentiles of modal floor altitude, whereas the right-hand lines at 2425 m are the 95 percentile of maximum floor altitude per cirque.

III. ASPECT CONCENTRATION

Slope aspects show greater concentration at the altitudes of headwalls. Focusing on steep slopes (>40°), the vector statistics of aspect can be compared with those of cirques. Vector means are consistently northward above 2200 m in Shulaps and 1900 m in Bendor (Tables III and IV). These are similar to vector means for cirque headwall aspects and glacier aspects. Shulaps means are 342-001°, 356° overall above 2200 m; and Bendor means are 012-014°, 008° overall above 1900 m. Headwall vector mean aspects are 007° and 018° respectively, and glaciers average 011° in both ranges. In lower altitude belts, various mean directions of steep slopes occur.

Steep slopes show relatively high vector strengths of 18-29%, 21% overall above 2200 m in Shulaps; and 14% overall

above 1900 m in Bendor but 14-22% in belts above 2100 m. The comparison reflects the broader range of cirque aspects in the more heavily glaciated Bendor Range.

Similarly in the English Lake District, slopes >45° at high altitude (above 300 m; Fig. 3) have a vector mean aspect of NE, (033°) as do the 157 cirques(048°): the vector strengths are 37% and 54%. These results are characteristic of mountains glaciated asymmetrically, and give further objective evidence of a glacial imprint. As yet it is not known whether asymmetry of steep slopes is found in mountain ranges where cirques face all directions and have no significant resultant vector. Consistency of steep slope aspects and cirque aspects is not found in the lightly glaciated Mission Ridge, east of Bendor and south of Shulaps but with a highest summit of only 2427 m. This ridge has a very steep southwest slope, part of the Seton Lake trough.

TABLE III. VECTOR MEAN AND STRENGTH FOR ASPECT OF SLOPES OVER 40°, BY ALTITUDE BANDS IN SHULAPS RANGE, B.C.;
the boundaries at 1957 and 2456 m are 05 and 95 percentiles of lowest altitude per cirque; 2610 m is the 95 percentile of maximum floor altitude per cirque; consistent northward tendency above 2200 m (in italics, bottom line) reflects cirque headwalls

Altitude (m)	Mean (°)	Strength (%)	Observations
Above 2610	**001**	**29**	7314
2456-2610	**360**	**24**	24433
2350-2456	**357**	**18**	25443
2250-2350	**351**	**18**	20074
2150-2250	**342**	**21**	15095
2050-2150	286	14	10554
1957-2050	219	21	10385
Above 2200	***356***	***21***	***85615***

In Romania, the gradient frequency distributions can be related to modal floor altitudes in the data of Mîndrescu and Evans (2014). In Table V the resulting signals for cirque floors (a decline in lower quartile: LQR) and cirque headwalls (increased standard deviations and inter-quartile ranges: SD & IQR) are related to the low (05) and high (95) percentiles of modal cirque floor altitudes, for the twelve ranges with more than four cirques. Although only six mountain ranges show a 'floor' signal of declining LQR, all but Bucegi show a 'headwall' signal. The ranges are listed in order of 'degree of glacial modification' calculated from seven cirque variables by Mîndrescu and Evans. The headwall signal is strongest for the 'most glaciated' ranges (the first three). Rodna, Maramureş and Ţarcu also give strong 'glacial' signals.

The innovative paper of Robl et al. (2015) graphed the hypsoclinometry of many massifs in the Alps, using a DEM with 50 m resolution. The continuing presence of glaciers is a complication, reducing gradients of the lower parts of cirque headwalls. Clear signals of both headwalls and cirque floors are found especially in the external massifs (Mont Blanc, Pelvoux-Écrins, Aar, Belledonne and Argentera), and in the Ligurian Alps and Dora Maira Massif (Robl et al., 2015, Figs. 6 & 8).

IV. CONCLUSIONS

From analyses of slope, aspect and altitude in British Columbia, Romania, England and the Alps, the best geomorphometric indication of glacial modification of mountains (by erosion) is the concentration of steep slopes, representing headwalls, around and above the altitudes of cirque floors. This is supported, in the common situation of asymmetric local glaciation, by consistent favoured directions of steep slopes at similar altitudes, with vector means comparable to those of cirques and present or former glaciers. There is also an increased standard deviation and inter-quartile range of slope gradients at these altitudes. The expected concentration of gentle slopes at altitudes of cirque floors is clear only where there are numerous well-developed cirques. Hypsometry alone – the concentration of area at certain altitudes – is not a reliable indicator of altitudes of glacial erosion.

TABLE IV. VECTOR MEAN AND STRENGTH FOR ASPECT OF SLOPES OVER 40°, BY ALTITUDE BANDS IN BENDOR RANGE, B.C.;
the boundaries at 1790 and 2300 m are 05 and 95 percentiles of lowest altitude per cirque; 2425 m is the 95 percentile of maximum floor altitude per cirque; consistent northward tendency above 1900 m (in italics, below) reflects cirque headwalls, and is stronger above 2100 m (black horizontal line)

Altitude (m)	Mean (°)	Strength (%)	Observations
Above 2425	**012**	**21.7**	51871
2300-2425	**007**	**15.9**	73199
2100-2300	**002**	**14.3**	125046
1900-2100	**014**	8.9	114425
1790-1900	061	7.4	59306
1500-1790	110	8.4	114671
Above 1900	***008***	***13.9***	***364541***

TABLE V. ALTITUDES WITH SLOPE GRADIENTS RELATED TO CIRQUE ALTITUDES, FOR 12 RANGES IN ROMANIA WITH MORE THAN FOUR CIRQUES

Mountain range	LQR rises	Modal Floor (p5……p95)	Increased SD & IQR	Max. altitude	n
Retezat	1800-2100	1760…2190	1800-2400	2509	84
Parâng	-	1830…2150	1850-2350	2518	51
Făgăraș	1875-2175	1830…2230	1900-2500	2544	206
Bucegi*	-	1940…2320	-	2505	11
Rodna	1700-1800	1520…1910	1700-2300	2303	45
Lotru*	-	1700…1960	1875-2150	2242	10
Cindrel*	-	1701…2020	1825-2200	2244	8
Godeanu*	-	1640…2010	1850-2200	2291	69
Maramureș	1475-1675	1465…1690	1475-1825	1956	27
Iezer*	-	1870…2170	1925-2200	2470	38
Țarcu*	1750-2050	1630…1980	1850-2100	2192	58
Călimani	1725-1975	1725…1975	1675-1875	2100	7

*ranges with summit plateaux. LQR = lower quartile, p = percentile, SD = standard deviation, IQR = inter-quartile range, n = number of cirques.

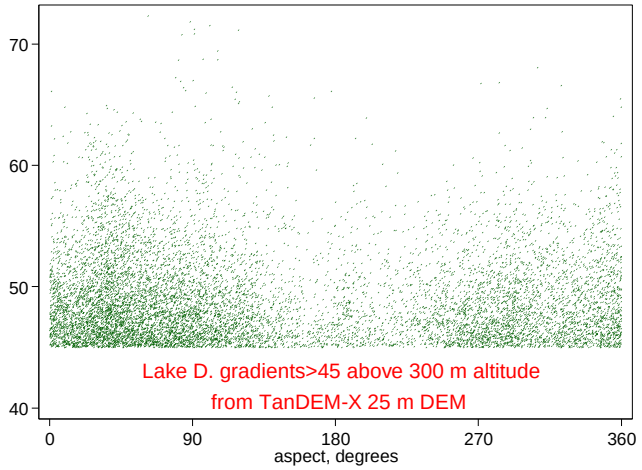

Figure 3. Gradients steeper than 45°, above 300 m altitude, in the English Lake District, from a gridded 25 m TanDEM-X DEM. Concentrations around north and northeast give a vector mean of 033°, with a strength of 37%.

ACKNOWLEDGEMENT

We are grateful to the German Aerospace Centre (DLR) for providing TanDEM – X DEM data for the Bridge River District under project DEM_METH1517.

REFERENCES

[1] Barr, I.D., Spagnolo, M., 2015. Glacial cirques as palaeoenvironmental indicators: Their potential and limitations. Earth-Science Reviews, 151: 48–78. http://dx.doi.org/10.1016/j.earscirev.2015.10.004.

[2] Crest, Y., Delmas, M., Braucher, R., Gunnell, Y., Calvet, M., Team ASTER, 2017. Cirques have growth spurts during deglacial and interglacial periods: evidence from 10Be and 26Al nuclide inventories in the central and eastern Pyrenees. Geomorphology, 278: 60–77. https://doi.org/10.1016/j.geomorph.2016.10.035.

[3] Egholm, D.L., Nielsen, S.B., Pedersen, V.K., Lesemann, J.E., 2009. Glacial effects limiting mountain height. Nature, 460: 884–887. https://doi.org/10.1038/nature08263.

[4] Evans, I.S., 2019. The erosion of glaciated mountains: evidence from hypsoclinometry. Revista de Geomorfologie, 21: 5–14. doi: 10.21094/rg.2019.006

[5] Evans, I.S., 2020. Glaciers, rock avalanches and the 'buzzsaw' in cirque development: Why mountain cirques are of mainly glacial origin. Earth Surface Processes & Landforms, 23 pp. doi: 10.1002/esp.4810.

[6] Evans, I.S., Cox, N.J., 2017. Comparability of cirque size and shape measures between regions and between researchers. Zeitschrift für Geomorphologie, 61, Suppl. 2: 81-103. Special Issue.

[7] Minár, J., Evans, I.S., Krcho, J., 2016. Geomorphometry: Quantitative Land–Surface Analysis (2nd. Edition). In: Reference Module in Earth Systems and Environmental Sciences. Elsevier, Amsterdam. DOI: 10.1016/B978-0-12-409548-9.10260-X.

[8] Mîndrescu, M., Evans, I.S., 2014. Cirque form and development in Romania: allometry and the buzz–saw hypothesis. Geomorphology, 208: 117–136. http://dx.doi.org/10.1016/j.geomorph.2013.11.019.

[9] Niculiță, M., Evans, I.S., 2018. Effects of glaciation on the clinometry and hypsometry of the Romanian Carpathians. Geomorphometry 2018. PeerJ Preprints https://doi.org/10.7287/peerj.preprints.27076v1.

[10] Robl, J.G., Prasicek, G., Hergarten, S., Stüwe, K., 2015. Alpine topography in the light of tectonic uplift and glaciation. Global & Planetary Change, 127: 34–49. http://dx.doi.org/10.1016/j.gloplacha.2015.01.008.

GEOMORPHOMETRY 2020 PERUGIA, ITALY JUNE 22 - 26 2020

3D marine geomorphometry for the Arctic Ocean

Igor V. Florinsky [a, §], Sergey V. Filippov [a], Alexander V. Govorov [b]
[a] Institute of Mathematical Problems of Biology
Keldysh Institute of Applied Mathematics, Russian Academy of Sciences
Pushchino, Moscow Region, 142290, Russia
[b] Department of Photogrammetry
Moscow State University of Geodesy and Cartography (MIIGAiK)
4 Gorokhovsky Lane, Moscow, 105064, Russia
[§] iflor@mail.ru

Abstract—**We develop a system for three-dimensional (3D) geomorphometric modeling of the Arctic Ocean submarine topography. Previously, low-resolution desktop versions of the system were created. In this article we present some results of the next stage developing multiscale, desktop and web versions of the system. We utilize a 500-m gridded digital elevation model (DEM) of the Arctic Ocean floor and adjacent land territories from the International Bathymetric Chart of the Arctic Ocean (IBCAO) ver. 3.0. To process, visualize, and operate the data, the following software are used: (1) Blender 2.79b, an open-source software for 3D modeling, rendering, and animation; (2) BlenderGIS addon for importing and processing geospatial data; (3) LandLord, a software for calculating geomorphometric variables; and (4) Verge3D, a toolkit for creating immersive web-based experiences. The main steps of the data processing are: (a) geomorphometric calculations; (b) importing the IBCAO DEM and morphometric models into Blender; (c) 3D modeling; and (d) exporting the 3D models into the web. A final version of the system will provide: Storage of the DEM of the Arctic Ocean floor; (2) Storage of models for 18 morphometric variables derived from the DEM; (3) Interactive, real-time 3D visualization of the morphometric models; and (4) Free access to this information via Internet.**

I. INTRODUCTION

Submarine topography is one of the major factors, which determine the course and direction of processes at the boundary between hydrosphere and lithosphere. Being a result of the interaction of endogenous and exogenous processes, submarine topography can also reflect the geological structure of a territory. Thus, bathymetric DEMs are used for solving problems of marine geomorphology, geology, and biology [1].

We develop a system for three-dimensional (3D) geomorphometric modeling of the Arctic Ocean floor [2]. Previously, low-resolution desktop versions of the system were created [3–5]. Here we present some results of the next stage of the project [6] developing multiscale, desktop and web versions of the system.

II. MATERIALS AND METHODS

As an input data, we utilize a 500-m gridded digital elevation model (DEM) of the Arctic Ocean floor and adjacent land territories from the International Bathymetric Chart of the Arctic Ocean (IBCAO) 3.0 [7, 8]. The DEM describes a territory measuring about 5,800 km × 5,800 km (Fig. 1). Depths and elevations range from –5,520 m to 5,110 m. A set of DEMs with resolutions of 1 km, 5 km, 10 km, and 15 km were extracted from the IBCAO DEM. All these DEMs are presented in the polar stereographic projection.

The main steps of the data processing are:

1. DEM smoothing. To suppress high frequency noise in the DEMs, they were smoothed.

2. Geomorphometric calculations. From the smoothed DEMs, we derived digital models of morphometric variables [9]: slope gradient, slope aspect, horizontal curvature, vertical curvature, mean curvature, Gaussian curvature, minimal curvature, maximal curvature, unsphericity curvature, difference curvature, vertical excess curvature, horizontal excess curvature, ring curvature, accumulation curvature, catchment area, dispersive area, topographic index, and stream power index.

3. Importing the IBCAO DEM and morphometric models into Blender.

4. 3D modeling. The Blender-based approach for 3D terrain modeling [10] includes the following key steps:

- Automatically creating a polygonal object from a DEM.
- Selecting an algorithm to model the 3D geometry.
- Selecting a vertical exaggeration scale.
- Selecting types, parameters, a number, and positions of light sources.
- Selecting methods for generating shadows.
- Selecting a shading method for the 3D model.
- Selecting a material for the 3D model surface.

Igor Florinsky, Sergey Filippov, and Alexander Govorov (2020) 3D marine geomorphometry for the Arctic Ocean:
in Massimiliano Alvioli, Ivan Marchesini, Laura Melelli & Peter Guth, eds., Proceedings of the Geomorphometry 2020 Conference, doi:10.30437/GEOMORPHOMETRY2020_22.

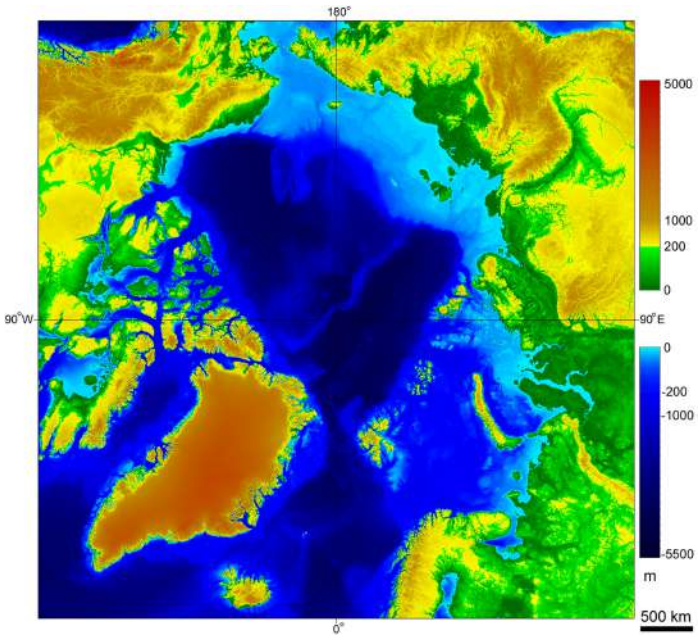

Figure 1. The IBCAO DEM: depths of the Arctic Ocean floor and elevations of adjacent regions of Eurasia and North America [3].

- Overlaying a texture on the 3D model.
- Setting a virtual camera(s).
- Rendering the 3D model.

5. Exporting the 3D models into the web.

To process, visualize, and operate the data, the following software are used:

- LandLord software for geomorphometric calculations [9].
- Blender 2.79b [11], an open-source software for 3D modeling, rendering, and animation.
- BlenderGIS addon [12] designed for import and processing of geospatial data.
- Verge3D [13], a powerful and intuitive toolkit, which allows Blender users creating immersive web-based experiences. (Blend4Web [14] and Sketchfab [15] packages may be used as alternative to Verge3D).

III. RESULTS AND DISCUSSION

Figures 2–5 display several examples of the 3D desktop morphometric models produced from DEMs with different resolutions ranging from 1 km to 15 km. Figure 6 represents an example of a 3D online model produced from the 15 km-gridded DEM.

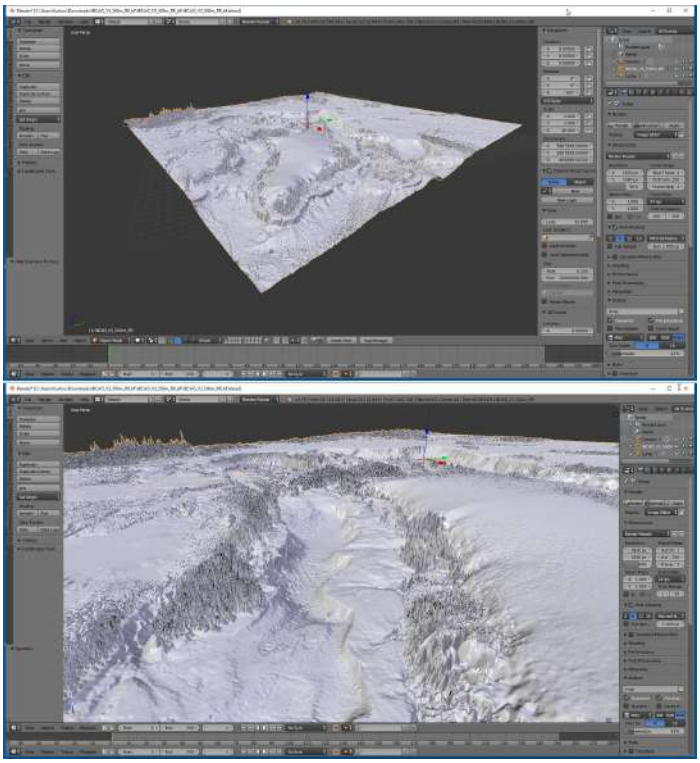

Figure 2. Examples of 1 km-gridded, 3D desktop monochromic models of the Arctic Ocean floor and adjacent regions presented within the Blender environment. General perspective view from the Atlantic (upper). Perspective view of the Buffin Bay and the Davis Strait from the Labrador Sea (lower) [6].

3D models clearly show the main features of the submarine topography manifested according to the physical and mathematical sense of a particular morphometric variable [5].

It is obvious that generalization level of the 3D model appearance depends mainly on the particular DEM resolution, although several smoothing applied to the DEMs before morphometric calculations and during 3D modeling also contribute to resulted smoothness of the models.

The created 3D morphometric models can be used in marine geomorphological, geological, and, probably, biological studies of the Arctic Ocean.

Our work allows expanding application areas of Blender software and its addons as convenient and efficient tools of scientific visualization.

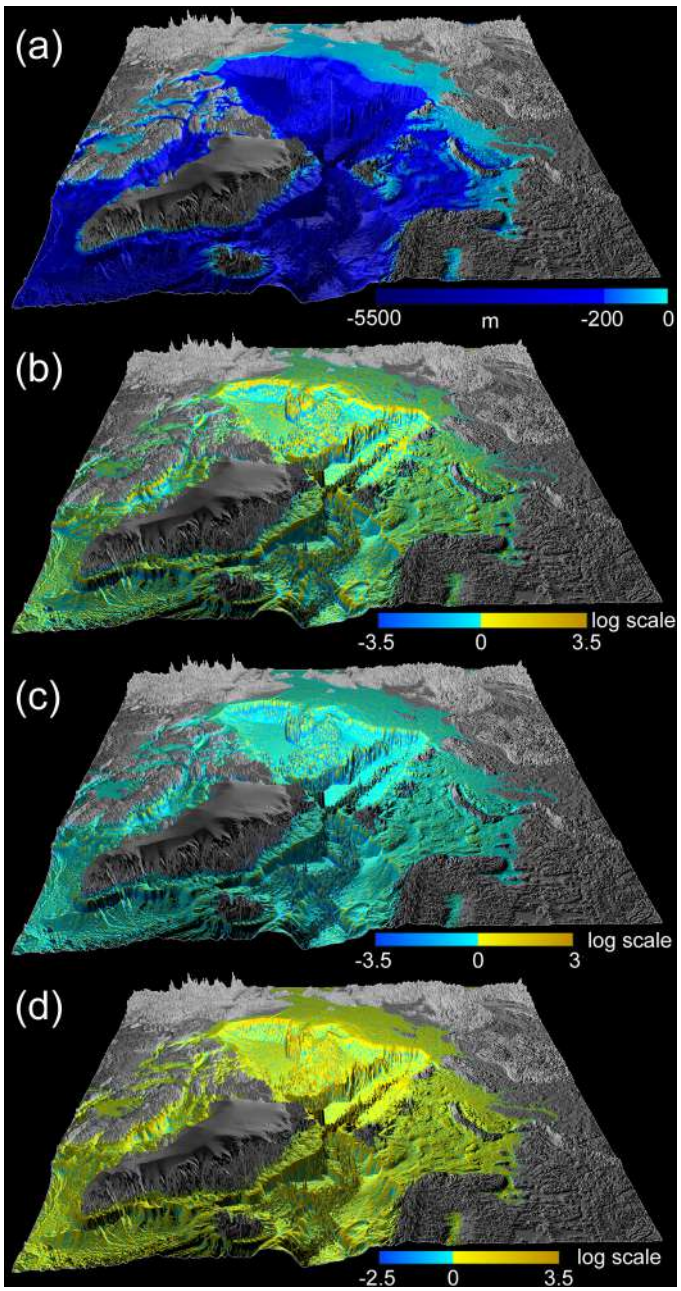

Figure 3. Examples of 5 km-gridded, 3D desktop models of the Arctic Ocean floor: (a) Depth. (b) Vertical curvature. (c) Minimal curvature. (d) Maximal curvature. Perspective views from the Atlantic [5].

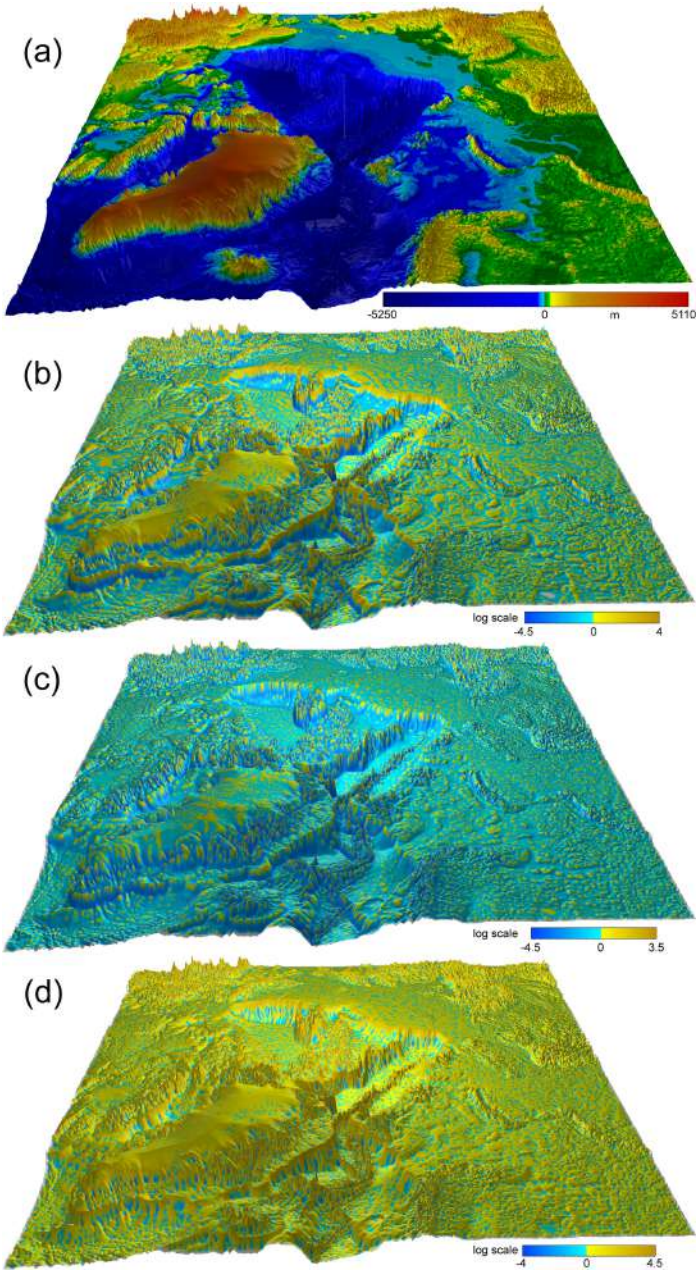

Figure 4. Examples of 10 km-gridded, 3D desktop models for the Arctic Ocean floor and adjacent territories: (a) Elevation/Depth. (b) Vertical curvature. (c) Minimal curvature. (d) Maximal curvature. Perspective views from the Atlantic [3].

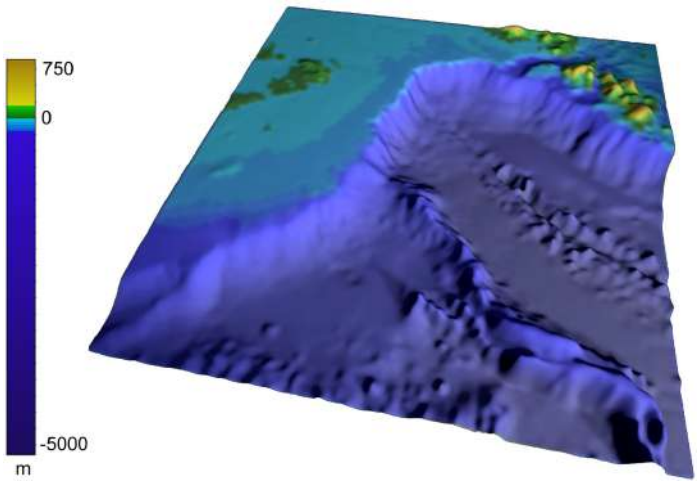

Figure 5. An example of 15 km-gridded, 3D desktop model for a portion of the Arctic Ocean floor (the Lomonosov Ridge): Elevation/Depth [10].

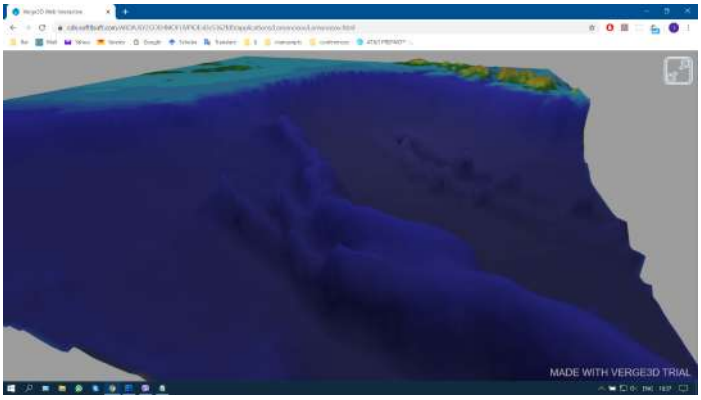

Figure 6. An example of a test, 15 km-gridded, 3D online model for a portion of the Arctic Ocean floor (the Lomonosov Ridge) presented within the Verge3D environment [6].

IV. CONCLUSIONS

We are now in the final phase of the project to develop the system for 3D geomorphometric modeling of the Arctic Ocean floor. Our experiments and results testify that the applied approach to the system development is flexible, effective, and functional. One of its advantages is that it is based on free and open-source software.

A final version of the system will provide:

- Storage of models for 18 morphometric variables derived from the IBCAO DEM.
- Interactive, real-time, 3D multiscale visualization of these morphometric models.
- Free access to this information via Internet.

V. ACKNOWLEDGMENTS

The study is supported by the Russian Foundation for Basic Research, grants ## 18-07-00223 and 18-07-00354.

REFERENCES

[1] Lecours, V., M.F.J. Dolan, A. Micallef, V.L. Lucieer, 2016. "A review of marine geomorphometry, the quantitative study of the seafloor". Hydrol. Earth Syst. Sci., 20(8), 3207–3244.

[2] Florinsky, I.V., S.V. Filippov, A.S. Abramova, Y.A. Zarayskaya, E.V. Selezneva, 2018. "Towards geomorphometric modelling of the topography of the Arctic Ocean floor". In: Bandrova, T. and M. Konečný, Eds., Proc. 7th Int. Conf. Cartogr GIS, 18–23 June 2018, Sozopol, Bulgaria, Vol. 1. Bulgarian Cartographic Association, Sofia, pp. 166–173.

[3] Florinsky, I.V. and S.V. Filippov, 2019. "Three-dimensional, low-resolution desktop geomorphometric modelling of the Arctic Ocean floor". In: Proc. OCEANS MTS/IEEE 2019 SEATTLE, Seattle, WA, 27–31 Oct. 2019, pp. 1–7.

[4] Florinsky, I.V. and S.V. Filippov, 2019. "Three-dimensional desktop morphometric models for the Arctic Ocean floor". Proc. Int. Cartogr. Assoc., 2, # 32.

[5] Florinsky, I.V. and S.V. Filippov, 2020. "Three-dimensional geomorphometric modeling of the Arctic Ocean submarine topography: A low-resolution desktop application". IEEE J. Ocean. Eng., doi:10.1109/JOE.2020.2969283.

[6] Florinsky, I., and A. Govorov, 2019. "Three-dimensional, multiscale system for geomorphometric modeling of the Arctic Ocean floor: Development of desktop and web applications using the Blender software". In: 2019 AGU Fall Meeting, San Francisco, CA, 9–13 Dec. 2019, # IN11B-18.

[7] IBCAO Version 3.0, 2012. National Centers for Environmental Information, NOAA, http://www.ngdc.noaa.gov/mgg/bathymetry/arctic/ibcaoversion3.html.

[8] Jakobsson, M. et al., 2012. "The International Bathymetric Chart of the Arctic Ocean (IBCAO) version 3.0". Geophys. Res. Lett., 39, # L12609.

[9] Florinsky, I.V., 2016. Digital Terrain Analysis in Soil Science and Geology, 2nd ed. Amsterdam, the Netherlands: Academic Press.

[10] Florinsky, I.V. and S.V. Filippov, 2019. "Three-dimensional terrain modeling with multiple-source illumination". Trans. GIS, 23(5), 937–959.

[11] Blender, 2003–2018. Amsterdam, the Netherlands: Stichting Blender Foundation, https://www.blender.org.

[12] BlenderGIS, 2020. San Francisco, CA: GitHub, Inc. https://github.com/domlysz/BlenderGIS.

[13] Verge3D, 2017–2020. Moscow: Russia: Soft8Soft, https://www.soft8soft.com/verge3d.

[14] Blend4Web, 2014–2019. Moscow, Russia: Triumph, https://www.blend4web.com/en.

[15] Sketchfab, 2020. New York, NY: Sketchfab, https://sketchfab.com.

GEOMORPHOMETRY 2020 PERUGIA, ITALY JUNE 22 - 26 2020

Geomorphometric diversity of closed depressions in the loess belt of east Poland (Nałęczów Plateau)

Leszek Gawrysiak[§], Renata Kołodyńska-Gawrysiak
Department of Geology, Soil Science and Geoinformation
Maria Curie Skłodowska University
Aleja Kraśnica 2CD, 20-718, Lublin, Poland
[§] leszek.gawrysiak@poczta.umcs.lublin.pl

Abstract—**Closed depressions (CDs, Fig. 1B) are typical geomorphological features of the loess belt in Europe. Although they are important elements of loess landscape in Europe, these depressions have been subject to no comprehensive studies of their geomorphometric properties. This paper presents a detailed case study of CDs in a loess region of east Poland (Nałęczów Plateau, Fig. 1A) investigating their morphometric features for a better understanding of the geodiversity of loess landscapes.**

The objective of the study was (1) the development of a methodology of delimitation of closed depressions and their watersheds, and (2) the analysis of their selected geomorphometric parameters in reference to land cover described in CLC2018. The detailed investigation concerned the Nałęczów Plateau (493.7km^2, east Poland) with a loess cover, where closed depressions are common elements of land relief. The extraction of depressions employed a high resolution (1x1 m) Digital Terrain Model; and the calculations were performed in SAGA-GIS and ArcGIS software. The calculation results were used for a quantitative description of the investigated landforms. Finally, Pearson correlation coefficients were calculated using pairs of parameters characterising depressions and watersheds in order to estimate correlations between them.

High diversity of CDs varying in size, length, depth, volume, and circularity ratio was found. Their watersheds also varied in terms of these parameters. Differences between CDs on agricultural land and in forests were determined. Part of these parameters were mutually correlated. The obtained results will be useful in describing the functioning of processes in other disciplines.

I. INTRODUCTION

A closed depression (CD) is a landform where the hillslopes encircle a common sediment depository, and the sediment eroded from the hillslopes by water and tillage erosion is trapped in the system [8]. Closed depressions (CDs) are typical geomorphological features of the loess belt in Europe as well as other loess regions in the World. The origin and evolution of CDs are highly debated in literature (see review in [3]). However, no comprehensive study of the geomorphic properties of these depressions has been made. Literature on the morphology of CDs is sparse, but several studies reported the basic dimensions of these landforms [3]. Preliminary research of detailed morphometric features of CDs was conducted in the loess areas of east Poland (Nałeczów Plateau) by Kołodyńska-Gawrysiak and Chabudziński [4, 5] and by Kołodyńska-Gawrysiak et al.[6] for better understanding of their origin and evolution. The Nałęczów Plateau (493.7 km^2) is covered by a compact loess belt of a differential thickness up to more than 20 m, and CDs are the primary element of its land relief.

The objective of this paper is to characterise the morphometric features of CDs in the Nałeczów Plateau to better recognise and understand the geodiversity of loess landscapes.

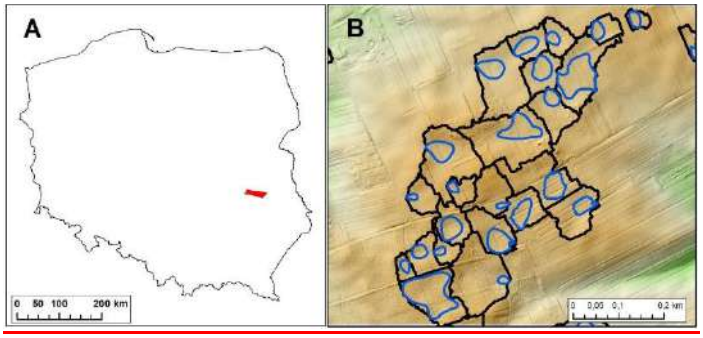

Figure 1. Location of the Nałęczów Plateau in Poland (A), and an example of closed depressions and their watersheds (B).

Leszek Gawrysiak and Renata Koéodynska-Gawrysiak (2020) Geomorphological influence assessment on natural conditions under climatic changes in the periglacial zone: in Massimiliano Alvioli, Ivan Marchesini, Laura Melelli & Peter Guth, eds., Proceedings of the Geomorphometry 2020 Conference, doi:10.30437/GEOMORPHOMETRY2020_23.

II. DATA AND METHODS

The analysis was based on a Digital Terrain Model (DTM) developed during project ISOK, including LiDAR scanning of Poland in the years 2011-2014 [9]. The DTM has a high spatial resolution of 1x1 m and vertical accuracy of 0.15 m [7]. Land cover was defined by means of CLC2018.

The Extraction of CDs from DTM employed the Closed Depressions function, included in the Basic Terrain Analysis module of SAGA-GIS [1]. The result was a grid of data containing all non-drainage surfaces with strongly differential areas. The visual analysis showed that cells defining depressions are grouped into areas of varying size, shape, and compactness. We noticed that landforms with an area of more than 200 m^2 are clearly isolated as compact areas. The next stage of processing involved the extraction of such landforms. Then, grid data were converted to vector polygons (shapefile), and depressions of anthropogenic origin were manually removed based on knowledge from field investigations and detailed analyses of their morphology and position in land relief. Shaded relief and coloured DTM were useful at this stage.

Next, the shape of polygons was smoothed using the "smooth polygon" tool (ArcGIS). Several attempts were made to find the optimum value of smoothing tolerance, and 30 m was eventually accepted. After smoothing, small artefacts were removed manually from some polygons. Finally, clear polygon data were analyzed by calculating the following: (1) area, (2) circularity ratio (Rk) [2], (3) depth, (4) volume, and (5) maximum length understood as diameter of circle enveloping polygon. Information concerning CLC2018 necessary to compare indices for areas of different types of land cover was assigned to polygons.

The next step was delimiting borders of watersheds of depressions by means of the "watershed tool" (ArcGIS), where polygons defining depressions were declared as pour points. The resulting grid data were converted to vector polygons (shapefile), and then morphometric indices were calculated, namely: (1) area, (2) circularity ratio (Rk), and (3) height difference within watershed.

The last stage was calculating Pearson correlation coefficients for pairs of indices of depressions, and between indices of depressions and watersheds.

III. RESULTS

A. Closed depressions

We distinguished 5419 closed depressions within the study area, with an area ranging from 0.02 to 3.66 hectares (Tab. 1). Landforms with an area of less than 0.1 ha (63.4%) were the most numerous. We found 236 (4.3%) largest forms with an area exceeding 0.5 ha. The total area of depressions was 7.5 km^2, accounting for 1.51% coverage of the Nałęczów Plateau. Depressions were the most common (Tab. 2) in agricultural areas (CLC code: 211, 222, 231, 242, 243) – 4412 landforms, constituting 81.4% of their total number (agriculture areas cover 72.75% of the Plateau). In forests (code 311, 312, and 313), we found 531 depressions (9.95%). Another outstanding land cover form was "discontinuous urban fabric" where we found 377 depressions (6.95%). In other categories (121, 122, 142, 222, and 231) depressions were not abundant (3.08%).

The average area of depressions in agricultural areas was 0.14 ha with a maximum of 3.46 ha. They were evidently smaller in forests, averaging 0.1 ha, although the largest depression (3.66 ha) was located in a forest.

TABLE 1. STATISTICS OF AREA (HA) OF CLOSED DEPRESSIONS

Range	0-0.05	0.05-0.10	0.10-0.15	0.15-0.20	0.20-0.25	0.25-0.30	0.30-0.35	0.35-0.40	0.40-0.45	0.45-0.50	> 0.50
Number	2006	1429	681	373	250	143	121	78	67	36	236

TABLE 2. DISTRIBUTION OF CLOSED DEPRESSIONS DUE TO CLC2018

class	112	121	122	142	211	222	231	242	243	311	312	313
number	377	7	105	9	3822	34	12	487	169	499	16	24

CLC2018 classes: 112 – Discontinuous urban fabric, 121 – Industrial or commercial units, 122 – Road and rail networks and associated land, 142 – Sport and leisure facilities , 211 – Non-irrigated arable land, 222 – Fruit trees and berry plantations, 231 – Pastures, 242 – Complex cultivation patterns, 243 – Land principally occupied by agriculture, with significant areas of natural vegetation, 311 – Broad-leaved forest, 312 – Coniferous forest, 313 – Mixed forest.

The depth of depressions (Tab. 3) was usually smaller than 1 m (5030 polygons, 92%), whereas the depth of most of them was in a range of 0.3-0.4 m (1068, 19.7%). The average depth of depressions was 0.49 m. 22 (0.4%) of them were classified as deepest (more than 2 m), with a maximum depth of 2.89 m. Depressions in agricultural areas had an average depth of 0.47 m. They were somewhat deeper in forests (average 0.61 m), and the deepest one (2.89 m) was located in a forest. Notice that the first category (0-0.2 m) includes shallow forms. Because of the vertical accuracy of the DTM (0.15 m) used in the analysis, some of them might be marked incorrectly. They constitute approximately 10% of the total number of CDs.

TABLE 3. DEPTH (M) OF CLOSED DEPRESSIONS

Range	0-0.2	0.2-0.4	0.4-0.6	0.6-0.8	0.8-1.0	1.0-1.2	1.2-1.4	1.4-1.6	1.6-1.8	1.8-2.0	>2.0
Number	581	2113	1275	692	369	171	98	50	33	16	22

The distribution of values (Tab. 4) of the circularity ratio (Rk) suggests that polygons of oval shape were most common. The mean value of Rk was 0.78, maximum reached 0.99, and minimum was 0.25. The largest, most complex polygons had an Rk value of approximately 0.5. The lowest values of the index

belonged to smaller polygons, usually with an area of less than 1000 m^2. Depressions in forests had a higher mean value of Rk (0.83) than those in agricultural areas (0.78).

TABLE 4. CIRCULATORY RATIO (RK) OF CLOSED DEPRESSIONS

Range	≤ 0.40	0.4-0.5	0.5-0.6	0.6-0.7	0.7-0.8	0.8-0.9	0.9-1
Number	67	188	403	730	1178	1630	1224

The maximum length of depressions (Tab. 5) was in a range between 16.9 and 355.7 m. The mean value was 50.1 m. The most frequent interval was 25-30 m (14.4%). Landforms with a length of up to 50 m were dominant (66.2%). We found 116 longest polygons with more than 150 m, accounting for 2.1%. The average length of depressions in forests was 40.4 m, and in agricultural areas 50.9 m.

TABLE 5. MAXIMUM LENGTH OF CLOSED DEPRESSIONS (M).

Range	< 20	20-40	40-60	60-80	80-100	100-120	120-140	140-160	>160
Number	131	2576	1445	589	288	164	88	42	97

The volume of closed depressions (Tab. 6) reached 38 123.1 m^3. The lowest value was 5.6 m^3, and mean 555.3 m^3. Depressions with a volume of up to 100 m^3 were dominant (44.5%), and large depressions (exceeding 1000 m^3) were relatively abundant (611, 11.3%). The mean volume of depressions throughout the study area was approximate to that in agricultural areas, and equaled 554.2 m^3. In forests the mean value was lower – 420.9 m^3. The depression with the largest area also had the highest volume (38,123 m^3).

TABLE 6. VOLUME (M3) OF CLOSED DEPRESSIONS

Range	0-100	100-200	200-300	300-400	400-500	500-600	600-700	700-800	800-900	900-1000	>1000
Number	2412	895	446	287	214	153	147	96	88	69	611

B. Watersheds

The area of watersheds (Tab. 7) varied from 0.037 to 20 hectares, averaging 0.97 ha. The most frequent class was 0-0.5 ha (43.2%), and watersheds with an area of up to 1 ha accounted for 71.1%. Watersheds of depressions in agricultural land had a mean area of 0.99 ha. It was considerably lower in forests, reaching 0.67 ha. The largest watershed in forests had an area of 9.36 ha. Watersheds in the class of over 5 ha only constituted 1.9%. The total area of watersheds in the Nałęczów Plateau was 5.26 km^2 (10.67%).

TABLE 7. AREA (HA) OF WATERSHEDS OF CLOSED DEPRESSIONS

Range	0-0.5	0.5-1.0	1.0-1.5	1.5-2.0	2.0-2.5	2.5-3.0	3.0-3.5	3.5-4.0	4.0-4.5	4.5-5.0	>5.0
Number	2341	1513	692	304	171	120	71	47	33	21	105

The circularity ratio (Tab. 8) was considerably smaller than in the case of closed depressions, and reached 0.54, with a mean value of 0.30. The most frequent class was 0.30 0.35 (30.2%). Together with the lower (0.25 0.30) and higher (0.35 0.40) class, they accounted for 69.2%. The mean Rk value of watersheds in forests (0.31) was approximate to that in agricultural areas.

TABLE 8. CIRCULATORY RATIO (RK) OF WATERSHEDS OF CLOSED DEPRESSIONS

Range	≤0.10	0.10-0.15	0.15-0.20	0.20-0.25	0.25-0.30	0.30-0..35	0.35-0.40	0.40-0.45	0.45-0.50	> 0.50
Number	15	148	405	796	1233	1366	967	393	80	15

Height differences within watersheds (Tab. 9) were in a range of 0.26 22.98 m, with a mean value of 3.12 m. The most frequent class was 1 2 m (32.9%). Its frequency was approximate to that of class 2-3 m (32.2%). The highest class (> 10 m) included 1.97% of depressions. The greatest height difference (22.09 m) was determined for a watershed located in an agricultural area. Watersheds in agricultural areas had a lower (3.09 m) mean value than those in forests (3.27 m).

TABLE 9. HEIGHT DIFFERENCES (M) WITHIN WATERSHEDS.

Range	0-1	1-2	2-3	3-4	4-5	5-6	6-7	7-8	8-9	9-10	>10
Number	326	1486	1457	915	488	302	152	97	62	44	89

C. Correlation of parameters

The analysis of relations between parameters involved the calculation of Pearson correlation coefficients between parameters of depressions (Table 10), and between depressions and their watersheds (Table 11). High (important) values of coefficients were obtained for depressions in most cases of pairs of indices (6 to 10). In the case of indices of depressions to watersheds only 5 (out of 15) reached an important value – the area of depressions increased with the watershed area, and volume and maximum length were correlated with area and height differences within watersheds.

TABLE 10. PEARSON CORRELATION COEFFICIENTS BETWEEN PARAMETERS OF CLOSED DEPRESSIONS (BOLDED IMPORTANT VALUES)

	Depth	Rk	Volume	Length
Area	**0.69**	-0.30	**0.93**	**0.90**
Depth		-0.15	**0.64**	**0.74**
Rk			-0.23	-0.48
Volume				**0.76**

TABLE 11. PEARSON CORRELATION COEFFICIENTS BETWEEN PARAMETERS OF CLOSED DEPRESSIONS (CD) AND THEIR WATERSHEDS

Watershed / **CD**	Area	Depth	Rk
Area	**0.61**	0.25	-0.14
Depth	0.45	0.27	-0.08
Rk	-0.15	-0.02	0.16
Volume	**0.56**	**0.64**	-0.12
Length	**0.59**	**0.74**	-0.48

IV. CONCLUSIONS

The processing and analysis provided data for creating a database of closed depressions, their watersheds, and morphometric parameters in the Nałęczów Plateau. The application of a high resolution Digital Terrain Model permitted precise delimitation of all depressions, including those not subject to inventory so far. First, borders of watersheds of closed depressions were successfully delimited. The precise data provided the basis for the calculation of accurate morphometric parameters. They show high diversity of closed depressions and their watersheds. Closed depressions strongly vary in size (0.02-3.66 ha), depth (0.1-2.89 m), circularity ratio (0.25-0.99), length (16.9-355.7 m), and volume (5.6-38.123 m^3). We noticed differences in the morphology of depressions and watersheds in agricultural and forested areas, expressed in differences of values of the analysed parameters. CDs located in forests have smaller mean area and length, but are usually deeper and have more regular shape (higher Rk). Watersheds in agricultural areas are larger with a similar circularity ratio, and those in forests are somewhat deeper than those on agricultural land.

We noticed important correlations between most parameters of closed depressions and some for watersheds. Parameters of CDs are mutually corelated, except for the circularity ratio. In reference to the correlation of CDs and watersheds, only area/area, volume/area, volume/depth, length/area, and length/depth show significant correlation values.

Because the total area of non-drainage surfaces in the Nałęczów Plateau exceeds 10%, they presumably play an important role in the functioning of hydrological, geomorphological, and soil processes. CDs and their watersheds have been so far ignored in detailed investigations in these disciplines. Detailed data regarding the issue will improve the quality of research of loess areas.

REFERENCES

[1] Conrad O., Bechtel B., Bock M., Dietrich H., Fischer E., Gerlitz L., Wehberg J., Wichmann V., Boehner J., 2015. System for Automated Geoscientific Analyses (SAGA) v. 2.1.4. Geosci. Model Dev., 8, 1991-2007, doi:10.5194/gmd-8-1991-2015

[2] Gregory K.J., Walling D.E., 1973. Drainage Basin Form and Processes. A Geomorphological Approach, Edward Anrold Ltd., London, s.456

[3] Kołodyńska-Gawrysiak R., Poesen J., 2017. Closed depressions in the European loess belt – natural or anthropogenic origin? Geomorphology 288: 111-128

[4] Kołodyńska-Gawrysiak, R., Chabudziński, Ł., 2012. Morphometric features and distribution of closed depressions on the Nałęczów Plateau (Lublin Upland, SE Poland). Annales UMCS, sec. B LXVII (1), 45–61.

[5] Kołodyńska-Gawrysiak, R., Chabudziński, Ł., 2014. The types and function of closed depressions in modern loess landscape of Nałęczów Plateau (Lublin Upland, E Poland). Annales UMCS 69 (1), 61–77.

[6] Kołodyńska-Gawrysiak, R., Harasimiuk, M., Chabudziński, Ł., Jezierski, W., Telecka, M., 2015. Geological conditions of the distribution of closed depressions in the Nałęczów Plateau (Lublin Upland, E Poland): are they an origin determinant? Landform Analysis 29, 9–18.

[7] Kurczyński Z., Stojek E., Cisło-Lesicka U., 2015. Zadania GUGiK realizowane w ramach projektu ISOK. [in:] Podręcznik dla uczestników szkoleń z wykorzystaniem produktów LiDAR, GUGiK, Warszawa, ss.22-58

[8] Norton L. D., 1986. Erosion-sedimentation in closed drainage basin in Northwest Indiana. Soil Sci. Soc. Am. J., 50, 209-213.

[9] Woźniak P., 2015. High Resolution Elevation Data in Poland [in:] Geomorphometry for Geoscience, Jasiewicz Z., Zwoliński Z., Mitasova H., Hengl T., (ed.), Ministry of Science and High Education of Poland, Adam Mickiewicz University in Poland, ss.13-14

GEOMORPHOMETRY 2020 PERUGIA, ITALY JUNE 22 - 26 2020

Geomorphometric characteristics of the high mountains in North Macedonia

Ivica Milevski[§], Bojana Aleksova[1], Sonja Lepitkova[2]
[1]Institute of Geography, Faculty of Sciences, Gazi Baba bb, 1000 Skopje, North Macedonia
[2]UGD, Faculty of Natural and Technical Sciences, Stip
[§] ivica@pmf.ukim.mk

Abstract— **As a result of powerful local and regional geotectonic movements, the landscape of North Macedonia (25,713 km^2) has a typical chequerboard topography with frequent changes of mountains and depressions. There are 38 mountain ranges, of which 13 extending above 2000 m are defined as high, while the highest - Korab, reach 2753 m. Because of their geomorphological and overall significance, geomorphometric features of these 13 dominant high mountain ranges are analyzed in this work. The data are calculated from a previously prepared 15-m DEM with particular attention to hypsometry, slope gradient, aspect, and curvature. Based on these variables, a simple classification of the high mountain ranges is made.**

I. INTRODUCTION

As uplifting morphostructures mountains are the predominant elements of the landscape in North Macedonia. The highest mountain massifs are mostly found in the western and central parts (Fig. 1); there are only two from 13 mountains above 2000 m in eastern parts of the country: Osogovo (2252 m) and Belasica (2029 m). According to a peak altitude of the mountains in the Balkan Peninsula, mountains in North Macedonia are divided into three groups: high mountains (2000-2753 m) with a subgroup of very high mountains (2500-2753 m), medium-high mountains (1000-2000 m) and low mountains (below 1000 m). The lowest altitude limit for a mountain is set to 700 m of absolute elevation and 500 m of relative altitude [1]. Because of the geotectonic setting, mountains in western and central parts (in the West-Macedonian zone, the Pelagonian massif, and the Vardar Zone) have a general NW-SE direction. In contrast, in the eastern part of the country, they are E-W elongated (because of the predominant N-S extensional regime). Mountains in the west and central part are generally composed of marbles (Jakupica, Suva Gora), lime-stones (Bistra, Jablanica, Galičica, Šara), granites (Pelister) or other compact rocks. For reasons, these mountains have usually narrow, sharp ridges and peaks and deeply incised valleys. Mountains in the eastern part of the country, are dominantly composed of erodible crystalline rocks (schists) and, consequently, show a more subdued relief, rounded ridges, and peaks, and less deeply incised valleys. However, both groups of mountains were shaped during the Neogene–Pleistocene [2].

All of the above differences are well reflected in the mountain morphology, which can be seen in their geomorphometry as well. In this regard, Milevski [3, 4] perform the first morphometric analysis of the mountain ranges in North Macedonia, based on 3"SRTM DEM.

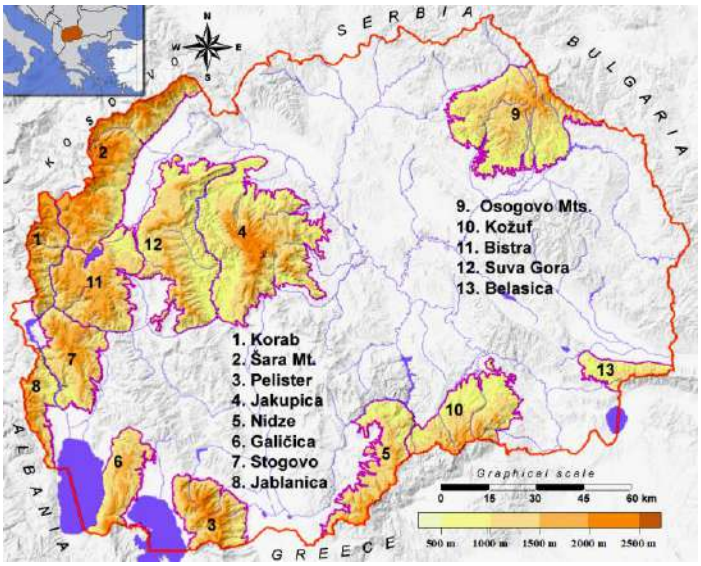

Figure 1. Geographic position of the high mountain ranges in North Macedonia

II. METHODOLOGY

In this work, geomorphometrical analyses of the high mountains in Macedonia are further improved and based on much more accurate 15-m DEM of the State Agency of Cadaster of North Macedonia. According to our tests, this model has a very good average horizontal and vertical accuracy of +/- 1.3 m, with maximum errors up to +/-4 m [5, 6]. Mountain range borders are vectorized manually with a combination of hypsometric criteria (following characteristic contours) and morphologic criteria

Ivica Milevski, Bojana Aleksova and Sonja Lepitkova (2020) Geomorphometric characteristics of the high mountains in North Macedonia: in Massimiliano Alvioli, Ivan Marchesini, Laura Melelli & Peter Guth, eds., Proceedings of the Geomorphometry 2020 Conference, doi:10.30437/GEOMORPHOMETRY2020_41.

(tracking clearly expressed morphological boundaries). However, it was a difficult and subjective task as the mountains in some parts gradually pass through hilly terrain to plains and valleys. After this, mountain extents are clipped from the 15-m DEM and processed to further calculations performed mostly in SAGA GIS software.

III. RESULTS

According to the data in Table 1, Šara Mt. has the highest mean altitude of 1610 m, followed by Korab with 1573 m, while the third is Pelister with 1477 m. With 1384 m, Bistra Mountain is the fourth immediately after Pelister (Baba Mountain), although by peak altitude (2163 m) it ranks eleventh. That is because of a significant area in the 1500-2000 m zone, with a large karst planation surface and few karst poljes on it. The mean altitude of all analyzed mountain ranges is 1257 m, which is 427 m more than the mean altitude (829 m) of North Macedonia [2].

Table 1. Basic morphometric features of the high mountains in North Macedonia including altitudes of the highest (Hmax) peak, average altitude (Hav), slope and area (A) of each mountain range.

	Mountain	Hmax m	Hav m	Slope °	A km^2
1	Korab	2753	1573	25.3	289.5
2	Šara Mt.	2748	1610	22.9	828.6
3	Pelister	2601	1477	23.4	396.6
4	Jakupica	2540	1127	22.1	1272.7
5	Nidže	2520	1190	22.2	460.0
6	Galičica	2288	1289	18.3	346.3
7	Stogovo	2268	1345	21.4	458.0
8	Jablanica	2256	1319	21.7	207.6
9	Osogovo Mt.	2252	1072	21.3	981.0
10	Kožuf	2165	1056	21.2	543.9
11	Bistra	2163	1384	20.8	643.7
12	Suva Gora	2061	1072	21.8	923.4
13	Belasica	2029	830	23.5	167.5
	Average	**2357**	**1257**	**22.0**	**578.4**

The data for the mean slopes show that Korab, Šara Mountain, and Pelister have the highest values (from 25.3° to 22.9°). The reasons are steep mountainsides (fault slopes), deeply incised river valleys, sharp ridges and peaks on the top shaped with strong glacial erosion during Pleistocene [7, 8]. Jakupica (22.1°) and Suva Gora (21.8°) have lower values because of large karst plains on it. Galičica Mountain have has the lowest value for mean slope (only 18.3°), due to the large karst plains with few karst poljes and uvalas. Bistra Mountain (20.8°) has an almost identical situation, but here mountainsides are almost vertically incised by the Radika Canyon, resulting in a higher mean slope [9]. Overall, the average slope gradient of the high mountains in North Macedonia is 22°, well above the average slope of the whole country of 15.1° [2].

As Figure 2 shows, the curves of mean slope against altitude are irregular, with frequent indents (representing planation surfaces and terraces) and maxima (representing steep slopes, escarpments, and sides of sharp peaks and ridges). Usually, the steepest average gradients are below 1000 m of altitude as a result of steep slopes and deeply incised valleys, as well as in the highest parts on the ridge and peak sides [4].

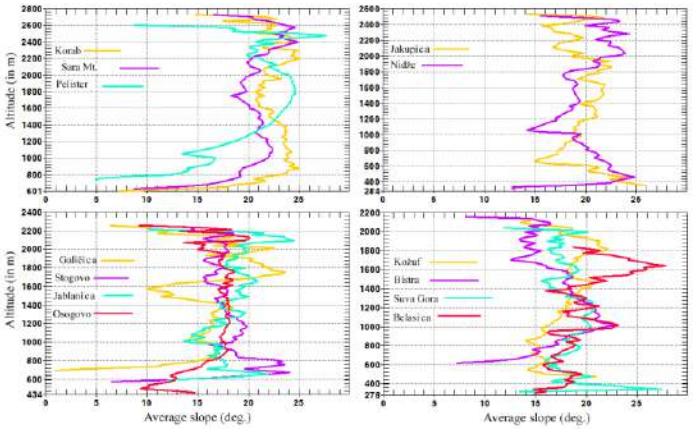

Figure 2. Average slopes against altitude of each high-mountain range in North Macedonia.

At the base of the mountains and on the top of most peaks and ridges, the slope is lower because of the gradual flattening of the terrain. However, mountains highly affected by Pleistocene glaciation (most of them in the western part of the country), show prominent peaks of the average slope above 2000 m. That is the case with Korab (2100-2500 m), Šara (2200-2600 m), Pelister (2300-2500 m), Galičica (1900-2150 m) and Jablanica (2050-2200 m). Usually, they represent steep slopes of cirques, U-valleys, ridges, and sharp peaks. At the same time, there are distinctive indentations in higher parts of the above and some other mountain ranges related to too large karst planation surfaces. Thus, Galičica have has remarkable indents (and planation surfaces) on 1500-1600 m, 1900-1950 m, and 2150-2250 m, Bistra Mountain on 1700-2050 m, and Jakupica on 2000-2400 m. There are also indents representing large old fluvial-denudation surfaces on Korab (1600-2100 m), Šara (1600-2200 m) and Pelister (2100-2300 m). Part of these surfaces is fulfilled with glacial deposits. Bellow 2100 m, Pelister which is typical, almost symmetrical horst, has a regular curve with a broad maximum of the gradient at 1600-2000 m. This contrasts with the Kožuf Mountains which have mean gradients between 14° and 22° from the foothills to the highest parts [3].

The terrain curvature is an important morphological and geomorphometric element that indicates the shape of slopes: convex, straight or concave. Ridges and peaks have convex curvature, plains or fields and surfaces with a uniform slope have

straight curvature, while valley bottoms and depressions have concave curvatures [10]. In this work, the types of the slope are represented by the SAGA GIS convergence index which is similar to plan curvature but gives much smoother results [11]. The calculation uses the aspects of surrounding cells, i.e. it looks to which degree surrounding cells point to the center cell. The result is given as percentages, negative values correspond to convergent, positive to divergent flow conditions. Minus 100 would be like a peak of a cone, plus 100 a pit, and 0 an even slope [12]. On all mountains, the curvature changes with elevation from concave (in the lowest parts) to convex (in the highest areas).

The graph in Fig. 3 show that the high mountain ranges in North Macedonia are dominated by straight to convex curvatures. Terrains with extremely convex slopes (summits area) are found on Galičica (0.9%), Kožuf (0.8%), Jablanica (0.75%), Bistra (0.7%), Belasica (0.7%), Nidze with Kozjak (0.69%), and Osogovo Mountain (0.68%). On these, numerous non-prominent peaks appear in relation to their total areas. On the other hand, Pelister (0.2%), Šar Planina (0.3%) and Korab (0.36%), compared to their total areas have smaller numbers of peaks, but usually much sharper. Mountains with the highest relative proportion of concave slopes are Kožuf (4.5%), Osogovo Mountain (4.4%) and Bistra (4.1%).

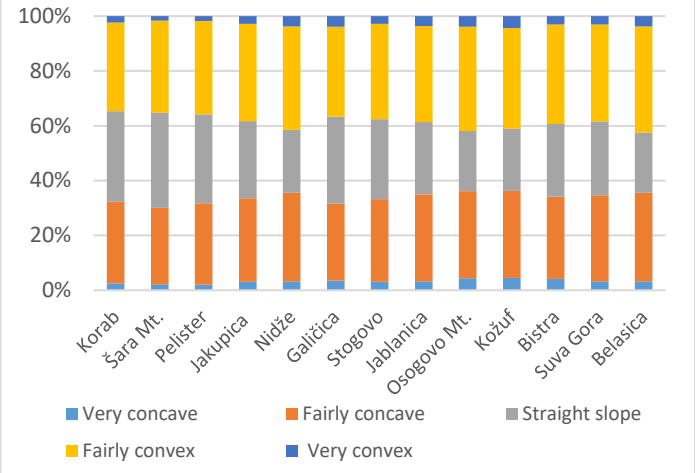

Figure 3. Graph of terrain curvature (convergence index) classes of the high mountains in North Macedonia (in %).

Aspects are an important geomorphometric element which is a result of geotectonic-structural and geomorphologic-evolutionary processes and they are important for the intensity of erosion. The high mountains in Macedonia had a high diversity of aspects as a result of dominant ridge direction, an extension of the larger river valleys, and extension of the mountain ranges in relation to the country borders. Because of the borders, a realistic view of aspect distributions is given only for the ranges which are wholly located in Macedonia: Jakupica, Stogovo, Bistra, Suva Gora and mostly Galičica range. Their aspect distributions, together with the Osogovo Mountains taken because of characteristic almost E-W stretching (as a whole, in natural borders) are presented in Fig. 4.

Interestingly only the Galičica and Stogovo Mountains show distinctive bi-directional aspect distributions (W-E and SW-NE) exactly in opposite to their elongations. The reason for that is poor lateral relief dissection. On the contrary is Osogovo Mountain, where aspects distribution is the same as its elongation (ENE-WSW) mostly because of frequent valleys incised in perpendicular directions. A relatively similar situation is with Jakupica and Suva Gora, while Bistra Mountain which is without clear elongation have an uneven distribution of aspects. However, on all 6 mountains except on Suva Gora, west and east aspects are dominant. Actually, that is the same for all 13 mountains, where western aspects are dominant (by a number of ranges), followed by eastern ones (by area). This is consistent with the dominant Dinaric-Hellenidic (N-S and NW-SE) direction of most ranges in Macedonia. Exceptions are Nidže, Kožuf, Osogovo and Belasica Mountains, which are W-E oriented because of the Aegean extensional neotectonic regime [13].

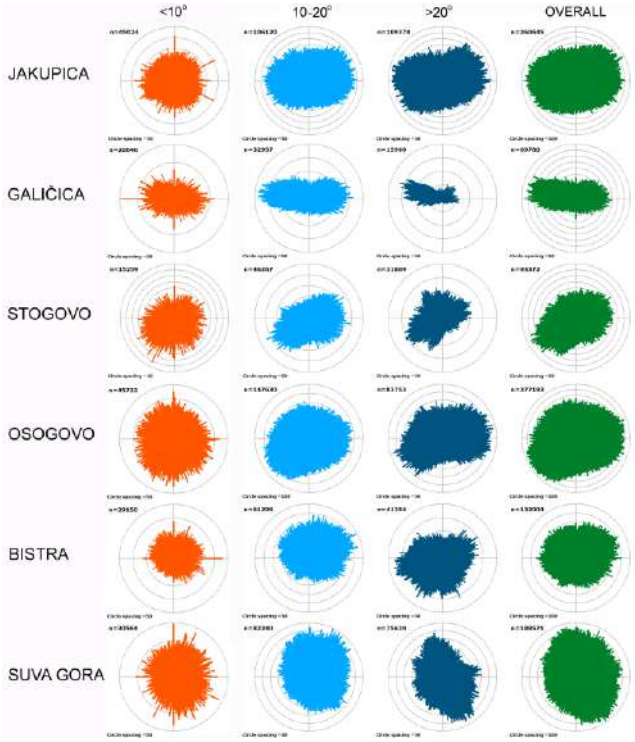

Figure 4. Aspects vs slopes for selected high mountains in North Macedonia.

With further analyses, the average gradients for each aspect were calculated. The data shows that the most common aspects do

not have the greatest slopes but the opposite. This is because a smaller slope increases the area with a given aspect. In fact, the most common aspects represent long, extensive mountain slopes that are perpendicular to the mountain direction. Aspects with the greatest slope gradients generally represent steep valley sides of rivers deeply incised into the mountain ranges, or along their rims. Steep slopes have great erosive potential, especially where facing south.

IV. CONCLUSION

Because of variable structural and geomorphic evolution, high mountains (higher than 2000 m) in North Macedonia have significant morphometric differences, clearly evident in their hypsometry, slope gradient, aspect, and convergence. According to the mean values of these variables, morphometric classification of the mountain ranges is made and they are classified into three groups. The first is a group of very high mountains (regarding the Balkan Peninsula conditions), with steep slopes: Korab, Šar Planina, and Pelister. In the second group are mountains with moderate altitude, slope, and convexity: Nidze, Stogovo, Jablanica, Suva Gora and Bistra. According to its characteristics, Jakupica (Mokra) Range lies between the first and second groups. The third group includes the lower ranges, with gentle slopes and large planation surfaces: Galičica, Osogovo, Kožuf, and Belasica. This classification is strongly related to the geotectonic position and mountain evolution. Thus, the first and second groups of mountain ranges belong to the inner Dinaric and Hellenic geotectonic belt characterized by intensive E-W tectonic compression especially during the Tertiary [14]. Numerous remnants from LGM with cirques, narrow ridges and sharp peaks extending above the karst planation surfaces (on 1600-2000 m), make distinctive morphology of these ranges. Unlike them, except for Galičica, the third group is closer to the Carpatho-Balkanic geotectonic belt, with a highly expressed N-S extensional regime of development.

Previous semi-automated geomorphometric classification is based only on the basic characteristics of 13 analyzed mountains in North Macedonia. However, with further improvements of variables and adjusting limiting values, automated classification [15] can be used at least for the high mountains on the Balkan Peninsula. Beyond purely theoretical research approaches, geomorphometric correlations may have practical significance for better structural and morphological interpretations, as well as for some erosion potential modeling [16] and geohazards indicators.

REFERENCES

[1] Kolčakovski, D., Milevski, I., 2012. "Recent Landform Evolution in Macedonia". In: Recent Landform Evolution. The Carpatho-Balkan-Dinaric Region, Editors Lóczy D., Stankoviansky M., Kotarba A. Springer Geography, 413-442.

[2] Milevski, I., 2015. "General Geomorphological Characteristics of the Republic of Macedonia". Geographical Reviews, 48, Skopje, 5-25.

[3] Milevski, I., 2011. "Morphometric classification of high mountain ranges in the Republic of Macedonia". Geomorphologia Slovaca et Bohemica 2/2011, 32-45.

[4] Milevski, I., 2016. "Morphometry and Land Use on the High Mountains in the Republic of Macedonia". In: Sustainable Development of the Mountain Regions - Southeastern Europe, Editor G. Zhelezov. Springer, London, 63-74.

[5] Milevski, I., Gorin, S., Markoski, B., Radevski, I., 2013. "Comparison of Accuracy of DEM's Available for the Republic of Macedonia". Proceedings from the 3rd International Geographic Symposium - GEOMED 2013, Kemer, Antalya, Turkey, 10-13 June 2013, 165-172.

[6] Milevski, I., 2014. "Slope Values Accuracy vs Resolution of the Digital Elevation Models (Example of the Republic of Macedonia)". Proceedings of 5th ICC-GIS Conference; Eds: Bandrova T & Konecny M., Vol. 2, Varna, 568-575.

[7] Kuhlemann, J., Milivojević, M., Krumrel, I., Kubik, P., 2009. "Last glaciation of the Šhara Range (Balkan Peninsula): Increasing dryness from the LGM to the Holocene". Austrian Journal of Earth Sciences v.102, Vienna, 146-158.

[8] Ribolini, A., Bini, M., Isola, I., Spagnolo, M., Zanchetta, G., Pellitero, R., Mechernich, S., Gromig, R., Dunai, T., Wagner, B., Milevski, I., 2018. "An Oldest Dryas glacier expansion on Mount Pelister (Former Yugoslavian Republic of Macedonia) according to 10 Be cosmogenic dating". Journal of the Geological Society. Vol. 175, Issue 1, 100-110.

[9] Temovski, M., Milevski, I., 2015. "DEM based geomorphometric analyses of karst surface in the Republic of Macedonia". In: Geomorphometry for Geosciences. Eds: Jasiewicz J, Zwolinski Z, Mitasova H, and Hengel T. Geomorphometry.org, Poznan, Poland, 65-68.

[10] Hrvatin, M., Perko, D., 2002. "Determination of surface curvature by digital elevation model and its application in geomorphology". GIS in Slovenia, Ljubljana, 65-72. (in Slovenian)

[11] Olaya, V., 2004. "A gentle introduction to SAGA GIS". The SAGA User Group e.V., Gottingen, Germany, 208 p.

[12] Conrad, O., 2011. SAGA-GIS Convergence Index, Wiki Documentation, http://sourceforge.net/apps/trac/saga-gis/wiki/ta_morphometry_1. On-line [March 18th, 2012]

[13] Burchfiel, C.B., King, W.R., Nakov, R., Tzankov, T., Dumurdzanov, N., Serafimovski, T., Todosov, A., Nurce, B., 2008. "Patterns of Cenozoic Extensional Tectonism in the South Balkan Extensional System". In: Earthquake Monitoring And Seismic Hazard Mitigation In Balkan Countries. Editor: Husebie S.E. NATO Science Series: IV: Earth and Environmental Sciences, 2008, Volume 81, I, 3-18.

[14] Dumurdzanov, N., Serafimovski, T., Burchfiel, C., 2004. "Evolution of the Neogene-Pleistocene Basins of Macedonia". In: Geological society of America Digital Map and Chart Series 1 (Accompanying notes). Boulder, Colorado, 1-20.

[15] Drâguț, L., Eisank, C., 2011. "Automated classification of topography from SRTM data using object-based image analysis". In: Geomorphometry 2011 edited by Hengel T., Evans S.I., Wilson P.J., and Gould M., Redlands, CA, 113-116.

[16] Zingg, A. W., 1940. "Degree and Length of Land Slope as it Affects Soil Loss in Runoff". Agric. Eng., 21(2), 59-64.

GEOMORPHOMETRY 2020 PERUGIA, ITALY JUNE 22 - 26 2020

Using high-resolution ICESat-2 point clouds to evaluate 1-3 arc second global digital elevation models

Tera M. Geoffroy, Peter L. Guth§
Department of Oceanography
United States Naval Academy
572C Holloway Road
Annapolis MD 21402 USA
geoffroy.tera@gmail.com, pguth@usna.edu

Abstract— **ICESat-2 is a new sensor which has potential to create a digital elevation model. This study measures the effectiveness of an ICESat-2 photon point cloud against other traditional DEMS. The photon point cloud does not have sufficient data to create a new DEM. ICESat-2 data does, however, show how the free global digital one arc second elevation models SRTM, ALOS, and ASTER penetrated the canopy, and the extent to which they represent a digital surface model (DSM) versus a bare earth digital terrain model (DTM). ALOS and SRTM have better canopy penetration compared to ASTER. All three show peak returns at about the midpoint of the canopy recorded by ICESat-2. For this assessment the ICESat-2 elevation data performs better than the photon data, with a significantly reduced volume of data.**

I. INTRODUCTION

A high-resolution point cloud provides a 3D elevation model of topography. Millions of data points are placed within this 3-dimensional cloud with geo-referenced to x, y, and elevation. In this study, we populated the point cloud from the photon data of NASA's ICESat-2. The launch of the ICESat-2 occurred in the fall of 2018, making it an exciting new data source [1]. The 1354 ground tracks of the satellite repeat in a 91 day orbit cycle [1]. The expected lifetime of the ATLAS laser altimeter attached to ICESat-2 is five years. [1].

We looked at data from Brazil to evaluate two things: (1) the accuracy of global 1-3 arc second DEMs which measure some surface above the ground, and (2) the possibility of using ICESat-2 to improve those models. To confirm the applicability of the results, we looked at two additional areas in California and Virginia.

II. METHODS

We evaluated three near global digital models in this study: ASTER [2], AW3D30 [3], and SRTM [4]. (Table 1). These all have 1" spacing, about 30 m, and are the best free DEMs covering most of the earth. The ASTER data from the Advanced Spaceborne Thermal Emission and Reflection Radiometer from NASA was downloaded from NASA's EarthData site [5]. The AW3D30 data from the Advanced Land Observation Satellite from JAXA was downloaded from JAXA's ALOS Global Digital Surface Model webpage [6]. The SRTM data from the Shuttle Topography Mission from NASA and NGA was downloaded from USGS' EarthExplorer [7].

We used two different forms of the ICESat-2 data, from OpenAltimetry [8]. The satellite collects data on six parallel tracks along the satellite path; all share the same trackid. Two tracks, 90 m apart, have strong and weak beams, and are 3.3 km from the next pair of beams. The ATL8 elevation data measures the ellipsoidal ground elevation and the canopy height. The ATL02 data set detects individual photons spaced approximately 0.7 m apart with an associated quality level. Away from the poles, with each 91 day cycle the data collection shifts laterally, increasing the coverage area.

For the elevation data we converted the ground elevation to the EGM2008 geoid, and added the canopy elevation to get the elevation of the top of the canopy. To this database, at the location of each ICESat-2 record, we added the interpolated elevations and slopes of the global DEMs, and the land cover category.

We converted the photon data into a point cloud with the LAS format. The beam, track identifier, confidence level, and acquisition data are all stored in the LAS file. At this stage we filtered the points to remove those with lower quality, and converted the elevations to the EGM2008 geoid to match the global DEMs. We then created a grid with the density of the ISESat-2 photons within each 1"x1" cell of the global DEM. For all cells with at least 25 photons, we create a database similar to the one with the elevation data.

Tera Geoffroy and Peter Guth (2020) Using high-resolution ICESat-2 point clouds to evaluate 1-3 arc second global digital elevation models:

in Massimiliano Alvioli, Ivan Marchesini, Laura Melelli & Peter Guth, eds., Proceedings of the Geomorphometry 2020 Conference, doi:10.30437/GEOMORPHOMETRY2020_29.

Table 1. Global DEMs used

DEM	Spacing	Source	Producer	Precision	Years Acquired	Ref	Source
SRTM (v3)	1"	Radar	NASA	Integer	2000 (11 days)	[4]	[7]
ASTER GDEM	1"	Stereo NIR imagery	NASA / JAXA	Integer	2000-2013	[2]	[5]
ALOS World 3D AW3D30	1"	Stereo pan imagery	JAXA	Integer	2006-2011	[3]	[6]

III. DISCUSSION

Table 2 summarizes the data for the three areas, for both the elevation and photon data. For all three areas, with both the elevation and photon data, there is ICESat-2 data in much fewer than 1% of the cells in the corresponding 1" global DEM.

Figure 1 displays the distribution of points from the three DEMS as well as the point cloud ground and canopy top. Though the majority of the points seem to be in a comparable range, the ASTER data is consistently above the other DEMS in elevation. Figure 2 shows the distribution of the data along a single track and beam in parallel with the ICESAT-2 elevation data.

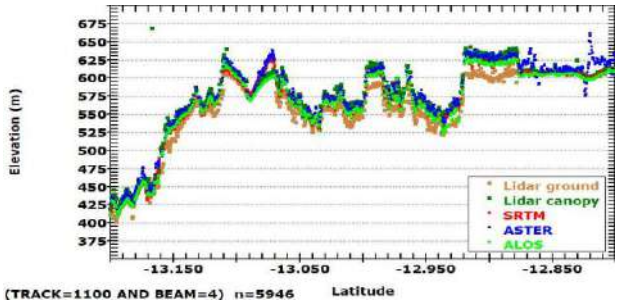

Figure 1. ICESat-2 photon data in Brazil and the three global DEMs.

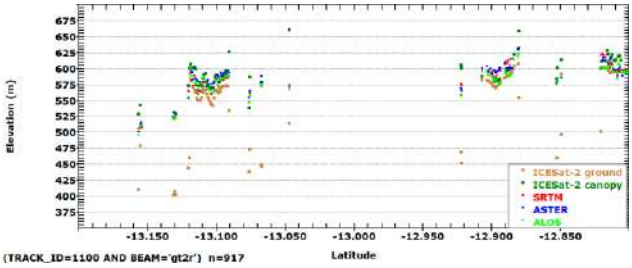

Figure 2. ICESat-2 elevation data in Brazil and the three global DEMs.

Figure 3 shows the percentage of values that falls between the ground and canopy top for each DEM for the three study areas. The California data shows the most consistency from the three DEMS in terms of percentage that falls within the point cloud. However, a good deal of data still falls both above and below the point cloud. The Brazil data shows that the ASTER data is mostly above the point cloud. The most compatible dataset to the Brazil photon point cloud is the ALOS DEM. The Virginia dataset shows that the majority of the dataset for all three DEMS falls above the point cloud.

The ICESAT-2 elevation data is also shown in Figure 3, where there are many fewer DEM elevations above the canopy top. The worst alignment occurs in Brazil and in Virginia with the ASTER DEM, a lot of the data falls above the ICESAT-2 data. In Brazil, all three DEMS have almost an equal amount of data below the dataset as inside of it. In the Virginia dataset, the ALOS DEM also has a lot of data beneath the ICESAT-2 elevation data.

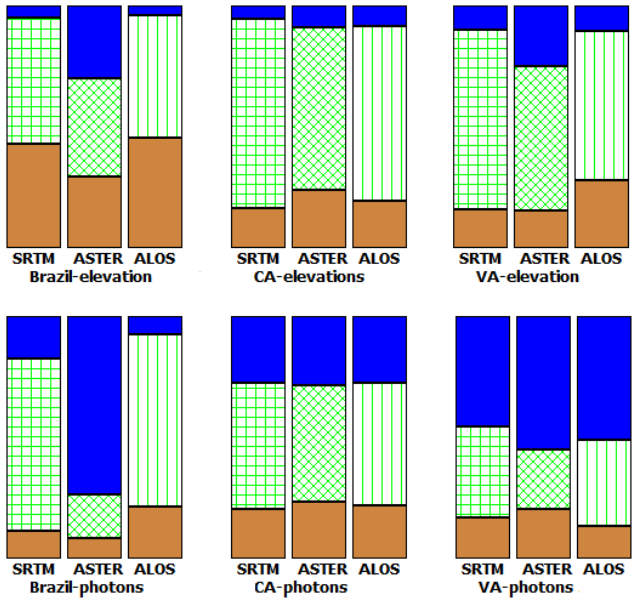

Figure 3. Proportion of data that falls within the point cloud among the three elevation models.

Figure 4 shows the distribution within the canopy of the DEM elevations. The elevations are scaled from 0 at the base of the canopy (lowest point cloud elevation in the cell) to 1 at the canopy top (highest elevation in the cell); the green shading highlights this range. A value of 2 indicates the point is twice the height of the canopy, and a value of -1 indicates the DEM elevation post was the height of the canopy below the ground level. In California, there is a division among the data with a large number of values above the point cloud and another large number of

values at the ground of the point cloud data. In Virginia, it appears that SRTM has the most data in the middle of the cloud and that ALOS has a large number of points above the cloud. In Brazil, ASTER is mostly outside of the cloud, with a small number of values within the cloud. In this region of study, SRTM appears to be mostly within the recorded point cloud canopy as well.

Table 2. ICESat-2 study regions

AREA	LOCATION	1" CELLS	Points per cell	ICESat-2 elevations (m)	SRTM slope (%) and std dev	Canopy height (m) and std dev
Brazil-elevation	S13.31° W59.28°	26,717	2	182 to 713		8.78±21.52
CA-elevations	N39.86° W123.802°	75,893	2	-15 to 1764	24.50±18.42	24.31±13.97
VA-elevation	N39.17° W78.57°	4790	2	225 to 820		18.37±13.58
Brazil-photons	S14.14° W60.73°	4321	40	-76 to 1329	4.42±3.73	20.51±69.76
CA-photons	N39.86° W123.802	122,909	86	-310 to 1749	10.95±15.57	58.21±111.25
VA-photons	N38.47° W78.23°	74,250	91	15 to 1114	7.46±7.87	7.67±11.91

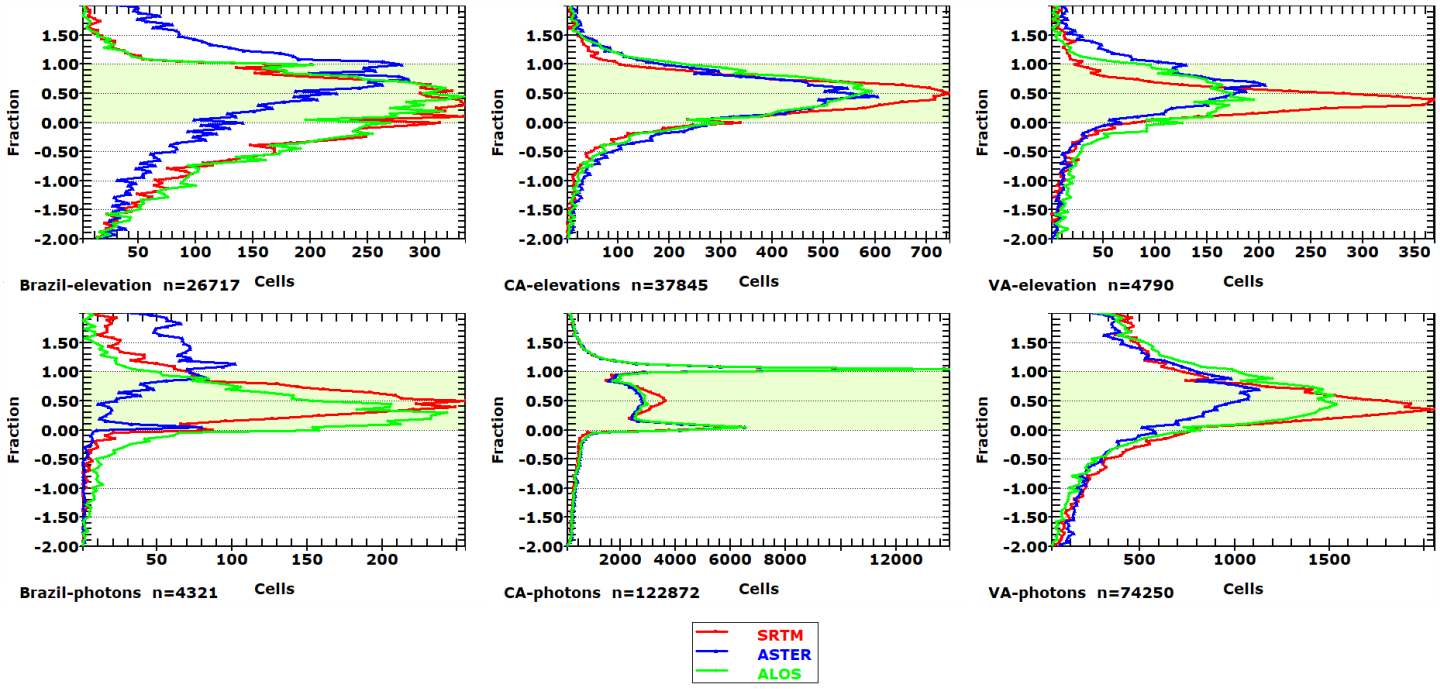

Figure 4. Fraction of data that falls within the elevation envelope and photon point cloud.

In comparison to the photon data, the elevation data appears to better correspond to the DEMs in Figure 4. The majority of the DEM data falls within the highlighted canopy region in California and Virginia. In Brazil, the DEM that disagrees most with the elevation data is ASTER. However, there are more DEM postings contained within the point cloud for ALOS and SRTM than the photon cloud counterpart.

The results of this paper are very different than the results of Guth [13] looking at lidar point clouds. The LIDAR point cloud is much more dense than the ICESat-2 point cloud , with thousands of points in each 1" cell compared to under 100, and with complete spatial coverage rather than a single altimeter track. As a result, the LIDAR point cloud provides much more coverage and provides a better assessment of the DEM .

IV. RESULTS AND CONCLUSION

The three global DEMS provide a good overview of the region, and are highly correlated with each other. The ICESat-2 data provides valuable ground truth to show how well the visible, infrared, and radar sensors penetrated into the canopy. This supports previous interpretations that ASTER in particular provides a lower quality DEM [10,11].In comparison, ICESat-2 data covers only a tiny fraction of the area. Data is currently available for 4-5 cycles of ICESat-2 data; if the satellite lasts for its 5 year design lifetime, even in cloud free regions it is unlikely to collect enough data to create a 1" DEM. Nevertheless, it will provide supplementary information. ICESat-2 will be useful in comparing great changes over a rapid period of time, such as glacier melt and deforestation.

In the analysis of the photon data it is apparent that in Brazil there are many low outliers. We examined these outliers with many different possibilities. We examined the land cover, that is, the ground classification of the vegetation covering the region. Figure 5 depicts the DEM data within the photon point cloud by ground classification. Compared to the entire data, the photon data is higher compared to the three DEMS for the open broadleafed deciduous forest as well as the mosaic grassland. We also analyzed the slope of the Brazil region in order to determine if high degrees of slope were responsible for problematic altimeter readings, without significant results. This indicates that the method of ICESat-2 photon data may bring inaccuracies unexplained by slope or land cover.

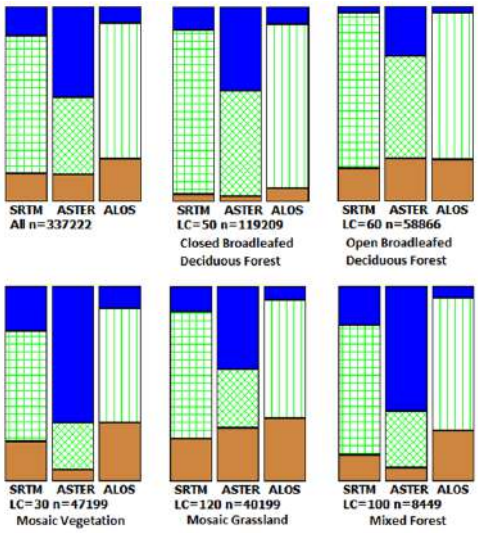

Figure 5. Fraction of DEM data within the ICESAT-2 point cloud by land cover classification

V. ACKNOWLEDGMENTS

All analysis was done with the MICRODEM program [12], including new code to deal with the ICESat-2 data and automate the analysis steps. We thank Ian Evans for a very helpful review.

REFERENCES

[1] Thomas A. Neumann, Anthony J. Martino, Thorsten Markus, Sungkoo Bae, Megan R. Bock, Anita C. Brenner, Kelly M. Brunt, John Cavanaugh, Stanley T. Fernandes, David W. Hancock, Kaitlin Harbeck, Jeffrey Lee, Nathan T. Kurtz, Philip J. Luers, Scott B. Luthcke, Lori Magruder, Teresa A. Pennington, Luis Ramos-Izquierdo, Timothy Rebold, Jonah Skoog, Taylor C. Thomas, "The Ice, Cloud, and Land Elevation Satellite – 2 mission: A global geolocated photon product derived from the Advanced Topographic Laser Altimeter System, Remote Sensing of Environment." Volume 233,2019.

[2] ASTER:Advanced Spaceborne Thermal Emission and Reflection Radiometer, n.d. Retrieved frrom https://asterweb.jpl.nasa.gov/

[3] T.Tadono, J.Takaku, F. Ohgushi, M. Doutsu and K. Kobayashi, "Updates of 'AW3D30' 30 M-MESH global digital surface model dataset, 2017 *IEEE International Geoscience and Remote Sensing Symposium (IGARSS)*, Fort Worth, TX, 2017,pp. 5656-5657.

[4] Shuttle Radar Topography Mission, n.d. Retrieved from https://www2.jpl.nasa.gov/srtm/

[5] Earthdata Search, n.d. Retrieved from https://search.earthdata.nasa.gov/search/

[6] ALOS Global Digital Surface Model "ALOS World 3D-30m (AW3D30)",n.d. Retrieved from https://www.eorc.jaxa.jp/ALOS/en/aw3d30/index.htm

[7] USGS, n.d. EarthExplorer-Home. Retrieved from https://earthexplorer.usgs.gov/

[8] OpenAltimetry, n.d. Retrieved from https://openaltimetry.org/data/icesat2/

[9] ESA. Land Cover CCI Product User Guide Version 2. Tech. Rep. (2017). Available at: maps.elie.ucl.ac.be/CCI/viewer/download/ESACCI-LC-Ph2-PUGv2_2.0.pdf

[10] Guth, P.L., 2010. "Geomorphometric comparison of ASTER DEM and SRTM". Join Symposium of ISPRS Technical Commission IV, Orlando, FL, p. 10.

[11] Hengl, T., and Reuter, H.I., 2011, How accurate and usable is GDEM? A statistical assessment of GDEM using Lidar data: In Geomorphometry 2011, edited by T. Hengl, I. S. Evans, J. P. Wilson and M. Gould, 45-48. Redlands, CA, 2011. http://www.geomorphometry.org/HenglReuter2011

[12] Guth, P.L., 2009, Geomorphometry in MICRODEM, In Hengl, T., Reuter, H.I. (eds), Geomorphometry: concepts, software, applications. Developments in Soil Science Series, Elsevier, p.351-366. Program at https://www.usna.edu/Users/oceano/pguth/website/microdem/microdemdown.htm.

[13] Guth, P.L., 2020, Using high-resolution lidar point clouds to evaluate 1-3 arc second global digital elevation models: Geomorphometry 2020.

GEOMORPHOMETRY 2020
PERUGIA, ITALY
JUNE 22 - 26 2020

Coastal dune modelling from airborne LiDAR, terrestrial LiDAR and Structure from Motion–Multi View Stereo

Carlos H. Grohmann[1*], Guilherme P.B. Garcia[2], Alynne A. Affonso[1], Rafael W. Albuquerque[1]
(1) Institute of Energy and Environment, University of São Paulo, São Paulo, Brazil
(2) Institute of Geosciences, University of São Paulo, São Paulo, Brazil
all authors: Spatial Analysis and Modelling Lab (SPAMLab, IEE-USP)
* *corresponding author:* guano@usp.br

Abstract—**In this work, we present an analysis of the Garopaba dune field, southern Brazil, based on data from Airborne LiDAR (ALS - surveyed in 2010), Terrestrial LiDAR (TLS - surveyed in 2019) and Structure from Motion–Multi View Stereo (SfM-MVS - surveyed in 2019). Although sand dunes are commonly regarded as a challenge to traditional photogrammetry due their homogeneous texture and spectral response, in this research image matching was successful in all areas of the survey due the presence of superficial features (footprints and sandboard tracks) and visibility of the sedimentary stratification, highlighted by heavy minerals. The SfM-MVS DEM accuracy was evaluated by comparison with a TLS DEM, resulting in RMSE of 0.08m and MAE of 0.06m. Displacement of dune crest lines from the ALS and SfM-MVS DEMs resulted in a migration rate of ≈5 m/year between 2010 and 2019, in good agreement with rates derived from satellite images and historical aerial photographs of the same area. SfM-MVS is a low-cost solution with fast and reliable results for 3D modelling and continuous monitoring of coastal dunes.**

I. Introduction

To better understand the dynamic environments in which aeolian dune fields occur, repeated topographic surveys of the landscape are needed [1]. As the sand supply of dune fields is sensitive to patterns of wind and rainfall, changes in dune field volume and morphology can be related to climate change [2].

Digital Elevation Models (DEMs) of aeolian dunes can be constructed by several methods such as traditional field techniques (levelling, Total Station), interpolation of contour lines or Differential/Real-time kinematic (RTK) GPS points, LiDAR (Light Detection and Ranging) surveys, either airborne (ALS – Airborne Laser Scanner) or terrestrial (TLS – Terrestrial Laser Scanner) and, more recently, Structure from Motion–Multi View Stereo (SfM-MVS) [3-5]. Remotely Piloted Aircrafts (RPAs) have been used as platform for SfM-MVS image collection and for lightweight LiDAR systems [6].

In this work, we present an analysis of the Garopaba dune field, southern Brazil, based on DEMs from ALS (surveyed in 2010), TLS and SfM-MVS (both surveyed in 2019). Altimetric accuracy of the SfM-MVS DEM was validated by comparison with TLS data collected during the same fieldwork campaign of the RPA flights. The use of SfM-MVS for aeolian dunes modelling is recommended and the factors that contributed to a successful 3D reconstruction are discussed.

II. Methods

The Garopaba dune field, located in southern Brazil, is composed of unvegetated and vegetated aeolian dunes. The unvegetated dunes are represented by mostly barchanoid chains, while the vegetated ones include parabolic dunes, blowouts and foredunes [7] (Fig. 1).

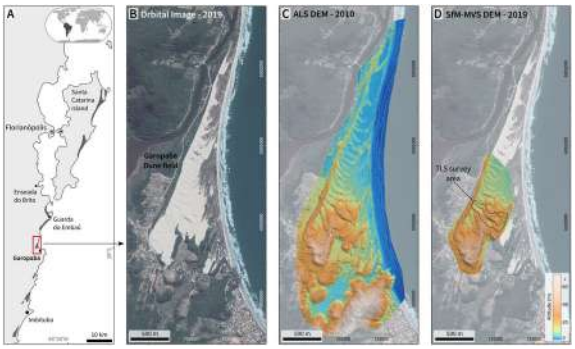

Figure 1. A) Location of study area in southern Brazil; B) Satellite image of the Garopaba dune field (image date: 07-30-2017); C) ALS DEM (2010); D) SfM-MVS DEM (2019), with TLS survey area shown. Elevation colour scale is the same for C and D. Shaded relief illumination: N25º, 30º above horizon.

Carlos Grohmann, Guilherme Garcia, Alynne Affonso and Rafael Albuquerque (2020) Coastal dune modelling from airborne LiDAR, terrestrial LiDAR and Structure from Motion--Multi View Stereo: in Massimiliano Alvioli, Ivan Marchesini, Laura Melelli & Peter Guth, eds., Proceedings of the Geomorphometry 2020 Conference, doi:10.30437/GEOMORPHOMETRY2020_30.

ALS data were collected on October 2010 by Geoid Laser Mapping Co. using an Optech ALTM 3100 sensor with a saw-tooth scanning pattern, density of about 4 points/m^2, measured from an altitude of ≈1,200m (≈4,000ft). Raw LiDAR data (with up to four laser pulses) were processed by Geoid and delivered with vertical accuracy of 0.15m (1σ) and horizontal accuracy of 0.5 m (1σ). ALS first returns were imported into GRASS-GIS as vector points and interpolated with bilinear splines to create a DEM with 0.5m spatial resolution (Fig. 1C).

TLS data (110 point clouds) were collected with a FARO Laser Scanner Focus^{3D} S120. To overcome the heterogeneous distribution of data common to TLS, with a very high density of points near the scanner, the full point cloud was subsampled in FARO Scene with a minimum distance filter of 2cm between points. This point cloud was gridded to a raster in GRASS-GIS using the mean elevation value of LiDAR points within 10cm cells (r.in.xyz module). To fill empty (null) cells, the raster was converted to vector and a DEM with 10cm spatial resolution was created by interpolation with bilinear splines (Fig. 4A).

Images for the SfM-MVS reconstruction were acquired by a DJI Phantom 4 Pro RPA (1" CMOS 20MP sensor, global shutter). Flight missions were executed with height above takeoff point of 100m (pixel size ≈2.7cm) and 75% overlap along and across-track. Six missions were flown, covering an area of ≈869,000m^2 with 810 images. Weather conditions during fieldwork were of dark skies with light rains scattered throughout the day. The SfM-MVS workflow was processed in Agisoft Metashape Pro version 1.5.14. In the SfM step, images were aligned with 'High' accuracy; the MVS reconstruction was set to 'High' quality and 'aggressive' depth filtering. The full SfM-MVS point cloud was subsampled (thinned) with LAStools by extracting every 125th point, imported into GRASS-GIS as vector points and interpolated with bilinear splines to a DEM with 0.5m resolution. The thinning value was determined after experimentation, and the goal was to obtain a similar number of points, within the interpolation area, for the ALS and SfM point clouds (Table 1).

TABLE I. OVERVIEW OF DATASETS USED IN THIS STUDY

Dataset	*DEM Area (m^2)*	*# points*	*points/m^2*
ALS (full)	4,434,722	11,574,555	2.6
ALS (SfM area)	740,922	2,380,005	3.2
SfM-MVS (full)	740,922	344,595,132	465.1
SfM-MVS (thin 125th pt)	740,922	2,376,632	3.2
SfM-MVS (TLS area)	80,413	28,158,102	350.1
SfM-MVS (10 cm grid)	80,413	8,039,750	99.9
TLS (full)	80,413	1,187,708,492	14770.1
TLS (2 cm filter)	80,413	170,141,709	2115.8
TLS (10 cm grid)	80,413	7,028,118	87.4

The point cloud datasets are available via the OpenTopography Facility. The following datasets were used in this study: OpenTopography ID OT.032013.32722.1 (ALS), OTDS.072019.32722.1 (SfM), OTDS.102019.32722.1 (TLS).

III. RESULTS

The DEMs produced from the TLS (Fig. 2A) and SfM-MVS (Fig. 2B) are very similar, without any major difference in elevation or in the reconstruction of topographic features. Upon a closer inspection, the SfM-MVS DEM presents a small scale surface roughness not visible in the TLS DEM. To visually evaluate this difference, surface roughness of the DEMs was calculated as the standard deviation of slope [8] in a 5x5 pixels neighbourhood (0.5×0.5 m).

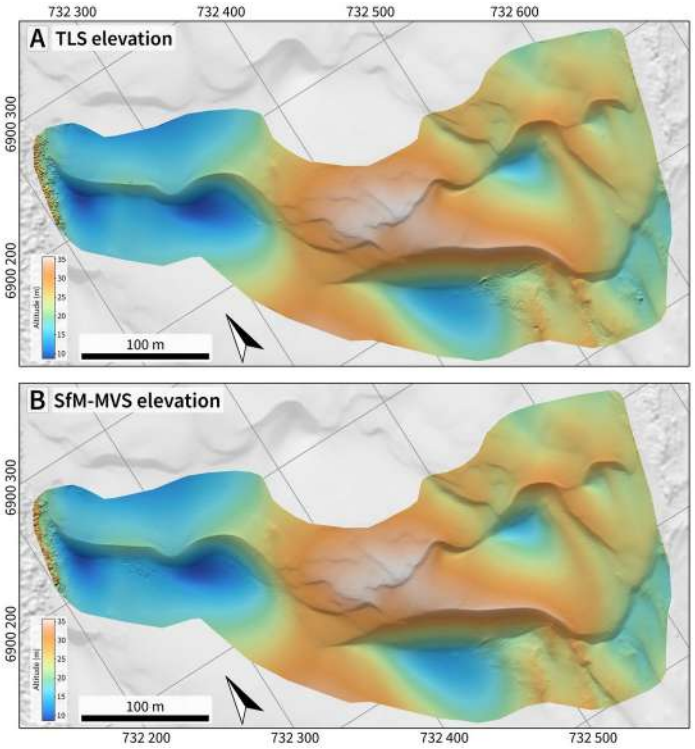

Figure 2. A) TLS DEM; B) SfM-MVS DEM. Elevation colour scale is the same for A and B. Shaded relief illumination: N25º, 30º above horizon.

The TLS DEM has a smooth surface, with higher roughness values on vegetated areas and over some of the places where the TLS equipment was positioned (Fig. 3A). These spots can be related to a small mismatch between adjacent scans, where in one there is no data (under the scanner), so the gridding procedure cannot compensate the difference and the result is a small circular patch of the terrain slightly above or below its surroundings. Dune crests are well marked by above-average roughness. Footprints and track marks are also visible, with lower roughness values. The SfM-MVS DEM shows a widespread distribution of low and average roughness values (Fig. 3B). While the dune crests can be identified, track marks are no longer visible and the patch of vegetation near the sandboard tracks cannot be discriminated based on its roughness. A set of footprints seen in the central-eastern portion of the TLS roughness map is not visible in the SfM-MVS roughness because the SfM-MVS survey was carried out before the TLS survey could cover that area.

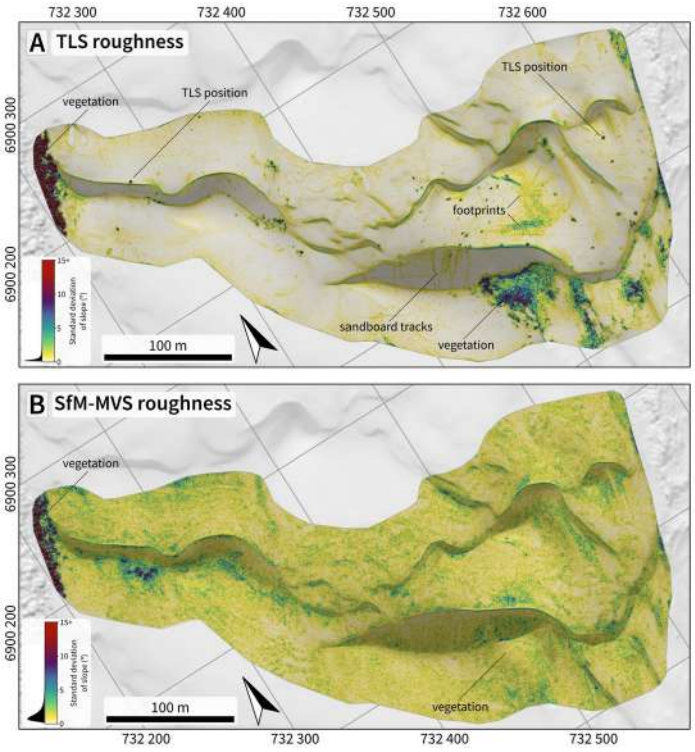

Figure 3. Surface roughness maps, calculated as the standard deviation of slope in a 5x5 window: A) TLS; B) SfM-MVS. Roughness colour scale is the same for A and B.

The vertical accuracy of the SfM-MVS DEM was calculated from a set of 2,000 random points, resulting in RMSE of 0.08m and MAE of 0.06m.

Besides a good correlation to the TLS DEM, the full SfM-MVS DEM (Fig. 4B) shows a good fit with elements of the landscape that didn't experienced significant change between the surveys, such as the road bordering the dune field to west and southwest (in grey in Fig. 4C, indicating no elevation difference).

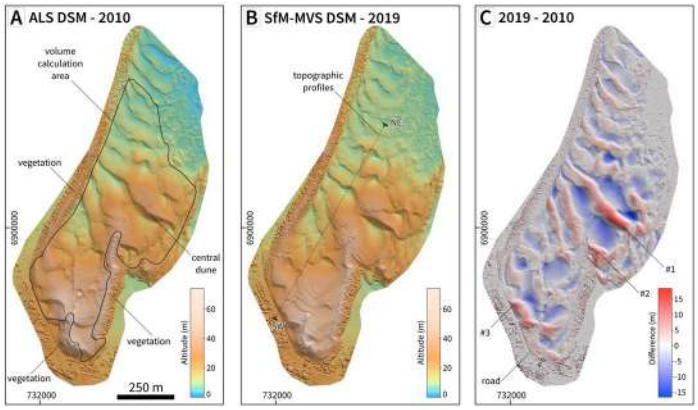

Figure 4. A) ALS DEM (2010), with volume calculation area polygon; B) SfM-MVS DEM (2019), with topographic profiles location; C) DEM of differences (2019-2010). Numbers in C are discussed in the text.

Some notable differences are indicated as #1,#2 and #3 in Fig. 4C: #1 marks the highest positive difference (where the SfM-MVS surface is above the ALS), related to the migration of a large 'central dune' with accumulation of sand towards a vegetated ridge in #2; #3 shows the migration of the dune field over the road. In this place, the town hall needs to remove the sand periodically to keep the road open.

The polygon for volume calculation encloses only unvegetated areas in both surveys (see Fig. 4A). Using the ALS and SfM DEMs with 0.5 m resolution, the calculated sand volumes were 9,035,115.45 m^3 for 2010 and 9,010,844.95 m^3 for 2019 (a decrease of 24,270.50 m^3 or 0.2%).

Dune crest displacement lines drawn over the DEMs (Fig. 5) yielded a mean azimuth of 215.5º and mean length of ≈44.5m (mean: 44.3m, median: 44.7m). A mean length of 44.5m in 9 years corresponds to a dune migration rate of ≈5 m/year. We consider these rates to be in agreement with rates of 6-7 m/year derived from interpretation of historical aerial photographs and satellite images with coarser spatial resolution [9].

Topographic profiles (Fig. 6) illustrate dune movement from 2010 to 2019, with migration of the lee side and relatively less change over the stoss side of large compound dunes.

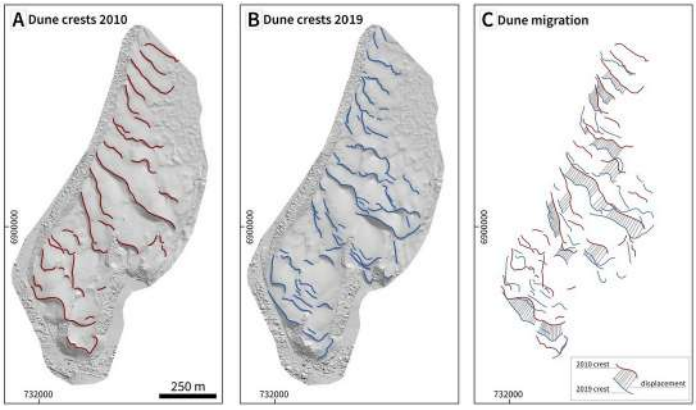

Figure 5. Determination of dune migration between 2010 and 2019 surveys. A) dune crests of 2010, over shaded relief image of ALS DEM; B) dune crests of 2019, over shaded relief image of SfM-MVS DEM; C) displacement lines (grey) connecting crest lines.

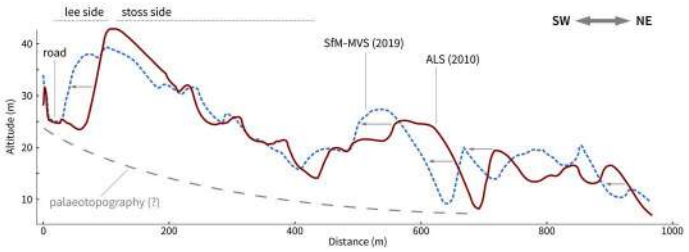

Figure 6. Topographic profiles across the dune field (location in Fig. 4B.)

IV. DISCUSSION

Although sand dunes are commonly regarded as a challenge to traditional photogrammetry due their homogeneous texture and spectral response, yielding poor results in image matching, the presence of superficial features (footprints and sandboard tracks) and visibility of the sedimentary stratification highlighted by heavy minerals, allowed a successful SfM-MVS reconstruction.

ALS might be acquired in little time, but it is by far the most expensive, imposing a serious constraint on repeated surveys, especially for researchers in developing countries or without access to state-funded coastal monitoring programs.

TLS has an intermediate cost of acquisition (since the equipment can be rented and operated by the research team) but it demands more fieldwork and more processing time. In our case we needed three days for the TLS survey and around three weeks of full-time work to produce a DEM of ≈80,400m^2.

We were able to cover ≈740,900m^2 with six RPA missions in under three hours. Processing time in a medium-range workstation (i.e., i7 processor, dedicated GPU) was ≈13 hours.

SfM-MVS is a low-cost solution capable of delivering fast and reliable results for 3D modelling and continuous monitoring of coastal dunes.

ACKNOWLEDGMENT

We would like to thank the financial support of FAPESP (grants #2009/17675-5, #2016/06628-0) and CNPq (grants #423481/2018-5, #304413/2018-6). This study was financed in part by CAPES Brasil – Finance Code 001 through PhD scholarships to G.P.B.G, A.A.A. and R.W.A. This work acknowledges the services provided by the OpenTopography Facility with support from the National Science Foundation under NSF Award Numbers 1557484, 1557319, and 1557330.

REFERENCES

[1] Conlin, M., Cohn, N., Ruggiero, P., 2018. A Quantitative Comparison of Low-Cost Structure from Motion (SfM) Data Collection Platforms on Beaches and Dunes. Journal of Coastal Research 34 (6), 1341–1357.

[2] Gaylord, D. R., Foit, F. F., Schatz, J. K., Coleman, A. J., 2001. Smith Canyon dune field, Washington, U.S.A: relation to glacial outburst floods, the Mazama eruption, and Holocene paleoclimate. Journal of Arid Environments 47 (4), 403 – 424.

[3] Mitasova, H., Overton, M., Harman, R. S., 2005. Geospatial analysis of a coastal sand dune field evolution: Jockey's Ridge, North Carolina. Geomorphology 72, 204–221.

[4] Gonçalves, J., Henriques, R., 2015. UAV photogrammetry for topographic monitoring of coastal areas. ISPRS Journal of Photogrammetry and Remote Sensing 104, 101 – 111.

[5] Guisado-Pintado, E., Jackson, D., Rogers, D., 2019. 3D mapping efficacy of a drone and terrestrial laser scanner over a temperate beach-dune zone. Geomorphology 328, 157–172.

[6] Solazzo, D., Sankey, J.B., Sankey, T.T. and Munson, S.M., 2018. Mapping and measuring aeolian sand dunes with photogrammetry and LiDAR from unmanned aerial vehicles (UAV) and multispectral satellite imagery on the Paria Plateau, AZ, USA. Geomorphology, 319, 174-185.

[7] Martinho, C. T., Giannini, P. C. F., Sawakuchi, A. O., Hesp, P. A., 2006. Morphological and depositional facies of transgressive dunefields in the Imbituba-Jaguaruna region, Santa Catarina State. Journal of Coastal Research SI39, 143–168.

[8] Grohmann, C. H., Smith, M. J., Riccomini, C., 2010. Multiscale Analysis of Topographic Surface Roughness in the Midland Valley, Scotland. Geoscience and Remote Sensing, IEEE Transactions on 49 (4), 1200–1213.

[9] Mendes, V. R., Giannini, P. C. F., Guedes, C. C. F., DeWitt, R., de Abreu Andrade, H. A., 08 2015. Central Santa Catarina coastal dunefields chronology and their relation to relative sea level and climatic changes. Brazilian Journal of Geology 45, 79 – 95.

GEOMORPHOMETRY 2020 PERUGIA, ITALY JUNE 22 - 26 2020

Using high-resolution lidar point clouds to evaluate 1-3 arc second global digital elevation models

Peter L. Guth[§]
Department of Oceanography
United States Naval Academy
572C Holloway Road
Annapolis MD 21402 USA
[§] pguth@usna.edu

Abstract—**Widely available lidar point clouds have 2-10 returns per m², which translates to 1500-10,000 points corresponding to each elevation posting in a 1" (arc second) digital elevation model (DEM). The lidar point cloud approximates the 3D earth surface observed by the visible, near infrared, and radar sensors used to create the DEMs, and allows estimation of the canopy penetration by the sensor. Canopy is broadly defined as the range of elevations within the 1" cell including effects from vegetation, slope, and man-made features. In open terrain, the SRTM, ALOS, and ASTER global DEMs approximate the ground surface. With significant canopy, the DEMs are closer to the top of the canopy, with the SRTM the lowest near the midpoint of the canopy. The ASTER does the poorest job of matching the lidar surface.**

I. INTRODUCTION

The digital elevation model (DEM) serves as the backbone for many studies in earth science, hydrology, land use planning and management, and military operations. The goal of most DEMs is to sample the bare earth, or digital terrain model (DTM), the land's surface stripped of vegetation and man-made features like buildings and power lines. Lidar provides extremely high resolution on the order of 1 m grid spacing and can produce either a DTM or a DSM, but only a few countries currently have freely available lidar data. For free near global coverage, the best resolution is 1" (arc second, approximately 30 m). Table 1 shows 4 DEMs at this scale, and three additional DEMs at 3" (about 90 m). All use the WGS84 datum, and all have orthometric heights except for TandemX which has ellipsoidal heights.

The SRTM, ASTER, and ALOS DEMs have comparable scales, and rely on three independent creation methods. SRTM was created during a single 11 day radar mission, while ASTER and ALOS used multiple collections of stereo imagery over multiple years and all seasons. At their scale, temporal and seasonal changes should not greatly affect most of their coverage area. GSDEM and MERIT attempt to deal with shortcomings in the data, notably holes, and create an improved, merged data set, while Tandem X and Copernicus DEM provide lower resolution free data based on much higher resolution commercial data.

This paper will show how well the SRTM, ASTER, and ALOS DEMs manage to penetrate canopy by comparing their elevations with high density lidar point clouds which record data from the top of the canopy to the ground, and if the DEMs are DTMs or DSMs.

Table 1. Free global DEMs with 1-3" spacing

DEM	Spacing	Source	Producer	Precision	Years Acquired	Ref	Download
SRTM (v3)	1"	Radar	NASA	Integer	2000 (11 days)	[1]	[2]
ASTER GDEM	1"	Stereo NIR imagery	NASA / JAXA	Integer	2000-2013	[3]	[4]
ALOS World 3D AW3D30	1"	Stereo pan imagery	JAXA	Integer	2006-2011	[5]	[6]
GSDEM-30	1"	Radar + stereo NIR imagery + stereo pan imagery	China	Float		[7]	[8]
MERIT	3"	Radar + Stereo pan imagery	Univ. Tokyo	Float		[9]	[10]
Tandem_X	3"	Radar	DLR	Float	2010-2015	[11]	[12]
Copernicus DEM	3"	Edited radar (Tandem_X)	Airbus/ESA	Float		[13]	

Peter Guth (2020) Using high-resolution lidar point clouds to evaluate 1-3 arc second global digital elevation models:

in Massimiliano Alvioli, Ivan Marchesini, Laura Melelli & Peter Guth, eds., Proceedings of the Geomorphometry 2020 Conference, doi:10.30437/GEOMORPHOMETRY2020_31.

Table 2. Lidar data sets used for comparison with 1” global DEMs

AREA	LOCATION	1" CELLS	Points per cell	Lidar elevation range (m)	SRTM slope (%) and std dev	Canopy height (m) and std dev
ANNAP	N38.99° W76.49°	7911	9942	-38 to 79	3.05±3.04	15.97±11.53
BLED	N46.37° E14.10°	3808	8050	474 to 642	8.58±12.62	17.12±15.28
CA	N39.85° W123.77°	12,606	7178	161 to 671	34.07±13.51	43.62±8.95
CO	N39.32° W106.28°	12,090	1910	3107 to 3704	25.46±13.87	20.76±10.34
ICOD	N28.37° W16.70°	38,913	1577	-2 to 1005	15.65±12.66	15.97±11.45
OAHU	N21.50° W158.19°	15,477	2984	95 to 988	40.60±26.38	36.03±19.31
VA	N38.62° W78.36°	3087	5753	582 to 994	32.55±13.65	32.05±6.76
VEGAS	N36.51° W115.08°	3176	4969	1772 to 2159	31.96±13.83	16.54±6.15

Within a lidar point cloud, the range of elevations in any region depends on the slope of the terrain and height of features above the ground sampled by the lidar. Trees represent the predominant above ground features, but modern lidars also increasing have many returns from utility lines which are not identified by the national mapping agencies in the delivered lidar products. These features would also have been imaged by the radar, visible, and near IR sensors used for global DEM generation, and this research seeks to quantify the penetration achieved by the sensors and see how far they depart from the desired DTM and instead reflect a digital surface model (DSM).

II. METHODS

Lidar point clouds in LAS or LAZ format from national mapping agencies cover a range of environments (Table 2) [14,15,16,17]. One arc second Geotiff DEMs [2,4,6] cover the areas with the lidar data sets. Lidar points classified as low or high noise were excluded from analysis, but all other returns are included. With the region of lidar coverage, the lidar points corresponding to each 1”x1” grid cell in the DEM were extracted and statistics computed. These points represent the “canopy” of the cell and include the ground, buildings, vegetation, power lines, and any other features. The canopy also includes the range of elevations due to the slope of the ground, and provides an estimate of ground truth for what is present in the cell. The sensors creating the global DEMs imaged the surface represented by the cloud and derived a single elevation, at a different time, season, or even a composite of multiple views over a period of years.

Figure 1 shows a 1” single cell, and the uneven distribution of lidar returns within its canopy and elevations from the three global DEMs. Figure 2 depicts the canopy penetration along a profile showing the lidar classifications with ground, buildings, and vegetation. Figure 3 shows a simplified, longer profile with the upper and lower limits of the lidar point cloud and the three global DEMs.

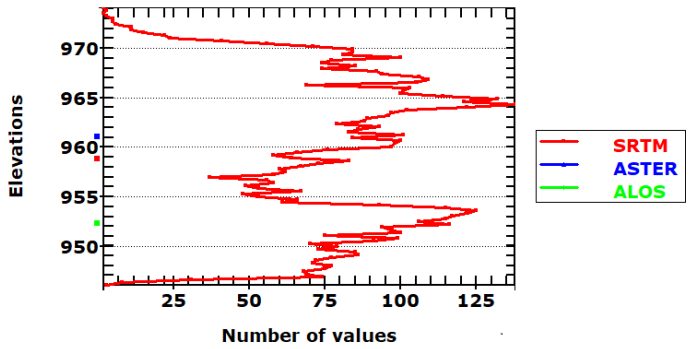

Figure 1. Point cloud density for 1”x1” cell, and elevation from 3 global DEMs on the left axis.

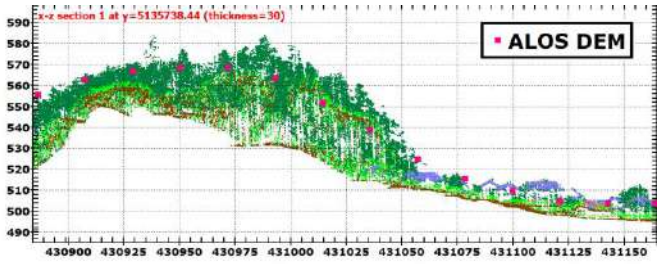

Figure 2. Slice through classified point cloud with the ALOS grid postings.

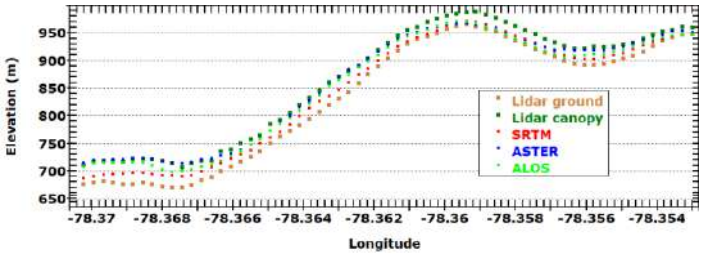

Figure 3. Profile of the ground and canopy top, and the DEM elevations.

Figures 1-3 reveal the micro-scale details of canopy penetration. To scale up the analysis, Figure 4 shows the proportion of the cells where the DEM elevation was above, within, or below the point cloud. This varies greatly by location and with the DEM. Figure 5 shows the distribution of the DEM elevations within the canopy of the lidar points. The elevations are scaled from 0 at the base of the canopy (lowest lidar elevation in the cell) to 1 at the canopy top (highest elevation in the cell); the green shading highlights this range. A value of 2 indicates the DEM point is twice the height of the canopy, and a value of -1 indicates the DEM elevation post was the height of the canopy below the ground level. As an alternative scaling, the percentile position in the point used the density of returns, from 0% at the ground to 100% at the top of the canopy. This is not linear, as seen in Figure 1 when there are peaks in density at 954 and 964 m, and very few returns above 970 m. The percentile scaling shows the same general patterns at the linear scaling in Fig. 5, but cannot extrapolate scaling for point outside the canopy range.

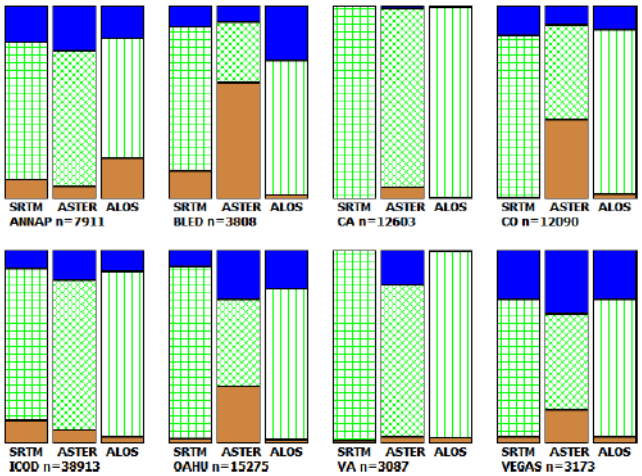

Figure 4. Proportion of DEM elevations above (blue), within (green), and below (brown) the point cloud.

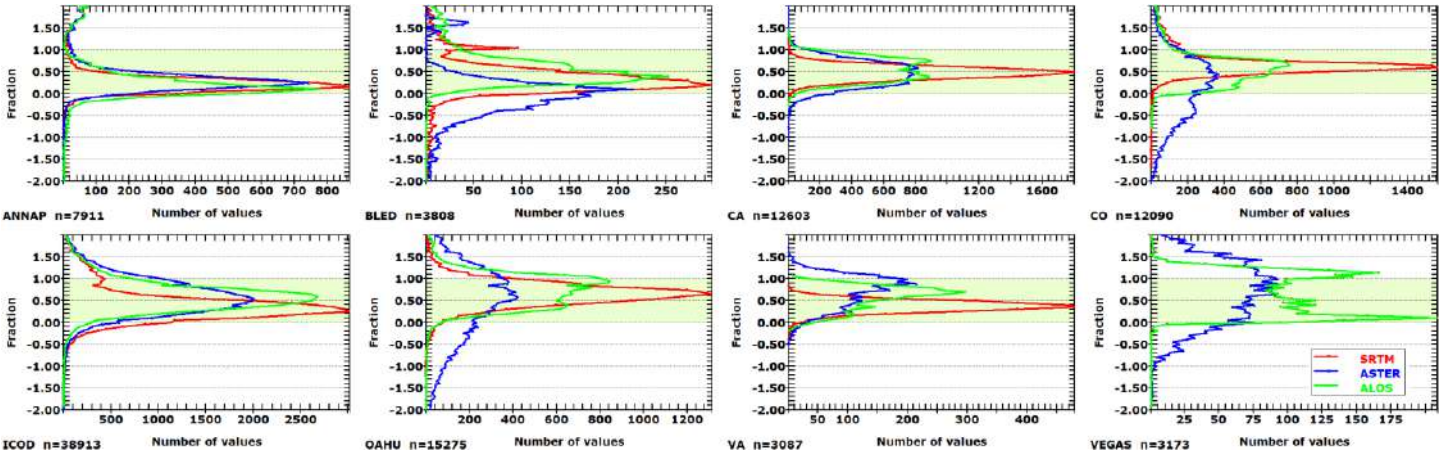

Figure 5. Distribution of the DEM postings within a linear scaling of the point cloud for the eight areas in Table 2. For the Vegas area SRTM is identical to ALOS.

III. Results and Conclusions

Canopy penetration with the sensors used for the SRTM, ALOS, and ASTER DEMs varies with the terrain. The elevations are closest to the ground, defined by the lowest lidar points, in relatively open terrain with many man-made features (ANNAP, BLED, and ICOD). These also contain the least steep terrain.

ASTER consistently shows the most points that do not lie within the lidar-defined canopy. It has many points (BLED, CO, OAHU, and VEGAS) below the ground level defined by the lidar data. A number of studies have found ASTER's quality problematic [19, 20], but it remains useful for its ability to image terrain where SRTM has challenges.

In forested terrain (CA, CO, OAHU, VA), SRTM elevations show a sharp peak concentration in about the middle of the canopy defined by the lidar. The ALOS and ASTER show a less clearly defined peak, with a tendency to record a higher position within the canopy implying that the radar achieved better penetration through vegetation. The northern hemisphere winter acquisition probably enhanced signal penetration for SRTM; ALOS and ASTER collected over a period of years and have variable season of acquisition. ALOS has a tendency for a bimodal distribution of returns from the canopy.

Future work will concentrate on the following extensions:

- Comparisons of grids created from lidar with global DEMs. The lidar can create either a DSM, DTM, or NVS (non-vegetated surface), and the global DEM would be closest to a DSM, so the comparison is not straight forward, and also requires a resampling method (min, max, mean, median, closest to the center of the cell). These regions had an average of 1500 to 10,000 points per 1" (about 900 m²) cell, allowing a lot of statistical manipulation of the data.
- Comparison of the global DEM with clouds composed only of the lidar points classified as ground. While the ground remains the goal for the global DEMs, their sensors do not readily penetrate vegetation or buildings.
- Incorporating land cover classification into the analysis.
- Adding the freely available 90 m global DEMs to the analysis.

IV. ACKNOWLEDGMENTS

All analysis was done with the MICRODEM program [21], including new code to automate the analysis steps. I thank Ian Evans for a very helpful review.

REFERENCES

[1] Farr, T. G., et al., 2007. "The Shuttle Radar Topography Mission". Rev. Geophys., 45, RG2004, doi:10.1029/2005RG000183.

[2] USGS, 2020, "Earth explorer home". https://earthexplorer.usgs.gov/

[3] NASA/METI/AIST/Japan Space systems, and U.S./Japan ASTER Science Team, 2001. "ASTER DEM Product [Data set]". NASA EOSDIS Land Processes DAAC. Accessed 2020-02-03 from https://doi.org/10.5067/ASTER/AST14DEM.003

[4] Earthdata, 2020. "EARTHDATA Search". https://search.earthdata.nasa.gov/search/

[5] Tadono, T., Takaku,J., Tsutsui, K., F. Oda, and Nagai, N., 2015. "Status of ALOS World 3D (AW3D) global DSM generation. Proceeding 2015 IEEE International Geoscience and Remote Sensing Symposium (IGARSS), 3822-3825, doi:10.1109/IGARSS.2015.7326657

[6] JAXA, 2020. "Precise Global Digital 3D Map "ALOS World 3D" Homepage", https://www.eorc.jaxa.jp/ALOS/en/aw3d/index_e.htm

[7] Yue, L., Shen, H., Liu, L., Yuan, Q., and Zhang, L., 2019. "A Global Seamless DEM Based on Multi-Source Data Fusion (GSDEM-30): Product Generation and Evaluation". https://www.preprints.org/manuscript/201906.0036/v1

[8] http://sendimage.whu.edu.cn/res/DEM_share/ Link broken Feb.29, 2020.

[9] Yamazaki, D., D. Ikeshima, R. Tawatari, T. Yamaguchi, F. O'Loughlin, J. C. Neal, C. C. Sampson, S. Kanae, and P. D. Bates, 2017. "A high-accuracy map of global terrain elevations". Geophys. Res. Lett., 44, 5844-5853, doi:10.1002/2017GL072874.

[10] Yamazaki, D., 2018,"MERIT DEM: Multi-Error-Removed Improved-Terrain DEM". http://hydro.iis.u-tokyo.ac.jp/~yamadai/MERIT_DEM/index.html

[11] Rizzoli, P., Martone, M., Gonzalez, C., Wecklich, C., Borla Tridon, D., Brautigam, B., Bachmann, M., Schulze, D., Fritz, T., Huber, M., Wessel, B., Krieger, G., Zink, M., and Moreira, A., 2017. "Generation and performance assessment of the global TanDEM-X digital elevation model". ISPRS Journal of Photogrammetry and Remote Sensing, Vol 132, pp. 119-139.

[12] DLR, 2020. "The TanDEM-X 90m Digital Elevation Model". https://geoservice.dlr.de/web/dataguide/tdm90/#access015

[13] Airbus, 2020. "Copernicus DEM product handbook". https://spacedata.copernicus.eu/documents/12833/20611/GEO1988-CopernicusDEM-SPE-002_ProductHandbook_I1.00/150167c3-3687-4f8e-9745-658ec29b3df0

[14] Agencia rs za Okolje, 2020. "LIDAR". http://gis.arso.gov.si/evode/profile.aspx?id=atlas_voda_Lidar@Arso

[15] Centro del Descargas, 2020. "Products". http://centrodedescargas.cnig.es/CentroDescargas/locale?request_locale=en

[16] OpenTopography, 2020. https://opentopography.org/

[17] USGS, 2020. "TNM download". https://viewer.nationalmap.gov/basic/

[18] Maryland, 2020. "Maryland statewide lidar download tool". https://lidar.geodata.md.gov:8443/ExpressZip

[19] Guth, P.L., 2010. "Geomorphometric comparison of ASTER DEM and SRTM". Join Symposium of ISPRS Technical Commission IV, Orlando, FL, p. 10.

[20] Hengl, T., and Reuter, H.I., 2011, How accurate and usable is GDEM? A statistical assessment of GDEM using Lidar data: In Geomorphometry 2011, edited by T. Hengl, I. S. Evans, J. P. Wilson and M. Gould, 45-48. Redlands, CA, 2011. http://www.geomorphometry.org/HenglReuter2011

[21] Guth, P.L., 2009, Geomorphometry in MICRODEM, In Hengl, T., Reuter, H.I. (eds), Geomorphometry: concepts, software, applications. Developments in Soil Science Series, Elsevier, p.351-366. Program at https://www.usna.edu/Users/oceano/pguth/website/microdem/microdemdown.htm .

GEOMORPHOMETRY 2020 PERUGIA, ITALY JUNE 22 - 26 2020

High-resolution geomorphometry – towards better understanding the genesis and contemporary processes in erosional sandstone landscapes

Kacper Jancewicz[§], Piotr Migoń, Wioleta Kotwicka, Milena Różycka
Institute of Geography and Regional Development
University of Wrocław
Plac Uniwersytecki 1, 50-137 Wrocław, Poland
[§] kacper.jancewicz@.uwr.edu.pl

Abstract—**The paper explores the topic of how geomorphometric analysis of high-resolution digital elevation models can be used within a spectrum of current geomorphological research focused on sandstone areas of very complex topography. Geomorphometric approach is applied to the study of tabular hills, valley (canyon) systems and connectivity in surficial drainage patterns. It offers means to advance comparative studies of residual relief using various morphometric indices, helps to distinguish canyon reaches of various origins and is useful to identify sinks within plateaus and reconstruct drainage patterns and pathways. Additionally the study provides an assessment of available LiDAR-based DEMs in terms of their capability to represent such a complex relief.**

I. INTRODUCTION

In terms of complexity, land surfaces vary enormously. Whereas standard geomorphometric tools perform fairly well in most situations, areas of specific relief and high topographic complexity pose a challenge which tools to use and how to adjust them to receive a quantitative representation of relief which would be objective and faithful as possible.

Among such extremely complex areas are dissected sandstone tablelands, where intricate joint-controlled patterns of rock elevations and topographic depressions represent very unusual topography, lacking many features of typical fluvio-denudational landscapes such as hierarchical drainage patterns, well defined water divides and moderately inclined slopes. Instead, they host tabular hills, grid-like patterns of clefts and gorges, boulder-filled canyons and sinkholes. Therefore, they are an interesting case in geomorphic and geomorphometric studies and yet, remain well away from the mainstream of contemporary geomorphology.

Such highly complex erosional topographies are widespread in Central Europe, across Germany, Czechia and Poland (Fig. 1). They have generated scientific interest since the 19C, but very few attempts to quantify the relief have been made. However, things started to change in the recent decade [1] due to release of high-resolution, LiDAR-based digital elevation models which provide an excellent opportunity to examine the applicability of geomorphometric tools to these highly specific areas. Here, the focus is on geomorphology of sandstone-capped tabular hills (mesas and buttes), valley shapes and networks, and surface versus subsurface drainage systems.

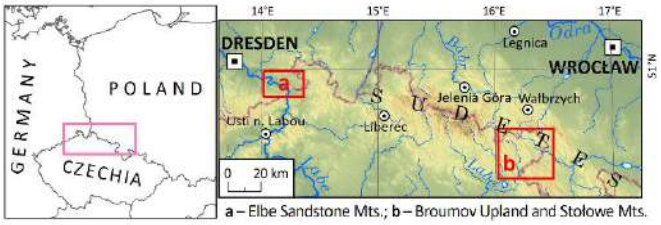

Figure 1. Location of study areas.

II. METHODS

Software-wise, the study is based on existing tools and algorithms implemented in ArcGIS and SAGA-GIS environment. Additionally, Global Mapper 18 software was used during pre-processing of elevation data.

A. Remarks on the elevation datasets and data pre-processing

The location of the study areas dictated the use of three LiDAR-based digital elevation grid datasets, all of 1x1 m resolution:

a) Polish *Numeryczny Model Terenu* (NMT), based on point cloud of 4–6 pts/m^2 density (original .las point cloud is available); mean vertical error = 0.15 m [2];

Kacper Jancewicz, Piotr Migon, Wioleta Kotwicka and Milena Rozycka (2020) High-resolution geomorphometry Çô towards better understanding the genesis and contemporary processes in erosional sandstone landscapes in Massimiliano Alvioli, Ivan Marchesini, Laura Melelli & Peter Guth, eds., Proceedings of the Geomorphometry 2020 Conference, doi:10.30437/GEOMORPHOMETRY2020_32.

b) German *Digitale Geländemodell* (DGM1), based on point cloud of 10 pts/m^2 density (original .las point cloud is available); mean vertical error = 0.15 m [3];

c) Czech *Digitální model reliéfu České republiky 5. generace* (DMR5G), based on point cloud of 1.6 pts/m^2 density [4] (original .las point cloud is not available); mean vertical error up to 0.3 m [5].

While all the above DEMs provide currently the most accurate and detailed representation of the surface within the study areas, their accuracy may be remarkably lower within areas of complex relief at the local scale and considerable elevation differences within the rock-cut landscape [4]. Many times, field work revealed that even high-resolution DEMs failed to show some typical elements of sandstone landscape such as cubically-shaped boulders or whole caprock fragments. This is mainly because of errors during point classification [6] and the issue can be solved by customized filtering of the point cloud if such one is accessible (Fig. 2). Hence, it is recommended that within complex erosional sandstone landscapes, the elevation data preprocessing shall be intertwined with detailed on-site observations.

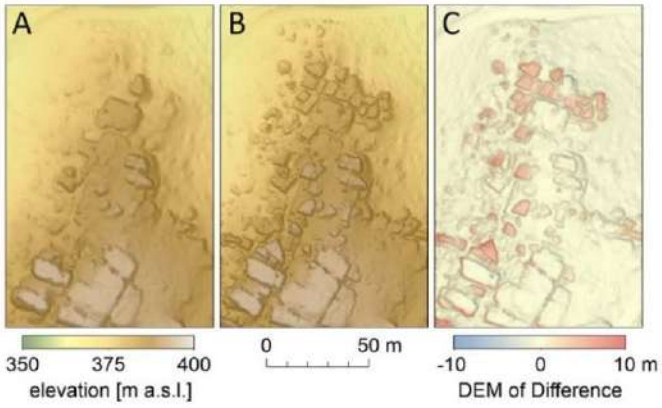

Figure 2. Labyrinth (Elbe Sandstone Mountains, Saxony, Germany), a fine example of how significant parts of caprock, while not represented by the raster version of DGM1 (A), can be restored after semi-manual filtering of primary point cloud (B). In this case, the elevation difference is up to 10 m (C).

B. Morphometric features of tabular hills

Tabular hills (mesas) are among characteristic landforms in platform areas and yet, it seems that no protocol exists to describe them quantitatively and hence, to facilitate comparative analysis. As an attempt to address the problem, selected mesas from the Elbe Sandstone Mountains were characterized by five morphometric parameters:

a) area of the mesa top surface;

b) Sinuosity Index of mesa rim (SI), defined as:

$$SI = P_{MR}/P_{mbr} \quad (1)$$

where:
$P_{MR} - perimeter\ of\ mesa\ rim$
$P_{mbr} - perimeter\ of\ minimum\ bounding\ rectangle\ enclosing\ the\ mesa\ top\ surface$ (Fig. 3A)

c) the percentage of slopes > 45° within the mesa top surface (in plan) (Fig. 3B);

d) the percentage of slopes > 60° within the bounding escarpments (in plan) (Fig. 3C);

e) the percentage of surface where Morphometric Protection Index (MPI) > 0.6 within the mesa top surface. MPI is a SAGA-GIS algorithm which returns an equivalent to the positive openness [7]; herein, MPI values exceeding 0.6 indicate the development of deep clefts and thus, the degree of fragmentation of the mesa top surface (Fig. 3D).

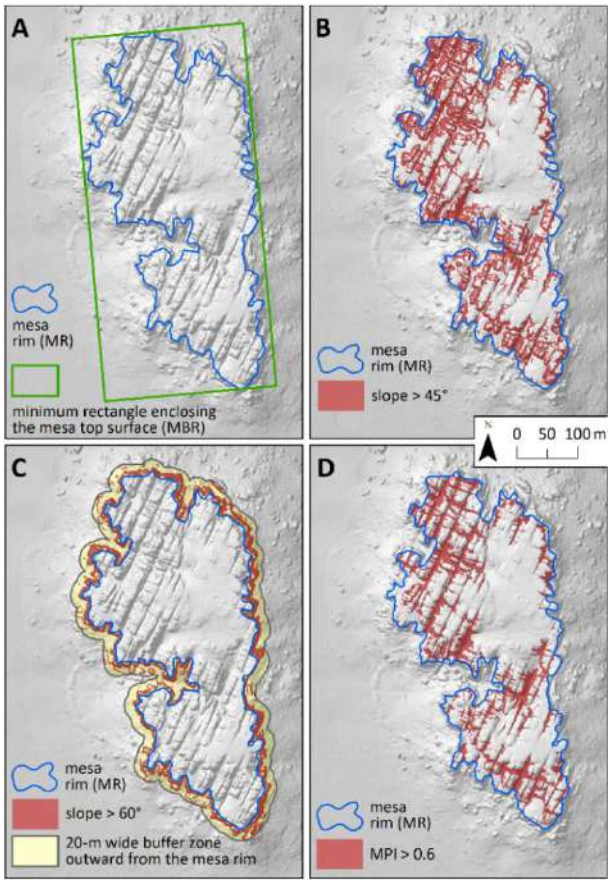

Figure 3. Selected morphometric parameters of a tabular hill on the example of Pfaffenstein (Elbe Sandstone Mts., Saxony, Germany).

Beside allowing for comparative analysis, in this particular area the variability of these parameters was explained in terms of

directional evolution of residual hills, from a plateau through the mesa stage to a residual butte or boulder-covered hill [8].

C. Morphological diversity of cleft-and-valley systems

In regularly jointed sandstones grid-like patterns of passageways between bedrock elevations form, difficult to analyse using conventional measures pertinent to drainage networks. In addition, many passageways are dry and lack channels. Therefore, simple measures of valley form and pattern were supplemented by MPI analysis, found to provide valuable insights into the nature of concave landforms and their diversity (Fig. 4).

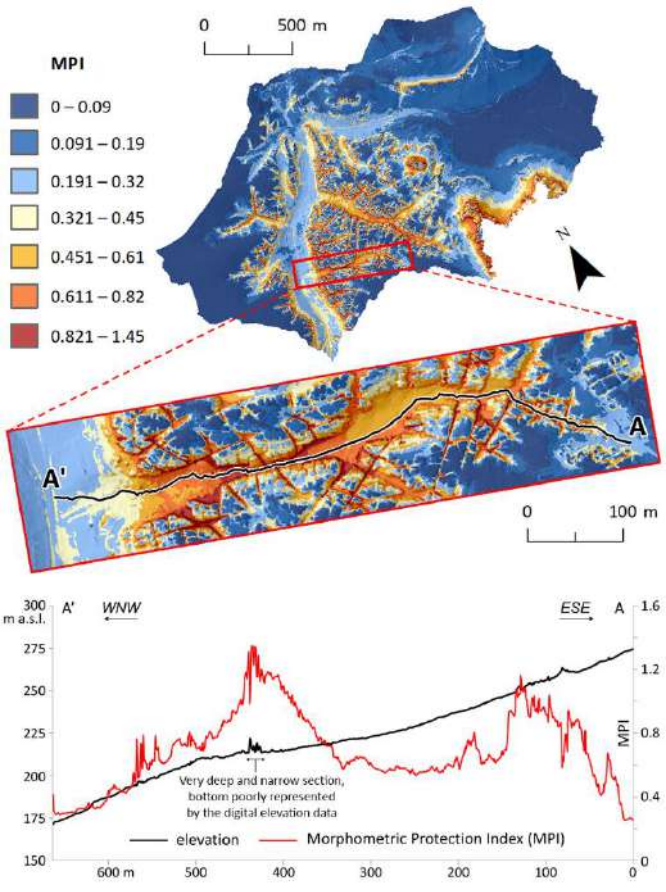

Figure 4. Geomorphic diversity of cleft-and-valley system on example of a small drainage basin located NE from Bad Schandau (Elbe Sandstone Mountains, Saxony, Germany). Longitudinal profile depicts morphological change along a selected canyon using Morphometric Protection Index, where high values coincide with narrow and deep sections.

Spatial diversity of valley forms includes unusual morphology of valley floors, with thick boulder fills. This topic was explored using Terrain Ruggedness Index (TRI) as a measure of variability [9]. The spatial extent of valley floor was, in this particular case, delimited automatically, basing on the criterion of maximum relative height above modelled stream network (2 m). Field work confirmed that high TRI values indicate particularly thick and irregular boulder fills, likely from long-term in situ disintegration of the sandstone rock mass.

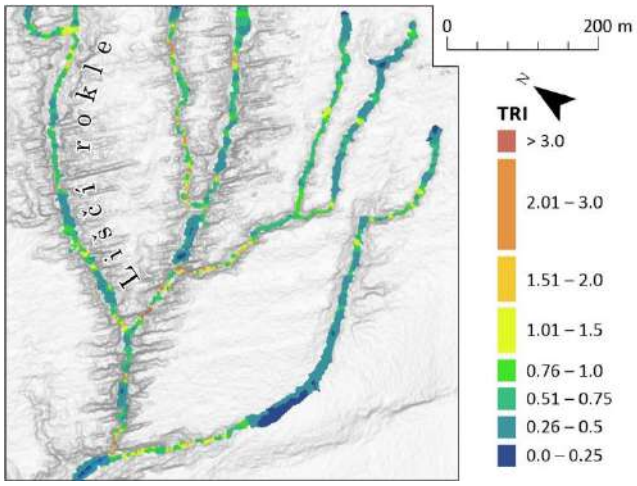

Figure 5. Spatial distribution of TRI values in the Liščí rokle cleft-and-valley system (Broumov Upland, Czechia).

D. Drainage connectivity patterns

Topographic and geological features of sandstone terrain may induce the occurrence of discontinuous surface drainage patterns and predominant subsurface drainage. We focused on spatial distribution of sinks as well as modelling of Topographic Wetness Index (TWI) [10] in contrasting geomorphic settings [11]:

$$TWI = ln\frac{SCA}{tan\beta} \quad (2)$$

where:
SCA – *specific catchment area calculated using the Multiple Flow Direction method* [12]; β – *local slope in degrees*.

Further procedure of TWI analysis involved data reclassification and, thus, delimitation of zones of predicted surficial flow where TWI values were above mean value plus one or two standard deviations [13], leading to the identification of numerous disconnectivity sites within the system (Fig. 6).

III. Results and Pathways of Further Research

Up to now, the high-resolution morphometric approach has proved to be a significant aid in detailed studies of sandstone relief in terms of:

a) provision of quantitative information which, while not standalone, enables the reevaluation and enhancement of classic schemes of sandstone landform evolution [8, 14];

b) support to the study of distribution and genesis of thick boulder-fills within valley floors in the canyonlands, which are in some parts – regardless the season – impenetrable due to vegetation and terrain obstacles [15];

c) assessment of the variety of surficial and subsurface drainage patterns, depending on the topographic position within the specific landform types [11].

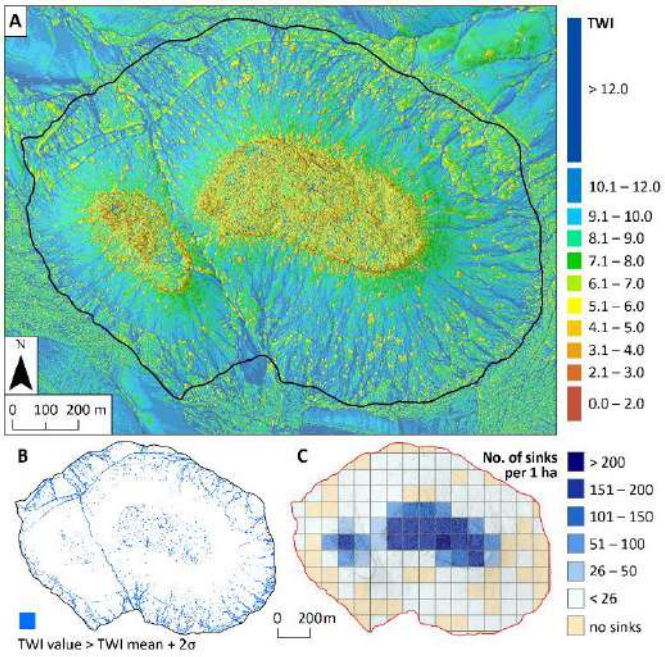

Figure 6. Disconnected surface drainage pattern of the Szczeliniec Wielki mesa (Stołowe Mts., Poland) revealed by TWI spatial distribution (A), zones of high (those above mean value plus two standard deviations) TWI values (B) and sink density map (C) [11].

The results, as well as the set of tools and indices, have to be seen as work in progress. Given the relatively broad spectrum of research undertaken so far or being planned, we aim to further develop the morphometric protocol, especially towards semi-automated classification of the different cleft/ valley/canyon types as well as to morphometrically-aided landform mapping. Still, notable obstacles in implementing any universal morphometric workflow basing on high-resolution LiDAR data reside in the quality of the data itself. These may vary quite significantly, depending on the study area location and, as such, may prevent any direct comparisons of morphometric features without detailed field prospection and validation. Nevertheless, ongoing improvement of the elevation data quality is indisputable and, hopefully, this will support synergic progress in sandstone geomorphometry which is very specific.

References

[1] Migoń, P., M. Kasprzak, 2016. Pathways of geomorphic evolution of sandstone escarpment in the Góry Stołowe tableland (SW Poland) – insights from LiDAR-based high-resolution DEM. Geomorphology 260, 51–63.

[2] Kurczyński, Z., E. Stojek, U. Cisło-Lesicka, 2015. "Zadania GUGiK realizowane w ramach projektu ISOK". [In:] P. Wężyk [ed.], Podręcznik dla uczestników szkoleń z wykorzystania produktów LiDAR. (Handbook for users of training courses in the use of LiDAR products). Informatyczny System Osłony Kraju przed nadzwyczajnymi zagrożeniami, 2nd ed. Główny Urząd Geodezji i Kartografii, Warszawa, pp. 22–58.

[3] "Produkt- und Qualitätsstandard für Digitale Geländemodelle. Version 3.0", 2019. Arbeitsgemeinschaft der Vermessungsverwaltungen der Länder der Bundesrepublik Deutschland (AdV) (15 pp).

[4] Paleček, V., P. Kubíček, 2018. Assessment of accuracy in the identification of rock formations from aerial and terrestrial laser-scanning data. ISPRS International Journal of Geo-Information 7, 142.

[5] Brázdil, K., 2016. Technická Zpráva k Digitálnímu Modelu Reliéfu 5. Generace DMR 5G. Zeměměřický úřad, Vojenský geografický a hydrometeorologický úřad, Praha (12 pp.).

[6] Sithole, G., G. Vosselman, 2004. "Experimental comparison of filter algorithms for bare-earth extraction from airborne laser scanning point clouds". ISPRS Journal of Photogrammetry and Remote Sensing 59, 85–101.

[7] Yokoyama, R., M. Shirasawa, R.J. Pike, 2002. "Visualizing topography by openness: a new application of image processing to Digital Elevation Models". Photogrammetric Engineering and Remote Sensing 68, 257–266.

[8] Migoń, P., M. Różycka, K. Jancewicz, F. Duszyński, 2018. "Evolution of sandstone mesas – following landform decay until death". Progress in Physical Geography 42 (5), 588–606.

[9] Riley, S.J., S.D. DeGloria, R. Elliot, 1999. "A terrain ruggedness index that quantifies topographic heterogeneity". Intermountain Journal of Sciences 5, 23–27.

[10] Beven, K.J., M.J. Kirkby, 1979. "A physically based variable contributing area model of basin hydrology". Hydrological Sciences Bulletin. 24 (1), 43–69.

[11] Jancewicz, K., P. Migoń, M. Kasprzak, 2019. "Connectivity patterns in contrasting types of tableland sandstone relief revealed by Topographic Wetness Index". Science of the Total Environment 656, 1046–1062

[12] Quinn, P., K. Beven, P. Chevallier, O. Planchon, 1991. "The prediction of hillslope flow paths for distributed hydrological modelling using digital terrain models". Hydrological Processes 5, 59–79.

[13] Różycka, M., P. Migoń, A. Michniewicz, 2017. "Topographic Wetness Index and Terrain Ruggedness Index in geomorphic characterisation of landslide terrains, on examples from the Sudetes, SW Poland". Zeitschrift für Geomorphologie 61 (Suppl. 2), 61–80.

[14] Migoń, P., F. Duszyński, K. Jancewicz, M. Różycka, 2019. "From plateau to plain – using space-for-time substitution in geoheritage interpretation, Elbsandsteingebirge, Germany". Geoheritage 11 (3), 839–853.

[15] Duszyński, F., K. Jancewicz, P. Migoń, 2018. "Boulder caves, roofed slots and boulder-filled canyons – evidence for subsurface origin, Broumov Highland, Czechia". International Journal of Speleology 47 (3), 343–359.

GEOMORPHOMETRY 2020 PERUGIA, ITALY JUNE 22 - 26 2020

Can multiscale roughness help computer-assisted identification of coastal habitats in Florida?

Vincent Lecours[§] & Michael C. Espriella
School of Forest Resources & Conservation
University of Florida
7922 NW 71st Street, Gainesville, Florida, USA, 32606
[§] vlecours@ufl.edu

Abstract—**Coastal habitats are of natural, economic, and cultural importance in Florida, and there is a need for effective approaches to map and monitor them. Geographic Object-Based Image Analysis (GEOBIA) was previously applied to an orthomosaic and a Digital Surface Model (DSM) to automatically delineate oyster reef, salt marsh, and mudflat habitats in Little Trout Creek, Florida. Here we evaluated whether a multiscale measure of roughness has the potential to improve this GEOBIA workflow in this context where oysters are spectrally similar to the two other habitat types. Our results show that multiscale roughness can be used to distinguish the different coastal habitat types studied. The level of roughness of mudflats is usually higher at broader scales, and the magnitude of that roughness is relatively small. Marsh roughness was highest at finer scales, and its magnitude was higher compared to other habitat types likely due to marshes' vegetation cover, which is captured in the DSM. The highest magnitudes of roughness for oysters were smaller than, and found at slightly broader scales than, the highest roughness for marshes. Our results were strongly affected by edge effects because the studied habitats are discrete and discontinuous. Multiscale roughness has the potential to help delineate coastal habitats in Florida, but more work is needed to better understand the multiscale topographic patterns of different coastal habitats in Florida and elsewhere.**

I. Introduction

Coastal habitats like oyster reefs and salt marshes provide economic opportunities as well as vital ecosystem services such as shoreline erosion control, habitat and nursery for a variety of species, and water filtration. However, many of these ecosystem services are threatened by natural and anthropogenic factors (*e.g.*, coastal development, sea-level rise, hurricanes). Mapping and monitoring coastal habitats are critical to improving scientific understanding of the complex dynamics of coastal ecosystems, to better inform management, planning, and conservation efforts.

Florida's coastal waters are the most economically valuable, have the highest recreational use, and have one of the highest concentrations of coastal communities in the United States. At a 2007 workshop, regional, state, and federal partners concluded that although mapping coastal resources was a top priority, the lack of a standard, reproducible approach was hindering broad-scale efforts [1]. With the increased likelihood of extreme weather events [2] that have the potential to impact coastal habitats in Florida [3], there is a critical need to develop an effective and reproducible mapping and monitoring workflow that can be used to answer questions in a variety of contexts (*e.g.*, sea-level rise, community resilience, hurricane impact assessments).

In a recent article, Espriella *et al.* [4] proposed a reproducible approach to detect and delineate three types of coastal habitats – oyster reefs, salt marshes, and mudflats – in imagery collected with Unoccupied Aircraft Systems (UAS). The approach is centered on a two-level Geographic Object-Based Image Analysis (GEOBIA) [5] that first identifies and extracts water areas from the data before classifying the remaining objects into their respective habitats. Both the RGB mosaic and the Digital Surface Model (DSM), produced using structure-from-motion photogrammetry, were used as inputs. However, with an overall classification accuracy of 79%, that GEOBIA alone may not be robust enough for accurate temporal monitoring. Oysters had the lowest overall separability from the other habitats, which is problematic from a management perspective; oysters are one of the most important living coastal resources actively managed in the Gulf of Mexico, are suffering from major declines in the area, and thus are of particular interest.

In nature, oyster reefs are more structurally complex than marsh and mudflats, at multiple scales. Therefore, we hypothesize that geomorphometry can provide a means to help differentiate these habitats from each other. While Espriella *et al.* [4] derived local measures of terrain attributes (*e.g.*, rugosity, relative position) at multiple independent spatial scales [6] using relatively few search neighborhoods [7], their feature-space optimization to select the variables best fit to recognize the different habitats did not identify any DSM-derived variables as being relevant. Here, we evaluate the potential of a multiscale measure of roughness [8] – as opposed to independent measures of roughness derived at multiple scales – to help distinguish oyster reefs, salt marshes, and mudflats from each other.

Vincent Lecours and Michael Espriella (2020) Can multiscale roughness help computer-assisted identification of coastal habitats in Florida?: in Massimiliano Alvioli, Ivan Marchesini, Laura Melelli & Peter Guth, eds., Proceedings of the Geomorphometry 2020 Conference, doi:10.30437/GEOMORPHOMETRY2020_24.

II. METHODS

UAS imagery was collected on December 8th, 2018 at low tide, at the mouth of Little Trout Creek (29° 15' 34.98" N, 83° 4' 29.68" W), on the west coast of Florida (Fig. 1). The imagery was collected at nadir using a DJI Inspire 2 equipped with a Zenmuse X7 35 mm RGB sensor. The UAS was flown 60 m above ground level, with an 80% along-track overlap and 75% across-track overlap. Four checkered targets were evenly distributed across the scene and located using a Trimble 5800 real-time kinematic positioning system. In addition to the orthomosaic, a DSM was produced using structure-from-motion photogrammetry in Pix4D Mapper v. 4.2.27. The total area surveyed covered approximately 0.116 km^2 and provided data with a 0.66 cm spatial resolution (Fig. 2), with a root mean square error of 0.3 cm in longitude and latitude, and 0.1 cm in elevation for the residuals of control points.

FIGURE 1. LOCATION OF THE STUDY AREA: LITTLE TROUT CREEK, FLORIDA, USA.

The GEOBIA ruleset of Espriella *et al.* [4] was applied to the data. The resulting classification was used to extract 37 oyster reefs, 22 salt marshes, and 33 mudflats areas from the DSM. The areas were selected because they were fully encompassed within the extent of the data (*i.e.*, no areas from the boundaries of the mosaic). Each extracted area was entered in the "Multiscale Roughness" tool of WhiteboxTools v. 1.1.0 [9], with search neighborhood radii ranging from 1 grid cell to 9,751 grid cells, which corresponds to the length of the longest feature (a salt marsh of about 64 m; cf. center of Fig. 2 and Fig. 3). The tool produced two main outputs: a raster that indicates, for each pixel, the size of the search neighborhood at which the measured roughness was the highest, and a raster displaying the magnitude of the measured roughness at that scale. Descriptive statistics of the two output types were calculated for each habitat type.

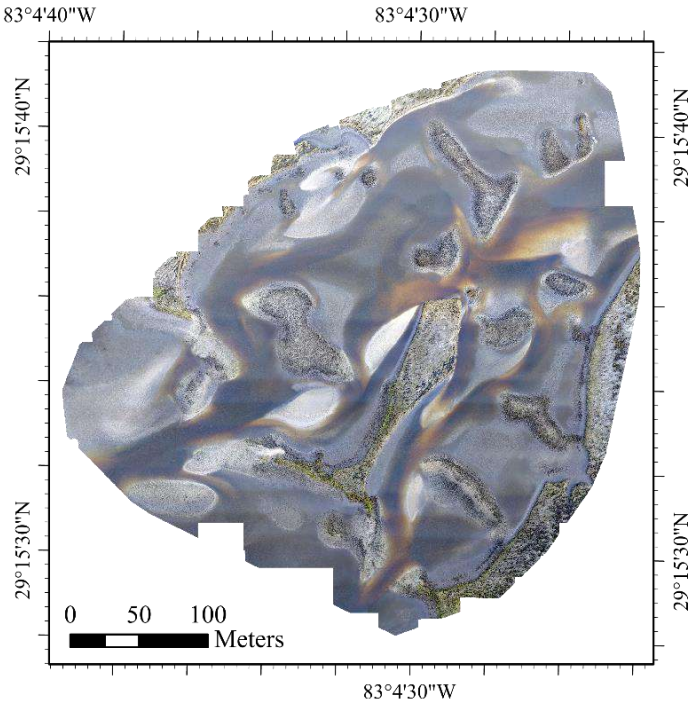

FIGURE 2. UAS IMAGERY COLLECTED AT LOW TIDE ON DECEMBER 8TH, 2018.

III. RESULTS AND DISCUSSION

Figure 3 presents the GEOBIA classification results and the scale and magnitude outputs for all the studied habitats. The spatial distributions of the scale and magnitude values seem to be influenced by the geometry of the features and the quality of the DSM. For instance, high-magnitude values were found on long and narrow features, and broader-scale values were found in areas of interpolation artifacts where the presence of water affected DSM production. In general, magnitude is the most promising output to differentiate the three studied coastal habitats (Fig. 3); patches of mud displayed a much lower magnitude than other habitat types, which was expected considering the less complex nature of mudflats, and salt marshes displayed a much higher magnitude than other habitat types, likely because of the presence of a vegetation cover captured in the DSM. Oyster reefs, which are the most heterogeneous habitats, had intermediate magnitudes of roughness at intermediate scales.

These observations are confirmed by the analysis of the statistical distributions of scale and magnitude (Tab. 1). On

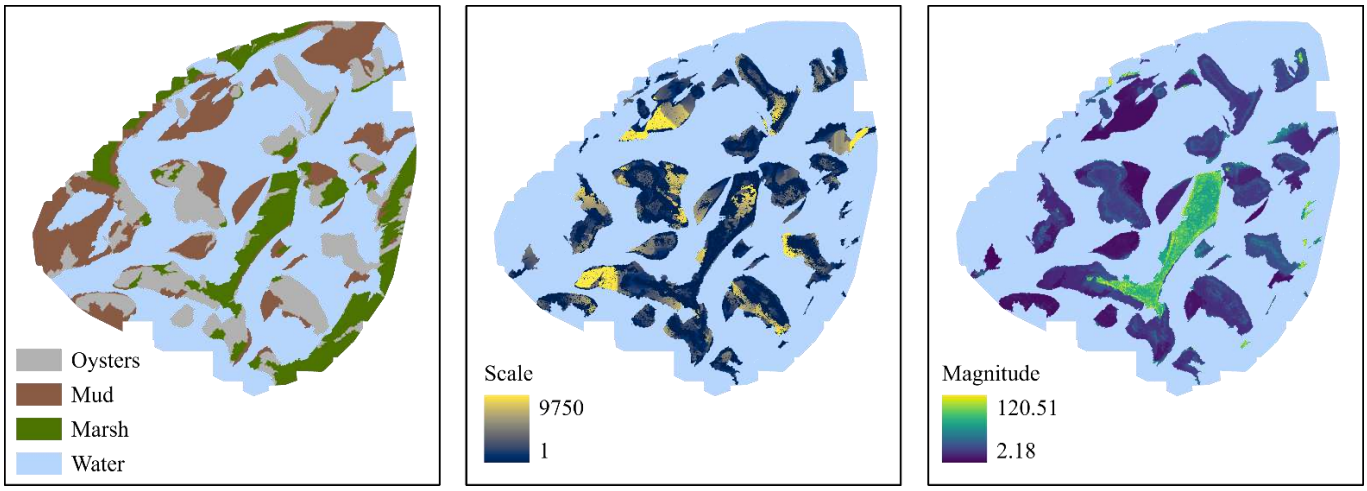

FIGURE 3. GEOBIA CLASSIFICATION, AND SCALE AND MAGNITUDE OF THE MULTISCALE ROUGHNESS MEASURE APPLIED TO THE EXTRACTED FEATURES.

average, the scale of maximum roughness was broader for mudflats than for oysters and marshes. However, averages are likely biased by outliers caused by edge effects: the skewness of the distributions for scale shows that they are highly skewed for marsh and oysters, and moderately skewed for mudflats. Distributions of scale for marshes and oysters are leptokurtic, and that of mudflats is platykurtic. The distributions of magnitudes for mudflats and oysters are heavily skewed, with a high and sharp peak and long and fat tails caused by many outliers. The distribution of magnitudes for marshes is relatively symmetrical but platykurtic, with a short and thin tail. Given these results, we do not expect that the averages presented in Tab. 1 are fully representative. We adjusted them by manually removing outliers from the distribution and obtained revised averages for scale of 1,231.66 (≈9.4 m) for marshes, 1,980.06 (≈19.6 m) for mudflats, and 1879.68 (≈15.0 m) for oysters. However, the median values suggest that patterns of highest roughness can be found at about 1.5 m for marshes, 12.9 m for mudflats, and 5.3 m for oysters, which is more consistent with what can be observed in the field in terms of habitat complexity and habitat patch size. Setting these results into the natural context can thus serve as additional evidence that edge effects influenced some of the statistics (*e.g.*, average, standard deviation). In fact, the cumulative distributions of scale for all habitat types showed a stabilization in slope between 125 and 400, which corresponds to 0.8 to 2.6 m, indicating that most of the high measured roughness would be found at scales finer than 3 m.

It is noteworthy that all habitat types reached a local peak of maximum roughness at search radii of 30 cells (oysters and mud) or 33 cells (marsh), which corresponds to 21±1 cm. While this is an interesting result, it should be interpreted with caution: given the different natures of the habitat types, it is improbable that they display local roughness at almost the same exact scale (with a precision of 6 mm). A possible explanation is that intrinsic noise is present in the DSM at this specific scale range and captured by the analysis. In terms of magnitude, the statistical distributions confirm that magnitudes of roughness are generally smaller for mudflats and higher for marshes.

TABLE 1. DESCRIPTIVE STATISTICS OF THE SCALE AND MAGNITUDE OF THE MULTISCALE ROUGHNESS MEASURE FOR EACH HABITAT TYPE.

	Scale			Magnitude		
	Marsh	Mud	Oyster	Marsh	Mud	Oyster
Number of Cells	154,945,348	238,774,206	438,236,795	154,945,348	238,774,206	438,236,795
Minimum	1	1	1	3.90	2.18	3.31
Maximum	9,750	9,750	9,750	108.65	120.51	101.21
Average	1,428.40	2,973.09	2,276.70	21.34	7.90	10.77
Median	229	1,948	804	25.76	6.30	9.82
Standard Deviation	2,287.13	3,127.44	2,943.04	11.01	5.64	5.47
Variance	5,230,967.94	9,780,854.37	8,661,511.55	121.33	31.76	29.88
Skewness	2.00	0.87	1.30	-0.10	2.91	3.15
Kurtosis	6.19	2.51	3.48	1.77	14.55	17.43

This work is an initial exploration of the potential of measures of multiscale topographic patterns to help identify coastal habitats. However, limitations include the use of the results of an imperfect spectral-based GEOBIA classification to guide the selection of habitat features for this analysis. For instance, Fig. 4 shows that one of the objects identified as marsh is partly misclassified: only the central section of this object is a vegetated salt marsh – the surrounding habitat is oysters. However, the entirety of this area was considered as marsh for the analysis because it was based on the objects defined and classified by the GEOBIA workflow. Both the scale and magnitude of the multiscale roughness captured that difference, with the marsh having a finer-scale roughness of higher magnitude than the surrounding oysters. This directly highlights the potential of these

measures to augment the GEOBIA and differentiate coastal habitats in Florida.

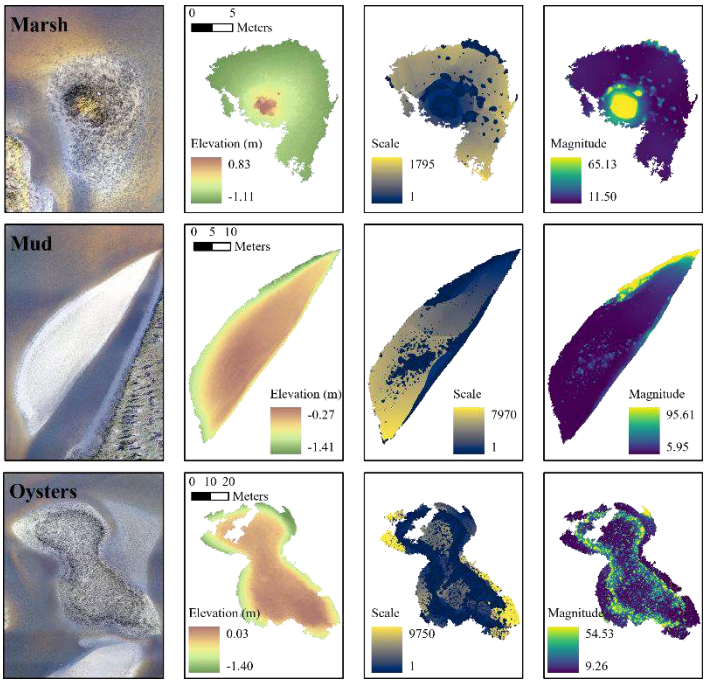

FIGURE 4. EXAMPLE OF ORTHOMOSAIC, DSM, AND THE SCALE AND MAGNITUDE COMPONENTS OF THE MULTISCALE ROUGHNESS MEASURE FOR ONE OF THE 22 SALT MARSHES, ONE OF THE 33 MUDFLATS, AND ONE OF THE 37 OYSTER REEFS STUDIED.

Another limitation of this work is that each of the 92 features studied was analyzed independently, which artificially increased edge effects. The complex dynamics of this coastal ecosystem mean that oysters can be directly adjacent to mudflats and marshes. As such, analyzing a patch of multiple habitats as one, then separating it into different habitats post-analysis before computing statistics could have reduced the influence of edge effects. However, this would be very computationally intensive given the size of the DSM (24 GB).

IV. CONCLUSIONS

Coastal geomorphometry has recently been identified as a future application of geomorphometry that will present challenges due to the presence of features both over and under the waterline [10]. Here we presented such an application, and these challenges were highlighted by a strong influence of edge effects and feature geometry that artificially increased the average scale at which maximum roughness was observed and the average magnitude of that roughness. However, we concluded that mudflats display relatively smaller amplitudes of roughness over broader scales and that salt marshes display the highest roughness over relatively finer scales. Oyster reefs showed intermediate patterns of roughness, with both amplitudes and scales between those of the two other habitat types. While we hypothesized that oyster reefs would show the highest roughness at the finest scales, the finer-scale patterns of salt marshes may be explained by the presence of characteristic vegetation on the marshes, which creates relatively high roughness patterns in the DSM. Future work should repeat the analyses using a Digital Terrain Model (DTM) instead of a DSM. In theory, the DTM would preserve the complex fine-scale structures of oyster reefs while omitting the vegetation over salt marshes that created local roughness. Denoising algorithms could also be applied to the models to ensure that the multiscale analyses capture the scales at which patterns are observed rather than the noise in the data. Finally, because we demonstrated that multiscale roughness shows potential to help differentiate coastal habitat types from each other, we recommend evaluating the suitability of other multiscale geomorphometric measures, such as multiscale topographic position [11], multiscale maximum spherical standard deviation [8], multiscale maximum difference from mean elevation [11], and multiscale topographic anisotropy [12] for the identification of coastal habitats.

REFERENCES

[1] Robbins, L., S. Wolfe, E. Raabe, 2008. “Mapping of Florida’s coastal and marine resources: setting priorities workshop”. USGS Open-File Report, 1157, 32 p.

[2] Gao, Y., J.S. Fu, J.B. Drake, Y. Liu, J.-F. Lamarque, 2012. “Projected changes of extreme weather events in the eastern United States based on a high resolution climate modeling system”. Environ. Res. Lett. 7, 1-12.

[3] Unmenhofer, C.C., G.A. Meehl, 2017. “Extreme weather and climate events with ecological relevance: a review”. Philos. T. R. Soc. B. 372, 1-13.

[4] Espriella, M., V. Lecours, P.C. Frederick, E.V. Camp, B. Wilkinson, 2020. “Quantifying intertidal habitat relative coverage in a Florida estuary using UAS imagery and GEOBIA”. Remote Sens. 12(4), 677, 1-17.

[5] Blaschke, T., 2010. “Object based image analysis for remote sensing”. ISPRS J. Photogramm. Remote Sens. 65, 2-16.

[6] Grohmann C.H., C. Riccomini, 2009. “Comparison of roving-window and search-window techniques for characterizing landscape morphometry”. Comput. Geosci. 35, 2164-2169.

[7] Deng, Y., J.P. Wilson, 2008. “Multi-scale and multi-criteria mapping of mountain peaks as fuzzy entities”. Int. J. Geogr. Inf. Sci. 22, 205-218.

[8] Lindsay, J.B., D.R. Newman, A. Francioni, 2019. “Scale-optimized surface roughness for topographic analysis”. Geosci. 9(7), 322.

[9] WhiteboxTools, https://jblindsay.github.io/ghrg/WhiteboxTools/index.html

[10] Lecours, V., M.F. Dolan, A. Micallef, V.L. Lucieer, 2016. “A review of marine geomorphometry, the quantitative study of the seafloor”. Hydrol. Earth Syst. Sci. 20, 3207-3244.

[11] Newman, D.R., J.B. Lindsay, J.M.H. Cockburn, 2018. “Evaluating metrics of local topographic position for multiscale geomorphometric analysis”. Geomorphology 312, 40-50.

[12] Newman, D.R., J.B. Lindsay, J.M.H. Cockburn, 2018. “Measuring hyperscale topographic anisotropy as a continuous landscape property”. Geosci. 8, 278.

GEOMORPHOMETRY 2020
PERUGIA, ITALY
JUNE 22 - 26 2020

Estimating the spatial distribution of vegetation height and ground-level elevation in a mesotidal salt marsh from UAV LiDAR-derived point cloud

Daniele Pinton[§], Alberto Canestrelli, Christine Angelini, Benjamin Wilkinson, Peter Ifju, Andrew Ortega

University of Florida
Department of Civil and Coastal Engineering
1949 Stadium Road, Gainesville, FL, USA
[§] daniele.pinton@ufl.edu

***Abstract*— Salt marshes are transitional wetlands placed between ocean and land, which act as natural defenses against coastal hazards. The amount of organic and inorganic deposition, which is strongly influenced by vegetation characteristics, is one of the main drivers for the survival of salt marshes. Vegetation also favors the dissipation of wind waves and storm surges. For these reasons, an accurate description of canopy characteristics in salt marshes is critical for their preservation and management. For this purpose, airborne LiDAR (Light Detection And Ranging) has become an accessible and cost-efficient tool to map large wetland areas. However, the limited horizontal resolution of airborne-derived point clouds (~1 m) prevents the direct extraction of ground elevation and vegetation height if not coupled with other data sources, such as RGB or hyperspectral images. Uncrewed Aerial Vehicles (UAV) have become an affordable and cost-efficient tool to map targeted salt marshes quickly. Although LiDAR is capable of measuring surface elevations, laser penetration is limited in dense salt marsh vegetation. The limited ability of the laser to penetrate dense vegetation hinders its usefulness for surveying tidal marsh platforms. For UAV-borne LiDAR, a reliable method to extract ground elevation and vegetation height from high-resolution point clouds is yet not available. Here we derive a new formulation for converting the 3D distribution of UAV derived points into vegetation height and ground-level elevation without the support of other data sources. Our formulation has been calibrated on the surveyed vegetation height in a *Spartina alterniflora* marsh in Little Sapelo Island, Georgia, USA, and successfully tested on an independent dataset. Our method produces high-resolution (40×40 cm^2) maps of ground elevation and vegetation height, thus capturing the large gradients in the proximity of tidal creeks.**

I. INTRODUCTION

The increased interest in wetland health is related to their progressive degradation and conversion in open water areas and mudflats. The leading causes of these transformations are the human interaction and the increasing sea-level rise [1]. As estuarine wetlands, salt marshes are an essential environment for many ecological, anthropologic, and economic reasons. They protect shorelines from storms, sequester carbon, improve water quality, and provide habitat for fisheries [2]–[4]. Salt marshes are the result of ecological and physical interactions [5], which requires numerical modeling to quantify the connections between hydrodynamic, morphological, and environmental processes [6], usually interested by non-linear effects. Long term evolution of salt marshes is characterized using empirical models. However, short term evolution processes that require higher precision are described using physical models [7]. In both cases, vegetation plays a central role, mitigating the effect of the meteorological agents and modulating the sedimentation and flooding patterns in the marsh area [8], [9]. In particular, vegetation influences the vertical flow velocity, producing additional frictional forces. These forces are mainly based on vegetation characteristics, such as the thickness of the vegetation layer that is strongly correlated to the ground-level elevation. Considering these reasons, an accurate description of both ground elevation and vegetation in salt marshes is essential for their management and conservation. LiDAR technology has been successfully used for many applications in wetlands, such as mapping forested wetlands [10] and quantifies the effects of sea-level rise in coastal salt meadows [11]. However, Airborne LiDAR data may not provide adequate representation of the creek network on the marshes [12], due to the low resolution of the surveyed datasets (~1 m). Unmanned Aerial Vehicle (UAV) is becoming a standard technology used for numerous purposes, such as high-resolution mapping [13], agricultural [14], and shoreline surveys [15], as well as for the estimation of vegetation biomass [16], [17]. More precise representation of the complex salt marsh morphodynamic and biological properties, as the vegetative cover [18] can be obtained using UAV-borne LiDAR point clouds, which higher resolution (~5 cm), is due to the lower flight altitude and the higher laser pulsation frequency.

The objective of this study is the production of high resolution (40×40 cm^2) maps of ground elevation and vegetation height using UAV-borne LiDAR, to describe the complexity of the tidal network crossing the salt marshes. With this goal, we derived a new formulation that converts UAV-based LiDAR point clouds into ground-level elevation and vegetation height. Our formulation has been calibrated

Daniele Pinton, Alberto Canestrellli,Christine Angelini, Benjamin Wilkinson,Peter Ifju and AndrewOrtega (2020)

Estimating the spatial distribution of vegetation height and ground level elevation in a mesotidal salt marsh from UAV LiDAR derived point cloud:

in Massimiliano Alvioli, Ivan Marchesini, Laura Melelli & Peter Guth, eds., Proceedings of the Geomorphometry 2020 Conference, doi:10.30437/GEOMORPHOMETRY2020_33.

from surveyed height data on a 0.26 km^2 *Spartina alterniflora* salt marsh in Little Sapelo Island, Georgia, USA. *S. alterniflora* is the predominant macrophyte in this area [1]. Its stems range from 20 cm to 2 m in height. While short *S. alterniflora* occupies the higher marsh platform with stem heights of 0.20–0.60 m, tall Spartina fills the lower marsh and creek banks with heights up to 2 m. The results were successfully tested on an independent dataset. The determination of more accurate and high-precision vegetation and topographic characteristics will be beneficial for the numerical description of coastal wetlands processes.

II. METHODS

A. Measurements

Field measurements were carried out on the 22nd of November 2019, in conjunction with a UAV-LiDAR survey. The data were acquired during a low tide event to avoid the effects of the tide on the survey.

Twenty-seven Ground Control Points (GCPs) were positioned on the marsh. Their geographic coordinates were measured to verify the accuracy of the acquired LiDAR point cloud. The vertical elevation and geographic position data were collected during a high-precision RTK-GPS survey. Their position was decided to cover the marsh domain homogeneously, allowing a proper verification of the accuracy of the collected LiDAR point cloud. The GCPs were placed 1 m above the ground level to make them visible for the surveying staff and to avoid to be covered by the tall vegetation and high tide.

Sixty-eight 40×40 cm^2 plots were randomly set in the study area, and their geographic coordinates and vertical elevation were surveyed. The spatial distribution of the plots was decided to cover all the marsh domain and to collect homogeneously distributed values in the plausible range of the measured vegetation height (~0.20-2.00 m). Each plot was located in a homogeneous area in terms of elevation and vegetation height. The vegetation height was measured, collecting the length of three *Spartina alterniflora* stems. The minimum, the mean and the maximum values of vegetation height were recorded. To confirm the measured data, we collected RGB images using a field-based tool for measurement, made of: (i) a wooden panel at a 45-degree angle to the ground, (ii) a horizontal-looking Distianert 12 megapixel Trail Camera with 80 m detection range, and a 125° field of view, connected to the panel and (iii) a red background board with a calibration scale [19]. The elevation and position data were collected using an RTK-GPS (Trimble R6 GNSS ±2 cm vertical and ±1 cm maximum horizontal accuracy) in the Universal Traversal Mercator (UTM) WGS84 17N reference system. The elevation data were measured with respect to the WGS84 ellipsoid.

We surveyed the study area with a UAV-borne LiDAR on the 22nd of November 2019, during a low tide event, to minimize the effects of the tide on LiDAR survey. The LiDAR system used to acquire the data employed a Velodyne VLP-16 Puck Lite. This scanner is comprised of 16 beams and acquires 600,000 points per second by including dual returns. The scanner is georeferenced with a Novatel STIM-300 Intertial Measurement Unit and GNSS receiver. The GNSS data were post-processed using a local base station. This local base station data was processed using OPUS (https://www.ngs.noaa.gov/OPUS/) to provide an accurate solution to enable PPK processing. (Post Processed Kinematics). This system is mounted on a DJI M600 airframe, which has an average of 20 minute flight time and is capable of flying pre-programmed waypoint missions. This flight was operated at 40 m altitude with 50 m flight line spacing. The acquired point cloud has an average density of ~500 points/m^2.

To maximize the accuracy in vegetation and ground-level elevation description, the acquired point cloud was filtered by applying two cut-off filters, removing: (i) the points with an elevation higher than 2.50 m above the MSL and lower than 1.20 m below the MSL, that describe the freshwater forest placed at the north-western boundary of the domain and the surface of the Duplin River, respectively and (ii) the points collected outside the study area. Both filters were performed using the CloudCompare software.

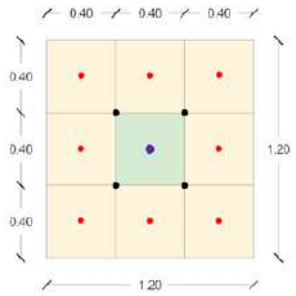

Figure 1. 3×3 cell stencil used in the determination of ground level elevation. The ground-level elevation in the central cell indicated as *(n,e)* was calculated using the eight surrounding yellow cells. The red dots are the minimum elevation values detected in every 0.4×0.4 m^2 cell. The black dots are the values calculated in the fourth step. The blue central dot is the final ground elevation level defined in the stencil.

B. Parameters estimation

Once filtered, LiDAR data were associated with the RTK-GPS data and the vegetation heights surveyed in the marsh, to define possible relations. Sixty-eight smaller point clouds were extracted and analyzed in the neighborhood of each surveyed plot. To calculate the ground-level elevation, the domain area and the LiDAR dataset were divided into 0.40 m × 0.40 m cells, using a 2737×1379 grid, whose gridlines were oriented in the North and East directions. Each cell location was identified by two indexes, (*n)* and (*e)* (north and east). The ground level in the salt marsh domain was calculated considering the local distribution of the minimum elevation values collected by the UAV-based LiDAR in a 3x3 cell stencil centered in *(n,e),* corresponding to a square 1.20x1.20m^2 area (Figure 1). The procedure was implemented based on the following assumption: since over the marsh the gradients in ground elevation are small, cells larger than 0.4x0.4 m^2 have a higher probability that at least one laser beam bypasses the vegetation and reaches the ground, thus reducing the error in estimating the real ground elevation by using the minimum elevation of the point cloud within the cell. The effects of the creeks, the holes, and sometimes the adverse impact stagnant water can have on the reflected laser beam, inevitably decrease the amount of the minimum elevation detected in their proximity using the overlying point cloud. To avoid that, we analyzed the distribution of the elevation values collected with the point cloud, using the following workflow for every *(n,e)* cell.

The algorithm developed to describe the ground-level elevation starting from the collected point cloud is based on the following steps:

1. **STEP 1**: Once the LiDAR dataset was split into *(n,e)* subsets, indicated as $PC_{n,e}$.
2. **STEP 2**: the elevation and the geographic coordinates of the lowest point in each (*n,e)* cell were identified and placed in the cell's centroids (red dots, Figure 1). The minimum elevation value was calculated as:

$$z_{\min,n,e} = min[h_k] \qquad h_k \in PC_{n,e} \tag{1}$$

where h_k is the elevation of the *k* points contained in the $PC_{n,e}$ subset.

3. **STEP 3**: For each (*n,e)* cell, a regression plane was determined using the geographic position of the lowest points detected in its 3×3 cells stencil (red dots in Figure 1). The mean slope of the plane ($S_{n,e}$) and the vertical range of the nine minimum elevation points ($R_{n,e}$) for each stencil were calculated as:

$$S_{n,e} = (|S_n| + |S_e|)/2 \tag{2}$$

$$R_{n,e} = max[z_{\min,i,j}] - min[z_{\min,i,j}] \quad \mathrm{i} = 1,3;\ \mathrm{j} = 1,3 \tag{3}$$

where S_n and S_e are the slope in the two main directions (east and north) of the regression plane of each (*n,e)* cell.

4. **STEP 4**: Two elevation values were attributed to the four vertexes of the central cell (black dots in Figure 1) of the 3×3 stencil. These values correspond to the minimum and the mean z_{min} calculated in the four cells surrounding each vertex. Two additional regression planes were determined from the two calculated datasets. The midpoint elevation of the two planes indicated as $Mean_{zmin,}$ and Min_{zmin} respectively, were calculated and placed in the middle of the 3×3 stencil.
5. **STEP 5**: The cells close to the creeks were identified using a threshold of 0.30 on the slope and 0.30 m on the vertical range, calculated as described at STEP 3. The thresholds were chosen, analyzing the shape of the point cloud in the proximity of the creeks. The ground elevation value ($Z_{G,n,e}$) of the (*n,e)* cells was calculated as follows:

$$\begin{cases} Z_{G,n,e} = Mean_{zmin} & if\ S_{n,e} > 0.30 \cup R_{n,e} > 0.30\ \mathrm{m} \\ Z_{G,n,e} = Min_{zmin} & \text{otherwise} \end{cases} \tag{4}$$

In the proximity of the creeks, $Mean_{zmin}$ was preferred to Min_{zmin}, avoiding the underestimation of the ground level obtained using the mean of the minimum values detected in the 3x3 stencil. In the marsh platform, where the effect of the ground elevation gradients is negligible, Min_{zmin} was preferred to $Mean_{zmin.}$

6. **STEP 6**: A correction on ground level was done as follows:

$$Z_{G,n,e} = min[z_{\min,2,2}] \quad if\ min[z_{\min,2,2}] < z_{min,min} \tag{5}$$

The method allows considering as valid the minimum value detected in the central cell when its elevation is lower than the values obtained using the two regression planes.

7. **STEP 7**: Finally, to remove the effect of the creeks, the $h_{i,j}$ points contained in the cells of the 1.20×1.20 m^2 stencil were shifted using the following procedure, obtaining a modified local point cloud:

$$\begin{cases} h_{i,j} = h_{i,j} + Z_{G,n,e} - z_{\min,i,j} & if\ z_{\min,i,j} < Z_{G,n,e} \\ h_{i,j} = h_{i,j} & if\ z_{\min,i,j} > Z_{G,n,e} \end{cases} \tag{6}$$

The ground level and a modified point cloud in which we removed the effects of high ground-level gradients were obtained, applying the procedure to the salt marsh area. The process was done using a MATLAB based algorithm. Vegetation height was calculated as the difference between the maximum elevation value of the point cloud, and the calculated ground level in the 3x3 cell stencil. The reduction of the error in the estimation of the ground level decreases the error in the calculation of the vegetation height (Figure 2).

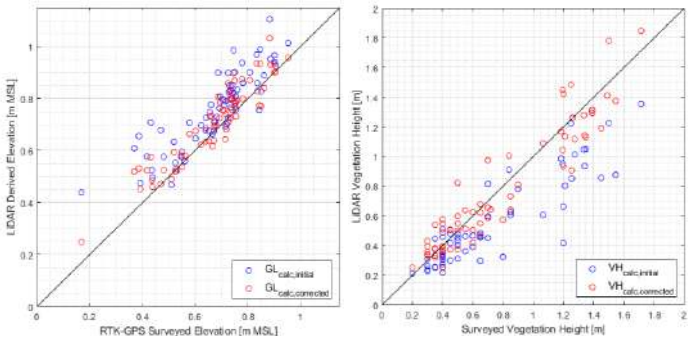

Figure 2. Displacement of ground level elevation (left) and vegetation height (right) Blue and red dots indicate the values obtained before and after the LiDAR correction.

III. RESULTS AND CONCLUSIONS

An accurate description of ground-level elevation and vegetation properties over estuarine wetlands is a crucial and challenging need in the safeguard and restoration of these delicate and useful ecosystems. Here we introduce a new algorithm for an accurate and high-resolution description of salt marshes.

The results showed in Figure 3 demonstrate as our model describes the complex tidal network of the salt marsh, producing high resolution (40×40 cm^2) maps of ground elevation (Figure 3, top-right) and vegetation height (Figure 3, bottom-right), thus capturing the large gradients in the proximity of tidal creeks. As illustrated in Figure 2, the application of our corrective process considerably reduces the error in the ground level estimation. The Mean Absolute Error (MAE) decreased from 8.78 cm to 5.34 cm; the Mean Error passed from -8.2 cm to -3.9 cm; the Maximum Error lowered from 27.7 cm to 15.2 cm. As shown in Figure 2, the correction procedure results essential also to reduce the error in vegetation determination. The Mean Error lowered from 15.3 cm to 1.2 cm, the MAE changed from 18.0 cm to 11.2 cm, and the Maximum Error reduced from 78.3 cm to 34.8 cm. The considerable reduction in the determination errors proved the affordability of the developed algorithm. The performed regression analysis shows the strong relationship between the surveyed vegetation height and the value obtained from the LiDAR point cloud, with an R^2=0.88 and a MAE=1.7 cm. The same agreement was observed between the surveyed ground-level elevation and the value obtained from the LiDAR point cloud, with an R^2=0.87 and a MAE=4.4 cm. The accuracy of the acquired UAV-based LiDAR was verified using the GCPs acquired in the salt marsh using the GPS-RTK system, obtaining a maximum absolute error

of +4.4 cm and a mean absolute error of +2.0 cm, which is in agreement with the ±2 cm of vertical accuracy of the GPS station.

We want to underline as this method does not require additional datasets to perform the identification of the parameters of interest. We would also emphasize that although we have used MATLAB in the all the manipulations related to the LiDAR point cloud, our algorithm is readily reproducible in every similar source code, and does not require any special devices or commercial software. The parameters obtained by the model will then be used as a base for a more efficient description of wetlands modifications using numerical modeling strategies.

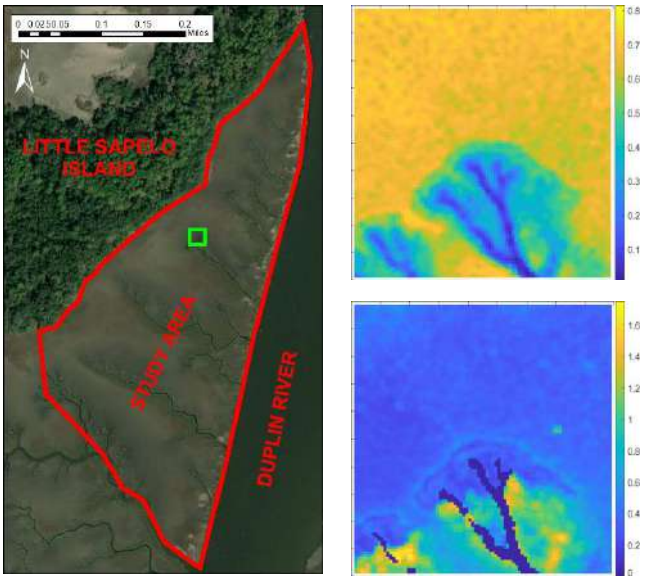

Figure 3. Example of spatial distribution of ground-level (top right) elevation and vegetation height (bottom right) calculated in a 40x40 m^2 area (green square, figure left) contained in the considered salt marsh domain (red polygon, figure left). Both parameters are displayed in meters.

REFERENCES

[1] C. Hladik, J. Schalles, and M. Alber, "Salt marsh elevation and habitat mapping using hyperspectral and LIDAR data," *Remote Sens. Environ.*, vol. 139, pp. 318–330, 2013.

[2] D. F. Boesch and R. E. Turner, "Dependence of fishery species on salt marshes: The role of food and refuge," *Estuaries*, vol. 7, no. 4, pp. 460–468, 1984.

[3] L. Pendleton *et al.*, "Estimating Global 'Blue Carbon' Emissions from Conversion and Degradation of Vegetated Coastal Ecosystems," *PLoS One*, vol. 7, no. 9, 2012.

[4] Barbier E. B., Hacker SD, Kennedy C, Koch EW, Stier AC, and Silliman BR, "The value of estuarine and coastal ecosystem services," *Ecol. Monogr.*, vol. 81, no. 2, pp. 169–193, 2011.

[5] M. Marani, A. D'Alpaos, S. Lanzoni, L. Carniello, and A. Rinaldo, "Biologically-controlled multiple equilibria of tidal landforms and the fate of the Venice lagoon," *Geophys. Res. Lett.*, vol. 34, no. 11, pp. 1–5, 2007.

[6] E. Mcleod, B. Poulter, J. Hinkel, E. Reyes, and R. Salm, "Sea-level rise impact models and environmental conservation: A review of models and their applications," *Ocean Coast. Manag.*, vol. 53, no. 9, pp. 507–517, 2010.

[7] S. Temmerman, G. Govers, S. Wartel, and P. Meire, "Spatial and temporal factors controlling short-term sedimentation in a salt and freshwater tidal marsh, Scheldt estuary, Belgium, SW Netherlands," *Earth Surf. Process. Landforms*, vol. 28, no. 7, pp. 739–755, 2003.

[8] S. Temmerman, T. J. Bouma, G. Govers, Z. B. Wang, M. B. De Vries, and P. M. J. Herman, "Impact of vegetation on flow routing and sedimentation patterns: Three-dimensional modeling for a tidal marsh," *J. Geophys. Res. Earth Surf.*, vol. 110, no. 4, pp. 1–18, 2005.

[9] S. Fagherazzi, 2 , 1 Matthew L. Kirwan, 2, 3 Simon M. Mudd, 4 Glenn R. Guntenspergen, 8 Stijn Temmerman, 5 Andrea D'Alpaos, 6 Johan van de Koppel, 7 John M. Rybczyk, and 10 and Jonathan Clough11 Enrique Reyes, 9 Chris Craft, "Numerical model of salt marsh evolution: ecological, geomorphic, and climatic factors," *Med. sans Front.*, vol. 50, no. 2011, p. 79, 2012.

[10] M. C. Richardson, C. P. J. Mitchell, B. A. Branfireun, and R. K. Kolka, "Analysis of airborne LiDAR surveys to quantify the characteristic morphologies of northern forested wetlands," *J. Geophys. Res. Biogeosciences*, vol. 115, no. 3, pp. 1–16, 2010.

[11] J. E. Moeslund, L. Arge, P. K. Bøcher, B. Nygaard, and J. C. Svenning, "Geographically comprehensive assessment of salt-meadow vegetation-elevation relations using LiDAR," *Wetlands*, vol. 31, no. 3, pp. 471–482, 2011.

[12] J. E. Chassereau, J. M. Bell, and R. Torres, "A comparison of GPS and lidar salt marsh DEMs," *Earth Surf. Process. Landforms*, vol. 36, no. 13, pp. 1770–1775, 2011.

[13] Y. Lin, J. Hyyppä, and A. Jaakkola, "Mini-UAV-borne LIDAR for fine-scale mapping," *IEEE Geosci. Remote Sens. Lett.*, vol. 8, no. 3, pp. 426–430, 2011.

[14] G. Grenzdörffer *et al.*, "UAVs in Agriculture : Perceptions , Prospects , and " Probably Not "," *Int. Arch. Photogramm. Remote Sens. Spat. Inf. Sci.*, vol. 1, pp. 1207–1213, 2008.

[15] M. Uysal *et al.*, "3D Shoreline Mapping Using an Unmanned Aerial Vehicle where," *FIG Congr. 2018*, vol. Conference, 2018.

[16] J. Wang, Z. Liu, H. Yu, and F. Li, "Mapping Spartina alterniflora biomass using LiDAR and hyperspectral data," *Remote Sens.*, vol. 9, no. 6, pp. 1–14, 2017.

[17] R. Wang and J. A. Gamon, "Remote sensing of terrestrial plant biodiversity," *Remote Sens. Environ.*, vol. 231, no. May, 2019.

[18] D. Wang, X. Xin, Q. Shao, M. Brolly, Z. Zhu, and J. Chen, "Modeling aboveground biomass in Hulunber grassland ecosystem by using unmanned aerial vehicle discrete lidar," *Sensors (Switzerland)*, vol. 17, no. 1, pp. 1–19, 2017.

[19] J. F. Schalles, C. M. Hladik, A. A. Lynes, and S. C. Pennings, "Landscape estimates of habitat types, plant biomass, and invertebrate densities in a Georgia salt marsh," *Oceanography*, vol. 26, no. 3, pp. 88–97, 2013.

GEOMORPHOMETRY 2020 PERUGIA, ITALY JUNE 22 - 26 2020

DEM from topographic maps - as good as DEM from LiDAR?

Bartłomiej Szypuła
University of Silesia in Katowice
Faculty of Natural Sciences, Institute of Earth Sciences
Będzińska 60, 41-200 Sosnowiec, Poland
e-mail: bartlomiej.szypula@us.edu.pl

Abstract— **Digital elevation models play a significant role in geomorphological research. For geomorphologists reconstructing landform and drainage structure is frequently as important as elevation accuracy. Consequently, large-scale topographic maps (with contours, height points and watercourses) constitute excellent material for creating models in fine resolution. The purpose of the conducted analyses was to assess the quality of such topo-DEM and comparing it with a reference model derived from laser scanning (LiDAR-DEM). The analysis also involved derivative maps of geomorphometric parameters (local relief, slope, curvature, aspect) generated on the basis of topo-DEM and LiDAR-DEM. Moreover, comparative classification of landforms was carried out. It was indicated that topo-DEM is characterised by good elevation accuracy (RMSE <2 m) and reflects the topography of the analyzed area surprisingly well. For an area of several dozen km^2 topo-DEM with 10×10 m resolution proved more efficient than detailed (1×1 m) LiDAR-DEM.**

I. INTRODUCTION

Digital elevation models are commonly used in earth sciences and play a central role in environmental modelling across a range of spatial scales. There are many freely-available global DEMS (ASTER GDEM, AW3D30, DTED-2, EU-DEM, SRTM), but their quality is not always sufficient for conducted studies. If we talk about the local scale, DEM resolution of 25-30 m is usually too low. Obviously, low spatial resolution of the DEMs affects their low accuracy (horizontal and vertical). For this reason, higher resolution models must be used. As we know, nowadays the most accurate height data for creating high-resolution models are LiDAR data. Unfortunately, they are not always available for all interesting areas, especially if we are interested in comparative analyzes with historical data. Topographic maps come to our rescue, because they are an extremely valuable source of information about the heights and nature of the relief of a given area. Contour lines in combination with height points and water bodies and flows are great material for creating digital elevation models. The main goal of this study was to carry out investigations into the quality assessment of DEM derived from topographic maps (topo-DEM) for geomorphometric purposes. To achieve this goal it was decided to compare the accuracy of topo-DEM with reference to DEM derived from laser scanning (LiDAR-DEM). I tried to answer the questions: What is the vertical accuracy of topo-DEM versus LiDAR-DEM? and Can a topo-DEM produce similar results for geomorphometric analyses to LiDAR-DEM? To answer these questions comparison of elevation differences between a topo-DEM and a LiDAR-DEM were done, calculations of basic geomorphometric parameters and landform classification using Topographic Position Index were conducted.

II. DATA AND METHODS

Data that was used in this study were: topo-DEM and LiDAR-DEM (Fig. 1). topo-DEM was build on the base 4 sheets of the topographic maps in 1:10,000 scale [1]. Altogether, most of the contour lines (circa 750 km) and all 362 points with described altitude were digitized from the maps. I assumed that since the map scale is 10,000, the size of the smallest element on the map is 1x1 mm and in reality it is 10x10 m. So, I was decided to create a topo-DEM with the resolution of 10x10 m. topo-DEM was made in PUWG-1992 (EPSG: 2180) coordinate system, and the heights of points relate to the Normal Height System Kronsztadt 86 [2]. Digitalization, creating topo-DEM, all analyses and calculations, and DEMs visualizations were performed in the ArcGIS environment [3]. I have used the Topo-to-Raster tool from ArcGIS Toolbox to generate topo-DEM. The Topo-to-Raster tool creates hydrologically correct DEMs and is based on the ANUDEM algorithm developed by Hutchinson [4-5]. This method applies an interpolator specifically designed to create a surface that more closely represents a natural drainage surface and better preserves both ridgelines and stream networks from input contour data. Therefore, all the watercourses and water

Bartéomiej Szypula (2020) DEM from topographic maps - as good as DEM from LiDAR?:
in Massimiliano Alvioli, Ivan Marchesini, Laura Melelli & Peter Guth, eds., Proceedings of the Geomorphometry 2020 Conference, doi:10.30437/GEOMORPHOMETRY2020_34.

reservoirs with an area ≥ 500 m^2 were used as breaklines to support the interpolation process. LiDAR-DEM [6] is a DEM derived by Airbone Laser Scanning (ALS) method. This DEM has 1x1 m horizontal resolution, vertical accuracy of 0.2 m [7] and use the same as topo-DEM coordinate system (EPSG: 2180). The LiDAR-DEM was used as reference model.

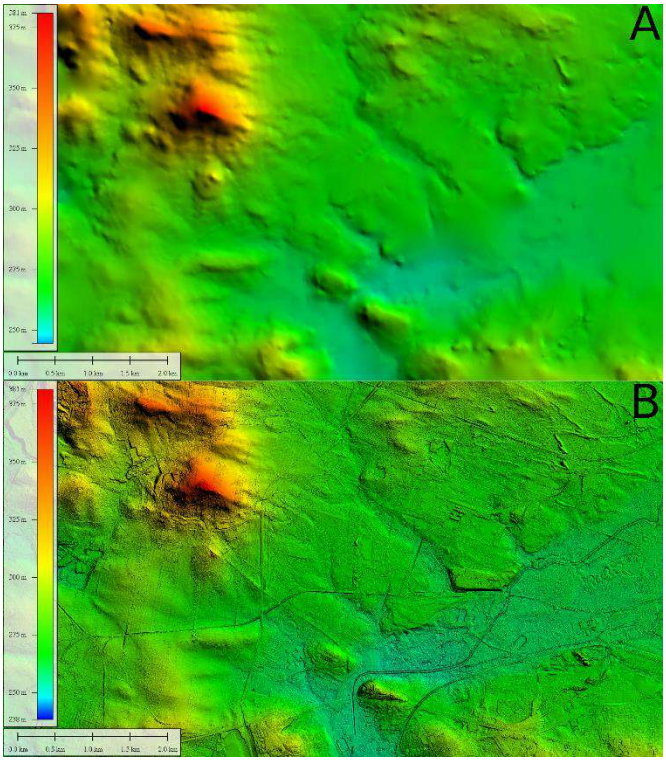

Figure 1. Fragment of the study area - hypsometry map on the base topo-DEM (A) and LiDAR-DEM.

The performed analyses can be divided into few stages:
First, the course of contours generated from the topo-DEM was compared with original contours from topographic maps. Then 100 checkpoints were randomly generated for which elevations read from the topographic map and from the topo-DEM were compared.
Second, reference data were derived by ground surveying with the application of high precision GPS RTK Leica Viva CS10. In total, 149 points for the entire area were measured. Distribution of checkpoints was not very regular because it was related to specific landform types (over 20 checkpoints in each type). Average accuracy of all the GPS RTK surveys was 1cm (horizontal) and 1.3 cm (vertical).

Third, detailed comparative analysis of topo-DEM with LiDAR-DEM was done. In the beginning elevation differences between topo-DEM and LiDAR-DEM were calculated. I used differential elevation map to show spatial distribution of elevational changes between both DEMs. I also used result conformity of elevations between DEMs, proposed by Szypuła [8]. This method consists in comparing both DEMs cell-by-cell and calculating the differences between them; values express how many percent of the first DEM grid cells are in accordance with the same grid cells of second DEM. The last basic geomorphometric parameters were calculated and compared.
Fourth, classification of landforms for both models using the Topographic Position Index [9] was made. TPI method is a classification system based on the difference between a cell elevation value and the average elevation of the neighborhood around that cell. Positive values mean the cell is higher than its surroundings (summit or near the top of a hill or a ridge), while negative values mean it is lower (at or near the bottom of a valley). TPI values near zero could mean either a flat area or a mid-slope area.

III. RESULTS

3.1. topo-DEM versus source topographic maps

All the 10-m contours from the model were generated and compared with the original contours from the topographic maps. The vast majority of the contours generated from the topo-DEM exactly matched the original course of the contours from maps (so, the method has recreated a model with the same characteristics as the original). Next 100 checkpoints were randomly generated, for which elevations from the topographic maps were read and compared with the elevations obtained from the topo-DEM. The differences in the compared elevations ranged from -1.68 to +2.06 m. The values of the MAE and RMSE were < 0.2 m, and SD was 0.4 m, which is a very good outcome.

3.2. topo-DEM versus LiDAR-DEM - elevation differences

The histograms with elevation distribution of both DEMs are similar and show typical right-skewed (positive) distribution. This situation indicates the prevailing number of altitude values below average elevation values. Firstly, vertical accuracy of both DEMs was checked by comparing with GPS RTK measurements (the same locations read from the DEMs and measured in the field). LiDAR-DEM MAE value was only 0.13 m, and RMSE and SD 0.48 m (after checking it appeared that differences exceeding 0.75 m occur only in 4 points). The mean elevation of all checkpoints is also exactly the same as GPS RTK (Tab. 1). topo-DEM MAE value was 0.72 m and RMSE and SD less was 0.97 m. The biggest differences did not exceed 3 m (but only for 2 points). These are quite good results.

Table 1. Elevation differences between GPS RTK measurements and DEMs

DEM	Resolution [m]	Elevation differences [m]					Mean elevation [m a.s.l.]
		Min	Max	MAE	RMSE	SD	
LiDAR -DEM	1.0	-3.7	+3.4	0.13	0.48	0.48	288.2
topo-DEM	10.0	-3.6	+3.1	0.72	0.97	0.97	288.3

Then, elevation differences between topo-DEM and LiDAR-DEM were calculated. LiDAR-DEM was converted to 10x10 m resolution. The accuracies of topo-DEM can be described by maximum elevation differences: -20.48 m and +22.4 m. However, these extremely high values did not affect small MAE (1.16 m), RMSE (1.69 m) and SD (1.83 m) because errors bigger than ±10 m are only 0.34 % of all compared values. Fig. 2 shows spatial distribution of elevational changes between both models. The largest elevation differences occurred in places heavily transformed by man: a sewage treatment plant, a former coal mine or a rubbish dump. These are the areas with the smallest number of height information (the course of the contours was uncertain and often incomplete and there were no height points). Final values of result conformity was calculated for different elevation ranges: ± 0.1 m, 0.25 m, 0.5 m, 1.0 m and 2.0 m. It is interesting that more than 63 % of the study area has result conformity value for the height difference of ± 1m and for more than 86 % of the area it is ± 2 m. It generally shows how accurate topo-DEM is.

*3.3. topo-DEM versus LiDAR-DEM - geomorphometric parameter*s

The following parameters were calculated: altitude, local relief, slopes, curvatures and aspect. Starting with the altitude one has to state that, despite the same resolution (10x10 m), LiDAR-DEM is much more detailed. This concerns elements related to human activity (embankments and road-rail incisions, excavations and dumps, artificial river channels, anthropogenic flats) in particular. The altitude range is very similar (LiDAR-DEM 239.1-381.0 and topo-DEM 244.4-380.8 m a.s.l. see Fig. 1). Maximum, mean and SD values of the altitude are practically the same.

Next, local relief - calculations were made in filter windows (3x3, 10x10 and 25x25 cells) to check how the values are distributed. Results showed that the biggest differences between the models occur for the 3x3 cells neighborhood. This situation confirms much greater detail of LiDAR-DEM compared to topo-DEM. The larger the filtering window (neighborhood) is, the more convergent and similar the results are.

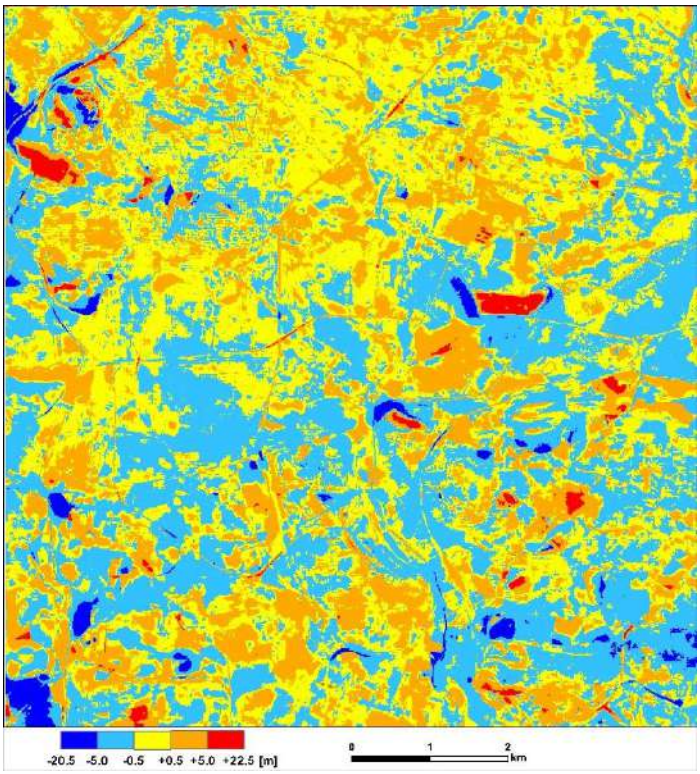

Figure 2. Map of elevational changes between LiDAR-DEM and topo-DEM

The spatial image of the calculated slopes is very similar to the local relief in the 3x3 cells neighborhood. Certainly, LiDAR-DEM showed a lot of small forms (lines of embankments and road incisions) that cannot be seen on topo-DEM. However, the main features of the relief are very clear. Higher maximum slope values occur in LiDAR-DEM but the mean and SD values are more similar.

The situation is different when we look at curvatures. Usually, expected values for an area with moderate relief can vary from -0.5 to +0.5, while for steep and mountainous relief the values can be much higher. In this case, a picture of spatial distribution is much more interesting than the values themselves. The curvature map on the basis of topo-DEM is clear and reflects and highlights characteristic elements of the topography well. Unfortunately, the map based on LiDAR-DEM is practically unreadable due to being too detailed (even though both maps are in the same resolution).

The last analyzed parameter was aspect. The distribution of the aspects, shows that a map derived from topo-DEM is much better for analyzing because the image is more generalized. LiDAR-DEM aspects introduce too much noise, so the picture is not clear.

The analysis of the polar plot and the percentage values for particular directions clearly show that the general quantitative-statistical picture is the same for both DEMs (differences in percentage from 0.3 to 1.7 %).

3.4. topo-DEM versus LiDAR-DEM - landform classification

I was decided to apply 10-class landform classification proposed by Weiss [9] (Fig. 3). In general, spatial distribution of the main landforms is similar. Classification on the basis of the topo-DEM is more balanced, slightly generalized compared to LiDAR-DEM. It seems that better visual effects are given by topo-DEM classification; the image is less overloaded. Although the reality is probably more efficiently reflected by LiDAR-DEM, the reception of the simplified (generalized) image is much better and easier to understand because we focus on dominant elements, avoiding unnecessary details. Moreover, quantitative analysis of landforms showed that results from both models were almost identical (the same statistical image).

IV. CONCLUSIONS

Elevation accuracy of the analyzed topo-DEM in 10x10 m resolution corresponds to the precision of the source topographic maps (1:10,000) with the MAE of 1-2 m and very close as compared with the LiDAR-DEM (MAE 1.16 m, RMSE 1.69 m and SD 1.83 m).

LiDAR-DEM converted to a 10x10 m (downsampling), is great DEM, but it turned out to be too detailed for studies of an area of this size (tens of km^2). This had a particularly adverse effect on maps with slopes, curvatures, aspects and landform classifications. Too much details caused information overload and blurred the spatial image, making maps unreadable. A topo-DEM coped well with the presentation of topography: it emphasized and reflected the most characteristic and dominant relief features. Maps of derived geomorphometric parameters and landform classification showed statistical and spatial distribution of the relief very well. These results confirmed the significance of geomorphological accuracy in geomorphometric analysis.

It should be remembered that topo-DEM is poor at dealing with low-relief areas due to the lack of detailed height information on maps. In these places, the high-resolution or even generalized (downsampled) LiDAR model is invaluable.

The above informations about topo-DEMs may be useful when: a) there is no high-resolution LiDAR DEM for the given area, but there are topographic maps that can be used to create a DEM; b) there is a need to create a DEM of a given area based on historic topographic maps and compare it with the contemporary DEM; c) topo-DEM can be used as reliable data to reduce the errors of freely-available global DEMs.

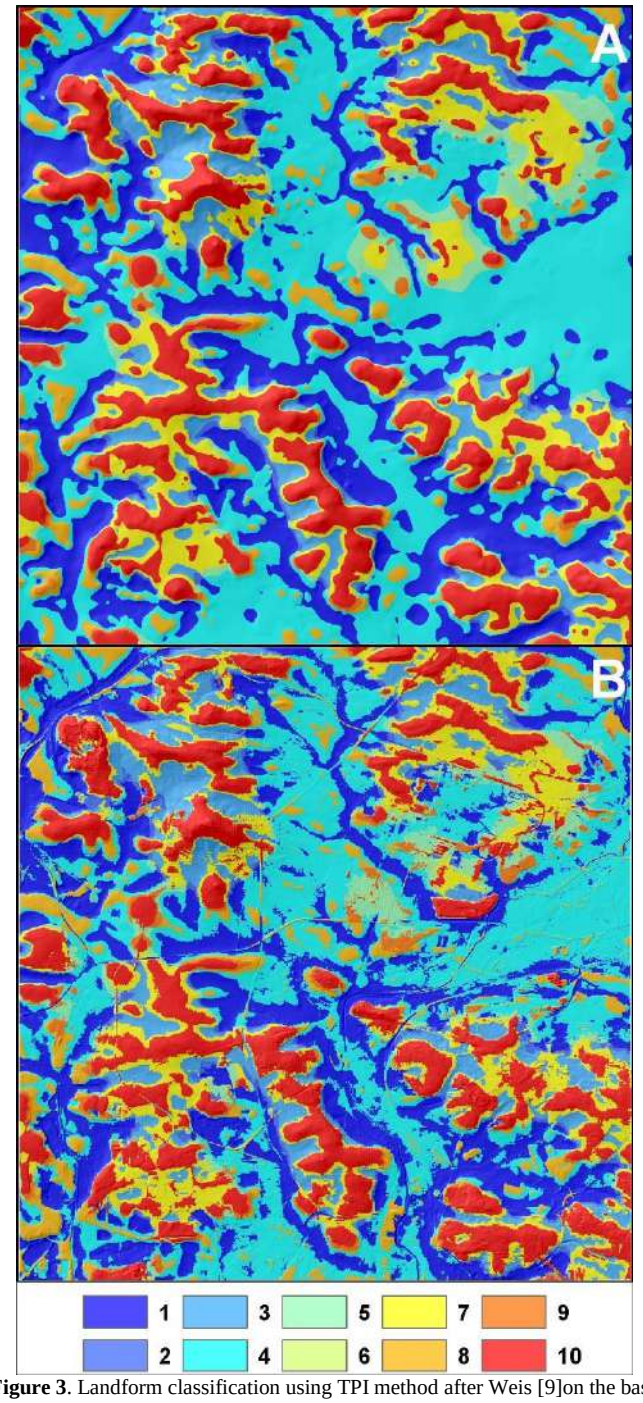

Figure 3. Landform classification using TPI method after Weis [9]on the base topo-DEM (A) and LiDAR-DEM (B): 1 - incised streams, 2 - shallow valleys, 3 – headwaters, 4 - wide valleys and depressions, 5 - small plains, 6 - open slopes, 7 - upper slopes, 8 - local ridges, hills in valleys, 9 - midslope ridges, small hills in plains, 10 - tops, high ridges

REFERENCES

[1] Topographic Map of Poland, 1:10,000, 1993. Sheets: M-34-51-C-c-4, M-34-51-C-d-3, M-34-63-A-a-2, M-34-63-A-b-1. Head Office of Geodesy and Cartography, Warszawa.

[2] Kadaj R.J., 2002. "Polskie układy współrzędnych. Formuły transformacyjne, algorytmy i program". AlgoRes soft, Rzeszów, 52 p (in Polish).

[3] ESRI (Environmental Systems Research Institute), 2017. ArcGIS Desktop: Release 10.5. Redlands, CA.

[4] Hutchinson M.F., 1989. "A new procedure for gridding elevation and stream line data with automatic removal of spurious pits". Journal of Hydrology 106, 211–232.

[5] Hutchinson M.F., 2011. "ANUDEM Version 5.3. User Guide". Fenner School of Environment and Society, Australian National University, 25 p.

[6] Numeryczny model terenu, 2014. Surveyor General of Poland, Warszawa.

[7] CODGiK (Central Office of Geodesy and Cartography), 2015. "Digital elevation data" http://www.codgik.gov.pl/index.php/zasob/numeryczne-dane-wysokosciowe.html

[8] Szypuła B., 2016. Geomorphometric comparison of DEMs built by different interpolation methods. Landform Analysis 32, 45-58.

[9] Weiss A., 2001. "Topographic positions and landforms analysis". ESRI International User Conference. San Diego, CA, 9-13.

GEOMORPHOMETRY 2020
PERUGIA, ITALY
JUNE 22 - 26 2020

Mathematical modelling of long profiles in a tectonically active area: Observations from the DEM-based geomorphometry of the Rangit River, India

Sayantan Das[§1], Lopamudra Roy[1], Arindam Sarkar[2], Somasis Sengupta[3]
[1] *Department of Geography, Dum Dum Motijheel College, Kolkata*
[2] *Department of Geography, P.K.H.N. Mahavidyalaya, Howrah*
[3] *Department of Geography, The University of Burdwan*
[§] sayantdas@gmail.com

Abstract—**The longitudinal profile of a river is one of the most popular indicators for assessing the degree of tectonic and structural control in a fluvial system. Sensitive to long-term tectonic, structural and climatic regimes, long profiles have been employed all over the globe and the anomalies in the long profiles are often been interpreted as evidence of active tectonic deformation. With the advent of high-resolution DEM datasets such as, SRTM, ASTER, etc. many large rivers of the world have been studied and analysed with respect to structure and tectonics. The present study is one such attempt for the Himalayan Rangit River in Eastern India. Physiographically located in the Eastern Himalayan Division of the Himalayas, this river is a small, steep-gradient tributary of the Tista River, debouching its waters into the Tista River near Melli (27°04'47"N, 88°25'56"E). SRTM DEM at 30 m resolution was procured for the area and the drainage network and the watersheds of the major tributaries as well as the trunk stream were extracted using the D8 routine in an ArcGIS environment. The long profiles were smoothened by the 11-point Moving Average method so as to remove all the major artefacts and spikes that may have arisen due to the inherent limitations in the SRTM dataset. This was followed by mathematical modelling of long profiles and estimation of the SL Index. Steep segments in the rivers were identified by normalizing the SL Indices and comparing with the average SL index. Finally, the shape of the long profiles was quantified from the power law regression equation between basin area and channel slope.**

Analysis of the long profiles of the Rangit River and its major tributaries reveals elevated magnitudes of most of the long profile parameters suggesting intense erosional regimes in the rivers. It is a well-known fact that the Himalayas are under active tectonic movement due to continuous collision of the Indian plate with the Eurasian landmass. Therefore, it may be concluded that the anomalous characteristics of the long profiles in the Rangit River and its tributaries may be ascribed to active tectonic deformation.

I. INTRODUCTION

Fluvial systems are characterized by extreme sensitivity of landscape. Any change in the prevailing climatic and tectonic conditions is invariably reflected by the changes in the river morphology and form. These changes are often difficult to comprehend at shorter spatial and temporal scales. Therefore, longitudinal profiles which take into consideration a river from its source to the mouth, is often used as proxies for ascertaining the degree of lithological, structural and tectonic control on the rivers [1,3,7,8,11,13,19]. The shape and form of the longitudinal profile of a river is result of the complex interplay between lithology, structure, tectonics, climate and catchment hydrology [11,14].

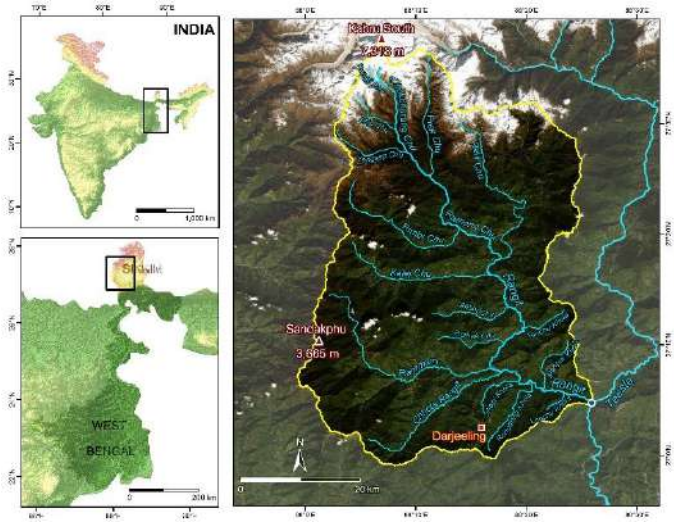

Figure 1. The Rangit Basin (delineated by yellow) along with its principal stream and tributary. The asymmetric basin is characterized by greater number of tributaries on the western side (right bank of the main channel).

Sayantan Das, Lopamudra Roy,Arindam Sarkar and Somasis Sengupta (2020)

Mathematical modelling of long profiles in a tectonically active area: Observations from the DEM-based geomorphometry of the Rangit River, India:

in Massimiliano Alvioli, Ivan Marchesini, Laura Melelli & Peter Guth, eds., Proceedings of the Geomorphometry 2020 Conference, doi:10.30437/GEOMORPHOMETRY2020_35.

Furthermore, the role of climate and hydrological processes on the longitudinal profiles of the rivers has also been investigated [12,20]. Long profiles have also been analysed for understanding the control of lithology [1,2,5], distribution of stream power [16,18], identification of knick zones [9,10].

This paper attempts to understand the river longitudinal profiles by statistical modeling. Also, the longitudinal profile derivatives such as, Stream Gradient Index, Concavity, etc. have been quantitatively determined so as to make a broad generalization of the long profile characteristics for a tectonically active area such as the Himalayas. The present area for study—the Rangit River basin is located in the Eastern Himalayas (~2,150 km^2, Fig. 1) and characterized by its steep-gradient.

II. METHODOLOGY

In all, the longitudinal profiles of 16 major tributaries of the Rangit River as well as the profile of the main channel of the Rangit River in the Eastern Himalayas were extracted and analysed in ArcGIS. For extracting the longitudinal profiles of these streams, the 12.5 m resolution ALOS PALSAR DEM was downloaded from the official website. Since the ALSO PALSAR DEM falls in the category of Ortho-DEM, it was gravitational corrected and imported in the ArcGIS environment. To generate the long profiles of the rivers from SRTM-DEM data, the following procedure was adopted:

The depression-less ALOS PALSAR DEM was subjected to the 'Hydrology' Routine in the ArcGIS software to get the stream segments. These streams were divided into segments of 50 m length. This is in accordance with the resolution of ALOS PALSAR data (12.5m) so as to ensure that the same cell was not extracted for two points. These stream segments were converted into points and only the end points of each segment were extracted to the newly created point file. The elevation of each point along with its x-y coordinates were extracted by the "Feature to DEM" routine of ArcGIS. The data obtained were exported to the Microsoft Excel software for further analysis. Using the distance formula (Eq. 1), the distances of the extracted points from one another was computed.

$$d = \sqrt{(x_2 - x_1)^2 + (y_2 - y_1)^2} \qquad (1)$$

where, d = distance between points x1 and x2, x1 = x-coordinate (in meters) of point x1, y1 = y-coordinate (in meters) of point y1, x2 = x-coordinate of point x2, y2 = y-coordinate of point y2

The distances were then cumulated taking the source as origin (zero) and then the distances of all the points from the source of the river were obtained.

Due to stepping in adjacent elevations and the effect of water bodies (dams) the long profiles derived from DEM are not as smooth and accurate as those produced from other techniques [4,18], especially for low-gradient reaches. In the present study, first the artificial spikes were deleted and smoothing of the long profiles using a 11-elevation points moving average (5 points upstream and 5 points downstream), was carried out. Then the long profiles were obtained by taking the distance on the horizontal axis and elevation on the vertical axis. Further analysis involved the following:

A. Description of the long profile forms:

The form and characteristics of the river long profiles were studied and compared with the concave=up profile of a river under steady-state equilibrium [6,13].

B. Normalized Long Profiles:

There is a possibility that the slight to noteworthy differences in the long profile shapes is because of the difference in basin relief and size (surrogate for power and discharge). Therefore, the long profile length and relief were normalized to minimize the effects of these two variables and highlight the effects of tectonics and/or lithology. The elevations and distances were divided by the head (i.e. maximum basin relief) and the total stream length, respectively to normalize the long profiles [8,15].

C. Mathematical Modeling: Curve Fitting

To describe the form of the long profiles simple linear, logarithmic, exponential and power-law regression models were fitted to the elevation versus distance data in the Rangit River and its tributaries.

The best fit model is one which minimizes the sum of squares of residuals and which also gives the minimum standard deviation of residuals [17]. It is also indicated that when the channel bed grain size is greater than the capacity of the river for transportation, the long profile shows a low degree of concavity and hence a better linear function fit [8]. As the transportation and deposition of channel sediment approaches dynamic equilibrium, the long profile better fits the exponential function. As the system approaches the graded profile, the channel sediment grain size will decrease downstream and hence the long profile fits more suitably for the logarithmic function. With further increase in the profile concavity, the power function becomes more appropriate. Thus, the evolution sequence should be linear--□-- exponential--□--logarithmic--□--power [8]. Therefore, the long profiles of the Rangit River and its tributaries were mathematically modeled.

D. Semi-logarithmic Profiles

Generally, the long profiles of the rivers are plotted on a semi-logarithmic paper in order to neutralize the exponential increase in

the distance from the headwaters [2,13]. A river under graded condition is expected to be in a state of balance between uplift and erosion rate and hence the long profiles of such rivers would plot as a straight line on a semi-logarithmic paper. Such linear plots are generally observed for areas of uniform lithology or under relative tectonic stability. On the other hand, if a river flows through a tectonically active area characterized by uplift exceeding denudation or over resistant rocks, its long profile displays convexity. Therefore, the long profiles of the rivers under consideration were plotted on the semi-logarithmic graph paper with distance on the logarithmic scale.

E. Stream Gradient Index:

The gradient of a graded river usually decreases downstream as the discharge increases, and the longitudinal profile of this river can be often approximated by a straight line on a semi logarithmic plot [6]:

$$H = C - K\ln L \quad (2)$$

Where, H = elevation, L = distance from the source, and C and K are constants. K, the slope of this idealized profile, is called the stream gradient index [6] and can be evaluated by:

$$K = Hi - Hj / \ln Li - In Lj \quad (3)$$

Where, i and j refer to two points along the river profile. The SL Index can be used to characterize a relatively short reach (segment) of the river as well as the entire profile. By comparing the river long profiles to the ideal semi-logarithmic profiles, the significance of anomalous gradients can be evaluated in the context of the discharge increasing downstream.

F. Identification of steep segments/zones:

It is known fact that a segment of the river with anomalously high SL Index has high stream energy corresponding to resistant rock area (control of lithology) or differential uplift zone (control of tectonics) [2,8]. For this purpose, an index called Normalized Stream Gradient Index (NSL) was proposed [13]. The SL Index of each reach or segment of the river isdivided by the idealized gradient index (k), which is the slope of the graded river profile, to obtain the NSL for each reach or segment of the river [13].

Mathematically, the statement can be represented as:

$$NSL = SL / k \quad (4)$$

Where, NSL = Normalized Gradient Index for a given reach or segment, SL = stream gradient index for the given stretch, and k = slope of the idealized Hack's graded profile.

Segments having SL/k $\geqslant$ 2 are regarded as significantly steeper, whereas the reaches with SL/k $\geqslant$ 10 are classified as extremely steeper reaches [13]. These attributes are characteristically associated with the areas undergoing uplift. In the present study, the points characterized by anomalously high SL values were identified using the criterion SL/k $\geqslant$ 10.

G. Long Profile Concavity:

This was derived from the power logarithmic regression relationship between upstream drainage area and channel slope. The upstream drainage area is considered as a proxy for discharge [8,10,16,20]. The relationship that has been used to calculate the long profile concavity and steepness is described below:

$$S = K_s A^{-\theta} \quad (5)$$

Where, S is the channel slope, A is the basin area, θ is the concavity and Ks is the steepness index.

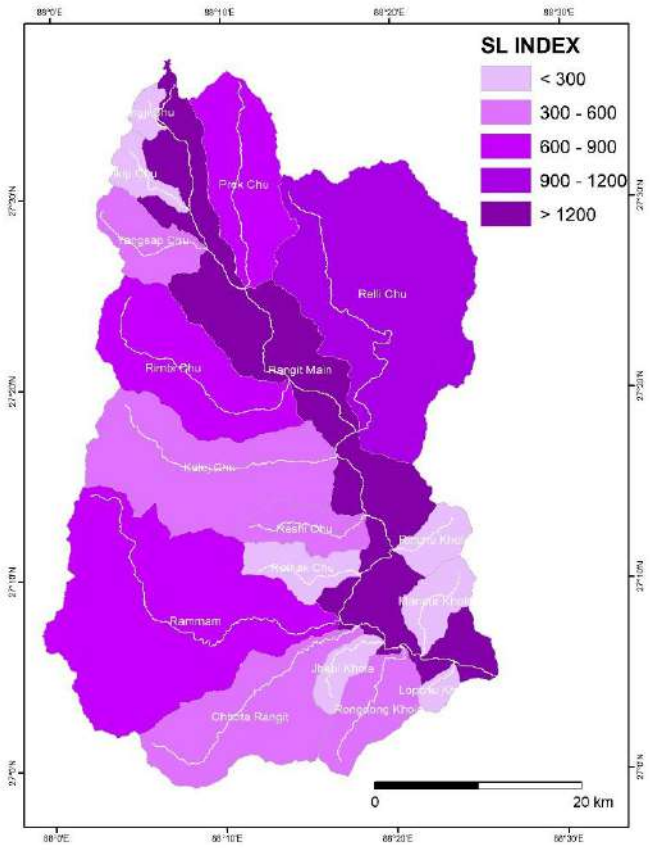

Figure 2. The SL index map of the Rangit Basin. The higher values of SL index imply steep gradients, often associated with the areas undergoing recent tectonic deformations.

III. Results and conclusions

The long profiles reveal that none of the rivers in the Rangit Basin display the typical concave-up profile which one would associate with a river under uniform lithology and long-term tectonic stability. Rather, as expected for a tectonically active region, the long profiles are, more or less, characterized by steep upper segments. Similarly, the semi-logarithmic profiles of the rivers under review do not exhibit the straight line. In fact all the profiles display above-grade conditions suggesting intense erosional regime. Most of the long profiles display the best fit for exponential equation. This means that the system has not yet reached the steady-state and is approaching the condition of dynamic equilibrium with channel bed grain size greater than the capacity of the river for transportation [8]. However, in the upper reach of the river, the tributaries display best fit for linear model which implies that the upper reach of the rivers are characterized by elevated erosion rates.

The stream gradient (SL) indices of the rivers range from 300–1200 which implies tectonic resurgence (Fig. 2). An important observation is that the left bank tributaries displaying higher values of SL index. Furthermore, analysis of the maps displaying the Normalized SL Index (NSL) reveals that a number of steep segments are predominantly concentrated in the upper reach of the Rangit River. Also in the lower reach such steep segments are found. An important characteristic in the lower reach is that there are a number of barbed drainages, an important signature of drainage reorganization due to tectonics.

Finally it can be concluded that geomorphometry can be a very efficient tool in deciphering the morphological adjustments of the rivers due to tectonic and lithology. The Rangit River, located in the Eastern Himalayas, display ample evidence of a river under active tectonic deformation. High values of SL Index supplemented by the right-skewed asymmetry of the river and high SL Indices of the right bank tributaries points out possibilities of the river gaining more are to the right at the cost of left.

References

[1] Begin, Z.B., 1975. “Structural and lithological constraints on stream profiles in the Dead Sea Region, Israel”. J Geol, 83(1), 97-111.

[2] Bishop, P., R.W. Young, I. McDougall, 1985. “Stream profile change and long-term landscape evolution: Early Miocene and Modern rivers of the East Australian Highland Crest, Central New South Wales, Australia”. J Geol, 93(4), 455-474.

[3] Chen, Y.C., Q. Sung, C.N. Chen, J.S. Jean, 2006. “Variations in tectonic activities of the central and south-western foothills, Taiwan, Inferred from river Hack profiles”. Terr. Atmos. Ocean. Sci., 17(3), 563-578.

[4] Das, S., P.P. Patel, S. Sengupta, 2016. “Evaluation of different digital elevation models for analyzing drainage morphometric parameters in a mountainous terrain: a case study of the Supin–Upper Tons Basin, Indian Himalayas”. SpringerPlus, 5(1544), 1-38.

[5] Goldrick, G., P. Bishop, 2007. “Regional analysis of bedrock stream long profiles: Evaluation of Hack’s SL form, and formulation and assessment of an alternative (the DS Form)”. Earth Surf Proc Land., 32(5), 649-671.

[6] Hack, J.T., 1973. “Stream profile analysis and stream-gradient index”. J Res US Geol Surv, 1, 421-429.

[7] Kale, V.S., S. Sengupta, H. Achyuthan, M.K. Jaiswal, 2014. “Tectonic controls upon the Kaveri River drainage, cratonic Peninsular India: Inferences from longitudinal profiles, morphotectonic indices, hanging valleys and fluvial records”. Geomorphology, 227, 153-165.

[8] Lee, C.S., L.L. Tsai, 2009. “A quantitative analysis for geomorphic indices of longitudinal river profile: A case-study of the Choushui River, Central Taiwan”. Environ. Earth Sci., 59, 1549-1558.

[9] Pederson, J.L., C. Tressler, 2012. “Colorado River long-profile, metrics, knickzones and their meaning”, Earth Planet. Sci. Lett., 345-348, 171-179.

[10] Perez-Pena, J.V.P., J.M. Azanon, A. Azor, J. Delgado, F. Gonzalez-Lodeiro, 2009. “Spatial analysis of stream power using GIS: SLk anomaly maps”. Earth Surf Proc Land., 34(1), 16-25.

[11] Rice, S.P., M. Church, 2001. “Longitudinal profiles in simple alluvial systems”. Water Resour. Res., 37(2), 417-426.

[12] Roe, G.H., D.R. Montgomery, B. Hallet, 2002. “Effects of orographic precipitation variations on the concavity of steady-state river profiles”. Geology, 30(2), 143-146.

[13] Seeber, L., V. Gornitz, 1983. “River profiles along the Himalayan arc as indicators of active tectonics”. Tectonophysics, 92(4), 335-337, 341-367.

[14] Shepherd, R.G., 1985. “Regression analysis of river profiles”, J Geol, 93(3), 377-384.

[15] Seidl, M.A., W.E. Dietrich, J.W. Kirchner, 1994. Longitudinal profile development into bedrock: An analysis of Hawaiian Channels, The Journal of Geology, 102(4), 457–474.

[16] Sklar, L.S., W.E. Dietrich, 1998. “River longitudinal profiles and bedrock incision models: Stream power and the influence of sediment supply”. In. Rivers over rock: Fluvial processes in bedrock channels, Geophys Monogr, 107, 237-260.

[17] Snow, R.S., R.L. Slingerland, 1987. “Mathematical modeling of graded river profiles”, J Geol, 95(1), 15-33.

[18] Snyder, N.P., K.X. Whipple, G.E. Tucker, D.J. Merritts, 2000. “Landscape response to tectonic forcing: Digital Elevation Model analysis of stream profiles in the Mendocino triple junction region, northern California”. Geol Soc Am Bull, 112(8), 1250-1263.

[19] Whittaker, A.C., 2012. “How do landscapes record tectonics and climate?” Lithosphere; 4(2), 160–164.

[20] Zaprowski, B.J., F.J. Pazzaglia, E.B. Evenson, 2005. “Climatic influences on profile concavity and river incision”. J Geophys Res, 110, F03004.

GEOMORPHOMETRY 2020
PERUGIA, ITALY
JUNE 22 - 26 2020

Tectonic Geomorphology of West Bangalore by analysing the Chick Tore river basin, Karnataka, India, Using ASTER DEM

Divyalakshmi K.S[1], Yogendra Singh and Biju John
National Institute of Rock Mechanics
Bangalore -560071, India
divyalakshmi.nirm@gmail.com

Abstract- **The study of tectonic geomorphology and morphometry is considered as a valuable tool in active tectonic studies. The present study carry out geomorphologic analysis in an area where a historic earthquake was reported. The study area is a small river (Chick Tore) basin, broadly showing a dendritic pattern, covering an area of 116 km^2 and having four 4th order tributaries. The area is crisscrossed by NW-SE, N-S and NE-SW trending lineaments. For morphometric analysis, the area is demarcated into 43 sub basins. Two pockets of anomalous basin asymmetry are observed southwest of the main trunk of the river. Transverse topography factor indicates that on either side of the NW-SE trending lineament, through which the Chick Tore river is flowing, are deflected on opposite directions. Valley floor width to valley height ratio along the NW-SE and NE-SW trending drainage segments also shows varying values (0.27 to 2.31) however, relatively higher values are observed along the NW-SE trending main trunk close to the junctions where N-S and NE-SW lineaments are crossing. The study observed that the area falls in uniform lithology and ongoing tectonic adjustments along the main NW-SE trending lineament are reflecting as drainage anomalies.**

I. INTRODUCTION

Bangalore city is the fastest growing city and fifth biggest city in India. The city is vulnerable even to average earthquakes, because the buildings of all kinds from mud buildings to RCC (Reinforced Cement Concrete) framed structures are constructed without proper building codes and with increasing population [1]. However, the occurrence of damaging earthquakes in various parts of similar intraplate tectonic settings indicates reactivation of pre-existing structural weaknesses/faults [2]. Indian plate is one of the complexly deformed parts in the world which had also become the source of various devastating earthquakes in the past along the pre-existing zone of weakness. However, the information on historic earthquakes are also lacking in such terrain to determine the long-term activity of the faults. Over the years, studies across the globe indicate that careful geomorphologic analysis can identify potentially active faults even from areas of moderate seismicity [3, 5, 6, 7, 8, 9, 10, 11, 12, 13]. Numerous geomorphic indices are formulated for quantitative assessment of the tectonically active area [3, 4, 6, 14, 15]. The present study is based on the fact that the geomorphology of a terrain indicates an amount of interaction between surficial and tectonic processes and also the control of climatic conditions over them [16]. Thus, the present study deals with the quantitative evaluation of structures falling with in the study area, using the elements of tectonic geomorphology.

II. STUDY AREA

The study area forms NNE- SSW trending Chick Tore basin of 5th order lies in the west of Bangalore, Karnataka (Fig. 1). This area is broadly falling under Seismic zone II of seismic zonation map of India a Low Damage Risk Zone [17]. However, an average earthquake nearby can induce heavy damage as mentioned above. The study area had already experienced an earthquake of intensity V (Ms=5.0) in the year 1916 [17]. The NNE- SSW trending Arkawati River is the major river draining in this area. The present study area is limited to the catchment of NW-SE trending Chick Tore, one of the tributaries of Arkawati River covering ~ 116 km^2.

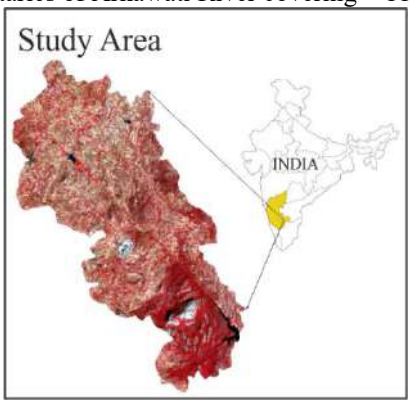

Fig.1 Study area shown as FCC of land sat image.

The general topography of the area shows the elongated hills trending NE-SW in the south eastern part. The area is mostly mid-range relief (1221m to 720 m), and most of the drainages flow along a gentle gradient.

The area regionally exposes rocks belonging to the peninsular Gneissic complex in which Clospet Granite belongs to Lower Proterozoic age. These rock units are intruded by basic dykes, acid dykes, and syenite and carbonatite bodies of Dharmapuri alkali complex of upper Proterozoic age.

The Clospet Granite, pink and grey, is prominently exposed as NNW-SSE trending body varying in width from about 15 km forms the basic rock unit in the study area.

III. METHODOLOGY

The present study extracted of drainages of Chick Tore from ASTER DEM using Hydrology tool of the spatial analysist and further calculated stream orders. The same has been validated with the georeferenced SOI toposheets. The watershed subdivided into 43 sub basins of 2nd and 3rd order streams using the snap pour point. The parameters like basin area, mid line and elevations are calculated using Arc GIS 10.6. The Transverse topographic symmetry factor and Valley floor width to valley height ratio are calculated from the Aster DEM.

IV. ANALYSIS

A] Lineament and drainage network

The NW-SE lineaments are found to be regionally the most persistent features within the study area. The NW-SE trending Chick Tore is also following along one such lineament (Fig.2). Though the main trunk of the river is of 5th order, there are several first order streams joining from south to the main trunk. Several closely spaced first order streams are joining the main trunk from north in the south-eastern side of the main trunk.

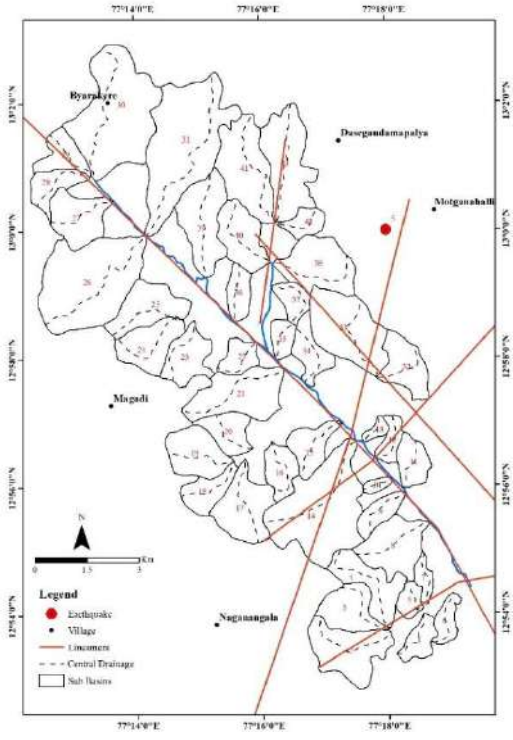

Fig. 2 Drainage basins and lineaments. Cnetral drainages and earthquakes are also shown.

Though most of the drainages joining from southern side of the drainage at right angle (NE-SW) to the main drainage, there are obvious curves towards northwest for many of them before its confluence with the main trunk. On the other hand, drainages joining from north meets the main trunk at an acute angle (N-S). It should be also noted that there are three 4th order and three 3rd order streams joining to the main trunk from south whereas only one fourth order and three 3rd order streams joining from the north to the main trunk. In the NE side of this river another parallel lineament is observed. In addition to that there are some NE-SW and N-S trending lineaments observed in the area appears to be influenced the drainage system.

B] Morphometric studies

Asymmetry Factor (AF), Transverse Topography Symmetry Factor (T) and Valley floor/Valley width ratio (V_f) are the geomorphic indices used in this study to detect the anomalies in the drainage system (Table 1).

Table 1: Formula used for calculating the various geomorphic indices

Indices	Formula	Remarks
Asymmetry Factor (AF)	AF = 100× (Ar/At)	Where, Ar = Right half of area of basin while facing downstream, At = Total area of the basin [14]
Transverse Topography Symmetry Factor (T)	$T=(D_a/D_d)$,	where D_a is the distance from the stream channel to the middle of its drainage basin and D_d is the distance from the midline to the basin divide [6]
Valley floor width to valley height ratio	$V_f = 2V_{fw}/[[E_{ld} - E_{sc}] + [E_{rd} - E_{sc}]$	Where V_{fw} is the width of valley floor, E_{ld} and E_{rd} are the respective elevations of the left and right valley divides, and E_{sc}, is the elevation of the valley floor [3]

B.1] Asymmetry factor

It is originally derived to detect the tectonic tilt of the basin areas [6, 18]. For a stream network flowing in a stable setting and uniform lithology, the AF would be falling close to 50. In all other cases there will be a change in value deviating on either side of 50 depending on the direction of drainage migration [6, 20].

The AF was calculated for all the 43 sub basins demarcated for the morphometric analysis and the value AF ranges from 22 to 78. If we consider a deviation of 10 for this structurally controlled terrain as normal values of AF, then it is observed that only 23 basins are falling in this range and 20 basins show anomalous AF (more than 10 from the perfect value of 50). Out of these 6 basins deviate more than 20 from the perfect value of 50. The highest anomaly basins (deviations more than 20) are observed mostly south of the main trunk of the river that is southern side of the study area. This may indicate that the tectonic disturbance may be more in the southern side of the NW-SE trending lineament.

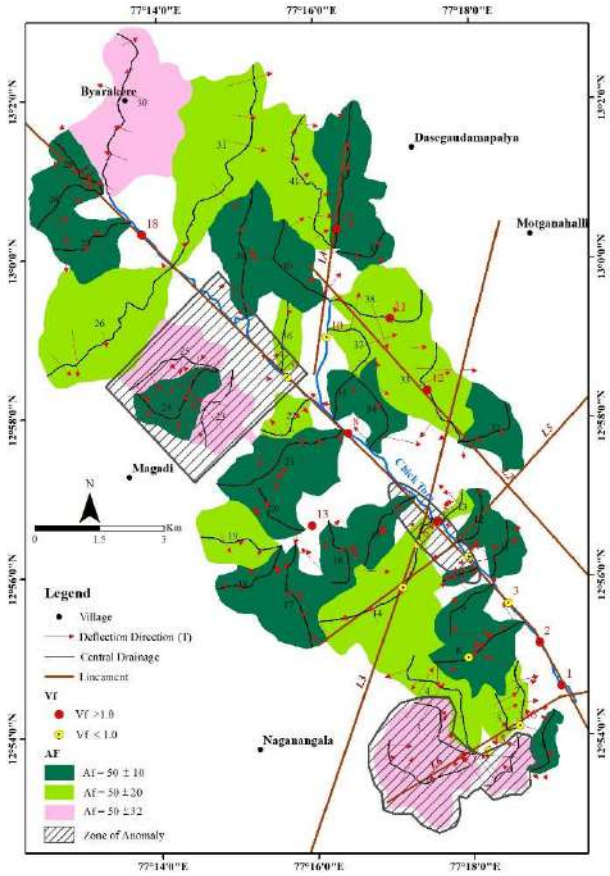

Fig. 3. Details of morphometric studies

B.2] Transverse topographic Symmetry factor (T)

Regional measurements of transverse topographic asymmetry are useful for recognition of several geological process of landscape evolution [19]. Similar studies carried out in the southern Peninsular India identified active faults [20, 21].

In the present study 'T' factor is calculated for the main trunks of all the 43 basins at different reaches. The direction of the arrows indicates the migration direction of the drainage from its original path. Higher the value of ratio, bigger will be the length of the arrow, which may indicate tilting of the terrain or conspicuous shifting of drainage from its original path.

The present analysis indicates that the drainage deflections are low in magnitude close to the main trunk of Chick Tore river though they show a consistent direction towards northwest in the southwestern side. It also indicates that on either side of the NW-SE trending lineament, through which the Chick Tore river is flowing, are deflected on opposite directions. The highly asymmetrical basins (Af) observed in the southern corner of the study area show a converging nature of T factor. The basins north of Magadi too show converging nature of T factor in the highly asymmetric basins. In contrary the T factors in the basin nos. 30 and 31 are diverging. Diverging pattern is also observed in the basins located between two NW-SE trending lineaments. East or north directed T factors are prominent in basins west of the NS trending lineament.

B.3] Valley floor width valley height ratio

Valley floor width - valley height ratio (V_f) is another geomorphic index developed by [3] for quantitative assessment for tectonically influenced geomorphic feature (e.g. SW USA [3, 22], Costa Rica [13], Oregon Coast Range, USA [23], southeast Spain [12], North western Himalaya, [24].

In the present study V_f is calculated at 18 locations across different reaches of the drainage system where the drainages follow straight course or/and following lineaments (table 2). The eight locations measured along the main trunk of Chick Tore river varied between 0.43-2.31. It is interesting to note that the highest value (2.31) of maturity of the river valley is observed at the beginning of the 4th order segment. In the downstream side of the main trunk, the valley appears to be more erosional. The ratio measured along the N-S trending 4th order stream also shows a relatively high value in the upstream side than that of one measured between two NW-SE trending lineaments. In contrary the ratios are very low along NE trending drainages flowing along the lineaments in the southern side of the main trunk.

Table 2: Values for Valley floor Valley Width ratio at different location

Loc.	E ld	E rd (m)	Esc (m)	Floor width (m)	Vf
1	800	810	700	123.31	1.17
2	870	830	720	162.03	1.25
3	1226	861	720	139.41	0.43
4	940	870	740	148.26	0.90
5	940	870	740	273.75	1.66
6	940	860	750	76.80	0.51
7	1126	920	780	109.90	0.45
8	880	900	760	132.68	1.02
9	850	942	780	65.51	0.56
10	977	850	780	97.39	0.73
11	940	920	820	117.88	1.07
12	880	860	800	76.79	1.10
13	1003	953	800	292.84	1.65
14	1126	960	820	122.52	0.55
15	970	925	740	95.73	0.46
16	970	925	740	55.94	0.27
17	965	884	820	147.86	1.41
18	912	979	820	290.08	2.31

V CONCLUSION

Chick Tore is a 5th order river having four 4th order tributaries flowing through uniform lithology (closepet granite). The main trunk of the river is flowing along a NW-SE trending lineament. Though this drainage broadly shows dendritic pattern several first order streams joining to the main trunk. The topographic asymmetries are inferred as selective preferred drainage migration. Morpometric studies identified anomalous values at three zones close to the NW-SE trending lineament as marked in figure 3. The spatial relationship of seismicity and the river valley raises the suspicion that the NW-SE trending valley is fault controlled and that the preferred drainage deflections are the result of local tectonic adjustments. The present study observed that the ongoing tectonic adjustments along the main NW-SE trending lineament are reflecting as drainage anomalies.

Acknowledgement

The ASTER data is down loaded from earth explorer USGS. The authors are thankful to the Director, National Institute of Rock Mechanics for his encouragement and support.

REFERENCE

[1] Sitharam, T.G. and Anbazhagan, P. (2006), 'Seismic Hazard Analyasis for the Bangalore Region'. Natural Hazards (2007) 40:261-278.

[2] Sykes, L.R. (1978), 'Intraplate seismicity, reactivation of preexisting zones of weakness, alkaline magmatism, and other tectonism postdating continental fragmentation', *Review of Geophysics,* **16**, 621–688.

[3] Bull, W. B. and McFadden, L. D. (1977), 'Tectonic geomorphology north and south of the Garlock fault, California. In: D.O. Doehring (Ed.), Geomorphology in arid regions', Publications in Geomorphology, State University of New York and Binghamton, pp 115-138.

[4] Burbank, D. W. and Anderson, R. S. (2001), 'Tectonic Geomorphology', Blackwell Science Publications.

[5] Champel, B., Van der, B. P., Mugnier, J. L. and Leturmy, P. (2002), 'Growth and lateral propagation of fault-related folds in the Siwaliks of western Nepal: Rates, mechanisms, and geomorphic signature', *Journal of Geophysical Research* **107** (2111), 2-1–2-18.

[6] Keller, E. A. and Pinter, N. (1996), 'Active Tectonics', Prentice Hall International (UK) Ltd, London. (6)

[7] Malik, J. N., Sohoni, P. S., Merh, S. S. and Karanth, R.V. (2001), 'Active tectonic control on alluvial fan architecture along the Kachchh Mainland Hill Range, Western India', *Zeithschrift für Geomorphologie* **45** (1), 81–100.

[8] John, B (2018), 'Importance of Geological Studies in Earthquake Hazard Assessment'. In *Integrating Disaster Science and Management: Global Case Studies in Mitigation and Recovery. Elsevier Book* Chapter 2, pp. 27-40.

[9] Riquelmea, R., Martinod, J., Herail, G., Darrozesa, J. and Charrierb, R. (2003), 'A geomorphological approach to determining the Neogene to Recent tectonic deformation in the Coastal Cordillera of northern Chile (Atacama)', *Tectonophysics,* **361**, 255–275.

[10] Schumm, S.A., Dumont, J.F. and Holbrook, M.J. (2002), *Active Tectonics and Alluvial Rivers*. Cambridge University Press, Cambridge, pp. 276.

[11] Seeber, L. and Gornitz, V. (1983), 'River profiles along the Himalayan arc as indicators of active tectonics', *Tectonophysics,* **92**, 335–367.

[12] Silva, P. G., Goy, J. L., Zazo, C. and Bardaji, T. (2003), 'Fault-generated mountain fronts in southeast Spain: geomorphologic assessment of tectonic and seismic activity', Geomorphology, 50, 203–225.

[13] Wells, S. G., Bullard, T. F., Menges, C. M., Drake, P. G., Karas, P. A., Kelson, K. I., Ritter, J. B. and Wesling, J. R. (1988), 'Regional variations in tectonic geomorphology along a segmented convergent plate boundary, Pacific coast of Costa Rica', *Geomorphology* **1**, 239–266.

[14] Keller, E.A. and Pinter, N. (2002), 'Active Tectonics: Earthquakes, Uplift, and Landscape'. Prentice, Hall, New Jersey.

[15] Peters, G. and Van Balen, R.T.,(2007), 'Tectonic geomorphology of the northern Upper Rhine Graben', *Germany. Glob. Planet. Chang,* **58,** 310–334

[16] Bull, W.B., (1991), 'Geomorphic responses to climatic change'. *Oxford University Press, New York,* 326 pp.IS 1893 (Part 1) 2002.

[17] GSI, (2000), Seismotectonic *Atlas of India and its Environs*. GSI Spec. Publ. no. 72.

[18] Hare, P. W. and Gardner, T. W. (1985), 'Geomorphic indicators of vertical neotectonism along converging plate margins, Nicoya Peninsula, Costa Rica'; In *Tectonic Geomorphology* (eds) Morisawa M and Hack J T (Boston: Allen and Unwin), pp. 75–104

[19] Cox, R.T., Van Arsadle, R.B. and Harris, J.B. (2001), 'Identification of possible quaternary deformation in the north eastern Mississipi embayment using quantitative geomorphic analysis of drainage basin assymmnetry', Geolo. Soc. Am. Bull., 113, 615-624. 160

[20] John, B. and Rajendran, C. P. (2008), 'Geomorphic indicators of Neotectonism from the Precambrian terrain of peninsular India: A study from the Bharathapuzha Basin, Kerala', *J. Geol. Soc. India,* **71**, 827–840.

[21] Singh, Y., John, B., Ganapathy G.P., George, A., Harisanth, S., Divyalakshmi, K.S. and Kesavan, S. (2016), 'Geomorphic observations from southwestern terminus of Palghat Gap, South India and their tectonic implications', Journal of Earth System Science 25 (4), 821-839.

[22] Rockwell, T.K., Keller, E.A. and Johnson, D.L. (1984), 'Tectonic geomorphology of alluvial fans and mountain fronts near Ventura, California', In: Morisawa, M., Hack, T.J. (Eds.), Tectonic Geomorphology. Publications in Geomorphology, State University of New York, Binghamton, pp. 183– 207.

[23] Rhea,S.(1993), 'Geomorphic observations of rivers in the Oregon Coast Range From a regional reconnaissance perspective', Geomorphology, 6(2), 135 -150.

[24] Malik J. N. and C. Mohanty. (2007), 'Active tectonic influence on the evolution of drainage and landscape: Geomorphic signatures from frontal and hinterland areas along the Northwestern Himalaya, India'. Journal of Asian Earth Sciences, 29, 604–618.

GEOMORPHOMETRY 2020 PERUGIA, ITALY JUNE 22 - 26 2020

Detecting paleosurface remnants on open access digital elevation models

Bernadett Dobre, István Péter Kovács, Titusz Bugya
Doctoral School of Earth Sciences
University of Pécs
Ifjúság street 6, 7624 Pécs, Hungary
§berneeg@gamma.ttk.pte.hu

Abstract—**Using different openly accessible digital elevation models to classify terrain forms are applied broadly in geomorphometry research. But to use those DEMs properly we must know their capabilities in altering environments. Throughout our research we give a brief overview about the applicability of the openly accessible, 30 meter pixel sizing DEMs in a semi-arid study area. While examining a wide range of digital elevation models (DEMs) we are able to add our novel experiences to widen the current knowledge of DEM relevancies. In our case study we investigate different elevation models with GIS tools and commonly adopted statistics in order to evaluate the possibility to detect peak forms as possible paleosurface remnants. Our research outcome can benefit other related geomorphometric analysis and gives a new approach for paleosurface detection.**

I. Introduction

The possibility of analysing a wide range of open access global or quasi-global digital elevation models gives an outstanding possibility for several research areas such as geomorphology, hydrology and further associated geosciences. Using semi-automated surface recognition on these DEMs we have an opportunity to observe and classify numerous geomorphological forms and features [1, 2]. Our aim was to detect paleosurface remnants and through qualitative and quantitative evaluation find the most appropriate DEM regarding the above mentioned purpose.

1.1. Theoretical background

Due to the recurrent quaternary climate changes the landscape continuously formed related to changing presence of erosion and accumulation. As a result of these recurrent processes various surface remnant had been reserved in altering forms. Usually, older surface remnants can be found as noticeable peaks and summits [3]. The ability of detecting peaks and summits can lead to a more detailed paleogeographical researches.

1.2. Study area

Our study area is located in the the Desatoya Mountains along the border of Churchill and Lander counties in Nevada as a part of the Great Basin. The Great Basin is a semi-arid to arid region, where our study area has an average annual precipitation approx. 250-360 mm/yr, which the majority is falling as snow in the winter months [4].

The landscape of the research area is a mountainous region with steep slopes and valleys and alluvial plains.

1.3. Examined DEMs

In our study we tested four different digital elevation models. The first is a 30 meter resolution DEM, which was derived from open access Lidar points with 6.21 pts/m^2 point density for 61 km^2 area [5]. This model was also used as a validation for the other observed DEMs. We used three different global models to examine the study area: TanDEM-X with 30 meter resolution, SRTM1 v3.0 and ASTER GDEM v3.0. The TanDEM-X dataset was created using X-band SAR instruments and released by the German Aerospace Center (DLR) in 2016 [6]. The other studied interferometric DEM was the SRTM1 model imagined with C-band SAR, released by the collaboration of NASA, NGA, ASI and DLR in 2015 [7, 8]. Finally, we examined the latest version of ASTER GDEM photogrammetric model created by the METI and NASA and released at 2016 [9, 10].

II. Methods

Firstly, the above mentioned Lidar point cloud was downloaded, then Lidar data points we interpolated for a 1 and a 30 meter resolution reference DEM, using regular spline tension interpolation method with the GRASS GIS's default parameters. Descriptive and error statistics for each model were also calculated. The r.geomorphon GRASS module has been run [11], where the core size reflects to the sizes of the searched remnants. Using the module's outcomes, we created histograms to explore possible absence of the paleosurface groups. As a qualitative evaluation we edited maps and surface profiles to aid proper visualization.

2.1. Applied softwares

Throughout the research, GIS data processing was performed in GRASS GIS 7.6.1. [12], while for visualization we both used QGIS 3.4.6. and GRASS GIS 7.6.1. softwares. In order to reference the TanDEM-X heights to the EGM96 geoid we run F477 program provided by NGA [13]. The implementation and presentation of the statistical calculation were carried out in RStudio version 1.2.5033.

Bernadett Dobre, Istvín Pter Kovícs and Titusz Bugya (2020) Detecting paleosurfaces on open access DEMs in semi-arid study area: in Massimiliano Alvioli, Ivan Marchesini, Laura Melelli & Peter Guth, eds., Proceedings of the Geomorphometry 2020 Conference, doi:10.30437/GEOMORPHOMETRY2020_37.

2.2. Descriptive statistics and error measures

To evaluate the vertical accuracy of the DEMs, we created Dem of Differences (DoD) for each of the models and also calculated the following error metrics: RMSE, MAE (1), SD (2) and R^2 [14, 2, 1]. Throughout the calculations the reference DEM was the 30 meter Lidar model.

$$MAE = \frac{1}{n}\sum_{j=1}^{n}|y_j - \hat{y}_j| \quad (1)$$

$$SD = \sqrt{\frac{\sum|x - \bar{x}|^2}{n}} \quad (2)$$

2.3. Semi-automated recognition process

The detection of the paleosurface remnants *r.geomorphon* GRASS GIS module was evaluated [11, 15], which contains ten different surface feature categories. Knowing that our paleosurface interpretation is related to peak/summit forms, we used the summits category. Firstly we used *r.mapcalc* to select the summit category from the r.geomorphon output. Later the *r.thin modul was used* to "skeletonize" the output raster map. Following that we used *r.to.vect* to vectorize the selected areas which were transformed to points with the *v.to.point* function. Finally, we added a new column to the attribute table and refreshed it with the elevation data using *v.what.rast* module. The output text file contains the x and y coordinates and the elevation, therefore it was appropriate to create histograms with various core sizes in order to explore the presence of the different paleosurfaces. Those histograms were clasterized and summarized in the Fig. 1 and Fig. 2.

III. Results and Conclusions

Examining the research outcome, seven distinct groups of possible paleosurfaces were detected. Five of them stand out sharply, while the rest of them can be interpreted as sub-surfaces also. The surfaces related to lower elevation are clearly separated, however the middle of the histogram is quite variant (Fig. 1.). The summits occurring at higher elevations are clearly separable at the same time due to its larger extents and also more eroded (Fig. 2.).

While examining the statistical parameters on Table 1., the TanDEM-X model was proved to be the most accurate considering RMSE, MAE and also R^2 value. The SRTM1 model stands close to the TDX, which could be a result of the same imaging system. The ASTER GDEM came out as the least precise of all.

On Fig. 3. A, the ASTER GDEM showed less precise on lower elevation with numerous misdetection, moreover the number of intersection proved lower compared to any other DEM. The SRTM1 (Fig. 3. B) model had almost twice as much many intersecting point as the ASTER DEM.

The TanDEM-X model (Fig. 3. C) gave the most impressive match with the Lidar model, practically twice as many as the SRTM1.

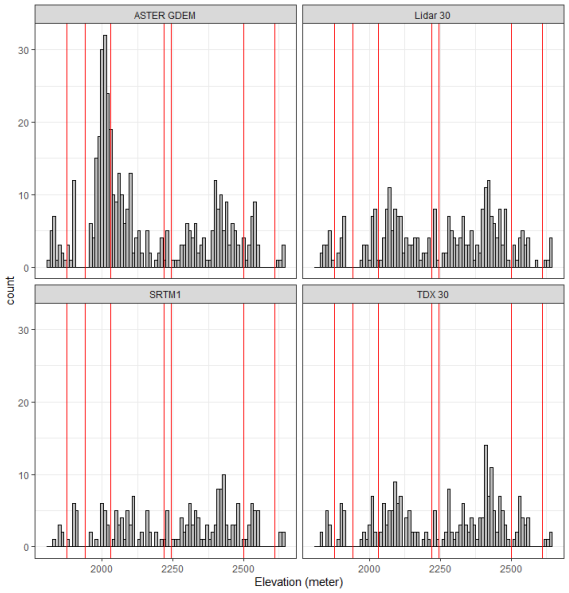

Figure 1. Histogram of each DEM with possible paleosurface remnants (dashed red lines)

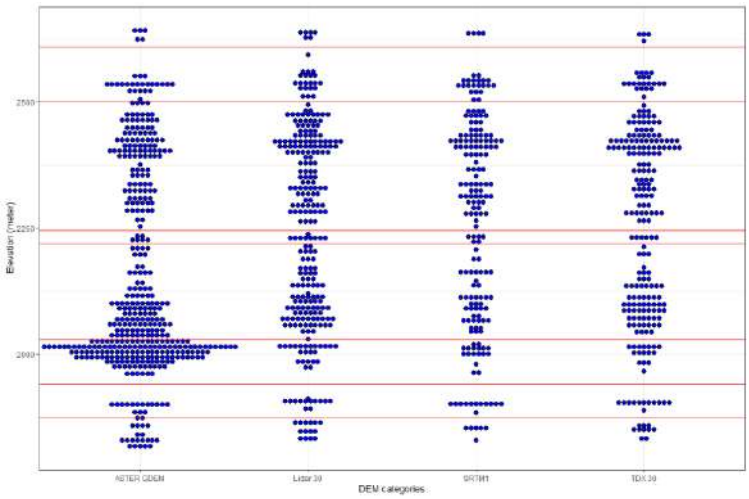

Figure 2. The dot plot of each DEM with the possible paleosurfaces (solid red lines)

Data	Imaging system	Wavelength	Pixel spacing	RMSE	MAE	R^2
SRTM1	SAR-C	5,66 cm	30	4,966	3,599	0,9996
ASTER	OPTICAL	0,52–10,95 µm	30	9,581	6,979	0,9985
TDX30	SAR-X	3,1 cm	30	3,381	2,415	0,9998
Lidar	OPTICAL	1064 nm	30	-	-	1

Table 1. Basic parameters and measure statistical errors of each DEM.

The remnant detection was successful on all of the models, while the TanDEM-X gave the most accurate outcome compared to the Lidar DEM, which was expected knowing its resolution. SRTM1 model proved also accurate enough and quite similar to the TanDEM-X, mostly also by the reason of the similar data acquisition techniques used for DEM creation. On Fig. 3. A, the ASTER GDEM showed less precise on lower elevation with numerous misdetection, moreover the number of intersection proved lower compared to any other DEM. The SRTM1 (Fig. 3. B) model had almost twice as much many intersecting point as the ASTER DEM. The TanDEM-X model (Fig. 3. C) gave the most impressive match with the Lidar model, practically twice as many as the SRTM1.

High number of the remnants can be interpreted as both fluvial and lacustrine erosion, furthermore the frequent tectonics [4] could leave a mark too, but this can only be the conclusion of a later research.

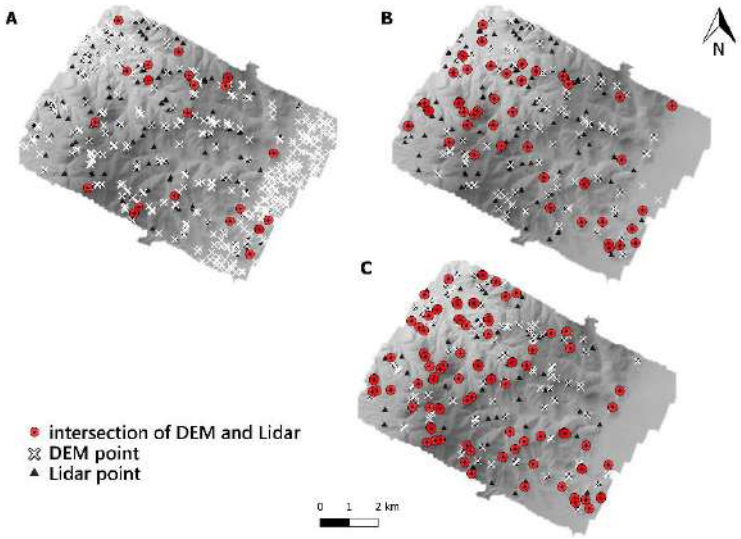

Figure 3. Intersection of DEM points and Lidar points, where A=ASTER GDEM, B=SRTM1, C=TDX

REFERENCES

[1] Sandip Mukherjee, P.K. Joshi, Samadrita Mukherjee, Aniruddha Ghosh, R.D. Garg, Anirban Mukhopadhyay 2013. Evaluation of vertical accuracy of open source Digital Elevation Model (DEM). International Journal of Applied Earth Observation and Geoinformation, 21, 205-217.

[2] Józsa, E., Fábián, S. Á., & Kovács, M. 2014. An evaluation of EU-DEM in comparison with ASTER GDEM, SRTM and contour-based DEMs over the Eastern Mecsek Mountains. Hungarian Geographical Bulletin, 63(4), 401–423.

[3] Bugya, T. 2009. Identification of Quaternary fluvial terraces using borehole data and digital elevation models. Zeitschrift Für Geomorphologie, Supplementary Issues, 53(2), 113–121.

[4] Chambers, Jeanne C.; Miller, Jerry R., eds. 2011. Geomorphology, hydrology, and ecology of Great Basin meadow complexes—implications for management and restoration. Gen. Tech. Rep. RMRS-GTR-258. Fort Collins, CO: U.S. Department of Agriculture, Forest Service, Rocky Mountain Research Station. 125 p.

[5] http://opentopo.sdsc.edu/datasetMetadata?otCollectionID=OT.102016.26911.1

[6] Grohmann, C. H. 2018. Evaluation of TanDEM-X DEMs on selected Brazilian sites: Comparison with SRTM, ASTER GDEM and ALOS AW3D30. Remote Sensing of Environment, 212, 121–133.

[7] Farr, T. G., Rosen, P. A., Caro, E., Crippen, R. E., Duren, R., Hensley, S., … Alsdorf, D. E. 2007. The Shuttle Radar Topography Mission. Reviews of Geophysics, 45(RG2004), 1–33.

[8] Guth, P. L. 2010. Geomorphometric Comparison of ASTER GDEM and SRTM. ISPRS Archives – Geospatial Data and Geovisualization: Environment, Security, and Society, 1–10. Orland

[9] Abrams, M. 2016. ASTER global DEM version 3, and new ASTER Water Body Dataset. ISPRS Annals of Photogrammetry, Remote Sensing and Spatial Information Sciences, 107–110. Prague: Copernicus Publications.

[10] ASTER Global Digital Elevation Map Announcement. 2011. Retrieved March 11, 2019, from https://asterweb.jpl.nasa.gov/gdem.asp

[11] Stepinski, T. F., & Jasiewicz, J. 2011. Geomorphons - a new approach to classification of landforms. In T. Hengl, I. S. Evans, J. P. Wilson, & M. Gould (Eds.), Proceedings of Geomorphometry 2011 pp. 109–112. Redlands: International Society for Geomorphometry.

[12] Hofierka, J., Mitasova, H., & Neteler, M. 2009. Geomorphometry in GRASS GIS. In T. Hengl & H. I. Reuter (Eds.), Geomorphometry: Concepts, Software, Applications. Developments in Soil Science, vol. 33 (pp. 387–410). Amsterdam: Elsevier.

[13] https://earthinfo.nga.mil/GandG/wgs84/gravitymod/egm96egm96.html

[14] Ismail Elkhrachy 2018. Vertical accuracy assessment for SRTM and ASTER Digital Elevation Models: A case study of Najran city, Saudi Arabia. Ain Shams Engineering Journal, 9, 1807-1817.

[15] Michal Veselský, Peter Bandura, Libor Burian, Tatiana Harciníková, and Pavel Bella 2015. Semi-automated recognition of planation surfaces and other flat landforms: a case study from the Aggtelek Karst, Hungary. Open Geosciences, 1, 799-811.

The relationship between Bedrock geometry and soil solum at a regional scale

Javad Khanifar[§], Ataallah Khademalrasoul[§]
Soil Science Department, Faculty of Agriculture
Shahid Chamran University of Ahvaz, Iran
[§] khanifar@yahoo.com; [§] Ataalahsoil@gmail.com

Abstract—**One of the main goals of geomorphometry is to derive the geometry attributes from a topographic surface that can be used as predictive variables in the soil-landscape analysis. In this study, the relationship between geometry attributes of bedrock topography and soil solum in a regional scale was investigated. For this study, seven geometry attributes (slope gradient, slope aspect, plan curvature, profile curvature, cross-sectional curvature, maximum curvature and minimum curvature) of terrain surface (DTM) and bedrock surface (DBM) was calculated. The multivariate adaptive regression splines (MARS) was applied for modeling and Mann-Whitney U test for assessing the statistically differences of the geometry attributes across the groups of DTM and DBM. The results showed that there are remarkable differences between DTM and DBM geometry attributes, especially the slope gradient, profile curvature, maximum curvature and minimum curvature. MARS modeling showed that there is a remarkable difference between the relationships of DTM and DBM geometry attributes and soil solum and the model fitted based on DBM geometry attributes performs better in prediction. In our opinion, the idea of using bedrock topography for geomorphometric modeling of soil properties still needs further investigation, especially in terms of scale issue.**

Keywords— Bedrock topography, Geomorphometry, Soil-landscape analysis, MARS.

I. INTRODUCTION

Topography is the most important pedogenic factor known in a high relief landscape that has a significant influence on the spatial variability of soil properties, especially soil depth, by controlling hydro-geomorphic processes [1, 2]. The relationship between soil and topography can be used to mapping soil patterns of a landscape which this process is called soil-landscape analysis and the development of modern digital techniques such as geomorphometry has led to advances in its methodology [3, 4]. One of the main purposes of geomorphometry analysis is to derive geometry attributes from a digital elevation model (DEM), which can be used as predictive environmental variables in digital soil mapping (DSM) [5]. When the rate of relief in the landscape is reduced, it is often that the ability of geometry attributes to predict soil properties is also diminished, as it becomes much harder to extract topographic information from a DEM. As relief declines, the need for high quality DEM is generally increased, although it is still not accessible in many least developed countries. In a geomorphologic unit such as the plain, because it lacks significant relief, the topography and spatial resolution of DEM will have lower impact on soil-landscape analysis. On the other hand, it seems that in the absence of easy available environmental variables, severe sampling from the soil along with interpolation methods would be an effective method in spatial prediction of the soil properties, which would also require high costs. One idea is that bedrock topography may be used instead of terrain topography for geomorphometric modeling of soil properties. Bedrock is the consolidated solid rock beneath unconsolidated surface materials, such as soil and gravel. The bedrock has been exposed in some areas at earth surface, but in areas it may be more than a thousand meters deep below the surface [6]. Estimating depth to bedrock is an important issue in geophysical science that can be of particular application in many fields of the earth sciences. Depth to bedrock affects energy and water cycles and can be considered as an input parameter for modeling natural hazards such as earthquakes and landslides [7]. This study was conducted to investigate the idea of using bedrock topography for soil-landscape analysis at a regional scale.

II. METHODS

The study was conducted in an area located between the four provinces of Henan, Shandong, Jiangsu and Anhui in western China (114° 05′ to 118° 16′ E and 32° 50′ to 35° 54′ N). The region has an area of 129560 km^2 and the survey of land cover product images (MCD12Q1) of MODIS satellite sensor shows that the major land use of the study area is agricultural. The bedrock elevation map shown in Figure (1) has a spatial resolution of 250 m and is generated from the difference the STRM elevation data and depth to bedrock data that are having same spatial resolution. Depth to bedrock data were obtained from http://globalchange.bnu.edu.cn and details about production and accuracy of this data are discussed in [7]. In this study, it has been

Javad Khanifar and Ataallah Khademalrasoul (2020) The relationship between Bedrock geometry and soil solum at a regional scale:
in Massimiliano Alvioli, Ivan Marchesini, Laura Melelli & Peter Guth, eds., Proceedings of the Geomorphometry 2020 Conference, doi:10.30437/GEOMORPHOMETRY2020_38.

observed that in areas with high DEM value, depth to bedrock value is low. According to Figure (1), the lowest and highest values of bedrock elevation are -354 and 1096 m, respectively, which are around of these two points the highest and lowest depths to bedrock respectively.

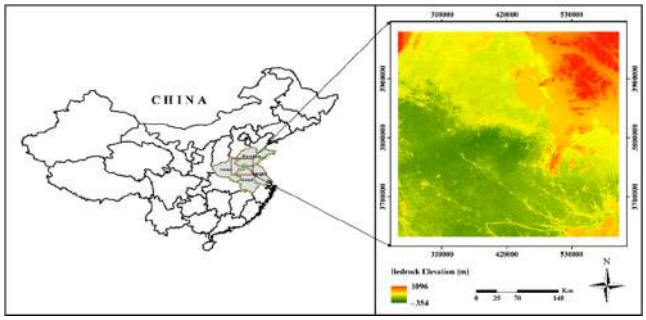

Figure 1. The location of the study area.

Soil solum data used in modeling have been extracted from the ISRIC's global database of soil profiles [8]. Solum is the upper part of the soil profile where soil formation processes are active. Solum in the soil consists of the A, E and B horizons. The activities of soil fauna and flora are largely limited to the solum [9]. In this study, the geometric attributes of slope gradient, slope aspect, plan curvature, profile curvature, cross-sectional curvature, maximum curvature and minimum curvature of DEM raster and bedrock surface raster was calculated in SAGA software (v.7.5.0) by fitting the quadratic function parameters in a locally moving neighborhood analysis window (NAW) (via least squares) as described by Wood (1996) [10]. In this paper, we call the geometry attributes group of the terrain surface and the bedrock surface DTM and DBM, respectively. Mann-Whitney U test was used for assessing the statistically differences of geometry attributes across the groups of DTM and DBM. The Spearman correlation test and the multivariate adaptive regression splines (MARS) were used to investigate the relationship between soil solum and DTM and DBM geometry attributes. MARS is a nonparametric modeling technique developed by Friedman (1991) [11] and can be viewed as generalization of stepwise linear regression or a modification of tree regression (CART) [12].This technique does not impose or consider any underlying assumptions about the functional relationship between explanatory and response variables, and model the nonlinear relationships between these variables by a set of separate piecewise linear segments (splines) of differing gradients (slope). This method divides the space of the explanatory variables into smaller pieces and fits a spline function at each piece, which the breakpoints between the pieces and these functions are called knots and basic functions, respectively [13]. In order to develop an optimal model that has a more accurate estimation, the MARS modeling was performed with different settings including maximum basic function in the first step, maximum degree of interaction between the independent variables and the penalty parameter. Evaluation of the MARS fitted models was performed using k-fold cross validation (k = 10).

III. RESULTS AND CONCLUSIONS

The results of descriptive statistics of the soil solum data are presented in Table (1). The skewness and kurtosis coefficients indicate that the solum property of soil does not have a normal distribution. In geomorphometric modeling of soil properties it is appropriate not to normalize the data because it reduces the effect of hot spots in the modeling. Soil solum has a coefficient of variation (CV) of 80.80 %, which seems that the large extent of the study area and its land use type are the main reason for the increase in CV.

Table 1. Descriptive statistics of Soil Solum Depth (n = 74).

Soil Property	Minimum	Maximum	Mean	Median
Solum Depth (cm)	12.00	150.00	37.80	26.00
	S.D.	**C.V. (%)**	**Skewness**	**Kurtosis**
	30.55	80.80	2.38	5.17

S.D. = Standard deviation. C.V. = Coefficient of Variation

After geomorphometric analysis, the values of each of the DTM and DBM geometry attributes were extracted for the location of the sampling points. The statistical analysis results of the extracted values of geometry attributes are shown in Figure (2) and Table (2). When geometry attributes, especially curvatures, are derived from topographic surface of the bedrock, a relatively wide range of positive and negative values can be observed which indicating a high variability in topographic surface bending among sampling areas. But in the DTM geometry attributes, the values range and hence the bending variability is significantly reduced. Mann-Whitney U test results (table 2) showed that the difference between slope gradient, profile curvature, maximum curvature and minimum curvature was significant across the DTM and DBM geometry attributes.

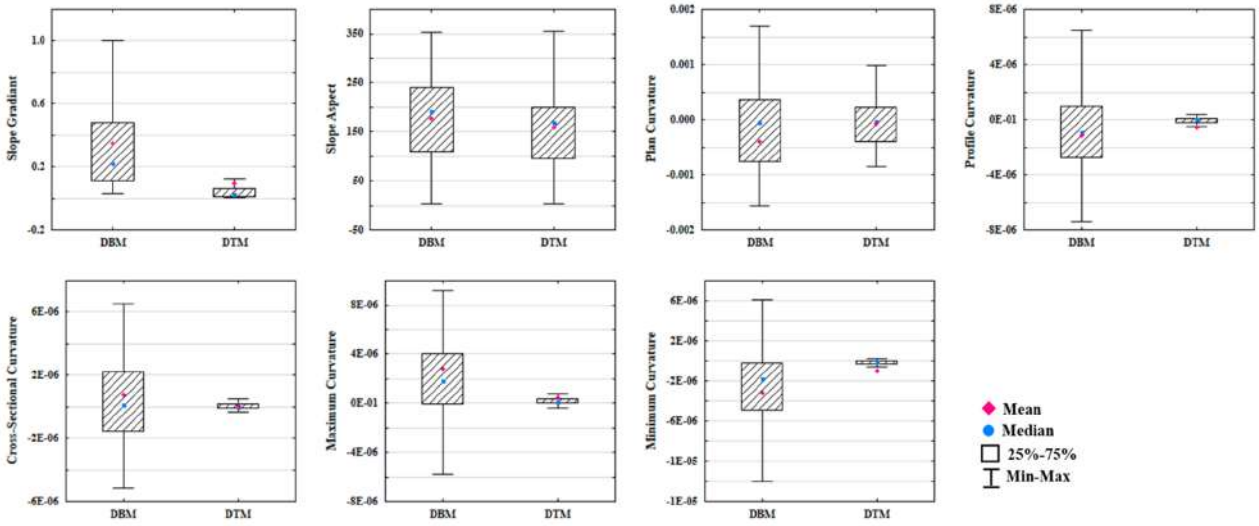

Figure 2. Descriptive statistics of DTM and DBM geometry attributes.

Table 2. Mann-Whitney U Test results used for assess a statistically significant differences between DBM and DTM (n = 2).

Geometry Attributes	Chi-square	df	P-value
Slope Gradient	64.98	1	0.00
Slope Aspect	2.62	1	0.11
Plan Curvature	0.13	1	0.72
Profile Curvature	4.27	1	0.04
Cross-Sectional Curvature	0.19	1	0.66
Maximum Curvature	11.81	1	0.00
Minimum Curvature	18.15	1	0.00

There is a difference between the correlation of DTM and DBM geometry attributes with soil solum. So that none of the DTM geometry attributes have significant correlation with soil solum but the plan curvature (at the 5 % level), cross-sectional curvature and minimum curvature (at the 1 % level) that are derived from bedrock topography have significant correlation with soil solum (table 3).

Table 3. Spearman correlation coefficients among soil depth and geometry attributes of bedrock surface (DBM) and terrain surface (DTM) at the study area (n=74).

DBM	Solum Depth	DTM	Solum Depth
Slope Gradient	-0.155	Slope Gradient	0.219
Slope Aspect	0.022	Slope Aspect	0.172
Plan Curvature	-0.277	Plan Curvature	-0.127
Profile Curvature	0.163	Profile Curvature	-0.1
Cross-Sectional Curvature	0.301	Cross-Sectional Curvature	0.145
Maximum Curvature	0.165	Maximum Curvature	0.187
Minimum Curvature	0.337	Minimum Curvature	-0.146

Correlation is significant at the 0.05 level.
Correlation is significant at the 0.01 level.

The results of soil solum modeling by DTM and DBM geometry attributes using MARS are presented in Table (4). The MARS models based on DTM and DBM were able to justify 31 and 45% of the soil solum depth variations in the study area, respectively, which this may indicate that DBM geometry attributes are better predictors for soil solum. Test results of the fitted MARS models by k-Fold cross validation show that the prediction accuracy of the two models is low, but the DBM-based model performs more accurate than the DTM model. MARS has fitted 5 basic functions based on DBM geometry attributes for soil solum modeling, some of which result from the multiplying of two or three basic functions due to the degree of interaction being set to 3 for modeling. The basic functions and the final formula for calculating the soil solum depth which developed based on DBM geometry attributes are presented in Table (4).

Table 4. Results of modeling between soil solum depth and geometry attributes of bedrock surface (DBM) and terrain surface (DTM) Using MARS.

Model	Learn R-Sq.	Test R-Sq.
DBM	0.45	0.14
DTM	0.31	-0.19

Solum depth model based on DBM :

BF4 = max(0, 0.756769 - SLOPE);
BF9 = max(0, MAXIMUM_CU + 8.98505e-007) * BF4;
BF15 = max(0, SLOPE - 0.460765);
BF18 = max(0, ASPECT - 303.408) * BF9;
BF20 = max(0, ASPECT - 164.834) * BF9;

Solum depth = 35.4004 + 18.071 * BF15 + 1.3763e+006 * BF18 - 101313 * BF20;

The overall results of this study show that there are remarkable differences between DTM and DBM geometry attributes and their relationship with soil solum. Although geometry attributes of bedrock surface are more correlated with soil solum and the MARS model fitted based on them has a higher accuracy in the prediction soil solum, this issue still needs further investigation. Preparing a high spatial resolution bedrock topography map requires specialized tools such as Ground Penetrating Radar (GPR) and is costly, but it is recommended that a fine-scale study be conducted to examine more accurately the relationship between bedrock topography and soil properties in different geoform units.

REFERENCES

[1] Graham, R. C. 2000. "Factors of soil formation: topography". In Certini, G, R. Scalenghe, (Eds). "Soils: Basic concepts and future challenges". Cambridge University Press, pp: 151-163.

[2] Moore, I. D., R. B. Grayson, A. R. Ladson, 1991. "Digital terrain modelling: a review of hydrological, geomorphological, and biological applications". Hydrological processes, 5(1), 3-30.

[3] Gopp, N. V., T. V. Nechaeva, O. A. Savenkov, N. V. Smirnova, V. V. Smirnov, 2017. "The methods of geomorphometry and digital soil mapping for assessing spatial variability in the properties of agro gray soils on a slope". Eurasian soil science, 50(1), 20-29.

[4] Park, S. J., P. L.Vlek, 2002. "Soil-landscape analysis as a tool for sustainable land management". 36(1), 31-49

[5] Pike, R. J., I. S. Evans, T. Hengl, 2009. "Geomorphometry: a brief guide". In Hengle, T., H.I. Reuter (Eds). "Geomorphometry: Concepts, Software, Applications". Elsevier, Amsterdam, pp: 3-30

[6] Shangguan, W., T. Hengl, J. M. de Jesus, H. Yuan, Y. Dai, 2017. "Mapping the global depth to bedrock for land surface modeling". Journal of Advances in Modeling Earth Systems, 9(1), 65-88.

[7] Yan, F., W. Shangguan, J. Zhang, B. Hu, 2020. "Depth-to-bedrock map of China at a spatial resolution of 100 meters". Scientific Data, 7(1), 1-13.

[8] Batjes N.H, E. Ribeiro, A.J.M. van Oostrum, 2019. "Standardised soil profile data for the world (WoSIS snapshot - September 2019)", https://doi.org/10.17027/isric-wdcsoils.20190901.

[9] Patel, S. V., B. A. Golakiya, S. G. Savalia, H. P. Gajera, 2008. "Glossary of Soil Sciences", first ed. International Book Distributing Co.

[10] Wood, J. 1996. "The Geomorphological characterisation of Digital Elevation Models". Diss., Department of Geography, University of Leicester, U.K.

[11] Friedman, J.H., 1991. "Multivariate adaptive regression splines". The Annals of Statistics 19, 1e141.

[12] Hastie, T., R. Tibshirani, J. Friedman, 2009. "The Elements of Statistical Learning: Data Mining, Inference and Prediction", second ed. Springer.

[13] Zhang, W., A. T. Goh, 2016. "Multivariate adaptive regression splines and neural network models for prediction of pile drivability". Geoscience Frontiers, 7(1), 45-52.

GEOMORPHOMETRY 2020
PERUGIA, ITALY
JUNE 22 - 26 2020

4D geometrical and structural analysis of ground ruptures related to 2016 earthquakes in Sibillini mountains (Central Italy)

Marco Menichetti[1§], Daniela Piacentini[1], Emanuela Tirincanti[1], Matteo Roccheggiani[1]
[1]Dipartimento di Scienze Pure e Applicate, Università di Urbino, 61029, Urbino (PU)
[§] marco.menichetti@uniurb.it

Abstract—**3D multi-temporal reconstructions (4D) of the geometries and the kinematics of a portion of the 35 km coseismic surface ruptures related to 2016 Central Italy earthquakes are presented. The analysis integrates a traditional structural field survey with the data extracted from 3D point cloud models. These models were generated using a Structure-from-Motion (SfM) algorithms applied to georeferenced low-altitude aerial digital photos, both zenithal and oblique, acquired with small Unmanned Aerial Vehicles (UAV). Several comparisons were performed between data measured in the field and the same data detected on the point cloud models. The results show errors of a few cms, where models generally overestimate the real data. The coseismic ground ruptures typically show multiple overlapping scarps that can be divided into kinematic sets that occur throughout the width of the pre-existing SW dipping normal fault zones.**

I. INTRODUCTION

A detailed field mapping concerning the spatial geometries of the surface of coseismic ruptures belonging to active faults is the basis for the identification of seismogenic structures and represents an important step toward assessing the recurrence intervals and magnitude of earthquakes [1]. Data of fracture distributions, fault offsets, and links between geometries along the fault strands are the essential tools for extrapolating and constraining the depth of the fault plane from a kinematic point of view. Finally, kinematic fault analysis integrated with geophysical data, allowing to constrain any seismotectonic model.

Earthquakes producing coseismic surface deformation generate offsets in the landforms that are linked to the kinematics and the magnitude of the seismic events. Even though their importance in the seismic hazard assessment and subsequent reduction procedure, the accurate ground rupture morphologies, and their structural geometries remain uncertain. In many cases, the relevant extension of the coseismic ruptures and the morphologically complex landscape required long-time fieldwork to recognize and survey each strand of the fractures [1, 2].

The integration of geological and seismological data remains one of the main objectives for identifying active faults and assessing their potential hazard. While large data sets of instrumental seismological data are easy to gather, especially with modern digital seismic stations, field geological data remain very demanding in terms of human and economic resources, especially in remote areas. However, evolving technologies have allowed remotely sensed data to be used to obtain a lot of equivalent information. A complete and detailed survey of the geometries of coseismic ruptures is central to define the kinematic and the dynamic relationships of active faults and the regional seismic hazard [3].

A significant sequence of earthquakes occurred in the Sibillini mountains in Central Italy from August to October 2016. On August 24th, a Mw 6.1 earthquake struck the southernmost area between the town of Amatrice (Rieti province) and Arquata del Tronto (Ascoli Piceno province) (Fig. 1). Several ground ruptures along different strands of SW dipping extensional faults developed for more than 20 km in the M. Vettore area. The October 26th Mw 6.0 earthquake was centred in the Visso area (Macerata province), approximately 30 km northwest of the previous event. Following this event, only a few coseismic fractures have been surveying because, on October 30th, a new seismic event of Mw 6.5 occurred in the area near Norcia (Perugia province) [4]. This event occurred between the epicentres of the preceding earthquakes. It reactivated existing ground fractures and produced further ruptures over a larger area, including the northernmost sector of the Sibillini mountains, extend from the Tronto river valley in the south to the Chienti river valley in the north, over a distance of about 40 km (Fig. 1) [5, 6].

In this study, results of 3D multi-temporal reconstructions (4D) of the geometries and the kinematics of the coseismic surface ruptures are presented. These were obtained integrating a traditional structural field survey, with the data extracted from 3D point cloud models generated applying a Structure-from-Motion

Marco Menichetti, Daniela Piacentini , Emanuela Tirincanti and Matteo Roccheggiani (2020)
4D geometrical and structural analysis of ground ruptures related to 2016 earthquakes in Sibillini mountains (Central Italy):
in Massimiliano Alvioli, Ivan Marchesini, Laura Melelli & Peter Guth, eds., Proceedings of the Geomorphometry 2020 Conference, doi:10.30437/GEOMORPHOMETRY2020_39.

(SfM) algorithms to digital aerial low altitude photos. These images are a part of a larger dataset of more than 15k 2D zenithal and oblique aerial photos taken along 35 km of coseismic ruptures. This dataset was acquired using a small commercial remotely piloted aircraft, commonly referred as Unmanned Aerial Vehicle (UAV) or drone [6].

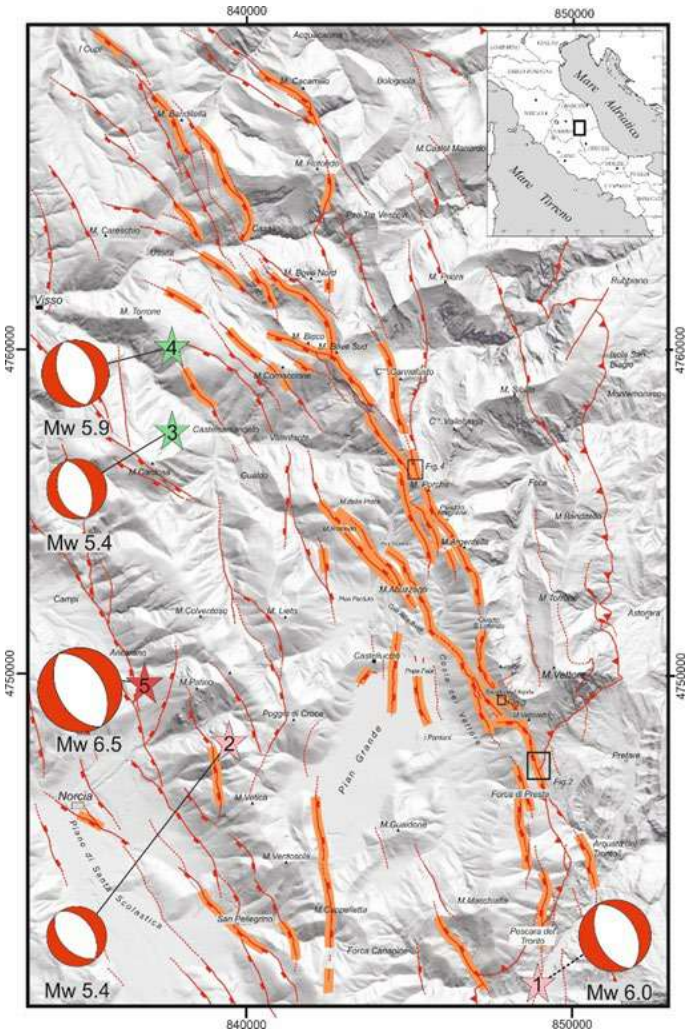

Figure 1. Structural map of the main Plio-Quaternary normal faults (barbs in the hw) and the Mio-Pliocenico Sibillini thrust (triangle in the hw). The seismic ruptures are highlighted in orange and the stars represent the epicenters of main earthquakes. Location of the study area is indicated in the box at the top right.

II. METHODS

The in-field structural survey of the coseismic ruptures consists of acquiring the geometrical parameters, regularly sampled along each rupture strand, needed to define the spatial relationships between vertical and horizontal displacement. Usually in the field, these data are difficult to acquire, not only in the morphological complex and steeply mountain areas, because the apparent offset is normally measured. Moreover, structural analysis, paleoseismological studies, and quantitative geomorphological analysis need high-resolution terrain data (i.e., Digital Elevation Model) to characterize the landscape.

In the last years, a new generation of flying platform systems ready-to-use (i.e., like small UAVs with maximum weight < 25 kg) can acquire georeferenced low-altitude aerial digital photographs, both zenithal and oblique. The spatial camera position and orientation are determined by on board GNSS (Global Navigation Satellite System) units and by IMU (Inertial Measurement Unit) and geotagged on the photos together with other flight parameters.

At the same time, the photogrammetry techniques benefit of the new computer vision algorithms to transform 2D images into 3D topographic surfaces [7]. The Structure-from-Motion (SfM) algorithms are an alternative method of producing topographical data to respect the traditional stereo photogrammetry or airborne and terrestrial LiDAR [8]. The use of the photos limits the use of this technique in the vegetated area and therefore, the digital model of the terrain corresponds to the visible surface (Digital Surface Model - DSM). On the other hand, the possibility of combine oblique and zenithal photos both aerial and terrestrial permits to analyze the point cloud model from a different point of view and detect features otherwise invisible. A consumer-grade camera and the availability of commercial and open-source software where the SfM algorithms are implemented, allow producing accurate and georeferenced 3D points clouds, DSM, and orthomosaic [9]. Before planning a survey, it is necessary to define the required resolution (i.e., the size of the feature be resolved). This latter depends on the Ground Sampling Distance (GSD): pixel distance between two points. GSD is geometrically linked with the acquisition camera parameters (physical size of the sensor, resolution, and focal length) and the flight altitude or the distance from the object.

The accuracy and the precision of the generated points cloud can be improved exploiting the known sizes or the coordinates (X, Y, Z) of the objects visible in the utilized photos. Onboard, a Global Navigation Satellite System (GNSS) gives a decimeter precision, while spatial well-distributed Ground Control Points (GCP), with coordinates known with respect to a referenced system (i.e., UTM – WGS84), guarantee a centimeter accuracy. However, the precision and accuracy are influenced by environmental conditions, including wind, air temperature, and atmospheric moisture that also affect the GNSS receivers [7]. The survey of few km long strips in the steep mountain slopes where the seismic ruptures are localized presents various problems for

georeferencing the model. The use of objects with known size has been preferred respect to position and measure the GCP. The derived point clouds have a good precision (centimeters), and low accuracy (meters) respects the geospatial reference frames. For each 3D cloud model, the possible survey errors, including reprojection and camera location errors are known and consistent with the size of surveyed features [8].

Several checks and comparison were performed between data of offset measured in the field and the same data detected on the point cloud model. The results show errors of a few cm, less 5%, where the model generally overestimates the real data. Finally, the quality of the topographic and geological 3D point clouds can be improved using several techniques including editing, resampling as well as, using different reprocessing methods or filters.

During the second semester of the 2016 and the 2017, along 35 km of coesismic ruptures, we used two commercial quadcopter drones to acquire more than 15k, 2D zenithal and oblique aerial photos. These platforms are equipped with a stabilized camera mount, producing geotagged photos in RAW format, georeferenced through two GNSS units (GPS and GLONASS) located above the camera gimbal. The model DJI Phantom 3 Pro equipped with a Sony sensors Exmor of size of 1/2.3" with a calibrated FOV 94°, 20 mm f/2.8 lens allows photo resolution of 12.76 Mpixel. The model DJI Phantom 4 Pro equipped with a Sony sensors Exmor of size of 1" with a calibrated FOV 84°, 24 mm f/2.8 lens allows photo resolution of 20 Mpixels.

The digital images were processed using Structure from Motion algorithms obtaining eighteen 3D point cloud models with more 10^7 points for each area. These were generated, including DSM and orthomosaics with centimeter resolution (Fig.2).

These point clouds permitted to generate a fully rendered 3D DSM where the geological structures, like faults and fractures and the displacements of several centimeters, can be easily traced and measured. From the microtopography map, features such as small water channels, upper and lower slope angles are easily detected and quantitatively analyzed. The attitude of these discontinuities, expressed by offset, dip direction and dip, was measured using a combination of GIS tools, integrated and verified with the digital field survey checks, and subsequently processed via the traditional geometrical spatial methods using structural statistical tools.

Some areas, especially in the M. Vettore sector (Fig. 3), were surveyed before and after the October 30 event, making possible a 4D kinematic reconstruction of the coseismic ruptures. Comparison of the multi-temporal point clouds in fact permit to define the kinematics of the fault strands for each of the two main earthquake events (Fig. 4).

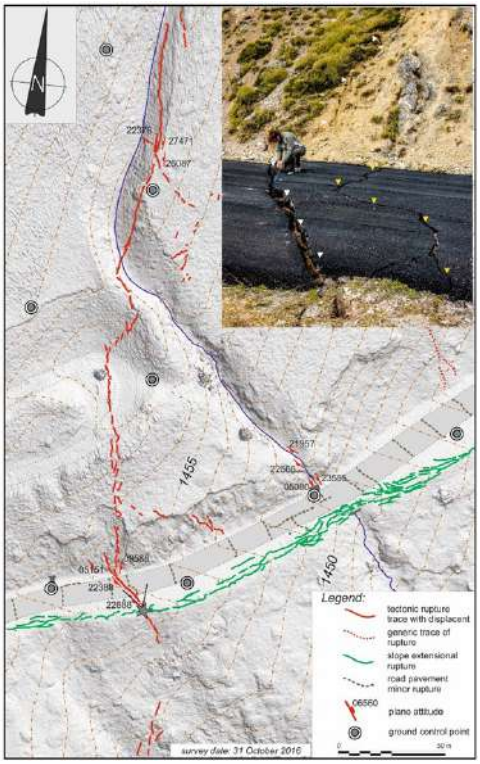

Figure 2. Digital surface model (DSM) with a resolution of 2 cm/pixel, of the SSE slope of M. Vettoretto, along the road SP 477. The contour lines refer to the orthometric height (EGM96 – geoid H 47.251 m). In the photo (taken in the point represented with the grey star) the offset within the road pavement of about 13 cm is observable; the white triangles indicate the coseismic ruptures of the October 30 2016 earthquake, while the yellow triangles indicate the reactivation of the August 24 coseismic ruptures. Location of the area is shown in Fig.1.

Figure 3. Oblique aerial view of the M. Vettore rupture. The arrow indicates a person. Location of the area is shown in Fig.1

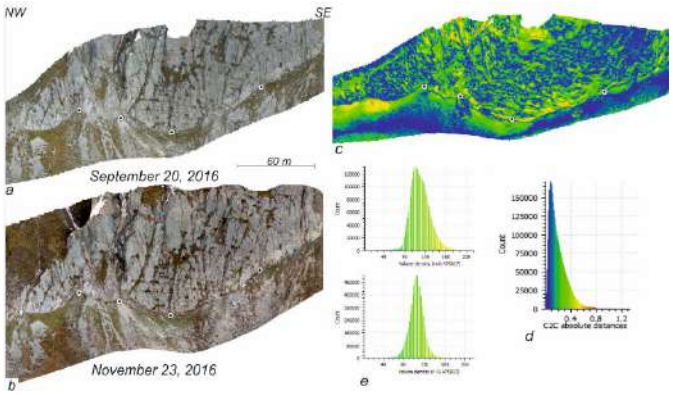

Figure 4. 3D point clouds of a portion of M. Vettore ruptures acquired on September 20, 2016 (a) and on November 23, 2016(b). Dotted circle are the GCP. In (c) the 4D point cloud derived comparing the two dataset. The graphs show the distribution of the absolute distance between the two clouds (d) and the volume density distribution for each point cloud (e). Location of the area is shown in Fig.1.

III. RESULTS AND CONCLUSIONS

The along-strike displacement versus distance of the fault planes and ground ruptures was analyzed along several cross-sections. The surface ruptures generally crossing the already known normal faults. They have a continuous extent of ~35 km and consist of open cracks and vertical dislocations or warps (2 m maximum throw) orientated NW-SE (Fig. 5). At least 12 fault strands SW dipping, with an average angles of 65°, and whose geological offsets are many hundred meters have been surveyed. Four reactivated ground ruptures NE dipping, less steep than the normal fault, and whose geological offsets are few hundred meters have been also observed. Structural relations such as fracture length and distributions, fault offsets, shear zone width, links between geometries along the fault strands provide insight regarding the mechanics of earthquake rupture. These parameters are the input for any seismic-hazard analysis, engineering design criteria, and studies of fault rupture dynamics. The extension and distribution of the coseismic fault slip in the near-surface give insight into the initiation, propagation, and cessation of dynamic ruptures and the structural evolution of the faults. The distribution and internal configuration of the rupture zones often display complex structures comprising two or more anastomosing, synthetic slip-surfaces. Looking in three dimensions, the degree of complexity is seen to vary, and parts of a rupture zone with multiple slip-surfaces can alternate with parts with a single surface. These ruptures typically show multiple overlapping scarps that can be divided into kinematic sets that occur throughout the width of the pre-existing fault zones. The spatial variation records the evolution of the fault zone with more complex structures arising from several processes including a linkage between different rupture segments, which shows to be a common fault growth mechanism.

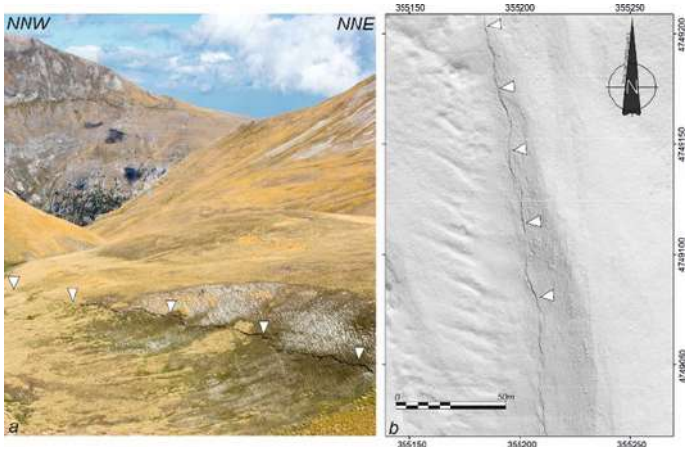

Figure 5. Aerial oblique view of the eastern slope of the M. delle Porche where coseismic ruptures of October 30, 2016 are visible (a) and the DSM (EPSG 32633) of the same area (b). The white triangles represent the shared points between the two images. Location of the area is shown in Fig.1.

REFERENCES

[1] Scholz, C., 2002. "The Mechanics of Earthquakes and Faulting". Cambridge University Press. doi:10.1017/CBO9780511818516.008.

[2] McCalpin J., 2009. "Paleoseismology". International geophysics Elsevier, vol. 95, 613 p.

[3] Menichetti, M., D. Piacentini, F. Troiani, G. Guidotti, A. Napolitano, 2016. "Remote sensing investigation techniques for the analysis of rocky slope stability in remote areas: a test from the Sierra Madre Occidental, Mexico." Rend. Online Soc. Geol. It., 39, 113-116.

[4] Chiaraluce, L., R. Di Stefano, E. Tinti, L. Scognamiglio, M. Michele, E. Casarotti, M. Cattaneo, P. De Gori, C. Chiarabba, G. Monachesi, A. Lombardi, L. Valoroso, D. Latorre, S. Marzorati, 2017. "The 2016 Central Italy seismic sequence: a first look at the mainshocks, aftershocks, and source models". Seismol. Res. Lett., 88(3), 757–771.

[5] Civico, R., S. Pucci, F. Villani, L. Pizzimenti, P.M. De Martini, R. Nappi, R., the Open EMERGEO Working Group, 2018. "Surface ruptures following the 30 October 2016 Mw 6.5 Norcia earthquake, central Italy". Journal of Maps, 14:2, 151-160.

[6] Roccheggiani, M., A. Tamburini, E. Tirincanti, M. Menichetti, 2018. "Automated detection of surface ruptures associated with the 2016 Central Italy earthquake sequence by Sentinel-1 SAR interferometry data". Proceedings of the 9th International INQUA meeting on Paleoseismology, Active Tectonics and Archeoseismology, 229-232.

[7] Carbonneau, P.E., J.T. Dietrich, 2017. "Cost-effective non-metric photogrammetry from consumer-grade sUAS: implications for direct georeferencing of structure from motion photogrammetry". Earth Surf. Process. Landforms, 42, 473– 486.

[8] Turner, D., A. Lucieer, C. Watson, 2012. "An automated technique for generation georectified mosaics from ultra-high resolution Unmanned Aerial Vehicle (UAV) imagery, based on structure from motion (SfM) point clouds". Remote Sens., 4, 1392–1410.

[9] Westoby, M.J., J. Brasington, N.F. Glasser, M.J. Hambrey, J.M. Reynolds, 2012. "Structure-from-Motion' photogrammetry: A low-cost, effective tool for geoscience applications". Geomorphology, 179, 300–314.

GEOMORPHOMETRY 2020 PERUGIA, ITALY JUNE 22 - 26 2020

Geomorphometry helps to distinguish between mountain fronts of various origin (Sowie Mts., SW Poland)

Kacper Jancewicz, Milena Różycka, Mariusz Szymanowski, Piotr Migoń[§]
Institute of Geography and Regional Development, University of Wrocław
pl. Uniwersytecki 1, 50-137 Wrocław, Poland
[§] piotr.migon@uwr.edu.pl

Abstract—**Mountain fronts may have more than one origin and not all of them are necessarily fault-controlled. Their occurrence may also reflect the presence of significant lithological boundary and result from differential erosion. In this study we apply various geomorphometric and geostatistical measures to two mountain fronts in SW Poland in order to check whether they can help to discriminate between fault- versus rock-controlled fronts. The results show that these two mountain fronts differ in terms of the distribution of altitudes, morphometric characteristics of drainage basins and gradient changes along stream profiles, although the discrimination is not as clear-cut as might be expected. However, given homogeneous lithology of the elevated terrain, the hypothesis assuming variable origin of range-bounding fronts receives support.**

I. INTRODUCTION

Many mountain ranges worldwide rise abruptly from the surrounding less elevated terrains, often along approximately straight lines. These topographically distinct marginal zones are called mountain fronts and it is usually implicitly assumed that they owe their origin to uplift of the mountains relative to the foreland and their position indicates the course of an active fault [1,2]. To facilitate comparative analysis of mountain fronts and to assess their state of activity various morphometric measures have been proposed [1] and these are almost routinely used nowadays. However, mountain fronts may have more than one origin. The mountain – piedmont junction may correspond to a lithological boundary and if this is the case, long-term differential erosion produces a topographic escarpment which separates highland terrain in more resistant rock from lowland terrain in weaker formations. Such lithological boundaries may follow ancient fault lines, so that the presence of a fault is not necessarily the evidence of active tectonics.

In this presentation we apply various morphometric and geostatistical measures to two mountain fronts which mark the topographic boundaries of the Sowie Mts. block in SW Poland (Fig. 1). The NE-facing front is of tectonic origin and fault activity has continued into the Quaternary [3], whereas the SW-facing front follows the lithological boundary along an old fault zone inherited from Late Palaeozoic times. Thus, they appear to be of different origin and this may be reflected in different geomorphometric signatures. Consequently, the primary aim of this exercise is to test this hypothesis and to identify opportunities and limits of geomorphometric approach to distinguish between fronts of different origin. Advantageous for this study is the fact that the Sowie Mts. block is built predominantly of gneiss and hence, both marginal zones show similar geology. Thus, the influence of rock factor on geomorphometric properties of the footwall is considerably reduced.

II. METHODS

Mountain fronts were characterized using the following approaches and measures, presented in more detail in the subsequent parts of the paper:

(1) mountain front sinuosity and spacing ratio;

(2) distribution of altitudes in 2 km wide buffer zones extending from the base of a mountain front into the elevated block. This part of the study is based on geostatistical approach and semivariogram analysis to address the structure of variability of altitude;

(3) drainage basin characterization by means of selected morphometric parameters pertinent to shape and relief, commonly applied in morphotectonic studies. The second step involved cluster analysis. In total, 59 drainage basins were subject to analysis, including 32 along the NE front and 27 along the SW one;

(4) analysis of stream longitudinal profiles by means of stream length–gradient index (SL index) [4].

Kacper Jancewicz, Piotr Migon, Wioleta Kotwicka and Milena Rozycka (2020). Geomorphometry helps to distinguish between mountain fronts of various origin (Sowie Mts., SW Poland): in Massimiliano Alvioli, Ivan Marchesini, Laura Melelli & Peter Guth, eds., Proceedings of the Geomorphometry 2020 Conference, doi:10.30437/GEOMORPHOMETRY2020_40.

A LiDAR-based DEM of original 1x1 m resolution was the primary source of data used in this study.

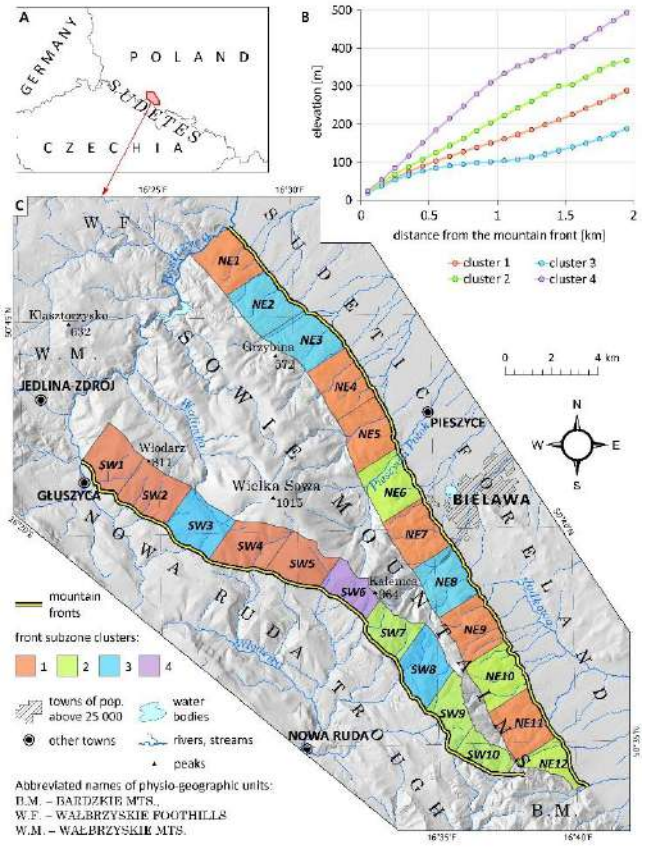

Figure 1. Study area (A), mean semivariograms of altitude (B), subdivision of frontal zones following cluster analysis of semivariograms (C).

III. GEOMORPHOMETRIC CHARACTERISTICS

A. Parameters of mountain fronts

The parameter of sinuosity does not show any evident difference between two opposite mountain fronts. For the NE front, the value obtained is 1.05, whereas slightly higher value of 1.1 was calculated for the SW front. Although in detail the NE front is better approximated by the straight line, no deep indentations and expansions of flat-floored valleys into the mountain mass occur along the SW front either. The mean distance between exit points of individual drainage basins is nearly identical for both mountain fronts, being 0.88 for the NE front and 0.94 for the SW one. By contrast, spacing ratio shows more variability, being nearly twice higher for the NE front (2.81 versus 1.68).

Geostatistical approach to mountain front characterization was based on semivariogram analysis. Semivariance, given as below, is a measure of similarity/dissimilarity of observations (that is DEM grid) as a function of a separating distance [5].

$$\gamma(h) = \frac{1}{2N(h)} \sum_{i=1}^{N(h)} [z(i) - z(i+h)]^2$$

where:

$\gamma(h) - semivariance\ for\ observations\ separated\ by\ distance\ h$
$N(h)$
$- number\ of\ pairs\ of\ observations\ separated\ by\ distance\ h$
$z(i) - altitude\ in\ i\ location$
$z(i+h) - altitude\ in\ i+h\ location$

More than 20 empirical semivariograms, for 2.5 km wide sectors of the front-parallel buffer zone, were prepared for comparative analysis (NE1–12, SW1–10; Fig. 1). Given that the variability in altitude depends not only on distance between observations but also on direction in which the analysis is performed (anisotropy), directional semivariograms, instead of omni-directional ones, were created. To do so, a single direction perpendicular to the mountain front base, in which the highest variability of data is observed, was determined on the basis of semivariogram maps. For each semivariogram constant input parameters, such as lag size (100 m), number of lags (max 20), angular tolerance (45°), bandwidth distance (2 lags) were adopted.

To identify subzones similar in terms of variability in altitude as a function of distance between observations, k-means method for non-hierarchical clustering was implemented. In this approach each subzone was treated as an observation described by a sequence of semivariances calculated for each lag in this subzone. The similarity of observations was quantified using Euclidean metric. Semivariance was re-calculated to relative elevations, to facilitate interpretations. Four clusters were distinguished, including one represented only by one sector (Fig. 1). According to this approach, the entire Sowie Mts. block may be subdivided into two parts. In the north-western part both mountain fronts show similar morphometric characteristics, with particular sectors belonging to clusters 1 and 3, whereas the south-eastern one is more diversified and notably, cluster 1 is not at all represented along the southern section of the SW frontal zone.

B. Drainage basins

Morphometric characteristics of river basins, frequently used in morphotectonic studies, were ascribed to 59 entities (Fig. 2) in order to examine the differences between the units located on the

opposite sites of the Sowie Mts. block. In the first step, the coefficient of variation (CV) for each measure was calculated to identify and eliminate the variables that do not discriminate the observations efficiently (CV < 10%). The degree of correlation between the parameters was assessed by Spearman's correlation coefficient, the application of which was determined by both statistical distribution of the variables examined by Shapiro-Wilk normality test and the presence of the outliers. From each pair of variables characterized by statistically significant rho value the parameter with the higher average degree of correlation with other measures was eliminated. This approach enabled us to reduce the total number of parameters taken into consideration from six to four (circularity ratio – CIRC, drainage basin compactness – COMP, hypsometric integral – HI, mean slope – MEAN_SLO).

To detect the statistical differences in the parameters values between the river basins corresponding to different mountain fronts both, t-test and its non-parametric equivalent (Mann-Whitney-Wilcoxon test) were applied (Table 1). When the homogeneity of variance between two independent groups of observations were violated in the light of Levene's test (p-value < 0.05), the Welch correction were introduced in the former. Statistically significant differences between independent groups were observed for CIRC and HI parameters. In both cases they appear related to different geomorphic histories of both range-bounding fronts. Tectonic activity along the NE front triggers headward erosion, so that streams cut back into the main ridge, shifting the divide westward. In this way, they become more elongated, as reflected in lower values of CIRC. This decreases the size of west-facing catchments and reduces erosional power of streams, resulting in higher values of HI.

Table 1. Statistically significant differences in the parameter values between river basins located on the opposite sites of the Sowie Mts. block.

Parameter	Shapiro-Wilk normality test for independent river basin groups (p-values)		Tests of significance of differences (p-values)
	1 – 32	33 – 59	
CIRC	0.9255	0.1008	t-test 0.0004
COMP	0.3610	0.1256	t-test 0.1381
HI	0.9300	0.0317	Mann-Whitney-Wilcoxon 0.0137
MEAN_SLO	0.1091	0.1388	t-test 0.3740

Test results significant at 0.05 level are in red.
Numbers of river basins according to Fig. 2.

Non-hierarchical multivariate k-means clustering was performed in order to distinguish groups of river basins similar to each other from morphometric perspective (Fig. 2). To determine the optimal number of clusters pseudo *F* statistics [6] was calculated. The differences between three independent groups of observations in terms of morphometric characteristics were then testing statistically with the application of ANOVA and its non-parametric alternative (Kruskal-Wallis test). As all tests results were significant at 0.05 level, multiple pair-wise comparisons between groups were performed in order to identify clusters different one from another. Statistically significant differences were not confirmed only in two out of 12 cases in the light of applied post-hoc tests (Dunn's with Benjamini-Yekutieli correction after Kruskal-Wallis and Tukey HSD after ANOVA with no Welch correction), which underlined morphometric similarities between clusters 2 and 3 and clusters 1 and 3 in terms of circularity ratio and drainage basin compactness, respectively.

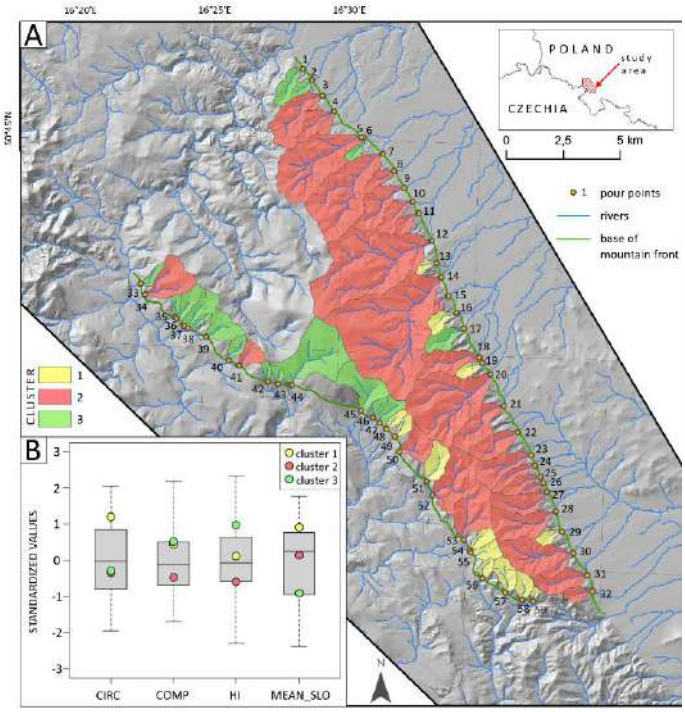

Figure 2. Results of drainage basin analysis: A – spatial pattern, B – statistical distribution of parameters, with dots corresponding to the average values. Note the predominance of cluster 2 along the fault-controlled NE mountain front and much less consistent pattern along the SW front.

C. Longitudinal stream profiles

Stream profiles in the Sowie Mts. used to be analyzed in the neotectonic context in the past [3,7], but based on low-quality elevation data and for the NE front only. Here, SL-index was calculated for 40 m long river sections, with the use of a "downstream moving segment". Index values were ascribed to points (segment mid-points) placed regularly every 10 m along the stream. The SL index was calculated for 40 perennial streams more than 2 km long, crossing the mountain fronts (24 and 16 streams for NE and SW front, respectively). Preliminary results were manually filtered in order to remove points of anthropogenically-induced extreme SL values. Further analysis concerned the change of SL values with the distance from the mountain front. It was based on mean minimum, mean maximum and mean SL values within zones of 100 m interval, generated with use of Euclidean distance from the mountain front line.

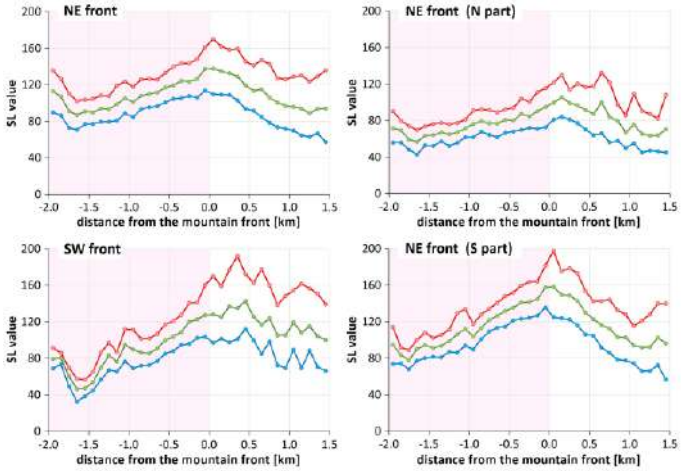

Figure 3. Aggregate downstream change of SL values along the main streams crossing mountain fronts of the Sowie Mts. Block. Explanation of colours: red – mean maximum, green – mean, blue – mean minimum. Data for the NE front were additionally split into the N (drainage basins 1–11, see Fig. 2) and S part (drainage basins 16–32), to highlight the differences within the front.

The results showed certain differences between the opposite fronts. Along the NE-facing front the highest mean SL values are noted at the mountain–piedmont junction and they are more evident in the southern sector, corresponding with higher relief of the entire frontal zone. By contrast, no analogous pattern exists along the SW-facing front and both mean and maximum values continuously rise going downstream, beyond the mountain front.

IV. CONCLUSIONS

Morphometric parameters, both simple and more complex, are often used in morphotectonic analysis [2,8,9]. The novelty of our approach is twofold. First, we applied geomorphometric approach to two opposite fronts of a mountain range, apparently of different origin – one clearly tectonic, another one more complex and significantly controlled by differential erosion. The purpose of this exercise was to explore whether geomorphometric measures will reveal evident differences between the two fronts. Although the differences are not as clear-cut as expected, they nevertheless appear in all three crucial components of this analysis: (a) spatial structure of variability of altitude within the frontal zones; (b) drainage basin characteristics shown by means of cluster analysis; (c) spatial distribution of SL index values across both fronts. Second, we tested geostatistical approach to the whole relief of frontal zones, not very often applied in such context and were able to show differences both within and between mountain fronts. This seems to be a promising avenue of research and will be subject to further inquiry.

This presentation is a contribution to Research Project no. 2015/19/B/ST10/02821, supported by the National Science Centre.

REFERENCES

[1] Bull, W.B., McFadden, L.D., 1977. "Tectonic geomorphology north and south of the Garlock Fault, California". In: Doehring, D.O. (Ed.), Geomorphology in Arid Regions. Proceedings of the 8th Annual Geomorphology Symposium, State University of New York at Binghamton, pp. 115–138.

[2] Bull, W., 2007. "Tectonic Geomorphology of Mountains: A New Approach to Paleoseismology". Blackwell Publishing, Oxford.

[3] Krzyszkowski, D., Migoń, P., Sroka, W., 1995. "Neotectonic Quaternary history of the Sudetic Marginal Fault, SW Poland". Folia Quaternaria 66, 73–98.

[4] Hack, J., 1973. "Stream-profile analysis and stream-gradient index". U.S. Geological Survey Journal of Research 1, 421-429.

[5] Cressie, N.A.C., 1991. "Statistics for spatial data". New York, Wiley.

[6] Caliński, T., J. Harabasz, 1974. "A dendrite method for cluster analysis". Communications in Statistics 3, 1-27.

[7] Krzyszkowski, D., Olejnik, W., 1998. "The role of neotectonics in the Quaternary evolution of the landscape of the Sowie Mts, Sudetes, southwestern Poland". Geologia Sudetica 31, 221–239.

[8] Ferraris, F., Firpo, M., Pazzaglia, F.J., 2012. "DEM analyses and morphotectonic interpretation: The Plio-Quaternary evolution of the eastern Ligurian Alps, Italy". Geomorphology 149–150, 27–40.

[9] Pérez-Peña, J.V., Azor, A., Azañón, J. M., Keller E. A., 2010. "Active tectonics in the Sierra Nevada (Betic Cordillera, SE Spain): Insights from geomorphic indexes and drainage pattern analysis". Geomorphology 119, 74–87.

GEOMORPHOMETRY 2020 PERUGIA, ITALY JUNE 22 - 26 2020

Geomorphometric characteristics of the high mountains in North Macedonia

Ivica Milevski[§], Bojana Aleksova[1], Sonja Lepitkova[2]
[1]Institute of Geography, Faculty of Sciences, Gazi Baba bb, 1000 Skopje, North Macedonia
[2]UGD, Faculty of Natural and Technical Sciences, Stip
[§] ivica@pmf.ukim.mk

Abstract— **As a result of powerful local and regional geotectonic movements, the landscape of North Macedonia (25,713 km^2) has a typical chequerboard topography with frequent changes of mountains and depressions. There are 38 mountain ranges, of which 13 extending above 2000 m are defined as high, while the highest - Korab, reach 2753 m. Because of their geomorphological and overall significance, geomorphometric features of these 13 dominant high mountain ranges are analyzed in this work. The data are calculated from a previously prepared 15-m DEM with particular attention to hypsometry, slope gradient, aspect, and curvature. Based on these variables, a simple classification of the high mountain ranges is made.**

I. INTRODUCTION

As uplifting morphostructures mountains are the predominant elements of the landscape in North Macedonia. The highest mountain massifs are mostly found in the western and central parts (Fig. 1); there are only two from 13 mountains above 2000 m in eastern parts of the country: Osogovo (2252 m) and Belasica (2029 m). According to a peak altitude of the mountains in the Balkan Peninsula, mountains in North Macedonia are divided into three groups: high mountains (2000-2753 m) with a subgroup of very high mountains (2500-2753 m), medium-high mountains (1000-2000 m) and low mountains (below 1000 m). The lowest altitude limit for a mountain is set to 700 m of absolute elevation and 500 m of relative altitude [1]. Because of the geotectonic setting, mountains in western and central parts (in the West-Macedonian zone, the Pelagonian massif, and the Vardar Zone) have a general NW-SE direction. In contrast, in the eastern part of the country, they are E-W elongated (because of the predominant N-S extensional regime). Mountains in the west and central part are generally composed of marbles (Jakupica, Suva Gora), lime-stones (Bistra, Jablanica, Galičica, Šara), granites (Pelister) or other compact rocks. For reasons, these mountains have usually narrow, sharp ridges and peaks and deeply incised valleys. Mountains in the eastern part of the country, are dominantly composed of erodible crystalline rocks (schists) and, consequently, show a more subdued relief, rounded ridges, and peaks, and less deeply incised valleys. However, both groups of mountains were shaped during the Neogene–Pleistocene [2].

All of the above differences are well reflected in the mountain morphology, which can be seen in their geomorphometry as well. In this regard, Milevski [3, 4] perform the first morphometric analysis of the mountain ranges in North Macedonia, based on 3"SRTM DEM.

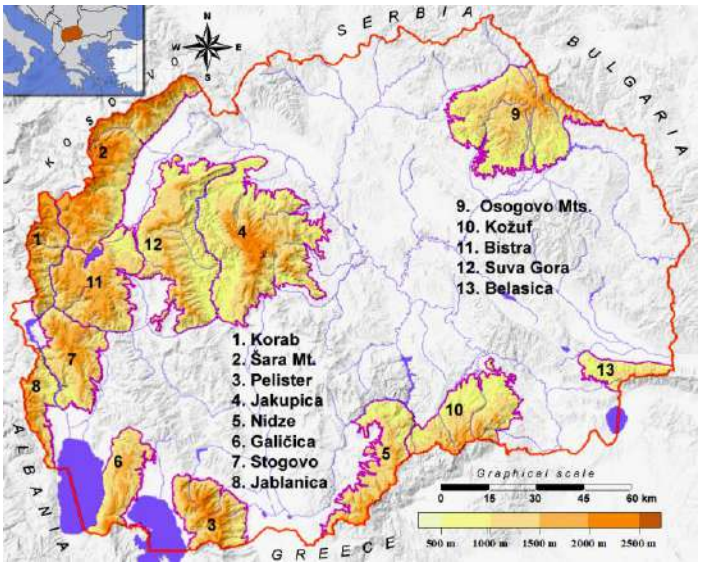

Figure 1. Geographic position of the high mountain ranges in North Macedonia

II. METHODOLOGY

In this work, geomorphometrical analyses of the high mountains in Macedonia are further improved and based on much more accurate 15-m DEM of the State Agency of Cadaster of North Macedonia. According to our tests, this model has a very good average horizontal and vertical accuracy of +/- 1.3 m, with maximum errors up to +/-4 m [5, 6]. Mountain range borders are vectorized manually with a combination of hypsometric criteria (following characteristic contours) and morphologic criteria

Ivica Milevski, Bojana Aleksova and Sonja Lepitkova (2020) Geomorphometric characteristics of the high mountains in North Macedonia: in Massimiliano Alvioli, Ivan Marchesini, Laura Melelli & Peter Guth, eds., Proceedings of the Geomorphometry 2020 Conference, doi:10.30437/GEOMORPHOMETRY2020_41.

(tracking clearly expressed morphological boundaries). However, it was a difficult and subjective task as the mountains in some parts gradually pass through hilly terrain to plains and valleys. After this, mountain extents are clipped from the 15-m DEM and processed to further calculations performed mostly in SAGA GIS software.

III. RESULTS

According to the data in Table 1, Šara Mt. has the highest mean altitude of 1610 m, followed by Korab with 1573 m, while the third is Pelister with 1477 m. With 1384 m, Bistra Mountain is the fourth immediately after Pelister (Baba Mountain), although by peak altitude (2163 m) it ranks eleventh. That is because of a significant area in the 1500-2000 m zone, with a large karst planation surface and few karst poljes on it. The mean altitude of all analyzed mountain ranges is 1257 m, which is 427 m more than the mean altitude (829 m) of North Macedonia [2].

Table 1. Basic morphometric features of the high mountains in North Macedonia including altitudes of the highest (Hmax) peak, average altitude (Hav), slope and area (A) of each mountain range.

	Mountain	Hmax m	Hav m	Slope °	A km^2
1	Korab	2753	1573	25.3	289.5
2	Šara Mt.	2748	1610	22.9	828.6
3	Pelister	2601	1477	23.4	396.6
4	Jakupica	2540	1127	22.1	1272.7
5	Nidže	2520	1190	22.2	460.0
6	Galičica	2288	1289	18.3	346.3
7	Stogovo	2268	1345	21.4	458.0
8	Jablanica	2256	1319	21.7	207.6
9	Osogovo Mt.	2252	1072	21.3	981.0
10	Kožuf	2165	1056	21.2	543.9
11	Bistra	2163	1384	20.8	643.7
12	Suva Gora	2061	1072	21.8	923.4
13	Belasica	2029	830	23.5	167.5
	Average	**2357**	**1257**	**22.0**	**578.4**

The data for the mean slopes show that Korab, Šara Mountain, and Pelister have the highest values (from 25.3° to 22.9°). The reasons are steep mountainsides (fault slopes), deeply incised river valleys, sharp ridges and peaks on the top shaped with strong glacial erosion during Pleistocene [7, 8]. Jakupica (22.1°) and Suva Gora (21.8°) have lower values because of large karst plains on it. Galičica Mountain have has the lowest value for mean slope (only 18.3°), due to the large karst plains with few karst poljes and uvalas. Bistra Mountain (20.8°) has an almost identical situation, but here mountainsides are almost vertically incised by the Radika Canyon, resulting in a higher mean slope [9]. Overall, the average slope gradient of the high mountains in North Macedonia is 22°, well above the average slope of the whole country of 15.1° [2].

As Figure 2 shows, the curves of mean slope against altitude are irregular, with frequent indents (representing planation surfaces and terraces) and maxima (representing steep slopes, escarpments, and sides of sharp peaks and ridges). Usually, the steepest average gradients are below 1000 m of altitude as a result of steep slopes and deeply incised valleys, as well as in the highest parts on the ridge and peak sides [4].

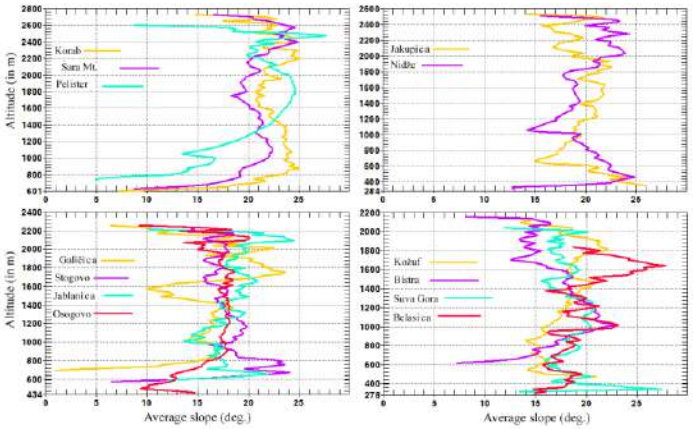

Figure 2. Average slopes against altitude of each high-mountain range in North Macedonia.

At the base of the mountains and on the top of most peaks and ridges, the slope is lower because of the gradual flattening of the terrain. However, mountains highly affected by Pleistocene glaciation (most of them in the western part of the country), show prominent peaks of the average slope above 2000 m. That is the case with Korab (2100-2500 m), Šara (2200-2600 m), Pelister (2300-2500 m), Galičica (1900-2150 m) and Jablanica (2050-2200 m). Usually, they represent steep slopes of cirques, U-valleys, ridges, and sharp peaks. At the same time, there are distinctive indentations in higher parts of the above and some other mountain ranges related to too large karst planation surfaces. Thus, Galičica have has remarkable indents (and planation surfaces) on 1500-1600 m, 1900-1950 m, and 2150-2250 m, Bistra Mountain on 1700-2050 m, and Jakupica on 2000-2400 m. There are also indents representing large old fluvial-denudation surfaces on Korab (1600-2100 m), Šara (1600-2200 m) and Pelister (2100-2300 m). Part of these surfaces is fulfilled with glacial deposits. Bellow 2100 m, Pelister which is typical, almost symmetrical horst, has a regular curve with a broad maximum of the gradient at 1600-2000 m. This contrasts with the Kožuf Mountains which have mean gradients between 14° and 22° from the foothills to the highest parts [3].

The terrain curvature is an important morphological and geomorphometric element that indicates the shape of slopes: convex, straight or concave. Ridges and peaks have convex curvature, plains or fields and surfaces with a uniform slope have

straight curvature, while valley bottoms and depressions have concave curvatures [10]. In this work, the types of the slope are represented by the SAGA GIS convergence index which is similar to plan curvature but gives much smoother results [11]. The calculation uses the aspects of surrounding cells, i.e. it looks to which degree surrounding cells point to the center cell. The result is given as percentages, negative values correspond to convergent, positive to divergent flow conditions. Minus 100 would be like a peak of a cone, plus 100 a pit, and 0 an even slope [12]. On all mountains, the curvature changes with elevation from concave (in the lowest parts) to convex (in the highest areas).

The graph in Fig. 3 show that the high mountain ranges in North Macedonia are dominated by straight to convex curvatures. Terrains with extremely convex slopes (summits area) are found on Galičica (0.9%), Kožuf (0.8%), Jablanica (0.75%), Bistra (0.7%), Belasica (0.7%), Nidze with Kozjak (0.69%), and Osogovo Mountain (0.68%). On these, numerous non-prominent peaks appear in relation to their total areas. On the other hand, Pelister (0.2%), Šar Planina (0.3%) and Korab (0.36%), compared to their total areas have smaller numbers of peaks, but usually much sharper. Mountains with the highest relative proportion of concave slopes are Kožuf (4.5%), Osogovo Mountain (4.4%) and Bistra (4.1%).

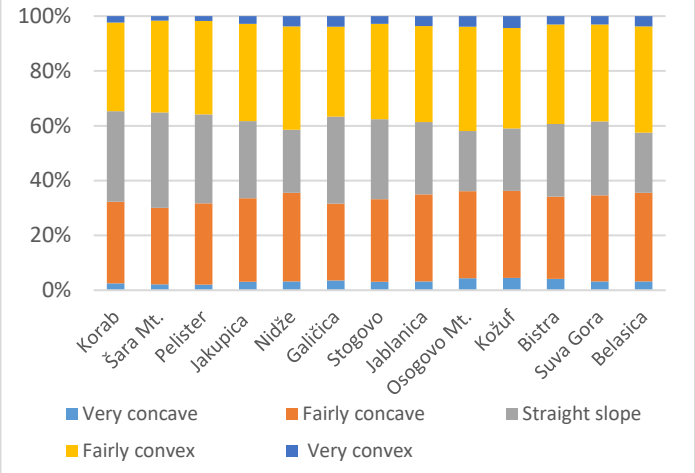

Figure 3. Graph of terrain curvature (convergence index) classes of the high mountains in North Macedonia (in %).

Aspects are an important geomorphometric element which is a result of geotectonic-structural and geomorphologic-evolutionary processes and they are important for the intensity of erosion. The high mountains in Macedonia had a high diversity of aspects as a result of dominant ridge direction, an extension of the larger river valleys, and extension of the mountain ranges in relation to the country borders. Because of the borders, a realistic view of aspect distributions is given only for the ranges which are wholly located in Macedonia: Jakupica, Stogovo, Bistra, Suva Gora and mostly Galičica range. Their aspect distributions, together with the Osogovo Mountains taken because of characteristic almost E-W stretching (as a whole, in natural borders) are presented in Fig. 4.

Interestingly only the Galičica and Stogovo Mountains show distinctive bi-directional aspect distributions (W-E and SW-NE) exactly in opposite to their elongations. The reason for that is poor lateral relief dissection. On the contrary is Osogovo Mountain, where aspects distribution is the same as its elongation (ENE-WSW) mostly because of frequent valleys incised in perpendicular directions. A relatively similar situation is with Jakupica and Suva Gora, while Bistra Mountain which is without clear elongation have an uneven distribution of aspects. However, on all 6 mountains except on Suva Gora, west and east aspects are dominant. Actually, that is the same for all 13 mountains, where western aspects are dominant (by a number of ranges), followed by eastern ones (by area). This is consistent with the dominant Dinaric-Hellenidic (N-S and NW-SE) direction of most ranges in Macedonia. Exceptions are Nidže, Kožuf, Osogovo and Belasica Mountains, which are W-E oriented because of the Aegean extensional neotectonic regime [13].

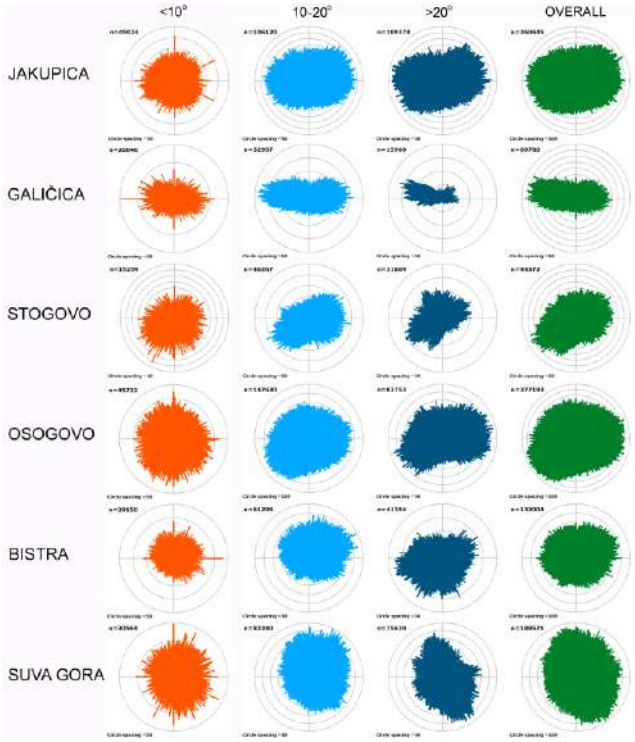

Figure 4. Aspects vs slopes for selected high mountains in North Macedonia.

With further analyses, the average gradients for each aspect were calculated. The data shows that the most common aspects do

not have the greatest slopes but the opposite. This is because a smaller slope increases the area with a given aspect. In fact, the most common aspects represent long, extensive mountain slopes that are perpendicular to the mountain direction. Aspects with the greatest slope gradients generally represent steep valley sides of rivers deeply incised into the mountain ranges, or along their rims. Steep slopes have great erosive potential, especially where facing south.

IV. CONCLUSION

Because of variable structural and geomorphic evolution, high mountains (higher than 2000 m) in North Macedonia have significant morphometric differences, clearly evident in their hypsometry, slope gradient, aspect, and convergence. According to the mean values of these variables, morphometric classification of the mountain ranges is made and they are classified into three groups. The first is a group of very high mountains (regarding the Balkan Peninsula conditions), with steep slopes: Korab, Šar Planina, and Pelister. In the second group are mountains with moderate altitude, slope, and convexity: Nidze, Stogovo, Jablanica, Suva Gora and Bistra. According to its characteristics, Jakupica (Mokra) Range lies between the first and second groups. The third group includes the lower ranges, with gentle slopes and large planation surfaces: Galičica, Osogovo, Kožuf, and Belasica. This classification is strongly related to the geotectonic position and mountain evolution. Thus, the first and second groups of mountain ranges belong to the inner Dinaric and Hellenic geotectonic belt characterized by intensive E-W tectonic compression especially during the Tertiary [14]. Numerous remnants from LGM with cirques, narrow ridges and sharp peaks extending above the karst planation surfaces (on 1600-2000 m), make distinctive morphology of these ranges. Unlike them, except for Galičica, the third group is closer to the Carpatho-Balkanic geotectonic belt, with a highly expressed N-S extensional regime of development.

Previous semi-automated geomorphometric classification is based only on the basic characteristics of 13 analyzed mountains in North Macedonia. However, with further improvements of variables and adjusting limiting values, automated classification [15] can be used at least for the high mountains on the Balkan Peninsula. Beyond purely theoretical research approaches, geomorphometric correlations may have practical significance for better structural and morphological interpretations, as well as for some erosion potential modeling [16] and geohazards indicators.

REFERENCES

[1] Kolčakovski, D., Milevski, I., 2012. "Recent Landform Evolution in Macedonia". In: Recent Landform Evolution. The Carpatho-Balkan-Dinaric Region, Editors Lóczy D., Stankoviansky M., Kotarba A. Springer Geography, 413-442.

[2] Milevski, I., 2015. "General Geomorphological Characteristics of the Republic of Macedonia". Geographical Reviews, 48, Skopje, 5-25.

[3] Milevski, I., 2011. "Morphometric classification of high mountain ranges in the Republic of Macedonia". Geomorphologia Slovaca et Bohemica 2/2011, 32-45.

[4] Milevski, I., 2016. "Morphometry and Land Use on the High Mountains in the Republic of Macedonia". In: Sustainable Development of the Mountain Regions - Southeastern Europe, Editor G. Zhelezov. Springer, London, 63-74.

[5] Milevski, I., Gorin, S., Markoski, B., Radevski, I., 2013. "Comparison of Accuracy of DEM's Available for the Republic of Macedonia". Proceedings from the 3rd International Geographic Symposium - GEOMED 2013, Kemer, Antalya, Turkey, 10-13 June 2013, 165-172.

[6] Milevski, I., 2014. "Slope Values Accuracy vs Resolution of the Digital Elevation Models (Example of the Republic of Macedonia)". Proceedings of 5th ICC-GIS Conference; Eds: Bandrova T & Konecny M., Vol. 2, Varna, 568-575.

[7] Kuhlemann, J., Milivojević, M., Krumrel, I., Kubik, P., 2009. "Last glaciation of the Šhara Range (Balkan Peninsula): Increasing dryness from the LGM to the Holocene". Austrian Journal of Earth Sciences v.102, Vienna, 146-158.

[8] Ribolini, A., Bini, M., Isola, I., Spagnolo, M., Zanchetta, G., Pellitero, R., Mechernich, S., Gromig, R., Dunai, T., Wagner, B., Milevski, I., 2018. "An Oldest Dryas glacier expansion on Mount Pelister (Former Yugoslavian Republic of Macedonia) according to 10 Be cosmogenic dating". Journal of the Geological Society. Vol. 175, Issue 1, 100-110.

[9] Temovski, M., Milevski, I., 2015. "DEM based geomorphometric analyses of karst surface in the Republic of Macedonia". In: Geomorphometry for Geosciences. Eds: Jasiewicz J, Zwolinski Z, Mitasova H, and Hengel T. Geomorphometry.org, Poznan, Poland, 65-68.

[10] Hrvatin, M., Perko, D., 2002. "Determination of surface curvature by digital elevation model and its application in geomorphology". GIS in Slovenia, Ljubljana, 65-72. (in Slovenian)

[11] Olaya, V., 2004. "A gentle introduction to SAGA GIS". The SAGA User Group e.V., Gottingen, Germany, 208 p.

[12] Conrad, O., 2011. SAGA-GIS Convergence Index, Wiki Documentation, http://sourceforge.net/apps/trac/saga-gis/wiki/ta_morphometry_1. On-line [March 18th, 2012]

[13] Burchfiel, C.B., King, W.R., Nakov, R., Tzankov, T., Dumurdzanov, N., Serafimovski, T., Todosov, A., Nurce, B., 2008. "Patterns of Cenozoic Extensional Tectonism in the South Balkan Extensional System". In: Earthquake Monitoring And Seismic Hazard Mitigation In Balkan Countries. Editor: Husebie S.E. NATO Science Series: IV: Earth and Environmental Sciences, 2008, Volume 81, I, 3-18.

[14] Dumurdzanov, N., Serafimovski, T., Burchfiel, C., 2004. "Evolution of the Neogene-Pleistocene Basins of Macedonia". In: Geological society of America Digital Map and Chart Series 1 (Accompanying notes). Boulder, Colorado, 1-20.

[15] Drâguț, L., Eisank, C., 2011. "Automated classification of topography from SRTM data using object-based image analysis". In: Geomorphometry 2011 edited by Hengel T., Evans S.I., Wilson P.J., and Gould M., Redlands, CA, 113-116.

[16] Zingg, A. W., 1940. "Degree and Length of Land Slope as it Affects Soil Loss in Runoff". Agric. Eng., 21(2), 59-64.

GEOMORPHOMETRY 2020 PERUGIA, ITALY JUNE 22 - 26 2020

Geomorphometry and statistics-based approach for recognition of areas of enhanced erosion and their morphotectonic interpretation

Milena Różycka[§], Piotr Migoń
Institute of Geography and Regional Development
pl. Uniwersytecki 1, 50-137 Wrocław, Poland
[§] milena.rozycka@uwr.edu.pl

Abstract—**Areas of enhanced erosion may be considered as markers of tectonic processes as far as the signals resulting from non-tectonic controls of landform evolution can be isolated. In this study spatial distribution of strong erosional signal recorded in morphometric attributes of the land surface, longitudinal stream profiles and valley morphology is examined and confronted with lithological diversity of the area.**

I. INTRODUCTION

Areas of enhanced erosion may indicate higher tectonic activity (as uplift drives erosion), lower resistance of bedrock to erosional factors and forces, or abundant precipitation. These controls frequently occur in combination and thus, one of the most important and challenging tasks in tectonic geomorphology is to separate the signal resulting from different controlling variables and to avoid overinterpretations.

In this study we first aim at identification of areas whose morphometric properties may reflect the enhancement of erosional processes, whatever reasons stood behind. To do so, a few different approaches were involved, all basing on morphometric and statistical analysis of various datasets. These include maps of spatially continuous morphometric parameters derived from LiDAR-based DEM, as well as discrete measures calculated for specific locations and ascribed to points or lines.

The protocol for identification of erosional 'hotspots' was applied to the Orlickie-Bystrzyckie Mountains Block (Sudetes, Central Europe), which owes its emergence to late Cenozoic uplift resulting from stresses from the Alps and the Carpathians, with the superimposed effects of long-term rock-controlled denudation. As lithological diversity of the area is high, the influence of bedrock properties on geomorphological markers of uplift needs to be considered in more detail. By contrast, spatial distribution of rainfall is relatively uniform over the area.

II. METHODS

A. *Erosional signal in morphometric attributes of the land surface*

To distinguish highly dissected terrains eight morphometric parameters with the potential to record erosional signal were selected in the first step. These include:

(1) relative elevation (rel_elev)

(2) standard deviation of elevation (std_elev)

(3) coefficient of variation of elevation (cv_elev)

(4) Terrain Ruggedness Index (TRI, [1])

(5) standard deviation of curvature (std_curv, [2,3])

(6) slope

(7) Topographic Wetness Index (TWI, [3,4])

(8) Valley Depth (val_dep, [5])

These parameters were derived form LiDAR-based DEM, resampled to 30x30 m spatial resolution. Most of them were calculated for the local neighbourhood, that is within 5x5 moving window. The approach is based on the assumption that the increase in values of the parameters reflects an increase in erosional dissection of the area, although this may be debatable for TWI.

To eliminate variables that do not discriminate observations efficiently, the coefficient of variation for each parameter was calculated. As for all eight variables it exceeds 10%, there was no need to eliminate any of them in this step.

As some of the parameters were suspect to be highly correlated, the correlation analysis was performed in order to eliminate variables which replicate information. The selection of the Spearman's correlation coefficient, as a measure of mutual

Milena Rozycka and Piotr Migon (2020) Geomorphometry and statistics-based approach for recognition of areas of enhanced erosion and their morphotectonic interpretation: in Massimiliano Alvioli, Ivan Marchesini, Laura Melelli & Peter Guth, eds., Proceedings of the Geomorphometry 2020 Conference, doi:10.30437/GEOMORPHOMETRY2020_71.

dependency, was determined by both statistical distribution of the variables (far from being normal) and the presence of outlier observations. Prior to correlation analysis median filter was applied to all parameters as a smoothing technique. This was dictated by relatively small neighbourhood for the calculation of some parameters and thus their high differentiation in space.

In the correlation matrix all pairs of variables characterized by the absolute value of Spearman's correlation coefficient equal or exceding 0.8 were identified. From each of these pairs the parameter with the higher average degree of correlation with other variables was eliminated. This approach enabled us to reduce the total number of parameters taken into consideration in this study from eight to four (cv_elev, std_curv, TWI, val_dep).

Nearly 2 million points ascribed to the central parts of the raster cells and characterized by a sequence of four selected parameters were then subject to clustering procedure in order to distinguish objects similar to each other from morphometric perspective and thus possibly recording the erosional signal of similar strength. Such a great number of observations prevents the application of hierarchical clustering algorithms and from the non-hierarchical ones the k-means method was selected. In order to determine the optimal number of clusters to distinguish (Fig. 1), the pseudo *F* statistics, also known as Caliński-Harabasz index [6], was calculated. As only two groups of observations should be created in the light of this measure, the alternative elbow method was also applied, but no clear indication of the optimal number of clusters was obtained in this way.

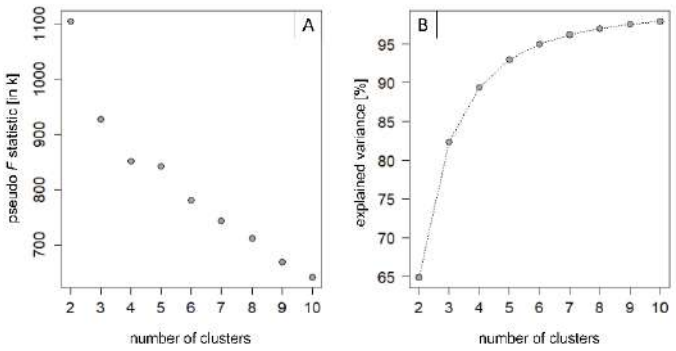

Figure 1. The attempts to establish optimal number of clusters with the use of Caliński-Harabasz pseudo *F* statistic (A) and elbow method (B).

B. Erosional signal in stream longitudinal profiles and valley morphology

To identify 'erosional' sections of the streams, that is channel segments abnormally steep in respect to the adjacent ones, stream length–gradient index (SL index) [7] was applied. It was calculated for 400 m long river segments according to the formula below (1):

$$SL = (\Delta H/\Delta L)L \quad (1)$$

where:

ΔH – change in elevation

ΔL – horizontal length of the segment

L – distance to the highest point in the channel

All river segments with the local slope possibly affected by anthropogenic elements (roads, bridges, reservoirs) were excluded from further analysis. Channel segments of higher steepness, that is those characterized by higher SL-index values, were identified in two different ways. In the quantile-based approach they were distinguished as those exceeding upper tercile, quartile and quintile of SL-index statistical distribution in which all examined river segments in the study area were taken into account. In the alternative, model-based approach erosive segments of river channels were recognized as follows. In the first step the chart presenting the variablity of SL-index along the river course was plotted for each stream separately (Fig. 2A). To this plot a linear model was adjusted and the residuals for each location were computed. For the positive ones the average residual value was calculated. All river segments typified by residuals exceeding this value were considered 'erosive'. This procedure was repeated also in local slope analysis, in which distance between the river segment (its midpoint) and the spring of a river (L) was not considered. The only difference was the adjustment of the logarithmic curve to the data, instead of the linear trend (Fig. 2B).

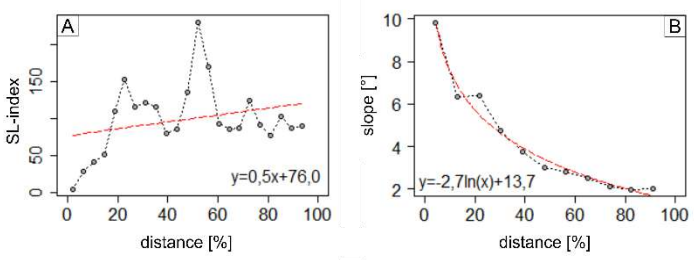

Figure 2. Variability of SL-index (A) and local slope (B) along exemplary streams with adjusted models.

In the final distinction (aggregate approach) erosive segments of river channels were identified as locations of superposition of 20% of observations with the highest SL-index values (quantile-based approach) and those distinguished as erosive in both model-based approaches (Fig. 2).

In the identification of erosive sections of river valleys, that is segments shaped by intensive river downcutting, valley floor width –valley hight ratio (V_f index) given by formula (2) was applied [8].

$$V_f = \frac{2V_{fw}}{(E_{rd} - E_{sc}) + (E_{ld} - E_{sc})} \quad (2)$$

where:

V_{fw} – valley floor width

E_{rd}, E_{ld} – elevation of right and left divides

(E_{sc} – elevation of stream channel

As many minor streams crossing the mountain-piedmont junction in the eastern part of the study area do not have any distinctive valley forms, the delimitation of which is essential for the purpose od V_f index calculation, this analysis was restricted to the western slope of the Orlickie Mountains.

The V_f index was calculated for the same locations for which SL-index was computed in order to allow their comparative analysis, mostly in terms of mutual correlation. Contrary to the latter, lower values of V_f index are indicators of more intensive erosion related to river downcutting. For identification of erosive valley segments the quantile-based approach, similar to the one introduced in the SL-index analysis, was applied.

As V_f index does not take account of slope of valley sides in a direct way, spatial distribution of steep valley sides (that is raster cells with the slope exceeding the upper quartile of statistical distribution) was also examined.

C. Lithological control on indicators of erosional signal

To assess the influence of diversified lithology on erosional dissection the non-parametric chi-square test of independence was performed. The categorical variable was considered in two different levels: general and detailed. While in the former the distinction was made only between crystalline basement and sedimentary cover, lithological diversity in the latter was considered in a more detailed way.

In chi-square test of independence the comparison is made between observed (empirical) values of a numeric variable with the theoretical ones established on the basis of the marginal distribution [9]. The assumption of the null hypothesis is that the numeric variable does not depend on the categorical one. The test statistic is given as below (3):

$$\chi^2 = \sum_{i=1}^{k}\sum_{j=1}^{s} \frac{(n_{ij} - n'_{ij})^2}{n'_{ij}} \quad (3)$$

where:

n_{ij} – observed values

n'_{ij} - expected values

k, s – number of levels in both variables

Given the null hypothesis is true, the test statistic has chi-squared distribution with (k-1)(s-1) degree of freedom. For significant test results mosaic plots were used to illustrate the pattern of deviation from independence [10].

In this study the numeric variable was expressed relatively, that is as percentage of area occupied by 'erosive' cluster within different lithological units or, respectively, as the length of erosive segments of river channels or valleys.

III. RESULTS AND INTERPRETATION

Given that no clear indication of the optimal number of groups to distinguish in the clustering procedure was obtained in the light of the elbow method, this number was established arbitrarily as five (Fig. 3A). As the cluster-specified average values do not maintain the same order for the parameters taken into consideration (Fig. 3B), it is not possible to rank the clusters in terms of increasing signal of erosional dissection. Nevertheless, basing on both their spatial and statistical characteristics, clusters no. 3 and 4 were considered as carriers of the strongest erosional signal.

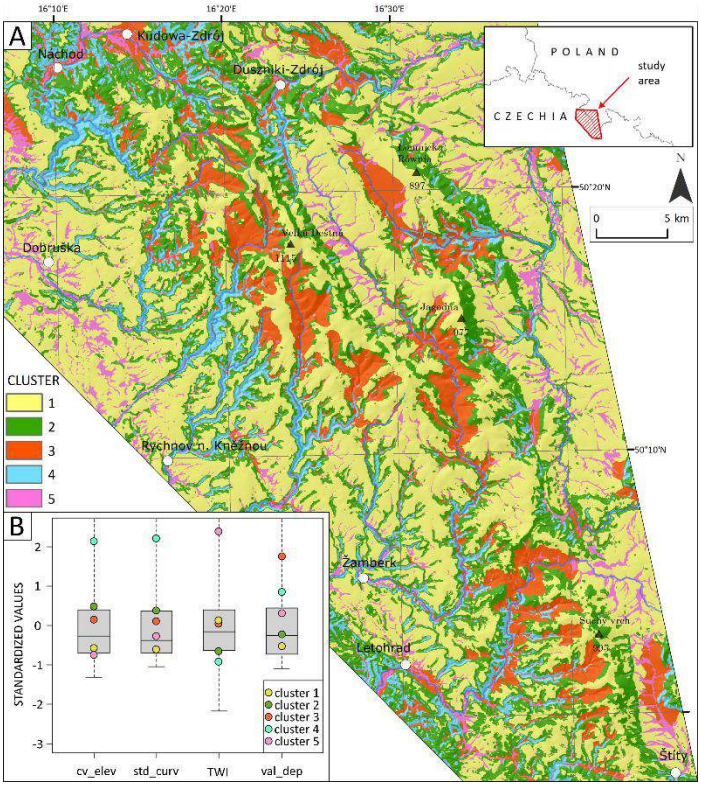

Figure 3. The results of k-means clustering (A) with the average values of all parameters calculated for each cluster separately (B).

Erosive segments of river channels obtained on the basis of the aggregate approach were sparse and short. Therefore, the quantile-based approach to their identification was solely included in further interpretations. Surprisingly, no statistically significant correlation between SL- and V_f index values calculated for the same locations was demonstrated (rho = -0,26).

In the final distinction of areas, whose morphometric properties may reflect the enhancement of erosional processes, the superposition of the most 'erosive' clusters (3 and 4 on Fig. 3) and erosive segments of river channels and river valleys, both identified in the SL and V_f quantile-based approaches, was considered (Fig. 4). The spatial distribution of steep valley sides was also taken into account.

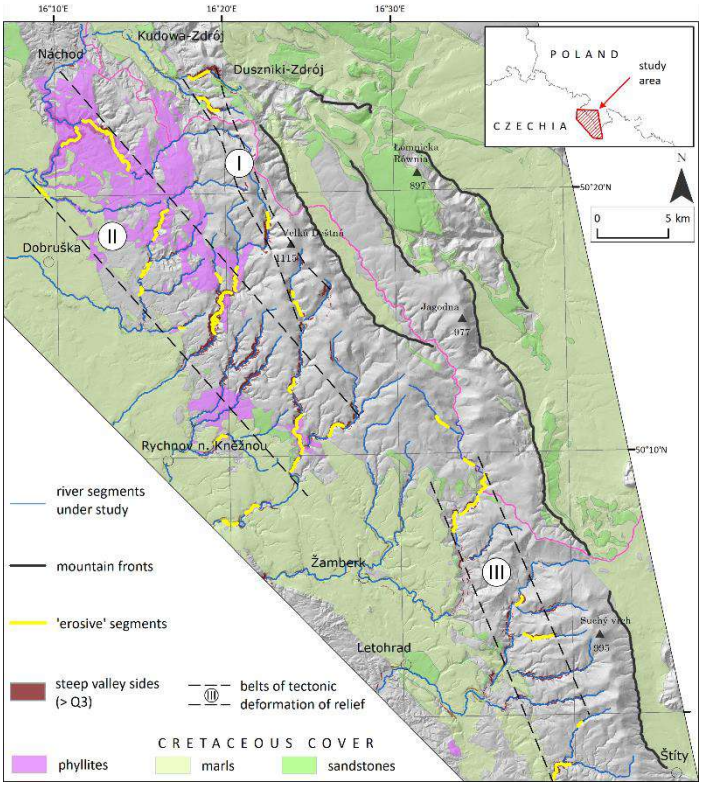

Figure 4. Belts of tectonic deformation of relief distinguished on the basis of spatial distribution of erosive segments of river channels and river valleys identified by SL- and V_f index and their affiliation to the most 'erosive' clusters (no. 3 and 4 on Fig. 3). Basement rocks other than phyllites are indicated in grey.

As the influence of lithological diversity of the area can be considered minor (Fig. 5), the erosive signal recorded in morphometric attributes of the land surface, longitudinal stream profiles and valley morphology is interpreted as the response to geologically recent and ongoing uplift of the area.

Three belts of tectonic deformation of relief, elongated parallel to the morphological NNW–SSE axis of the mountain block, were recognized (Fig. 4). The spatial pattern of variable intensity of endogenic processes is consistent with the geological situation of the region, especially with the distribution of remnants of the Cretaceous sedimentary cover.

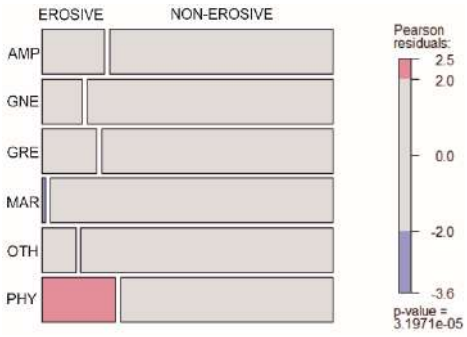

Figure 5. Relationships between relative frequencies of segments identified as erosive (see Fig. 4) in total length of the streams for different lithological units. Note statistically significant overrepresentation of these segments within phyllites (AMP – amphibolites, GNE – gneisses, GRE – greenschists, MAR – marls, OTH – other metamorphic schists, PHY – phyllites).

This paper is a contribution to Research Project no. 2015/19/N/ST10/01530, supported by the National Science Centre.

REFERENCES

[1] Riley, S., S. DeGloria, R. Elliot, 1999. "A Terrain Ruggedness Index that quantifies topographic heterogeneity". Intermountain Journal of Sciences 5, 23-27.

[2] Zeverbergen, L., C. Thorne, 1987. "Quantitative analysis of land surface topography". Earth Surface Processes and Landforms 12, 47-56.

[3] Moore, I., R. Grayson, A. Landson, 1991. "Digital terrain modelling: A review of hydrological, geomorphological and biological applications". Hydrological Processes 5, 3-30.

[4] Sørensen, R., U. Zinko, J. Seibert, 2006. "On the calculation of the Topographic Wetness Index: Evaluation of different methods based on field observations". Hydrology and Earth System Sciences 10, 101-112.

[5] Conrad, O., B. Bechtel, M. Bock, H. Dietrich, E. Fischer, L. Gerlitz, J. Wehberg, V. Wichmann, J. Böhner, 2015. "System for Automated Geoscientific Analyses (SAGA) v. 2.1.4.".Geoscientific Model Development 8, DOI: 10.5194/gmd-8-1991-2015.

[6] Caliński, T., J. Harabasz, 1974. "A dendrite method for cluster analysis". Communications in Statistics 3, 1-27.

[7] Hack, J., 1973. "Stream-profile analysis and stream-gradient index". U.S. Geological Survey Journal of Research 1, 421-429.

[8] Bull, W., 2007. "Tectonic Geomorphology of Mountains: A New Approach to Paleoseismology". Blackwell Publishing, Oxford, pp. 316.

[9] McHugh, M., 2013. "The chi-square test of independence". Biochemia Medica 23, 143-149.

[10] Meyer, D., A. Zeileis, K. Hornik, 2006. "The strucplot framework: Visualising multi-way contingency tables with vcd". Journal of Statistical Software 17, 1-48.

GEOMORPHOMETRY 2020 PERUGIA, ITALY JUNE 22 - 26 2020

Suspected signature of active tectonism in Palghat Gap, India

Yogendra Singh[1], Biju John, Divyalakshmi KS
National Institute of Rock Mechanics, Seismotectonic Department,
Eshwar Nagar, Banashankari Bangalore 560070
Karnataka, India
[1]lamyans.yogendra@gmail.com

Abstract- **The present study is an attempt to identify the signature of ongoing tectonic adjustments within a major watershed, peninsular India, which has experienced several earthquakes including a M=6.0 event. Previous studies have also identified an active fault within the watershed. This watershed is criss-crossed by several lineaments in which NW-SE and NE-SW trending lineaments are regionally more conspicuous. In the present study quantitative analysis of 29 sub basins of Bharthapuzha watershed is carried out by analysing their Hypsometric curves and hypsometric integral. The study found that the basins east of the epicentre of 1900 earthquake, northeast of lineament 4 (NW-SE), apparently indicating higher relative uplift, which is further supported by the ongoing seismicity observed in the north eastern side of the lineament.**

I. INTRODUCTION

Studies conducted in last few decades have identified a number of evidences for neotectonism within the cratonic region of Peninsular India, which was once considered as tectonically stable [1,2,3,4]. In some part of Peninsular India drainage networks are also considered to be tectonically controlled [5]. Studies conducted, using the geomorphic indices and morphometric tools, in peninsular India had identified several potential seismogenic structures as a first step of seismic hazard assessment [6,7,8,9]. Studies elsewhere in Peninsular India also suggest that the damaging earthquakes in this region can occur at places where it is least expected, due to long return period [1]. Thus, the present study is focused to identify evidence of active tectonism through morphometric analysis.

The Coimbatore earthquake M=6.0 is the largest event reported in the southern peninsular India falling with in the major watershed called Bharthapuzha [10]. In the present study, quantitative analysis of Bharthapuzha watershed using Hypsometric curve and Hypsometric integral for the individual sub basins were carried out to understand the ongoing tectonic activity.

II. STUDY AREA

The E-W trending Palghat Cauvery shear zone is one of the prominent Precambrian shear zone in peninsular India. The Palghat Gap, a conspicuous geomorphic break, is also coincides with this shear zone [11,12,13]. Bharathapuzha and its tributaries constitute the drainage network in the gap area, which is generally controlled by E-W trending lineaments [14]. The Gap region consists of 250-km long and 30-km wide low land ('gap') bordered by ridges and hills. The structural elements in the gap region are consistent with a ductile shear zone (Palghat-Cauvery Shear zone), defined by a large E-W dextral oblique-slip component, which may have been associated with Proterozoic tectonic events [15]. Based on thermobarometric studies large-scale exhumation of lower to mid-crustal rocks is identified in the Palghat gap region [16]. The exhumed low-mid-crustal basement rock in the area suggests a north south compression during late Proterozoic (900-550 Ma) [16]. Earlier studies identified a NW-SE trending fault located in the south western corner of the Bharathapuzha watershed as active [6,17].

In this region some of the NW-SE lineaments are defined by emplacement of basic dykes connected with Deccan volcanism [18,19]. There are four prominent NW-SE trending structures in the basin. The F1 is identified as active fault [17]. The lineament L1 is continuing from the central part of Kerala state called Idamalayar lineament which is also the location for dyke emplacement. The lineament L4 is merging with L2 and is spatially associated with the epicentre of M=6.0 earthquake. Historical and recent data also suggest that several earthquakes have occurred in the Palghat Gap between 1865 and 2007, (e.g. [20]).

III. METHODOLOGY

The present study used ASTER (Advanced Spaceborne Thermal Emission and Reflection Radiometer) DEM as basic elevation data. For analysis DEM and other available data reprojected to make similar projection. Drainages, watershed and sub watershed boundaries were extracted from ASTER data using Arc GIS 10.6. Spatial analyst tool. Baharthapuzha watershed and sub basins within the watershed are derived based on the largest flow accumulation points in the area. On the basis of third and fourth order drainage, 29 sub watersheds were derived for the present study. The derived sub watersheds are converted to the features for calculating the area and other parameters. The elevation and area were calculated using the modelling tool of the Arc GIS. The lineaments are demarcated using the Landsat 7 data.

Yogendra Singh, Biju John and KS Divyalakshmi (2020) Suspected signature of active tectonism in Palghat Gap, India:

in Massimiliano Alvioli, Ivan Marchesini, Laura Melelli & Peter Guth, eds., Proceedings of the Geomorphometry 2020 Conference, doi:10.30437/GEOMORPHOMETRY2020_42.

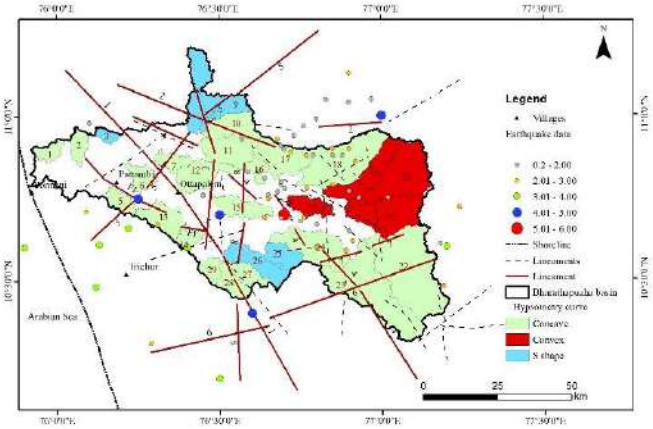

Figure 1. Map showing the spatial distribution seismicity and basin with different shapes of hypsometric curved obtained.

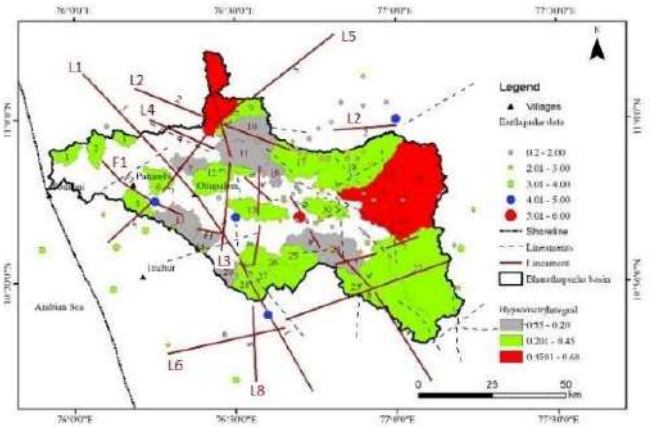

Figure 2. Map showing the spatial distribution seismicity and Hypsometric Integral values with in the study area.

IV. Results and Discussion

A. Hypsometry Curve

Hypsometric curves are non-dimensional measure of the proportion of the catchment area above a given elevation. The hypsometric curves are related to geomorphic and tectonic evolution of drainage basins in terms of their forms and process [23]. Three types of landforms, namely, young, mature and monadnock were identified on the basis of hypsometric curve shape [21, 23].

Hypsometry curves derived for 29 sub watersheds of Bharthapuzha drainage system indicates that 62% sub watershed are concave upward, indicative of old stage topography [23]. The studies carried out by John and Rajendran 2008 have identified a NW-SE trending active fault (F1, Desamangalam fault) which is the source of ongoing seismicity, since 1989 in this area.

Three sub-basins (19, 20 and 21) in the eastern side of the watershed are in convex upward, which represents the youthful stages (Fig. 3) [21, 23]. The basin no. 30, which is located very close to the epicentre of 1900 Coimbatore earthquake is also showing convexity in the profile. Apart from this there are several 'S' shaped curves observed in the area which are located between L1 and L4 lineaments. The basins 12, 15, and 22 falling between L1 and L4 also show convexity in the upper part of the curve. Similarly, basins 2 and 3 located at the northwest of Desamangalam fault also show convexity in the profile (fig 1 & 2).

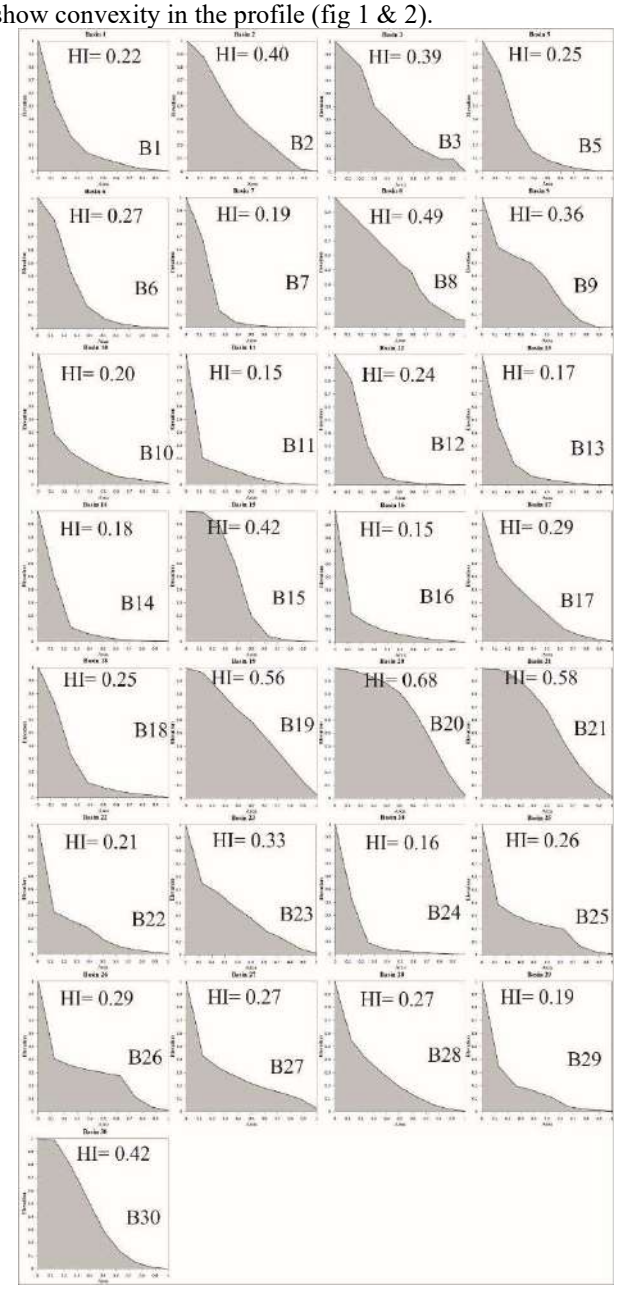

Figure 3: Hypsometric profile & HI for 29 sub basins

B. Hypsometric Integral (HI)

Hypsometric integral controls the shape of a hypsometric curve and thereby provides clues for landform evolution [21]. The high value of hypsometric integral related to youthful

topography, active tectonics. The intermediate value of HI indicates the mature stage. The low values of HI are related to the older landscapes, which got more eroded and doesn't reflect any activity in terms of recent tectonics [22].

In this area HI values are ranging from 0.15 to 0.68 and mean value is 0.312. Considering 0.312 as a mean value the entire basin is divided into three categories <0.20 is considered as lower values and 0.20 to 0.45 is considered as the medium values and above >0.45 is considered as highest values. The 48.27 % (14) basins are falling in the intermediate region and 31.03% (9) basin are flowing the trend of very low HI and 20.68 % (6) basin are flowing the high HI index. It is observed that along the lineament 4 which is spatially associated with M=6.0 earthquake shows as older landscape where as high values are observed in the basins located in the north eastern side of this lineament. Between the lineaments 1 and 4 most of the basins are observed as mature. It is also to be noted that the basins close to the debouching area (Arabian sea) in the line of Desamangalam fault show a mature stage than an old stage that observed in the central part of the catchment area (Fig 1 & 2).

V. CONCLUSION

Bharathapuzha watershed in an unique drainage system flowing through a low lying terrain within western ghats. The occurrence of several low magnitude earthquakes and a magnitude of 6.0 (in 1900) and an identified active fault signifies the need for detailed study. The present study identified basins indicating the youth stage and also high values of HI in the northeast of the NW-SE trending lineament passing through east of Palghat. Between the lineaments L1 and L4 most of the basins are observed as mature where it shows selective convexity (uplift) in hypsometric profile. Tectonic adjustment of Desamangalam fault also appears to be reflecting as basins of mature values and also have convex in the hypsometry profile. Thus, the present study suggests a detailed investigation in this area is required to understand the nature of active tectonic adjustments.

References

[1] John, B (2018), 'Importance of Geological Studies in Earthquake Hazard Assessment'. In *Integrating Disaster Science and Management: Global Case Studies in Mitigation and Recovery. Elsevier Book* Chapter 2, pp. 27-40.

[2] Radhakrishna, B.P. (1968), 'Geomorphological approach to the charnockite problem'. *Jour. Geol. Soc. India*, v.9, pp.67-74.

[3] Vaidyanadhan, R. (1977), 'Recent advances in Geomorphic studies of peninsular India: A review'. *Indian Jour. Earth Sci*. (Ray Volume), pp.13-35

[4] Valdiya, K.S. (1998), 'Late Quaternary movements and landscape rejuvenation in southeastern Karnataka and adjoining Tamilnadu in Southern Indian shield'. *Jour. Geol. Soc. India*, v.51, pp.139-166.

[5] Sinha-Roy, S. and Mathai, T. (1979), 'Development of western continental margin of India and plateau uplift as related to geology and tectonics of Kerala', *Workshop on Status, Problems and Programmes in Indian shield,* pp. 235–271

[6] John, B. and Rajendran, C. P. (2008), 'Geomorphic indicators of Neotectonism from the Precambrian terrain of peninsular India: A study from the Bharathapuzha Basin, Kerala', *J. Geol. Soc. India,* **71**, 827–840.

[7] Ramasamy, S. M., Kumanan, C. J., Selvakumar, R. and Saravanavel, J. (2011), 'Remote sensing revealed drainage anomalies and related tectonics of South India', *Tectonophysics,* **501**, 41–51.

[8] John, B., Divyalakshmi, K. S., Singh, Y., and Srinivasan., C. (2013),'Use of SRTM Data for a Quick Recognition of the Active Tectonic Signatures'." In *Geomorphometry 2013*. Nanjing, China, 2013.

[9] Singh, Y., John, B., Ganapathy G.P., George, A., Harisanth, S., Divyalakshmi, K.S. and Kesavan, S. (2016) 'Geomorphic observations from southwestern terminus of Palghat Gap, South India and their tectonic implications', Journal of Earth System Science, 125(4), 821-839.

[10]Basu, K. L. (1964), 'A note on the Coimbatore earthquake of 8th February 1900', Indian J. Meteor. Geophys. 15, 281– 286.

[11]Arogyaswami, R.N.P., 1962. 'The origin of the Palghat Gap'. Rec. *Geol. Surv. India* 93, 129–134.

[12]Drury, S. A., Harris, N. B., Holt, R. W., Smith, R. G. J. and Wightman, R. T. (1984), 'Precambrian tectonics and crustal evolution in South India', *Jour. Geology,* 92, 3-20.

[13]Subramaniam, K.S., Muraleedharan, M.P., 1985. 'Origin of the Palghat Gap in South India—a synthesis'. *J. Geol. Soc. India* 26, 28–37.

[14]John, B. (2003), 'Characteristics of near surface crustal deformation associated with shield seismicity: Two examples from peninsular India'; *Unpublished PhD theses*, *Cochin University of Science and Technology*.

[15]D'Cruz, E., Nair, P.K.R. and Prasannakumar, V. (2000), 'Palghat gap— a dextural shear zone from the south Indian granulite terrain', *Gondwana Res*. **3**, 21–31.

[16]Ravindrakumar, G.R. and Chacko,T. (1994), 'Geothermobarometry of mafic granulites and metapelite from Palghat Gap; South India: Pertological evidence of isothermal uplift and rapid cooling', *Jour Metamorphic Geo.,* **1**, 479-492

[17]John, B. and Rajendran, C. P. (2009), 'Evidence of episodic brittle faulting in the cratonic part of the peninsular India and its implications for seismic hazard in slow deforming regions', *Jour Tectonophys,* 471, 240–252.

[18]Krishnaswami, V. S. (1981), 'The Deccan volcanic episode: Related volcanism and geothermal manifestations; In: Deccan volcanism (eds) Subbarao K V and Sukheswala R.N', *Geol. Soc. India Memoir,* **3**, pp. 1–7.

[19]Nair, M. M. (1990), 'Structural trend line patterns and lineaments of the Western Ghats, south of 13^0 latitude', J. *Geol. Soc. India*, **35,** 99–105.

[20]Rajendran, C.P. and Rajendran K. (1996), 'Low-moderate seismicity in the vicinity of Palghat gap, South India and its implication', *Current Science,* **70**, 304–307.

[21]Sinha Roy, S., (2002), 'Hypsometry and landform evolution: a case study in the Banas drainage basin, Rajasthan, with implications for Aravalli uplift'. Journal of Geological Society of India, 60, 7–26.

[22]Hamdouni, R.El., Irigaray, C., Fernandez, T., Chacon, J. and Keller, E. A. (2008). 'Assessment of relative active tectonics, Southwest Border of Sierra Nevada (southern Spain)'. Geomorphology, 96 (1–2), 150–173.

[23] Strahler, A.N. (1964). Quantitative geomorphology of drainage basins and channel networks. In V.T. Chow (Ed.), Handbook of Applied Hydrology, McGraw Hill, New York, pp 39-76

GEOMORPHOMETRY 2020 PERUGIA, ITALY JUNE 22 - 26 2020

A data-driven method for assessing the probability for terrain grid cells of initiating rockfalls on a large area

Massimiliano Alvioli[§], Michele Santangelo, Federica Fiorucci, Mauro Cardinali,
Ivan Marchesini, Paola Reichenbach, Mauro Rossi
Istituto di Ricerca per la Protezione Idrogeologica, Consiglio Nazionale delle Ricerche,
Via Madonna Alta 126, I-06128 Perugia, Italy
[§]massimiliano.alvioli@irpi.cnr.it

Abstract—**Rockfalls are one harmful kind of landslide, due to their rapidity, destructive potential and high probability of occurrence on steep topographies, often found along transportation corridors. Various factors can trigger rockfalls, including intense rainfall and seismic activity, and diverse phenomena affect their occurrence, like rock weathering and fracturing. Existing approaches for the assessment of rockfall susceptibility range from purely phenomenological to purely deterministic, physically based methods. A common requirement for many approaches is the need to locate the potential point locations of source areas, often located uphill on cliffs. Application of a physically based model, in particular, allows the calculation of material runout stemming from rockfalls originating from such point locations. In this work, we propose a method for the location of rockfall source points, on a digital elevation model, suitable for large areas. We deem the method as data-driven, because it relies on expert delineation of potential source areas from Google Earth images in few sample locations, representative of the study area at large. We measure the slope distribution of grid cells encompassed by expert-mapped source areas, and generalize the distribution of sources to the whole of the study area. We apply the method to a corridor of about 17,000 km in length and varying width, containing the entire Italian railway network. The map of source areas represents the main input for a physically based simulation of rockfall trajectories with the model STONE, and likely of other similar physically based or phenomenological models for rockfall runout assessment.**

I. INTRODUCTION

Location of potential sources of rockfalls requires expert analysis of the cliffs in the study area, which is typically a time consuming and expensive procedure. This makes identification of potential sources a limiting factor for systematic rockfall studies over large areas. Existing analyses are limited to individual hillslopes or portions of slopes along transportation corridors of limited length. Moreover, a reliable extraction of potential sources requires availability of high-resolution images and digital elevation models (DEMs), which allows observation of existing sources [1-2], or continuous monitoring of slopes with various technologies, typically feasible in small areas [3, 4]. Moreover, once a potential source is located on a digital model, it is desirable to assign a probability for the likelihood of that location to evolve into an actual rockfall [5].

The common way of straightforwardly selecting source areas is to establish a slope threshold above which any grid cell acts as a potential rockfall source. In this work, we describe a method to both locate and assign a probability of failure in a homogeneous way in a very large area.

The procedure presented here represents nothing but a starting point for the assessment of rockfall susceptibility, or rockfall hazard, depending on the additional available data and purpose of the study [6]. In fact, for such purposes, we run STONE, a kinematic model to simulate rockfall trajectories originating from given source pixels on a digital topography [7]. Additional inputs of the model are friction and energy restitution grids of parameters, initial velocity of the simulated falling boulders, and other optional quantities [1, 7-9]. The model assumes point-like boulders, considering them in a state of either free fall, bouncing or rolling, at each time step of the simulation. Trajectories end when the boulders exhaust their initial kinetic energy due to simulated friction with the terrain (air drag is neglected).

II. METHODS

In this work, we performed the following steps to calculate the probability for grid cells to initiate rockfalls on a 10 m-resolution DEM of Italy (TINITALY) [10]:

1) selection of a 1 km-wide buffer around the railway track;
2) selection of the set of slope units (SUs) [11, 12] intersecting the buffer;
3) expert mapping of a subset of potential rockfall source areas within the selected SUs, in regions we considered representative of the conditions that could trigger rockfalls in the particular topographic unit [13] under investigation;

Massimiliano Alvioli, Michele Santangelo, Federica Fiorucci, Mauro Cardinali, Ivan Marchesini, PaolaReichenbach and Mauro Rossi (2020)

A data-driven method for assessing the probability for terrain grid cells of initiating rockfalls on a large area:

in Massimiliano Alvioli, Ivan Marchesini, Laura Melelli & Peter Guth, eds., Proceedings of the Geomorphometry 2020 Conference, doi:10.30437/GEOMORPHOMETRY2020_43.

4) development of a statistical procedure to generalize the source areas of point 3) to different grid cells, with the same characteristics in terms of local terrain slope, within the same topographic unit [14];
5) visual analysis of the source areas map obtained from the statistical procedure of point 4), in relation to the railway track, and assimilation in the final source area map of potential source areas left out by the procedure;
6) additional set of analysis, not described here, necessary for execution of the program STONE [7].

In point 2) above, we introduced the use of slope units. A national SU map is available for the whole of Italy [11, 12]. An extension of the method and software first described in Ref. [14] allowed preparation of such map. Slope units are suitable for landslide modeling [14, 15], particularly where available data is heterogeneous [15]. In our case, using SUs also allows to put a well-defined spatial boundary around the railway track, with some confidence that the runout of simulated rockfalls stays within the boundary.

In point 3) above, we introduced topographic units of Italy. We adopted a (slightly) revised version of the units from Ref. [13], as in Ref. [12]. This step allows selection of representative areas for expert mapping in each of the 29 different units, and statistical generalization of them within physiographical homogeneous areas. Table I lists the total area of each topographic unit and, in each of them, the area covered by slope units selected for simulation.

Point 4) consisted in a regression of the distribution of the number of grid cells encompassed by the expert-mapped source areas as a function of their slope, S, using a suitable functional form. We opted for a non-linear quantile regression with a single parameter probability function P_{FIT}, of the following form:

$$P_{FIT}(S) = c\,\left(\frac{S}{90}\right)^4, \qquad (1)$$

where S is expressed in degrees and c is the regression parameter. We assigned values of probability with a lower bound, set as the minimum between 0.1 and the value that provides a map in which 80% of the mapped sample has non-null probability.

III. Results and conclusions

The procedure described by the enumerated list in Section II applies to each of the topographic units adopted in this work. Table I and Fig. 1 summarize the results of the procedure.

The statistical procedure produces a 10 m x 10 m grid map aligned with the TINITALY DEM used in this work. We assigned grid cells with the probability for a rockfall trajectory to originate from within that specific location. Thus, cell-by-cell comparison between modeled probability and expert-mapped source areas is meaningful. To this end, we calculated the percentage of grid cells encompassed by polygons representing mapped source areas in which the statistical procedure assigned non-null probability, and the number of cells with values of probability larger than 0.8.

Table I lists results for each of the topographic sections in which we run the statistical procedure independently.

ZONE CODE	**Total Area** [km^2]	**SU Area** [km^2]	**HR** (Total)	**HR** (P > 80%)
1.1	16,274	1,590	77%	0.13
1.2	35,735	2,620	80%	0.19
2.1	32,702	373	80%	0.27
2.2	9,426	164	11%	0.06
2.3a	3,103	458	75%	0.16
2.3b	1,298	88	-	-
3.1	2,322	332	16%	0.00
3.2	3,991	1,778	51%	0.04
4.1	22,393	2,067	78%	0.07
4.2	16,835	1,894	79%	0.09
4.3	4,920	457	77%	0.13
4.4	8,097	1,585	75%	0.14
4.5	12,890	1,379	79%	0.18
4.6	6,203	383	50%	0.03
4.7	5,337	598	59%	0.09
4.8	4,262	511	48%	0.03
5.1	25,346	2,086	58%	0.12
5.2	6,136	972	79%	0.05
5.3	6,375	859	62%	0.04
6.1	9,023	930	78%	0.10
6.2	20,236	706	44%	0.11
6.3	1,731	-	-	-
7.1&7.2	14,285	2,195	56%	0.12
7.3	5,321	691	46%	0.09
7.4	1,499	210	80%	0.28
8.1	16,404	428	63%	0.14
8.2	258	-	-	-
8.3	1,946	4	58%	0.21
8.4	2,844	42	76%	0.22

Table I. Numerical evaluation of the statistical generalization for the probability of grid cells to initiate a rockfall trajectory (see text). We also list the total area of each section (Zone code, Ref. [10, 12]) and the area occupied by selected slope unit area.

We evaluated the agreement between expert-mapped areas and statistical generalization by hit rate, HR = TP = (TP + FN), where TP stands for true positives and FN for false negatives.

Figure 1 shows a sample subset of the results, in four of the 29 units. The figure shows the empirical probability for a grid cell of initiating a rockfall, represented by slope values calculated for the set of 10 m x 10 m grid cells encompassed by the expert-mapped

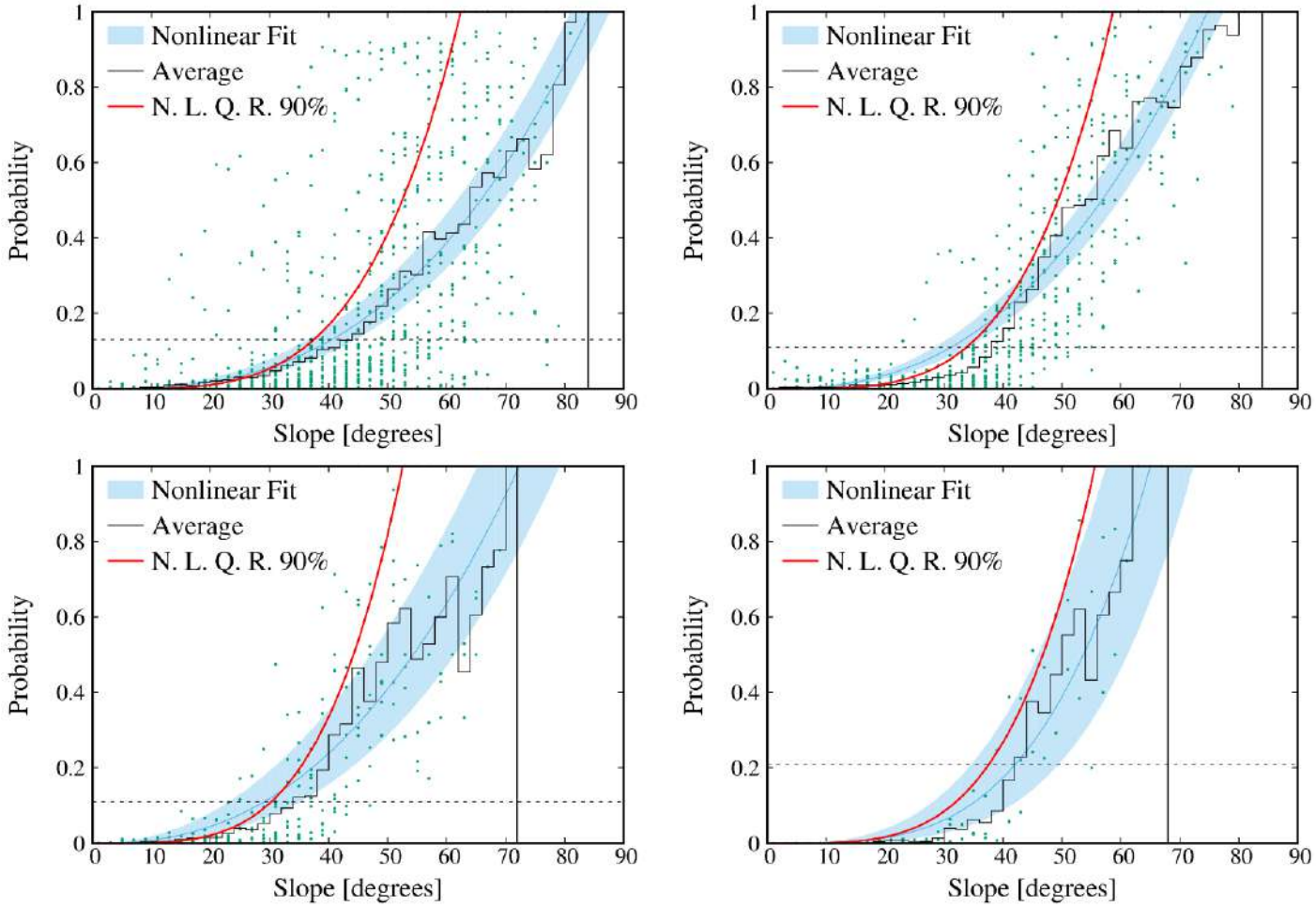

Figure 1. Example result of statistical assessment of the probability of a grid cell with given slope to represent a source area for rockfalls. Data (green dots) and numerical models (curves) correspond to four out of the 29 topographic from Ref. [10, 12], adopted in this work. The red curve, a non-linear 90% quantile regression corresponding to Eq. (1), is the adopted model. The horizontal line represents the probability limit under which probability is set to null.

polygons (green dots). The figure also shows different curves, corresponding to the following quantities. Blue curve with confidence band: a non-linear fit with an expression similar to Eq. (1), but with the exponent also being a fitting parameter. Black curve: piecewise average of the data values. Red curve: the 90% non-linear quantile regression, *i.e.* the function of Eq. (1) with a value of c that leaves 90% of the data points below the curve. Our choice falls on the last quantity, as anticipated, because both the other ones would assign many cells with large values of slope with very small probability of generating rockfalls. We empirically observed that it is not the case.

Numerical results listed in Table I indicate that in three of the units the map produce by the proposed procedure accounts for 80% of the mapped source areas in three topographic units; the agreement is poor (less than 16%) in two units and low (less than 50%) in four units. We show no results for a few units, in which we do not expect rockfalls at all (no mapped source areas), or they do not overlap with the railway track.

We can make sense of the low values of hit rate appearing in Table I with the following considerations. We hypothesized a relationship between the probability of a grid cell of initiating a rockfall and local slope. This represents a good compromise between an acceptable overall time needed for the procedure over a large study area and a realistic product, for our purposes, but it certainly does not embed all of the local terrain properties of that influence the expert criteria applied for mapping potential source

areas. Errors may also arise from the discrepancy between the DEM used in the analysis and the apparent resolution of Google Earth imagery, especially in the locations with largest relief, in which we are mostly interested. Eventually, we used a DEM generated from a triangulated irregular network (TIN); visual inspection of a shaded relief generated form the DEM highlighted locations in which the triangulation used to prepare the DEM is manifest, which surely affects the slope map nation-wide.

Numerical results in Table I correspond to comparisons limited to the slope units overlapping with a buffer along the national railroad network. Applicability of this method for a national rockfall susceptibility map remains to be investigated.

Preliminary results of simulations of rockfall trajectories with the STONE program were compared with mapped rockfalls in the Italian Inventory of Landslide Phenomena Inventory of landslide phenomena, known as IFFI [17, 18]. The IFFI inventory contains over 620,000 landslide polygons, of which 4,051 correspond to rockfalls. Rockfall polygons contain both source and runout areas. The comparison shows nice agreement with empirical evidence. Detailed results, and assessment of their impact on the national railway network, will be reported elsewhere.

ACKNOWLEDGEMENTS

This work was partially supported by RFI gruppo Ferrovie dello Stato Italiane.

REFERENCES

[1] Santangelo, M., M. Alvioli, M. Baldo, M. Cardinali, D. Giordan, F. Guzzetti, I. Marchesini, P. Reichenbach, 2019. "Brief communication: Remotely piloted aircraft systems for rapid emergency response: road exposure to rockfall in Villanova di Accumoli (Central Italy)". Natural Hazards and Earth System Sciences 19, 325-335. DOI: 10.5194/nhess-19-325-2019

[2] Santangelo, M., I. Marchesini, F. Bucci, M. Cardinali, M. Cavalli, S. Crema, L. Marchi, M. Alvioli, F. Guzzetti, 2020. "Exposure to landslides in rural areas in Central Italy". Journal of Maps (in press). DOI: 10.1080/17445647.2020.1746699

[3] Carlà, T., et al., 2019. "Rockfall forecasting and risk management along a major transportation corridor in the Alps through ground-based radar interferometry". Landslides 16, 1425-1435.DOI: 10.1007/s10346-019-01190-y

[4] Giordan, D., A. Manconi, F. Remondino, F. Nex, 2017. "Use of unmanned aerial vehicles in monitoring application and management of natural hazards". Geomatics, Natural Hazards and Risk, 8:1, 1-4.
DOI: 10.1080/19475705.2017.1315619

[5] Mavrouli, O., J. Corominas, 2020. "Evaluation of maximum rockfall dimensions based on probabilistic assessment of the penetration of the sliding planes into the slope". Rock Mechanics and Rock Engineering DOI: 10.1007/s00603-020-02060-z. (In press)

[6] Agliardi, F., G. Crosta, 2003. "High resolution three-dimensional numerical modelling of rockfalls". International Journal of Rock Mechanics and Mining Sciences 40, 455-471. DOI: 10.1016/S1365-1609(03)00021-2

[7] Guzzetti, F., G. Crosta, R. Detti, F. Agliardi, 2002. "STONE: a computer program for the three-dimensional simulation of rock-falls". Computers & Geosciences 28, 1079-1093. DOI: 10.1016/S0098-3004(02)00025-0

[8] Guzzetti, F., P. Reichenbach, S. Ghigi, 2004. "Rockfall hazard and risk assessment along a transportation corridor in the Nera Valley, Central Italy". Environmental Management 34, 191-208. DOI: 10.1007/s00267-003-0021-6

[9] Guzzetti, F., P. Reichenbach, G.F. Wieczorek, 2003. "Rockfall hazard and risk assessment in the Yosemite Valley, California, USA". Natural Hazards and Earth System Sciences 3, 491-503. DOI: 10.5194/nhess-3-491-2003

[10] Tarquini, S., et al., 2007. "Tinitaly/01: a new triangular irregular network of Italy". Annales Geophysicae 50, 407-425. DOI: 10.4401/ag-4424

[11] Alvioli, M., Marchesini, I., Guzzetti, F., 2018. "Nation-wide, general-purpose delineation of geomorphological slope units in Italy". In: Geomorphometry 2018, Boulder, CO, USA. pp. 1-4. DOI:1 0.7287/peerj.preprints.27066v1

[12] Alvioli, M., F. Guzzetti, I. Marchesini, 2020. "Parameter-free delineation of slope units and terrain subdivision of Italy". Geomorphology 358, 107124. DOI: 10.1016/j.geomorph.2020.107124

[13] Guzzetti, F., P. Reichenbach, 1994. "Towards a definition of topographic divisions for Italy". Geomorphology 11, 57-74. DOI: 10.1016/0169-555X(94)90042-6

[14] Alvioli, M., I. Marchesini, P. Reichenbach, M. Rossi, F. Ardizzone, F. Fiorucci, F. Guzzetti, 2016. "Automatic delineation of geomorphological slope units with r.slopeunits v1.0 and their optimization for landslide susceptibility modeling". Geoscientific Model Development 9, 3975-3991. DOI: 10.5194/gmd-9-3975-2016

[15] Jacobs, L., M. Kervyn, P. Reichenbach, M. Rossi, I. Marchesini, M. Alvioli, O. Dewitte, 2020. "Regional susceptibility assessment with heterogeneous landslide information: slope unit- vs. pixel-based approach". Geomorphology 356, 107084. DOI: 10.1016/j.geomorph.2020.107084

[16] Alvioli, M., Marchesini, I., Guzzetti, F., 2020. "Poster presentation: Automatic Delineation of Slope Units and Terrain Classification of Italy". Ibid.

[17] Trigila, A., Iadanza, C., Spizzichino, D., 2010. "Quality assessment of the Italian landslide inventory using GIS processing". Landslides 7, 455-470. DOI: 10.1007/s10346-010-0213-0

[18] ISPRA, 2018. "Landslides and floods in Italy: hazard and risk indicators - Summary Report 2018". Technical report. The Institute for Environmental Protection and Research. Via Vitaliano Brancati, 48 - 00144 Roma. URL: http://www.isprambiente.gov.it.

GEOMORPHOMETRY 2020 PERUGIA, ITALY JUNE 22 - 26 2020

Towards a consistent set of land-surface variables for landslide modelling

Andrei Dornik
Department of Geography, West University of Timisoara, Bd. V. Parvan 4, 300223, Timisoara, Romania

Lucian Drăguț
Department of Geography, West University of Timisoara, Bd. V. Parvan 4, 300223, Timisoara, Romania

Marinela Adriana Chețan
Department of Geography, West University of Timisoara, Bd. V. Parvan 4, 300223, Timisoara, Romania

Takashi Oguchi
Center for Spatial Information Science, The University of Tokyo, 5-1-5 Kashiwanoha, Kashiwa-shi, Chiba, 277-8568, Japan

Yuichi Hayakawa
Center for Spatial Information Science, The University of Tokyo, 5-1-5 Kashiwanoha, Kashiwa-shi, Chiba, 277-8568, Japan
Faculty of Environmental Earth Science, Hokkaido University, N10W5 Kita-ku, Sapporo, Hokkaido, 060-0810, Japan

Mihai Micu
Institute of Geography, Romanian Academy, 023993, Bucharest, Romania

Abstract—**This study aims at identifying a set of land-surface variables (LSVs) that enable consistent results in landslide modelling, within the context of automatic landslide mapping. The experiments were conducted in six study areas in Japan, Romania and USA. From an initial set of 24 LSVs, the most consistent predictors of landslide scarps in all study areas were selected through correlation analysis and variable importance investigation: negative topographic openness (radius 1500 m), slope height, and slope gradient. These three LSVs were further employed to model scarps' presence/absence with logistic regression. The results were compared against logistic regression models built on: 1) the best combination of locally fit LSVs (variable number of predictors, ranging from two to five across study areas), which was determined with backward stepwise logistic regression, and 2) a number of six variables reported in literature to best describe terrain properties. The predictive performance of the model built on the three LSVs came close to 1) and exceeded it in two cases, and outperformed 2), except for two cases. We conclude that negative topographic openness, slope height, and slope, which account for scarps shape, position on the slope, and landsliding favorability respectively, have a potential of generalization across landscape conditions in the prediction of scarps presence/absence.**

I. INTRODUCTION

Data-driven landslide modelling relies mainly on land-surface variables (LSVs) for automatic mapping, as well as for susceptibility assessment [1]. While LSVs are easy to obtain form Digital Elevation Models (DEMs), a consistent approach in selecting the ones that are the most relevant to landslides is still missing [2]. This lack of consistency makes the results of modelling dependent on the skills and experience of the analyst, thus hampering the comparison between models [3] and preventing their transferability to other areas [4].

Here we report preliminary results of an experiment that aims at finding a set of LSVs capable to help in identifying landslide scarps in various landscape conditions.

II. STUDY AREAS

The tests were conducted in six study areas, of different environmental conditions. Three study areas are located in the Buzău county, Romania, at the contact between the Romanian Carpathians and the Subcarpathian Hills, covering 121.7 km^2 (B1), 261.6 km^2 (B2) and 85.1 km^2 (B3) respectively. The annual mean temperature in these areas varies between 4-9°C and the total annual precipitation between 800-1200 mm. These areas are prone to numerous landslides, caused on the one hand by a clay rich substrate and high amount of precipitation, and on the other hand by their location in one of the European seismic hotspots.

Two study areas are located in the southeast of Honshu Island, Shizuoka Prefecture, Japan. The areas are humid and temperate with annual rainfall of approximately 2100 mm and annual mean temperature of 15°C. They are located in a tectonic active zone dominated by medium and high slopes, recording numerous landslides. One area covers 35.9 km^2 (J1) and the second one, 82.5 km^2 (J2).

The sixth study area (U), located in Utah, USA, has a relatively homogeneous lithology dominated by mixed-clastic and limestone deposits and covers an area of 299.2 km^2. The area receives on average 560-600 mm of annual precipitation that falls primarily as snow, while temperatures typically range from -11 to 27°C.

Andrei Dornik, Lucian Dragut, Marinela Adriana Chetan, Takashi Oguchi, Yuichi Hayakawa and Mihai Micu (2020) Towards a consistent set of land-surface variables for landslide modelling: in Massimiliano Alvioli, Ivan Marchesini, Laura Melelli & Peter Guth, eds., Proceedings of the Geomorphometry 2020 Conference, doi:10.30437/GEOMORPHOMETRY2020_44.

III. METHODS

A. Data

In the Buzău study areas there are available databases of landslide scarps compiled from different sources, such as archive data, detailed geomorphological field mapping, local authority databases, digital stereographic photo interpretation using color aerial ortho-photographs [5].

For the Japanese study areas we used inventories of landslide scarps provided by the National Research Institute for Earth Science and Disaster Resilience, Japan (NIED) [6-8].

In Utah we used the Landslide Inventory Polygons developed by professional scientists from Utah Department of Natural Resources and Utah Geological Survey. The polygons were built using LiDAR, stereo aerial photography, other data, and field reconnaissance.

In order to avoid differences in modelling results caused by differences in sampling intensity, the existing databases were reduced to contain approximately the same number of scarps. One point was randomly selected within each landslide scarp, and the same number of points was also randomly selected outside scarp polygons as absence data. The databases for each study area, containing between 204 and 220 points, were split into training (70%) and test (30%) subsets.

Besides landslide inventories, Shuttle Radar Topography Mission (SRTM) 1 arc second (ca. 30 m) digital elevation model (DEM) was available at the US Geological Survey website and was downloaded from the USGS Earth Explorer Interface. The DEM resolution is suitable for this analysis, since the average size of scarps is 14.9, 9.96 and 4.18 ha in B1, B2, B3, respectively, 2.26 ha in J1, 2.58 ha in J2 and 3.24 ha in U.

B. Land-surface variables

A number of 24 LSVs, which have been predominantly used in landslide modelling, were derived from DEM. To avoid multicollinearity of variables we conducted a correlation analysis, to retain only the non-correlated terrain variables. The threshold for variable removal was set to 0.6 for correlation coefficient.

Subsequent processing was conducted in order to ensure that all terrain variables have a normal distribution [9].

C. Variable importance analysis

In order to select a generalizable subset of terrain variables for landslide modelling, the uncorrelated variables were subjected to variable importance (VI) analysis using Random Forest (RF) [10]. VI analysis was conducted with randomForest package in R [11] and was based on the mean decrease in accuracy (MDA) algorithm implemented by Liaw and Wiener [12].

D. Landslide modelling

The identified generalizable subset of variables, arising as important predictors in all study areas were used subsequently to conduct landslide modelling (named LSM_VI).

To assess the performance of the identified set of LSVs, we conducted analyses based on the best model specific to each study area, identified with backward stepwise logistic regression (named LSM_best_model).

In addition, we tested the set of generalizable LSVs against six terrain variables (named LSM_tasse), proposed by Lecours et al. [13] to be used in environmental studies, as the six variables capture more than 70% of the topographic structure of an area. These variables are: relative difference to mean elevation value, standard deviation of DEM, easterness, northerness, local mean and slope.

Logistic regression was used for modelling and the results were evaluated both in terms of model fit using training data and model prediction performance using test data. The model fit was evaluated through the Akaike information criterion (AIC), and the prediction performance through overall accuracy and area under the receiver operating characteristic (ROC) curve (AUC) measures.

IV. RESULTS AND DISCUSSION

A. Correlation analysis

Correlation analysis revealed 14 non-correlated LSVs: elevation, slope, profile curvature, plan curvature, convexity, easterness, northerness, mid-slope position, negative topographic openness, positive topographic openness, slope length, slope height, texture, valley depth.

B. Selection of a generalizable set of LSVs

Fig. 1 shows the results of VI analysis in the six study areas. The first variable that showed as important predictor in all study areas is negative topographic openness (radius 1500 m), with MDA values higher than 10%. Slope height stood out also as important predictor in five out of six study areas, with MDA larger than 10%. In B3, slope height recorded a MDA value of 8.7, however being one of the most important five variables. Slope also recorded high MDA values, in U recording the highest value within all tests (38%), and over 10% in B2 and B3. Slope was also an important predictor in B1 with a MDA value of 8.1%. These three variables were thus selected as the generalizable set for LSM_VI model. We interpret negative openness as a generalized concavity that accounts for the shape of the landslide scarps; slope heights would describe the scarp position, and slope gradient is well known as the main topographic predisposing factor for mass movements.

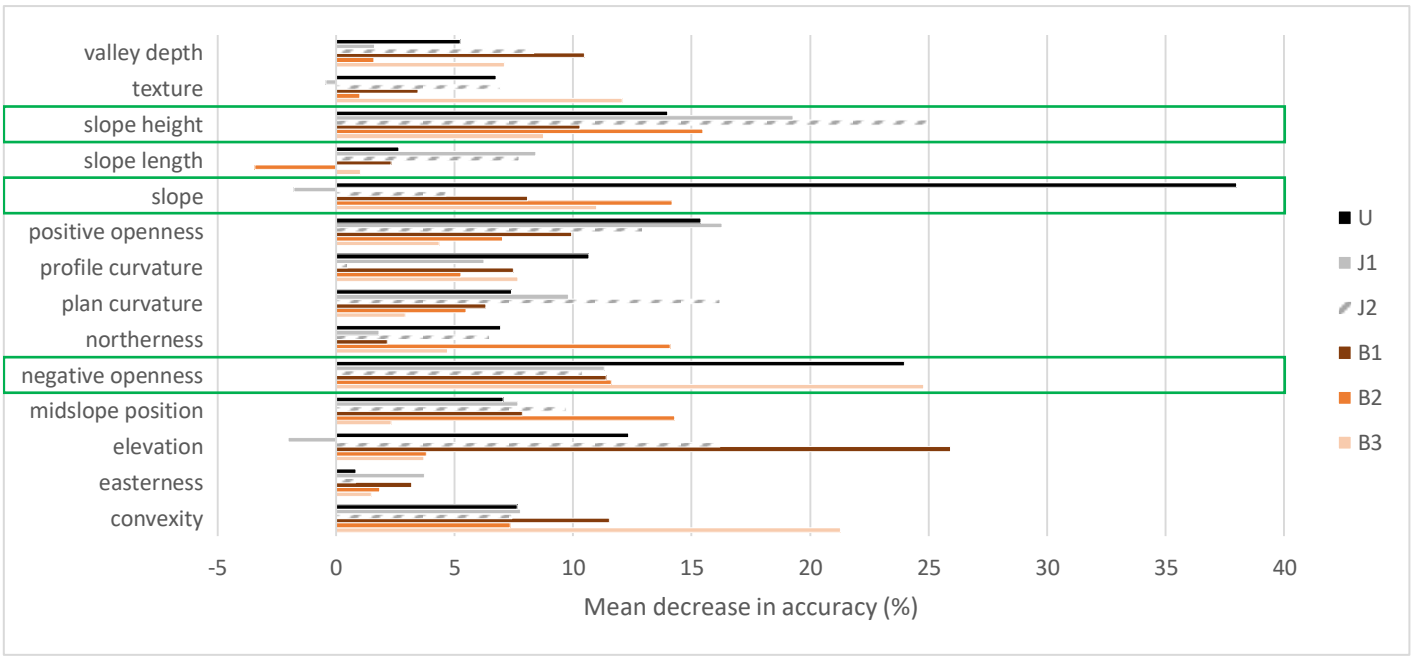

Figure 1. Variable importance expressed as mean decrease in accuracy in the six study areas.

Other variables were more location specific, highlighted as important predictors only in one to three study areas. For example, convexity, elevation and valley depth recorded MDA values higher than 10% in B1, midslope position and northerness in B2, positive openness in J1, elevation and plan curvature in J2, and profile curvature in U. Other terrain variables like easterness, slope length and texture were among the least important variables in all study areas.

C. Models evaluation

In terms of model fit measured by AIC, our proposed model was relatively similar to the best model, losing between only 7.4 in study area U and 28.8 in B3. The other study areas recorded AIC value larger by less than 20. Comparing our proposed model with LSM_tasse, in five out of six cases LSM_VI model was better with AIC value lower by 2.6, 4.6, 9.1, 13.7 and 14.2. In study area B2, LSM_tasse model was better than our model, by 12.4 (Table 1).

Overall accuracy of LSM_VI recorded values lower than the best model in four out of six cases, however by only 1-7%. In study areas J1 and B3 our proposed model performed better than the best model, by 2 and 12% respectively. In four out of six cases our proposed model overperformed LSM_tasse, recording overall accuracies higher by 3, 5, 11 and 15%. In study area U the models had the same accuracy, 70%. Only in one case, B1, LSM_tasse performed better than LSM_VI, by 12%. The absolute values of overall accuracy for LSM_best_model range between 52 and 74%, for LSM_VI between 56-70%, and for LSM_tasse between 53-70% (Table 1).

In terms of AUC, the best model performed better than our proposed model only in two cases (J2 and B1), by 0.01 and 0.1, in other two cases the models performing identical (B2 and B3), with an AUC of 0.65. In J1 and U, LSM_VI performed better than the best model, by 0.09 and 0.03. Compared to LSM_tasse, our proposed model recorded higher AUC values in five out of six cases, with differences ranging between 0.01 and 0.16. Only in study area B1, LSM_tasse recorded an AUC higher than LSM_VI, by 0.12. The absolute values of AUC ranged between 0.63-0.82 for LSM_best_model, 0.63-0.83 for LSM_VI and 0.63-0.81 for LSM_tasse (Table 1).

The results should be interpreted also regarding the number of variables, being well known that between two similar models, it should be preferred the simpler one. While the LSM_VI used three terrain variables and LSM_tasse used six variables, the best model used various numbers of variables, ranging from 2 in J1 to 5 in B2.

Table 1. Models fit and prediction performance assessment.

Study area		AIC			Overall accuracy			AUC		
	Var. no. best model	LSM_best_ model	LSM_VI	LSM_ tasse	LSM_best_ model	LSM_VI	LSM_ tasse	LSM_best_ model	LSM_VI	LSM_ tasse
J1	2	186.70	197.30	206.40	0.52	0.64	0.53	0.63	0.72	0.64
J2	4	178.60	188.10	202.30	0.74	0.70	0.55	0.82	0.81	0.65
B1	3	167.80	183.90	188.50	0.63	0.56	0.68	0.73	0.63	0.75
B2	5	168.30	185.30	172.90	0.64	0.59	0.56	0.65	0.65	0.63
B3	4	158.70	187.50	201.20	0.62	0.64	0.59	0.65	0.65	0.64
U	4	147.80	155.20	157.80	0.71	0.70	0.70	0.80	0.83	0.81

V. CONCLUSIONS

We found three LSVs with the potential of describing satisfactorily landform scarps in various landscape conditions. Negative topographic openness, slope height, and slope account for scarps shape, position on the slope, and landslide favorability respectively.

The logistic regression model based on these three LSVs produced results comparable to models built on locally calibrated LSVs, as well as to a model built on a double number of LSVs.

REFERENCES

[1] Reichenbach, P., et al., *A review of statistically-based landslide susceptibility models.* Earth-Science Reviews, 2018. **180**: p. 60-91.

[2] Budimir, M., P. Atkinson, and H. Lewis, *A systematic review of landslide probability mapping using logistic regression.* Landslides, 2015. **12**(3): p. 419-436.

[3] Guzzetti, F., et al., *Landslide hazard evaluation: a review of current techniques and their application in a multi-scale study, Central Italy*. Geomorphology, 1999. **31**(1-4): p. 181-216.

[4] Cama, M., et al., *Improving transferability strategies for debris flow susceptibility assessment: Application to the Saponara and Itala catchments (Messina, Italy).* Geomorphology, 2017. **288**: p. 52-65.

[5] Sîrbu, F., et al., *Scaling land-surface variables for landslide detection.* Progress in Earth and Planetary Science, 2019. **6**(1): p. 44.

[6] Shimizu, F., et al., *Landslide maps series 14 "Shizuoka".* Technical Note of the National Research Institute for Earth Science and Disaster Resilience, p 221, 2002.

[7] Uchiyama, S., et al., *The NIED landslide mapping team.* 2012.

[8] Oyagi, N., S. Uchiyama, and M. Ogura, *Explanations of landslide distribution maps.* Technical note of the National Research Institute for Earth Science and Disaster Resilience, 2015. **vol 394, pp 391-314**.

[9] Csillik, O., I. Evans, and L. Drăguţ, *Transformation (normalization) of slope gradient and surface curvatures, automated for statistical analyses from DEMs.* Geomorphology, 2015. **232**: p. 65-77.

[10] Breiman, L., *Random forests.* Machine learning, 2001. **45**(1): p. 5-32.

[11] R Core Team, *R: A language and environment for statistical computing. R Foundation for Statistical Computing*. 2015: p. Vienna, Austria, http://www.R-project.org/.

[12] Liaw, A. and M. Wiener, *Classification and regression by randomForest.* R news, 2002. **2**(3): p. 18-22.

[13] Lecours, V., et al., *Towards a framework for terrain attribute selection in environmental studies.* Environmental Modelling & Software, 2017. **89**: p. 19-30.

GEOMORPHOMETRY 2020
PERUGIA, ITALY
JUNE 22 - 26 2020

Incorporating ground cracks in the estimation of post-seismic landslide susceptibility

Shui Yamaguchi, Mio Kasai§,
Research Faculty of Agriculture
Hokkaido University
Kit-9, Nishi-9, Kita-ku, Sapporo, Japan
§kasaim@for.agr.hokudai.ac.jp

Abstract—**An intense earthquake not only induces numerous landslides over a broad area, but can also trigger landslides; this is because the ground loses strength when strong tremors occur. Following an earthquake, landslide susceptibility should be appraised immediately to avoid further disasters and enable safe and prompt restoration work to proceed in the affected region. This study developed a topographic index to represent a soil mass with dense seismic ground cracks (DCI), to allow the degree of ground disturbance to be expressed on a local scale. The index was then used as a conditioning factor in a statistical model based on the weight of evidence (WoE) approach, to assess the correlation between DCI and landslides and estimate landslide susceptibility. An analysis of 38 post-seismic slides was conducted in a 2 km^2 area of the Aso region in Kyushu, Japan, where a powerful earthquake (Mw 7.0) struck in April 2016. Tectonic, seismic, lithological, climatic, and vegetational conditions were assumed to be similar over the area due to its small size, and only topographic conditioning factors were considered. The results demonstrated a correlation between DCI and post-seismic landslide occurrence, and the area under the receiver operating characteristic curve (AUC) indicated slightly greater model accuracy when DCI was included. Further studies using larger datasets are required to develop an appropriate model to express the relationships between the index and controlling factors, to improve the accuracy of post-seismic slide susceptibility assessments.**

I. INTRODUCTION

An intense earthquake can trigger numerous landslides over a broad area, causing damage to human lives, property, and infrastructure. Following an earthquake, an area will remain prone to landslides because ground that is affected by strong tremors requires months to years to recover its strength. Under these circumstances, landslide susceptibility should be appraised as soon as possible to avoid further disasters and enable safe and prompt restoration work to begin in the area. Appraisals are often made by the "direct method" [1], i.e., identifying topographic features indicative of slope instability, such as ground cracks, slope knick lines, and steep slopes, via field survey and/or examining aerial photographs or topographic maps derived from a light detection and ranging (LiDAR) survey. However, this is time-consuming and labor-intensive work, and the outcome can vary according to the skill of the operators. As an alternative, landslide susceptibility can also be estimated indirectly using a statistical model incorporating tectonic, lithological, climatic, hydrologic, topographic, and vegetation conditioning factors [2]. This method has been widely applied to co-seismic slides [3,4,5], while it has rarely been used for post-seismic slides, possibly because of a shortage of information regarding landslides after an intense earthquake. An appropriate and accurate model for post-seismic slides would facilitate assessments of landslide susceptibility over a broad area.

In this study, we attempted to develop a statistical model to appraise post-seismic landslide susceptibility by considering seismic ground cracks. The location of the ground cracks is a key issue when using the direct method, but is rarely considered in statistical models, due to the coarse resolution of elevation data and the difficulty of digital expression of the features. A 2 km^2 area of the Aso region in Kyushu, Japan, where a powerful earthquake (Mw 7.0) occurred in April 2016, was selected for the analysis (Figure 1). As the first step, an index to represent soil mass with dense seismic ground cracks (DCI) was proposed by employing a surface roughness filter. The DCI, together with topographic factors selected following a field survey [6], was then assessed using the weight of evidence (WoE) approach [7], to examine the correlation between the indices and the occurrence of landslides, and estimate landslide susceptibility. Finally, landslide susceptibility estimations were compared with versus without use of the DCI, to determine the improvement in the model achieved by incorporating seismic ground cracks into the set of conditioning factors.

Shui Yamaguchi and Mio Kasai (2020) Incorporating ground cracks in the estimation of post-seismic landslide susceptibility:
in Massimiliano Alvioli, Ivan Marchesini, Laura Melelli & Peter Guth, eds., Proceedings of the Geomorphometry 2020 Conference, doi:10.30437/GEOMORPHOMETRY2020_45.

II. STUDY AREA

The study area was located on a flank of the caldera wall of the Aso volcano, underlain by Middle Pleistocene pyroxene, andesite, and pyroclastic rock. The 2016 earthquake caused 76 slides and numerous cracks over an area of 2 km^2. A further 38 landslides were later induced by rainfall; these were of the shallow translational type, and some of them yielded a debris flow. Landslides increased in size continuously following the earthquake; this phenomenon was not accounted for in this study. A landslide inventory was compiled based on aerial photographs and LiDAR survey data acquired simultaneously in January 2015, and in April and August 2016. Slopes where landslides were initiated were targeted for the analysis; therefore, sediment transfer and deposition zones were not included in the inventory. Tectonic, seismic (e.g. peak ground acceleration), lithological, and climatic conditions were presumed to be equal throughout the study area due to its small size. The entire area was covered with aged *Cyptomeria japonica*.

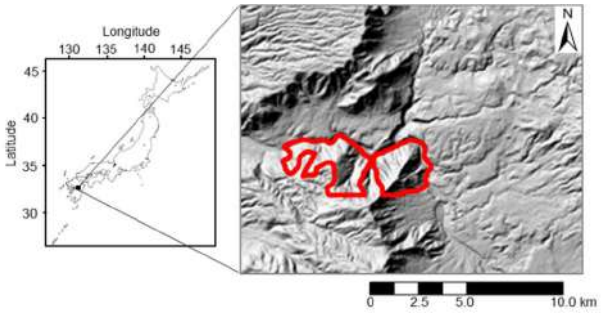

Figure 1. Study area (outlined in red)

III. METHODS

The DCI was derived from a surface roughness filter, based on the assumption that crack formation is associated with an increase in roughness. In this study, we applied a standard deviation of a slope angle for 3 × 3 cells, σ_s, proposed by [8], to the filter, using a 1-m digital elevation model (DEM). We assumed that cracks appeared in cells where the change in standard deviation from pre- (January 2013) to post- (April 2016) earthquake conditions ($\sigma_{s\ chg}$) was greater than or equal to a threshold value (C_m). The change was calculated as follows:

$$\sigma_{s\,chg} = \sigma_{s\,post} - \sigma_{s\,pre} \quad (1)$$

where the subscript indicates the timing of the LiDAR survey used to produce two DEMs. We compared the spatial distributions of $\sigma_{s\,chg}$ and seismic ground cracks identified in the field, or based on topographic maps generated after the earthquake, to determine C_m. Then, cells with $\sigma_{s\,chg} \geq C_m$ were converted into points to calculate the point density using a kernel density function with a bandwidth of 10 m for each 1-m cell in the ArcGIS software environment. The density was defined as DCI.

The WoE method [7] was applied to estimate the susceptibility to post-seismic landslides. A bivariate model was used to examine the correlation between DCI and the occurrence of post-seismic landslides. We randomly selected 68% of the landslides (26) to train the model; the remaining 12 were used for testing. The correlation between a certain conditioning factor class and landslides is given by the contrast, C, as follows:

$$C = W^+ - W^- \quad (2)$$

where W^+ is the positive weight of evidence for a certain conditioning factor class, and W^- is the negative weight of evidence for the class for a 1-m cell. They are given by:

$$W^+ = \ln\frac{P(F|L)}{P(F|\overline{L})} \quad (3)$$

$$W^- = \ln\frac{P(\overline{F}|L)}{P(\overline{F}|\overline{L})} \quad (4)$$

where L indicates the presence of a landslide, F indicates the presence of a value within a certain conditioning factor class, $\overline{L}$ indicates the absence of a landslide, $\overline{F}$ indicates the absence of a value within a certain conditioning factor class, $P(F|L)$ is the probability of a 1-m landslide cell conditioning a value within a certain conditioning factor class, $P(F|\overline{L})$ is the probability of a cell outside of a landslide containing a value within a certain conditioning factor class, $P(\overline{F}|L)$ is the probability of a 1-m landslide cell not containing a value within a certain conditioning factor class, and $P(\overline{F}|\overline{L})$ is the probability of a cell outside of a landslide not containing a value within a certain conditioning factor class. The combination of positive W^+ and negative W^-, or high C, suggests a positive relationship between landslide occurrence and that conditioning factor class. In contrast, a combination of negative W^+ and positive W^- indicates a negative relationship. If landslide occurrence is independent of the factor class, then W^+ and W^- both equal 0. The classes of DCI and other conditioning factors, slope angle, plan and profile curvature, and topographic wetness index (TWI) obtained for each 1-m cell are shown in Table 1. The plan and profile curvature values for each cell provided excessively detailed topographic information, and appeared not to show the effects of slope profiles on landslide occurrence appropriately. Therefore, we averaged these values within a 10-m radius of each cell, as described previously by [9], and incorporated the results into the model. The variance inflation factor (VIF) of the included factors ranged from

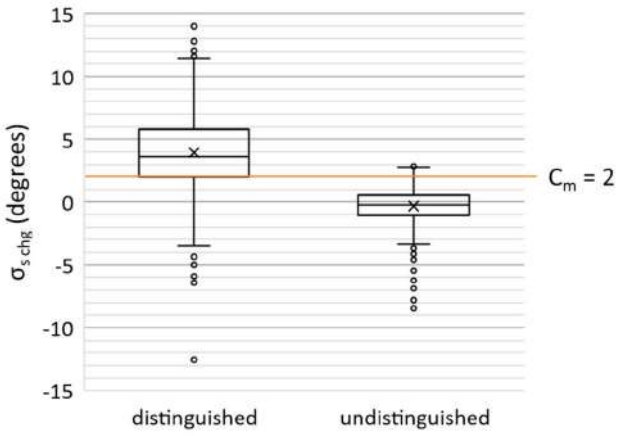

Figure 2. Box plots of $\sigma_{s\,chg}$ for the locations with cracks distinguished and undistinguished. The interquartile range is represented by the box. Upper whiskers: 1.5 times the interquartile range above the third quartile. Lower whiskers: 1.5 times the interquartile range below the first quartile. Outliers are plotted as dots. The horizontal line represents the median value of $\sigma_{s\,chg}$.

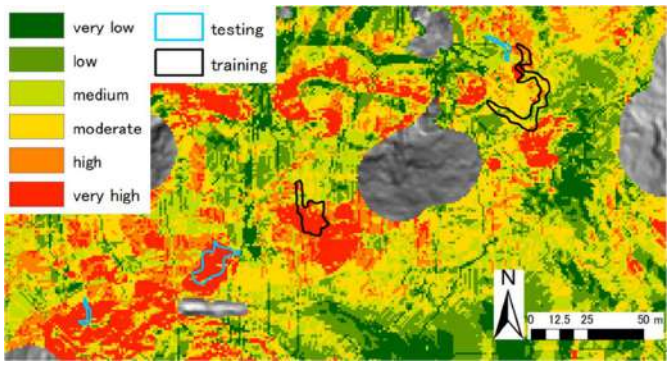

Figure 3. A part of susceptibility map for post-seismic slides. Areas of co-seismic slides were omitted from the analysis. Susceptibility is categorized into 5 classes, very high (10%), high (10%), moderate (20%), medium (20%), low (20%) and very low (20%).

1.03 to 1.13, confirming their independence. *C* values obtained for each conditioning factor were summed for each 1-m cell and used as a landslide susceptibility index for the cell. The accuracy of the models with/without use of the DCI was compared based on the area under the receiver operating characteristic curve (AUC) for true and false positive rates.

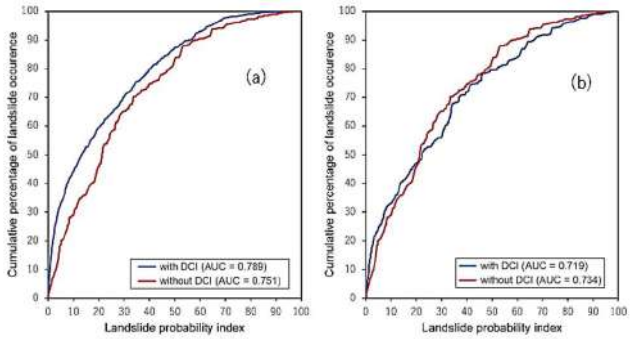

Figure 4. ROC curves calculated for (a) training and (b) testing slides.

IV. Results and Discussion

The standard deviation of slope angle increased by more than 2° after the earthquake in 75% of the locations where ground cracks were identified; therefore, we set C_m as 2° (Figure 2). Table 1 shows a negative contrast for DCI values < 0.2, which increased in classes with high DCI values. Overall, the factor that had the greatest influence on post-seismic slides was a DCI value over 0.6. The results suggest that integration of the DCI was favorable for estimating susceptibility to post-seismic landslides. Profile curvatures from -4 to 0, which corresponded to knick lines, and slope angles from 35° to 50° were other topographic features closely associated with landslide occurrence; this finding was consistent with a previous field investigation of post-seismic landslides in the same region [6]. A profile curvature < -4 corresponded to abrupt profile changes, such as cliff tops. Positive contrasts for the 0–4 plan curvature classes demonstrated concave slopes where landslides were likely to occur, whereas those > 4 mainly indicated narrow ridges.

Part of a post-seismic-slide susceptibility map is presented as an example in Figure 3. When using the DCI, the AUC values for training and testing slides were 0.79 and 0.72, respectively (Figure 4), which were within the range considered acceptable by the model [10]. In contrast, the AUC values for cases without DCI were 0.75 for training slides and 0.73 for testing slides (Figure 4). We obtained a slight improvement in the training data, but no improvement in the testing data upon incorporating DCI, despite the close association of the index with landslide occurrence (Table 1). This result can be partly explained by the manner in which the topographic features were represented by conditioning factors, and also by deficits in the bivariate model, which did not consider associations among controlling factors. In addition, a small number of landslide data, particularly in the testing dataset, disproportionately affected the modelling results. Further study

using larger datasets is required to find the most appropriate combination of topographic factors and statistical model to increase the accuracy of post-seismic slide susceptibility assessments. Tectonic, seismic, lithological, climatic, and vegetation conditions should also be considered to extend the applicability of the model and help to prevent disasters caused by post-seismic landslides during restoration work undertaken after powerful earthquakes.

Table 1. Contrast for conditioning factors.

Conditioning factor	class	W^+	W^-	contrast
DCI	−0.2	-0.440	0.673	-1.113
	0.2−0.4	0.499	-0.193	0.692
	0.4−0.6	0.968	-0.090	1.057
	0.6−	1.899	-0.041	1.940
Slope angle (degree)	−20	-2.184	0.098	-2.283
	20−25	-1.503	0.067	-1.570
	25−30	-0.696	0.066	-0.762
	30−35	-0.075	0.013	-0.089
	35−40	0.329	-0.091	0.420
	40−45	0.568	-0.146	0.714
	45−50	0.371	-0.047	0.418
	50−	-0.005	0.001	-0.005
Plan curvature	−-4	-1.760	0.074	-1.835
	-4−-2	0.032	-0.004	0.036
	-2−0	-0.261	0.082	-0.342
	0−2	0.320	-0.193	0.513
	2−4	0.326	-0.056	0.382
	4−	-0.520	0.041	-0.561
Profile curvature	−-4	-1.252	0.036	-1.289
	-4−-2	0.469	-0.060	0.528
	-2−0	0.449	-0.387	0.835
	0−2	-0.424	0.193	-0.617
	2−	-1.422	0.098	-1.520
TWI	−2	0.050	-0.042	0.091
	2−4	-0.059	0.034	-0.092
	4−6	0.236	-0.042	0.277
	6−	-1.378	0.038	-1.415

REFERENCES

[1] Van Westen, C.J., N. Rengers, R. Soeters, 2003. “Use of geomorphological information in indirect landslide susceptibility assessment”. Nat. Hazards 30, 399-419.

[2] Reichenbach, P., M. Rossi, B.D. Malamud, M. Mihir, F. Guzzetti, 2018. “A review of statistically-based landslide susceptibility models”. Earth Sci Rev 180, 60-91.

[3] Tanyaş, H., M. Rossi, M. Alvioli, C.J. van Westen, I. Marchesini, 2019. “A global slope unit-based method for the near real-time prediction of earthquake-induced landslides”. Geomorphology 327, 126-146.

[4] Tanyaş, H., C.J. van Westen, C. Persello, M. Alvioli, 2019. “Rapid prediction of the magnitude scale of landslide events triggered by an earthquake”. Landslides 16, 661-676.

[5] Nowicki Jessee, M.A., M.W. Hamburger, K. Allstadt, D.J. Wald, S.M. Robeson, H. Tanyaş, M. Hearne, E.M. Thompson, 2018. “A global empirical model for near-real-time assessment of seismically induced landslides”. J. Geophys. Res. Earth Surf. 123-8, 1835-1859.

[6] Committee for Seismic Crack Counterplan in the Tateno District, 2019. “Field Investigation Report”. Kumamoto Prefecture.

[7] Bonham-Carter, G.F., 1994. “Tools for Map Analysis: Multiple Maps”. Geographic Information Systems for Geoscientists: Modelling with GIS, Pergamon (Elsevier Science Ltd), pp. 267-338.

[8] Frankel, K.L., and J.F. Dolan, 2007. “Characterizing arid region alluvial fan surface roughness with airborne laser swath mapping digital topographic data”. J. Geophys. Res. Earth Surf. 112, F02025.

[9] Toda, K., 2012. "Development of the microtopographical map by using airborne LIDAR DEM". J. Jpn. Soc. Erosion Control Eng. 65-2, 51-55.

[10] Hosmer, D.W., and S. Lemeshow, 2000. “Assessing the Fit of the Model”. Applied Logistic Regression, John Wiley and Sons, Inc., pp. 143 -202.

GEOMORPHOMETRY 2020 PERUGIA, ITALY JUNE 22 - 26 2020

Methodological Improvement for Reconstructing the Paleo-topography of Lombok Island before the Samalas AD 1257 Eruption

Mukhamad N. Malawani[§, β], Franck Lavigne[§], Bachtiar W. Mutaqin[β]
[§]Laboratory of Physical Geography – CNRS Meudon
University of Paris 1 – Pantheon Sorbonne
1 Place Aristide Briand, 92195, France
[β]Environmental Geography, Universitas Gadjah Mada
mukhamad.malawani@lgp.cnrs.fr; malawani@ugm.ac.id

Abstract—**Paleo-topographic reconstruction due to volcanic eruptions is a fascinating study, especially if the erupting volcano has a large magnitude of the eruption. Recently, at least three previous studies present well-organized methods and computational analysis for paleo-topography reconstruction. By reviewing those research and did a simple test, we found that there are small gaps that need to be improved. This paper is proposed an improvement method for paleo-topography reconstruction. It is important to notice that this improved methodology is not technically based, but only focused on a conceptual framework. The improvement review involves five variables, i.e., 1) the present-day topography, 2) stratigraphic composite, 3) data correlation, 4) paleo-channel validation, and 5) final paleo-topography validation. This improvement will be applied in future research in a complete reconstruction of Lombok island paleo-topography before the Samalas AD 1257 eruption.**

I. INTRODUCTION

Samalas volcano is located in Lombok Island, Indonesia. This volcano experienced a significant eruption in AD 1257 which is known as one of the most significant volcanic eruptions in recent human history [1], [2]. This eruption is speculated to have caused the climatic change at both the local and global scales [2]–[4]. As a local impact, Lombok paleo-topography has been mostly buried by the volcanic deposits in the western, northern, and eastern regions (Fig. 1). The dynamic impact at the local scale has been reconstructed along the eastern part of Lombok Island, adjacent to Alas Strait [5]. The eastern part reconstruction showed that the morphology dramatically changed due to pumice-rich PDC deposit, which thickness ranged up to 30 m. The burial deposit significantly changed the pattern of the valleys from 1257 to the present day.

The landscape prior to the 1257 eruption has not been fully reconstructed yet especially in the northern and western parts. A study from Ref. [5] is useful as baseline because it emphasized that burial deposit consists of pumice-rich PDC deposits; sand with pumice fragments (laharic); flood derived deposits (sand material domination), and reworked materials with limited or no pumice deposits. A similar study of paleo-topography reconstruction was also previously performed in the Sarno River plain (Italy) due to Somma-Vesuvius eruption in AD 79 [6],[7]. The method from Ref. [6], [7] has been then improved by Ref. [5] for reconstructing eastern part of Lombok. However, those methodologies especially from Ref. [5] is still possible to be improved in order to reconstructing the northern and eastern part 13th century topography of Lombok Island. This paper provides proposed methods for reconstructing paleo-topography.

II. METHODS

This paper presents a methodological review especially from Ref. [5] and Ref. [7], to enhance a better methodological framework. Five fundamental proposed variables for nearly future improvement were applied in Mataram city, western part Lombok Island (Fig. 1). The first variable is present-day topography. The paleo-topography modeling is depending on the present topography input, which can be represented using DEM (digital elevation model). A study from Ref. [7] has mentioned that present topography is the most importance as a variable predictor. The second variable is composite stratigraphy. The third one is a correlation between various data input, e.g. cores data, wells data, outcrops, etc. The fourth variable is paleo-channel validation. The last one is the paleo-topography validation method.

Mukhamad Malawani, Franck Lavigne and Bachtiar Mutaqin (2020) Methodological Improvement for Reconstructing the Palaeo-topography of Lombok island before the Samalas AD 1257 Eruption: in Massimiliano Alvioli, Ivan Marchesini, Laura Melelli & Peter Guth, eds., Proceedings of the Geomorphometry 2020 Conference, doi:10.30437/GEOMORPHOMETRY2020_46.

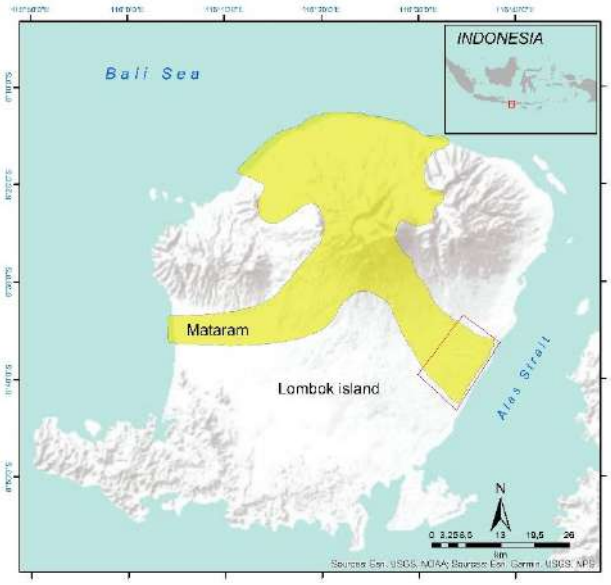

Figure 1. Mataram city, located in the western part of Lombok Island. Yellow color represents areas that have been buried by PDC deposits from the 1257 eruption of Samalas volcano [1], [4]. Red box adjacent to Alas Strait is the previous paleo-topography reconstruction performed by Ref. [5].

III. RESULTS AND CONCLUSIONS

A. Present-day topography/elevation data

Indonesia has been published a free DEM data source in national coverage, namely DEMNAS data with the best resolution in 8 meter. The DEMNAS data can be accessed in: http://tides.big.go.id/DEMNAS/login.php. Compared to topography data (contour) from RBI (Rupa Bumi Indonesia/ Indonesia Topographic Map), DEMNAS data provides better data as shown in Fig. 2. The SRTM and ASTER GDEM resolution data are even lower (30m respectively). The DEMNAS is preferable to use for a basic data of present-day topography. However, for paleo-topographic reconstruction, present-day topography is not sufficient only using DEM data. Geodetic measurement of x,y,z data is essential by putting some ground control point (GCP) data as a reference detailed coordinate. The number of GCP points is custom, depending on the area and topographic form [8]. As comparison, digital elevation model (DEM) used in the Sarno River plain stated as high resolution DEM, but the detailed resolution has not mentioned neither its type nor source-generated. It is only mentioned that the expected result in scale 1:5,000 [7]. For the eastern part of Lombok, present day DEM was generated from Indonesia Topographic Map (RBI) in scale 1:25,000 [5]. Basically, aerial photography is the fastest way for obtaining present day DEM, but for a densely vegetated area this method is slightly difficult to apply [9], also an aerial photograph is costly. Therefore, the combination between DEMNAS data and GCP measurement will produce better present-day elevation model with better resolution.

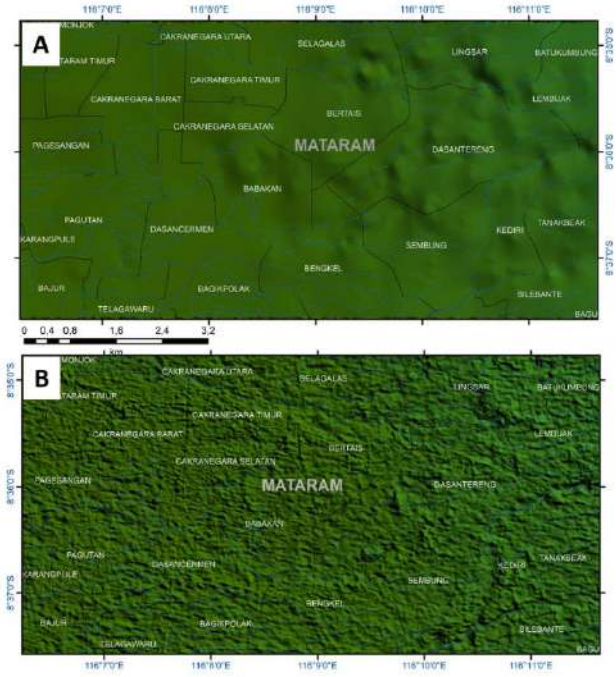

Figure 2. Comparison of DEM data derived from RBI contour map (A) and DEMNAS (B). As shows in the figure, DEMNAS data has more detailed morphology expression.

B. Stratigraphic Composite

Composite stratigraphy was reconstructed in the western part of Lombok using deep core data from the Government of Nusa Tenggara Barat Province (Fig. 3). In this composite stratigraphy, information of paleosol and and physical characteristics of rock, especially pumice, is essential to better understand the arrangement of buried materials since the 13th century eruption. Stratigraphic reference from Ref. [4] also useful for the contruction of stratigraphic composite. This stratigraphic composite method has been applied in Merapi volcano for reconstructing the dynamic buried materials since 4,800 years BP to present [10]. Previous modeling in the eastern part of Lombok does not display any stratigraphic composite information because in this area PDC rich deposits from Samalas AD 1257 is dominant, so the rock layers condition is mostly similar.

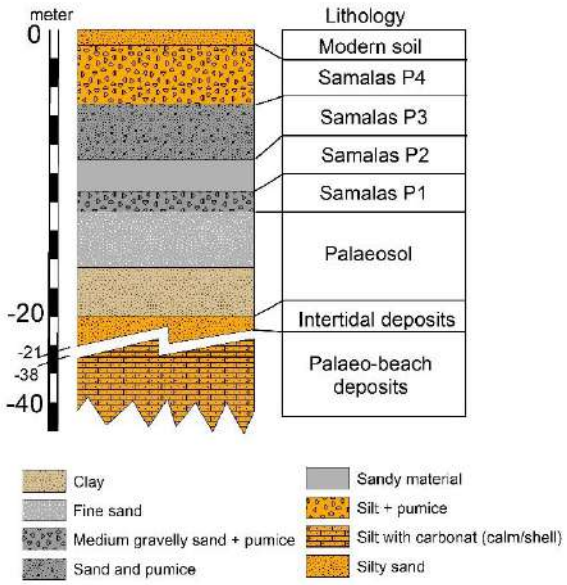

Figure 3. Stratigraphic composite from several deep core data in Islamic Centre of Lombok island. The term of Samalas P1-P4 (ejected material during eruption phase 1-4) and paleo-beach deposits lithology is refers to Ref.[1], [4]. Paleosol is selected as former surface topography, while modern soil and Samalas P1-P4 are buried material after 13th century.

C. Data correlation

The composite stratigraphy is the main reference of bedding classification. Other lithology data such as outcrops, wells data, boreholes must be correlated to the main stratigraphic reference. Borehole data can be obtained using percussion drill or soil auger. For the western and northern part of Lombok, we proposed a correlation order as shows in Fig. 4. We suggest that the main stratigraphic reference for correlation purpose is deep core data, while the numerous data is wells data because it is easy to obtain from wellsman. Usually when they made a wells, they were recorded the material found at every depth. In addition, the distribution of data is considerable by using grid method. Each grid should be represented by minimum of a wells data.

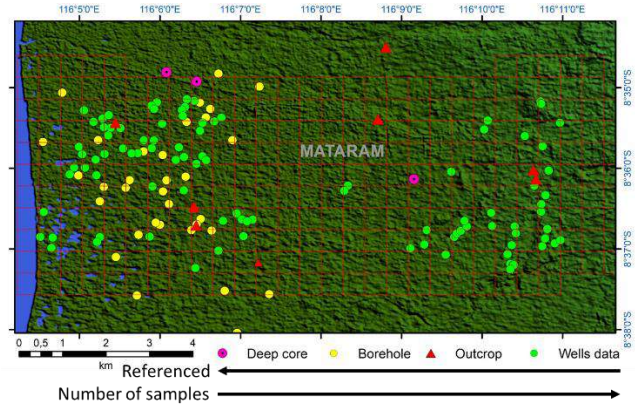

Figure 4. The data availability and its correlation order in Mataram city, which consist of cores, boreholes, outcrops, and wells data.

D. Paleo-channel validation

Interpreted resistivity data can be used as paleo-channel validation. Fig. 5 shows the suspected paleo-channel in Mataram city. Cross-section was performed in north-south direction. Resistivity data can well detect the paleo-channel especially if there was a wide river valley. Buried material form volcanic deposits follows the past topographic form as shown in Fig. 5. Both of Sarno River plain and eastern part of Lombok are performing paleo-channel reconstruction. The method is slightly similar by using "watershed" modeling in GIS software and geological data inventory. This method is robust and rapid but need more validation strategies by using resistivity data.

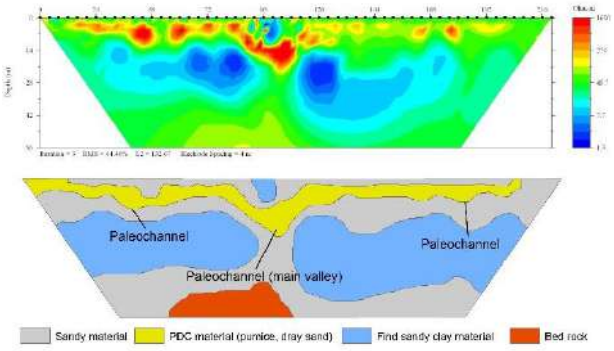

Figure 5. Suspected paleo-channel generated from resistivity data interpretation.

E. Paleotopography validation

A simple test of RMSE (rot-mean square error) was calculated in some area of Mataram 13th century topography using wells data inventory. The modeling of paleo-topography (Fig. 6) is shows a good validation with the value of RMSE 0.447. The interpolation methods are using IDW. Comparing to Ref. [5], [7] modeling, the data used in this test is limited, but shows proper validation. In this case, we noted that RMSE is a basic for validation, but we proposed additional validation methods. The first is calculating RMSE in three different locations, such as in the ridge (hilly), plain, and valley. We believe that they will have a different estimated error. Comparison of topographic section between paleo and present-topography is also useful for selecting the location for error calculation (Fig. 7). The second is performing random outcrops observation or borehole test in those three different locations to searching the real base of paleo-topography. When the random point is used for validation, we believe it will be resulting in more satisfied validation than using data input for modeling.

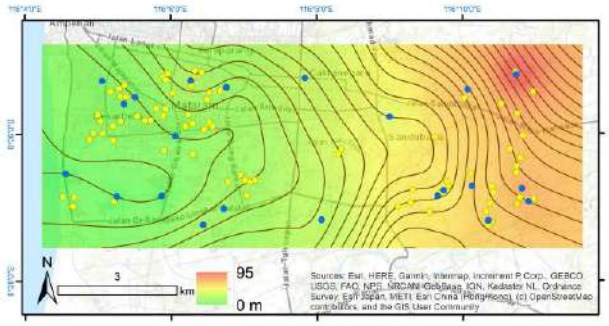

Figure 6. The preliminary paleo-topography of the 13th century in Mataram, modeled using wells data inventory (yellow dot) and additional reference points (blue dot).

In conclusion, we assumed that better paleo-topography reconstruction should build from a better conceptual methodological framework. Even if results from Ref. [7] and Ref. [5] are convinced, we have shown that they can be improved using additional strategies. The proposed method described in this paper starts from data input, then stratigraphically analysis, and validation strategy. The data processing technic is not explained in detail because we focused on the conceptual framework. This improvement review will be applied in near future research for a complete work.

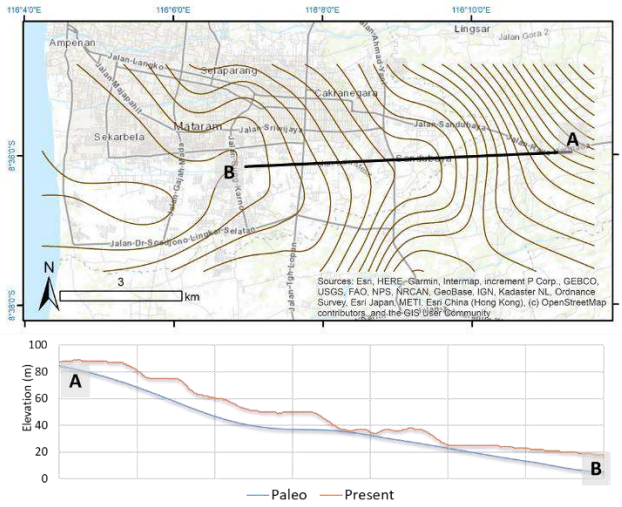

Figure 7. Comparison between paleo and present-day topographic profile of Mataram. Profile line A-B shows that paleo-topography is rather smooth with minor topographic expression.

REFERENCES

[1] F. Lavigne *et al.*, "Source of the great A.D. 1257 mystery eruption unveiled, Samalas volcano, Rinjani Volcanic Complex, Indonesia," *Proc. Natl. Acad. Sci. U. S. A.*, vol. 110, no. 42, pp. 16742–16747, 2013.

[2] C. M. Vidal *et al.*, "The 1257 Samalas eruption (Lombok, Indonesia): The single greatest stratospheric gas release of the Common Era," *Sci. Rep.*, vol. 6, no. October, 2016.

[3] S. Guillet *et al.*, "Climate response to the Samalas volcanic eruption in 1257 revealed by proxy records," *Nat. Geosci.*, vol. 10, no. 2, pp. 123–128, 2017.

[4] C. M. Vidal *et al.*, "Dynamics of the major plinian eruption of Samalas in 1257 A.D. (Lombok, Indonesia)," *Bull. Volcanol.*, vol. 77, no. 9, 2015.

[5] B. W. Mutaqin *et al.*, "Landscape evolution on the eastern part of Lombok (Indonesia) related to the 1257 CE eruption of the Samalas Volcano," *Geomorphology*, vol. 327, pp. 338–350, 2019.

[6] S. Vogel and M. Märker, "Reconstructing the Roman topography and environmental features of the Sarno River Plain (Italy) before the AD 79 eruption of Somma-Vesuvius," *Geomorphology*, vol. 115, no. 1–2, pp. 67–77, 2010.

[7] S. Vogel, M. Märker, and F. Seiler, "Revised modelling of the post-AD 79 volcanic deposits of Somma-Vesuvius to reconstruct the pre-AD 79 topography of the Sarno River plain (Italy)," *Geol. Carpathica*, vol. 62, no. 1, pp. 5–16, 2011.

[8] E. Oniga, A. Breaban, and F. Statescu, "Determining the optimum number of ground control points for obtaining high precision results based on UAS images" p. 5165, 2018.

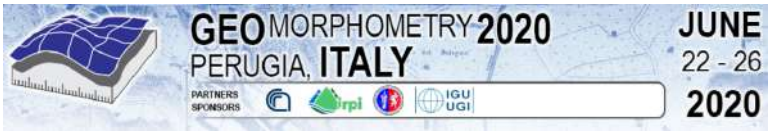

Slope – catchment area relationship for debris-flow source area identification

Ivan Marchesini[§], Mauro Rossi, Massimiliano Alvioli, Michele Santangelo, Mauro Cardinali
Istituto di Ricerca per la Protezione Idrogeologica
Consiglio Nazionale delle Ricerche
via Madonna Alta 126, I-06128 Perugia, Italy
[§] ivan.marchesini@irpi.cnr.it

Abstract— **Classification of the source areas of debris flow, mud flows, debris avalanches is fundamental for the zonation of the territory susceptibility to the propagation of these type of landslide phenomena. Here we describe and discuss the data and the methods adopted to derive empirical equations useful to identify and to classify the possible source areas of fast moving landslides at regional and national scale in Italy. The empirical equations were derived based on a large catalogue of debris flows and the fitting of quantile regression curves. We used a 10m resolution DEM and an inventory of more than 4000 landslides distributed on three different Italian regions. Results highlight that differences exist between the equation parameters derived for confined and unconfined debris-flows.**

I. INTRODUCTION

In a recent review paper, [1] defines debris flow as a "*Very rapid to extremely rapid surging flow of saturated debris in a steep channel. Strong entrainment of material and water from the flow path*". Here, with the term debris flow we refer to the general class of flow-like landslides including also mud-flows and debris-avalanches.

Location of the debris flows initiation zones depends on multiple factors such as geomechanic characteristics of the potentially entrained material [2], erosion of the channel banks [3], wildfire occurrence [4], effect of forest harvesting [5] which are hard to collect at regional or national scale.

Many authors demonstrated a relationship between geomorphometric parameters and debris-flow source areas (e.g [6–10]) and in particular terrain slope and flow accumulation seem to play a relevant role in defining the possible initiation zone for the debris flows. Previous research has established also a distinction between channelized and hillslope (confined or unconfined) debris flows, i.e. between phenomena occurring within incised channels or on slopes made by unconsolidated sediments ([8,11–15].

In the framework of a project aimed at defining the areas prone to debris-flow propagation at national scale, we designed a preliminary procedure to identify and to classify the possible debris-flow source areas (initiation zones) only based on the analysis of geomorphometric information. Procedure is based on the analysis of the geomorphometric characteristic of the landslides source areas available for three large areas in the north, south and central Italy. Here, besides describing the research settings and the input data, we discuss the results.

II. DATA

The research data used for this study are a Digital Elevation Model (DEM) and a debris-flow inventory map.

The used DEM is the Tinitaly DTM [16,17] with a ground resolution of 10 m × 10 m, and projection UTM WGS 84 zone 32N (EPSG:32632). It is the most detailed DEM available for the whole country. [16] describe the uncertainties and inhomogeneity present within the final product. The DEM was produced through the integration of all the topographic data available in Italy starting at least from the 1:25000 scale. Therefore, intuitively, the DEM reflects the quality and, above all, the spatial resolution of the input data used. In particular, it should be noted that where the available topographic cartography is made up of poorly detailed data, the listed points subsequently interpolated by triangulation are very scattered. Consequently, the triangle areas (TIN) resulting from the triangulation carried out in areas such as the one just described are significantly larger than the area of a final DEM cell (100 m^2). Arguably, topographic information in regions where the average value of the TIN area is significantly higher than the TINITALY cell area may be affected by locally important errors such as excessive generalizations and artifacts that can cause errors in the experiment. However [16] demonstrated that very high values of the triangle areas are expected in the flat (alluvial plains) areas, which are not interesting for the present study. Clearly, this problem remains where such excessive generalizations occur in non-flat areas.

Ivan Marchesini, Mauro Rossi, Massimiliano Alvioli, Michele Santangelo and Mauro Cardinali (2020) Slope--catchment area relationship for debris-flow source area identification: in Massimiliano Alvioli, Ivan Marchesini, Laura Melelli & Peter Guth, eds., Proceedings of the Geomorphometry 2020 Conference, doi:10.30437/GEOMORPHOMETRY2020_47.

Debris-flow inventory maps, were carried out through geomorphological studies based on comparative analysis of stereoscopic aerial images taken in different years, associated with targeted or diffuse (depending on the working scale) field surveys.

Figure 1 shows the location of the debris-flow inventory maps produced by IRPI and used for the purpose of this work.

The inventory maps cover a total territory of 10,948 km^2, ~3% of the national territory and count 4004 polygons. We acknowledge that the original inventory was made of lines, which were buffered of 20 meters to account for small inaccuracies due to the mismatch between the debris-flow geometries and the DEM. Even if other inventories are available for the Italian territory (e.g. the Italian IFFI catalogue [18] or the Valle d'Aosta inventory [19]), only this inventory was used to perform the experiment, since for it we have full consciousness of the implementation techniques, methodologies and data used, and therefore of its limits and its potential.

III. METHODS

According to the literature, we considered the channelized and the hillslope debris-flows and we analyzed separately the three different areas in the north (Lombardy), south (Sicily) and center (Umbria) of Italy.

A. Hillslope and channelized debris flows

The classification of the inventory polygons into channelized and open slope debris-flow was based on the usage of a slope units maps available for the entire country [20]. Slope units are mapping units delimited by drainage and divide lines and are portions of terrain, defined by the general requirement of maximizing homogeneity within a single unit and heterogeneity between different ones [21]. The spatial intersection (∩) between vector

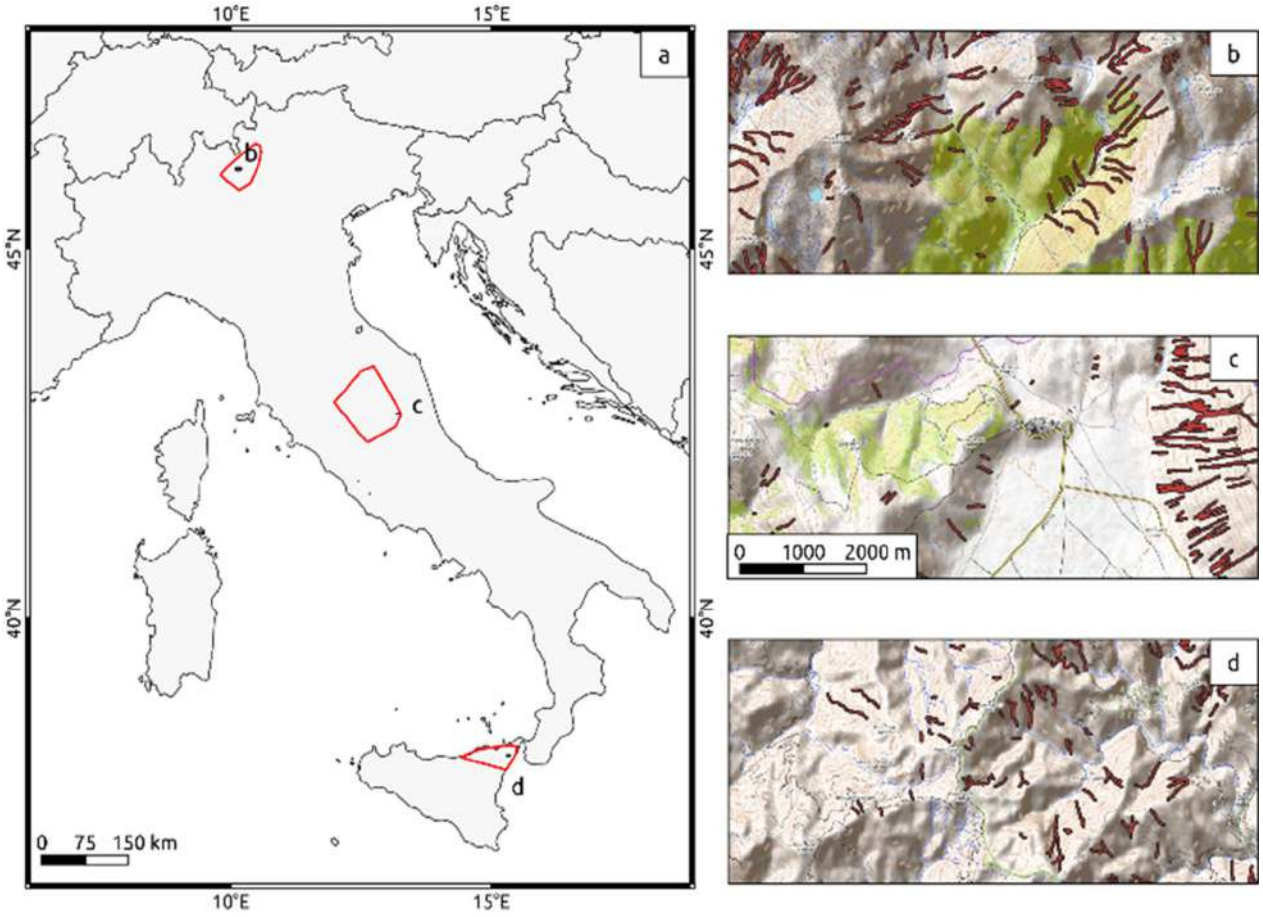

Figure 1. a) convex hull of the debris-flow inventory maps. b). c), d) insets showing details of the inventory

cartography of slope-units and landslide inventories produces a new cartography of vector polygons. Reason is due to the fact that, where the limits of the slope units (typically the drainage lines) intersect those of the polygons representing the debris flows, the latter are split. Landslides completely included inside the slope units, on the other hand, maintain their original geometry. The analysis of the ratio (A_{ratio}) between the areas of the polygons resulting from the aforementioned intersection and the areas of the corresponding landslide polygons in the original inventories, allows to identify polygons which are split by the intersection process and that, as a consequence, are located in the valleys delimiting the slope units. These original polygons are classified as channelized debris flows. More in detail it is assumed that a polygon corresponds to a channeled debris flow if the $A_{ratio} < 0.95$, otherwise it is assumed that it represents a hillslope debris flow.

B. Statistical model for the classification of the source areas of debris flows

The channelized and hillslope debris flow inventory is used to derive a statistical model aimed to assign, to each cell a value that expresses, in terms of probability, the propensity of that pixel (cell) to be a source area of debris flows.

The approach used is based on the assumption that the uppermost portion of the polygons representing the debris flows (in the inventories), can be considered their source areas. In particular, the procedure is based on the following steps: (i) identification of the uppermost portion of each polygon (cells where the elevation non-exceedance probability is larger than 90%), (ii) calculation of slope (β) and flow accumulation (A) for those cells, (iii) exclusion of cells having flow accumulation smaller than 500 m^2 (selecting only those cells that receive a given surface runoff), (iv) linear quantile regression in the bi-logarithmic scale log(tan(β)) and log(A), assuming a power law equation.

$$tan(\beta)=c*A^b$$

where c and b are the coefficient and the exponent of the power law, and are calibrated by a quantile regression. Six quantile regression lines were derived for the following percentiles: 5%, 10%, 25%, 75%, 90%, 95%. These linear functions are indicated as follows $\beta_{05}(A)$, $\beta_{10}(A)$, $\beta_{25}(A)$, $\beta_{75}(A)$, $\beta_{90}(A)$, $\beta_{95}(A)$ and shown in Figure 2 for the different study areas and the channelized and hillslope debris flows.

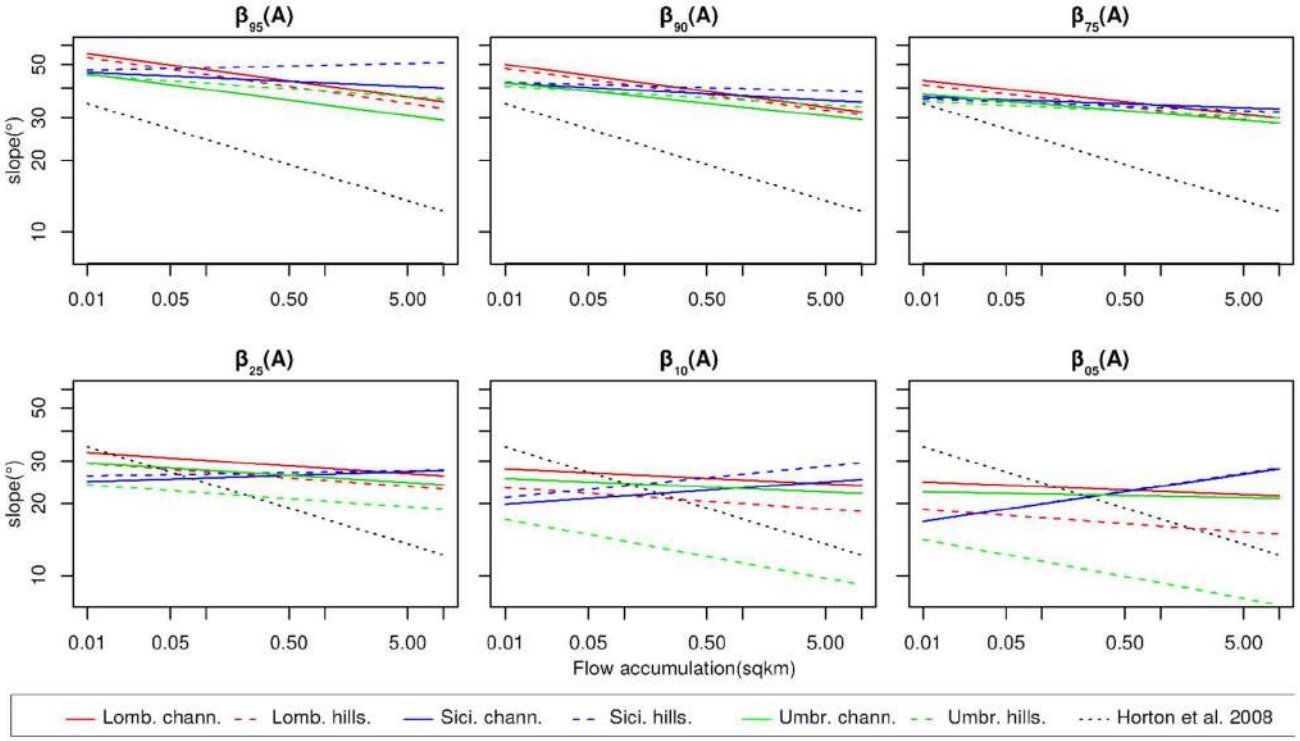

Figure 2. Quantile regression functions for the different study areas and the channelized and hillslope debris flows.

IV. RESULTS AND CONCLUSIONS

Figure 2 shows that the trend of the quantile linear functions derived for Lombardy and Umbria is similar to that observed by other authors [9,22]: debris flow source areas are located on steep areas when the flow accumulation area is small, while they may also be present in less sloping areas when the flow accumulation area is larger. The $\beta_{95}(A)$ and $\beta_{05}(A)$ functions shows that the source areas of debris flows tend to be absent on both low slope and high slope areas. Reasons for not observing source areas in flat zones is trivial. In very steep zones, instead, the cause of the scarce presence of initiation zones is (at least partly) imputable to the fact that debris flows mobilize unconsolidated materials that can hardly be found on steeply sloping areas.

Interestingly, we observe that for quantiles 75, 25, 10 and 5, the channelized functions always return higher values than those obtained for the hillslope functions. A possible explanation for this might be that channel sediments offer more resistance to be entrained, by drag force exerted by the flowing surface water, as opposed to the unconsolidated sediments lying on the slopes.

For the Sicilian inventory, a poorer correlation between slope and flow accumulation areas is observed. Here, the location of the debris flow source areas seems to be independent from the flow accumulation value.

Figure 2 also portrays, for reference, the equation, proposed by [9] and used by [22], which was derived as a lower limit boundary for the data collected by the authors. Even if the slope coefficient of this equation is markedly different from any of the functions derived in the present work, we observe that it only intersects the $\beta_{05}(A)$, $\beta_{10}(A)$, $\beta_{25}(A)$ functions which represent different realizations of the lower limit of the data used in the present work.

We acknowledge that not all the areas resulting by the application of the quantile functions can be considered as initiation zones since actually they also depend on other factors (see Section 1) which are not considered in the present study. However, this study provides results (functions) that can be used to conservatively identify and classify the portions of the territory which net of other factors, can be considered more prone to trigger rapid-moving landslides.

REFERENCES

[1] O. Hungr, S. Leroueil, L. Picarelli, The Varnes classification of landslide types, an update, Landslides. 11 (2014) 167–194. https://doi.org/10.1007/s10346-013-0436-y.

[2] F.D. Milne, M.J. Brown, M.C.R. Davies, G. Cameron, Some key topographic and material controls on debris flows in Scotland, Q. J. Eng. Geol. Hydrogeol. 48 (2015) 212–223. https://doi.org/10.1144/qjegh2013-095.

[3] O. Hungr, S. McDougall, M. Bovis, Entrainment of material by debris flows, in: M. Jakob, O. Hungr (Eds.), Debris-Flow Hazards Relat. Phenom., Springer, Berlin, Heidelberg, 2005: pp. 135–158. https://doi.org/10.1007/3-540-27129-5_7.

[4] S.H. Cannon, J.E. Gartner, Wildfire-related debris flow from a hazards perspective, in: M. Jakob, O. Hungr (Eds.), Debris-Flow Hazards Relat. Phenom., Springer, Berlin, Heidelberg, 2005: pp. 363–385. https://doi.org/10.1007/3-540-27129-5_15.

[5] F. Imaizumi, R.C. Sidle, R. Kamei, Effects of forest harvesting on the occurrence of landslides and debris flows in steep terrain of central Japan, Earth Surf. Process. Landf. 33 (2008) 827–840. https://doi.org/10.1002/esp.1574.

[6] J. Blahut, C.J. van Westen, S. Sterlacchini, Analysis of landslide inventories for accurate prediction of debris-flow source areas, Geomorphology. 119 (2010) 36–51. https://doi.org/10.1016/j.geomorph.2010.02.017.

[7] C.-Y. Chen, F.-C. Yu, Morphometric analysis of debris flows and their source areas using GIS, Geomorphology. 129 (2011) 387–397. https://doi.org/10.1016/j.geomorph.2011.03.002.

[8] J.W. Godt, J.A. Coe, Alpine debris flows triggered by a 28 July 1999 thunderstorm in the central Front Range, Colorado, Geomorphology. 84 (2007) 80–97. https://doi.org/10.1016/j.geomorph.2006.07.009.

[9] D. Rickenmann, M. Zimmermann, The 1987 debris flows in Switzerland: documentation and analysis, Geomorphology. 8 (1993) 175–189. https://doi.org/10.1016/0169-555X(93)90036-2.

[10] V. Wichmann, T. Heckmann, F. Haas, M. Becht, A new modelling approach to delineate the spatial extent of alpine sediment cascades, Geomorphology. 111 (2009) 70–78. https://doi.org/10.1016/j.geomorph.2008.04.028.

[11] J.-C. Chen, C.-W. Lin, L.-C. Wang, Geomorphic characteristics of hillslope and channelized debris flows: A case study in the Shitou area of central Taiwan, J. Mt. Sci. 6 (2009) 266–273. https://doi.org/10.1007/s11629-009-0250-0.

[12] D.M. Cruden, D.J. Varnes, LANDSLIDES: INVESTIGATION AND MITIGATION. CHAPTER 3 - LANDSLIDE TYPES AND PROCESSES, Transp. Res. Board Spec. Rep. (1996). https://trid.trb.org/view/462501 (accessed February 27, 2020).

[13] R.H. Guthrie, A. Hockin, L. Colquhoun, T. Nagy, S.G. Evans, C. Ayles, An examination of controls on debris flow mobility: Evidence from coastal British Columbia, Geomorphology. 114 (2010) 601–613. https://doi.org/10.1016/j.geomorph.2009.09.021.

[14] A. Lorente, S. Beguería, J. C. Bathurst, J.M. García-Ruiz, Debris flow characteristics and relationships in the Central Spanish Pyrenees, Nat. Hazards Earth Syst. Sci. 3 (2003) 683–692. https://doi.org/10.5194/nhess-3-683-2003.

[15] S. Zhang, L.-M. Zhang, H.-X. Chen, Q. Yuan, H. Pan, Changes in runout distances of debris flows over time in the Wenchuan earthquake zone, J. Mt. Sci. 10 (2013) 281–292. https://doi.org/10.1007/s11629-012-2506-y.

[16] S. Tarquini, I. Isola, M. Favalli, F. Mazzarini, M. Bisson, M.T. Pareschi, E. Boschi, TINITALY/01: a new triangular irregular network of Italy, Ann. Geophys. (2007).

[17] S. Tarquini, L. Nannipieri, The 10m-resolution TINITALY DEM as a trans-disciplinary basis for the analysis of the Italian territory: Current trends and new perspectives, Geomorphology. 281 (2017) 108–115. https://doi.org/10.1016/j.geomorph.2016.12.022.

[18] A. Trigila, C. Iadanza, D. Spizzichino, Quality assessment of the Italian Landslide Inventory using GIS processing, Landslides. 7 (2010) 455–470. https://doi.org/10.1007/s10346-010-0213-0.

[19] M. Giardino, S. Ratto, M. Palomba, W. Alberto, M. Armand, M. Cignetti, The Debris Flows Inventory of the Aosta Valley Region: An Integrated Natural Hazards Assessment, in: C. Margottini, P. Canuti, K. Sassa (Eds.), Landslide Sci. Pract. Vol. 1 Landslide Inventory Susceptibility Hazard

GEOMORPHOMETRY 2020
PERUGIA, ITALY
JUNE 22 - 26 2020

Landslide topographic signature prediction using segmentation of roughness and Random Forest classification

Mihai Niculiță[§]
Department of Geography
Alexandru Ioan Cuza University of Iași
Caro II 20A, 700505 Iași, Romania
[§] mihai.niculita@uaic.ro

Abstract—**Landslides creates a typical rough topography which is clearly distinguishable from other types of roughness created by other geomorphological processes or agents. Starting from the idea of geometric signature of topography induced by landslide processes I fed geomorphological objects obtained from segmentation of roughness and their geomorphometry to a machine learning algorithm in order to be able to predict landslide topography presence. The results are good in terms of overall accuracy (0.72 sensitivity and 0.06 false positive rate), but further study is needed to improve the results and to test it in other physiographic settings. This approach of landslide presence prediction is of crucial importance for landslide hazard research, because landslides usually appear in areas previously affected by the process, and this information can be used in landslide susceptibility assessment.**

I. INTRODUCTION

Landslide induced topography exhibit a clear geomorphometric signature [1-3]. Landslide roughness is different from fluvial roughness mainly in scale. The landslide roughness is also defined by more smoothness than pure fluvial roughness. Geomorphometrical objects [4] delineated based on roughness delineate landform facets/segments that exhibit elevation deviation both vertically and horizontally. The target is to use statistical information on the geomorphometry of these segments, in order to predict their landslide/non-landslide status. The main idea is that landslide topography is rough and with curvature different than non-landslide topography, and this morphometric signature can be targeted using high-resolution Digital Elevation Models (DEMs) and Random Forest (RF).

The areas previously affected by landslides are more susceptible to be affected later by landslides [5,6], and a layer with the spatial extension of these landslides can be used in landslide susceptibility assessment [7,8].

Two study areas from Moldavian Plateau were selected for testing the proposed approach (Fig. 1 and 2).

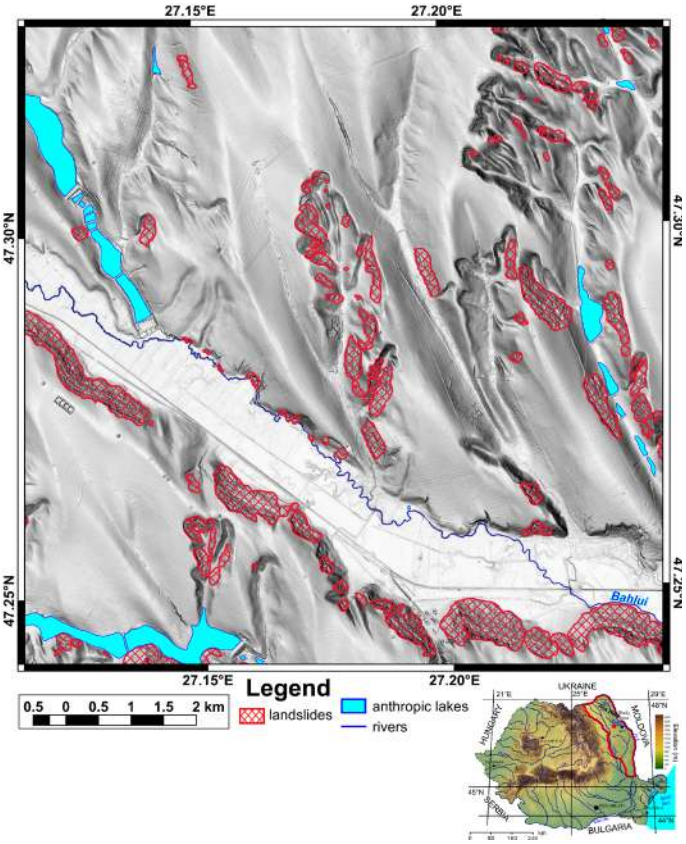

Figure 1. The northern study area and the landslide mapping (a high-resolution version is available at https://doi.org/10.6084/m9.figshare.12226673).

The two areas have a rectangular shape of 100 square km, and are in neighborhood of each other. In the northern study area, the landslide density (landslide surface proportion was computed from

Mihai Niculita (2020) Landslide topographic signature prediction using segmentation of roughness and Random Forest:
in Massimiliano Alvioli, Ivan Marchesini, Laura Melelli & Peter Guth, eds., Proceedings of the Geomorphometry 2020 Conference, doi:10.30437/GEOMORPHOMETRY2020_48.

the landslide inventory of [9]) is 7.53%, while in the southern study area the landslide density is 14,53%. Both relict, old and new landslides are present [10,11], with various typologies: flowslides, translational and rotational slides, and through landslide amalgamation compound and complex landslides appear mainly on the steep hillslopes of cuesta scarps [12,13].

II. METHODS

A DEM with a spatial resolution of 5 m was obtained from a 0.5 m spatial resolution bare earth LiDAR through bicubic resampling in SAG GIS [14]. Landslides were delineated using 2D and 3D views of hillshading, slopes and contours. All the areas affected by landslides were delineated without separating different landslide events, that are visible in topography. Relict landslides (see [11] for details on how the relative age was estimated) were not included in the delineation, mainly because their roughness is smoothed by the agricultural works (tillage and terraces).

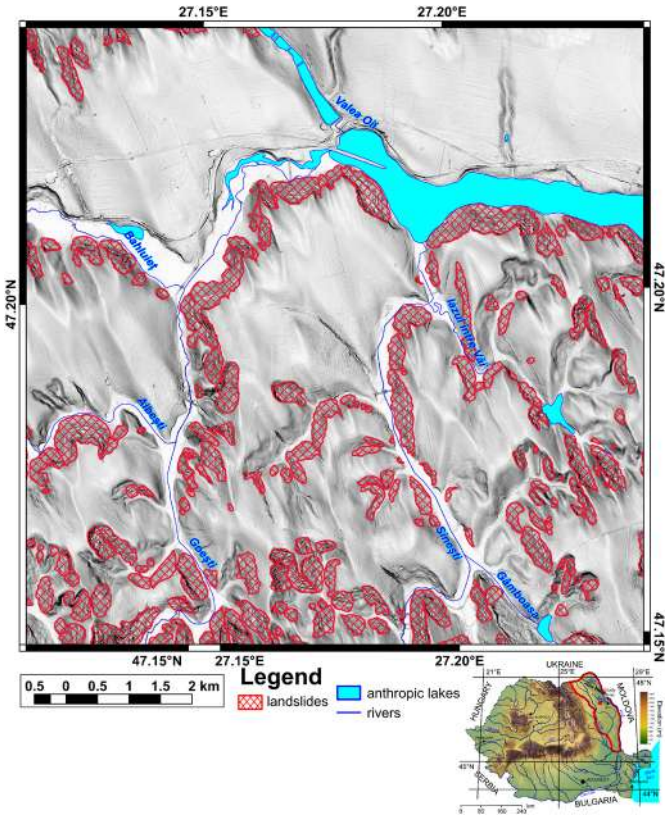

Figure 2. The southern study area and the landslide mapping (a high-resolution version is available at https://doi.org/10.6084/m9.figshare.12226838).

The landforms segments were obtained through watershed segmentation of the vectorial roughness measure [15] computed based on the DEM in SAGA GIS [14]. For every segment the descriptive statistics (minimum, maximum, mean, sum, standard deviation, multiples of 5 percentiles) of the following geomorphometric variables were generated: altitude, vectorial roughness measure [15], real area, terrain ruggedness index [16], texture [17], slope [18] and curvatures (profile, plan, cross-sectional, longitudinal, minimum, maximum) [19].

The Random Forest (RF) algorithm [20] implemented in R software [21] as randomForest package [22] was used for fitting the model. Latin hypercube sampling [23,24] was used to select the training dataset with the clhs package [25]. All the segments corresponding to the delineated landslides were selected in the training dataset while the latin hypercube sampling was used to select a double amount of non-landslide segments. The testing was performed on the southern study area dataset (external domain [26]). The RF parameters were tuned in order to derive the best model. An enough number of trees to grow (ntree=100), with a small number of variables randomly sampled as candidates at each split (mtry=3) and a small minimum size of terminal nodes (nodesize=1) are giving the best results. The performance of the models was evaluated in terms of confusion matrix, and not in terms of Out-of-bag (OBB) error. Another important aspect of tuning is the sampling and the class imbalance. The sampling was performed statistically (latin hypercube), but the class proportion is important and used together with priors of the class (classwt=c(0.1,0.9)) parameter of the RF model in order to deal with class imbalance.

III. RESULTS AND CONCLUSIONS

The confusion matrix for the northern study area, where the model was fit and for the southern study area, where the model was evaluated are shown in Table I.

TABLE I. THE CONFUSION MATRIX AND ITS MEASURES FOR THE NORTHERN STUDY AREA (FIRST ROW) AND SOUTHERN STUDY AREA (SECOND ROW)

RF parameters	OBB error	TP	TN	FP	FN	SNS	FPR
10000 segments from which 946 landslides, 100 ntree, 5 mtry, 1 nodesize	5.23	9223	147615	2698	4471	0.67	0.018
		14428	137798	8528	5593	0.72	0.058

Sensitivity and false positive rate are shown in order to assess an overall view of the result, since accuracy is not necessarily the best measure.

The sampling was performed statistically (latin hypercube), and the class imbalance is consistently dealt with this approach: the sampling keeps the proportion of landslide vs. non-landslide

segments, and the results are better with RF models that do not assign weights or priors for imbalanced classification. All the geomorphometric variables and their statistics (285) were used in the final model. In this way, all the geomorphometric information is used for the identification of landslide segments. The overall accuracy seems to be good enough, but the spatial results need to be investigated. It seems that especially the basal part of landslides is occupied by false negative segments and the crown by false positive segments (Fig. 3 and 4). False positive segments also appear on some relict landslides and in settlement areas, where there is a certain roughness related to be anthropic modifications of topography. Some unfiltered vegetation, and several gullies also are considered topography related to landslides by the model.

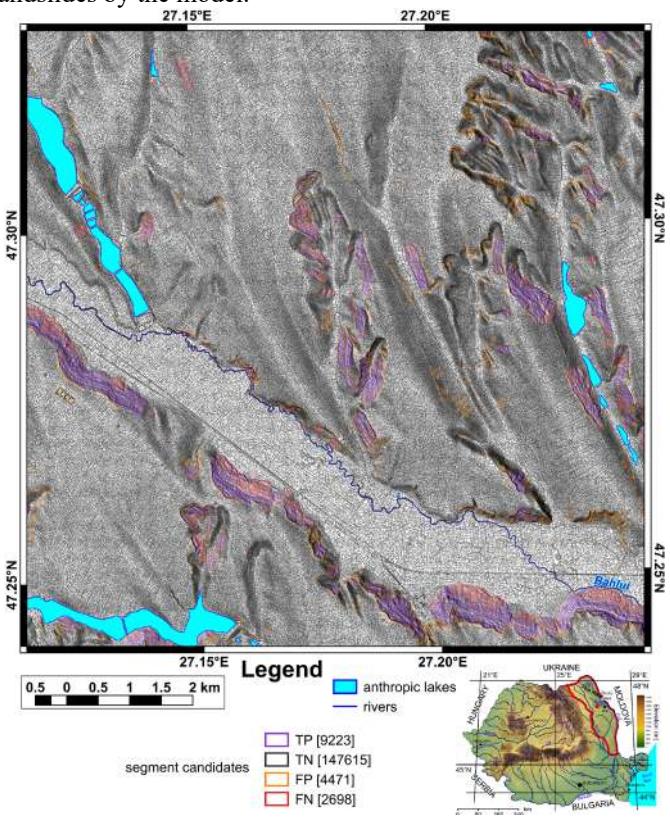

Figure 3. The northern study area and the predicted landslide segments. (a high-resolution version is available at https://doi.org/10.6084/m9.figshare.12226853).

IV. CONCLUSIONS

The landslide prediction based on roughness proved to be feasible in an object-based approach. The segments that are not predicted (the false negatives) are located mainly inside landslides, where the topography is not rough for various reasons (landslide mass deformation, agricultural works or lake presence). The segments that are predicted as landslides, but in fact are not (false positives), fall in three categories: i) settlements, ii) relict landslides, iii) river and gully incision. While the results can be considered satisfactory for now, future improvements are welcomed.

ACKNOWLEDGMENTS

This work was supported by a grant of Ministery of Research and Innovation, CNCS – UEFISCDI, project number PN-III-P1-1.1-PD-2016-0154, within PNCDI III. I am grateful to Prut-Bârlad Water Administration who provided me with the LIDAR data.

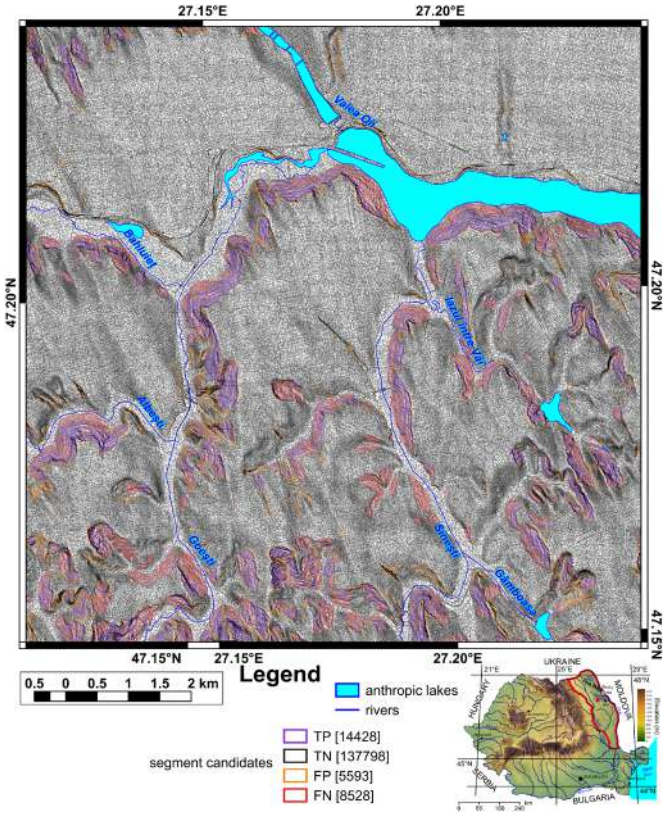

Figure 4. The southern study area and the predicted landslide segments. (a high-resolution version is available at https://doi.org/10.6084/m9.figshare.12226883).

REFERENCES

[1] Pike, R. J. 1988. "The geometric signature: Quantifying landslide-terrain types from digital elevation models". Mathematical Geology 20(5), 491-511.

[2] Marchesini, I., Rossi, M., Mondini, A. C., Santangelo, M., Bucci, F. 2014. "Morphometric signatures of landslides". In: Third Open Source Geospatial Research & Education Symposium, Espoo, Finland, 10-13 June 2014, pp 99-105.

[3] Rossi, M., Mondini, A. C., Marchesini, I., Santangelo, M., Bucci, F., Guzzetti, F. 2013. "Landslide morphometric signature". The 8th IAG/AIG International Conference on Geomorphology, Paris, France, 27-31 August, 2013.

[4] MacMillan, R. A., Shary, P. A. 2009. "Chapter 9 Landforms and Landform Elements in Geomorphometry". In: Geomorphometry - Concepts, Software, Applications. Developments in Soil Science. pp 227-254.

[5] Samia, J., Temme, A., Bregt, A., Wallinga, J., Guzzetti, F., Ardizzone, F., Rossi, M. 2016. "Do landslides follow landslides? Insights in path dependency from a multi-temporal landslide inventory". Landslides 14(2), 547-558.

[6] Samia, J., Temme, A., Bregt, A., Wallinga, J., Guzzetti, F., Ardizzone, F., Rossi, M. 2017. "Characterization and quantification of path dependency in landslide susceptibility". Geomorphology 292, 16-24.

[7] Samia, J., Temme, A., Bregt, A. K., Wallinga, J., Stuiver, J., Guzzetti, F., Ardizzone, F., Rossi, M. 2018. "Implementing landslide path dependency in landslide susceptibility modelling". Landslides 15(11), 2129-2144.

[8] Necula, N., Niculiță, M. 2017. "Landslide reactivation susceptibility modeling in Iași Municipality". Revista de geomorfologie 19, 101-117.

[9] Niculiță, M., Mărgărint, M. C. 2014. "Landslide inventory for Moldavian Plateau, Romania". In: International Conference Analysis and Management of Changing Risks for Natural Hazards Padua, Italy, 18-19 November 2014, AP3-1-9.

[10] Niculiță, M., Mărgărint, M. C., Cristea, A. I. 2019. "Using archaeological and geomorphological evidence for the establishment of a relative chronology and evolution pattern for Holocene landslides". PLoS One 14(12), e0227335.

[11] Niculiță, M., Mărgărint, M. C., Santangelo, M. 2016. "Archaeological evidence for Holocene landslide activity in the Eastern Carpathian lowland". Quaternary International 415, 175-189.

[12] Mărgărint, M. C., Niculiță, M. 2017. "Landslide Type and Pattern in Moldavian Plateau, NE Romania". In: Rădoane M, Vespremeanu-Stroe A (eds) Landform Dynamics and Evolution in Romania. Springer Geography, vol Springer Geography. Springer, Cham, pp 271-304.

[13] Niculiță, M. 2011. "A landform classification schema for structural landforms of the Moldavian platform (Romania) ". In: Hengl T, Evans IS, Wilson JP, M. G (eds) Geomorphometry 2011, Redlands, USA, September 7-11, 2011. pp 129–132.

[14] Conrad, O., Bechtel, B., Bock, M., Dietrich, H., Fischer, E., Gerlitz, L., Wehberg, J., Wichmann, V., Böhner, J. 2015. "System for Automated Geoscientific Analyses (SAGA) v. 2.1.4". Geoscientific Model Development 8(7), 1991-2007.

[15] Sappington, J. M., Longshore, K. M., Thompson, D. B. 2007. "Quantifying Landscape Ruggedness for Animal Habitat Analysis: A Case Study Using Bighorn Sheep in the Mojave Desert". Journal of Wildlife Management 71(5), 1419-1426.

[16] Riley, S. J., DeGloria, S. D., Elliot, R. 1999. "A terrain ruggedness index that quantifies topographic heterogenity". Intermountain Journal of Sciences 5(1-4), 23-27.

[17] Iwahashi, J., Pike, R. J. 2007. "Automated classifications of topography from DEMs by an unsupervised nested-means algorithm and a three-part geometric signature". Geomorphology 86(3-4), 409-440.

[18] Evans, I. S. 1979. "An integrated system of terrain analysis and slope mapping". Final report on grant DA-ERO-591-73-G0040. University of Durham, Durham, UK.

[19] Wood, J. 1996. "The geomorphological characterisation of digital elevation models. PhD Thesis, University of Leicester, Leicester, UK.

[20] Breiman, L. 2001. "Random Forests". Machine Learning 45(1), 5-32.

[21] R Team (2019) "R: A language and environment for statistical computing". version 3.6.2 edn. R Foundation for Statistical Computing, Vienna, Austria

[22] Liaw, A., Wiener, M. 2002. "Classification and Regression by randomForest". R News 2(3), 18-22.

[23] Minasny, B., McBratney, A. B. 2006. "A conditioned Latin hypercube method for sampling in the presence of ancillary information". Computers & Geosciences 32(9), 1378-1388.

[24] Roudier, P., Beaudette, D. E., Hewitt, A. E. 2012. "A conditioned Latin hypercube sampling algorithm incorporating operational constraints". In: Minasny B, Malone BP, McBratney AB (eds) Digital Soil Assessments and Beyond: Proceedings of the 5th Global Workshop on Digital Soil Mapping, Sydney, Australia, 2012, CRC Press, pp 1-6.

[25] Roudier, P., Brugnard, C., Beaudette, D., Louis, B. 2019. "clhs: Conditioned Latin Hypercube Sampling. version 0.7-2 edn. R package.

[26] Brenning, A. 2005. "Spatial prediction models for landslide hazards: review, comparison and evaluation". Natural Hazards and Earth System Science 5(6), 853-862.

GEOMORPHOMETRY 2020 PERUGIA, ITALY JUNE 22 - 26 2020

Relevance of morphometric predictors and completeness of inventories in earthquake-induced landslide susceptibility

Badal Pokharel[1 §], Massimiliano Alvioli[2], Samsung Lim[1]

[1]School of Civil and Environmental Engineering, The University of New South Wales, Sydney, Australia

[2]Istituto di Ricerca per la Protezione Idrogeologica, Consiglio Nazionale delle Ricerche, via M. Alta 126, 06128 Perugia, Italy

[§] b.pokharel@unsw.edu.au

Abstract— **Landslide susceptibility is the likelihood of landslide occurrence in a specific geographic location. A complicated interaction between various morphometric, climatic, seismic, and anthropogenic variables governs landslide susceptibility. Among these variables, morphometric causative factors are important for the generation of landslide susceptibility maps as they provide the basic information related to the topography. In fact, many morphometric variables are commonly included in landslide susceptibility analyses. Additionally, an accurate landslide inventory is a key input to both train and validate a classification model used to prepare susceptibility maps. The objective of this work is to investigate the significance of the causative factors, in relation to different landslide inventories, and their contribution to landslide susceptibility mapping. To do so, we selected a set of five earthquake-induced landslide inventories, developed independently in the aftermath of the 2015 Gorkha earthquake. We obtained landslide susceptibility maps in the framework of a logistic regression model using slope units as spatial mapping domains. We evaluated the significance of the different independent variables relying on p-values corresponding to the susceptibility maps obtained from each inventory. We examined the performance of susceptibility maps by pairwise comparison between the inventories, finding that the significance of variables is not entirely consistent for all inventories. This implies that preparation or selection of a landslide inventory for earthquake-induced landslide susceptibility is a non-trivial step. The pairwise validation of different maps also shows the robustness of the performance varies upon using different inventories.**

I. INTRODUCTION

The disastrous earthquake of a magnitude 7.8 at Gorkha, Nepal, on April 25, 2015 triggered numerous landslides in the central Nepal Himalayas. Many researchers carried out the post-earthquake assessment of landslides by producing inventories and susceptibility maps, however, the relevance of independent variables causing landslides has not been specifically analyzed. The factors contributing to the reliability of susceptibility maps calculated from such inventories are the completeness of inventories, the type of mapping units utilized for zonation, and the sampling balance between the inventories [1-2]. Furthermore, the choice of predictors, specifically the morphometric variables derived from a digital elevation model (DEM), is often made without addressing their significance, with a few exceptions [3].

In this study, we selected five existing landslide inventories mapped in the same region after the Gorkha earthquake event. We checked the relevance of the independent variables, performed accuracy assessment on each landslide susceptibility map and validated using the remaining inventories.

II. MATERIAL AND METHODS

In this work, we used five landslide inventories, for the landslide triggered by the Gorkha Earthquake 2015, prepared independently by [4-8]. The first four inventories are polygon-based and the last is point-based inventory. The study area covers the section of Rasuwa, Nuwkot and Sindhupalchowk districts (Figure 1). Table I shows the descriptive details about the five inventories and slope units used in this work.

Inventories	Landslides	Unstable SUs	Landslide area [km^2]	Landslide area (%)
[4]	1,264	66	10.82	0.74
[5]	1,780	87	9.68	0.66
[6]	1,765	81	14.28	0.98
[7]	359	54	3.68	0.25
[8]	371	63	Point inventory	

Table I. Details about landslide inventories used in this study.

In this work, we performed the following six steps:

Badal Pokharel, Massimiliano Alvioli and Samsung Lim (2020)

Relevance of morphometric parameters in susceptibility modelling of earthquake-induced landslides:

in Massimiliano Alvioli, Ivan Marchesini, Laura Melelli & Peter Guth, eds., Proceedings of the Geomorphometry 2020 Conference, doi:10.30437/GEOMORPHOMETRY2020_49.

Step 1: Five inventories were chosen so that they cover the most affected areas of the earthquake-triggered landslides in the central Nepal. One of the authors (BP) actively participated in preparing the inventory from Ref. [4].

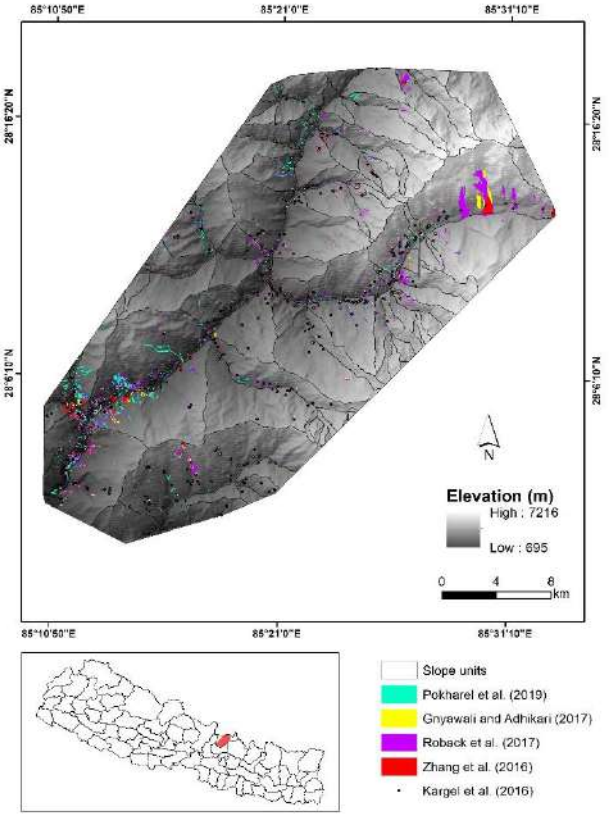

Figure 1. Map of study area. Slope units were delineated in GRASS GIS using the algorithm developed by Ref. [9]. Map is in EPSG:32645 reference system.

Step 2. A slope unit (SU) map over the study area was available for this study. The SU map was based on the algorithm developed in Ref. [9] and generalized to account for large areas in Ref. [10].

Step 3. We calculated 9 morphometric variables (raster maps) from the Cartosat-I DEM, and collected three dynamic parameters from the United States Geological Survey (USGS) Shake Maps published after the earthquake event [11] as independent variables responsible for the landslides.

Step 4. We characterized each SU with presence or absence of landslides and with descriptive statistics (mean and standard deviation) of independent variables [2,12,13], except for landforms classes, for which we used the dominant class in each SU. We selected the DEM derivatives as independent variables (Table II), following Ref. [1], who performed a similar analysis. The selected variables have a rather straightforward interpretation in terms of their effect on landslides.

Type	Independent variables	GRASS GIS module/Reference
Dynamic	PGA	[11]
Dynamic	PGV	[11]
Dynamic	MMI	[11]
Static	Slope	r.slope.aspect
Static	Topographic Wetness Index (TWI)	r.topidx [14]
Static	Vector Ruggedness Measure (VRM)	r.vector.ruggedness [15]
Static	Local relief	r.neighbors [16]
Static	Landform classes	r.geomorphon [16]
Static	Plan curvature	r.slope.aspect
Static	Profile curvature	r.slope.aspect

Table II. List of independent variables as studied in [1] and adopted in this work. We also show the specific method used to calculate descriptive statistics by specifying GRASS GIS modules.

Step 5. We chose the smallest number among the stable and unstable SUs (40, in the inventory from [5]) among the five different inventories to generate the training datasets. We randomly selected 75% of both stable and unstable SUs for each landslide inventory dataset, for a total of 60 SUs. We iterated this process for 20 times for each dataset and run the glm() function (generalized linear model, within the R language) to train the logistic regression (LR) – a widely used method in landslide susceptibility modelling. Then, we obtained descriptive statistics and run a χ-square test to calculate the p-values for all independent variables in 20 runs.

Step 6. We prepared boxplots showing the distributions of p-values associated to each inventory, stemming from the 20 runs. We checked the accuracy of the landslide susceptibility maps using area under curve (AUC), and validated the accuracy of the susceptibility map obtained from each inventory, on the slope units not used in the training step, selected from the same inventory and for the remaining for maps. The validation test corresponds to 20 runs as well, from which we calculated mean and standard deviation of AUC for each train/validation pair.

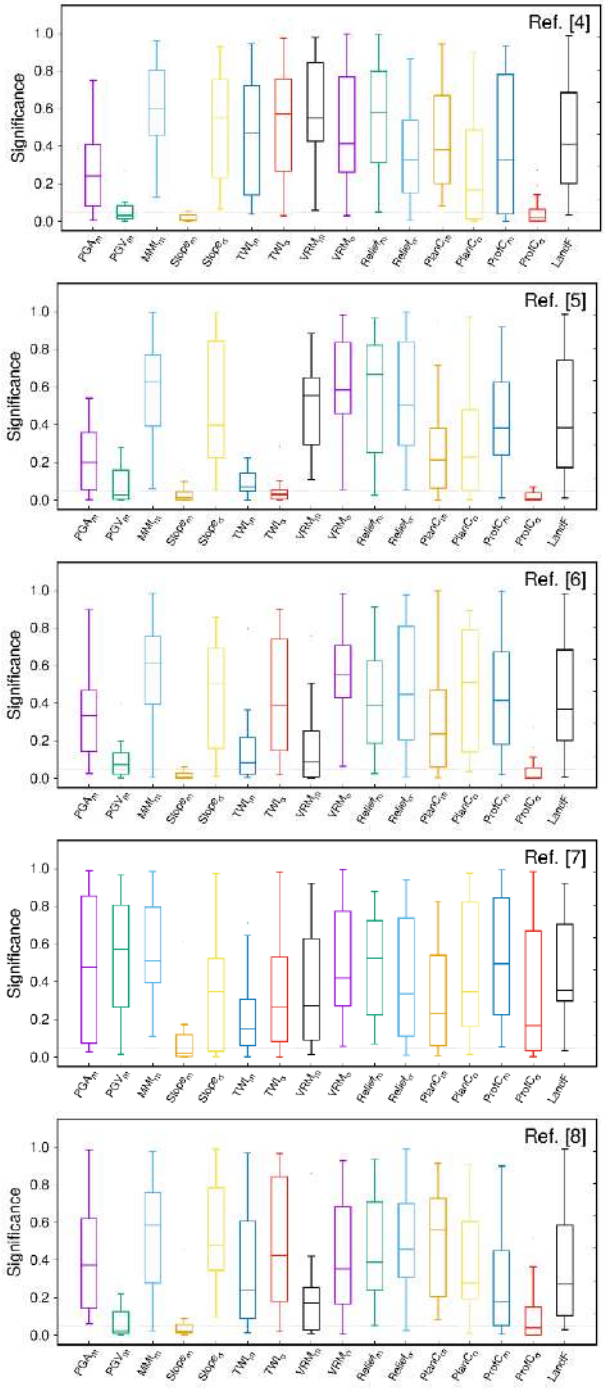

Figure 2. Distributions of the significance (p-value) of the different variables in the logistic regression, obtained from 20 runs of the susceptibility model for each inventory, with different random selections of the training dataset. The horizontal dashed line represents the 0.05 significance threshold.

Inventories	Significant predictors
Ref. [4]	PGV (mean), Slope (mean), Profile curvature (mean)
Ref. [5]	PGV (mean), Slope (mean), TWI (S.D) Profile curvature (S.D)
Ref. [6]	Slope (mean), Profile curvature (S.D)
Ref. [7]	Slope (mean)
Ref. [8]	PGV (mean), Slope (mean), Profile curvature (S.D)

Table III. Significance factors obtained for each inventory (p-value <0.05).

III. RESULTS AND CONCLUSIONS

Figure 2 shows boxplots of the distribution of p-values of each variable and for each landslide inventory dataset. Table III shows the variables for which the p-value was always smaller than 0.05, in all the 20 randomized runs of the LR. Although all inventories covered the same area, some inconsistency exists in the relevance of the predictors, which may be due to the different number and location of the landslides in the different inventories. In addition, for the same aerial extent, the number of stable and unstable slope units (i.e. of slope units containing no landslide or at least one landslide) differs for different inventories, which ultimately influences the content of landslide susceptibility maps. The morphometric variable that stood significant for all the inventories is slope (mean). Profile curvature (standard deviation) is invariably very significant for four inventories, while its significance was substantially smaller for the one from Ref. [7]. This implies that slope morphometry influences the spatial occurrence of landslide triggered by the Gorkha Earthquake 2015. We stress that the inventory from Ref. [7] contains the smaller number of landslides, which seems to produce a noticeable difference. Table IV lists the results for pairwise validation of the inventories in 20 runs for each. Performance was higher for each map if the validation data

Trained by	Validated by				
	[4]	**[5]**	**[6]**	**[7]**	**[8]**
[4]	**0.68±0.06**	0.71±0.06	0.68±0.05	0.58±0.06	0.68±0.06
[5]	0.63±0.06	**0.74±0.08**	0.71±0.06	0.53±0.07	0.65±0.06
[6]	0.63±0.06	0.73±0.07	**0.71±0.07**	0.57±0.07	0.69±0.04
[7]	0.58±0.07	0.59±0.08	0.62±0.07	**0.60±0.08**	0.61±0.07
[8]	0.70±0.07	0.70±0.08	0.70±0.07	0.62±0.07	**0.69±0.07**

Table IV. Pairwise validation between five inventories. The table shows mean ± standard deviation for AUC of testing/validating dataset.

was from the same inventory, which is expected. The testing sample of the inventory from Ref. [7] had lower performance. The inventories [4], and [8] had same relevant variables (Table III) but the model performances varied.

From our study, we may draw two main conclusions. First, the differences in significant predictors (within LR) creates a difficulty in interpretation and reliability of susceptibility maps. Among morphometric predictors, only mean slope and profile curvature are (almost) always significant – this is a relevant point, being morphometric variables the ones that stay constant across different earthquake events. Second, model performance (within LR) depends upon the number of landslides and/or completeness of the inventory. This is clearly shown by the inventory with smallest number of landslides ([7]) having the weakest performance. We stress that this point could be less relevant where the spatial extent of the study area is larger. Hence, it is necessary to make sure the inventories are representative, i.e. complete enough [17, 18], if one is to use them for landslide susceptibility.

ACKNOWLEDGEMENTS

The authors would like to thank the Australian Government Research Training Program at the University of New South Wales, Australia, for sponsoring this research.

REFERENCES

[1] Tanyaş, H., M. Rossi, M. Alvioli, C.J. van Westen, I. Marchesini, 2019. "A global slope unit-based method for the near real-time prediction of earthquake-induced landslides". Geomorphology 327, 126-146. DOI: 10.1016/j.geomorph.2018.10.022

[2] Tanyaş, H., C.J. van Westen, C. Persello, M. Alvioli, 2019. "Rapid prediction of the magnitude scale of landslide events triggered by an earthquake". Landslides 16, 661-676. DOI: 10.1007/s10346-019-01136-4

[3] Schlögel, R., I. Marchesini, M. Alvioli, P. Reichenbach, M. Rossi, J.P. Malet, 2018. "Optimizing landslide susceptibility zonation: effects of DEM spatial resolution and slope unit delineation on logistic regression models". Geomorphology 301, 10-20. DOI: 10.1016/j.geomorph.2017.10.018

[4] Pokharel, B., P.B. Thapa, 2019. "Landslide susceptibility in Rasuwa District of Central Nepal after the 2015 Gorkha Earthquake". J. Nepal Geological Society 59, 79-88. DOI: /103126/jngs.v59i0.24992

[5] Gnyawali K.R., B.R. Adhikari, 2017. "Spatial Relations of Earthquake Induced Landslides Triggered by 2015 Gorkha Earthquake Mw = 7.8". In: Mikoš M., Casagli N., Yin Y., Sassa K. (eds.) Advancing Culture of Living with Landslides. WLF 2017. Springer, Cham. DOI: 10.1007/978-3-319-53485-5_10

[6] Roback, K., M.K. Clark, A.J. West, D. Zekkos, G. Li, S.F. Gallen, D. Champlain, J.W. Godt, 2017. "Map data of landslides triggered by the 25 April 2015 Mw 7.8 Gorkha, Nepal earthquake". U.S. Geological Survey data release. DOI: 10.5066/F7DZ06F9

[7] Zhang, J., E. Liu, W. Deng, N.R. Khanal, D.R. Gurung, M.S.R. Murthy, S. Wahid, 2016. "Characteristics of landslide in Koshi River Basin, Central Himalaya". Journal of Mountain Science 13, 1711–1722. DOI: 10.1007/s11629-016-4017-0

[8] Kargel, J.S., Leonard, G.J., Shugar, D.H., et al., 2016, "Geomorphic and geologic controls of geohazards induced by Nepal's 2015 Gorkha earthquake", Science 351. DOI:10.1126/science.aac8353

[9] Alvioli, M., I. Marchesini, P. Reichenbach, M. Rossi, F. Ardizzone, F. Fiorucci, F. Guzzetti, 2016. "Automatic delineation of geomorphological slope units with r.slopeunits v1.0 and their optimization for landslide susceptibility modeling". Geoscientific Model Development 9, 3975-3991. DOI: 10.5194/gmd-9-3975-2016

[10] Alvioli, M., F. Guzzetti, I. Marchesini, 2020. "Parameter-free delineation of slope units and terrain subdivision of Italy". Geomorphology 358, 107124. DOI: 10.1016/j.geomorph.2020.107124

[11] USGS M7.8 - 36 km E of Khudi, Nepal Available online: http://earthquake.usgs.gov/earthquakes/eventpage/us20002926#scientific_finitefault:us_us20002926

[12] Rossi, M., F. Guzzetti, P. Reichenbach, A.C. Mondini, S. Peruccacci, 2010. "Optimal landslide susceptibility zonation based on multiple forecasts". Geomorphology 114, 129-142. DOI: 10.1016/j.geomorph.2009.06.020

[13] Rossi, M., P. Reichenbach, 2016. "LAND-SE: a software for statistically based landslide susceptibility zonation, version 1.0". Geoscientific Model Development 9, 3533–3543. DOI: 10.5194/gmd-9-3533-2016

[14] Cho, H., 2000. "GIS Hydrological Modeling System by Using Programming Interface of GRASS". Master's Thesis, Kyungpook National University, Korea.

[15] J.M. Sappington, K.M. Longshore, D.B. Thompson, 2007. "Quantifying Landscape Ruggedness for Animal Habitat Analysis: A Case Study Using Bighorn Sheep in the Mojave Desert". Journal of Wildlife Management 71, 1419-1426. DOI: 10.2193/2005-723

[16] Jasiewicz, J., T.F. Stepinski, 2013. "Geomorphons - a pattern recognition approach to classification and mapping of landforms". Geomorphology 182, 147-156. DOI: 10.1016/j.geomorph.2012.11.005

[17] Tanyas, H., L.Lombardo, 2020. "Completeness Index for Earthquake-Induced Landslides Inventories." Engineering Geology 264, 105331. DOI: 10.1016/j.enggeo.2019.10533

[18] Guzzetti, F., A.C. Mondini, M. Cardinali, F. Fiorucci, Santangelo, M., K.-T. Chang, 2012. "Landslide inventory maps: New tools for an old problem". Earth-Science Reviews 112, 42-66. DOI: 10.1016/j.earscirev.2012.02.001

GEOMORPHOMETRY 2020 PERUGIA, ITALY JUNE 22 - 26 2020

Volumetric assessment of river bank erosion using terrestrial laser scanning and high-resolution digital terrain modelling

Ján Šašak[§1], Michal Gallay[1], Jaroslav Hofierka[1], Ján Kaňuk[1], Miloš Rusnák[2], Anna Kidová[2]

1 - Institute of Geography, Faculty of Science, Pavol Jozef Šafárik University in Košice, Košice, Slovakia

2 - Department of Physical Geography, Geomorphology and Natural Hazards, Institute of Geography, Slovak Academy of Sciences, Bratislava, Slovakia

§ jan.sasak@upjs.sk

Abstract— **The dynamic geomorphological phenomena such as riverbank erosion require accurate and frequent mapping. In this study, we present a methodology for the assessment of volumetric changes in the river banks represented by high-resolution digital terrain models derived from 12 periodic terrestrial laser scanning surveys over the 3-year period. The methodology was applied to assess a sediment delivery from a cut-bluff induced by lateral erosion of the high-energy braided-wandering river Belá in West Carpathians. The slope-channel processes were identified as a significant sediment delivery contributor to the channel. Sliding activation was supported by channel incision and lateral erosion of the riverbanks. The amount of sediment supply from the cut-bluff to the channel was associated with the river discharge system.**

I. INTRODUCTION

The sediment from stream banks accounts for as much as 85% of watershed sediment yields [1]. It is a result of processes between the river channel and adjacent slopes, terraces, alluvial plains, and landforms often called a streambank erosion [2]. The bank erosion and bluff failure are commonly acting together resulting in a bank retreat dominantly located at the outside meander bend of a river [3,4].

Over the last decade, the laser scanning (LiDAR) technology has been applied in the research of bank erosion and failures by many authors. Grove et al. [5] and Nardi et al. [6] demonstrate the application of multi-temporal LiDAR mapping and high-resolution aerial imagery to determine processes and volumes of riverbank erosion at a catchment scale. The rates and spatial patterns of annual riverbank cliff erosion using sequential LiDAR and historical photography analyses present a unique tool for sediment erosion research [7-9]. Despite the development of quantitative assessment by application of high accuracy topography measurement, the complexity of the processes limits a better conceptualization of the phenomenon. Moreover, sufficiently accurate sediment transfer models predicting spatially-distributed elevation changes are still missing. A better understanding of the phenomenon requires high-resolution, multi-temporal spatially-distributed data documenting the processes [9].

The main aim of this paper is to present a methodology for calculation of volumetric and detailed morphological changes in the bank of the Belá River by multi-temporal, seasonal, and post-flood terrestrial laser scanning (TLS) and high-resolution digital terrain models (DTMs). This analysis helps to calculate spatial and temporal changes in the mechanism of mass movement from upper to lower bluff positions with a detailed assessment of morphological changes and sediment budget calculations.

II. METHODS

A. Study area

The area of interest comprises a system of a channel and cut-bluff of the Belá river near the village of Vavrišovo in West Carpathians, Slovakia (Fig. 1). The area was selected for long-term monitoring of the sediment budget and mass movement from valley slope into the river channel. Belá represents a natural laboratory of high energy gravel-bed river with braided-wandering river pattern formed by the confluence of Tichý potok and Kôprovský potok (creeks) draining the glacial troughs of Tichá dolina and Kôprová dolina in the western part of High Tatras (Vysoké Tatry). Belá is the main right-side tributary of the upper Váh River which is a major tributary of the Danube from West Carpathians. The drainage basin of Belá (244 km^2, minimal altitude 630 m a. s. l., maximal 2 494 m a. s. l.) is characterized by an asymmetric drainage network. Most of its course is predominated by longitudinal as well as transverse tectonic faults. The valley bottom is filled with typical non-cohesive glaciofluvial river sediments. The average annual discharge (1964-2006) is 3.5

Jan Sasak, Michal Gallay, Jaroslav Hofierka, Jan Kanuk, Milos Rusnak and Anna Kidova (2020)

Geomorphometry based geodiversity for Lesser Antilles:

in Massimiliano Alvioli, Ivan Marchesini, Laura Melelli & Peter Guth, eds., Proceedings of the Geomorphometry 2020 Conference, doi:10.30437/GEOMORPHOMETRY2020_50.

$m^3.s^{-1}$ at the gauging station Podbanské and 6.8 $m^3.s^{-1}$ at the confluence of Belá with Váh in Liptovský Hrádok [10]. The study area is located about 5.5 km northeast from the confluence of the Belá and Váh rivers. Hydrologic maximum of Belá occurs during spring floods generated by snowmelt in April/May and during summer floods from intensive rainfalls occurring often in the Tatry region in July/August [11].

The river undercuts a 30 m height terrace of the Mindel age (Fig. 1A). Terrace slope is covered by glacifluvial deposits from the Tatry Mountains and built by lithofacies of the Inner-Carpathian Paleogene formed by altering claystone and sandstone lithofacies. Coupling processes between the river and terrace slope are controlled by the river dynamics. Belá formed a wandering channel system in this section with an intensive valley floor reworking leading to channel migration associated with the arm abandonment.

B. Terrestrial laser scanning (TLS)

The area of the cut bluff has a complex microtopography locally obscured by growing trees and grass. For this reason, TLS was preferred to close-range photogrammetry from a drone. The Riegl VZ-1000 scanner was used for data collection with the maximum range set to 450 m and 300 MHz pulse rate frequency. Moreover, TLS did not require placing ground control points (GCP) prior to the survey as is the case of photogrammetry [9]. In our case, ground control (georeferencing) was performed based on 4 to 5 GCPs (black-white checkerboards) placed around each scanning position and recorded by a dual-frequency GNSS receiver in real-time kinematic mode. For this task, differential corrections of the Slovak Positioning Service (SKPOS) broadcasted within a mobile broadband network were used. There were about 20-30 GCPs measured during each TLS mission.

Systematic monitoring of the cut-bluff started in March 2016 and continued to November 2018 with a 3 months interval. There were 10 scan positions located within the study area (Fig. 1B). Local topographic conditions had changed frequently, therefore, scan positions were adjusted accordingly to capture the required land surface topography.

(A)

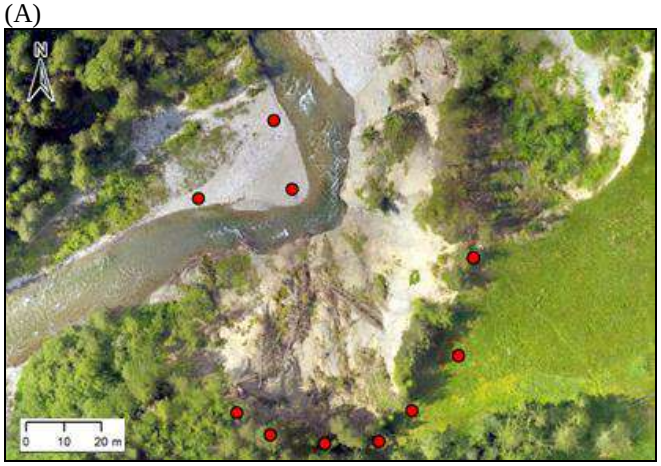

(B)

Figure 1. (A) Location of the study site in the West Carpathians, Slovakia, with detailed photographs of the cut-bluff from a vertical perspective. (B) Orthophoto image with positions of laser scanner (red dots).

C. Data processing

The TLS data obtained during a single campaign were processed in several steps. In the first step, the scanning positions were mutually registered in the project coordinate system. This step involved a manual change of position and orientation of every single scan (Coarse registration) and an automatic alignment using the MSA (MultiStation Adjustment) tool implemented in the

RiSCAN Pro software. The tool is based on the Iterative Closest Point (ICP) algorithm [12] minimizing the deviations between identical planes derived from each scan position. To keep the calculation of volumetric changes at a reasonable level of accuracy, the scans of each campaign were mutually oriented achieving the average standard error below a centimeter. Georeferencing a point cloud for each campaign was done with the GCPs in the S-JTSK national coordinate system (EPSG code: 5514) and the Baltic Sea vertical reference system after adjustment. The achieved standard errors were between 3 to 5 centimeters per unified point cloud in each campaign. Such an error resulted in a volumetric error that ranged between 100-300 m^3 across the 6000 m^2 of the area of interest.

To derive a DTM, ground points were extracted using the automatic Vegetation filter tool of the RiSCAN Pro software. The points classified as vegetation were visually inspected to verify the classification. The problematic places such as slope cliff, overhangs, main scarp could be classified as vegetation as well. These parts were then manually unclassified. The points classified as vegetation, noise, and other objects except terrain were removed from the point cloud. Overall, more than 70% of all points were removed by filtration, and only points representing the land surface were used in further data processing and analysis. The DTMs for each campaign were derived in GRASS GIS using the parallelized version of the regularized spline with tension and smoothing implemented in the v.surf.rst module [13]. The parameters of the interpolation function were identical for each model with smoothing 0.4, the minimum point distance (dmin) set to 0.09 m, and spatial resolution of the final DTM 0.1 m.

III. RESULTS

The Belá River is a dynamic and laterally unstable river system [14] and activation of slope failure is controlled by channel evolution and position of the channel on the valley floor. Channel movement and lateral erosion to the distinct contact of the cut-bluff slope triggers the mass transport into the channel. Frequent flooding affects the intensity of toe erosion and accelerates material removal and entrainment by water flow leading to changes in slope failure geometry and activation of block failures in the upper cut-bluff positions. The amount of relocated sediment during the monitoring period in relation to the river discharge is depicted in Fig. 2. It can be seen that erosion dominates the process of relocation and the marked changes occurred after strong hydrologic events. Further analysis is needed to interpret the volumetric changes more convincingly, e.g. using rainfall data.

The spatial pattern of the changes in the sediment volume is depicted in Fig. 3. The pattern of material gains and losses summarizes quantity and spatial variation of slope processes and mass movement. Spatial-temporal changes in mass replacement are evident. In the first monitoring periods from March 2016 to March 2017 slightly prevailing erosional processes over deposition with material deposition in the lower position and vertical movement in the upper position of bluff. In this cut-bluff stage, mass transport is a little higher over detectable limit calculated based on the cumulative effect of measurement and post-processing errors. Intensive toe erosion from March 2017 to June 2017 was documented and 3529 m^3 of cut-bluff material was eroded into the river channel. Intensive toe erosion is connected with river undercutting and high magnitude flood events occurred between monitoring campaigns. Increasing energy of water flow resulted to less cohesive claystone block destruction and collapsing lower slope parts into the channel. Morphometric changes in toe slope parts initiated sediment cascade from the upper slope position. These morphological changes was followed by period of mass deposition in former foot surface and accelerated erosion in downstream direction after channel bend extension. In the next period (September 2017 - November 2017), upper scarp material loss prevails resulting in erosion of 2394 m^3 of sediment. In both cases, winter periods are presented by a very small material displacement indicating a low interaction with frost weathering and thermal stress. In the first half of the year 2018, changes in the upper collapsed zone were recorded and mass movement acceleration from the main scarp occurred in the form of sliding blocks.

There were 3,130 m^3 of material eroded and 789 m^3 accumulated between April and June 2018. Then a massive scarp retreat occurred caused mainly by fluvial undercutting of the cut-bluff toe during snowmelt season in the Tatry Mountains. Erosion and removal of the material dominated further on (3,189 m^3 eroded, 549 m^3 accumulated) which can be primarily attributed to an extraordinary flash-flood event that occurred in late-July 2018. Subsequent forceful human interventions in the river channel and gravel extraction for river regulation preserved slope undercutting which resulted in the reduction of the mass movement on the cut-bluff slope. After the artificial measures, the erosion relocated only 639 m^3 in the upper zone of the cut-bluff and 641 m^3 were accumulated in its foot zone.

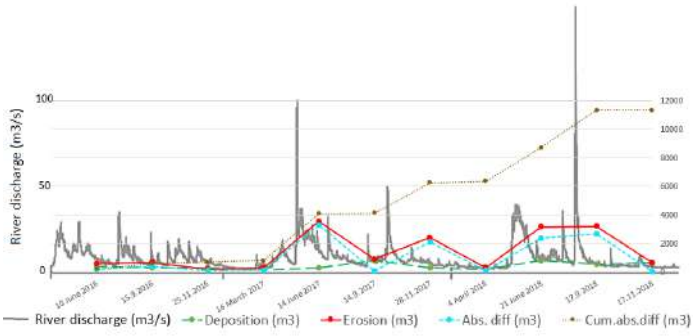

Figure 2. River discharge (left vertical axis) and the calculated volume of relocated sediment mass based on TLS monitoring (right vertical axis) in cubic meters.

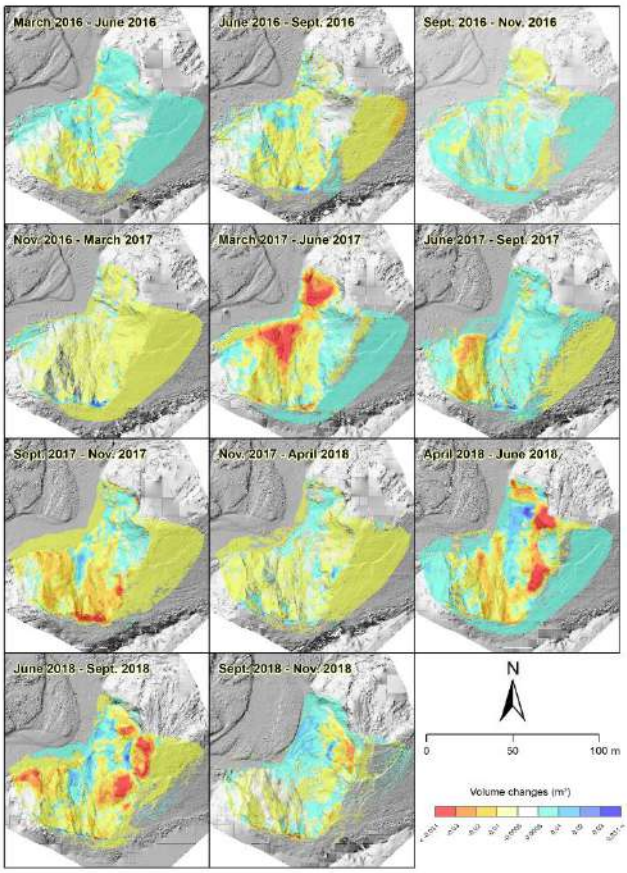

Figure 3. The difference between successive DTMs (DoD) presenting volumetric changes of cut-bluff slope material.

IV. CONCLUSIONS

Mass movement mechanism operation and processes of material movement from cut-bluff into the channel were measured by TLS techniques during three years and 12 monitoring campaigns. We have presented a methodology for the evaluation of volumetric changes in the river banks represented by high-resolution DTMs derived from periodic TLS surveys. The study also demonstrated the potential of this approach for a high accuracy assessment of sediment delivery to the river channel. Changes in the Belá River channel planform activated several failures in the 30m high river Pleistocene terrace and reactivated the studied cut-bluff slope in 2013. The results of this analysis along with the associated hydrological data provide insight into the physical mechanism of cut-bluff sliding. Future research will focus on the analysis of the connectivity between the river channel and the cut-bluff.

ACKNOWLEDGMENT

The research was financially supported by the Science Grant Agency (VEGA) of the Ministry of Education of the Slovak Republic and the Slovak Academy of Sciences (Grant Nr. 02/0098/18 and by the Slovak Research and Development Agency (APVV, Grant nr. 15-0054).

REFERENCES

[1] Simon, A., Curini, A., Darby, S.E., Langendoen, E.J., 2000. Bank and near-bank processes in an incised channel. Geomorphology 35, 193–217.

[2] Luppi, L., Rinaldi, M., Teruggi, L.B., Darby, S.E., Nardi, L., 2009. Monitoring and numerical modelling of riverbank erosion processes : a case study along the Cecina River (central Italy) 546, 530–546.

[3] O'Neal, M. a., Pizzuto, J.E., 2011. The rates and spatial patterns of annual riverbank erosion revealed through terrestrial laser-scanner surveys of the South River, Virginia. Earth Surf. Process. Landforms 36, 695–701.

[4] Yenes, M., Monterrubio, S., Nespereira, J., Santos, G., Fernández-Macarro, B., 2015. Large landslides induced by fluvial incision in the Cenozoic Duero Basin (Spain). Geomorphology 246, 263–276.

[5] Grove, J.R., Croke, J., Thompson, C., 2013. Quantifying different riverbank erosion processes during an extreme flood event. Earth Surface Processes and Landforms 38, 1393-1406.

[6] Nardi, L., Campo, L., Rinaldi, M., 2013. Quantification of riverbank erosion and application in risk analysis. Nat. Hazards 69, 869–887.

[7] De Rose, R.C., Basher, L.R., 2011. Measurement of river bank and cliff erosion from sequential LIDAR and historical aerial photography. Geomorphology 126, 132–147.

[8] Thompson, C., Croke, J., Grove, J., Khanal, G., 2013. Spatio-temporal changes in river bank mass failures in the Lockyer Valley, Queensland, Australia. Geomorphology 191, 129–141.

[9] Spiekermann, R., Betts, H., Dymond, J., Basher, L., 2017. Volumetric measurement of river bank erosion from sequential historical aerial photography. Geomorphology 296, 193-208.

[10] Majerčáková, O., Škoda, P., Danáčová, Z., 2007. Vývoj vybraných hydrologických a zrážkových charakteristík za obdobia 1961–2000 a 2001–2006 v oblasti Vysokých Tatier. Meteorologický Časopis 10, 205–210.

[11] Halmová, D., Pekárová, P., 2011. Statistical evaluation of the extreme flood and drought changes in the Belá River basin. In: Gomboš,M., Pavelková, D., Tall, A. (Eds.), Influence of Anthropogenic Activities on Water Regime of Lowland Territory. Physics of Soil Water, Institute of Hydrology SAS, Bratislava, pp. 125–133.

[12] He, Y., Liang, B., Yang, J., Li, S., He, J., 2017. An iterative closest point algorithm for registration of 3D laser scanner point clouds with geometric features. Sensors 17, 1-16.

[13] Hofierka, J., Lacko, M., Zubal, S., 2017. Parallelization of interpolation, solar radiation and water flow simulation modules in GRASS GIS using OpenMP. Computers & Geosciences. 107, 20–27.

[14] Kidová, A., Lehotský, M., Rusnák, M., 2016. Geomorphic diversity in the braided-wandering Belá River, Slovak Carpathians, as a response to flood variability and environmental changes. Geomorphology 272, 137–149.

GEOMORPHOMETRY 2020
PERUGIA, ITALY
JUNE 22 - 26 2020

The role of pre-landslide morphology in statistical modelling of landslide-prone areas

Stefan Steger
Institute for Earth Observation
Eurac Research
Viale Druso 1, I-39100 Bolzano/Bozen, Italy
stefan.steger@eurac.edu

Abstract—**The ultimate goal of most statistically-based landslide susceptibility studies is to portray areas that a more or less prone to future slope instability. A number of strategies have been presented to sample the position of the underlying training observations (i.e. landslide locations) within raster-based landslide susceptibility models. Previous research emphasized that the location of past landsliding should preferably be represented by variables that describe the conditions before landslide occurrence (pre-landslide conditions). The assumption behind is that an in-depth description of post-landslide conditions might hamper the identification of susceptible terrain that did not fail yet, but is likely to be affected by future landsliding. In practice, however, data on pre-landslide conditions is rarely available. This contribution outlines the main outcomes of recently published research Ref. [1]. The aim was to elaborate differences between landslide susceptibility models based on post-landslide digital terrain models (DTMs) and their counterparts calibrated with approximated pre-landslide DTM derivatives. In this context, also the associated effects of raster resolution and landslide size were considered. The pairwise model comparisons (post- vs. pre-landslide) showed that the DTM raster resolution and the size of the geomorphic phenomena of interest (i.e. smaller vs. larger landslides) controlled whether and how the modelling results differed. The experiments indicate that commonly available post-landslide DTMs can still reasonably be utilized to derive landslide susceptibility models in case they are resampled to a comparably low resolution (i.e. with respect to landslide size).**

I. Introduction

Almost all published landslide susceptibility models are based on topographic variables derived from (recent) DTMs. Available spatial information on past landsliding frequently refers to a time before the available DTM data was acquired (e.g. geomorphological landslide inventories) [2]. Since landslide phenomena are likely to leave a distinct signature on earth surface topography, the question arises whether statistical models trained with recent post-landslide DTM derivatives (e.g. slope angle, curvature indices, aspect) are appropriate to identify generally landslide-prone terrain that was not yet affected by slope instability. Intuitively, pre-landslide conditions should be preferred for a statistical spatial landslide prediction task [3–7]. The analysis associated with this contribution [1] investigated differences between grid-based landslide susceptibility models based on post-landslide topographies and their counterparts based on an approximated pre-landslide morphology. It was tested whether the underlying DTM resolution and the size of the landslide phenomena play a critical role on (i) how the models differ (post- vs. pre-landslide models) and on (ii) the (f)utility to consider pre-landslide topography in susceptibility modelling.

II. Study Area and Data

The 12 km² large landslide-prone hillslopes of the Dreiklang area (Vorarlberg, Austria, Fig. 1) served as a test site for the experiments [8]. A multi-temporal landslide inventory which consists of 366 polygons (mean size 842 m², median 427 m²) build the basis for the analyses (for more details refer to Ref. [1]). Environmental variables were extracted from a 1:50,000 lithological map, a 1 m airborne Light Detection And Ranging (LiDAR) DTM and multi-temporal land cover information [9].

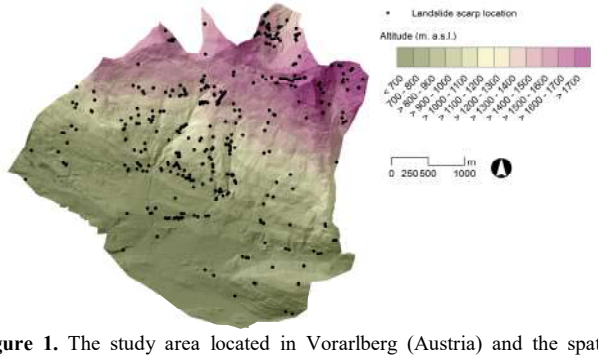

Figure 1. The study area located in Vorarlberg (Austria) and the spatial distribution of the 366 mapped landslide scarp locations.

Stefan Steger (2020) The role of pre-landslide morphology in statistical modelling of landslide-prone areas:

in Massimiliano Alvioli, Ivan Marchesini, Laura Melelli & Peter Guth, eds., Proceedings of the Geomorphometry 2020 Conference, doi:10.30437/GEOMORPHOMETRY2020_51.

III. METHODS

The workflow, described in more detail in Ref. [1], comprised A. an initial approximation of pre-landslide topography and a derivation of commonly used topographic variables (different resolutions) and B. a separate statistically-based modelling of landslide susceptibility (post- vs. pre-landslide topography) followed by an in-depth result evaluation.

A. Data preparation

Pre-landslide topography was approximated automatically by (i) deleting mapped landslides areas from the original 1 m DTM and by (ii) refilling the resultant *'landslide holes'* with interpolated elevation values (TIN interpolation followed by moving window-based smoothing of rasterized values). The newly generated pre-landslide DTM and the original post-landslide DTM were resampled bilinearly to a resolution of 2.5 m, 5 m, 10 m and 25 m to derive frequently used topographic variables: slope, profile slope curvature (i.e. convergence index) and slope orientation (i.e. northness and eastness) (Fig. 2). The effect of landslide size on the modelling results was evaluated by preparing two equally sized response variables (183 landslides each) that contain landslide information on (i) relatively large phenomena (> median landslide polygon size) and (ii) comparably small landslides (< median).

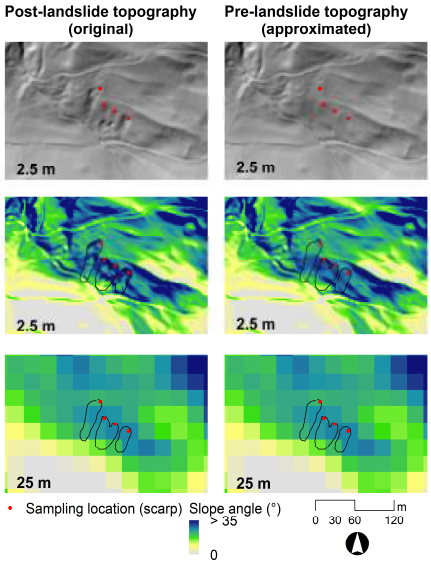

Figure 2. Visual impression of post-landslide topography (left column) and approximated pre-failure topography (right column). The underlying cell size is displayed at the bottom left of each plot.

B. Modelling and model evaluation

Generalized linear (mixed) models were trained separately for data sets associated with different raster resolutions and the two landslide size groups. The (fixed effect) predictor set of the final models contained the variables slope, convergence index, northness, eastness and lithology. Land cover classes were introduced as a random intercept to 'average out' an expected varying completeness of landslide information among land cover units according Ref. [10]. The model evaluations focused on a pairwise comparison of post-landslide models with their pre-landslide equals using different criteria: the discriminatory power of variables (based on the Area Under the Receiver Operating Characteristic, AUROC), predictive performance (based on k-fold cross-validation), the effect size of variables (i.e. odds ratio), variable importance and the spatial pattern of the final maps [1].

IV. RESULT SUMMARY

The evaluations exposed that landslide susceptibility models trained with post-landslide topographic variables can, but must not differ from models that consider an approximated pre-landslide topography. The pairwise comparisons (post-landslide vs. pre-landslide) highlighted that the detail in terrain representation (i.e. raster resolution) as well as the size of mapped landslides controlled whether or not the respective models differed. For instance, differences in the discriminatory power of the variables slope and convergence diminished with a decreasing raster resolution. Most distinct differences were observed for models associated with high resolutions and larger landslides (Fig. 3).

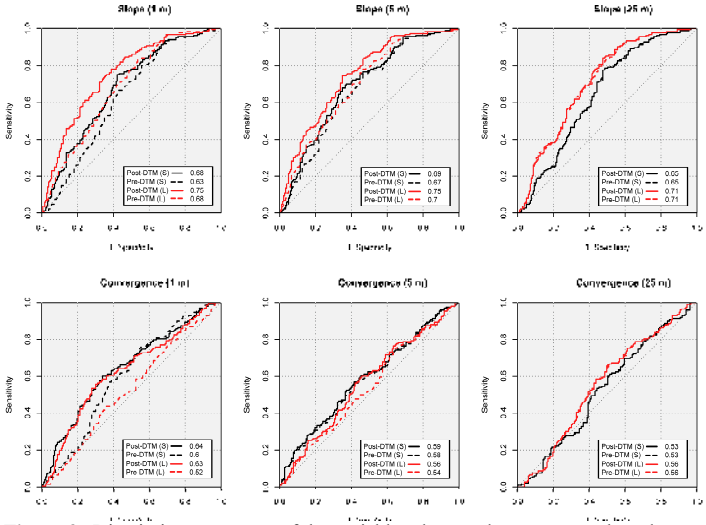

Figure 3. Discriminatory power of the variables slope and convergence based on single-variable logistic regression for different raster resolutions (1 m, 5 m , 25 m) and the two landslide size groups (S: smaller landslides in black, L: larger in red). Confrontations of the AUROCs reveal decreasing differences among the models (post- vs. pre-landslide) with coarser raster resolutions. At higher raster resolutions, larger differences were observed for models based on larger landslides (confront straight and dashed red lines and associated AUROCs).

Similar trends were observed when evaluating the multiple-variable models by means of estimated predictive performances, the effect size of variables and the relative importance of variables: higher similarity of post-landslide and pre-landslide models in case the models were based on lower raster resolutions (e.g. 10 m , 25 m) and smaller landslides. At a spatial resolution of 25 m, differences between the modelling results were negligible. Difference maps of classified landslide susceptibility maps (Fig. 4) visually highlight (i) a considerable portion of dissimilarly classified raster cells for high resolution maps which are based on larger landslides (top right) and (ii) similar predictions for lower resolution maps based on smaller landslides (bottom left).

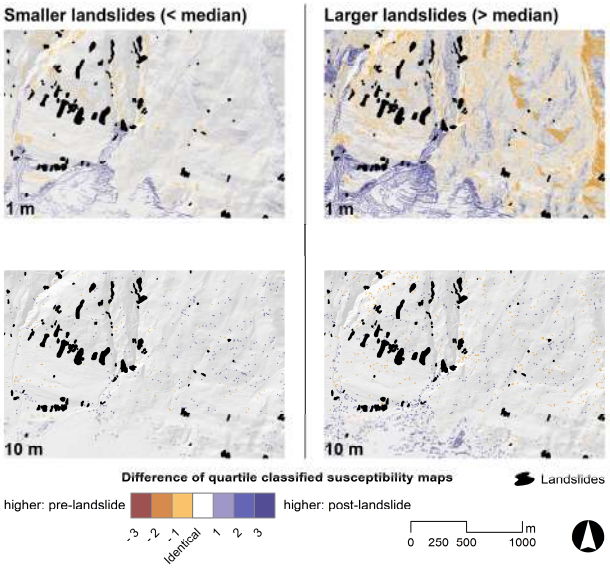

Figure 4. Difference of quartile classified susceptibility maps. The highest (lowest) portion of dissimilarly predicted cells can be observed for maps based on a higher (lower) raster resolution and larger (smaller) landslides. The underlying cell size is displayed at the bottom left of each plot. Note that the expressions "smaller landslides" (left column) and "larger landslides" (right) relate to the training data. Mapped landslides of both size groups are shown in each map.

V. CONCLUSION

The study [1] showed that an undesired too detailed description of landslide morphology within raster-based landslide susceptibility models can not only be minimized by estimating pre-landslide topography, but also by simply resampling a DTM to a lower spatial resolution and by excluding topographic variables that predominantly reflect the geomorphic remnants of past slope failure. For larger deep-seated movements, an approximation of pre-landslide topography or an application of alternative spatial units (e.g. slope-units, [11]) is recommended. Critical decisions in statistical landslide modelling, such as the selection of variables and raster resolution, should not be based on model performance estimates, but on the ultimate goal of a study: identification of landslide-prone terrain (i.e. emphasis on generalization and the future) or landslide detection (i.e. emphasis on describing the past). DTM derivatives that mainly depict landslide morphology may be of limited use to identify not yet failed susceptible terrain [1]. It is planned to investigate the (f)utility to approximate pre-failure conditions in the context of dynamic physically-based slope stability modelling.

ACKNOWLEDGMENTS

The author thanks Elmar Schmaltz for sharing landslide data and Thomas Glade for the coordination of the BioSlide project in which the original research [1] was conducted. Thanks also to the federal state of Vorarlberg for providing LiDAR data and the torrent and avalanche control for providing landslide archive data.

REFERENCES

[1] Steger, S., E. Schmaltz, T. Glade, 2020. "The (f)utility to account for pre-failure topography in data-driven landslide susceptibility modelling". Geomorphology 354, 107041.

[2] Reichenbach, P., M. Rossi, B.D. Malamud, M. Mihir, F. Guzzetti, 2018. "A review of statistically-based landslide susceptibility models". Earth-Science Reviews 180, 60–91.

[3] Atkinson, P.M., R. Massari, 1998. "Generalised linear modelling of susceptibility to landsliding in the Central Apennines, Italy". Computers & Geosciences 24(4), 373–385.

[4] Clerici, A., S. Perego, C. Tellini, P. Vescovi, 2006. "A GIS-based automated procedure for landslide susceptibility mapping by the Conditional Analysis method: the Baganza valley case study (Italian Northern Apennines)". Environ Geol. 50(7), 941–961.

[5] Schlögel, R., I. Marchesini, M. Alvioli, P. Reichenbach, M. Rossi, J.-P. Malet, 2018 "Optimizing landslide susceptibility zonation: Effects of DEM spatial resolution and slope unit delineation on logistic regression models". Geomorphology 301, 10–20.

[6] Süzen, M.L., V. Doyuran, 2004. "A comparison of the GIS based landslide susceptibility assessment methods: multivariate versus bivariate". Environmental Geology 45(5), 665–679.

[7] Van Den Eeckhaut, M., T. Vanwalleghem, J. Poesen, G. Govers, G. Verstraeten, L. Vandekerckhove, 2006. "Prediction of landslide susceptibility using rare events logistic regression: A case-study in the Flemish Ardennes (Belgium)". Geomorphology 76(3–4), 392–410.

[8] Steger, S., E. Schmaltz, A.C. Seijmonsbergen, T. Glade, 2020. "The Walgau – a landscape shaped by landslides". in Embleton-Hamann, C. (Ed.): "Landscapes and Landforms of Austria". Geomorphological Landscapes of the World. (in press)

[9] Schmaltz, E., S. Steger, T. Glade, 2017. "The influence of forest cover on landslide occurrence explored with spatio-temporal information". Geomorphology 290, 250–264.

[10] Steger, S., A. Brenning, R. Bell, T. Glade, 2017. "The influence of systematically incomplete shallow landslide inventories on statistical susceptibility models and suggestions for improvements". Landslides 14(5), 1767–1781.

[11] Alvioli, M., Marchesini, I., Reichenbach, P., et al., 2017. "Automatic delineation of geomorphological slope units with r.slopeunits v1.0 and their optimization for landslide susceptibility modeling". Geosci. Model Dev. 9(11), 3975–3991.

GEOMORPHOMETRY 2020 PERUGIA, ITALY JUNE 22 - 26 2020

Assessing the impact of lava flows during the 2020 unrest of the Svartsengi volcanic system on the Reykjanes peninsula, Iceland

Simone Tarquini[§a], Massimiliano Favalli[a], Melissa A Pfeffer[b], Mattia de' Michieli Vitturi[a], Sara Barsotti[b], Gro B. M. Pedersen[c], Bergrún A Óladóttir[b,c], Esther H Jensen[b]

[a]Istituto Nazionale di Geofisica e Vulcanologia
via Cesare Battisti 53, I - 56125 Pisa, Italy
[b]Icelandic Meteorological Office
Bústaðavegur 7 - 9, 105 Reykjavík, Iceland
[c]Nordic Volcanological Center, Institute of Earth Sciences, University of Iceland
Askja - Sturlugata 7, 102 Reykjavík
[§] simone.tarquini@ingv.it

Abstract—**In January 2020, inflation up to 5 cm was detected in the volcanic system of Svartsengi, Reykjanes peninsula (Iceland). The inflation was probably linked to the movement of magma which was estimated to be at a depth of 3-5 km. Shortly after the detection of the inflation, the Scientific Advisory Board responsible for tackling the unrest deemed possible that the unrest could evolve into an effusive eruption. We used both the MrLavaLoba and the DOWNFLOW codes to simulate the area potentially inundated by lava flows in order to assess the hazard posed in case of an effusive eruption. The DOWNFLOW code was used to create a suite of 10,000 simulations which were used to derive maps of the lava flow hazards. These maps can be dynamically updated to account for ongoing modifications suggested by the geophysical signals of the monitoring system. The MrLavaLoba code, in turn, was tuned based on the historical lava flows in the area, so it would be ready to simulate potential lava flow fields if an eruption began. At the time of writing (April 2020), the area appears have experienced two intrusions and is currently in a waning phase. However, the lava flow modeling carried out constitutes an example of rapid response during an ongoing crisis. The post-processing of DOWNFLOW simulations can also allow for preliminary estimations of the time left before lava flow inundates given targets, providing effective support for stakeholders.**

I. INTRODUCTION

In mid-January 2020, inflation was detected in the south of the Reykjanes peninsula (Iceland), within the Svartsengi volcanic system. The inflation was accompanied by an earthquake swarm, and was centered close to Thorbjörn, a hill immediately to the North of the town of Grindavík (Fig. 1).

The collected geophysical data suggested that a magma body was moving upwards through the feeding system of Svartsengi, modeled to be at a depth of 3-5 km. The maximum deformation observed from the GPS stations was about 8 cm (as of end-April 2020; vedur.is). If the magma reached the surface, lava flows would have threatened inhabited areas (~ 3500 people), important facilities (e.g. a geothermal powerplant) and the main road linking the capital Reykjavík to the international airport. It was important to assess the possible impact from lava flows using models.

The present contribution summarizes how we used numerical lava flow modeling to prepare for a potential eruption and enhance mitigation planning during the crisis. At the time of writing the present abstract (end-April 2020), a second period of inflation has stalled and it appears that the unrest of Svartsengi is in a potentially temporary waning phase. However, we deemed useful to document the work carried out during the initial intrusion, which could be of use in the future.

II. METHODS

Throughout the duration of the crisis, all the data collected by the monitoring system and the results provided by data post-processing were discussed during Scientific Advisory Board meetings. The board was formed by a team of scientists from Icelandic institutions and local stakeholders. The reports of the board meetings were rapidly published online (Icelandic Met Office website, vedur.is), to provide timely communication to the whole community. We carried out a series of lava flow numerical

Simone Tarquini, Massimiliano Favalli, Melissa Pfeffer, Mattia De' Michieli Vitturi, Sara Barsotti, Gro Pedersen, Bergrn Arna ôladttir and Esther Hjensen (2020):

Assessing the impact of lava flows during the unrest of Svartsengi volcano in the Reykjanes peninsula, Iceland:

in Massimiliano Alvioli, Ivan Marchesini, Laura Melelli & Peter Guth, eds., Proceedings of the Geomorphometry 2020 Conference, doi:10.30437/GEOMORPHOMETRY2020_52.

simulations to assess the hazard posed by possible lava flows in the area. As the computational domain, we used a digital elevation model of the Reykjanes peninsula from the Arctic DEM with a 10 m- grid-size, which is an adequate resolution for lava flow simulations [1]. Geological maps of the area and the relevant literature were studied to collect and analyze all the visible eruptive fissures, with the aim of getting information about possible future vents and about the eruption style. The last known eruptions in the area occurred in the time interval 1210-1240 AD. Within that period, three separate effusive episodes erupted from the Svartsengi fissure swarm. The largest eruption formed the Arnarseturshraun lava, estimated to be 0.3 km^3 in volume and to cover an area of 20 km^2. The duration of each historical eruption spans from a few days up to several weeks, with the entire eruptive episode lasting decades. Given the spatial orientation and the length of the historical eruptive fissures (up to 12 km long), it was necessary to consider possible vent opening in a large area around the ongoing inflation.

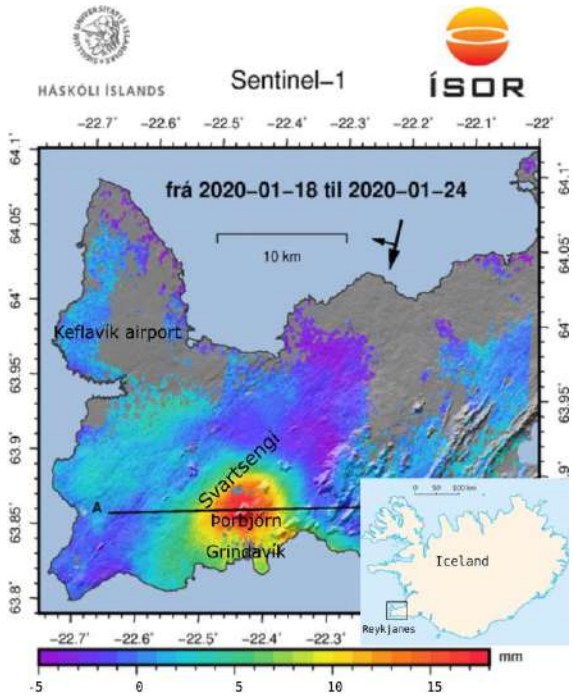

Figure 1. An InSAR measurement (InSAR: interferometric analysis of synthetic aperture radar images) based on satellite information showing the inflation during the period from Jan 18-24. The red colour indicates an inflation of around 15 mm during the period. (Vincent Drouin, ISOR). The inflation continued in the following weeks up to a maximum of about 5 cm. This figure has been downloaded from the Icelandic Met Office website during the crisis (vedur.is).

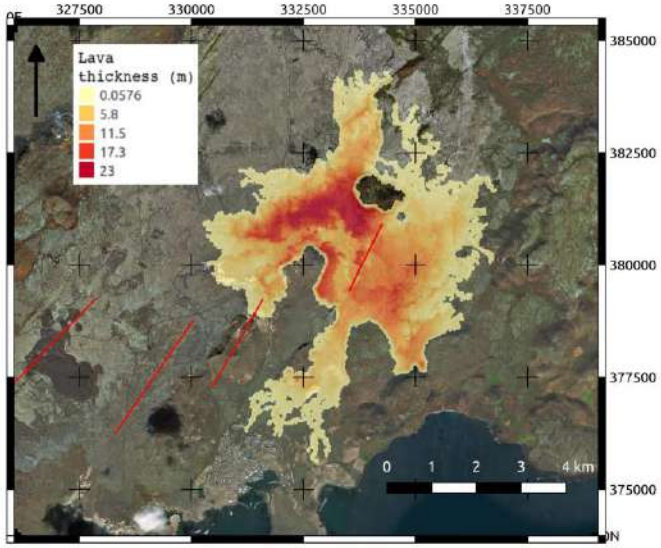

Figure 2. MrLavaLoba simulation from an eruptive fissure to the North-East of the Grindavík town. Red lines represent some of the possible eruptive fissures considered in the present work. 150 M m^3 of erupted lava considered.

A. Lava flow simulation codes

To perform numerical simulations, we decided to use both the MrLavaLoba code [2, https://github.com/demichie/MrLavaLoba] and the DOWNFLOW code [3]. Both codes are probabilistic in nature and provide an output area possibly inundated by the flowing lava. Both codes are essentially based on the computation of the steepest descent, but they differentiate in how the deviation from the bare steepest descent path is computed. MrLavaLoba can also explicitly account for the syn-emplacement modifications of the topography (i.e. it accounts for the erupted volume), and this capability can be specifically useful when the eruption promotes the formation of a thick lava deposit. The tuning of MrLavaLoba to a given scenario can imply several runs, because of the wide spectrum of possible combinations among the tunable parameters. A MrLavaLoba run can take minutes to hours on a PC, with the run time changing based on input parameter choices (for example, defining too many lobes to be generated leads to longer run times). In the present case, the preliminary tuning session lasted 4-6 hrs. Once the initial tuning is done, however, MrLavaLoba allows further additional calibration refinements which can potentially cope with the actual complexity of the lava flow emplacement process [4, 5]. The DOWNFLOW code, in comparison, does not explicitly account for the erupted volume, and takes only into account the

pre-emplacement topography (details can be found in the Ref. [3]). In spite of its simplicity, DOWNFLOW has been demonstrated to be effective during several volcanic crises [1]. Additional characteristics of the DOWNFLOW code are that it is easy to tune (essentially only one parameter), and it is very fast (a few seconds for each run), making this code ideal for the creation of a large suite of simulations [6, 7].

III. RESULTS AND CONCLUSIONS

The two codes were used in parallel. MrLavaLoba was tuned to a spectrum of possible eruptive scenarios, in order to reproduce a range of lava deposit thicknesses and lava flow lengths based on given erupted volumes (e.g. Figure 2). We considered that, if an effusive event actually occurred, this code could have allowed to account for the specific emplacement style (e.g. a given thickening) by iteratively modifying the tuning of the code parameters on the basis of the available data from the monitoring system [8].

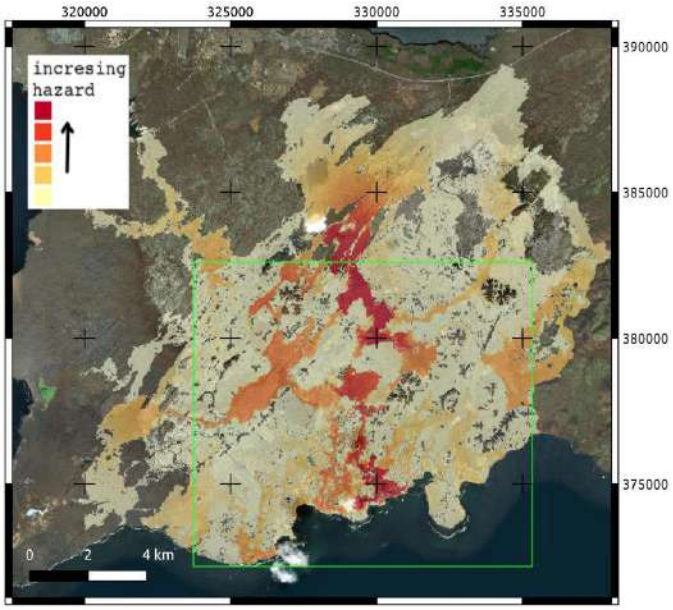

Figure 3. Lava flow hazard map of the area potentially affected by an eruption linked to the inflation in the Reykjanes peninsula. The map was derived by post-processing DOWNFLOW simulations triggered from a grid of about 10,000 computational vents (bounding box of the grid in green).

DOWNFLOW, instead, was used to derive a large database of lava flow simulations triggered from a regular 100 m-spaced grid of about 10,000 vents covering a wide area around Thorbjörn. This database was obtained in about 10 h by using a cluster for parallel computing hosted at the National Institute of Geophysics and Volcanology in Pisa (Italy). The database of simulations was then post-processed considering a given probability density function (pdf) of future vent opening (quantifying the opening probability of each vent), and a given probability of reaching a given maximum flow length.

We initially set a uniform pdf of vent opening, so that the opening probability is equal at each potential vent. The latter settings allow to highlight the effect of other factors than vent position, such as topography and flow length, in the resulting flow propagation. Based on the available geological mapping of this area, we set a uniform probability of reaching a flow length between 0 and 7 km, obtaining the hazard map in Figure 3. This map shows a maximum probability of lava flow inundation extending north from the south coast halfway through the green square (Figure 3).

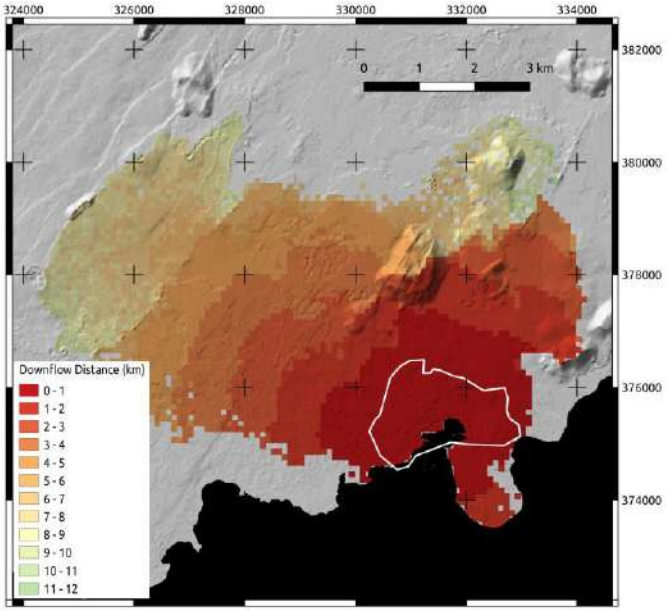

Figure 4. Map showing, at each point, the remaining down-flow distance to reach the town of Grindavík (enclosed by the white polygon). Down-flow distances are measured along the lava flow path computed by the simulations.

We derived additional hazard maps by considering different pdf of vent opening since the geophysical data (e.g. inflation, earthquakes) suggested that the probability of opening may be higher in certain areas than elsewhere. As an example, in the early days of the crisis, it was suggested that a more likely site of eruption was along the westernmost of the four possible

eruptive fissures illustrated in Figure 2 (red segments), thus we created a pdf of vent opening assigning a uniform probability to all the computational vents laying within 100 m from the fissure, and 0 to all the other vents. From an operational viewpoint, we remind that a post-processing iteration of the described database takes about half an hour.

A different type of post processing of the same database of DOWNFLOW simulations allows to "invert" the map to visualize specific characteristics of the simulated lava flows with respect to given "targets", i.e. a given asset vulnerable to the potential lava flow [6, 9]. Figure 4 shows a map in which each point is attributed with the minimum distance a lava flow venting at (or reaching) that point has still to travel, along the simulation path, to reach the town of Grindavík (with a population of 3,300). During the present crisis, it was possible that an effusive vent could open quite close to the town. For this reason, stakeholders where especially interested in the assessment of the "time left" for possible evacuation. We note that the map of Figure 4 constitutes a significant step forward in that direction, because upon estimation of a range of possible average lava flow front advancement velocity, the down-flow distance can be easily translated into an estimation of the time left for evacuation. On the basis of a preliminary literature review [10 - 12] we believe a reasonable range of lava flow front advancement velocity is between 5 and 150 mh^{-1}, and we propose alternative color legends for Figure 4 providing the time left for minimum and maximum advancement velocities (Figure 5).

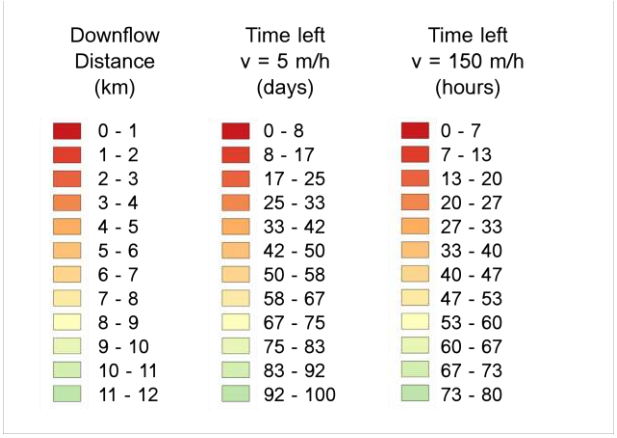

Figure 5. Alternative color legends for the map in Figure 4. From the left: The default legend showing the down-flow distance; the "time left" legend assuming a lava flow front advancement velocity (v) of 5 mh^{-1}; and the "time left" legend assuming a lava flow front advancement velocity of 150 mh^{-1}.

All the maps created during this work (including those showed in the present abstract) have been presented and discussed during Scientific Advisory Board meetings, and constituted effective support to the decision makers.

REFERENCES

[1] Tarquini, S., M. Favalli, 2016. "Simulating the area covered by lava flows using the DOWNFLOW code". *Geological Society, London, Special Publications*, *426*(1), 293-312.

[2] De' Michieli Vitturi, M., & Tarquini, S. (2018). MrLavaLoba: A new probabilistic model for the simulation of lava flows as a settling process. *Journal of Volcanology and Geothermal Research*, *349*, 323-334.

[3] Favalli, M., Pareschi, M. T., Neri, A., & Isola, I. (2005). Forecasting lava flow paths by a stochastic approach. *Geophysical Research Letters*, *32* (3).

[4] Tarquini, S., de' Michieli Vitturi, M., Jensen, E. H., Pedersen, G. B., Barsotti, S., Coppola, D., & Pfeffer, M. A. (2018). Modeling lava flow propagation over a flat landscape by using MrLavaLoba: the case of the 2014–2015 eruption at Holuhraun, Iceland. *Ann. Geophys.* 62:228.

[5] Applegarth LJ, Pinkerton H, James MR, Calvari S (2010b) Morphological complexities and hazards during the emplacement of channel-fed `a`ā lava flow fields: a study of the 2001 lower flow field on Etna. *Bull Volcanol* 72:641–656.

[6] Favalli, M., Tarquini, S., Fornaciai, A., & Boschi, E. (2009). A new approach to risk assessment of lava flow at Mount Etna. *Geology*, *37*(12), 1111-1114.

[7] Favalli, M., Tarquini, S., Papale, P., Fornaciai, A., & Boschi, E. (2012). Lava flow hazard and risk at Mt. Cameroon volcano. *Bulletin of V4olcanology*, *74*(2), 423-439.

[8] Harris, A. J. L., Carn, S., Dehn, J., Del Negro, C., Guðmundsson, M. T., Cordonnier, B., ... & De Groeve, T. (2016). Conclusion: recommendations and findings of the RED SEED working group. *Geological Society, London, Special Publications*, *426*(1), 567-648.

[9] Richter, N., Favalli, M., de Zeeuw-van Dalfsen, E., Fornaciai, A., Fernandes, R. M. D. S., Pérez, N. M., ... & Walter, T. R. (2016). Lava flow hazard at Fogo Volcano, Cabo Verde, before and after the 2014-2015 eruption. *Natural Hazards & Earth System Sciences*, *16*(8).

[10] Pedersen, G. B. M., Höskuldsson, A., Dürig, T., Thordarson, T., Jonsdottir, I., Riishuus, M. S., ... & Sigmundsson, F. (2017). Lava field evolution and emplacement dynamics of the 2014–2015 basaltic fissure eruption at Holuhraun, Iceland. *Journal of Volcanology and Geothermal Research*, 340, 155-169.

[11] Sigurðsson O (1974). Jarðeldar á Heimaey 1973. *Týli* 4, 5–26.

[12] Einarsson Þ (1974). Gosið á Heimaey í máli og myndum. *Heimskringla*. Reykjavík

GEOMORPHOMETRY 2020
PERUGIA, ITALY
JUNE 22 - 26 2020

Differences between terrestrial and airborne SFM and MVS photogrammetry applied for change detection within a sinkhole in Thuringia, Germany

Markus Zehner[§], Helene Petschko, Patrick Fischer, Jason Goetz
Friedrich Schiller University Jena,
Institute of Geography,
Grietgasse 6, 07743 Jena, Germany
[§] markus.zehner@uni-jena.de

Abstract—**Structure from motion (SFM) combined with multi view stereo (MVS) reconstruction is a cost effective method to assess topographic change, to analyse long term development and to perform risk assessments. The objective of this study was the comparison of two image acquisition methods, terrestrial handheld and UAV based photography regarding the detectable changes over time and the differences between the point clouds of the 'Äbtissingrube' – a sinkhole in Thuringia, Germany. The imagery was taken yearly from 2017 to 2019 with both UAV and handheld camera. The 3D point clouds were processed within Agisoft PhotoScan Pro. Additionally the point precisions were estimated with SFM_Georef and the differences in the resulting point clouds were compared using multiscale model to model cloud comparison with precision maps (M3C2-PM) in CloudCompare. The resulting differences are 10.2 percent of detectable change between the 2019 UAV and terrestrial point cloud with a mean detectable change of 9.0 mm. Change detection from 2017 to 2019 shows 61.1 percent of detectable change and a mean detectable change of 59.6 mm within the sinkhole. The resulting coverage of the sinkhole was generally higher by the point clouds derived from UAV in comparison to the handheld camera.**

I. INTRODUCTION

Structure from motion (SFM) and multi view stereo (MVS) reconstruction, originating from computer vision algorithms by Ref. [1], are applied widely within the analysis of earth surface processes in the last years to create dense 3D point clouds of surfaces out of optical imagery [2]. Although implemented in various open source programs, Agisoft PhotoScan Pro is preferred in many scientific publications [3]. Terrestrial handheld photography is the most basic approach, at the cost of the limitation of viewing angles and position of the sensor [4]. UAVs supporting consumer grade cameras and flight stabilisation offer better options in sensor position and viewing angles. With the low cost and weight of consumer grade cameras, highly mobile survey methods are possible, including the usage of small UAVs for image acquisition [5]. SFM has already been applied at scales from large planar regions for digital elevation model creation, landslides, rivers and sinkholes to erosion measurements within the millimeter range in laboratory work [4, 6-9]. Research comparing accuracies of point clouds derived with SFM-MVS to those of TLS and LiDAR show no disadvantages, given careful GCP placement, calibration and a sufficient number of images [2, 3, 10, 11 and 12]. Less studies have compared the differences between using terrestrial or aerial imagery [13]. As a state of the art point cloud comparison method in complex topography the multiscale model to model cloud comparison (M3C2) by Ref. [14] is often applied. Assessing the spatial uncertainties within the derived point clouds resulting from the SFM-MVS algorithms and georeferencing is decisive for identifying areas of detectable change. Profound methods have been developed with UAV imagery based on the random variations within the SFM photogrammetry workflow deriving precision maps [15] or on the comparison of repeated surveys of the same surface within a short time span [16].

The objective of this study was the comparison of two image acquisition methods - terrestrial handheld and UAV based photography - regarding the detectable changes over time and the differences between the point clouds with precision maps from the same day. The comparison was based on imagery taken of the sinkhole Äbtissingrube in 2017, 2018 and 2019.

The sinkhole is located in Northern Thuringia on the Kyffhäuser Southern Margin Fault which causes low mineralized groundwater to rise and infiltrate the overlaying sedimentary rocks of the Permian, which are very good aquifers. Solution processes caused by the water are assumed to have triggered the formation of the sinkhole [17].

Markus Zehner, Helene Petschko ,Patrick Fischer, and Jason Goetz (2020)

Differences between terrestrial and airborne SFM and MVS photogrammetry applied for change detection within a sinkhole in Thuringia, Germany:

in Massimiliano Alvioli, Ivan Marchesini, Laura Melelli & Peter Guth, eds., Proceedings of the Geomorphometry 2020 Conference, doi:10.30437/GEOMORPHOMETRY2020_53.

II. METHODS

Data was recorded yearly in autumn for 2017, 2018 and 2019 with a terrestrial and an aerial approach. The UAV was maneuvered manually to record images from above and within the sinkhole. The terrestrial imagery was taken with a handheld camera from the edge of the sinkhole. Georeferencing was accomplished with ground control points (GCPs) by surveying targets laid out around the sinkhole with a GNSS (Leica Viva GS10 & GS15). Sensor characteristics and weather conditions that influence the results of the SFM are given in Table 1 and 2. Software for the analysis was Agisoft PhotoScan Pro 1.4.3, SFM_Georef 3.1 and CloudCompare 2.10 alpha.

Within PhotoScan Pro, all images were masked by hand to the extent of the sinkhole to reduce vegetation. SFM was used to create the sparse cloud, which represents prominent features within overlapping images as tie points. This was done with a key point limit of 40,000 and a tie point limit of 10,000 with masks applied to key points and adaptive camera model fitting. With the tie points, camera positions and viewing angles were reconstructed. The sparse clouds were filtered gradually to only contain points with a reprojection error, reconstruction uncertainty and projection accuracy of 0.2, 15 and 10 for UAV data and 0.2, 30 and 10 for terrestrial imagery respectively. These settings within PhotoScan Pro were used to reduce the possible tie points of the images to only high quality ones. The lowered reconstruction uncertainty in the terrestrial sparse clouds were to ensure that the sparse clouds do not show too large holes within the slopes where unobstructed ground surfaces were visible. The GCPs were marked manually within the imagery, upon which the sparse cloud was georeferenced. Then the camera alignment was optimized with the GCPs. With MVS reconstruction, all the imagery based on the prior estimated camera positions was matched in a three dimensional dense cloud with medium quality and mild depth filtering which represents the photographed structure.

Bundle adjustment was carried out with a 10,000 fold Monte-Carlo approach to generate precision maps with SFM_Georef containing precisions of each point in the sparse clouds for x, y and z axis [9, 15].

The precision maps were combined with the dense clouds within CloudCompare with a distance based spherical normal distribution interpolation. As the sparse clouds were thinner in vegetated areas, this lead to points without precision within the dense clouds. Normals were calculated using the quadric local surface model and minimum spanning tree. Comparison of the dense clouds was done with the M3C2 plugin with precision maps enabled [14]. Cylinders are created for each core point along the local normal direction to calculate the mean distance of the two clouds. By using the precision maps variable local differences in point quality are also considered [14]. Scales for the cylinders were calculated within the plugin. For each comparison the whole cloud was set as core points. Points of the resulting comparison without a value for uncertainty were ignored as these are for the most part changes due to vegetation. Then percentage of detectable change, i.e. where the level of detection was smaller than the distance of measured change, was calculated based upon the initial cloud in each comparison. Mean and median for measured change and the level of detection were calculated for the area where detected change was observed.

Obstruction by vegetation is a large challenge with optical data, as shorter wavelengths are not able to penetrate foliage and result in local loss of surface information. To minimize the impact of the survey on the study area and to not risk any further collapse, vegetation was not cleared within the sinkhole. Furthermore any disruption by accessing the sinkhole would have impacted the results. Over the survey period, large areas at the bottom of the sinkhole became overgrown with dense vegetation so that not all vegetation within the sinkhole could be masked out.

Table 1: Survey characteristics

	Date	Lighting	Vegetation	GCPs
2017	22. March	Steep incidence	Dry brown	8
2018	22. Nov.	Diffuse lighting	Green, some snow	8
2019	05. Nov.	Steep incidence	Green	10

Table 2: Used sensors and resulting point clouds

Year	Sensor	Resolution	Focal length	Image count / used	Sparse Cloud	Dense Cloud
2017	DJI FC330	4000 x 3000	4 mm	353/353	37,037	2,651,375
	Nikon D3000	3872 x 2592	18/21 mm	221/94	13,051	2,311,397
2018	DJI FC6310	5472 x 3648	9 mm	564/542	54,443	8,767,159
	Nikon D3000	3872 x 2592	18 mm	169/157	30,820	2,402,887
2019	DJI FC330	4000 x 3000	4 mm	287/278	34,612	2,673,191
	Nikon D3000	3872 x 2592	18 mm	178/177	21,929	2,707,662

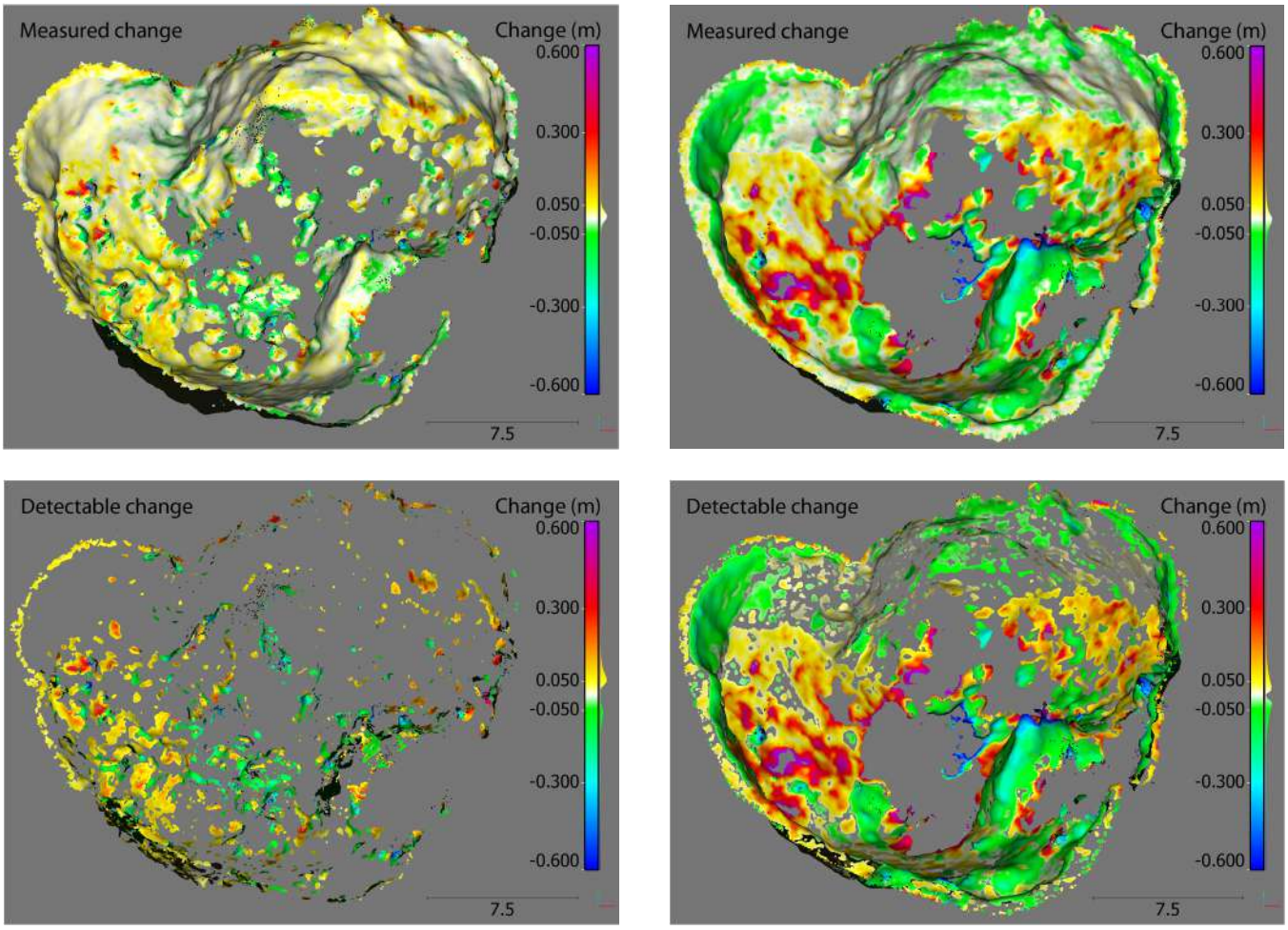

Figure 1. *Left:* Comparison of the dense clouds derived from 2019 terrestrial and aerial data, projected on the aerial cloud. *Right:* Comparison of the dense clouds derived from 2017 and 2019 aerial data, projected on the 2017 aerial cloud. Shown are points with a measured change of 0.6 m relative to the projected cloud, along with the density curve next to the color bar. The upper figures show the general measured change, where point precisions were present. The lower figures show detectable change, where the change measured was greater than the level of detection. The missing points in the figures are due to exclusion of points with measured change larger than 0.6 m, exclusion of points without point precision estimate (upper figures) and exclusion of non-detectable change (lower figures)

III. RESULTS AND CONCLUSIONS

A first result for the sensor comparison can be drawn from Table 2. The same filtering, except for a higher reconstruction uncertainty, results in more tie points out of the UAV data. The dense clouds show less difference in point count with exception of 2018. Here also the number of used images has to be accounted for: with the UAV approach, image recording was faster and more data could be acquired within each study. Manual operation of the handheld camera also lead to more blurred images, protruding branches from within the sinkhole were an additional limitation to the viewpoints. This is in line with findings from Ref. [3] as the accuracy of the point cloud does not increase linearly with the number of used images, but levels off to diminishing returns after a sufficient number [3].

The comparison of the dense clouds derived from the 2019 terrestrial and airborne data resulted in a percentage of detectable change of 10 % (273,068 out of 2,673,191, Figure 1 (on the left)). The mean and median of the measured change of the points of detectable change were 0.009 m and 0.049 m respectively with a

mean and median level of detection of 0.049 m and 0.047 m. The comparison of the dense clouds derived from aerial data from 2017 to 2019 shows 61 % of points with detectable change (1,618,638 out of 2,651,375, Figure 1 (on the right)). Here the mean and median of detectable change were 0.059 m and 0.022 m with mean and median of level of detection of 0.021 and 0.018 m.

Regarding the small number of points with detectable change in the sensor comparison, we conclude that the differences between photogrammetric results are minor. Therefore, the algorithms within Agisoft PhotoScan Pro create point clouds that represent the sinkhole with comparable precision. However, the reduced viewing angles in the handheld approach lead to more obstruction in this complex relief, as well as lower visibility of the targets used as GCPs. This lead to a less complete representation of the sinkhole in the point cloud derived from the terrestrial imagery and to potentially higher errors in georeferencing. Looking at the change detection between 2017 and 2019, the survey in 2017 and 2019 had comparable lighting as well as the same sensors in use. This plays an important factor as sensor type and lighting conditions influence the precision of SFM. Deriving the precision maps and applying them within the M3C2 point cloud comparison gives us confidence in the detectable changes within the years 2017 and 2019. Over the two year period we can identify areas where material disappeared and accumulated in areas with less vegetation.

REFERENCES

[1] Ullman, S., 1979 “The interpretation of visual motion”. Proceedings of the Royal Society of London. Series B. Biological Sciences, 203(1153), 405-426.

[2] Smith, M. W., J. L. Carrivick, and D. J. Quincey. 2016. "Structure from motion photogrammetry in physical geography." Progress in Physical Geography 40.2, pp. 247-275.

[3] Eltner, A, Kaiser, A., Castillo, C., Rock, G., Neugirg, F., & Abellán, A., 2016. "Image-based surface reconstruction in geomorphometry-merits, limits and developments". Earth Surface Dynamics 4.2.

[4] Klawitter, M., Pistellato, D., Webster, A., & Esterle, J., 2017. “Application of photogrammetry for mapping of solution collapse breccia pipes on the Colorado Plateau, USA”. The Photogrammetric Record, 32(160), 443-458.

[5] Fonstad, M. A., Dietrich, J. T., Courville, B. C., Jensen, J. L., & Carbonneau, P. E., 2013. “Topographic structure from motion: a new development in photogrammetric measurement”. Earth surface processes and Landforms, 38(4), 421-430.

[6] Nakano, T., Kamiya, I., Tobita, M., Iwahashi, J., & Nakajima, H., 2014. “Landform monitoring in active volcano by UAV and SFM-MVS technique”. The International Archives of Photogrammetry, Remote Sensing and Spatial Information Sciences, 40(8), 71-75.

[7] Esposito, G., Salvini, R., Matano, F., Sacchi, M., Danzi, M., Somma, R., Troise, C., 2017. “Multitemporal monitoring of a coastal landslide through SfM-derived point cloud comparison”. The Photogrammetric Record, 32(160), 459-479.

[8] Javernick, L., Brasington, J., Caruso, B., 2014. “Modeling the topography of shallow braided rivers using Structure-from-Motion photogrammetry”. Geomorphology, 213, 166-182.

[9] James, M. R., & Robson, S., 2012. “Straightforward reconstruction of 3D surfaces and topography with a camera: Accuracy and geoscience application”. Journal of Geophysical Research: Earth Surface, 117(F3).

[10] Westoby, M. J., Brasington, J., Glasser, N. F., Hambrey, M. J., Reynolds, J. M., 2012. “‘Structure-from-Motion’photogrammetry: A low-cost, effective tool for geoscience applications”. Geomorphology, 179, 300-314.

[11] Passalacqua, P., Belmont, P., Staley, D. M., Simley, J. D., Arrowsmith, J. R., Bode, C. A., Crosby, C., DeLong, S. B., Glenn, N. F., Kelly, S. A., Lague, D., Sangireddy, H., Schaffrath, K., Tarboton, D. G., Wasklewicz, T., Wheaton, J. M., 2015. “Analyzing high resolution topography for advancing the understanding of mass and energy transfer through landscapes: A review”. Earth-Science Reviews, 148, 174-193.

[12] Cook, K. L., 2017. “An evaluation of the effectiveness of low-cost UAVs and structure from motion for geomorphic change detection”. Geomorphology, 278, 195-208.

[13] Koci, J., Jarihani, B., Leon, J. X., Sidle, R. C., Wilkinson, S. N., Bartley, R., 2017. “Assessment of UAV and ground-based structure from motion with multi-view stereo photogrammetry in a gullied savanna catchment”. ISPRS International Journal of Geo-Information, 6(11), 328.

[14] Lague, D., Brodu, N., Leroux, J., 2013. “Accurate 3D comparison of complex topography with terrestrial laser scanner: Application to the Rangitikei canyon (NZ)”. ISPRS journal of photogrammetry and remote sensing, 82, 10-26.

[15] James, M. R., Robson, S., Smith, M. W., 2017. “3-D uncertainty-based topographic change detection with structure-from-motion photogrammetry: precision maps for ground control and directly georeferenced surveys”. Earth Surface Processes and Landforms, 42(12), 1769-1788.

[16] Goetz, J., Brenning, A., Marcer, M., Bodin, X. 2018. “Modeling the precision of structure-from-motion multi-view stereo digital elevation models from repeated close-range aerial surveys”. Remote sensing of environment, 210, 208-216.

[17] Petschko, H., Goetz, J., Böttner, M., Firla, M., Schmidt, S., 2017. “Erosion processes and mass movements in sinkholes assessed by terrestrial structure from motion photogrammetry”. In Workshop on World Landslide Forum. Springer, Cham, 227-235.

GEOMORPHOMETRY 2020
PERUGIA, ITALY
JUNE 22 - 26 2020

Quantifying geomorphic change in a partially restored gully using multitemporal UAV surveys and monitoring discharge and sediment production

Alberto Alfonso-Torreño[§], Álvaro Gómez-Gutiérrez, Susanne Schnabel
Research Institute for Sustainable Land Development (INTERRA)
University of Extremadura, Cáceres, Spain
[§] albertoalfonso@unex.es

Abstract—**Gully erosion in valley bottoms is a frequent process with negative consequences in the landscape. The development of new techniques and instruments allows the study of gullied channels with high spatial and temporal resolution. Here we present a detailed study of a valley bottom gully that was restored in 2017 with check dams. The channel is located in an experimental catchment, which is equipped with sensors to continuously monitor rainfall, discharge and suspended sediment concentration. The objectives of this work are (1) to analyze the effectiveness of operations carried out in the channel and (2) to elucidate the role of the former operations on the hydrological and sedimentological spatial and temporal dynamic. The methodology included the following steps: 1) field survey with a fixed-wing UAV to capture high-resolution aerial photographs and a GNSS to provide Ground Control Points (GCPs), 2) Structure-from-Motion photogrammetry to produce multi-temporal point clouds, DEMs and orthophotographs, 3) estimating topographic changes and 4) analyzing the relationship between rainfall and discharge events, sediment load and topographic changes. A spatially variable threshold was produced using a Fuzzy Inference System and considering different sources of errors. For the period 2017-2019 (i.e. after restoration activities), the gully showed a positive balance indicating accumulation of sediments (40.2 m^3) and hence a good performance of the restoration measures. The sediment load was reduced after dams installation, while runoff was not modified.**

I. INTRODUCTION

Gully erosion is one of the erosive processes that mostly contributes to shape the Earth surface. In fact, gully erosion represents one of the most significant types of soil degradation in the dehesa landscape, an agrosilvpoastoral land use system widespread in the SW Iberian Peninsula. Gullies are located in valley bottoms and studies have quantified the magnitude of these processes in a dehesa environment, determining for the period 2001-2007 an average gully erosion rate of 4.17 $m^3 y^{-1}$ [1]. Among the different restoration strategies, check dams are often used in Mediterranean areas [2-5]. Nevertheless, there are still few studies monitoring the effects of check dams on sediment dynamics [4].

In the last decade, recent advances in airborne-based surveying technologies, transformed the topographic data acquisition, replacing the method based on interpolating cross sections to estimate the volumetric change in channels [1, 6, 7]. The recent development of UAV platforms facilitates the acquisition of high resolution aerial photos from which Structure-from-Motion [8] photogrammetry can be applied to obtain point clouds, DEMs and orthophotos, being very useful to analyze geomorphic changes in gullies [9-10]. Geomorphic changes can be monitored through repeated and low-cost topographic surveys [11-12]. A DEM of differences (DoD) [13] is relevant to geomorphic studies because it provides a spatially distributed model of topographic change through time [14-15]. Uncertainties in topographic representation of a surface in a DEM have implications for DEM applications, these uncertainties or error can be considered as a spatially variable threshold. Several studies characterized error as being uniform across the entire DEM surface [14, 16]. Fuzzy inference systems (FIS) [17] allow estimating topographic changes from multiple factors that contribute to DEM uncertainty [13, 18]. The present work aims to analyze the effectiveness of operations carried out in the channel and to clarify the role of the former measures in the hydrological and sedimentological spatial and temporal dynamic of the gullied channel. Five high-resolution DEMs and orthophotographs were obtained from 2016 to 2019. In February 2017 (i.e. after the first survey) the gully was restored with check dams. Additionally, rainfall, discharge and suspended sediment were continuously monitored at the outlet of the catchment.

II. STUDY AREA

The study was conducted in the Parapuños experimental catchment (99.5 ha) in the SW of the Iberian Peninsula (Fig. 1). The area is representative of the dehesa land use system. The

Alberto Alfonso-Torreno, Alvaro Gomez-Gutierrez and Susanne Schnabel (2020)

Quantifying geomorphic change in a partially restored gully using multitemporal UAV surveys and monitoring discharge and sediment production:

in Massimiliano Alvioli, Ivan Marchesini, Laura Melelli & Peter Guth, eds., Proceedings of the Geomorphometry 2020 Conference, doi:10.30437/GEOMORPHOMETRY2020_54.

channel is a second order stream, which in the lower part of the catchment is incised into alluvial sediments. The main gully has a length about 850 m. Climate is Mediterranean with an average annual temperature of 16ºC and an average annual rainfall of 600 mm with high seasonality. The average altitude of the catchment is 396 m a.s.l. and the mean slope is 8%. The vegetation cover is composed of a disperse layer of Holm oak (*Quercus ilex va. rotundifolia*) and herbaceous plants in the understory. Livestock rearing is the main land use in the study area, with sheep and cows. Three different subsections were considered in the channel: (1) upper reach with restoration measures built in February 2017; (2) lower reach and (3) tributary reach.

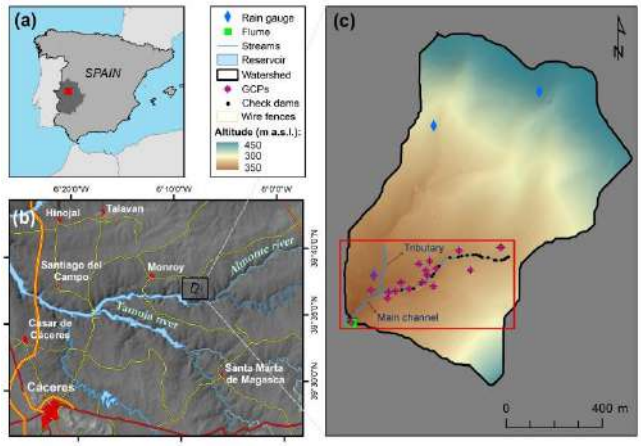

Figure 1. (a) Location of the study area in the Iberian Peninsula, (b) regional setting of the study area and (c) the gullied channel area represented by a red rectangle, including check dams and the GCPs represented by pink points.

III. MATERIAL AND METHODS

A. Monitoring rainfall, discharge and suspended sediment

The location of the measurement tools in the study area is presented in Figure 1c. The catchment is equipped with three tipping bucket rain gauges that recorded with a resolution of 0.2 mm at 5 minute intervals. Discharge was determined using a water depth probe installed in a weir at the outlet of the watershed, allowing measurement of a wide range of discharges (1-4000 l s^{-1}). Data analysis was conducted at different temporal scales: rainfall event, month and year. An event database was elaborated including rainfall events that generated runoff between September 2013 and August 2019. For event separation, a minimum period between two events of 1 hour without precipitation was used. The separation of base flow from direct runoff was through the technique of the normal depletion curve [19]. Flood discharges were identified as a flow increase of at least 1.5 times base flow prior to the rainfall event. At the event scale the following variables were used: antecedent rainfall, rainfall intensity, discharge (flood and base flow) and runoff coefficient (RC).

B. Field surveys and SfM workflow

The SfM-MVS workflow was fed with aerial photographs acquired by a fixed-wing UAV (Ebee by Sensefly) carrying on board a Sony WX220 sensor (18 Mpx). A total of 5 flights were conducted (24/03/2016, 16/02/2017, 25/10/2017, 03/05/2018 and 25/01/2019). Twenty GCPs were registered with a GNSS and used to scale and georeference the models (Fig. 1c). Pix4D software was used to process the UAV-derived photographs to produce point clouds, high-resolution DEMs and orthophotos.

C. DEMs of Difference and error analysis

Geomorphic change analysis was conducted through the DEM of difference approach [13], using the Geomorphic Change Detection (GCD) v7.1 add-in within ArcGIS Desktop v10.6. The DoD approach is based on the georeferencing error and the spatially variable error. The fuzzy inference system (FIS) method [13] was used to evaluate spatially variable errors. A two-input rule FIS system based on DEM slope and canopy height model (CHM) are used as indicators of vertical uncertainty. A third variable related to grassland was included applying a minimum level of detection (minLoD) based on the height of the grass in the different periods analyzed. The behavior of each variable on the final spatially variable error surface depends on the pre-designed membership functions. The process of defining membership functions for a variable can be thought of in two parts. First, the number of classes was identified (low, medium and high) to characterize the variable being described. Finally define the membership function that will describe the range of values covered by each class for the input or output. The total consequence membership function resulted in a raster output with values about elevation uncertainties. The FIS output used default MFs for the uncertainty (δz) and output was categorized into four classes (Low, Average, High, Extreme). Finally, a map of spatially vertical uncertainty (δz) of each DEM was obtained. Then, the elevation errors of each DEM were quantified in the DoD as described by [16, 20], with the following equation:

$$minLoD = t\ (\delta z_{DEMnew}{}^2 + \delta z_{DEMold}{}^2)^{0.5} \qquad (1)$$

where the minLoD is the critical threshold in the DoDs of significant topographic change for a 95% confidence interval, and σZ_{DEMnew} and σZ_{DEMold} are estimated uncertainties of the two compared DEMs. Topographic change was only considered in values greater than values of the error surface. Significant topographic changes were detected spatially and erosion and deposition volumes were calculated by multiplying the value by the pixel size of the resulting raster.

IV. RESULTS

A. *Photogrammetric results*

A total of 5 point clouds with a volumetric point density of 1504 pts m^3 on average were obtained and DEMs and orthophotographs with a GSD of 0.02 m resulted from the SfM processing. The total processing time (of the five models) for point clouds, Digital Terrain Model (DTM) and orthopotograph generations was almost 20 hours.

B. *Geomorphic change in the gully*

A total accumulation of 98.3 m^3 in the channel was estimated for the period 2016-2019, representing an annual deposition rate of 34.6 m^3 y^{-1}. Geomorphic change showed a high temporal variability, from -40.4 m^3 of net erosion experienced in P2 to 88.8 m^3 of net deposition during P3 (Table 1). All recorded-monitored variables experienced high temporal variability. The rainfall ranged from 476 mm (P3) to 182 mm (P2). The flood discharge ranged from 37277 m^3 in P3 (6 events with a Q > 100 l s^{-1}) to 3622 m^3 in P4 (1 event with a Q > 100 l s^{-1}). The largest amount of sediments was registered in P2 with 99.2 tons. The statistical analysis showed significant relationships between several variables (Table 2). Erosion-deposition values were highly correlated with rainfall, flood discharge, number of times Q > 100 l s^{-1} and maximum rainfall intensity in 60 minutes.

Table 1. Summary of the data registered during the study period: erosion or deposition, net volume difference (NVD), rainfall (P), flood discharge (Q), maximum peak discharge, the number of times discharge exceeding 100 l s^{-1}.

Period	**P1**	**P2**	**P3**	**P4**
Duration	24/03/2016 - 16/02/2017	16/02/2017 - 25/10/2017	25/10/2017 - 03/05/2018	03/05/2018 - 25/01/2019
Erosion (m^3)	-10.0	-46.7	-1.3	-14.9
Deposition (m^3)	65.7	6.3	90.2	6.6
NVD (m^3)	55.7	-40.4	88.8	-8.3
Rainfall (mm)	446.6	181.7	476.2	328.1
Events (N)	28	3	25	19
P mean (mm)*	11.0	26.1	11.5	10.1
Q (m^3)*	20165.1	18218.1	37277.4	3622.3
Q-max (l s^{-1})*	541.6	1237.2	1052.3	336.7
Q > 100 l s^{-1} (N)*	2	1	6	1
I60 (mm)*	4.7	8.8	4.1	6.4
RC (%)*	3.8	12.5	6.0	2.1
Sed. load (t)*	37.8	99.2	20.6	1.9

(*) Event scale

Table 2. Correlation matrix for NVD, rainfall, flood discharge (Q), maximum peak flood (Q-max), RC, sediment load and maximum 60-minutew rainfall (I60). Statistically significant values (p < 0.05) are highlighted

	NVD (m^3)	Rain *(mm)*	Q (m^3)	Q-max *l s^{-1}*	Q > 100 *(N)*	I-60 *(mm)*	RC *(%)*
Rainfall	**0.87**						
Flood discharge (m^3)	**0.88**	**0.59**					
Q-max (l s^{-1})	0.31	**0.55**	**0.90**				
Q > 100 l s^{-1} (N)	**0.92**	0.34	0.52	**0.68**			
I-60 (mm)	-0.11	**0.57**	0.22	0.37	0.35		
RC (%)	-0.16	0.38	**0.85**	**0.87**	**0.57**	0.14	
Sed load (kg)	-0.51	0.48	**0.84**	0.66	0.39	0.11	**0.55**

Different processes were observed in the gully, dominating the aggradation processes as determined by the topographic change analysis. Channel aggradation processes were observed, filling the channel bed and forming sediment bars at different locations along the gully, but also in the installed check dams. The source areas of these sediments are the hillslopes where sheet erosion takes place. Several erosion processes were also observed: a) channel bed erosion, due to the direct action of water flow and transported materials, b) lateral bank erosion and bank collapse produced by lateral incision followed by the collapse of the upper part of the banks, c) deepening and widening in a few headcuts where the tributary and the lower reach join and d) erosion downstream of the check dams. Only two lateral headcuts were advancing during P4.

C. *Effectiveness of restoration measures*

The total volume of sediments retained in the check dams are 11.7 m^3 from which 85% are accumulated in permanent check dams. The total volume of sediments accumulated in the check dams represents 12.4% of the upper reach deposition. Of the three periods analyzed with the restoration measures, the check dams in P4 did not retain sediments, it is a period characterized by net erosion. Nearly half of the total sediment volume (49%) retained in the check dams occurred in P2. During this period an event with 49.3 mm and a maximum flow of 1237.2 l s^{-1} occurred, producing a flood discharge of 18,136.7 m^3 which was the highest maximum flood registered since 2009-10.

Regarding sediment load at the outlet of the catchment, sediments transported in the channel came from two sources, the hillslopes (due to sheet erosion) and the valley bottoms (due to gully erosion). The average annual sediment load was 73.8 tons, equivalent to 0.72 t ha^{-1} y^{-1}. The interannual variation is very high, ranging from 0.07 to 1.86 t ha^{-1} y^{-1}. The first year after check dam's construction 561 mm of rainfall was recorded, generating 56,743 m^3 of discharge with a RC of 10.3%. This was the year with the third highest value of the RC, being the seventh highest in sediment production. Figure 2 presents the relationship between suspended sediment load and flood discharge which are significantly correlated. This analysis shows how sediment production was clearly reduced by the presence of check dams

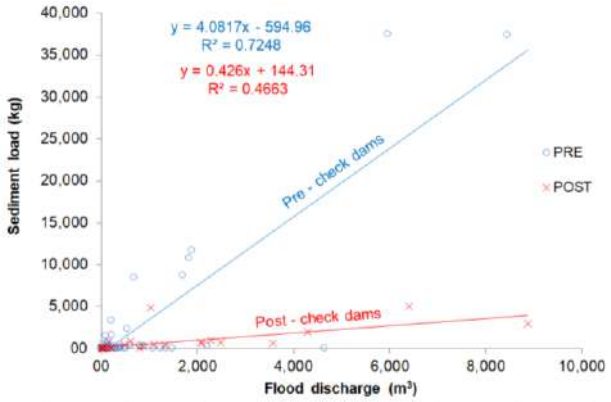

Figure 2. Relationship between flood discharge and sediment load depending on events pre or post check-dams.

V. CONCLUSIONS

Multi-temporal topographic (UAV+SfM photogrammetry) surveys have allowed us to analyze the effectiveness of restoration measures conducted in the channel and to study the hydrological and sedimentological dynamic after check dams' construction. Topographic changes were determined through the DEM of difference approach. The fuzzy inference system method was used to evaluate spatially variable errors. A total accumulation of 98.3 m^3 in the channel was estimated for the period 2016-2019. For the period after check dams construction, the gully showed a positive balance of 40.2 m^3 demonstrating the effectiveness of the restoration measures. Sediment load was reduced after check dam installation, though not affecting runoff generation. These results are valuable to quantify the magnitude of the erosive processes in dehesa landscapes and to understand the role of restoration measures in gullies.

ACKNOWLEDGMENTS

Alfonso-Torreño is a beneficiary of a PhD scholarship (PD16004) of the Regional Government of Extremadura and research was financed by the Spanish Ministry of Economy and Competitiveness (CGL2014-54822-R).

REFERENCES

[1] Gómez-Gutiérrez, Á., Schnabel, S., De Sanjosé, J.J., Lavado Contador, J.F., 2012. "Exploring the relationships between gully erosion and hydrology in rangelands of SW Spain". Zeitschrift für Geomorphologie, Supplementary Issues 56, 27–44.

[2] Castillo, V.M., Mosch, W.M., Conesa García, C., Barberá, G.G., Navarro Cano, J.A., López-Bermúdez, F., 2007. "Effectiveness and geomorphological impacts of check dams for soil erosion control in a semiarid Mediterranean catchment: El Cárcavo (Murcia, Spain)". Catena 70 (3), 416-427.

[3] Bombino, G., Gurnell, A.M., Tamburino, V., Zema, D.A., Zimbone, S.M., 2009. "Adjustements in cannel form, sediment calibre and vegetation around check-dams in the headwater reaches of mountain torrents, Calabria, Italy". Earth Surface Processes Landforms 34 (7), 1011-1021.

[4] Cucchiaro, S., Cavalli, M., Vericat, D., Crema, S., Llena, M., Beinat, A., Marchi, L., Cazorzi, F., 2019. "Geomorphic effectiveness of check dams in a debris-flow catchment using multi-temporal topographic surveys". Catena 174, 78-83.

[5] Alfonso-Torreño, A., Gómez-Gutiérrez, Á., Schnabel, S., Lavado Contador, J.F., Sanjosé Blasco, J.J., Sánchez Fernández, M., 2019. "sUAS, SfM-MVS photogrammetry and a topographic algorithm method to quantify volume of sediments retained in check-dams". Science of the Total Environment 678, 369-382.

[6] Griffiths, G.A., 1979. "Recent sedimentation history of the Waimakariri River, New Zealand". Journal of Hydrology (New Zealand), 18: 6-28.

[7] Ferguson, R., Ashworth P.J., 1992. "Spatial patterns of bedload transport and channel change in braided and near-braided rivers". In: Dynamics of Gravel-bed Rivers, Billi P, Hey RD, Thorne CR, Tacconi P (Eds). John Wiley & Sons Ltd; 477-492.

[8] Ullman, S., 1979. "The interpretation of structure from motion". Proceedings of the Royal Society B, 203, 405-426.

[9] Castillo, C., Pérez, R., James, M.R., Quinton, J.N., Taguas, E.V., Gómez, J.A., 2012. "Comparing the accuracy of several field methods for measuring gully erosion". Soil Science Society of America Journal 76, 1319.

[10] Gómez-Gutiérrez, Á., Schnabel, S., Berenguer-Sempere, F., Lavado-Contador, F., Rubio-Delgado, J., 2014. "Using 3D photo-reconstruction methods to estimate gully headcut erosion". Catena 120, 91–101.

[11] Xiang, J., Chen, J., Sofía, G., Tian, Y., Tarolli, P., 2018. "Open-pit mine geomorphic changes analysis using multi-temporal UAV survey". Environmental Earth Sciences 77, 220.

[12] Kaiser, A., Erhardt, A., Eltner, A., 2018. "Addressing uncertainties in interpreting soil surface changes by multitemporal high-resolution topography data across scales". Land Degradation & Development 29 (8), 2264-2277.

[13] Wheaton, J.M., Brasington, J., Darby, S.E., Sear D.A., 2010. "Accounting for uncertainty in DEMs from repeat topographic surveys: improved sediment budgets". Earth Surface Processes and Landforms 35, 136-156.

[14] Brasington, J., Langham, J., Rumsby, B., 2003. "Methodological sensitivity of morphometric estimates of coarse fluvial sediment transport". Geomorphology 53 (3–4), 299–316.

[15] Rumsby, B.T., Brasington, J., Langham, J.A., McLelland, S.J., Middeton, R., Rollinson, G., 2008. "Monitoring and modelling particle and reach-scale morphological change ingravel-bed rivers: applications and challenges". Geomorphology 93, 40–54.

[16] Brasington, J., Rumsby, B., McVey, R., 2000. "Monitoring and modelling morphological change in a braided gravel-bed river using high resolution GPS-based survey". Earth Surf. Processes Landforms 25 (9), 973–990.

[17] Milan, D.J., Heritage, G.L., Large, A.R.G, Fuller, I.C., 2011. "Filtering spatial error from DEMs: Implications for morphological change estimation". Geomorphology 125, 160-171.

[18] Prosdocimi, M., Calligaro, S., Sofia, G., Dalla Fontana, G., Tarolli, P., 2015. "Bank erosion in agricultural drainage networks: New challenges from structure-from-motion photogrammetry for post-event analysis". Earth Surface Processes Landforms 40 (14), 1891–1906.

[19] Horton, R.E., 1933. "The role of infiltration in the hydrologic cycle". Transactions, American Geophysical Union 14, 446–460.

[20] Lane, S. N., Westaway, R. M., & Murray Hicks, D., 2003. "Estimation of erosion and deposition volumes in a large, gravel-bed, braided river using synoptic remote sensing". Earth Surface Processes and Landforms 28, 249–271.

GEOMORPHOMETRY 2020 PERUGIA, ITALY JUNE 22 - 26 2020

A new and extendable global watershed and stream network delineation using GRASS-GIS

Giuseppe Amatulli[§]
School of Forestry and Environmental Studies - Center for Research Computing, Yale University, New Haven, CT-USA
Tushar Sethi, Longzhu Shen
Spatial Ecology, 35A, Hazlemere Road, Penn, Bucks HP10 8AD, U.K
Jaime Ricardo García-Márquez, Jens Kiesel, Sami Domisch
Leibniz-Institute of Freshwater Ecology and Inland Fisheries, Müggelseedamm 310, 12587 Berlin, Germany
[§] giuseppe.amatulli@gmail.com

***Abstract*—We used the hydrologically corrected digital elevation model (DEM) "MERIT Hydro" at a 3 arc-seconds (90 m) spatial resolution to derive a globally seamless, standardised stream network employing GRASS-GIS hydrological modules. Our main aim is to delineate a global stream network that extracts, in particular, small headwaters in greater spatial detail. We hence implement a low upstream area threshold (0.05 km^2) to initiate headwater streams, while using water bodies in the NHDPlusV2 dataset for calibration. The obtained hydrography layers (flow accumulation, flow direction, basins and stream network) are compatible with other r.stream.* modules within GRASS-GIS and hence the dataset can easily be customised and expanded by computing other hydrographical features.**

I. Introduction

The location and structure of streams and rivers underpin a myriad of patterns and processes in hydrology, geomorphology, geography and ecology. The wide availability of Digital Elevation Models (DEMs) and improvement in computational power have led to recent advances in terrain and hydrological analyses on the local and global scales. Extracting a stream network from DEMs is based on the computation of the upstream flow accumulation. It yields a potential analysis of geophysical features, but does not account for stream hydraulics or water availability. For the delineation of watershed and drainage networks, a large number of techniques and algorithms have been implemented [1-2-3-4]. Current algorithms are based on the natural phenomena that water follows the steepest and shortest direction along a relief, and accumulates along valleys, lowlands, flat areas and depressions.

In this study, we used the MERIT Hydro at 3 arc-seconds (90 m) spatial resolution and the NHDPlusV2 water bodies, which we processed using the hydrological modules within the Geographic Resources Analysis Support System (GRASS) open source GIS software [5] to derive a globally seamless and standardised hydrography. Unlike that of existing datasets, our aim is to represent headwaters at greater spatial detail, and create a product that can be re-ingested in GRASS-GIS to produce ancillary hydrographical features.

I. Data and method

A. Source layers

The MERIT Hydro dataset [6] was released in 2019 at a spatial grain of 90 m (3 arc-seconds) with the exception of Antarctica. It includes depression areas and hydrologically-adjusted elevation that incorporates, as an elevation correction factor, water occurrence datasets (G1WBM [7], GSWO [8], and OpenStreetMap [9]). The water occurrence datasets are used to modify the elevation satisfying the condition that "downstream is not higher than upstream". Here, it is important to consider that the G1WBM and GSWO are Landsat-derived, and therefore not useful for capturing small tributaries (smaller than 20-30m river width) or even large rivers under canopy cover. In contrast, OpenStreetMap is based on a direct survey of observed water bodies, therefore small tributaries are, depending on the region, depicted as a function of the survey effort. Currently, only a few countries represented in OpenStreetMap provide a high level of spatial accuracy for headwater streams. Therefore, our stream extraction algorithm has to be calibrated such that headwater streams can be delineated at maximum spatial accuracy.

In addition to MERIT Hydro, the NHDPlusV2 is a geo-spatial database of surface water features, developed by the US EPA Office of Water and by the US Geological Survey [10]. This dataset was derived from the US National Elevation Dataset (NED) in a 1 arc-second (~30 m) spatial resolution, and has about 3 million rivers at a 1:100,000-scale or higher [10] which has made it suitable to spatially validate the location of streams

Giuseppe Amatulli, Tushar Sethi, Longzhu Shen, Jaime Ricardo Garcia-Mírquez ,Jens Kiesel, and Sami Domisch (2020)

A new and extendable global watershed and stream network delineation using GRASS-GIS:

in Massimiliano Alvioli, Ivan Marchesini, Laura Melelli & Peter Guth, eds., Proceedings of the Geomorphometry 2020 Conference, doi:10.30437/GEOMORPHOMETRY2020_55.

that are derived from lower-resolution DEMs. The NHDPlusV2 is a reliable data source for locating water bodies, and can be therefore be used to calibrate the stream network delineation algorithm. For the calibration, we selected an area of 20 x 15 degrees in the Mississippi basin.

B. Basin delineation and stream network extraction methodology

In order to address the large demand on computer memory posed by the calculation of the flow accumulation, we used the Level-2 basin polygons from HydroBASINS [11-12] to divide the MERIT Hydro DEM into computational tiles (see Figure 1). We manually re-located and enlarged the tiles across the maximum number of cells possible (2^{31} −1, equivalent to ~2 bilion). This is the maximum number of cells that *r.watershed* can be processed by the RAM. We located the tiles in such a way that larger basins and 2.5 degrees of surrounding area were completely within the tiles. This allows maximum precision in basin delineation and stream network extraction. Using GRASS-GIS, we ran the following modules for each tile: *r.watershed, r.stream.extract, r.stream.basins*.

The command *r.watershed* requires a hydrologically-adjusted elevation as an input, which together with a depression raster map is able to compute flow accumulation and flow direction, using a multiple down-stream cells algorithm (-MFD flag) [13]. The *r.watershed* function also accepts the flow parameter that incorporates a raster map representing the amount of upstream area per cell. Therefore, we first calculated the surface-area of each cell using *r.cell.area* to compute the flow accumulation. Another parameter that influences the flow accumulation and ultimately the stream network location and length is convergence, which ranges from 1 to 10. Lower values result in higher divergence of flow direction, as opposed to higher values that indicate higher convergence.

After *r.watershed*, we ran *r.stream.extract* using flow accumulation and depression. In order to extract the stream we set the minimum upstream flow accumulation area (threshold) to 0.05 km^2 (~6 cells at the equator). This threshold is the minimum area necessary to initiate the channel head and hence results in higher stream density. The threshold typically differs by region [14], in according to climatic and geomorphological features. We note that this stream network delineation is part of a larger project aiming to calculate discharge at a monthly level. Hence, at a later stage we will shorten (prune) river sections and account for possible flow intermittency (flow > 0 m^3/sec) indicates stream presence and produces a dynamic representation that changes the stream dimension as a function of the monthly flow. The final output will be 12 monthly stream networks that differ in length and intermittencies.

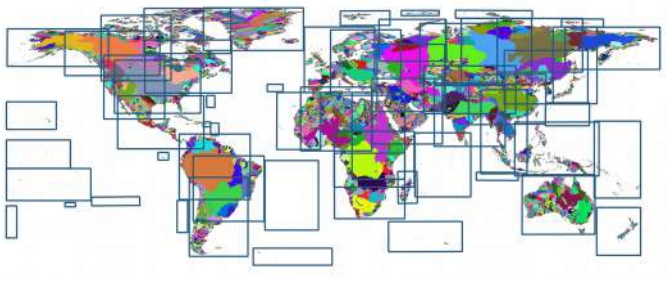

Figure 1: Global 1,608,114 drainage basins (random colours for illustrative purposes only) and computational tiles.

Transforming conventional static stream networks into a monthly dynamic representation overcomes the limitations of fixing *a priori* convergence parameters and the minimum upstream flow accumulation areas. The new computation will produce a stream network that is determined by the environmental characteristics found across each catchment. Stream discharge at a monthly level will be computed using a machine learning approach, which integrates meteorological factors, as well as geomorphometric features, soil types, land cover/use, among others. Hence, the stream length (stream presence if flow > 0 m^3/sec), will be modelled based on the interaction of these factors.

Subsequent to *r.stream.extract* we ran *r.stream.basins* to delineate basins using the flow direction and the previously calculated streams. For each tile, we retained only the complete basins and removed the ones adjacent to tile borders that were possibly truncated. We also used the same procedure (retain and remove) for the other hydrography layers, keeping the ones that belonged only to entire computed basins. Finally, we re-aggregated all of the hydrography layers to yield a complete global basin delineation.

In order to calibrate the best convergence value, we repeated the full processing chain for each of the 10 convergence factors available in GRASS-GIS, and spatially overlaid the newly-developed stream network on top of the one from NHDPlusV2. The convergence value that produced the maximum overlap between our computed stream network and the NHDPlusV2 network was considered the most appropriate value, and was used for the remainder of the global-scale implementation.

II. RESULTS

With the described procedure we were able to complete global layers for flow accumulation, flow direction, basins and stream networks. In total, we delineated 1,608,114 basins (see Figure 1), and for each we extracted constituent stream networks. These stream networks overlapped cleanly against the

NHDPlusV2, although some spatial overestimation in MERIT-DEM-derived streams is known. A final validation procedure will be conducted at the end of the project for accurate discharge computation. The final optimal convergence parameter equals 10 (see Figure 2). Once delineated, each basin can be used as a computational unit to calculate other hydro-geomorphological features, such as stream length, stream order or residence time. For context, flow accumulation can reach a maximum value of 5,509,644 km^2 (Amazon River), followed by 3,671,834 km^2 (Nile River) and 3,197,652 km 2 (Mississippi-Missouri River).

III. Conclusion

We demonstrated the processing of MERIT Hydro by means of r.watershed and *r.stream.** modules in GRASS-GIS to derive a stream network that more closely matches the observed spatial representation of streams and rivers. As demonstrated, the NHDPlusV2 can be used effectively to calibrate the convergence parameters.

Other regional and national stream networks can also be used to validate the final product. From a 5computational perspective, GRASS-GIS provides fast and flexible functions for hydrological modelling with automated scripting workflows, and allows the processing of very large datasets using efficient algorithms and memory management. We are in the process of accurately calibrating and validating stream network extraction and basin delineation worldwide. For the calibration and validation procedures, we will use detailed stream networks that are freely available from governmental institutions. The final products will be stored as hydrography layers that can be re-ingested into GRASS-GIS to produce ancillary hydrographical features.

IV. Acknowledgements

This study was supported in part by the facilities and staff at the Yale Center for Research Computing (YCRC) and by the Leibniz Competition (J45/2018).

References

[1] D. G. Tarboton, R. L. Bras, and I. Rodriguez-Iturbe, 1992. "A physical basis for drainage density," Geomorphology, vol. 5, no. 1, pp. 59–76.

[2] D. R. Montgomery and E. Foufoula-Georgiou, 1993. "Channel network source representation using digital elevation models," Water Resources Research, vol. 29, no. 12, pp. 3925–3934.

[3] R. A. Heine, C. L. Lant, and R. R. Sengupta, 2004. "Development and comparison of approaches for automated mapping of stream channel networks," Annals of the Association of American Geographers, vol. 94, no. 3, pp. 477–490.

[4] J. D. Pelletier, 2013. "A robust, two-parameter method for the extraction of drainage networks from high-resolution digital elevation models (dems): Evaluation using synthetic and real-world dems," Water Resources Research, vol. 49, no. 1, pp. 75–89.

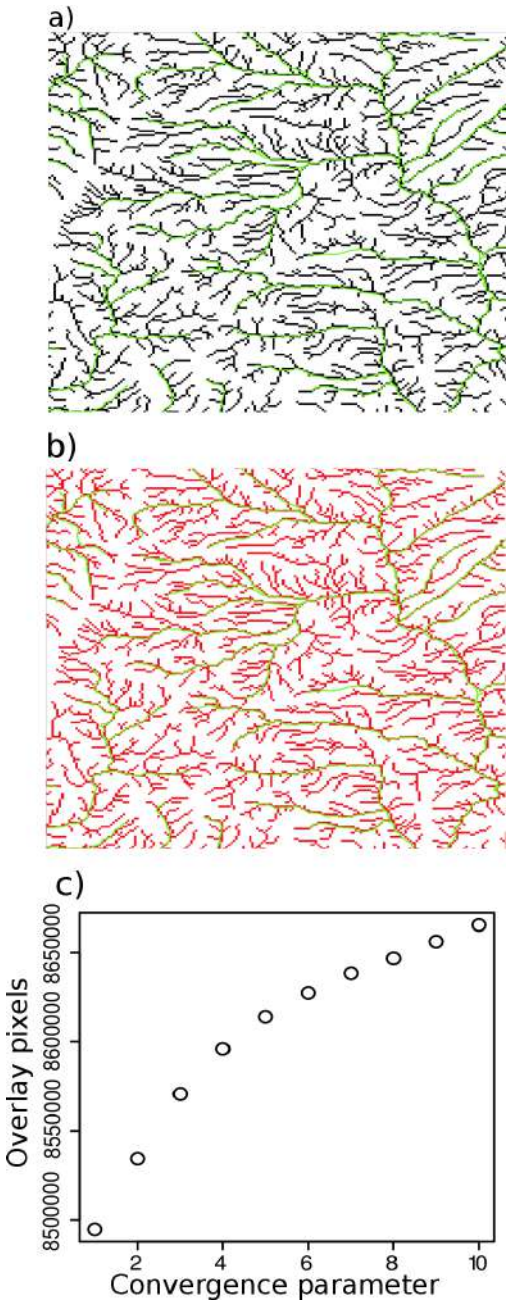

Figure 2. Convergence calibration. (A) The green lines represent the NHDPlusV2 stream network; the black lines show the newly-developed stream network generated using a convergence value of 1, while (B) the red lines represent the newly-developed stream network with a convergence value of 10. (C) The NHDPlusV2 and the newly-developed stream network pixels overlap as a function of the convergence.

[5] GRASS Development Team, Geographic Resources Analysis Support System (GRASS GIS) Software, Version 7.2, 2017. Open Source Geospatial Foundation.

[6] D. Yamazaki, D. Ikeshima, J. Sosa, P. D. Bates, G. H. Allen, and T. M. Pavelsky, 2019. “Merit hydro: a high-resolution global hydrography map based on latest topography dataset,” Water Resources Research, vol. 55, no. 6, pp. 5053–5073,.

[7] D. Yamazaki, M. A. Trigg, and D. Ikeshima, “Development of a global˜ 90 m water body map using multi-temporal landsat images,” Remote Sensing of Environment, vol. 171, pp. 337–351, 2015.

[8] [8] J.-F. Pekel, A. Cottam, N. Gorelick, and A. S. Belward, 2016. “High-resolution mapping of global surface water and its long-term changes,” Nature, vol. 540, no. 7633, pp. 418–422.

[9] OpenStreetMap contributors, 2017. “Planet dump retrieved from https://planet.osm.org .” https://www.openstreetmap.org.

[10] C. H. David, D. R. Maidment, G.-Y. Niu, Z.-L. Yang, F. Habets, and V. Eijkhout, , 2011. “River network routing on the nhdplus dataset,” Journal of Hydrometeorology, vol. 12, no. 5, pp. 913–934.

[11] B. Lehner, K. Verdin, and A. Jarvis, “New global hydrography derived from spaceborne el-evation data, 2008. “Eos, Transactions American Geophysical Union, vol. 89, no. 10, pp. 93–94.

[12] B. Lehner 2014, “Hydrobasins technical documentation, version 1. c,” HydroSHEDS.

[13] P. Quinn, K. Beven, P. Chevallier, and O. Planchon, 1991. “The prediction of hillslope flow paths for distributed hydrological modelling using digital terrain models,” Hydrological processes, vol. 5, no. 1, pp. 59–79.

[14] J. V. Vogt, R. Colombo, and F. Bertolo, 2003. “Deriving drainage networks and catchment bound-aries: a new methodology combining digital elevation data and environmental characteristics,” Geomorphology, vol. 53, no. 3-4, pp. 281–298.

GEOMORPHOMETRY 2020 PERUGIA, ITALY JUNE 22 - 26 2020

Drainage reversal revealed by geomorphometric analysis of fluvial terraces

Francesco Bucci[1§], Michele Santangelo[1], Francesco Mirabella[2], Andrea Mazzoni[2], Mauro Cardinali[1]

[1]Istituto di Ricerca per la Protezione Idrogeologica
Consiglio Nazionale delle Ricerche
via Madonna Alta 126, I-06128 Perugia, Italy
[2]Dipartimento di Fisica e Geologia
Università di Perugia
Piazza Università 1, I-06123 Perugia, Italy
§ francesco.bucci@irpi.cnr.it

Abstract— **Fluvial terraces preserve the paleo-profiles of rivers, recording the spatial and temporal changes of the landscape, and are key landforms in the study of river processes, active tectonics and paleoclimatology. In this paper we use an original mapping of different re-incised fluvial terraces, focusing on their attitude, to investigate the modification of flow direction of the Puglia River, a tributary of the Tiber River, in central Umbria, Italy. To obtain the attitude of the fluvial terraces, we start from the linear signatures of terrace edges mapped on aerial photographs and transferred into a GIS after raster tracing of the orthorectified image. Then, we build on a previous work aimed at obtaining bedding attitude information from bedding traces on the topographic surface, testing the capability of the method to provide information on the attitude of fluvial terraces. Results indicate the systematic dip toward SE of the highest terraces, while the lowest terraces dip to the W, in the same flow direction of the present-day Puglia River course. We interpret the results as the evidence of the southeastward flow of the ancient Puglia River, before bedrock incision, drainage inversion and deposition of the lowest terraces. We suggest a tectonic control as the main factor driving incision and river inversion in the landscape evolution of the area. We conclude encouraging the use of the same work flow to investigate fluvial related landforms elsewhere, in order to identify space/time changing of fluvial processes in diverse geologic, tectonic, and climatic setting.**

I. INTRODUCTION

Modification of rivers and their drainage basins is a poorly understood process associated with tectonically and/or climatically induced erosion, that strongly influence paleogeography, sediment budgets, and provenance. Such events may represent the geomorphological response to variation in rate, style, and locus of tectonic deformation, hence their identification and investigation is a key issue in active tectonic studies.

However, the reconstruction of ancient river systems is often hampered by the scattered distribution of rare and poorly preserved outcrops of fluvial sediments, a condition that undermines adequate stratigraphic and sedimentological studies, and requires the integration of geomorphological and morphometric investigations. In this contribution, we present a geomorphological e morphometric workflow aimed at identifying and measuring Earth surface changes related to the modification of rivers path and flow direction in an active extensional tectonic setting.

II. METHODS

Based on multi-scale interpretation of stereoscopic aerial photographs, we identify and map a system of fluvial terraces associated with the evolution of the Puglia River, a tributary of the Tiber River, in central Umbria, Italy (Figure 1). This involved the interpretation of two sets of stereoscopic pairs of aerial photographs: panchromatic, taken in 1955 (1:33,000) and colors, taken in 1977 (1:13,000). Thematic information was drawn manually on transparent plastic sheets placed over the older photographs (Figure 2a). Then, the geomorphological information was transferred into a GIS using a semi-automatic procedure designed to reduce mapping errors (Santangelo et al., 2015). The procedure consists in the ortho-rectification of the aerial photographs and in the subsequent raster tracing of the geomorphological elements portrayed on the image (Figure 2b). The procedure exploits the GRASS GIS script i.ortho.photo, which requires a number of input data, such as the scanning of the aerial photograph and the superimposed undeformable plastic film, a DEM, an orthophoto map, and the camera parameters of the aerial photograph (Rocchini et al, 2010). The output vector features are stored in different thematic shapefiles.

Francesco Bucci, Michele Santangelo, Francesco Mirabella, Andrea Mazzoni, and Mauro Cardinali (2020) Drainage inversion revealed by geomorphometric analysis of fluvial terraces: in Massimiliano Alvioli, Ivan Marchesini, Laura Melelli & Peter Guth, eds., Proceedings of the Geomorphometry 2020 Conference, doi:10.30437/GEOMORPHOMETRY2020_56.

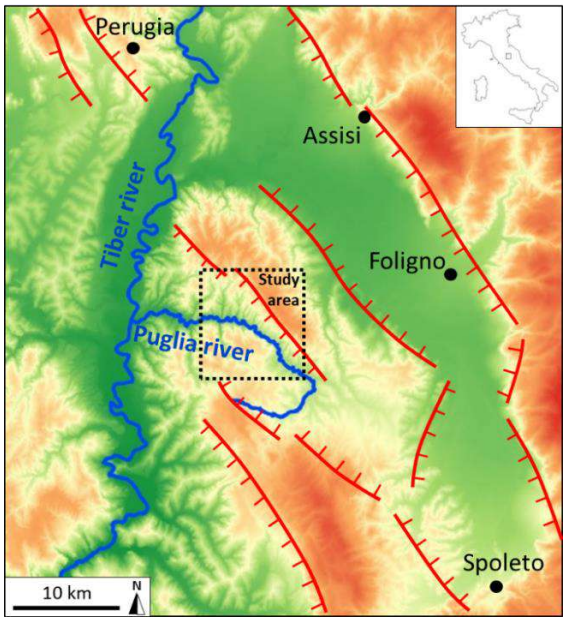

Figure 1. Location map of the study area in central Umbria, Italy. Main cities are indicated for easier geographical location. The area is crossed by the Puglia river, a tributary of the Tiber river. Map-scale main Quaternary normal faults with a clear morphological expression are also shown in red.

Among the others, we selected the fluvial terraces shapefile and we applied an open source processing chain that, starting from the aerial photo-interpreted boundary of fluvial terraces and the same DEM used for the orthorectification, produces a vector map of terraces attitudes. We define the terraces surface attitude as the combination of aspect and dip of the terraces surface. It has to be intended as the definition of bedding attitude. The procedure bases on a GIS tool, geobed.py (Marchesini et al., 2013), implemented using python in GRASS GIS environment and GNU-Linux OS. The geobed.py tool was developed in first place to reconstruct the attitude of bedding planes in layered terrains, and requires a bedding traces map and a DEM to be executed. In this contribution, we extend the application of the geobed.py tool to the reconstruction of the attitude of the fluvial terraces, hence a map of outer and inner edges of fluvial terraces were used in the place of the bedding trace map. The script iterates five steps for each terrace edge, and returns a point vector map containing information on dip angle, dip direction, and associated uncertainty. In the first step, the terrace edge is transformed into a 3D linear feature using the DEM. Secondly, the terrace edge is closed into a 3D polygon. Thirdly, a sequence of regularly spaced points is generated on the polygon boundary. A 3D Delaunay triangulation (Davis 1990) is then performed which outputs a nearly flat surface corresponding to the terrace surface. The slope and aspect raster maps of the terrace surfaces are then computed (step four).

Lastly, the mean values of slope (dip angle) and aspect (dip direction) of the terrace surface are estimated. The uncertainties of dip angle and dip direction are computed as (i) the standard deviation of the terrace slope map and (ii) as the circular variance (Davis 1990) and angular standard deviation (Butler 1992) of the terrace aspect map.

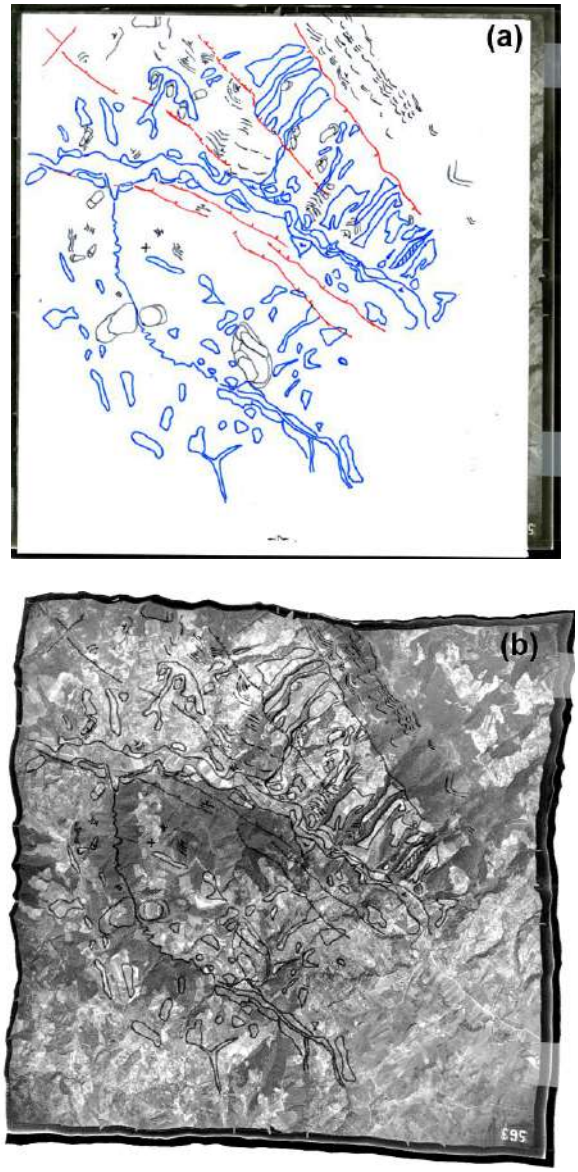

Figure 2. Thematic information drawn over the photograph. Different colors indicate different elements: red for faults, blue for terraces and alluvial deposits, black polygons for landslide, black lines for bedding traces (a). Orthorectification of the aerial photograph and the interpreted elements (b).

III. RESULTS AND CONCLUSIONS

Results indicate the general S-SE oriented dip direction of the highest terraces, while a roughly W-SW oriented dip direction, consistent with the present-day flow direction of the Puglia River and its right tributaries, results for the intermediate terraces. The lowest terraces generally converge toward the main river course as evidence of the contribution of the lateral streams to the terraces building (Figure 3).

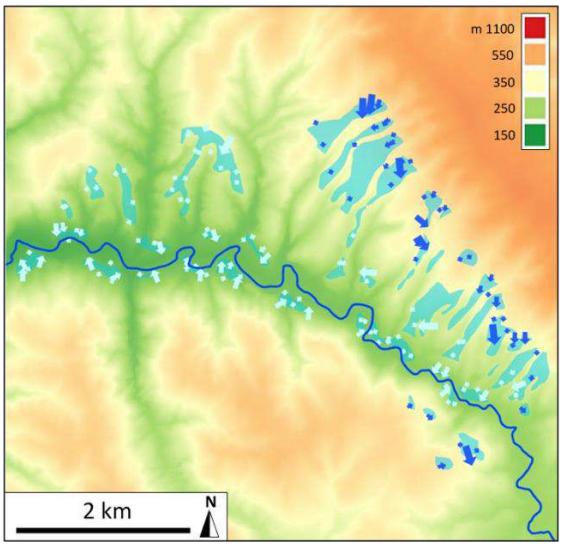

Figure 3. Main result of the analysis indicating different attitudes for terraced mapped at different elevations. Ciano polygons indicate the mapped terraces; blue arrows indicate the attitude of terraces located at highest elevation; light blue arrows indicate the attitude of terraces located at lower elevations and close to the present-day river course. Arrows size is inversely proportional to data uncertainty, measured as the angular standard deviation of the computed attitude values.

We interpret the results as the evidence of the southeastward flow of the ancient Puglia River, before reversal and deposition of the progressively lower terraces. Scattered sedimentological evidences, including pebble imbrication, composition, dimension and roundness, seems to confirm that the Puglia River reversed its course to westward flow in the recent geological past. Basing on an updated geological survey (Bucci et al., 2016) and original photo-geological information (Figure 2a), we document the structural control operated by normal faults on the geometry of the ancestral Puglia River Basin and propose that the drainage inversion was driven by progressive extension, consisting with an eastward migration of the normal fault activity. River reversal likely followed stream capture in response to enhanced fluvial erosion and uplift of the Puglia River basin, at the footwall of the NE dipping active normal fault bounding westward the Foligno Valley (Figure 1) (Mirabella et al., 2018). Future dating of the river terraces will allow determining the timing of the inversion of the Puglia River, and will help to constraint the space-time migration of fault activity. The findings are important in a more general perspective because open at the possibility to apply the same open source processing chain to detect, measure and model space/time changing of fluvial processes elsewhere, which in turn can be related to changing in rate, style, and locus of tectonic deformation, benefiting active tectonic studies.

REFERENCES

[1] Bucci, F., Mirabella, F., Santangelo, M., Cardinali, M. & Guzzetti, F. (2016). Photo-geology of the Montefalco Quaternary Basin, Umbria, Central Italy. Journal of Maps, https://doi.org/10.1080/17445647.2016.1210042

[2] Butler R.F. (1992). Paleomagnetism: Magnetic Domains to Geologic Terranes. Blackwell Scientific Publications – Boston. Oxford. http://www.geo.arizona.edu/Paleomag/book/.

[3] Davis J.C. (1990). Statistics and data analysis in geology, 2nd edn. John Wiley & Sons, Inc, New York

[4] Marchesini I., Santangelo M., Fiorucci F., Cardinali M., Rossi M., Guzzetti F. (2013). A GIS method for obtaining geologic bedding attitude. Margottini, C., Canuti, P., Sassa, K. (Eds.) Landslide Science and Practice, Volume 1: Landslide Inventory and Susceptibility and Hazard Zoning, ISBN 978-3-642-31324-0

[5] Mirabella, F., Bucci, F., Santangelo, M., Cardinali, M., Caielli, G., De Franco, R., Guzzetti, F. & Barchi, M.R. (2018). Alluvial fan shifts and stream captures driven by extensional tectonics in central Italy. Journal of the Geological Society. https://doi.org/10.1144/jgs2017-138

[6] Rocchini, D., Metz, M., Frigeri, A., Delucchi, L., Marcantonio, M., and Neteler, M. (2010). Robust rectification of aerial photographs in an open source environment, Computers Geosci., 39, 145–151, doi:10.1016/j.cageo.2011.06.002, 2011.

[7] Santangelo, M., Marchesini, I., Cardinali, M., Fiorucci, F., Rossi, M., Bucci, F., and Guzzetti, F. (2015). A method for the assessment of the influence of bedding on landslide abundance and types, Landslides, 12, 295–309, doi:10.1007/s10346-014-0485-x, 2015b

GEOMORPHOMETRY 2020 PERUGIA, ITALY JUNE 22 - 26 2020

Structural sediment connectivity assessment through a geomorphometric approach: review of recent applications

Marco Cavalli[§], Stefano Crema, Lorenzo Marchi
Research Institute for Geo-Hydrological Protection
National Research Council
Corso Stati Uniti 4, 35127 Padova, Italy
[§] marco.cavalli@irpi.cnr.it

Abstract— **Sediment connectivity, defined as the degree to which a system facilitates the transfer of water and sediment through itself by means of coupling relationships between its components, has become a key issue in sediment transfer processes analysis and one of the building blocks of modern geomorphology. The growing availability of high-resolution Digital Elevation Models (DEMs) offers new opportunities for the characterization of sediment connectivity spatial patterns. An index of sediment connectivity, based on DEM derivatives as drainage area, slope, flow length and surface roughness, has been recently developed along with related freeware software tool (SedInConnect). The index aims at depicting spatial connectivity patterns at the catchment scale to support the assessment of the contribution of a given part of the catchment as sediment source and define sediment transfer paths. The increasing interest in the quantitative characterization of the linkages between landscape units and the straightforward applicability of this index led to numerous applications in different contexts. Such works demonstrate that, when carefully applied considering the intrinsic limitations of the geomorphometric approach, the index can rapidly provide a spatial characterization of sediment dynamics, thus improving the understanding geomorphic system behavior and, consequently, hazard and risk assessment. This work presents and discusses the main applications of this sediment connectivity index.**

I. INTRODUCTION

In recent years, connectivity has emerged as a paramount property of geomorphic systems [1-3]. The growing interest of the earth sciences community on water and sediment connectivity led these concepts to become key issues in research on hydrological and sediment delivery processes and on the characterization of source to sinks pathways [e.g. 4-8].

The assessment of the degree of linkages exerted by coupling/decoupling relationship between different parts of a system is pivotal to comprehend the behavior of hydro-geomorphic systems and thus to predict their responses. Geomorphic coupling and connectivity play a relevant role in the assessment of the sediment budget in watersheds since they reflect the contribution of different processes that can have a large spatio-temporal variability.

Among the numerous definitions of connectivity available in literature, the one by Heckmann et al. [9] (*"…the degree to which a system facilitates the transfer of water and sediment through itself, by means of coupling relationships between its components. In this view, connectivity becomes an emergent property of the system state, reflecting the continuity and strength of runoff and sediment pathways at a given point in time*") is one of the most comprehensive. Accordingly, the interaction governed by geomorphic processes among natural landforms and man-made structures is fundamental to understand connectivity [10] (Fig. 1). The spatial configuration of system components and their potential linkage is known as *structural connectivity* whereas the term *functional connectivity* refers to the dynamics of geomorphic and hydrologic processes within the system [11].

The increasing availability of high-resolution Digital Elevation Models (DEMs) from different sources as LiDAR and Structure from Motion (SfM) paved the way to a more quantitative approach for assessing sediment connectivity. Recently, a geomorphometric index of sediment connectivity has been developed [12] along with related freeware software tool [13]. The index, based on the original work by Borselli et al. [14], aims at characterizing connectivity patterns at the catchment scale allowing to estimate the contribution of a given part of the catchment as sediment source and define sediment transfer paths.

In this work, this index of connectivity is presented along with its most recent applications in different contexts.

Marco Cavalli, Stefano Crema and Lorenzo Marchi (2020) Structural sediment connectivity assessment through a geomorphometric approach: review of recent applications: in Massimiliano Alvioli, Ivan Marchesini, Laura Melelli & Peter Guth, eds., Proceedings of the Geomorphometry 2020 Conference, doi:10.30437/GEOMORPHOMETRY2020_57.

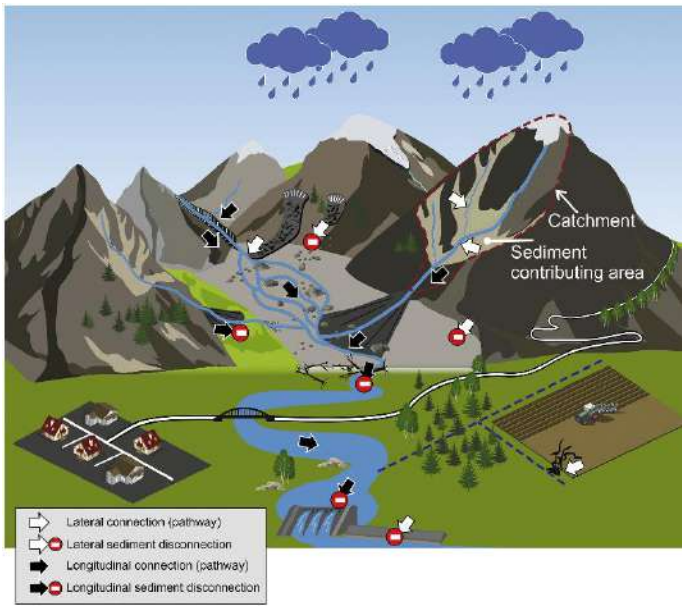

Figure 1. Schematic illustration of sediment connectivity distinguishing between lateral (i.e. hillslope-channel) and longitudinal (along channel network) and of the most relevant factors controlling it (modified from [9]).

II. THE INDEX OF CONNECTIVITY *IC*

Following the approach by Borselli et al. [14], the index of connectivity (*IC*) is computed as:

$$IC = log_{10}\left(\frac{D_{up}}{D_{dn}}\right) \quad (1)$$

where D_{up} and D_{dn} are the upslope and downslope components of connectivity, respectively (Fig. 2). *IC* is defined in the range of [$-\infty$,$+\infty$], with connectivity increasing for larger *IC* values.

The upslope component D_{up} represents the potential for downward routing of the sediment produced upslope and is estimated as follows:

$$D_{up} = \bar{W}\bar{S}\sqrt{A} \quad (2)$$

where $\bar{W}$ is the average weighting factor of the upslope contributing area, $\bar{S}$ is the average slope gradient of the upslope contributing area (m/m), and A is the upslope contributing area (m^2).

The downslope component D_{dn} takes into account the flow path length that a particle has to travel to arrive at the nearest target or sink:

$$D_{dn} = \sum \frac{d}{WS} \quad (3)$$

where d_i is the length of the flow path along the cell according to the steepest downslope direction (m), and W and S are the weighting factor and the slope gradient of the cell, respectively.

The weighting factor W in Eq. 2 and 3 is intended to represent the impedance to sediment transport and can be expressed in different ways. Cavalli et al. [12] refined the original index by Borselli et al. [14] in order to adapt it to the mountain environment and to better exploit high-resolution DEM. In particular, they proposed to use a surface roughness index [15] in place of the USLE/RUSLE C- factor adopted in [14] as weighting factor. Other modifications encompass the calculation of the slope along the flow direction and of the drainage area using the multiple flow D-infinity approach [16], replacing the single-flow direction algorithm used in the original version to capture flow paths on hillslopes where divergent flow occur. More details on the theoretical basis and the methodology can be found in Cavalli et al. [12]. A standalone freeware software (SedInConnect 2.3, [13]) implementing new features, as the possibility to normalize W according to Trevisani and Cavalli [17], was also developed to facilitate index computation. The software is available at https://github.com/HydrogeomorphologyTools/SedInConnect_2.3.

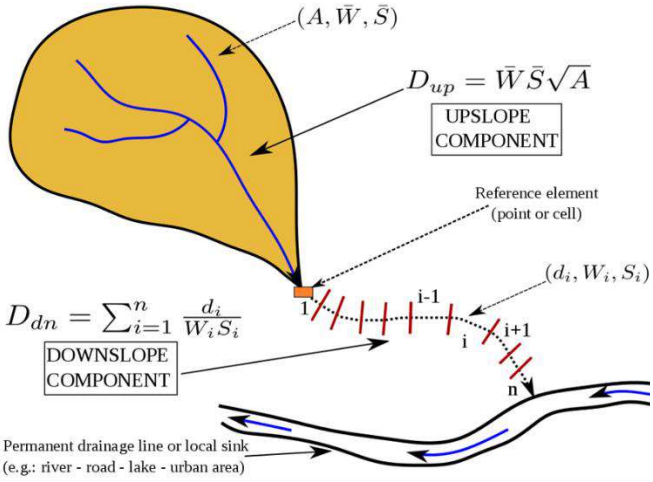

Figure 2. Representation of the components of the index of connectivity (from [13])

III. RECENT APPLICATIONS AND CONCLUSIONS

The version by Borselli et al. [14] was successfully applied to understand soil erosion patterns [18] and specific sediment yield variations [19]. Using a land-use based weighting factor permits to study the effects of different land use and land abandonment scenarios on sediment connectivity e.g. [20, 21]. Even if not meant for this purpose, *IC* has proven useful also for estimating

hillslope sediment delivery ratio (SDR) [22]. Jamshidi et al. [23], developed an algorithm integrating the SDR estimation approach by Vigiak et al. [22] to assess annual variability in sediment yields related to changes in vegetation. Hamel et al. [24] integrated *IC* into a new version of the InVEST model, a model aiming at quantifying and map ecosystem services, showing a great potential to quantify the sediment retention service. *IC* supported the interpretation of radioactive dose rate measurements after the Fukushima Dai-ichi Nuclear Power Plant accident in nearby catchments [25]. Another interesting application of this version of *IC* was carried out by Foerster et al. [26] in the Spanish Pyrenees. In [26], *IC* was computed in two catchments in contrasting seasons estimating the weighting factor based on fractional vegetation cover from hyperspectral data. This approach permitted to effectively identify hot spot erosion areas.

The herein presented version implementing roughness index as W factor, after its first application in two small adjacent catchments of the Eastern Alps [12], was extensively applied in different contexts especially in the mountain environment. Notable applications include the analysis of hillslope–channel coupling in a catchment in SW Turkey [27], sediment transfer dynamics in a formerly glaciated alpine valley [28], the impact of volcanic eruptions on sediment connectivity [29, 30] and sediment connectivity in proglacial areas [1, 31, 32]. *IC* has been successfully used in combination with sediment sources and/or landslide inventories in order to characterize such areas and optimize sediment management and to focus on the most critical hotspots [33, 34]. A valuable feature of *IC* arose from an application to 22 catchments in the Eastern italian Alps: if averaged at catchment scale, *IC* values can help distinguishing among different dominant processes (debris flow, bedload transport and intermediate behavior) [35]. Similar results were found in the Austrian Alps where *IC* was used together with other morphometric parameters to identify dominant processes acting in headwater catchments [36]. Most recently, the increasing availability of multitemporal high-resolution data offered the opportunity to integrate the time variable into the connectivity analysis [37, 38]. It is worth noting that the index values show a systematic decrease with increasing resolution [35, 39] and it has a strong dependency on catchment size. Furthermore, the use of different weighting factors can lead to different connectivity patterns. It is thus recommended to carefully choose the weighting factor according to the specific research aims. These limitations should be taken into account to produce reliable results that, given the simple index structure, must be always validated in the field.

In conclusion, *IC* has proved very promising for rapid spatial characterization of sediment dynamics both at catchment and regional scales. The reported applications demonstrate that a reliable assessment of sediment connectivity via a geomorphometric approach, especially when integrated with a sediment sources inventory, is useful for giving management priorities. This represents a key issue when dealing with sediment management and has important linkages with hazard and risk assessment and in relation to priorities of intervention at the catchment scale. Being a topography-based index, *IC* is focused on structural aspects of connectivity, and quality and resolution of DEMs may have significant impact on the results. Future development should consider process-based connectivity and incorporate temporal variability directly into the index. First attempt has been made by Kalantari et al. [40] who modified *IC* including a functional weighting factor based on surface runoff estimate by curve numbers and considering spatially and temporally variable forcing. Further research in this direction will help to conceive a new geomorphometric approach combining system configuration, processes and external forcing towards an improved caractherization of sediment and hydrological connectivity.

REFERENCES

[1] Cavalli, M., Vericat, D., Pereira, P., 2019. Mapping water and sediment connectivity. Science of the Total Environment 673, 763-767. https://doi.org/10.1016/j.scitotenv.2019.04.071

[2] Parsons, A.J., Bracken, L., Poeppl, R.E., Wainwright, J., Keesstra, S.D., 2015. Introduction to special issue on connectivity in water and sediment dynamics. Earth Surf. Process. Landf. 40, 1275–1277. https://doi.org/10.1002/esp.3714.

[3] Wohl, E., Brierley, G., Cadol, D., Coulthard, T.J., Covino, T., Fryirs, K.A., Grant, G., Hilton, R.G., Lane, S.N., Magilligan, F.J., Meitzen, K.M., Passalacqua, P., Poeppl, R.E., Rathburn, S.L., Sklar, L.S., 2019. Connectivity as an emergent property of geomorphic systems. Earth Surf. Process. Landf. https://doi.org/10.1002/esp.4434

[4] Bracken, L.J., Wainwright, J., Ali, G.A., Tetzlaff, D., Smith, M.W., Reaney, S.M., Roy, A.G., 2013. Concepts of hydrological connectivity: research approaches, pathways and future agendas. Earth-Sci. Rev. 119, 17–34. https://doi.org/10.1016/j. earscirev.2013.02.001

[5] Brierley, G., Fryirs, K., Jain, V., 2006. Landscape connectivity: the geographic basis of geomorphic applications. Area 38, 165–174. https://doi.org/10.1111/j.1475-4762.2006.00671.x.

[6] Fryirs, K., 2013. (Dis)connectivity in catchment sediment cascades: a fresh look at the sediment delivery problem. Earth Surf. Process. Landf. 38, 30–46. https://doi.org/10.1002/esp.3242.

[7] Poeppl, R.E., Keesstra, S.D., Maroulis, J., 2017. A conceptual connectivity framework for understanding geomorphic change in human-impacted fluvial systems. Geomorphology, Connectivity in Geomorphology From Binghamton 2016. 277, pp. 237–250. https://doi.org/10.1016/j.geomorph.2016.07.033

[8] Wohl, E., 2017. Connectivity in rivers. Prog. Phys. Geogr. Earth Environ. 41, 345–362. https://doi.org/10.1177/0309133317714972

[9] Heckmann, T., Cavalli, M., Cerdan, O., Foerster, S., Javaux, M., Lode, E., Smetanová, A., Vericat, D., Brardinoni, F., 2018. Indices of sediment connectivity: opportunities, challenges and limitations. Earth-Sci. Rev. 187, 77–108. https://doi.org/10.1016/j.earscirev.2018.08.004.

[10] Fryirs, K.A., Brierley, G.J., Preston, N.J., Kasai, M., 2007. Buffers, barriers and blankets: the (dis)connectivity of catchment-scale sediment cascades. CATENA 70, 49–67. https://doi.org/10.1016/j.catena.2006.07.007.

[11] Wainwright, J., Turnbull, L., Ibrahim, T.G., Lexartza-Artza, I., Thornton, S.F., Brazier, R.E., 2011. Linking environmental régimes, space and time: interpretations of structural and functional connectivity. Geomorphology, Geomorphology on Multiscale Feedbacks in Ecogeomorphology. 126, pp. 387–404. https://doi.org/10.1016/j.geomorph.2010.07.027.

[12] Cavalli, M., Trevisani, S., Comiti, F., Marchi, L., 2013. Geomorphometric assessment of spatial sediment connectivity in small Alpine catchments. Geomorphology 188, 31–41. https://doi.org/10.1016/j.geomorph.2012.05.007.

[13] Crema, S., Cavalli,M., 2018. SedInConnect: a stand-alone, free and open source tool for the assessment of sediment connectivity. Comput. Geosci. 111, 39–45. https://doi.org/10.1016/j.cageo.2017.10.009.

[14] Borselli, L., Cassi, P., Torri, D., 2008. Prolegomena to sediment and flow connectivity in the landscape: a GIS and field numerical assessment. Catena 75, 268–277. https://doi.org/10.1016/j.catena.2008.07.006

[15] Cavalli, M., Marchi, L., 2008. Characterisation of the surface morphology of an alpine alluvial fan using airborne LiDAR. Nat. Hazards Earth Syst. Sci. 8 (2), 323–333. https://doi.org/10.5194/nhess-8-323-2008

[16] Tarboton, D.G., 1997. A New Method for the Determination of Flow Directions and Upslope Areas in Grid Digital Elevation Models. Water Resour. Res. 33 (2), 309–319.

[17] Trevisani, S., Cavalli, M., 2016. Topography-based flow-directional roughness: potential and challenges. Earth Surf. Dyn. 4, 343–358. https://doi.org/10.5194/esurf-4-343-2016.

[18] López-Vicente, M., Quijano, L., Palazón, L., Gaspar, L., Navas, A., 2015. Assessment of soil redistribution at catchment scale by coupling a soil erosion model and a sediment connectivity index (central spanish pre-pyrenees). Cuad. Investig. Geográfica 41, 127–147. https://doi.org/10.18172/cig.2649.

[19] Sougnez, N., vanWesemael, B., Vanacker, V., 2011. Low erosion rates measured for steep, sparsely vegetated catchments in southeast Spain. CATENA 84, 1–11. https://doi.org/10.1016/j.catena.2010.08.010.

[20] López-Vicente, M., Poesen, J., Navas, A., Gaspar, L., 2013. Predicting runoff and sediment connectivity and soil erosion by water for different land use scenarios in the Spanish Pre-Pyrenees. Catena 102, 62–73.

[21] López-Vicente, M., Nadal-Romero, E., Cammeraat, E.L.H., 2017a. Hydrological Connectivity Does Change Over 70 Years of Abandonment and Afforestation in the Spanish Pyrenees. Land Degrad. Dev. 28 (4), 1298–1310.

[22] Vigiak, O., Borselli, L., Newham, L.T.H., McInnes, J., Roberts, A.M., 2012. Comparison of conceptual landscape metrics to define hillslope-scale sediment delivery ratio. Geomorphology 138, 74–88. https://doi.org/10.1016/j.geomorph.2011.08.026.

[23] Jamshidi, R., Dragovich, D., Webb, A.A., 2014. Distributed empirical algorithms to estimate catchment scale sediment connectivity and yield in a subtropical region. Hydrol. Process. 28 (4), 2671–2684.

[24] Hamel, P., Chaplin-Kramer, R., Sim, S., Mueller, C., 2015. A new approach to modeling the sediment retention service (InVEST 3.0): Case study of the Cape Fear catchment, North Carolina, USA. Sci. Total Environ. 524-525, 166–177.

[25] Evrard, O., Chartin, C., Onda, Y., Patin, J., Lepage, H., Lefèvre, I., Ayrault, S., Ottlé, C., Bonté, P., 2013. Evolution of radioactive dose rates in fresh sediment deposits along coastal rivers draining Fukushima contamination plume. Sci. Rep. 3. https://doi.org/10.1038/srep03079.

[26] Foerster, S., Wilczok, C., Brosinsky, A., Segl, K., 2014. Assessment of sediment connectivity from vegetation cover and topography using remotely sensed data in a dryland catchment in the Spanish Pyrenees. J. Soils Sediments 14 (12), 1982–2000.

[27] D'Haen, K., Dusar, B., Verstraeten, G., Degryse, P., de, Brue H., 2013. A sediment fingerprinting approach to understand the geomorphic coupling in an eastern Mediterranean mountainous river catchment. Geomorphology 197, 64–75. https://doi.org/10.1016/j.geomorph.2013.04.038.

[28] Meßenzehl, K., Hoffmann, T., Dikau, R., 2014. Sediment connectivity in the high-alpine valley of Val Müschauns, Swiss National Park – linking geomorphic field mapping with geomorphometric modelling. Geomorphology 221, 215–229.

[29] Ortíz-Rodríguez, A.J., Borselli, L., Sarocchi, D., 2017. Flow connectivity in active volcanic areas: use of index of connectivity in the assessment of lateral flow contribution to main streams. CATENA 157, 90–111. https://doi.org/10.1016/j.catena.2017.05.009.

[30] Martini, L., Picco, L., Iroumé, A., Cavalli, M., 2019. Sediment connectivity changes in an Andean catchment affected by volcanic eruption. Science of the Total Environment, 692, 1209-1222. DOI: 10.1016/j.scitotenv.2019.07.303

[31] Cavalli, M., Heckmann, T., Marchi, L., 2019. Sediment connectivity in proglacial areas. In: Heckmann, T., Morche, D. (Eds.), Geomorphology of Proglacial Systems: Landform and Sediment Dynamics in Recently Deglaciated Alpine Landscapes, Geography of the Physical Environment. Springer International Publishing, Cham, pp. 271–287https://doi.org/10.1007/978-3-319-94184-4_16.

[32] Micheletti, N., Lane, S.N., 2016. Water yield and sediment export in small, partially glaciated Alpine watersheds in a warming climate. Water Resour. Res. 52 (6), 4924–4943.

[33] Persichillo, M.G., Bordoni, M., Cavalli, M., Crema, S., Meisina, C., 2018. The role of human activities on sediment connectivity of shallow landslides. CATENA 160, 261–274. https://doi.org/10.1016/j.catena.2017.09.025.

[34] Tiranti, D., Cavalli, M., Crema, S., Zerbato, M., Graziadei, M., Barbero, S., Cremonini, R., Silvestro, C., Bodrato, G., Tresso, F., 2016. Semi-quantitative method for the assessment of debris supply from slopes to river in ungauged catchments. Sci. Total Environ. 554–555, 337–348. https://doi.org/10.1016/j.scitotenv.2016.02.150.

[35] Brardinoni, F., Cavalli, M., Heckmann, T., Liébault, F., Rimböck, A., 2015. Guidelines for assessing sediment dynamics in alpine basins and channel reaches: Final Report of the SedAlp Project, Work Package 4: Vienna.

[36] Heiser, M., Scheidl, C., Eisl, J., Spangl, B., Hubl, J., 2015. Process type identification in torrential catchments in the eastern Alps. Geomorphology 232, 239–247. https://doi. org/10.1016/j.geomorph.2015.01.007.

[37] Cucchiaro S., Cazorzi F., Marchi L., Crema S., Beinat A., Cavalli M., 2019. Multi-temporal analysis of the role of check dams in a debris-flow channel: Linking structural and functional connectivity. Geomorphology, 345, 106844. DOI: 10.1016/j.geomorph.2019.106844

[38] Llena, M., Vericat, D., Cavalli, M., Crema, S., Smith, M.W., 2019. The effects of land use and topographic changes on sediment connectivity in mountain catchments. Sci. Total Environ. https://doi.org/10.1016/j.scitotenv.2018.12.479.

[39] Cantreul, V., Bielders, C., Calsamiglia, A., Degré, A., 2018. How pixel size affects a sediment connectivity index in central Belgium. Earth Surf. Process. Landf. 43, 884–893. https://doi.org/10.1002/esp.4295.

[40] Kalantari, Z., Cavalli, M., Cantone, C., Crema, S., Destouni, G., 2017. Flood probability quantification for road infrastructure: Data-driven spatial-statistical approach and case study applications. Sci. Total Environ. 581-582, 386–398. https://doi.org/10.1016/j.scitotenv.2016.12.147.

GEOMORPHOMETRY 2020 PERUGIA, ITALY JUNE 22 - 26 2020

Fluvial inverse modelling for inferring the timing of Quaternary uplift in the Simbruini range (Central Apennines, Italy)

Michele Delchiaro[1§], Veronica Fioramonti[2], Marta Della Seta[1], Gian Paolo Cavinato[3], Massimo Mattei[2]

[1] Department of Earth Sciences, Sapienza University
Piazzale Aldo Moro 5, 00185 Rome, Italy
[2] Department of Sciences, Roma Tre University,
Largo San Leonardo Murialdo 1, 00146 Rome, Italy
[3] National Research Council, Office of Rome
Department of Earth Sciences, Sapienza University
Piazzale Aldo Moro 5, 00185 Rome, Italy
[§] michele.delchiaro@uniroma1.it

Abstract— **The regional topography of the Central Apennines results from convergence between the African and Eurasian plates that led to the formation of a Neogene NE-verging imbricate fold and thrust belt. During the final stages of the orogenic deformations, the whole area was affected by strong uplift and by extensional faulting oriented along the main direction of the Apennine chain. In this framework, the landscape evolution in subaerial conditions started diachronically and is testified by the relicts of clastic deposit at different height from base levels of the present drainage network. In the Simbruini range, there are no absolute dating records neither of the most ancient clastic units deposited after the Messinian thrust-top facies nor of tectonic events. Trying to fill this gap, we used geomorphometric analyses to infer the timing of the recent phases of the tectonic history of the Simbruini range. Specifically, we identified the main non-lithological knickpoints along the river longitudinal profiles, clustered their altimetric distribution and correlated them with the levels of continental clastic deposits reserved at different elevations. Furthermore, we inferred the uplift history of the range by applying the inverse modelling of the river longitudinal profiles. Assuming a block uplift model, the drainage network cutting the Simbruini range recorded on average about 2.4 Myr of tectonic history, characterized by variable base level fall rates (corresponding to uplift rates). According the average tectonic history, the highest base level fall rate of 690 m My $^{-1}$ was reached at 1.65 Ma, followed by the minimum of about 370 m My $^{-1}$, reached at 0.75 Ma, and by a second rise, up to a present-day value of 660 m My^{-1}.**

I. INTRODUCTION

The Central Apennine chain developed from the Late Oligocene to present, as a consequence of the convergence and the following collision between the African and Eurasian plates. The study area is located in the Simbruini-Ernici range, sited in the intermediate sector of the Central Apennines, a thrust-belt/foredeep system progressively migrating towards the NE [1-2] (Figure 1). It strikes NW-SE and is part of the Latium-Abruzzi paleogeographic domain made up of a carbonatic succession from Mesozoic to Miocene [3-4]. The range is bordered by the Latina Valley to the SW and the Roveto Valley to the NNE, filled with Tortonian to Messinian siliciclastic sediments, mainly deposited in feredeep basins [5]. The last recorded sedimentary cycle of the Central Apennine chain is given by the thrust-top clays and conglomerates (Messinian), that crop out scattered on the deformed bedrock units [6]. Specifically, the study area is located in the axial culmination of the antiformal central Simbruini range (Figure 1), where the strong uplift brought Triassic dolostones to be exposed, in correspondence of an important and complex tectonic lineament called the "Vallepietra - Filettino - Mt. Ortara Line" [6-7]

From the topography perspective the building of relief was slow during the phase of major crustal shortening occurred during Miocene-Pliocene, but strongly accelerated in the Quaternary, when the shortening slowed down and the whole area was affected by strong uplift and extensional faulting striking mainly NW-SE [8-10]. The landscape evolution in subaerial conditions started diachronically and is testified by the relicts of clastic deposit at different height from base levels of the present drainage network. Many Authors [8-10] reported on gently undulated low relief surfaces located in the mountain slopes and tops and interpreted as the remnants of old landscapes formed before the Quaternary uplift. Nevertheless, in the Simbruini range, there are no absolute

Michele Delchiaro, Veronica Fioramonti, Marta Della Seta, Gian Paolo Cavinato, and Massimo Mattei (2020)

Fluvial inverse modelling for inferring the timing of Quaternary uplift in the Simbruini range (Central Apennines, Italy):

in Massimiliano Alvioli, Ivan Marchesini, Laura Melelli & Peter Guth, eds., Proceedings of the Geomorphometry 2020 Conference, doi:10.30437/GEOMORPHOMETRY2020_58.

dating records neither of the most ancient clastic units deposited after the Messinian thrust-top facies and the evolution of tectonic events is still not well understood.

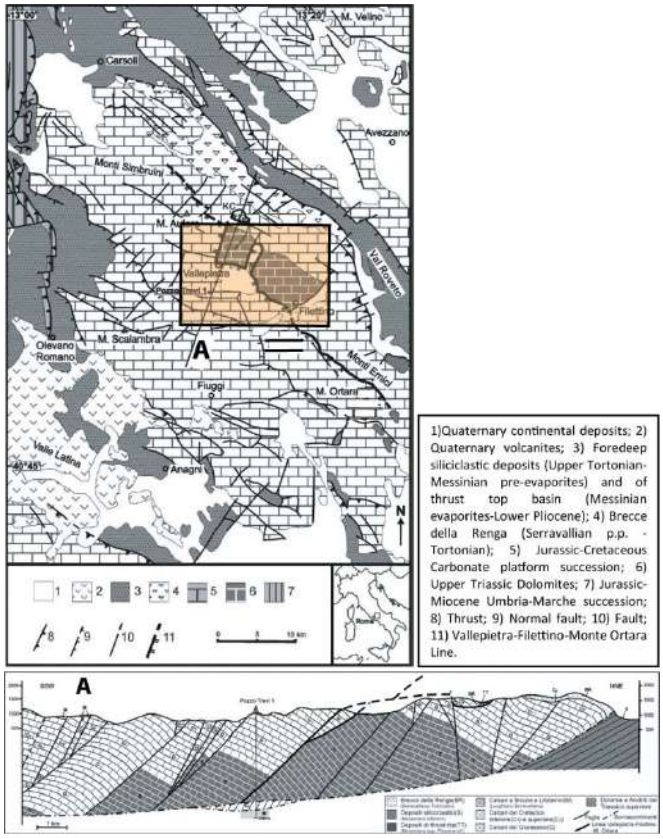

Figure 1. Structural map of the Central Apennines. In the rectangle it is locate the region of interest, the Simbruini range. It is also reported a geological cross-section (A) of the main structural units (modified from [9]).

In this framework, the general purpose is to shed light on final stages of the post-orogenic deformation in the central Simbruini range through geomorphometric analyses. Specifically, we identified the main non-lithological knickpoints along the river longitudinal profiles, constraining the final morpho-evolutionary stages of the valleys cutting the range. Furthermore, we attempted to reconstruct the uplift history of the range through the inverse modelling of the river longitudinal profiles.

II. METHODS

In tectonically active areas, the evolution of topography can provide key insights into the spatio-temporal variations of uplift. Fluvial landscapes record elements that reflect temporal and spatial variations in rock uplift rates which are experienced as base level changes. In rapidly evolving landscapes such as the valleys cutting the Simbruini range, the morphometric record of tectonic perturbation is limited to the most recent times. We investigated the plano-altimetric distribution of the main non-lithological knickpoints along the river longitudinal profiles of the valleys cutting the Simbruini range, included in the Aniene River drainage basin. Furthermore, after calibrating the river profiles with an erodibility value, we applied the inverse modelling of river longitudinal profiles, thus constraining the base level change histories that such knickpoints testify to.

The drainage network was extracted from the 10 m-resolution TINITALY Digital Elevation Model [11] using TopoToolbox, a set of Matlab functions for topographic analysis [12]. We performed the inverse modelling of the longitudinal profiles of the drainage network using a Matlab code gently provided by Sean Gallen.

A. Linear Stream Power Law for Inverse modelling

In detachment-limited conditions, typical of tectonically active regions, the evolution of the river profile is described by the stream power law (SPL) [13] as the change in elevation z of a channel point x through time t, which relates to the competition between erosion (E) and uplift (U):

$$\frac{dz(x,t)}{dt} = U(x,t) - E\,(x,t) \tag{1}$$

where fluvial erosion E is calculated as:

$$E\,(x,t) = K\,A\,(x)^{\,m}\,(\frac{dz\,(x,t)}{dx})^{n} \tag{2}$$

The powers m and n are positive constants controlling the erosion mechanism. Specifically, m depends on the climatic conditions and hydraulic properties of the discharge, and n is function of other erosional thresholds [14]. The erodibility, K, reflects the lithology, the climatic conditions and channel geometry. In the general case, K can vary in space and time, but in the treatment presented here, it is taken as a constant. A power-law relationship between the local channel slope (S) and the upstream drainage area (A) reveals the steady-state river profile:

$$S\,(x,t) = (\frac{E(x,t)}{K})^{\frac{1}{n}}\,A(x)^{-\frac{m}{n}} = k_s\,A(x)^{-\theta} \tag{3}$$

where $k_s = (E\,(t,x)\,/\,K)^{\,1/n}$ is known as the steepness index and m/n ratio or θ is defined as concavity index. According to the steady state conditions, the surface elevation, the erosion rate and the relative uplift rate do not vary over time, $U(x) = E(x)$, $n=1$ and the steepness index takes the form [15]:

$$k_s = \frac{E\,(x,t)}{K} = \frac{U(x,t)}{K} \tag{4}$$

If U and K are space-invariant, we can perform the integration of $(U/K)^{1/n}$ from a base level x_b to an arbitrary upstream point x of the channel to predict the elevation of a river profile [16]:

$$z(x) = z(x_b) + \left(\frac{U}{K {A_0}^m}\right)^{\frac{1}{n}} \chi \quad (5)$$

where A_0 is an arbitrary scaling area and χ is an integration of river horizontal coordinates defined by the equation:

$$\chi(x) = \int_{xb}^{x} \left(\frac{A_0}{A(x')}\right)^{\frac{m}{n}} dx' \quad (6)$$

The erosional wave celerity, $C(x) = K\,A(x)^m\,S(x)^{n-1}$, controls the speed at which perturbations travel along the channel [14]. The response time, τ(x), for perturbations to propagate from the river outlet, at $x = 0$, to a point x along the channel is expressed as [14]:

$$\tau(x) = \int_0^x \frac{dx'}{C\,(x')} = \int_0^x \frac{dx'}{K\,A\,(x')^m\,S\,(x')^{\,n-1}} = \frac{\chi\,(x)}{K\,{A_0}^m} \quad (7)$$

where x′ is an integration variable. The response time, τ(x), increases constantly with x, from the base level to the high channel reaches. τ-plot is the starting point for the linear inverse scheme to study the rock-uplift/base-level fall history recorded in the fluvial topography [14-15]. Concluding we assumed a spatially constant K and U as in a block uplift scenario employing the inverse approach stream power model solution proposed by Ref. [17-18].

III. Results and Conclusions

A plano-altimetric analysis of the major knickpoints distinguished based on their elevation drop, was conducted (Figure 2). Knickpoint histogram in Figure 2 shows quite well a cluster correlating to the highest clastic deposits (between 1550 and 1300 m a.s.l.) that are associated to the presence of a large anomalous patch of low relief/slope landscape. The low relief areas are especially visible in Vallepietra, Valgranara and Campocatino networks, are elevated by at least 700 m above the Aniene trunk channel and have low slope hanging reaches with increasing vertical drop towards downstream segments. The histogram shows also other two minor clusters of knickpoint at elevation of 1000-800 m a.s.l and 600-400 m a.s.l., respectively in the Valgranara, where another level of breccias crops out, and along the lower reach of the upper Aniene River valley. Major river systems were extracted that drain the upper valley of the Aniene River basin where drainage area exceeds 10^6 m^2. As described by Eq. 3, channel slope, S, and upstream drainage area, A, were plotted on a SA *log-log* plot (Figure 2) and used to calculate the channel concavity, θ. Moreover, the steepness index, ks, was computed to the entire drainage network using the obtained value of channel concavity.

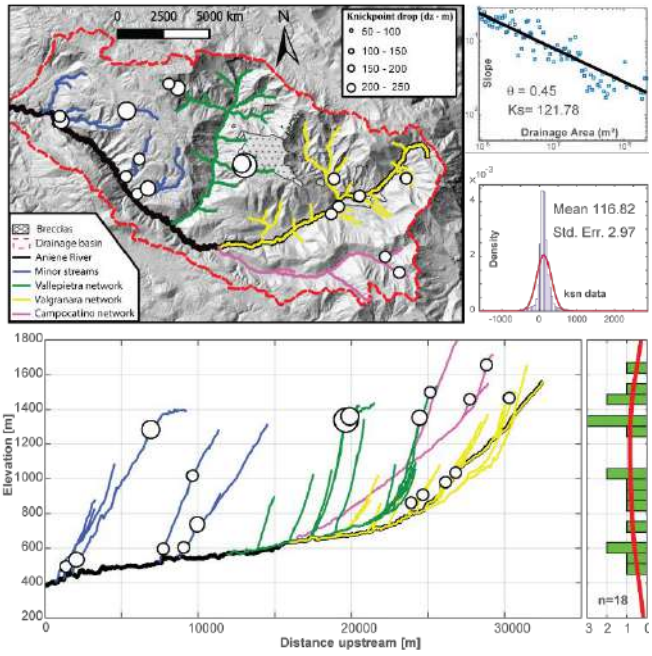

Figure 2. The planimetric view of the stream networks composing the upper Aniene River valley (including the Valgranara, Campocatino and Vallepietra sub-catchments) with the associated slope area plot and ksn density distribution. It is also reported the longitudinal profiles of the main streams of the drainage basin and knickpoint elevation histogram.

The average concavity, θ, relative to the entire drainage basin of the upper Aniene River valley is 0.45 while the steepness index, ks, 116.82 with a standard error of 2.97. In order to calibrate the erodibility K, we referred to literature data for the axial zone of the Central Apennines [9-10] by which provided an averaged uplift rate ranging from 0.5 to 0.7 mm yr $^{-1}$. In order to provide a sensitivity analysis on such a parameter, we find the max, mean and min K, applying Eq. 4 respectively between the max uplift rate and the min ks, the mean uplift rate and the mean ks, the min uplift rate and the max ks. We find that K_{max} = 6.04 X 10^{-6} m$^{0.1}$ yr^{-1}, K_{mean} = 5.14 X 10^{-6} m$^{0.1}$ yr^{-1}, K_{min} = 4.24 X 10^{-6} m$^{0.1}$ yr^{-1}. The inversion results were calibrated using the values of K_{est} and m (being $n = 1$ for the steady-state condition then θ = m = 0.45) with a time step size of 10 ka. In Figure 3, the stream network's elevation was reported in χ space and converted in τ space for the different values of K_{est} by applying Eq. 7. Regarding the linear river inversion curves under the block uplift assumption, the tectonic histories that we generically interpret as base level fall rate at the outlet point of the drainage system where

the tectonic Simbruini range ends, are as longer as K_{est} is greater ranging from 2.1 Ma with K_{max} to 2.9 Ma with K_{min}. Moreover, the base level fall rates are greater increasing K_{est}.

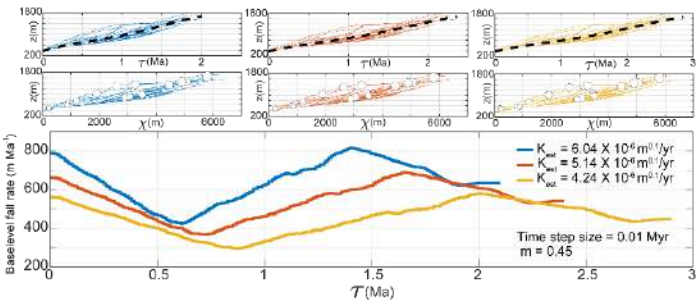

Figure 3. Empirical and best fit χ and τ plots of the stream networks of the upper Aniene River valley computed for K_{max}, K_{mean}, K_{min}. The linear river inversion curves obtained for the different values of K_{est} with the associated parameters chosen in the modelling.

The upper Aniene River valley records on average about 2.4 Myr of tectonic history. According to the average tectonic history in Figure 3, from 2.4 to 1.65 Ma, the base level fall rate constantly increases reaching the highest value of about 690 m My $^{-1}$. Then, from 1.65 Ma to 0.75 Ma it decreases except for a short period of time around 1.3 Ma where a slight increase is recorded. At 0.75 Ma the baselevel fall rate reaches its minimum of about 370 m My $^{-1}$ after which it rises again until to the present day with a value of about 660 m My $^{-1}$.

In conclusion, we tested the linear river inversion procedure in the Simbruini range in Central Italy, as an alternative tool for inferring the recent tectonic history from Pleistocene to the present day where it is still difficult to provide an accepted chronological evolution.

REFERENCES

[1] Dondi, L., Papetti, I., Tedeschi, D., 1966. "Stratigrafia del pozzo Trevi 1 (Lazio)". Geologica Romana, 5, 249-262.

[2] Pasquali, V., Castorina, F., Cipollari, P., Cosentino, D., Lo Mastro, S., 2007. "I depositi tardo-orogenici della Valle Latina meridionale: stratigrafia e implicazioni cinematiche per l'evoluzione dell'Appennino centrale". Bollettino della Società Geologica Italiana (Ital. J. Geosci.) 126 (1), 101-118.

[3] Cosentino, D., Cipollari, P., Marsili, P., Scrocca, D., 2010. "Geology of the central Apennines: a regional review". Journal of the Virtual Explorer, 36(11), 1-37.

[4] Carminati, E., Corda, L., Mariotti, G., Brandano, M., 2007. "Tectonic control on the architecture of a Miocene carbonate ramp in the Central Apennines (Italy): insights from facies and backstripping analyses". Sedimentary Geology, 198(3-4), 233-253.

[5] Devoto, G., Parotto, M., 1967. "Note geologiche sui rilievi tra Monte Crepacuore e Monte Ortara (Monti Ernici-Lazio nord-orientale)". Geologica Romana, 6, 145-163.

[6] Calamita, F., Di Domenica, A., Viandante, M. G., Tavarnelli, E., 2008. "Sovrascorrimenti younger on older o faglie normali ruotate: la linea Vallepietra-Filettino-Monte Ortara (Appennino centrale laziale-abruzzese)". Rendiconti online della Società Geologica Italiana, 1, 43-47.

[7] Cavinato, G. P., Parotto, M., Sirna, M., 2012. "I Monti Ernici: da peripheral bulge a orogeno. Stato dell'arte della ricercar". In " Geological summary of the Central Apennines... four decades later". Convegno in onore di Maurizio Parotto e Antonio Praturlon., Vol. 23, pp. 31-44.

[8] Calamita, F., Coltorti, M., Pieruccini, P., Pizzi, A, 1999. "Evoluzione strutturale e morfogenesi plio-quaternaria dell'Appennino umbro-marchigiano tra il preappennino umbro e la costa adriatica". Bollettino della Società Geologica Italiana, 118(1), 125-139.

[9] D'Agostino, N., Jackson, J. A., Dramis, F., Funiciello, R., 2001. "Interactions between mantle upwelling, drainage evolution and active normal faulting: an example from the central Apennines (Italy)". Geophysical Journal International, 147(2), 475-497.

[10] Molin, P., Fubelli, G., 2005. "Morphometric evidence of the topographic growth of the Central Apennines". Geografia Fisica e Dinamica Quaternaria, 28(3), 47-61.

[11] Tarquini, S., Nannipieri, L., 2017. "The 10 m-resolution TINITALY DEM as a trans-disciplinary basis for the analysis of the Italian territory: Current trends and new perspectives". Geomorphology, 281, 108-115.

[12] Schwanghart, W., Scherler, D., 2014. "TopoToolbox 2–MATLAB-based software for topographic analysis and modeling in Earth surface sciences". Earth Surface Dynamics, 2(1), 1-7.

[13] Howard, A. D., Kerby, G., 1983. "Channel changes in badlands". Geological Society of America Bulletin, 94(6), 739-752.

[14] Whipple, K. X., Tucker, G. E., 1999. "Dynamics of the stream-power river incision model: Implications for height limits of mountain ranges, landscape response timescales, and research needs". Journal of Geophysical Research: Solid Earth, 104(B8), 17661-17674.

[15] Kirby, E., Whipple, K. X., 2012. "Expression of active tectonics in erosional landscapes". Journal of Structural Geology, 44, 54-75.

[16] Perron, J. T., Royden, L., 2013. "An integral approach to bedrock river profile analysis". Earth Surface Processes and Landforms, 38(6), 570-576.

[17] Goren, L., Fox, M., Willett, S. D., 2014. "Tectonics from fluvial topography using formal linear inversion: Theory and applications to the Inyo Mountains, California". Journal of Geophysical Research: Earth Surface, 119(8), 1651-1681.

[18] Gallen, S. F., 2018. "Lithologic controls on landscape dynamics and aquatic species evolution in post-orogenic mountains". Earth and Planetary Science Letters, 493, 150-160.

GEOMORPHOMETRY 2020 PERUGIA, ITALY JUNE 22 - 26 2020

Guidelines for optimization of terrestrial laser scanning surveys over gully erosion affected areas

Fran Domazetović[§], Ante Šiljeg, Ivan Marić
Geospatial Analysis Laboratory (GAL)
Department of Geography, University of Zadar
Trg kneza Višeslava 9, 23000 Zadar
[§] fdomazeto@unizd.hr

Abstract — **Quantification and monitoring of complex geomorphic spatio-temporal changes requires multiple field surveys and creation of very-high resolution (VHR) digital elevation models (DEMs). Due to pronounced terrain roughness and complex surface topography modelling of gully erosion induced spatio-temporal changes can be very challenging. Although advanced geospatial technologies, such as terrestrial laser scanning (TLS), provide good basis for modeling of complex morphological features, certain limitations still exist that can lead to the overall devaluation in model quality. Most of these limitations are related to the non-systematic TLS survey approach, that lacks thorough survey planning and preparation phases.**

Main aim of our research was to provide guidelines for optimization of TLS surveys over gully erosion affected areas, through development of new systematic survey methodology. Established systematic TLS survey methodology allows multiple detection, quantification and monitoring of spatio-temporal changes, where survey characteristics are adjusted to the local terrain characteristics and specifications of available terrestrial laser scanner. Developed survey methodology was applied for TLS survey over chosen gully site at Pag Island, Croatia.

I. INTRODUCTION

Terrestrial laser scanning (TLS) represents state-of-the-art topographic modelling technique, that has broad application in various geomorphic researches, with special emphasis on application for detection, quantification and monitoring of various spatio-temporal changes (e.g. landslides (Kromer et al., 2017.), rockfalls (van Veen et al., 2017.), glacial dynamics (Fischer et al., 2016.), volcanism (de Zeeuw-van Dalfsen et al., 2017.), etc.).

As such, ground-based LiDAR surveys have been successfully implemented for monitoring of gully erosion induced spatio-temporal changes (e.g. headwall retreat (Rengers & Tucker, 2015; Goodwin et al., 2017.), volume of eroded material (Perroy et al., 2010; Castillo et al., 2012; Goodwin et al., 2017; Taylor et al., 2018.), etc.). However, pronounced terrain roughness and complex surface topography of certain gullies can lead to significant limitations and challenges in field scanning surveys, as well as in later modelling and creation of DEMs. For example, complex surface topography can obstruct laser beams from scanning certain areas (e.g. overhangs and steeper parts of gully headwall, inner deeper parts of gully channels), that can lead to introduction of "shadows" in collected point cloud (Perroy et al., 2010.) (Fig. 2.B). Such obstructed areas can lead to the overall devaluation in model quality and introduction of various errors (e.g. volume underestimation or overestimation (Bremer & Sass, 2012.)). Most of these limitations are related to the non-systematic TLS survey approach, that lacks thorough survey planning. However, such limitations can be eliminated through introduction of more scanning positions (Fig. 2.C) within systematic survey planning and preparation. Due to the time or resource constrains planning and preparation phases have been avoided or neglected in many TLS surveys, where scanning positions were determined on site, based entirely on user experience and judgment (Perroy et al., 2010; Bremer & Sass, 2012; Rengers & Tucker, 2015; Goodwin et al., 2016; 2017.).

Therefore, main aim of our study was to provide guidelines for optimization of TLS surveys over gully erosion affected areas, through development of new systematic survey methodology, that would allow multiple detection, quantification and monitoring of gully erosion induced spatio-temporal changes. Special emphasis in our research was given to the planning (1), preparation (2) and implementation (3) phases of TLS topographic surveys, that had to be accurate and repeatable. Established systematic TLS survey methodology allows multiple detection, quantification and monitoring of spatio-temporal changes, where survey characteristics are adjusted to the specifications of used terrestrial laser scanner (e.g. Faro M70; Stonex X300, etc.) and local terrain characteristics (terrain roughness, gully size and divergence, etc.).

Developed TLS survey methodology was applied on example of gully Santiš, located on SE part of Pag Island, Croatia (Fig. 1). Gully Santiš is simple, unbranched gully, with recent traces of active gully erosion. As such, this gully was perfect test site for validation of developed systematic TLS survey methodology.

Fran Domazetovic, Ante Siljeg and Ivan Maric (2020) Guidelines for optimization of terrestrial laser scanning surveys over gully erosion affected areas: in Massimiliano Alvioli, Ivan Marchesini, Laura Melelli & Peter Guth, eds., Proceedings of the Geomorphometry 2020 Conference, doi:10.30437/GEOMORPHOMETRY2020_59.

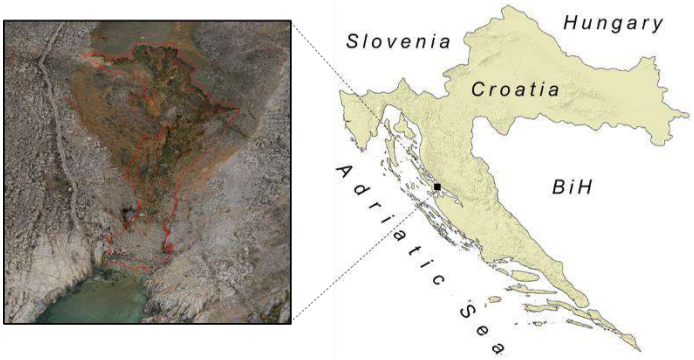

Figure 1. Study area covering gully Santiš within SE part of Pag Island, Croatia

II. METHODS

Field survey of chosen gully site was conducted on December 17, 2019 with Faro M70 terrestrial laser scanner (Fig. 2.A).

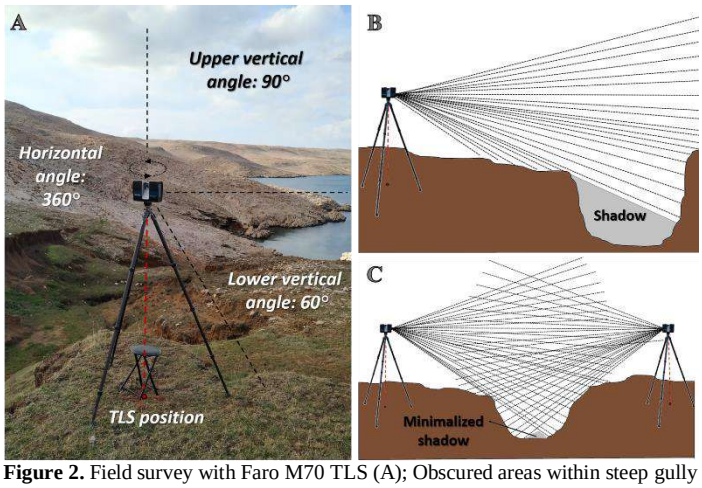

Figure 2. Field survey with Faro M70 TLS (A); Obscured areas within steep gully channels (B); Minimization of obscured areas with introduction of more TLS positions (C)

Whole systematic TLS survey methodology that was developed and applied within this research can be divided in four main steps: *survey planning* (A), *filed preparations* (B), *field TLS survey* (C), *creation and validation of gully model* (D).

A. Survey planning phase

TLS survey planning phase (A) is crucial phase in systematic TLS survey methodology, that serves as basis for all later activities. Planning of systematic TLS survey was performed in ArcGIS 10.1 software, based on available high resolution DEM of chosen study area. For that purpose, VHR DEM (2 cm spatial resolution) and digital ortophoto image (0.5 cm) of gully Santiš were derived from available data collected earlier by aerophotogrametric survey carried out with DJI Matrice 600 PRO drone.

First step in planning phase is *definition of study area extent* (A1), that in our case was defined by the extent of gully Santiš in initial DEM (1163 m²). Then *total number of scans* (A2) has to be determined, in respect to available survey time. As it was planned that survey lasts between 3 and 5 hours (due to short winter daylight), it was decided that survey will have around 8 scans (around 30 minutes per scan). In order to stay within 30-minute range per scan, scanning parameters in Faro M70 had to adjusted accordingly (resolution: ½; quality: 3x).

After determination of total number of scans, it is necessary to *find optimal positions for these scans* (A3), which was performed through the visibility analysis. Visibility analysis was performed by Interactive Visibility tool, where analysis parameters were adjusted to the specifications of Faro M70 laser scanner (Fig. 2; Table 1.).

Table 1. Specifications of Faro M70 used for adjustment of visibility analysis

MIN Range	MAX Range	Horizontal angle	Upper vertical angle	Lower vertical angle	TLS height
0.6 m	70 m	360º	90º	60º	1.9 m

Interactive Visibility tool was used to test more than 100 potential laser scanning positions, where areal spatial coverage and overlap were calculated for every tested position. From all tested potential TLS positions 8 locations with highest overlap and areal coverage were determined as optimal scanning location (Fig. 3.).

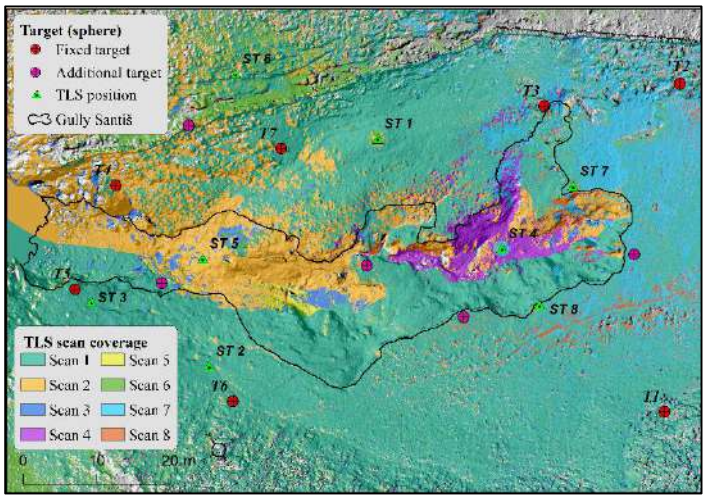

Figure 3. Visibility analysis carried out for 8 optimal TLS scanning positions

Final step in survey planning phase is *definition of optimal positions for survey reference targets* (A4). Survey reference targets (e.g. spheres, chessboards, etc.) are indications used in TLS surveys for accurate registration of multiple surveyed scans. As such, these targets have to be placed on exact XYZ location, which are identical for every repeated TLS survey and that won't be affected by ongoing gully erosion process. Therefore, optimal locations for these targets are on surrounding carbonate rocks, outside of the soil material affected by gully erosion. Visibility of every chosen target from defined 8 TLS positions was validated by *Line of sight* tool, which confirmed that at least three targets are visible from every TLS position. In total 7 targets were defined around study area and their height was set to 2 meters above ground, so that targets are visible from all parts of the gully.

B. Field preparations phase

Second phase in our methodology covers the field preparations (B) for later field TLS surveys, which includes *GPS stakeout of target positions* (B1), *construction of fixed and anchored target positions* (B2) and *GPS stakeout of scanner positions* (B3).

Seven target positions were stakeout and marked on the ground with Stonex S10 RTK GPS. At every marked target location fixed stands were carved in carbonate rock with Bosch hammer drill (Fig. 4.A) and leveled with self-leveling concrete (Fig. 4.B). Four anchors were then drilled in every fixed stand (Fig. 4.C), which serve as basis for metal poles that are holding the reference targets (spheres).

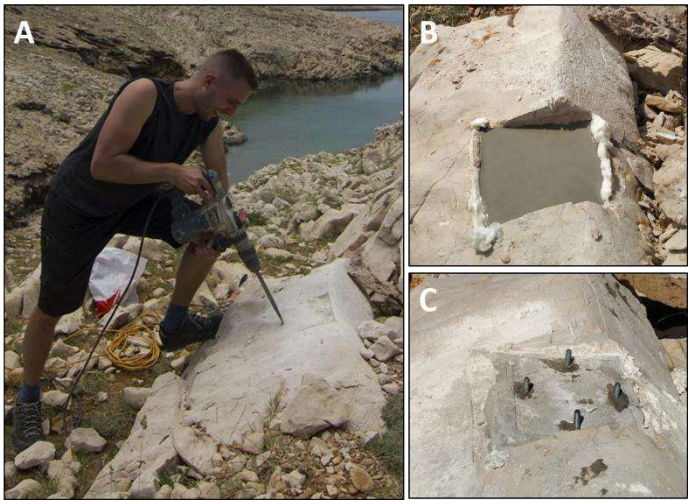

Figure 4. Construction of fixed target (sphere) stands with Bosch hammer drill (A); leveling of carved stand (B); fixed anchors for target poles (C)

Seven 2 m long metal poles were then used to fix targets above constructed stands. Metal poles can be dissembled and stored in-between two TLS surveys, while constructed TLS stands are protected from exposure to weather and salt depletion by nylon and gypsum protective caps.

After construction of all seven target stands, eight TLS scanning positions were stakeout and marked with red spray. Since most TLS positions are located within study area and within loose soil material, no permanent position marks haven't been made. In order to avoid disturbance of natural gully erosion process only red spray was used, as non-destructive marking method. Therefore, TLS positions have to be stakeout and marked with RTK GPS repeatedly before every new TLS survey.

C. Field TLS survey

Prior to the TLS field survey all seven reference targets (d = 69.5 cm) were placed on metal poles fixed to the constructed stands (Fig. 5.), while additional targets were placed in-between. Additional targets are optional, as they serve only to improve registration of collected scans, if main fixed targets are not sufficient. Precise coordinates of every TLS target, placed on top of metal pole was collected with 50-epoch RTK positioning using the Stonex S10 RTK GPS.

Figure 5. Reference target (sphere) placed on the fixed metal pole anchored to the constructed stand (A); one of seven target poles distributed around study area (B)

At the end, Faro M70 TLS mounted on carbon tripod was used to scan entire gully from all eight defined TLS positions.

D. Creation and validation of gully model

Collected scans were processed in Faro Scene 2019 software, which was used for registration of scans and creation of point cloud representing whole study site.

III. RESULTS AND CONCLUSIONS

A. Coverage of gully study area with TLS scans

Carried survey planning phase based on visibility analysis and eight defined optimal TLS positions resulted with very high percentage of study area coverage (over 95 %). Despite complex terrain morphology, survey planning minimized occurrence of shadows, as extend of obstructed areas were limited to the bottom of steep and incised sub-channels within the main gully channel.

Reference target stands prepared within survey preparation phase proved to be practical solution for accurate positioning of targets within and around the study area. Constructed target stands are allowing accurate multiple TLS surveys, as spheres are positioned on identical locations for every new survey.

Conducted TLS survey included eight scans that covered entire study area. Every scan lasted around 24 minutes, including time required for TLS setup and duration of scanning. In total scanning of the whole gully lasted around 3 h (3 hours, 10 minutes and 36 seconds).

B. Scans registration and point cloud creation

Collected eight scans were registered in Faro Scene through manual registration, with 1.7 mm mean horizontal target error and 2.9 mm mean vertical target error. Registered scans were used for creation of point cloud with 368 549 177 points. Created point cloud successfully covered whole study site, with exception of small obstructed areas at the bottom of steep headwall sections or within steep sub-channels (Fig. 6.). Thus, created point cloud has confirmed the accuracy and reliability of performed planning phase.

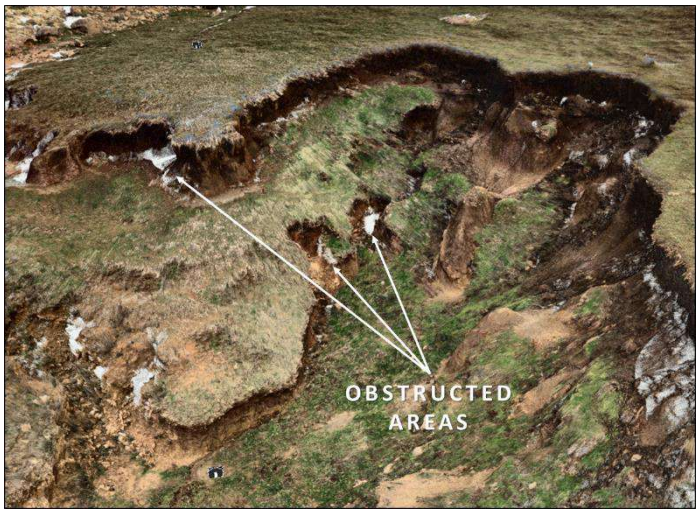

Figure 6. Initial part of gully Santiš represented within collected point cloud

In conclusion, developed systematic TLS survey methodology allowed accurate scanning of complex gully site. As planned, created point cloud successfully covered over 95% of complex gully surface, while obstructed areas were minimalized. Survey planning and preparation phases proved to be crucial for systematic scanning of complex morphological features, especially if multiple surveys and quantification of spatio-temporal changes are required.

Results of conducted survey will be compared with next systematic TLS survey, which is scheduled for June 17, 2020.

REFERENCES

[1] Bremer, M., & Sass, O. (2012). Combining airborne and terrestrial laser scanning for quantifying erosion and deposition by a debris flow event. Geomorphology, 138(1), 49-60.

[2] Castillo, C., Pérez, R., James, M. R., Quinton, J. N., Taguas, E. V., & Gómez, J. A. (2012). Comparing the accuracy of several field methods for measuring gully erosion. Soil Science Society of America Journal, 76(4), 1319-1332.

[3] de Zeeuw-van Dalfsen, E., Richter, N., González, G., & Walter, T. R. (2017). Geomorphology and structural development of the nested summit crater of Láscar Volcano studied with Terrestrial Laser Scanner data and analogue modelling. Journal of Volcanology and Geothermal Research, 329, 1-12.

[4] Fischer, M., Huss, M., Kummert, M., & Hoelzle, M. (2016). Application and validation of long-range terrestrial laser scanning to monitor the mass balance of very small glaciers in the Swiss Alps. The Cryosphere, 10(3), 1279-1295.

[5] Goodwin, N. R., Armston, J. D., Muir, J., & Stiller, I. (2017). Monitoring gully change: A comparison of airborne and terrestrial laser scanning using a case study from Aratula, Queensland. Geomorphology, 282, 195-208.

[6] Goodwin, N. R., Armston, J., Stiller, I., & Muir, J. (2016). Assessing the repeatability of terrestrial laser scanning for monitoring gully topography: A case study from Aratula, Queensland, Australia. Geomorphology, 262, 24-36.

[7] Kromer, R. A., Abellán, A., Hutchinson, D. J., Lato, M., Chanut, M. A., Dubois, L., & Jaboyedoff, M. (2017). Automated terrestrial laser scanning with near-real-time change detection–monitoring of the Séchilienne landslide. Earth surface dynamics, 5(2), 293-310.

[8] Perroy, R. L., Bookhagen, B., Asner, G. P., & Chadwick, O. A. (2010). Comparison of gully erosion estimates using airborne and ground-based LiDAR on Santa Cruz Island, California. Geomorphology, 118(3-4), 288-300.

[9] Rengers, F. K., & Tucker, G. E. (2015). The evolution of gully headcut morphology: a case study using terrestrial laser scanning and hydrological monitoring. Earth Surface Processes and Landforms, 40(10), 1304-1317.

[10] Taylor, R. J., Massey, C., Fuller, I. C., Marden, M., Archibald, G., & Ries, W. (2018). Quantifying sediment connectivity in an actively eroding gully complex, Waipaoa catchment, New Zealand. Geomorphology, 307, 24-37.

[11] van Veen, M., Hutchinson, D. J., Kromer, R., Lato, M., & Edwards, T. (2017). Effects of sampling interval on the frequency-magnitude relationship of rockfalls detected from terrestrial laser scanning using semi-automated methods. Landslides, 14(5), 1579-1592. Schlögel, R

GEOMORPHOMETRY 2020 PERUGIA, ITALY JUNE 22 - 26 2020

The surface stream function: representing flow topology with numbers

John Gallant[§]
CSIRO Land and Water
Black Mountain Laboratories
Clunies Ross St, Canberra ACT, Australia
[§] john.gallant@csiro.au

***Abstract*— This paper introduces the concept of the land surface stream function, a map that labels slope lines in a way that captures the topology of surface flow networks. When combined with elevation, the stream function forms a hydrological, rather than geographical, coordinate system that reflects the organisation of the landscape into nested catchments with hierarchical stream and ridge networks.**

The stream function map dramatically simplifies several otherwise complicated tasks related to the analysis of surface flow paths. It identifies a catchment at any scale with a pair of numbers, the minimum and maximum stream function for the catchment. It supports tracing of catchment boundaries from any point without needing to follow flow pathways within the catchment, and it has the potential to dramatically simplify the construction of surface flow nets for hydrological modelling.

I. INTRODUCTION

Flow across the landscape can be visualized with the aid of contour and slope lines. The shapes of the contour lines convey information about the form of the land surface and show specific features such as ridges, valleys, hilltops, saddles and depressions. Their spacing indicates the slope of the surface. Slope lines follow the direction of steepest descent and represent the paths of water flow across the land surface [1,2]. Slope lines are everywhere perpendicular to contour lines and suitably chosen slope lines divide the landscape into hydrological units of catchments and interfluves. In combination with the contour lines they create an orthogonal curvilinear mesh that can be used to partition the land surface into broad units (Maxwell's Hills and Dales) or more finely into stream tubes and elements for modelling surface flow [3-7]. Slope lines are also the basis for the mathematical formulation of specific catchment area [8].

Contour lines represent lines of constant elevation, but what quantity can be associated with a slope line? The surface stream function assigns values to slope lines so that the difference in value from one slope line to another equals the area between the two slope lines. With the addition of the stream function field, the orthogonal curvilinear mesh of contours and slope lines becomes a physically meaningful coordinate system. It is closely related to the stream function used in groundwater and other fluid flow applications, with the contour lines representing the potential and the slope lines representing the flux but using area rather than an actual material flow; this matches the way specific catchment area is used as a surrogate for flow in surface hydrology.

II. THE STREAM FUNCTION CONCEPT

A. Definitions

The properties of the stream function are intimately connected with the properties of slope lines. Every slope line runs from a peak to a sink, except for particular lines that terminate on a saddle at either the upper or lower end. Maxwell [1] envisaged slope lines running to underwater pits but in practice slope lines are considered to terminate at water bodies (lakes or the coastline). The lines that terminate on a saddle play important roles so are here given specific names:

- A **course line** runs from a saddle to a sink (or coastline)
- A **divide line** runs from a peak to a saddle

The divide and course lines are important *topological* features in the slope line network and the names are chosen to avoid using the names valley and ridge, which are here reserved for *topographic* features. Course lines often run along valleys but not always; likewise divide lines are often found on ridges but not always. In terms of slope lines, these definitions of valley and ridge are adopted here:

John Gallant (2020) The surface stream function: representing flow topology with numbers:
in Massimiliano Alvioli, Ivan Marchesini, Laura Melelli & Peter Guth, eds., Proceedings of the Geomorphometry 2020 Conference, doi:10.30437/GEOMORPHOMETRY2020_60.

- A **valley line** is a slope line to which many slope lines converge in a downslope direction heading towards a sink (or coastline)
- A **ridge line** is a slope line to which many slope lines converge in an upslope direction heading towards a peak

B. Stream function fundamentals

Each slope line has a unique stream function value not shared with any other line. Unlike contours there cannot be multiple disconnected line segments with the same value. The only exception to this is slope lines terminating on saddles where multiple slope lines share a stream function value as shown in the examples below, but even then the multiple line segments all touch at a single saddle.

In general, a point on the landscape has only one slope line running through it so has a single stream function value, but there are important exceptions. Because multiple slope lines connect to each peak, peaks have a range of stream function values. Likewise sinks have multiple slope lines and a range of stream function values. Ridge and valley lines are in practice considered to have a range of stream function values that varies along the line.

The basic relationship between stream function value, denoted by ψ, and conventional ideas of stream tube area and contributing and dispersal areas A and D is that the total area between the two slope lines (the stream tube area, see Figure 1) equals the change in stream function value between the lines:

$$\Delta\psi = \psi_2 - \psi_1 = A + D \quad (1)$$

Stream function is defined here such that ψ increases from left to right when looking downslope. Hence ψ increases when moving along a contour line in a clockwise direction around a peak and in a counter-clockwise direction around a sink. Note that this makes the (ψ, z) coordinate system left-handed (Figure 1).

C. Examples of stream function properties

Figure 2a shows an idealized small island with an area of 100 ha and a single peak in the centre at a height of 100 m. Slope lines are arranged around the island enclosing areas of 10 ha between each pair of lines so the stream function increases by 10 ha from one line to the next.

The location of the slope line with $\psi = 0$ is arbitrary, as only the differences in stream function value have any significance. The stream function increases clockwise around the island and reaches a maximum of 100, the island's area, on the other side of the starting slope line. Every contiguous land mass will have one of these lines of discontinuity where the stream function jumps by the total area of the land mass.

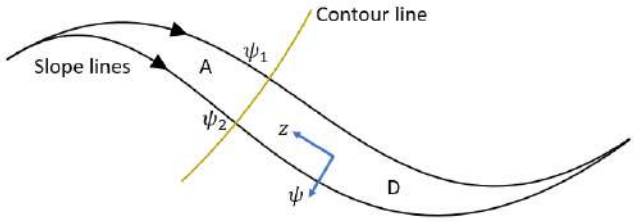

Figure 1. Plan view of a stream tube bounded by two nearby slope lines that terminate or merge at each end. Each slope line has an associated stream function value ψ. At any contour line along the stream tube, the total area of the stream tube is divided into the contributing area A above the contour line and the dispersal area D below the line. ψ and z form a left-handed curvilinear coordinate system.

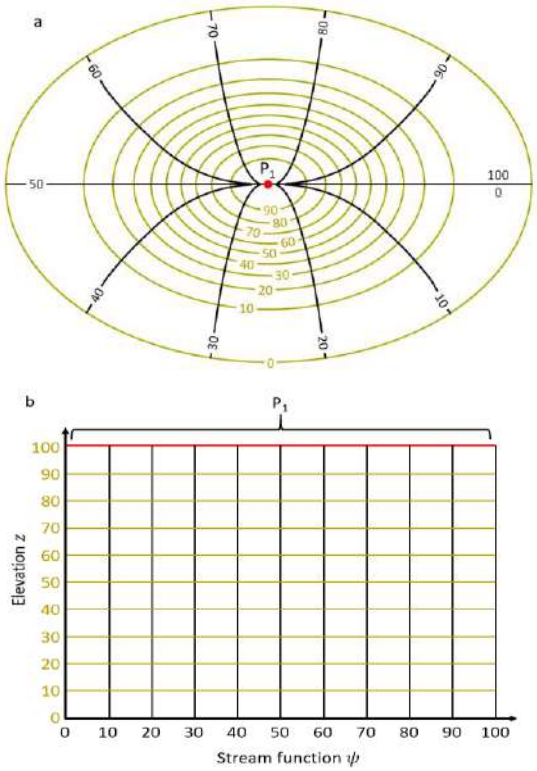

Figure 2. (a) An island of 100 ha area with a single peak P_1 at 100 m elevation. (b) The stream function map for the island showing contour and slope lines parallel to the z and ψ axes.

Figure 2b shows the same island in the hydrological (ψ, z) space. In this representation the contour lines are horizontal since they all have constant z values and the slope lines are vertical with constant ψ values. The peak P_1 appears as a horizontal line since all slope lines connect to it so it includes the full range of stream function values corresponding to the peak's dispersal area.

Figure 3a shows a similar island but with two peaks, P_1 and P_2 at heights of 70 and 100 m. Between the peaks there is a saddle K_1 at a height of about 45 m and the contour at the saddle elevation forms two closed loops in a figure-eight formation. The two peaks P_1 and P_2 still appear as horizontal lines since all the slope lines have their upper end at one of those two peaks.

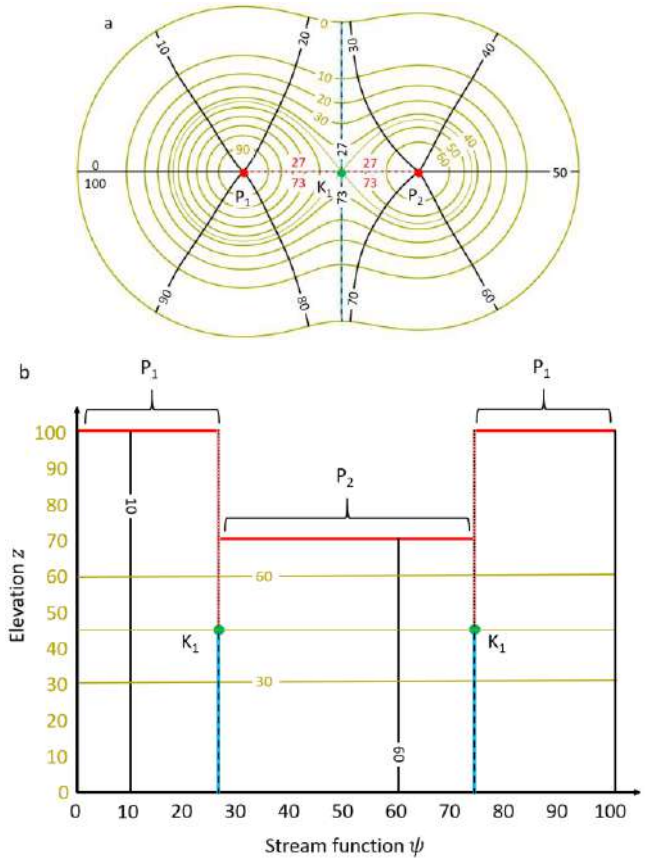

Figure 3. (a) An island with two peaks, P_1 and P_2 at elevations 100 and 70 respectively and an intervening saddle K_1 at an elevation of about 45. Divide lines (red with short black dashes) run from each peak to the saddle and course lines (blue with long black dashes) run from the saddle to both sides of the island. (b) The stream function map for the island showing the saddle K_1 with its two different stream function values. The labelled contour and slope lines correspond to the same labels in (a).

The saddle K_1 introduces significant changes to the topology of the flow lines and therefore changes in the structure of the island in (ψ, z) space. The fact that the saddle point K_1 is connected to two course lines that terminate on opposite sides of the island means that the saddle point has two different stream function values, 27 and 73 (note that integer values of ψ are used here for convenience, in reality they are real values). As a result, the saddle point K_1 appears twice in the (ψ, z) map with the same z but different ψ. The contour line through the saddle appears as a single line in the (ψ, z) map but still crosses K_1 twice because K_1 appears twice in that map. The contour lines at elevations 30 and 60 in the (ψ, z) map appear to both be simple lines, even though the contour at 60 m is two separate loops in (x, y) space. The discontinuity in stream function along the divide lines in (x, y) space is matched by discontinuities in x and y on the divide lines in (ψ, z) space.

The divide lines running from the peaks to the saddle have two stream function values, the same values as the two course lines, reflecting the fact that those slope lines effectively continue past the saddle as course lines to reach the coastline on opposite sides of the island. The dual values are valid on opposite sides of the lines and the values between them are not included: there is no slope line with $\psi = 50$ reaching peak P_1, for example. Divide lines create a discontinuity in the stream function.

Sinks behave in a complementary manner to peaks – they appear in (ψ, z) space as a horizontal line with a stream function range equal to their contributing area. Course lines from saddles connected to sinks have a discontinuity in stream function value.

D. Stream function in a real catchment

Figure 4 shows the geographic and stream function map for a 436 ha catchment in Australia (150° 42′ E 33°16′ S). Ridges and valleys, defined using a threshold area of 10 ha, are identified as thicker red and blue lines in the geographic map and as shaded red and blue areas in the stream function map. Much of the stream function map is occupied by valleys (blue regions) reflecting the fact that most slope lines run for most of their height along a valley line, which will usually be channelled. The branched valley network produces a set of nested truncated triangular regions in the (ψ, z) map. The sloped edges of those regions capture the changing range of ψ along the valley lines.

I. Applications

Because stream function captures flow topology in a numerical system it replaces many otherwise complex flow-tracing operations with much simpler operations. The examples here assume stream function is implemented on a raster where each

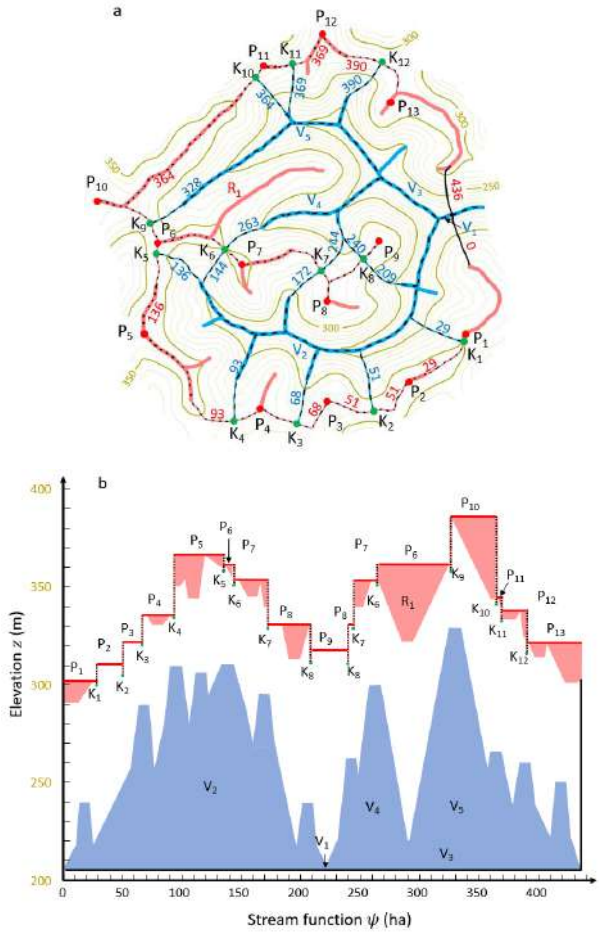

Figure 4. (a) A small catchment with branched ridge and valley networks. (b) The stream function map for the catchment. The blue and red shaded areas correspond to the blue valley lines and red ridge lines in (a).

cell has both a minimum and maximum value of stream function. The difference between the minimum and maximum is the sum of contributing area and dispersal area for the cell, as in Figure 1.

A. Catchments and partial catchments

Stream function defines the catchment of an outlet cell as all the cells satisfying:

$$\psi_{min} \geq \psi_{min,outlet} \text{ and } \psi_{max} \leq \psi_{max,outlet}$$

That inequality can be used to find all cells in a catchment or decide if a single location lies within a given catchment. It is also possible to trace the outline of a catchment using stream function without visiting any of the interior cells.

Along a stream reach from point A to point B, the area on the left side of the stream (looking downstream) has:

$$\psi_{min,A} \leq \psi_{min} \leq \psi_{min,B}$$

while the area on the right side of the stream has:

$$\psi_{max,B} \leq \psi_{max} \leq \psi_{max,A}$$

B. Flow nets for hydrological modelling

The original motivation for developing the stream function map was to simplify the creation of flow nets – all previous methods for producing them are based on contour data. Elements in a flow net are bounded by contour lines and slope lines; in the stream function map, these are just rectangles in (ψ, z) space. Despite this simplicity there are still complexities to overcome, particularly in the automated division of the landscape into elements of roughly uniform size, and the implementation is yet to be completed.

ACKNOWLEDGEMENTS

The development of the stream function concept and its implementations has taken many years. Early steps were supported by the CRC for Catchment Hydrology and Professor Joe Ritchie at Michigan State University. The bulk of the development of the Terrae software implementation was funded by Professor Bruno Basso at University of Basilicata and Michigan State University, and most of the details of the behaviour of stream function were worked out during that period. Prof Michael Hutchinson provided valuable insights at several key points during the development of the stream function methods.

REFERENCES

[1] Cayley, A. 1859. "On contour and slope lines" The London, Edinburgh and Dublin Philosophical Magazine and Journal of Science 18(120): 264-268.

[2] Maxwell, J.C. 1870. "On hills and dales" The London Edinburgh and Dublin Philosophical Magazine and Journal of Science 40: 421-427.

[3] Onstad, C.A. and Brakensiek, D.L. 1968. "Watershed simulation by the stream path analogy" Water Resources Research 4(5): 965-971.

[4] O'Loughlin, E.M. 1986. "Prediction of surface saturation zones in natural catchments by topographic analysis." Water Resources Research 22(5): 794-804.

[5] Moore, I.D. and Grayson, R.B. 1991. "Terrain-based catchment partitioning and runoff prediction using vector elevation data." Water Resources Research 27(6): 1177-1191.

[6] Dawes, W. R. and Short, D. 1994. "The significance of topology for modeling the surface hydrology of fluvial landscapes." Water Resources Research 30(4): 1045-1055.

[7] Moretti, G. and Orlandini, S. 2008. "Automatic delineation of drainage basins from contour elevation data using skeleton construction techniques." Water Resources Research 44: W05403.

[8] Gallant, J.C. and Hutchinson, M.F. 2011. "A differential equation for specific catchment area." Water Resources Research 47: W05535.

GEOMORPHOMETRY 2020 PERUGIA, ITALY JUNE 22 - 26 2020

The D8 implementation of the surface stream function

John Gallant[§]
CSIRO Land and Water
Black Mountain Laboratories
Clunies Ross St, Canberra ACT, Australia
[§] john.gallant@csiro.au

Abstract— **The land surface stream function has the potential to simplify many tasks related to the analysis of surface flow paths, but a practical implementation is required to make it usable. Three implementations of varying complexity have been developed and the simplest, based on D8 flow paths, is described in detail.**

While this simple method lacks fidelity to true flow paths it provides a usable approximation to the true stream function whenever areas anchored on stream channels are considered. To each cell, the method assigns a minimum and maximum stream function that can be used to delineate catchments and trace catchment boundaries without working through the interior of the catchment. It is not suitable for creating flow meshes because it ignores dispersal area.

I. Stream Function Implementations

The concept of the land surface stream function [1] is very appealing and provides a novel and informative way of viewing catchment structure. But a practical implementation is required before it can be used with real data.

Producing a stream function map from a grid digital elevation model is not a simple task. The method must capture the locations of peaks, sinks and saddles, construct the various lines – divide, course, ridge and valley lines – and calculate stream function on a regular grid accounting for the discontinuities along divide and course lines.

The general approach is to calculate contributing area A and dispersal area D within each cell or on each cell edge and use the sum $A + D$ as the difference in stream function in the cell or across the cell edge. The stream function value can then be accumulated from one cell to the next starting at an arbitrary zero point and accounting for the discontinuities and merging of lines.

Three implementations have been developed with varying degrees of simplification. The simplest method adopts the extreme simplification of forcing all slope lines to converge to a single line in each grid cell and uses the single-direction steepest descent to construct the slope lines between cells. Under this construction there are no dispersal areas and the stream function calculation closely follows the calculation of contributing area using the D8 method. Following the cell-to-cell connectivity in an orderly manner, each cell is assigned a minimum and maximum stream function value and the difference in values exactly equals the cell's D8 contributing area. Prior identification of peaks, sinks and saddles is not required in this method provided there are no depressions, which matches the typical application where contributing area is calculated. Peaks and ridge lines are considered to be located on cell corners and edges and their dispersal area is represented by the gap in stream function ranges for adjacent cells. While this extreme simplification prevents the proper construction of stream tubes and hillslope flow elements it still allows some of the most useful applications such as tracing catchment boundaries from points along streams and computing the hydrological significance of ridge lines.

The second method is a detailed implementation known as Terrae (outlined in [2]). It uses a novel method for computing A and D that assigns values to cell edges, allows convergence and divergence within cells and takes measures to control artificial dispersion. It identifies peaks, sinks and saddles and assigns dispersal and contributing areas to peaks and sinks respectively. Divide and course lines are explicitly constructed, and the magnitude of stream function discontinuity is assigned to each line using the peak and sink areas, accumulating values along chains of divide and course lines as needed. The stream function difference along each cell edge is $A + D$ plus the contributions from any discontinuities, with the sign defining positive or negative change in a clockwise direction. For each cell the sum of stream function differences around the four cell edges is zero except where the cell contains a peak or a sink. Starting at an arbitrary point a stream function value of zero is assigned to a cell corner and the difference in value along the edge, plus the change across any discontinuity, allows the stream function value to be

John Gallant (2020) The D8 implementation of the surface stream function:

in Massimiliano Alvioli, Ivan Marchesini, Laura Melelli & Peter Guth, eds., Proceedings of the Geomorphometry 2020 Conference, doi:10.30437/GEOMORPHOMETRY2020_61.

assigned to the corner at the far end of the edge. This process is repeated until all corners have been given a value. The method is complicated by the need to trace every divide and course line, including merging of lines along ridges and valleys, and to capture the discontinuity in stream function on every cell edge crossed by one of those lines.

The third method was inspired by the stark contrast in complexity for the first two methods. How can the very simple method capture the discontinuities at divide and course lines without having to explicitly identify them as Terrae does? The answer is that by following the tree structure of the steepest descent paths the simple method automatically steps around the discontinuities that are, as noted before, located on cell edges and corners. When slope line divergence and convergence are allowed, as in the full Terrae method, there is no simple tree structure to follow but the lines of discontinuity can still be forced to cell edges without much distortion of the stream function. This requires identification of peaks, sinks and saddles and those divide lines and course that contain discontinuities, as in Terrae, but there is no need to determine the change in stream function at the discontinuities. For this method to work, stream function values must be recorded at both ends of each cell edge so that the stream function value on an edge can take on different values on either side of the edge. After calculating A and D values for every cell edge the accumulation of stream function values can proceed as in Terrae but values are not propagated across divide and course lines that have discontinuities. Because a saddle creates discontinuities along either divide *or* course lines – never both – there is always a path to propagate stream function values around the end of discontinuities. When the full set of stream function values has been calculated the change in stream function across each discontinuity is automatically captured.

The simplest D8-based method is described here. The other methods will be described in papers currently in preparation and the implementations will be released with the papers.

II. THE D8 STREAM FUNCTION METHOD

In this method each cell is divided into 8 triangular segments and the stream function is calculated in units of 1/8 of cell area, so integer values can be used. Each cell is assigned a minimum and maximum stream function value.

Figure 1 shows a simple example for illustration of the method. The calculation starts at an arbitrary cell on a boundary (edge of DEM or coastline) that has an outflow, and the initial stream function value of 0 is assigned as the minimum value for that cell. In Figure 1 there is only one outflow cell, so that is the starting cell.

Within the cell being processed, each potential inflowing direction is considered in sequence in a counter-clockwise direction, starting from the outflow direction, and the stream function is incremented once for each change of direction. If an

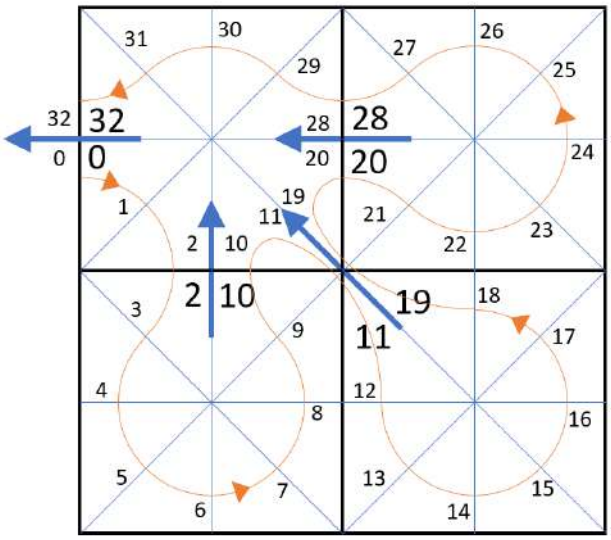

Figure 1. A simple D8 flow network showing flow paths (blue arrows) between cells (black squares). The cells are divided into eights representing the areas between each potential inflow direction (thin blue lines). The sequence of processing stream function is shown by the orange line and arrows. Stream function at each step is shown by the smaller numbers, while the larger numbers are the minimum and maximum stream function allocated to each cell.

inflow is found, the calculation shifts to the source cell and again starts by setting the cell's minimum stream function value to the current value and setting the flow direction to the cell's outflow direction.

When all eight inflowing directions have been considered and the flow direction matches the cells outflow direction, the cell's maximum stream function is set to the current stream function value and processing shifts to the downstream cell with the flow direction set to the inflow direction from the cell that has just been finished.

When the processing finishes tracing the tree for the initial cell, which has an outflow that exits the DEM or land area, the boundary is traced in a clockwise direction looking for another outflow that has not already been processed. If there are multiple disconnected land areas (islands), the search for an unprocessed outflow should continue across the DEM and each separate boundary traced to find all outflows.

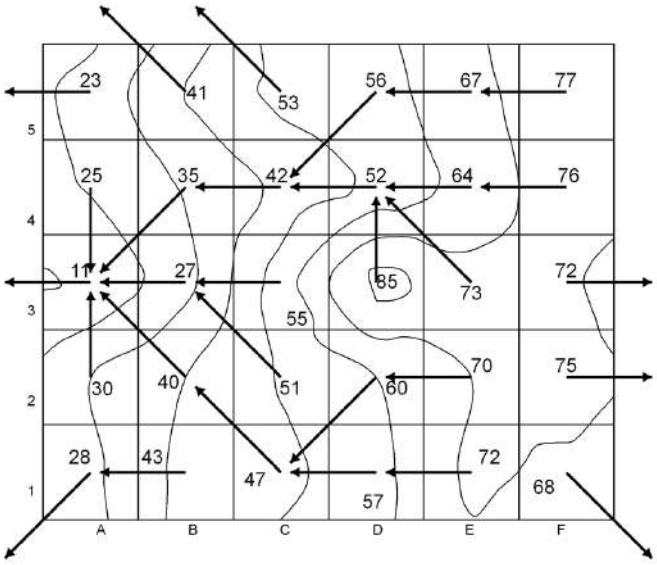

Figure 2. A synthetic example showing elevations, flow directions and contours (curved lines).

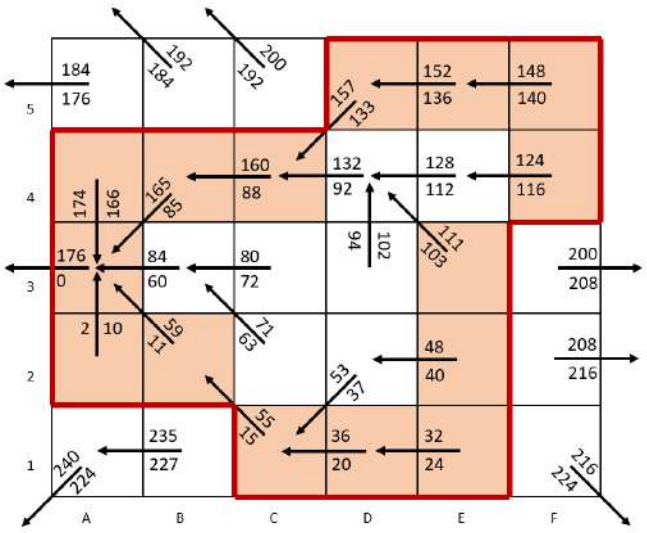

Figure 3. Minimum and maximum stream function values for the flow network of Figure 2. The shaded cells are the catchment boundary cells identified by the boundary tracing algorithm, and the catchment boundary itself is the outer edges of those cells, highlighted in red.

The path of processing and the intermediate stream function values are shown in Figure 1, as well as the minimum and maximum values assigned to each cell.

Figure 2 shows a larger area with a more complex flow network, labelled with elevations and showing contours. Most of the area is occupied by a single catchment that flows across the boundary of the DEM at cell A3. Figure 3 shows the stream function values for the same flow network.

III. Stream Function Applications

A. Contributing area

The difference in D8 stream function value between minimum and maximum is equal to the D8 contributing area of each cell, measured in units of 1/8th of the cell area. The stream function method takes only marginally more time to compute than contributing area and produces contributing area (in cells) as well as the two stream function results:

$$A = \frac{\psi_{max} - \psi_{min}}{8}$$

Note that this equation does not apply to stream function in general, only to this specific implementation where dispersal area is always zero due to the way flow paths are treated.

B. Catchment delineation

Given a cell A, any cell with stream function values within the range of that cell are inside the catchment of that cell. The catchment of cell A is comprised of all cells satisfying:

$$\psi_{min} > \psi_{min,A} \text{ and } \psi_{max} < \psi_{max,A}$$

This pair of conditions can be used to find all the cells that are within the catchment area of cell A, or to test whether an individual cell lies within cell A's catchment.

C. Measuring the hydrological significance of divide lines

The change in stream function across a divide line is a measure of the hydrological significance of the divide. For a minor divide where the slope lines either side of the divide converge after only a short distance, the difference in stream function is small. On a major divide, where the slope lines might not converge at all before they reach a coastline, the difference in stream function is large. This is similar to the maximum branch length described by Lindsay and Seibert [3] except that the difference in stream function value represents the area between the two slope lines rather than the length.

In the D8 implementation of stream function, the divide is between cells, so values in adjacent cells must be used, not the difference between maximum and minimum value in a single cell.

D. Tracing a catchment boundary

The D8 stream function supports tracing of catchment boundaries with a very simple algorithm. Starting at a catchment outlet, such as cell A3 in Figure 3, the minimum and maximum stream function values are noted. A current direction is set to the outflow direction for the starting cell. The adjacent cells are then examined, starting from the current direction and proceeding in a clockwise direction, looking for a cell that has stream function values within the range of the outlet cell. When such a cell is found, processing moves to that cell and it is marked as part of the catchment boundary. The current direction is reversed so that it points to the previous cell, and then rotated one step clockwise before continuing the examination of the adjacent cells. The process repeats until it arrives back at the starting cell. Figure 3 shows the cells identified by the boundary tracing algorithm starting at cell A3. The cells identified by this process are inside the catchment boundary and the boundary itself is the outer edges of those cells, identified by the heavy red line in Figure 3.

This algorithm is used by DamSite [4], a tool for identifying topographically favourable sites for constructing new dams. The DamSite method uses the set of catchment boundary cells identified using the D8 stream function to ensure that all saddle dams are accounted for, no matter how far from the main dam wall, when estimating the dam construction cost.

IV. CONCLUSIONS

The D8 implementation of the stream function is a very crude approximation to the full stream function because it completely ignores dispersal areas, but it captures many of the useful features of the stream function such as delineation of catchment areas and catchment boundaries. The algorithm to compute it is fast and takes little more computation than D8 contributing area.

REFERENCES

[1] Gallant, J.C., 2020. “The surface stream function: representing flow topology with numbers”. Geomorphometry 2020.

[2] Gallant, J.C. and Basso, B., 2013. “Creating a flow-oriented modelling mesh using the stream function”. Abstract for MODSIM2013, International Congress on Modelling and Simulation, Adelaide, 1-6 Dec 2013. https://www.mssanz.org.au/modsim2013/documents/MODSIM2013_Abstracts.pdf

[3] Lindsay, J.B. and Seibert, J. 2013. “Measuring the significance of a divide to local drainage patterns.” International Journal of Geographical Information Science 27(7):1453-1468. http://dx.doi.org/10.1080/13658816.2012.705289.

[4] Petheram, C., Gallant, J.C. and Read, A.M., 2017. "An automated and rapid method for identifying dam wall locations and estimating reservoir yield over large areas." Environmental Modelling and Software 92:189-201. http://dx.doi.org/10.1016/j.envsoft.2017.02.016.

GEOMORPHOMETRY 2020 PERUGIA, ITALY JUNE 22 - 26 2020

Second-order derivatives of microtopography for evaluating soil erosion

Michal Gallay §1, Jozef Minár[2], Ján Kaňuk[1], Juraj Holec[3], Anna Smetanová[4]
1 - Institute of Geography
Faculty of Science, Pavol Jozef Šafárik University in Košice, Košice, Slovakia
2 - Department of Physical Geography and Geoecology, Faculty of Natural Sciences, Comenius University, Bratislava, Slovakia
3 – Slovak Hydrometeorological Institute, Bratislava, Slovakia
4 – Research Group Ecohydrology and Landscape Evaluation, Technische Universität Berlin, Berlin, Germany

§ michal.gallay@upjs.sk

Abstract— **The relation of soil erosion induced by water and land surface morphology is usually reasoned by the influence of slope angle and slope length, or contributing area on the erosion-accumulation processes. These assumptions about geomorphometric properties often fail in flat topographies cultivated by humans in a long-term time span. This paper demonstrates the potential of various land surface curvatures in explaining the mosaic of erosion-accumulation processes in such flat regions taking the example of loess table of Danube Lowland (Slovakia). The area is covered by chernozems where erosion manifests itself as bright patches on aerial photographs for the reduced humic horizon. Soil samples from 185 soil cores are compared with the mosaic of various subforms of plan and profile curvature and also with mean and difference curvature and from *Index of Slope Energy Disequilibrium* (*ISED*). The analyses assumed generating a highly detailed and accurate terrain model capturing microtopography of the flat landscape. Curvatures that are best interpretable from the physical aspect are important for such an application. The historical structure of the land parcels determined the direction of ploughing. The historical structure mirrors itself in curvatures also after the land consolidation. The ISED parameter appears to be the most suitable in this context.**

I. INTRODUCTION

Soil erosion has been accompanying human land use and land management through millennia [1, 2]. Dependence of soil erosion on the geomorphometric variables reflects all generally used models of the soil erosion. Majority of them (e.g. RUSLE) consider a dependence of soil erosion on the slope gradient and slope length or contribution area. Only exceptionally the land surface curvatures are used, despite the influence of plan curvature on convergence or divergence and profile curvature on acceleration and deceleration of gravity flows is long term known, e.g. [3]. A suitable expression of the interplay of plan and profile curvature in the soil erosion process is a crucial problem. [4] suggested such unification of the influence of these two in the case of the transport capacity limited process. In their approach, the resultant net erosion/deposition is proportional to the sum of the plan and profile curvature, i.e. to the mean curvature.

We have derived a more general approach based on the analysis of Potential Energy on the land Surface applicable to mass flow - PES [5]. It points to the importance of the difference of profile and plan curvatures (i.e. difference curvature) on the erosion-accumulation process. Tillage erosion is a very important factor in relatively flat areas. Recent but also historical land use (size and orientation of fields) play a significant role not only in the soil profile change but also in microtopography modification. The last can also be identified using land surface curvatures.

A comparison of spatial variability of the soil erosion and land use structure and various kind of land surface curvatures is the main goal of the paper. However, because the soil erosion process is influenced by landforms of a small dimension and computation of land surface curvatures is strongly influenced by the DEM error, very detailed and precise DTM is a basic precondition for the realization of this goal.

II. METHODS

A. Study area

The Voderady study area is situated in the northwestern part of the Danube Lowland, in the Southwest Foreland of the West Carpathians (48°17'01.4"N, 17°34'45.5"E) [6]. It belongs to the Trnavská pahorkatina Hilly Land - one of five loess hill-dominated lands within the region. The study area is characterized by relatively flat topography partially transformed by Quaternary

Michal Gallay, Jozef Minar, Jan Kanuk, Juraj Holec and Anna Smetanova (2020) Second-order derivatives of microtopography for the evaluation of soil erosion: in Massimiliano Alvioli, Ivan Marchesini, Laura Melelli & Peter Guth, eds., Proceedings of the Geomorphometry 2020 Conference, doi:10.30437/GEOMORPHOMETRY2020_62.

tectonic uplift of micro-blocks up to 15 m above sunken micro-blocks [7]. The study area covers 2.6 km^2 with a part of a dry shallow valley situated on an uplifted block in the central part of the area (Fig. 1). The altitudes range from 122 to 147 m above sea level. The ridges are asymmetric in their altitude and slope with steeper SW-oriented hillslopes (up to 8°), while the majority of slopes lie between 0.75 and 3.5° in the area (Fig. 2). The valley bottom, in the central part of the area, is characteristic by concave-concave morphometric forms and slopes with inclination 0–1.7°. On the hillslopes, convex-convex morphometric forms are prevailing.

B. Soil erosion and related data

Soil erosion strongly influences the Chernozems in loess hilly land in the Slovak part of the Danube Lowland. It leads to the transformation of the original humus horizon to a brighter less humic horizon, which is easily distinguishable in terrain or on aerial photographs. Bright patches consist of eroded, non-eroded and accumulated soils. In non-eroded and accumulated parts, the mollic horizon is thicker due to in-situ development or accumulation of humus-rich material transported from the upper parts of slopes. The tilled parts of soils are being changed by the incorporation of bright material transported from eroded parts of slopes. There-fore visual interpretation of aerial images could bring incorrect results.

The more realistic picture of soil erosion is provided by the records of erosion and deposition from 314 soil cores [2, 8]. Difference between depth of the humic horizon in a given site and a standard depth of the humic horizon (not influenced by erosional – depositional processes) we considered as a measure of erosional (-) and depositional (+) processes (Fig. 1). As preliminary results pointed to a probable influence of the tillage erosion, the structure of historical land use was investigated too. The aerial orthoimagery valid to 1949 was used for visual comparison with the pattern of curvatures of the contemporary terrain surface. The historical orthoimage documents the distribution and orientation of small fields before the collectivization stage (Fig. 1).

C. Close-range UAV photogrammetry

The area was flown in two days of March 2018 with an unpiloted aerial quadcopter DJI Phantom 4 with an integrated 12-megapixel FC330 camera (focal length 3.61 mm) mounted on 3-axes gimbal. Prior to the flight, 19 ground control points (50 by 50 cm wooden cross marks) were placed in the field and located by a dual-frequency GNSS receiver Topcon Hyper II using real-time kinematic positioning method with a mobile broadband connection to the network of the Slovak real-time positioning service (SKPOS) within the national S-JTSK03 coordinate system (EPSG code: 5514) with vertical datum Baltic after adjustment (Bpv). The overall accuracy of the RTK GNSS positioning ranged between 1–2 cm (1σ). There were 2,244 natural colour images

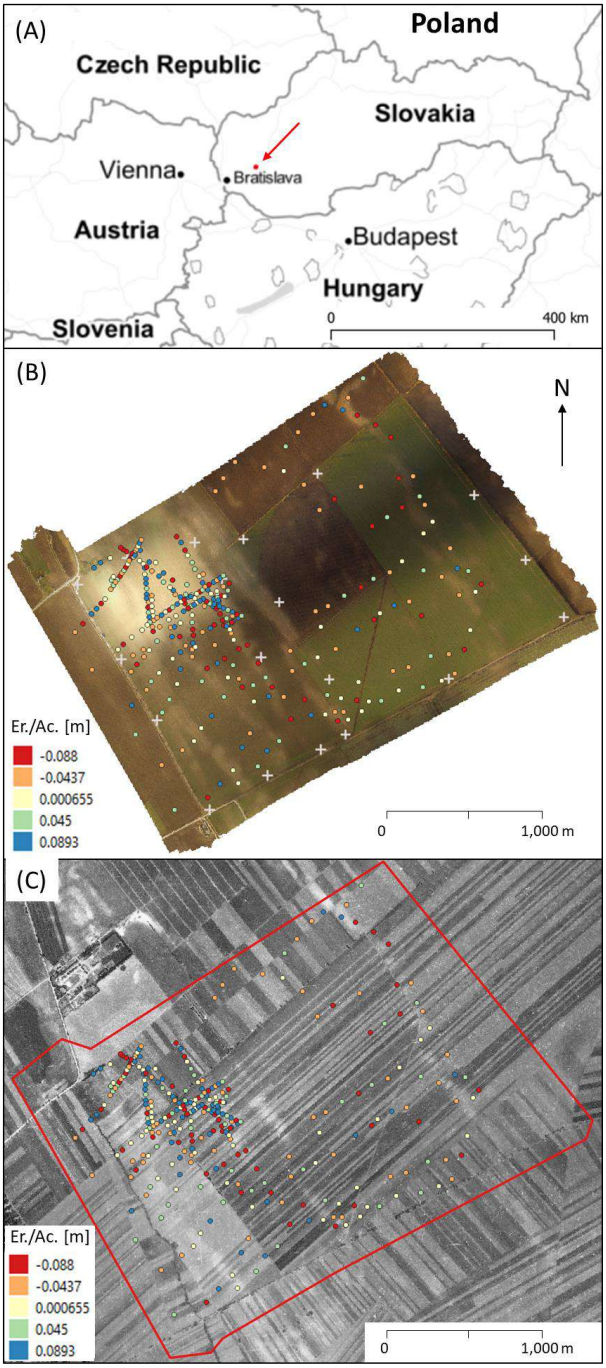

Figure 1. (A) Location of the study site in Slovakia, Central Europe with (c) Stamen Design Toner background layer. (B) Orthophotomosaic from UAV imagery acquired on 14 March 2018 with ground control points (grey cross hairs) and soil sampling locations coloured by the rate of erosion and accumulation in meters, (C) Orthophotomosaic from 1949 with the same soil sampling locations overlaid.

taken during 6 flights of 20 minutes duration from about 90 meters above the ground. The acquired imagery was processed by image matching method based on structure from motion in the Agisoft PhotoScan v1.4.1 software resulting in 3D point clouds and orthoimagery. Over 172 million points were extracted achieving an average point density of 55 points per m^2 a pixel size of 3.4 cm. The topography was reconstructed and from 4 to 9 overlapping images with a root mean square reprojection error of 0.85 pixels.

The original point cloud did not require extensive filtering of above-ground surface objects as the land was smoothly ploughed without crops on 2/3 of the area. About 1/3 were grown by wheat plants of 5 cm height which were not distinguishable from the ground (Fig. 1B). Points on trees and bushes were manually removed.

D. Digital terrain modelling

The cleaned point cloud was used to interpolate a digital terrain model (DTM) in the GRASS GIS software by regularized spline and smoothing implemented as the parallelized v.surf.rst module [9]. Default settings were used to generate a DTM of 25 cm cell size. The DTM was resampled to 2.25 x 2.25 m resolution by fitting a bivariate quadratic polynomial to a 9 x 9 cells moving window using least squares [10] implemented within the r.param.scale module of GRASS GIS. The purpose was to capture landforms above the scale level of particular furrows. Following land surface variables were then computed from the generalized DTM: slope gradient – S; profile curvature as normal slope line curvature [11] - $(k_n)_s$; profile curvature as the 2nd slope line derivative of altitude [12]; plan curvature as normal contour line curvature [13] – $(k_n)_c$; plan curvature as 2nd contour line derivative of altitude [12].

Mean curvature: $k_{mean} = \frac{(k_n)_s + (k_n)_c}{2}$

Difference curvature: $k_d = \frac{(k_n)_s - (k_n)_c}{2}$

Index of Slope Energy Disequilibrium [5]:

$$ISED = \frac{50 k_d}{\sin S}$$

The ISED expresses the percentage deviation of unit gravitational Potential Energy of Surface (PES) for mass flow from an equilibrium state.

III. Results and Discussion

The resulting data involve second-order derivatives as raster maps of parameters derived from the DTMs. Some of them are displayed in Fig. 2. The land surface curvatures provide generally higher correlation with erosion than the slope angle. The plan, profile, and mean curvatures (Fig.2) mirror the contemporary but also past cultivation/land use (Fig.1). The ISED parameter fuses the used curvatures and appears to be more relevant than the typically used kinds of curvature. The NE-SW oriented spatial structures visible in 1949 orthoimage are indicated by ISED. ISED pattern partially also follows the NW-SE direction of patterns from margins of the area. However, the scatterplot in Fig. 3 does not indicate a clear correlation of ISED and erosion/accumulation rates measured from the soil samples.

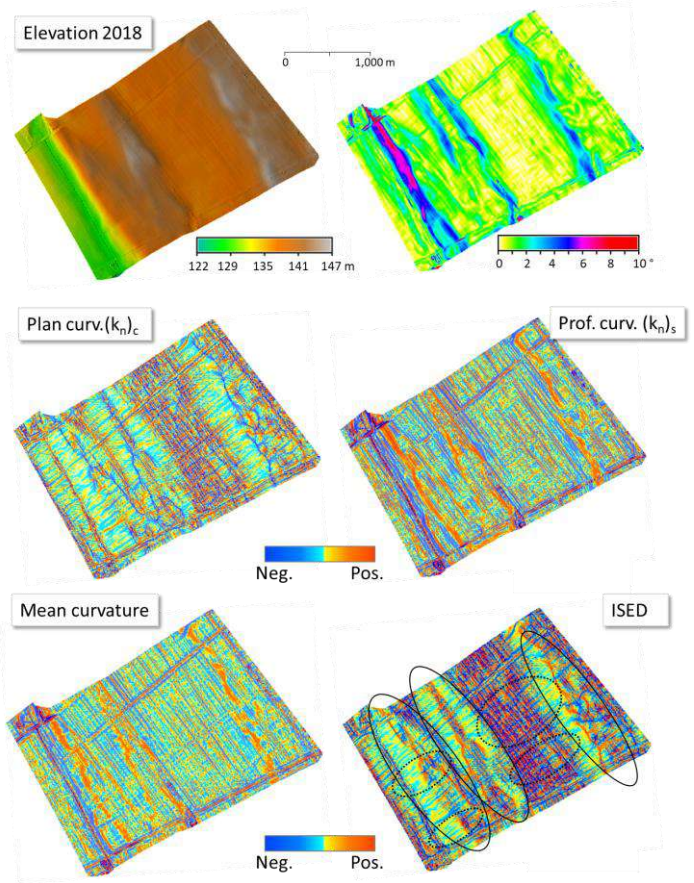

Figure 2. Terrain elevation and slope angle, and second-order elevation derivatives: plan curvature $(k_n)_c$, profile curvature as normal slope line curvature $(k_n)_s$ mean curvature, and index of slope disequilibrium (ISED) annotated with ellipses marking the reduced humic horizon (black solid line ellipses) and possible old morphological features resulting from past cultivation (black dotted ellipses).

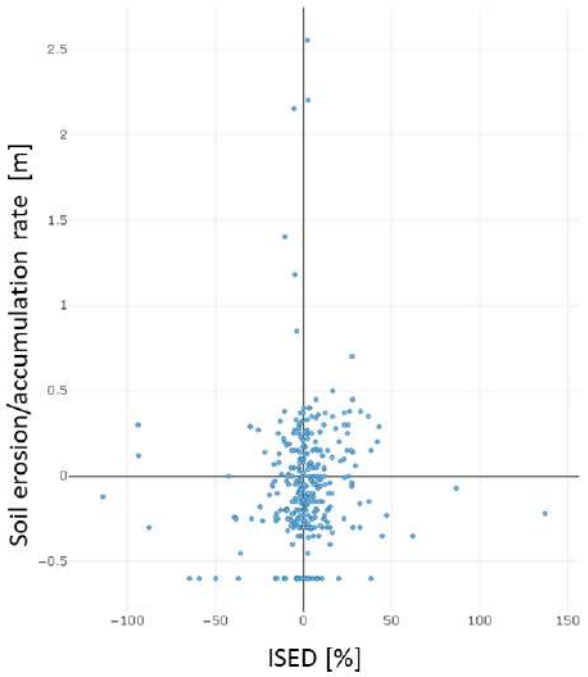

Figure 3. Scatterplot of the index of slope energy disequilibrium (ISED) and soil erosion (-)/accumulation (+) rate in meters.

IV. Conclusions

We used a high-resolution digital terrain model to derive first and second-order derivatives of elevation in a cultivated area with mild vertical relief and smooth topography. The pattern of cultivation at present markedly differs from the pattern from 70 years ago. The curvatures and index of slope disequilibrium (ISED) visually well correspond with the pattern of long-term erosion accumulation (with patches of the reduced humic horizon) but they also depict the pattern preserved from past cultivation (i.e. tillage direction). The newly defined ISED parameter was applied and it -better identifies both patterns. The visually apparent relationship of curvature-based parameters and erosion/accumulation values from soil cores is not convincingly supported by statistical analysis carried out so far. One of the reasons can be in varying scale-dependency of erosion and accumulation across the study area which requires further study. Therefore, the next steps will focus on multiscale analysis of the geomorphometric parameters and their relation with the field measured soil erosion/accumulation rate.

V. Acknowledgment

The research was financially supported by the Slovak Research and Development Agency (APVV, Grant nr. 15-0054).

References

[1] Dotterweich, M. (2008). The history of soil erosion and fluvial deposits in small catchments of central Europe: deciphering the long - term interaction between humans and the environment—A review. Geomorphology, 101, 192–208.

[2] Smetanová, A., Verstraeten, B., Notebaert, B., Dotterweich, M., & Létal, A. (2017). Landform transformation and long - term sediment budget for a Chernozem - dominated lowland agricultural catchment. Catena, 157, 24–34.

[3] Young, A., 1972. Slopes. Oliver and Boyd, Edinburgh.

[4] Mitas, L., Mitasova, H., 1998. Distributed soil erosion simulation for effective erosion prevention. Water Resources Research 34 (3), 505–516.

[5] Minár, J., Bandura, P., Holec, J., Popov, A., Gallay, M., Hofierka, J., Kaňuk, J., Drăguţ, L., Evans, I.S., 2018. Physically-based land surface segmentation: Theoretical background and outline of interpretations. PeerJ Preprints 6:e27075v1

[6] Minár, J., Bielik, M., Kováč, M., Plašienka, D., Barka, I. , Stankoviansky, M., Zeyen, H. (2011). New morphostructural subdivision of the Western Carpathians: an approach integrating geodynamics into targeted morphometric analysis. Tectonophysics, 502 (2011), pp. 158-174,

[7] Stankoviansky M., 1993, Vývoj reliéfu južnej časti Trnavskej tabule, Geografický časopis, 45, 1, 93–107.

[8] Smetanova, A., Burian, L., Holec, J., Minár, J. (2016): Bright patches on chernozems - from space to surface and soil properties. Geophysical Research Abstracts, 18, EGU2016-13499, European Geoscience Union, General Assembly.

[9] Hofierka, J., Lacko, M., Zubal, S., 2017. Parallelization of interpolation, solar radiation and water flow simulation modules in GRASS GIS using OpenMP. Computers & Geosciences. 107, 20–27.

[10] Wood, J., 1996. The Geomorphological characterisation of Digital Elevation Models. Diss., Department of Geography, University of Leicester, U.K online at: http://hdl.handle.net/2381/34503

[11] Krcho, J., 1973. Morphometric analysis of relief on the basis of geometric aspect of field theory. Acta Geographica Universit. Comenianae, Geographico–physica No 1, pp. 7–233.

[12] Zevenbergen, L.W., Thorne, C.R., 1987. Quantitative analysis of land surface topography. Earth Surface Processes and Landforms 12 (1), 47–56.

[13] Krcho, J. 1983. Teoretická koncepcia a interdisciplinárne aplikácie komplexného digitálneho modelu reliéfu pri modelovaní dvojdimenzionálnych polí., [Theoretical conception and interdisciplinary applications of the complex digital model of relief in modeling bidimensional fields]. Geografický časopis 35 (3), 265–291 (in Slovak).

GEOMORPHOMETRY 2020 PERUGIA, ITALY JUNE 22 - 26 2020

Response of alluvial river to active faulting example form Peninsular India

Biju John[1], Divyalakshmi KS, Yogendra Singh, Dhanil Dev SG
National Institute of Rock Mechanics, Seismotectonic Department,
Eshwar Nagar, Banashankari Bangalore 560070
Karnataka, India
[1]b_johnp@yahoo.co.in

***Abstract*-Alluvial rivers are highly sensitive to vertical adjustments along the faults that located across the river channels. The present study identified a pattern change of an alluvial river from the East coast of India, an oldest continental boundary in the Indian landmass. The study identified the structures responsible for the pattern change and the style of movement that caused the forced meandering. These structures are oriented along the NW-SE direction which is considered as favourable for movement in the present tectonic regime.**

I. INTRODUCTION

The east coast is the oldest continental boundary in Indian landmass (120 Ma since separation form Gondwana). The rocks in this region are highly weathered with laterite cover. The NW-SE trending Gundalakama fault is the prominent seismogenic structure that generated significant seismicity. During the routine geological investigation the authors came across the anomalous meandering path of Manneru river which is flowing along a gentle slope and having sharp turn. This lead us to a curiosity to understand the nature and reason for the pattern and whether it have any relation with active tectonism.

Geomorphic evaluation is a possible method for the analysis of alluvial river dynamics for identification of active faults [1]. The present study carried out under the presumption that even the smallest changes in topography affect the sinuosity of low gradient rivers [2]. In the present study also the attempt has been made to find the style of ongoing tectonic activity in the study area, along the east coast of India, by analysing the fluvial morphology of NE-SW trending Manneru River.

II. STUDY AREA

The area comprises metamorphic rock of Archean age overlined by Gondwana sedimentary rock, laterite and alluvium. The marine, fluvio marine and fluvial deposits are of quaternary age (Pleistocene – Holocene) with small outcrops of laterite of Pleistocene age observed in the coastal tract [3]. This area is broadly falling under Seismic zone III of seismic zonation map of India, Moderate damage corresponding to intensity VII of MM scale [4], and has also experienced couple of micro earthquakes in the recent past.

Upputeru is the tributary of the major river Manneru which is debouching into bay of Bengal. In general both the rivers flows along SW to NE and at Sanampudi it takes a right angled turn towards south east along a straight course and finally debouches into the Bay of Bengal. Although Upputeru and Mannar rivers show meandering as it is flowing through very gentle slope, the straight segments between meanders are the anomalies in this terrain.

III. METHODOLOGY

In the present study ASTER DEM is utilized for extracting the tributaries/ drainages. The same has been validated by extracting the drainage pattern from 1:50000 scale toposheets. Delineation of the lineament is carried out by using the Landsat 7 and Liss IV data. The major course of the river is segmented for different reaches based on change in style of course and sharp turn. River sinuosity index (SI) is calculated carried out as per the formula given in Table 1. Further the lineaments are identified as faults based on the field observations.

Table 1: Formula used for calculating the River Sinuosity

Indices	Formula	Remarks
River Sinuosity (SI)	SI =Curved Length of Drainage Segment/ Straight Length of Drainage Segment	[5]

IV. ANALYASIS

A. Lineaments and drainage

There are three prominent lineaments identified in the area. The NE-SW lineament 'L1' follows the course of the Upputheru and Manneru rivers (Fig. 1). There are two NW-SE trending lineaments, namely L2 and L3, influencing the course of NE trending rivers of the area. Two drainages, both named Upputeru, are joining at Pedapavani. After the confluence the Upputeru river further flow towards NE to join Manneru river near Manchavaram, where the lineament L2 is also crossing the river (Fig. 1). A small river named Elikeru which is flowing in the eastern side of the river is also

Biju John, KS Divyalakshmi,Yogendra Singh, SG Dhanil Dev (2020) Response of alluvial river to active faulting example form Peninsular India: in Massimiliano Alvioli, Ivan Marchesini, Laura Melelli & Peter Guth, eds., Proceedings of the Geomorphometry 2020 Conference, doi:10.30437/GEOMORPHOMETRY2020_63.

influenced by the L2 lineament and takes a right angled turn towards right to debouch into Bay of Bengal. It should be noted that some studies in peninsular India identified NW-SE trends as one of the favourable orientation for faults for reactivation in the present tectonic regime [6].

Both Upputeru and Manneru rivers are flowing through gentle slope and show strong meandering. However, after their confluence, the river goes through relatively straight path before forming another meander. The river takes a sharp turn towards SE along L3 lineament and follows a straight course to enter into Bay of Bengal.

B. River Sinuosity (SI)

As mentioned earlier the river has been divided into 10 segments to compare the sinuosity. The main trunk of the Manneru river is divided into six segments (Fig.1) where the main Upputeru river is divided into three for the calculation. The data shows that the manner river show highly anomalous (SI=1.61) in the third segment(Table 2). The subsequent segment (segment 4), however show a low anomaly (SI =1.25). The high value repeated in the downstream (segment 5; SI = 1.61) before it takes a sharp turn. The sinuosity value is the lowest one (1.08) in this segment (segment 6) which is debauching into Bay of Bengal. Similarly, Upputheru river show relatively low meandering values except for the segment (segment 9) joining Manneru river (SI =1.37).

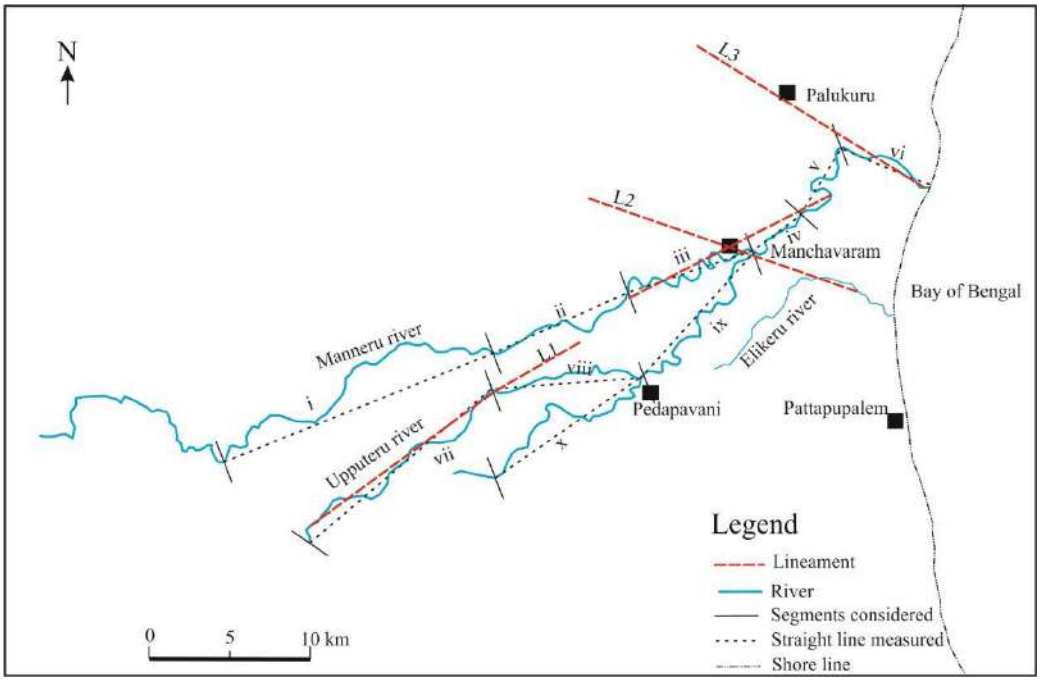

Figure 1: Anomalous pattern of Manneru and Upputeru Rivers

Table 2: River sinuosity calculated

Segment no	SI value
i	1.252
ii	1.163
iii	1.615
iv	1.250
v	1.610
vi	1.087
vii	1.202
viii	1.190
ix	1.370
x	1.330

C. Field Observations

During the search for the reasons of river pattern anomaly, faults exhibiting brittle deformations are observed along both the NW-SE trending lineaments. Along L2 the fault is traced across a second order drainage parallel to Manneru river (Fig 2). Brittle faulting is also observed at several locations along the lineament L3 (Fig.3). The faults show reverse movement and are oriented along the lineaments. Significantly both these structures are dipping towards Northeast.

Figure 2: Fault observed along L2

V. CONCLUSION

Over the years change in river pattern is often identified as adjustment along faults. The present study evaluated the sinuosity pattern and identified the causative structures as NW-SE trending faults. The reverse movement of the faults that run across the direction of the river apparently obstructs the downstream flow and forced the river to form meander in the upstream side. This also lead a straight course in the downstream side. For the lineament 2 the river appears to be failed to cut across the lineament and flows along it along a straight course. The present study could be a template for understanding influence of active faults on alluvial rivers in similar conditions.

Figure 3: Fault observed along L3

References

[1] Ouchi, S., (1985), 'Response of alluvial rivers to slow active tectonic movement', *Geol. Soc. Am. Bull,.* **96,** 504–515.

[2] Holbrook, J. and Schumm, S. A. (1999), 'Geomorphic and sedimentary response of the river to tectonic deformation: A brief review and critique of a tool for recognizing subtle epirogenic deformation in modern and ancient setting', *Tectonophy.,* **305,** 287–306.

[3] GSI (1999), 'Quardrangle Geological Map 57N'

[4] IS 1893-2012, 'Criteria for earthquake resistance design of structures Bureau of Indian standards'

[5] Leopold, L.B., Wolman, M.G. and Miller, J.P. (1964), 'Fluvial processes in geomorphology', Freeman, San Francisco, 511 pp.

[6] Gowd, T.N., Srirama Rao, S.V., Gaur, V.K., (1992), 'Tectonic stress field in the Indian subcontinent'. *J. Geophys. Res.* **97**, 11,879–11,888.

GEOMORPHOMETRY 2020 PERUGIA, ITALY JUNE 22 - 26 2020

Attempt at detecting cases of connectivity between rock glaciers and torrents using morphometrical indices

Mario Kummert[1], Xavier Bodin[1]
[1]Laboratoire EDYTEM, CNRS/University of Savoie-Mont-Blanc
Bvd de la Mer Caspienne 5, 73376 Le Bourget-du-Lac, France
mario.kummert@univ-savoie.fr

Abstract— **This contribution describes the application of a new approach aiming at detecting rock glaciers connected to the torrential network system in Alpine catchments. The method first uses morphometric variables to identify steep rock glaciers fronts. The sedimentary connection between these fronts and torrents is then assessed through the computation of a sediment connectivity index. Results are then compared to an inventory of connected rock glaciers performed by visual analysis of aerial images. 20 rock glaciers were identified as connected visually while 85 were detected via the geomorphometric approach. If the latter overestimated the level of connectivity for several cases, other error sources such as the use of low-quality input data or the uncertainties in the visual connectivity assessment were identified by the study.**

I. INTRODUCTION

The climatically-driven acceleration of rock glaciers has been largely documented for many mountain ranges, in particular in the European Alps [1-3]. The resulting increase in slope instabilities is likely to represent a threat to the integrity of infrastructures and activities that stand directly on permafrost [4] but also in valley bottoms [5]. In particular, the acceleration of rock glaciers creep rates is expected to increase the magnitude and/or the frequency of rock falls and debris flow events through enhanced release of rock debris at their margins [6,7]. However, it can be assumed that high surface velocities would only impact the occurrence of debris flows if an efficient sediment connection exists between rock glaciers fronts and vulnerable infrastructures such as roads or buildings [8]. Yet, there is a lack of knowledge in the potential propagation of gravitational and torrential processes, especially because the level of connectivity within the sediment cascade of alpine torrential catchments is generally not known. This is particularly the case for rock glaciers which are commonly identified in the European Alps through specific inventories but whose level of connectivity with torrential channels is rarely documented. With rock glaciers frequently presenting high surface velocities, knowledge about the location of rock glaciers efficiently connected to the torrential network system can be considered as important.

Assessing connectivity within Alpine catchments is not an easy task if one considers both structural connectivity, i.e. the direct proximity between slope units, and functional connectivity, i.e. the actual occurrence of sediment transfer from one upslope geomorphological unit to a downslope one [9]. If the structural connectivity can be relatively easy to retrieve from simple visual analysis of aerial images, the level of functional connectivity is often more difficult to establish. In a visual, qualitative approach, geomorphological indications such as the presence of fresh sediments in a channel or traces of fresh erosion at the margin of a landform can be used as clues to determine the occurrence of a functional connectivity between two slope units [8]. However, such visual, geomorphological approach remains quite subjective because it is clearly dependent on the geomorphological expertise of the observer. Recently, several studies proposed methods to infer connectivity in a semi-quantitative way using morphometric indices [10, 11]. Among these studies, the Index of Connectivity (IC) proposed by [10] and adapted from [12] is the most commonly used [13, 14]. The IC is well adapted to high mountains environments but only computes relative values of connectivity and is therefore not suited to differentiate connected landforms from unconnected ones [13, 14]. Specific adaptations must thus be undertaken in order to use the IC for the detection of rock glaciers connected to torrential channels, and thus to the Alpine valleys where most infrastructures lie.

In this work, we propose a new approach especially designed to detect rock glaciers connected to torrents at the regional scale. It reposes on the combination between the use of morphometric indices and the IC computed on a 5 meters DEM. The method is here tested on several catchments of the French Alps and compared for the same areas to an inventory of connected rock glaciers compiled solely based on geomorphological analysis of aerial images, as proposed by [8].

Mario Kummert and Xavier Bodin (2020) Attempt at a semi-automatic detection of connectivity between rock glaciers and torrents: in Massimiliano Alvioli, Ivan Marchesini, Laura Melelli & Peter Guth, eds., Proceedings of the Geomorphometry 2020 Conference, doi:10.30437/GEOMORPHOMETRY2020_64.

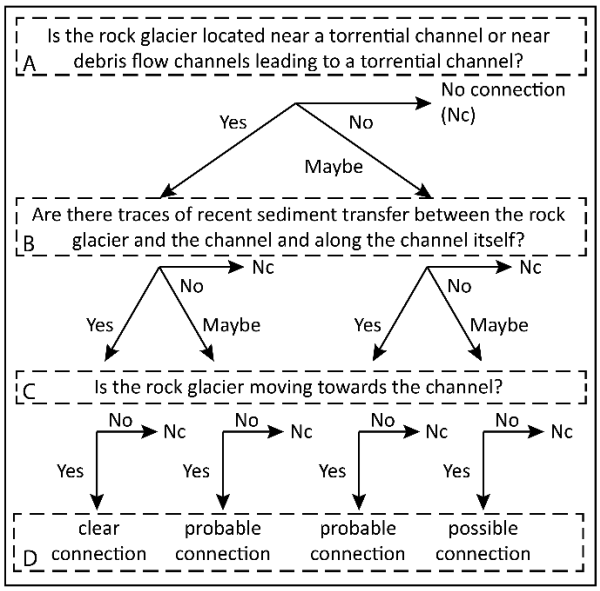

Figure 1. Conceptual workflow representing the different steps used for the visual detection of rock glaciers connected to torrential channels. Letters refers to the text.

II. METHODS

In this study, two main methodological approaches have been used to detect rock glaciers connected to the torrential network system. First, an inventory developed from visual geomorphologic interpretation of aerial images is proposed (Figure 1) and serves as a comparison basis with a second approach based on the aggregation of several morphometric indices. Both methods were applied in an area corresponding to the sub-catchments shown in Figure 2. These sub-catchments are characterized by the highest densities of active rock glaciers in the French Alps, hence their selection for the study.

A. Visual method

The inventory of rock glaciers connected to torrents is performed through visual observation of aerial images following the methodological framework developed by [8]. Compared to this previous study, the method applied here uses a slightly improved workflow which is shown in Figure 1. For each rock glacier previously inventoried in the study region [15], the structural connectivity is first inferred by visually determining the topographical proximity between the rock glacier and channelized structures leading to the main torrential channel (which in turn leads to the main valley, see A in Figure 1). When a rock glacier is detected as "structurally connected" to a torrent, the analysis continues by estimating the level of functional connectivity through the visual identification of recent sediment transfer activity between the rock glacier and the torrent until it reaches the main valley (B in Figure 1). Basically, traces of fresh sediments lying in the channel are interpreted as indicators for efficient functional connection while their absence points towards an inactive connection. Finally, the use of time series of aerial images allows a qualitative determination of the rock glaciers movement direction (C in Figure 1). This is useful to check if sediments are actually being actively transported towards the torrential channel or not. At the end of the workflow, different classes of connectivity can be assigned to each rock glacier as reported Figure 1 (D).

B. Morphometric approach

As the visual detection of connectivity remains subjective, the 2nd method applied here aims at detecting rock glaciers connected to torrents using morphometric parameters. Terrain curvature (with distinction between planar and profile curvature) and slope angle appear in the literature as the most important parameters to identify debris flow prone areas [16,17]. They are here calculated from the French IGN (National Geographical Institute) 5 meters DEM. Thanks to an already existing database of 35 frontal areas known as being directly connected to torrents in the western Swiss Alps [8], threshold curvature (planar and profile) and slope values could be determined by adding (maximal threshold value) and subtracting (minimal threshold value) the standard deviation to the mean value of each morphometric parameter respectively. The thresholded curvature (x2) and slope rasters obtained for the studied catchments were then coupled with the surface of rock glaciers as provided from existing polygon inventories [15] to highlight areas of rock glaciers where the morphology favors the occurrence of water-driven sediment transport (i.e. mainly the steep fronts). In a second step, the identified areas are intersected with zones where the IC [10] exceeds a threshold value (-2.8), also previously determined from zonal statistics performed on the 35 connected frontal areas detected in the western Swiss Alps. The targets used for the IC calculation are here the main rivers of the chosen catchments (Figure 2). As a result, areas of rock glaciers prone to water erosion and sediment transfer and for which the IC value exceeds a given threshold are detected. Each rock glacier for which such area exists is thus considered here as connected to the main valley river.

III. RESULTS

The application of the morphometric approach led to the identification of 85 rock glaciers connected to the valley bottom through the torrential network. As a comparison, 20 rock glaciers were classified as connected (classified as possible, probable or clear connection) by the use of the visual method. Among these 20 cases, 10 are identified as connected by both approaches while the rest is characterized by differing results (Figure 3). All the rock glaciers classified as "clear connection" by the visual method are also recognized as connected in by the morphometric approach.

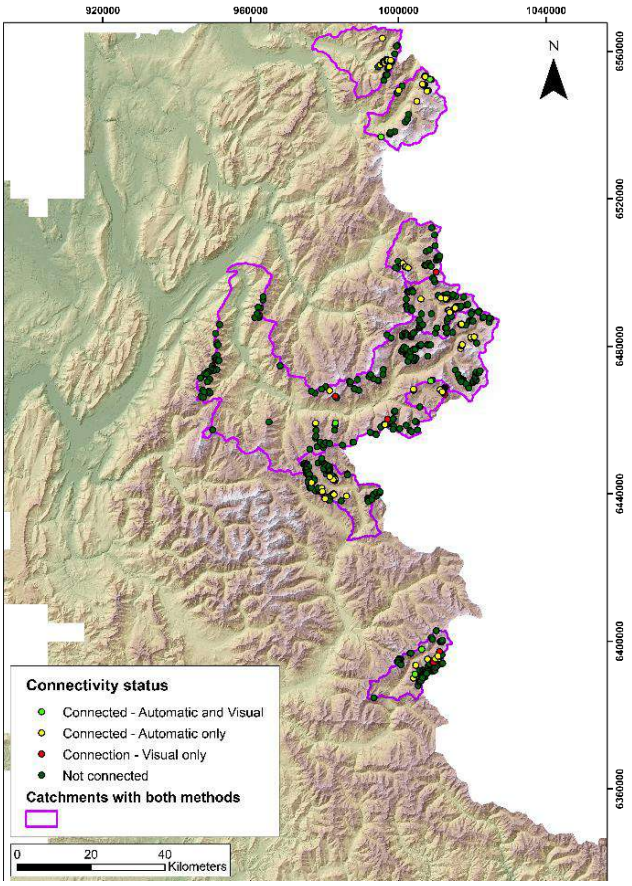

Figure 2. Subdivision of the French Alpes in 7 hydrological basins (purple polygons), within which both visual and automatic detection were carried out. The comparison between the results of both methods are represented with the colored dots on the map.

The main causes of discrepancy between the two approaches have been evaluated for each rock glacier identified as connected by one method or the other (or both) and are shown in Figure 3. If it appears that the most common reason of disagreement are errors in the automatic detection, two other sources of difference are characterized by significant percentages, namely errors in the rock glacier inventory (errors in the polygon outlining and errors in the landform interpretation) and undefined errors issuing from the difficulty to identify the error source between the visual and the morphometric approach (Figure 3). This is especially the case for rock glaciers located far from the main valley and separated from it by long flat channel sections which might stop debris flows propagation. In such cases, it is difficult to clearly identify which of the two approaches yields the correct connectivity status.

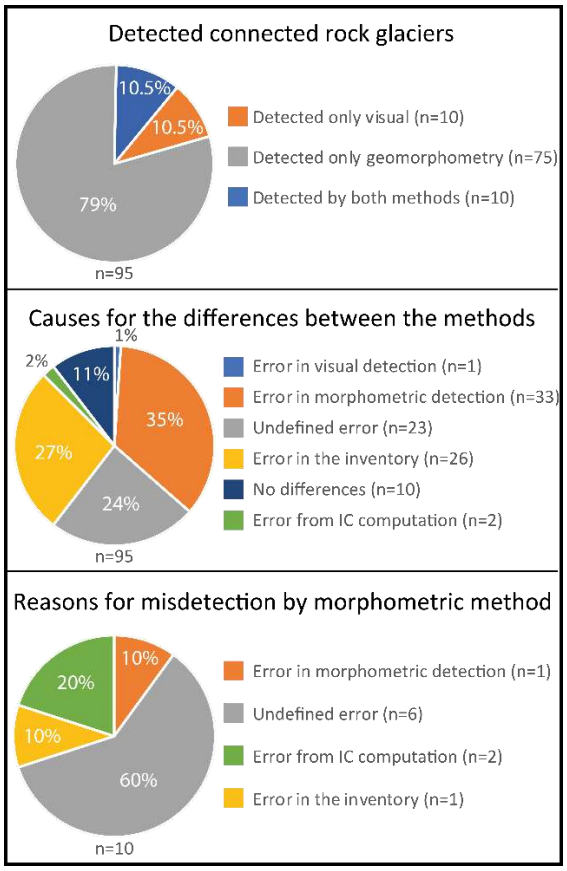

Figure 3. Pie charts showing the results and the relative performance in the detection of rock glaciers connected to torrential channels. The term "undefined error" is used when it is not clear which one of the semi-automatic or the visual method is yielding wrong results while "error from IC computation" refers to issues related to the choice of the target in the IC calculations. "Error in the inventory" designates mistakes in rock glaciers status and outlines in the original rock glacier inventory used as input data.

IV. Discussion

At first glance, the performance of the morphometric detection of connected rock glacier can be questioned, given the large number of cases identified as connected which do not appear in a more classical visual inventory. However, the results show that discrepancies between visually and morphometrically identified connected landforms do not only arise from errors in the morphometrical detection, but also from other sources of errors.

Among these other sources of error, the study underlines the primordial importance of good source data quality. Indeed, 27%

of all rock glaciers identified as connected (visual and/or morphometric) have been wrongly detected due to errors in the rock glacier inventory used as a base for the analysis. These errors comprise (i) talus slopes included by mistake in the inventory and (ii) bad delimitation of rock glaciers outlines preventing our approach to efficiently detect the fronts. In addition, our results show that determining which of the two methods yields wrong results is often difficult. This is for instance the case when a rock glacier is connected to the main channel but long flat sections may prevent the propagation of debris flows downstream. In such cases, we expect that the automatic method using morphometric parameters is probably more capable of identifying flat sections that will effectively decouple the upslope area from the valley.

Finally, part of the errors in the morphometric detection derives from misidentification of rock glaciers fronts. Indeed, it appeared that the developed approach sometimes detects debris flow prone areas in the rooting zones of rock glaciers and does not correspond to what was targeted (rock glaciers fronts). Future development of the method should thus imply a better use of morphometric variables in order to better distinguish rock glaciers fronts from steep areas in the rooting zones.

Improvements should also include a better identification of the target zones for the connectivity investigations. In this study, the targets used for the connectivity assessment and the IC computations the catchments main rivers as they generally coincide with the location of most vulnerabilities. However, cases may exist where vulnerable objects such as roads are located further upslope than the main river. Specific investigations using alternative targets could thus be sometimes necessary. Inventories of vulnerable objects could facilitate forthcoming developments.

V. Conclusion

The developed morphometric approach yielded quite promising results. It detected well cases of rock glaciers which were identified as clearly connected with the visual approach and partly detected rock glaciers classified as possibly connected and probably connected. The approach however slightly overestimated connectivity. Improvements in the morphometric detection of rock glaciers fronts could help enhance the quality of the results. We thus suggest to use the developed morphometric approach as a first step to identify potentially connected cases and to associate it with a more traditional visual analysis in a second step to verify the actual presence of an efficient connection.

References

[1] Roer, I., Kääb, A. and Dikau, R., 2005. Rockglacier acceleration in the Turtmann valley (Swiss Alps): probable controls. Norwegian Journal of Geography 59, 157-163.

[2] Kaufmann, V., Ladstädter, R. and Kienast, G., 2007. 10 years of monitoring of the Doesen rock glacier (Ankogel group, Austria) – A review of the research activities for the time period 1995-2005. In: Petrovic, D. (eds), Proceedings of the 5th Mountain Cartography Workshop, Bohinj, Slovenia, 29 March-April 2006, 129- 144.

[3] PERMOS, 2016. Permafrost in Switzerland 2010/2011 to 2013/2014. Noetzli, J., Luethi, R., and Staub, B. (eds.). Glaciological Report (Permafrost) of the Cryospheric Commission of the Swiss Academy of Sciences 12-15, 85 pp.

[4] Duvillard, P-A., Ravanel, L., Marcer, M. and Schoeneich, P., 2019. Recent evolution of damage and infrastructure on permafrost in the French Alps. Regional Environmental Change 19, 1281–1293.

[5] Zimmermann, M. and Haeberli, W., 1992. Climatic change and debris flow activity in high-mountain areas. A case study in the Swiss Alps. In: Greenhouse Impact on Cold Climate Ecosystems and Landscapes, Catena Supplement 22, 59–72.

[6] Harris, C., Davies, M. and Etzemüller, B., 2001. The assessment of potential geotechnical hazards associated with mountain permafrost in a warming global climate. Permafrost and Periglacial Processes 12, 145-156.

[7] Haeberli, W., Noetzli, J., Arenson, L., Delaloye, R., Gärtner-Roer, I., Gruber, S., Isaksen, K., Kneisel, C., Krautblatter, M. and Phillips, M., 2011 Mountain permafrost: Development and challenges of a young research field. Journal of Glaciology 56(200), 1043-1058.

[8] Kummert, M. and Delaloye, R., 2018. Regional-scale inventory of periglacial moving landforms connected to the torrential network system. Geographica Helvetica 73, 357-371.

[9] Lexartza-Artza, I. and Wainwright, J., 2009. Hydrological connectivity: Linking concepts with practical implications. Catena 79, 146-152.

[10] Cavalli, M., Trevisani, S., Comiti, F. and Marchi, L., 2013. Geomorphometric assessment of spatial sediment connectivity in small Alpine catchments. Geomorphology 188, 31–41.

[11] Heckmann, T. and Schwanghart, W., 2013. Geomorphic coupling and sediment connectivity in an alpine catchment - Exploring sediment cascades using graph theory. Geomorphology 182, 89–103.

[12] Borselli, L., Cassi, P. and Torri, D., 2008. Prolegomena to sediment and flow connectivity in the landscape: A GIS and field numerical assessment. Catena 75, 268-277.

[13] Messenzehl, K., Hoffmann, T. and Dikau, R., 2014. Sediment connectivity in the high-alpine valley of Val Müschauns, Swiss National Park – linking geomorphic field mapping with geomorphometric modelling. Geomorphology 221, 215-229.

[14] Tiranti, D., Crema, S., Cavalli, M. and Deangeli, C., 2018. An Integrated Study to Evaluate Debris Flow Hazard in Alpine Environment. Frontiers in Earth Science 6:60, 14pp.

[15] Marcer, M., Bodin, X., Brenning, A., Schoeneich, P., Charvet, R., and Gottardi, F. Permafrost Favorability Index: Spatial Modeling in the French Alps Using a Rock Glacier Inventory. Frontiers in Earth Science, 5:105, 17 pp.

[16] Fischer, L., Rubensdotter, L., Sletten, K., Stalsberg, K., Melchiorre, C., Horton, P. and Jaboyedoff, M., 2012. Debris flow modeling for susceptibility mapping at regional to national scale in Norway. In: Eberhardt, et al. (Eds.), Landslides and Engineered Slopes: Protecting Society through Improved Understanding. Taylor & Francis Group, London, pp. 723–729.

[17] Meyer, N.K., Schwanghart, W., Korup, O., Romstad, B. and Etzelmüller, B., 2014. Estimating the topographic predictability of debris flows. Geomorphology 207, 114-125.

GEOMORPHOMETRY 2020 PERUGIA, ITALY JUNE 22 - 26 2020

Mapping stream and floodplain geomorphic characteristics with the Floodplain and Channel Evaluation Tool (FACET) in the Mid-Atlantic Region, United States

Marina Metes[1,§], Kristina Hopkins[1], Labeeb Ahmed[2], Sam Lamont[3], Peter Claggett[1], and Greg Noe[1]
[1]U. S. Geological Survey (USGS), [2]Attain LLC, [3]Athenium Analytics
[§] USGS Maryland-Delaware-DC Water Science Center
5522 Research Park Drive
Baltimore, MD, 21228
mmetes@usgs.gov

Abstract—**Quantifying channel and floodplain geomorphic characteristics is essential for understanding and modeling sediment and nutrient dynamics in fluvial systems. The increased availability of high-resolution elevation data from light detection and ranging (lidar) has helped improve methods for extracting these metrics at a greater accuracy across regional scales. The Floodplain and Channel Evaluation Tool (FACET) was developed as an open source tool to calculate a suite of geomorphic metrics describing channel and floodplain geometry from high-resolution digital elevation models (DEMs), providing estimates of channel width, bank height, cross-sectional area, and floodplain extent. Field data from sites in the Chesapeake Bay and Delaware River watersheds were used to calibrate and validate FACET within five physiographic provinces in the Mid-Atlantic region of the United States. Stream banks were identified using either a slope-threshold method at cross sections, which are automatically generated at a user-defined interval along the delineated stream network, or by applying a curvature-threshold method for grid cells within a buffered distance from the stream network. The floodplain extent was mapped using a height above nearest drainage (HAND) grid and empirical regression models built for each physiographic province relating the HAND threshold to drainage area. Other user-defined input parameters within FACET control the sensitivity of calculations to DEM resolution, relief, and stream order, allowing for the ability to optimize FACET at multiple scales and/or regions if field survey data are available for calibration. Geomorphic metrics derived from FACET are currently being used to develop predictive models to estimate bank erosion and floodplain deposition to enhance our understanding of watershed sediment and nutrient budgets.**

I. INTRODUCTION

Sediment and nutrients in fluvial systems follow a dynamic cycle of erosion, transport, and deposition as they move through river systems [1]. Modeling the amount of sediment eroded from banks, deposited on floodplains, and exported from the system is essential for developing accurate watershed sediment and pollutant budgets for land and water resource decision making. Key parameters in these models are field-measured rates of sediment and nutrient fluxes and measurements of stream and floodplain geomorphic characteristics such as channel width, stream bank height, and floodplain width to scale field data to large stream networks. The increasing availability of high-resolution elevation datasets derived from lidar now makes it possible to obtain stream and floodplain geomorphic characteristics at finer watershed scales. The Floodplain and Channel Evaluation Tool (FACET) [2] was developed to allow for a regional-scale analysis of stream and floodplain geomorphic characteristics with minimal field data for calibration and calculation. To run FACET in the Mid-Atlantic region of the United States, a high-resolution DEM and knowledge of terrain in the area of interest to select appropriate input parameters are the only requirements needed to calculate the geomorphometry of stream banks and floodplains at the watershed scale.

II. METHODS

FACET was developed using open-source geospatial libraries in Python to calculate geomorphic metrics using lidar-derived DEMs. Field-based channel and floodplain characteristics were measured at 68 sites in the Chesapeake Bay and Delaware River

Marina Metes, Kristina Hopkins, Labeeb Ahmed, Sam Lamont, Peter Claggett, and Greg Noe (2020)
Mapping stream and floodplain geomorphic characteristics with the Floodplain and Channel Evaluation Tool (FACET) in the Mid-Atlantic Region, United States:
in Massimiliano Alvioli, Ivan Marchesini, Laura Melelli & Peter Guth, eds., Proceedings of the Geomorphometry 2020 Conference, doi:10.30437/GEOMORPHOMETRY2020_65.

Watersheds (Fig. 1). These data were used to calibrate the active floodplain extent and assess FACET metric accuracy.

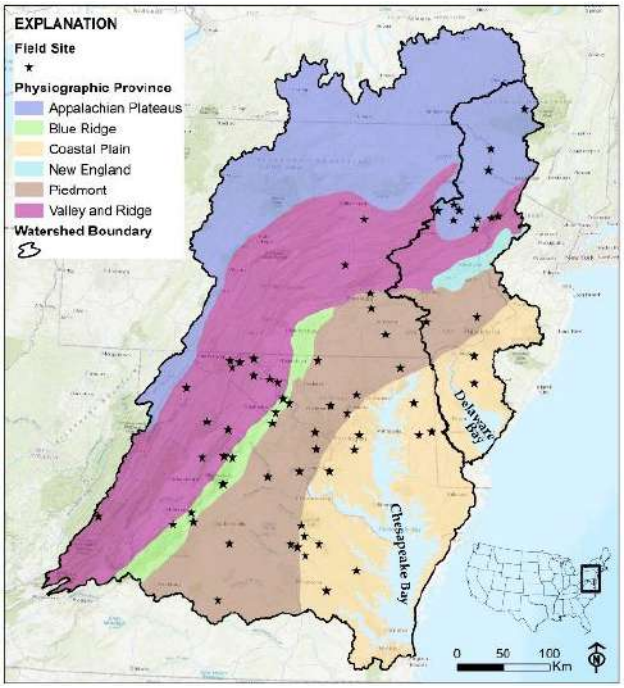

Figure 1. Location of 68 field sites spanning five physiographic provinces in the Chesapeake Bay and Delaware River Watersheds. Channel width, bank height, and floodplain width were measured at each field site. Bank erosion and floodplain deposition rates were estimated using dendrogeomorphology. Soil chemistry data collected at each site were also used to calculate sediment and nutrient fluxes.

A. FACET input data and pre-processing

Lidar-derived DEMs covering the study area varied in quality level (i.e., resolution, vertical and horizontal accuracy) and therefore were resampled to 3 meters for consistency. DEMs were hydrologically conditioned using pre-processing steps built into FACET. First, road-stream and railroad-stream intersections were identified as barriers to surface flow and breached. To ensure any additional barriers not breached in the first method were addressed, the fast breach algorithm in Whitebox Tools [3] was then applied to the DEM. D8 flow direction and contributing area were then calculated using Terrain Analysis Using Digital Elevation Models (TauDEM), version 5.3.7. [4], to delineate a stream network based on the end nodes of the U.S. Geological Survey (USGS) 1:24,000-scale High Resolution National Hydrography Dataset (NHD High Res.) [5].

B. Stream bank identification

FACET contains two separate methods to delineate stream banks [2]. The first is a slope break approach, which uses a series of cross sections placed perpendicular to the channel and spaced at user-defined intervals. Within the elevation profile of each cross section, a series of horizontal lines are spaced above the lowest point along the cross section at a user-defined vertical increment. Once the user-defined ratio between the length of a horizontal line and the next highest line is exceeded, FACET searches for a slope break that exceeds a user-defined threshold to identify the top of the bank on each side of the cross-sectional profile of the channel. Each bank point pair contains a measurement for bank height, bank angle, channel width, and channel area (Fig. 2).

The second method of bank detection is a raster-based curvature approach. FACET calculates curvature within a moving window along the stream network using two optional methods: mean curvature and wavelet-based [6]. Pixels within a buffered distance from the stream network falling within the curvature threshold are identified as banks. Mean channel widths from the curvature approach are summarized by stream segments. The user can adjust the moving window size, curvature threshold, and buffer distance.

C. Floodplain delineation

A height above nearest drainage (HAND) grid was generated using the TauDEM D-infinity vertical averaged distance downstream to identify the vertical distance between each pixel on the landscape to the location along the stream network to where it drains. HAND height thresholds corresponding to the edge of the floodplain mapped in the field were identified for 57 of the 68 field sites across five physiographic provinces: Appalachian Plateau, Blue Ridge, Coastal Plain, Piedmont, and Valley and Ridge (Table 1). The HAND threshold for each field site was related to drainage area and physiographic province in a linear regression model to predict unique HAND thresholds for unmeasured sites. Predictions were limited to drainage areas greater than 3 km^2 and less than 3000 km^2, reflecting the drainage area distribution of the field sites. HAND threshold predictions for each stream reach catchment were applied to the HAND grid to create a continuous floodplain raster for the watershed. (Fig. 2).

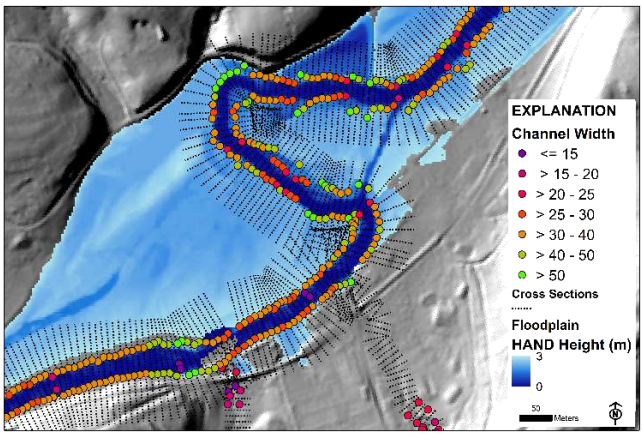

Figure 2. Example of banks derived using the slope break approach. A pair of bank points were identified for each cross section drawn perpendicular to the channel. Channel width, bank height, and other channel metrics were quantified at each cross section/bank point pair. Example also shows output of the HAND-derived floodplain along the reach.

III. Results and Conclusions

A significant relationship between HAND threshold and drainage area was identified for the Appalachian Plateau, Piedmont, and Valley and Ridge sites ($R^2 = 0.59$, $p < 0.001$). A static HAND threshold was used within the Coastal Plain (HAND = 1.65 m) and the Blue Ridge (HAND = 1.56 m) (Table 1).

Table 1. Mean and range of HAND thresholds corresponding to field-mapped active floodplain extent within each physiographic province.

Physiographic Province	Number of Field Sites	HAND Threshold Range (m)	HAND Threshold Mean (m)	Drainage Area Range (sq km)
Appalachian Plateau	9	0.2 - 1.8	1.04	52 - 285
Blue Ridge	8	0.6 - 1.9	1.56	11 - 26
Coastal Plain	14	0.6 - 3.8	1.65	33 - 2,792
Piedmont	13	0.7 - 5	2.55	20 - 1,604
Valley & Ridge	13	1 - 4.9	2.18	16 - 1,748

FACET accuracy was assessed using the root mean square error (RMSE), comparing the FACET-derived values for channel width, bank height, and floodplain width with the field-measured values of each metric along each overlapping reach (Fig. 3). FACET tended to overestimate channel width and bank height in the Blue Ridge region where the topography is more complex and the drainage area of field sites ranged from 11 to 26 km^2, indicating the ability for FACET to accurately detect banks in small mountainous headwater streams was limited. In the Coastal Plain, Piedmont, and Valley and Ridge regions where drainage areas of field sites were larger and banks were typically more defined, estimates from FACET match field values more closely. FACET tended to overestimate floodplain width in the Valley and Ridge region but did not consistently over or underestimate floodplain width in the Piedmont or Coastal Plain region. Other variables influencing FACET accuracy could be lidar quality and characteristics used to delineate floodplains in the field that are not as evident from lidar (e.g., microtopographic changes, flow-oriented debris, and shifts in vegetation type).

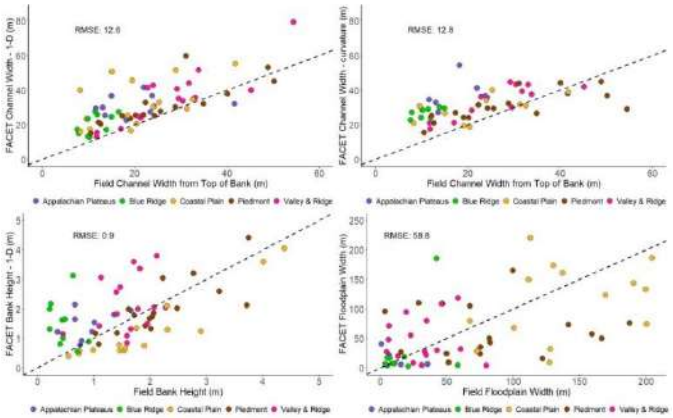

Figure 3. Plots showing the FACET versus field-derived measurements of channel width, bank height, and floodplain width for each of the 68 field sites, along with the root mean square error (RMSE) value for each comparison. Sites within each physiographic province are grouped by color.

FACET-derived geomorphic metrics are currently being used to scale up field measurements of sediment and nutrient fluxes calculated at each of the 68 field sites to predict fluxes from streambank erosion and floodplain deposition across the entire Chesapeake Bay and Delaware River Watersheds.

References

[1] Meade, R.H., 1982. Sources, sinks, and storage of river sediment in the Atlantic drainage of the United States. *The Journal of Geology*, *90*(3), pp. 235-252.

[2] Lamont, S.L., Ahmed, L., Metes, M.J., Claggett, P., Hopkins, K.G., and Noe, G.B., 2019. Floodplain and Channel Evaluation Tool (FACET). Version 0.1.0. [Software release]. U.S. Geological Survey.

[3] Lindsay, J.B., 2016. Efficient hybrid breaching-filling sink removal for flow path enforcement in digital elevation models. *Hydrological Processes*, *30*(6), pp. 846-857.

[4] Tarboton, D. G., 1997. A New Method for the Determination of Flow Directions and Contributing Areas in Grid Digital Elevation Models, *Water Resources Research*, *33*(2), pp. 309-319.

[5] U.S. Geological Survey, 2017. "National Hydrography Dataset Plus High Resolution (NHDPlus HR) – USGS National Map Downloadable Data Collection".

[6] Gangodagamage, C., Foufoula-Georgiou, E., Brumby, S.P., Chartrand, R., Koltunov, A., Liu, D., Cai, M. and Ustin, S.L., 2016. Wavelet-compressed representation of landscapes for hydrologic and geomorphologic applications. *IEEE Geoscience and Remote Sensing Letters*, *13*(4), pp.480-484.

GEOMORPHOMETRY 2020 PERUGIA, ITALY JUNE 22 - 26 2020

LITHOLOGY AND CHANNEL NETWORK INITIATION AND ORIENTATION: A CASE STUDY OF UPPER OGUN RIVER BASIN, SOUTHWESTERN NIGERIA

Adeyemi O. OLUSOLA[α], Adetoye FANIRAN[α]*

[α]Department of Geography, University of Ibadan, Ibadan, Nigeria.

**Corresponding Author: olusolaadeyemi.ao@gmail.com*

Abstract— **Several geomorphologists have highlighted the importance of structure on landform evolution. However, studies concerned with the impact of underlying structure on channel initiation and evolution are still growing. In this study, six-third order basins were selected systematically from Upper Ogun River Basin, Southwestern Nigeria for lithology and channel network initiation and orientation evaluation. Rose diagrams were used to present the influence of underlying lithological units on river network orientation and initiation. The approach here is to identify lineaments and river networks for each basin and compare the presented patterns. The study area is underlain by granites, migmatites, schists, pegmatites, quartzite, etc. with migmatite being the most obvious in terms of spread. Lineament and channel network pattern and orientation were extracted for each of the basins from Shuttle Radar Topography Mission (SRTM) at 30m resolution using Rockworks 15 and ArcGIS 10.2. The Rose diagram for the lineament trends suggests four major trends; E-W, N-S, SSE-SSW and NE-SW. Across these four major trends, the N-S and E-W were particularly dominant showing a bimodal distribution that has corresponding peaks on the length-orientation axis of the Rose diagram of the river channels. Since the general trend of tectonic grains within the Nigerian Basement Complex is relatively N-S, the main channels draining the selected basins in Upper Ogun appear to have been controlled along pre-existing weak zones in the country rocks.**

Introduction

Until recently, information about streams in humid tropics was limited to their description in relation to geological structure; there remain a large gap to fill as regards mechanics of how river channels and networks evolve, lithological units and channel network pattern, etc. Most studies especially in temperate regions or river channels with(out) glacial history have been studied and underlying interactions between process-form dynamics presented in the literature. The inherent characteristics observed in humid tropical regions as a result of differential weathering suggest that most valley settings and fluvial processes are unique in this area. However, narratives concerning humid tropical basins without glacial history are still growing. The problem, however, is that information on basins within a humid tropical region is too limited for any reasonable and definitive inferences and deductions to be made [1, 2]. Hence, the need to take advantage of big data available in Digital Elevation Models (DEMs) and emerging geo-computational tools cannot be overemphasized.

This study seeks to contribute to geomorphic understanding by using Digital Elevation Models (DEMs) to provide interactions between process and form within a typical drainage basin in Southwestern Nigeria. This will ensure the co-production of knowledge for locations with limited geomorphological understandings.

This study aims to understand the influence of lithology on river channel orientation. The use of Rose diagrams presents an avenue to highlight the influence of underlying lithological units on river network orientation and initiation.

I. METHODS

Basin determination and procedure

Seventeen (17) third-order basins were identified across the Upper Ogun River Basin using topographical maps and Geographic Information Systems. This involves the use of Shuttle Radar Topography Mission, SRTM, a Digital Elevation Model, DEM, at 30m resolution. The output from the DEM was cross-validated with topographical maps of 1:50 000 covering the entire basin. The 30meter DEM was projected in the Universal Traverse Mercator Zone 31N based on Nigerian Grid Datum. The directions of surface water flow, flow accumulation area and stream network coverage were obtained from a filled DEM based on the methods of [3], while a variety of methods were used to determine an appropriate flow accumulation area for a stream [4, 5].

Geoprocessing

The steps used in extracting the channel networks from Upper Ogun River Basin involves the clipping and processing of the DEM. Processing the DEM from the clipped DEM involves filling of depressions in the DEM, assignment of flow directions on the filled DEM and the calculation of flow accumulation on the flow direction using hydrological tools of the ArcToolbox (ArcGIS 10.x). After these processes, the channel network was then extracted using the con Tool and ordered using the Strahler

Adeyemi Olusola and Adetoye Faniran (2020) Lithology and channel network initiation and orientation: a case study of upper Ogun River basin, southwestern Nigeria: in Massimiliano Alvioli, Ivan Marchesini, Laura Melelli & Peter Guth, eds., Proceedings of the Geomorphometry 2020 Conference, doi:10.30437/GEOMORPHOMETRY2020_66.

method. The ordered stream network raster was then converted into vector.

After ordering, seventeen third-order basins were identified across the Upper Ogun Basin. The seventeen third-order basins which form the population of the study were then cross-validated with the topographical maps. After which the raster form of the channel networks was converted into vector form.

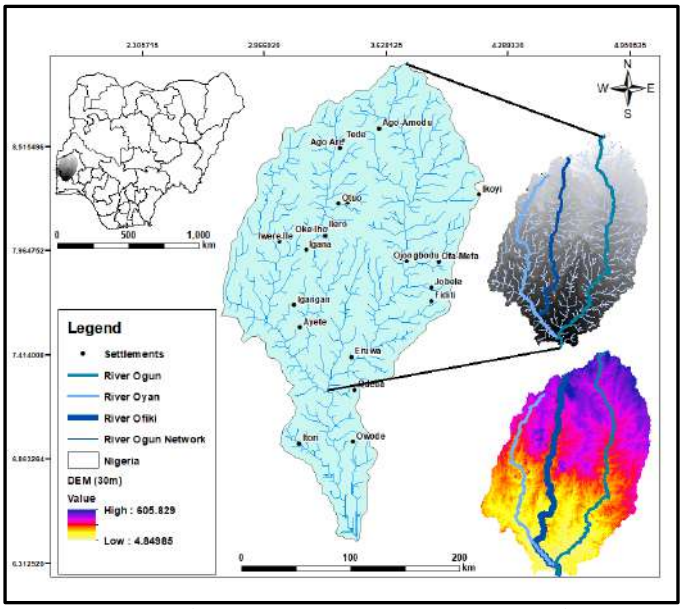

Figure 1. The extent of the Ogun River Basin showing a section of the Upper Ogun River Basin and the DEM

Sampling

To identify the basins to be studied, a systematic and random sampling technique was employed. The first step was to identify basins that were heterogeneous based on lithological variations. For a basin to be heterogeneous, it must have more than two lithological units within the basin, none of which must be more than seventy percent in terms of areal coverage across the basin. The benchmark of seventy percent was set for the study because the area is a basement complex and largely underlain by migmatites [6]. Applying this yardstick, six basins (Table 1) were selected from the population (Figure 2).

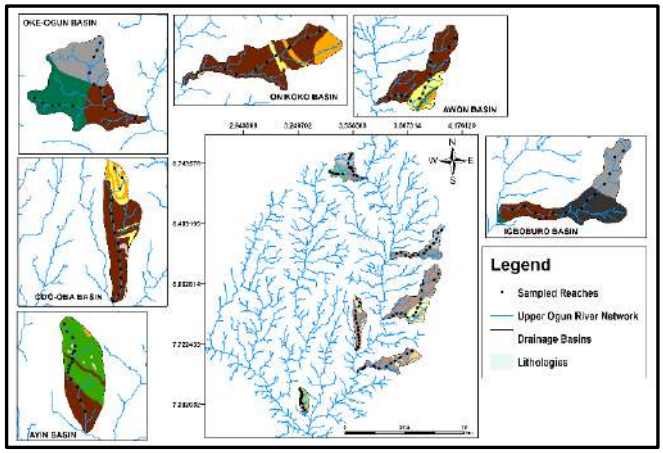

Figure 2. Selected third-order basins

Data Analyses

Topographic properties were extracted using System for Automated Geoscientific Analysis (SAGA) version 4.0.0, a GIS software. Rockware software was used in creating Rose diagrams for lineament patterns and channel networks

Table 1. Selected third-order basins

Basin ID	BASIN NAME	GEOLOGY
1	OKE-OGUN	OGe -Medium to coarse-grained hornblende; OGp – Coarse porphyritic and biotite hornblende granite; and M - Migmatite
2	IGBOBURO	OGp – Coarse porphyritic and biotite hornblende granite; M – Migmatite; and OPg – Prophyroblastic gneiss
3	AWON	Su – Undifferentiated Schists; Qs – Quartzite Schist; and P - Pegmatite
4	ONIKOKO	OGe – Medium to coarse-grained hornblende; M – Migmatite; and OGp – Coarse porphyritic and biotite hornblende granite
5	ODO-OBA	OGb – Coarse porphyritic biotite and biotite muscovite granite; OGh – Coarse porphyritic hornblende granite; and M - Migmatite
6	AYIN	OGu – Undifferentiated Older Granite; Su – Undifferentiated Schists; OGp – Coarse porphyritic and biotite hornblende granite

II. RESULTS AND CONCLUSIONS

Environmental factors such as climate, lithology, vegetation, etc exercise control through their direct and indirect impact on fluvial process and dynamics. Within a homogenous climatic zone, lithology stands to be one of the most important environmental factors to influence river channel morphology. Rose diagrams (Figure 3) present the influence of underlying lithological units on river network orientation and initiation. The approach here is to identify lineaments and river networks and compare the pattern. It has been established that known methods of relating lineament patterns to morpho-tectonic subsets are Rose diagrams [7, 8]. In recent times, other attributes can be generated from lineament properties especially since the advent of computer-aided programs. It is important to state here that the area is a Basement Complex with the occurrence of Inselbergs and domes across the entire landscape of the Upper Ogun River Basin (UORB) (Figure 1). The area is underlain by granites, migmatites, schists, pegmatites, quartzite, etc. with migmatite being the most obvious in terms of spread (Table 2).

The frequency and length of lineaments (fractures) in the Rose diagram for the study area (Figure 3) shows a bi-modal distribution in most cases along the EW-NS (East West – North South) and N-S (North-South) directions. The distributions (EW-NS and N-S) have corresponding peaks on the length-orientation axis of the Rose diagram of the river channels (Figure 3). Specifically, within the Oke-Ogun basin (Figure 3a), the lineament pattern showed a more N-S direction as the main lineament axis with other minor sub-trends show more of the E-W direction. The river network presents for its main channel an E-W trend with its tributaries showing largely ENE-WSW trends. By implication, the main channel of the basin is largely controlled by minor sub-trends of the lineaments. For the Igboburo basin (Figure 3b), the lineament trend shows E-W, N-S, SSW-NNE and ENE-WSW, while the channel network for the main channel showed E-W trend and its tributaries showing N-S and SSE-SSW trends. This implies that the main channel draining Igboburo basin is being controlled by the main structural trend. Awon basin (Figure 3c), showed a trend of N-S, E-W and SSE-SSW, while the river network presents a N-S trend. The implication here is that the main channel draining Awon basin is being controlled by the main structural trend in the N-S direction. Onikoko basin (Figure 3d) showed for its lineament trend E-W and SSE-SSW as its major trends, while the river network within the basin presents SSE-SSW as the trend direction for its main channel. In essence, the main channel draining the Onikoko basin is being controlled by the main structural trend along the SSE-SSW direction. Odo-Oba basin (Figure 3e), presents a dominant trend direction for its lineament along N-S, NE-SW, NNE-SSW and NWN-SES, while the main channel network as presented in the Rose diagram is along NNE-SSW and NWN-SES. For the Ayin basin (Figure 3), the main lineament trend is along N-W, while the minor sub-trends are along NE-SW direction. The main channel network presented a NW-SE direction. By extension, the main channel network within the Ayin basin is controlled by minor sub-trends of the lineament pattern.

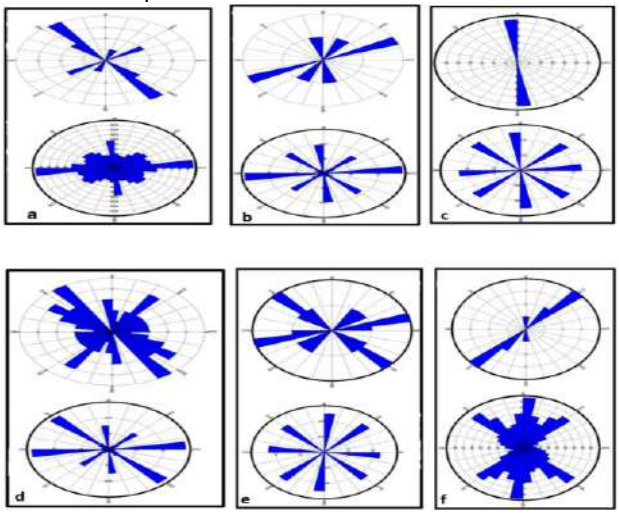

Figure 3. Rose diagram illustrating trends of lineament (upper Rose diagram) and channel network (lower Rose diagram) (a) Oke-Ogun Basin (b)Igboburo Basin (c) Awon Basin (d) Onikoko Basin (e) Odo-Oba Basin (f) Ayin Basin

In conclusion, the Rose diagram for the lineament trends suggests four major trends; the E-W, N-S, SSE-SSW and NE-SW. Across these four major trends, the N-S and E-W were particularly dominant. The general trend of tectonic grains within the Nigerian Basement is relatively in the N-S trend [9], the main channels draining the selected basins in Upper Ogun appear to have been controlled along pre-existing weak zones in the country. Hydro-geomorphologically, the E-W and N-S lineament trend as observed in this study can be tied to tectonic events that have affected the evolution of the Upper Ogun Basin [10]. Furthermore, it is established that groundwater flow in the Basement complex is likely to follow the path of porosity in fractures as well as weathered overburden [11]. It can, therefore, be implied that these two lineament orientation sets (N-S, E-W) could define the preferred orientation of groundwater occurrence within the Upper Ogun River Basin (UORB). Another far-reaching implication is the observation that the occurrence of the N-S and E-W trending lineaments in the area might suggest that they serve as active conduits connecting most springs in the area to the main channel.

REFERENCES

[1]. Twidale, C. R. 1976. On the survival of paleoforms, *American Journal of Science*, 276, 77-95.
[2]. Faniran, A., Jeje, L. and Ebisemiju, F. (2006). *Essentials of Geomorphology*, Penthouse Publications, Ibadan, Oyo State, Nigeria.
[3]. Jenson, S. K., & Domingue, J. O. (1988). Extracting topographic structure from digital elevation data for geographic information system analysis. *Photogrammetric engineering and remote sensing*, *54*(11), 1593-1600.
[4]. Reinfelds, I., Cohen, T., Batten, P., Brierley, G. (2004). Assessment of downstream trends in channel gradient, total and specific stream power: a GIS approach. *Geomorphology*, 60, 403–416.
[5]. Hayakawa, Y.S. and Oguchi, T., (2006). DEM-based identification of fluvial knickzones and its application to Japanese mountain rivers. *Geomorphology*, 78(1–2), pp.90–106.
[6]. Olusola, A.O. (2019). *Process-form dynamics of upper Ogun river basin, Southwestern Nigeria.* Unpublished PhD thesis submitted to the Department of Geography, University of Ibadan.
[7]. Smithurst, L.J.M. (1990). Structural remote sensing of South-West England. Proceedings of the Ussher Society, 7, pp.236-241.
[8]. Anifowose, A.Y.B. and Kolawole, F. (2012). Tectono-hydrological study of Akure Metropolis, Southwestern Nigeria. *Hydrology for Disaster Management*. Special Publication of the Nigerian Hydrological Sciences.
[9]. Oluyide, P. O. (1988). Structural trends in the Nigerian basement complex. *Precambrian Geology of Nigeria, Geological Survey of Nigeria, Kaduna*, 93-98.
[10]. Kolawole, F., (2012). Tectono-Hydrological Study of Akure Metropolis , Southwestern Nigeria. *Hydrology of disaster management*.
[11]. Wright, E.P. and Burgess, W.G. (1992). Hydrogeology of crystalline basement aquifers in Africa. *Geological Society Bulletin* (Special Publication), 66, pp.1-27.

GEOMORPHOMETRY 2020 PERUGIA, ITALY JUNE 22 - 26 2020

Morphometric and channel erosivity analysis of lateritic gully catchments using high resolution DTM and repeat survey Structure-from-Motion datasets

Priyank Pravin Patel[1§], Sayoni Mondal[1], Rajarshi Dasgupta[2]

[1]Department of Geography, Presidency University, 86/1, College Street, Kolkata - 700 073, West Bengal, India

[2]Department of Geography, East Calcutta Girls' College, P 237, Lake Town Road, Kolkata - 700 089, West Bengal, India

[§] priyank999@hotmail.com

Abstract— **Fine-scale gully catchment mapping is a prerequisite towards ascertaining any soil loss estimates from such areas. The use of high resolution Digital Terrain Models (DTM) has greatly facilitated extraction of minor gully features, but these remain essentially top-down views of the surface and do not capture erosional or morphological aspects formed on gully walls. However, Structure-from-Motion affords repeat survey capabilities that allow documentation and precise mapping of gully features and the main erosion channels, while also providing means of creating side-view looking 3-D models for documenting otherwise obscure features. Repeat such surveys provide the means for using a DEM differencing approach to quantify the amount of erosion and surface lowering in the gully catchment. Longitudinal profile analysis of the developed gully channels using standard hydraulic and steepness equations of the Detachment Limit Model also provide insights into the rill erosivity. The above methods have been used to analyze a lateritic badland tract in southwestern West Bengal in eastern India.**

I. INTRODUCTION

Gully research has often focused on quantifying their morphological parameters using erosion pins, total stations, laser profilometers and differential GPS[1], along with the use of remote sensing products and techniques, like very high resolution (VHR) satellite imageries and Digital Elevation Models (DEMs)[2,3,4]. The advent of airborne and terrestrial laser scanning[5] and image modeling through Structure-from-Motion & Multi-view Stereo (Sfm-MVS) technologies [6,7] now afford greater capability of using side-looking sensors to document gully wall morphological forms that were not always discernable from top-down satellite based sensor views. In the Indian context too, DEM generation from satellite stereo-data for terrain analysis[8] has been found especially suitable for demarcating and analyzing small catchments and gully fields[9].

The Gangani Tract, (locally known as *Ganganir Danga*, translated as *Land of Fire*, due to the deep ochre hues of the exposed rocks as a result of the presence of hydrated iron oxides), is situated near the small town of Garbeta ($22^0 51' 47''$ N, $87^0 21' 13''$ E) in Paschim Medinipur district, West Bengal, in eastern India. The area is part of the lateritic uplands situated in the northern and western portions of the district and is deeply gullied and riven by numerous channels that dissect the upper lateritic and lower elevation sandstone surfaces. Detailed mapping and morphometric characterization of the region is thus important for ascertaining the extent of rill and gully erosion occurring therein and the year-wise changes in the small gully catchments. Morphometric analysis of the incised channels developed on the exposed surfaces is also important to document their erosivity, that contributes directly towards the overall erosion occurring from the region.

II. METHODS

A high resolution 2 meter Digital Terrain Model (DTM) obtained from JAXA (Figure 1), generated using the ALOS Daichi satellite has been used to analyze the terrain attributes of the area. This dataset was used to extract the various gully basins and the traditional morphometric parameters for each of them, like basin hypsometric integrals. Alongside this, specific locations have been surveyed repetitively during the last 3 years using the Structure-from-Motion (SfM) technique, leading to the generation of multiple DTM datasets, which could be subtracted from each other to obtain the surface elevation changes.

Priyank Pravin Patel, Sayoni Mondal, and Rajarshi Dasgupta (2020)

Morphometric and channel erosivity analysis of lateritic gully catchments using high resolution DTM and repeat survey Structure-from-Motion datasets:

in Massimiliano Alvioli, Ivan Marchesini, Laura Melelli & Peter Guth, eds., Proceedings of the Geomorphometry 2020 Conference, doi:10.30437/GEOMORPHOMETRY2020_67.

Rebound RockSchmidt Hammer readings on the gully wall helped characterize the differential resistance of the surface lithologies to incision by overland flow. Longitudinal profile analysis of the formed gullies was done using the Detachment Limit Model[10] for characterizing erosion from bedrock channels, as per the following equations:

$$k_{sn} = \left(e/K\right)^{1/n} \quad (1)$$

k_{sn}- Normalized steepness index, e- Erosion rate, K- stream power coefficient combining lithology-rainfall aspects

$$\tau = \rho g \left(Q/W\right)^{0.6} S^{0.7} \quad (2)$$

Q- Discharge, W- Width, ρg- Specific weight of water, S- Slope, τ- shear stress generated by water flow in the gullies

III. Results and Conclusions

Use of the 2m DTM enables extraction of various morphological features of the badland tract, especially the fingerlike projections of the numerous gully heads. The older gully fields are larger with more total volume loss. When normalized by area, smaller younger gullies are more seen to be more erosive, with higher hypsometric integrals (Figure 2). Due to their higher erosivity, these younger gullies had also expanded at higher rates.

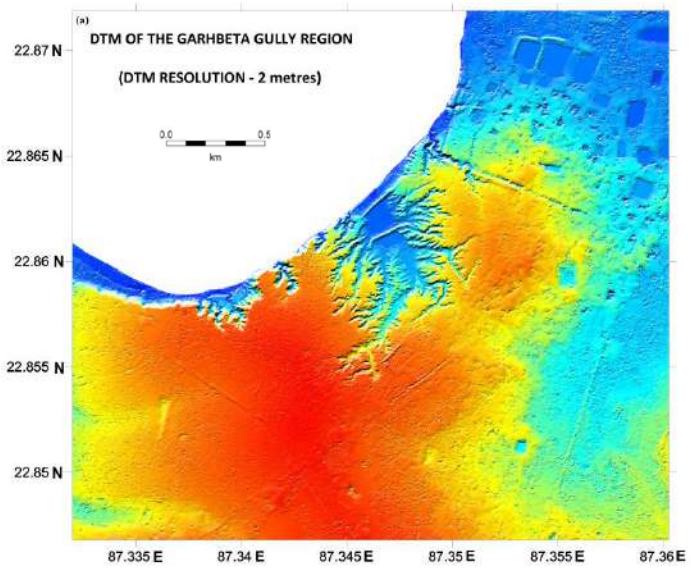

Figure 1. The 2 meter DTM of the Gangani Tract with the finger-like projections of the gullied landscape

The SfM method allowed creation of 3D representations of the gully wall and cave-forms (Figure 3), allowing their measurements, which would be otherwise impossible from spaceborne top-down images. Thus SfM-MVS provides a viable solution to not only represent them on screen but also the ability to view them interactively from all possible angles. Multi-temporal SfM datasets helped depict the micro-topographic changes in the dimensions of the rills and minor gully network and their rates of deepening were ascertained from DEM differencing such datasets.

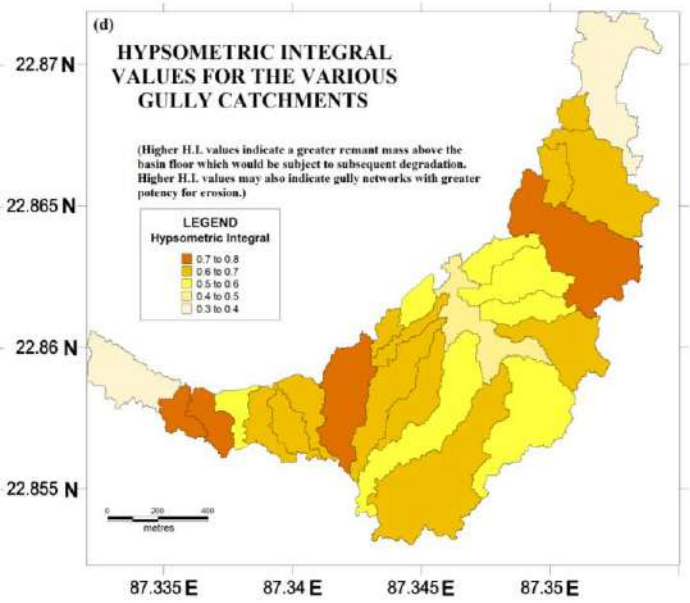

Figure 2. Hypsometric integral variations across the gully basins

Figure 3. SfM based 3-D model of a cave and earth pillar form [From Patel et al., 2020]

Extraction of the Ksn parameter and characterization of the channels on basis of their steepness values again revealed spatial variations, with the younger gullies in the western part of the Gangani Tract reporting the highest values and show marked breaks in their longitudinal profiles where the gully channel transitioned across different lithologies.

Plots of RockSchmidt hammer readings taken along the gully walls and floor show the lithological variations along the gully longitudinal profile and these could be correlated with the breaks and minor knickpoints seen along them, as ascertained from the Ksn analysis.

REFERENCES

[1] Castillo, C. *et al*., 2012. Comparing the accuracy of several field methods for measuring gully erosion. *Soil Sci. Soc. Am. J.* **76,** 1319-1332.

[2] Desprats, J.F. *et al.*, 2013. Mapping linear erosion features using high and very high resolution satellite imagery. *Land Degrad. Dev.* **24,** 22-32.

[3] Shruthi, R. B. V., Kerle, N., Jetten, V., Abdellah, L. & Machmach, I., 2015. Quantifying temporal changes in gully erosion areas with object oriented analysis. *Catena* **128,** 262-277.

[4] Perroy, R. L., Bookhagen, B., Asner, G. P. & Chadwick, O. A., 2010 Comparison of gully erosion estimates using air-borne and ground based LiDAR on Santa Cruz Island, California. *Geomorphology* **118,** 288-300.

[5] Gómez-Gutiérrez, A., Schnabel, S., Berenguer-Sempere, F., Lavado-Contador, F. & Rubio-Delgado, J., 2014. Using 3D photo-reconstruction methods to estimate gully headcut erosion. *Catena* **120,** 91-101.

[6] Frankl, A. *et al*., 2015 Detailed recording of gully morphology in 3D through image-based modelling. *Catena* **127,** 92-101.

[7] Christian, P. & Davis, J., 2016 Hillslope gully photogeomorphology using structure-from-motion. *Z. Geomorphol. Supp.* **60,** 59-78.

[8] Ranga, V., Poesen, J., Rompaey, A. V. & Pani, P., 2016. Detection and analysis of badland dynamics in the Chambal River Valley (India), during the last 40 (1971-2010) years. *Environ. Earth Sci.* **75,** 1-12.

[9] Patel, P. P., Dasgupta, R & Mondal, S., 2020. Using Ground-Based Photogrammetry for Fine-Scale Gully Morphology Studies: Some Examples. In: P. K. Shit et al. (eds.), Gully Erosion Studies from India and Surrounding Regions, pp. 207-220. Advances in Science, Technology & Innovation, Springer. https://link.springer.com/chapter/10.1007%2F978-3-030-23243-6_12

[10] Whipple, K. X. & Tucker, G. E., 2002. Implications of sediment‐flux‐dependent river incision models for landscape evolution. *Journal of Geophysical Research: Solid Earth* **107,** 2039.

GEOMORPHOMETRY 2020 PERUGIA, ITALY JUNE 22 - 26 2020

GIS-based geomorphometric analysis of stream networks in mountainous catchments: implications for slope stability

Daniela Piacentini[1§], Francesco Troiani[2], Mattia Marini[1], Marco Menichetti[1], Olivia Nesci[1]
[1] Dipartimento Scienze Pure ed Applicate DiSPeA
Università di Urbino Carlo Bo
Via Cà le Suore 2-4, I-61029 Urbino, Italy
[2] Dipartimento di Scienze della Terra
Università di Roma La Sapienza
P. le Aldo Moro 5, I-00185 Roma, Italy
§ daniela.piacentini@uniurb.it

Abstract—**This work presents the application and validation of a GIS-based toolbox called SLiX, devoted to extract Stream Length-gradient (SL) index values along stream networks starting from Digital Elevation Models (DEMs). SL anomalous values are helpful to outline significant deviations from the concave-up shape of river longitudinal profiles of bedrock streams within mountainous catchments. The spatial analysis of SL index may be suitable for detecting along stream knickzones, supporting the investigation of the process responsible for their formation such as active tectonics, landslides interacting with streambeds or variations in bedrock resistance to erosion. The application in a mountainous catchment localized in the central Apennines (Italy) confirmed the proper functionality of the tool and the potentiality of the SL spatial analyses. This analysis has been integrated by the study of the Slope-Area (SA) function, which provided the contributing area threshold value required for the extraction of the stream network. SA analysis also supported the geomorphological interpretation of the knickzones detected through the SLiX application. The combination of SL and SA analyses in the sample area within the central Apennines revealed practical for detecting a major knickzone at a paleo-lake originated by the run-out of a rockslide. The SA function allowed interpreting the knickzone as one of the slope-break typologies, suggesting its occurrence and upstream propagation before the emplacement of the mass movement.**

I. INTRODUCTION

Geomorphometric analysis of stream networks and the quantitative analysis of stream longitudinal profiles are useful for the landscape evolution modelling within mountainous catchments. The identification of anomalous gradients occurring along bedrock stream longitudinal profiles (i.e. knickzones), can be practical for detecting mass movements directly interacting with streambeds at the catchments scale [1]. Many geomorphometric indexes have been demonstrated to be suitable for detecting anomalies along stream long profiles [2 and reference therein]. In particular, the Stream Length-gradient (SL) index allows outlining significant deviations from the concave-up shape of stream long profiles supporting the geomorphological interpretation of the processes responsible for the knickzone formation, such as the presence of a geological structure not necessary active, the occurrence of a landslides or the variations of the bedrock resistance to erosion [3 and reference therein]. The analysis of the along stream distribution of the slope values and the contributing area (i.e. SA function) can be practical for the interpretation of the knickzone typology [4]. This analysis allows discriminating the slope-break category, which encompass upstream propagating knickzones due to major variations of the base level of erosion, from the vertical steps, generated by local disturbances (i.e. lithological changes, meander cut-off, stream damming).

The growing availability of information technologies allows facing the application of geomorphometric indices with new tools and taking advantage from GIS procedure. A GIS-based toolbox, named SLiX, has been proposed by Piacentini et al. (2020) [5] to extract SL index values with a reproducible, standardized and timesaving process. The tool allows avoiding an error-prone procedure consisting of several step-by-step phases for converting the DEM dataset in SL index values. In this work, the SLiX toolbox has been used in order to detect the knickzones correlated with the main slope instability occurring within a mountainous catchment located in the central Apennines (Italy) (Fig. 1). The study has been supported by the analyses of the SA function with the double aim of selecting the appropriate contributing area value

Daniela Piacentini, Francesco Troiani, Mattia Marini, Marco Menichetti and Olivia Nesci (2020)

GIS-based geomorphometric analysis of stream networks in mountainous catchments: implications for slope stability:

in Massimiliano Alvioli, Ivan Marchesini, Laura Melelli & Peter Guth, eds., Proceedings of the Geomorphometry 2020 Conference, doi:10.30437/GEOMORPHOMETRY2020_68.

for the channel initiation threshold [6, 7] and for supporting the interpretation of the process responsible for the formation of the along stream anomalous zones [4].

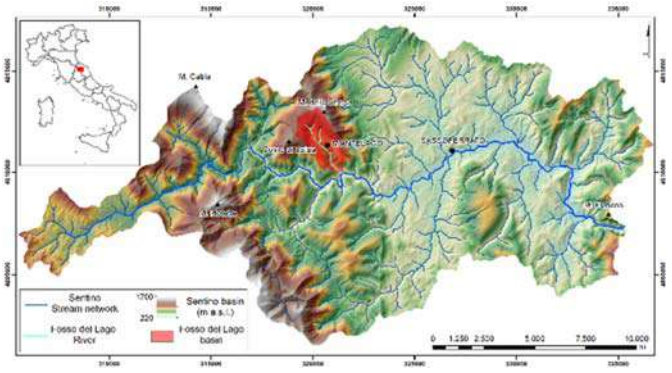

Figure 1. Location and altimetry of the study area coinciding with the Sentino catchment (Central Apennines, Italy). The location of the Fosso del Lago tributary has been also reported.

II. METHODS

The interactions between stream network and slope morphodynamics within the Sentino River basin has been investigated by means of a coupled geomorphometric analysis based on the computation of the Stream Length-gradient (SL) index and the study of the Slope-Area (SA) function. The analysis has been based on a 10 m cell-sized DEM, derived from altimetric dataset included in the topographic map, available in vector format at the scale of 1:10.000.

A. Computation and spatial analysis of the SL index

The SL index, according to Hack (1973) [8], is a suitable parameter to detect the deviations of a bedrock stream long profile from the steady-state conditions. In particular, SL may be to be a valid tool for identifying anomalous gradients along bedrock stream channels in mountainous catchments.

The SL Index is defined by the equation 1:

$$SL = \frac{dH}{dL} \times L \qquad (1)$$

where dH is the variation of elevation between two points of the stream channel, dL is the distance between the two points, and L is the total channel length from the channel initiation (Fig. 2).

The SL index values have been extracted taking advantage of the SLiX Toolbox [5] (Fig. 3). The toolbox allows, by means of a codified and timesaving process, to identify landscape portions where anomalous high values of SL Index occur and, consequently, where stream channels show peaks in the erosional dynamic (i.e. knickzones).

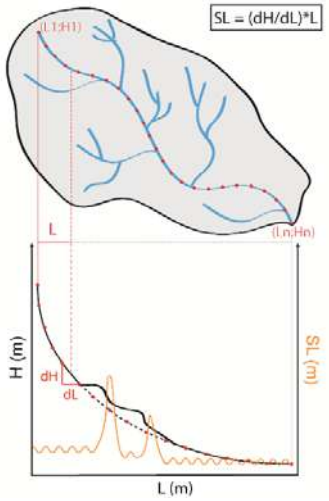

Figure 2. Parameters considered for the along stream calculation of SL index values following the Hack's equation (from [5]).

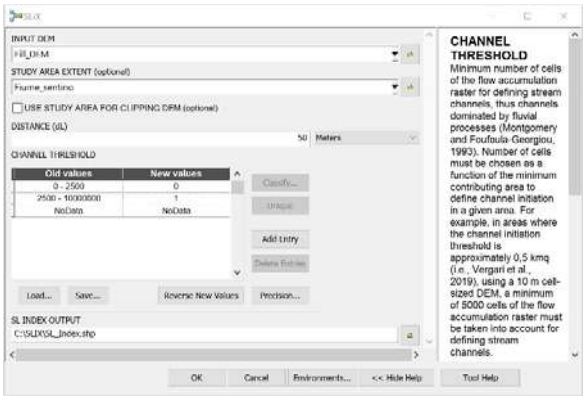

Figure 3. SLiX Toolbox mask [5].

B. Calculation and interpretation of the SA function

The SA approach is valid to explore the morphevolution of drainage basins in mountainous landscapes. In particular, the SA function demonstrated to be a valid way for detecting critical thresholds separating slope and channel process domains [6] and for supporting the interpretation of the different knickzone typologies that can characterize stream long profiles [4]. The SA function is pointed out by SA plots [9] where the slope, in m/m, is empirically expressed in function of the drainage area, in m^2.

The log form of this relationship is:

$$\log(S) = \log(k_s) + \theta \log(A) \qquad (2)$$

where k_s is the channel steepness index, and θ is the channel concavity index. Hence, the k_s and θ can be readily obtained from

the log–log plots [10], computed adopting the method proposed by Tarolli and Della Fontana (2009) [11]. In particular, computing the SA plot for the main channel, within a given catchment, can provide information on the typology of a knickzone. The slope-break typology will appear as a break on the SA scaling and, generally, is indicative of an upstream propagating knickzone generated as the response of the fluvial system to a major variation of the base-level of erosion [4 and reference therein].

III. RESULTS

The application of the SA analysis using the "total basin" method provided the value of contributing area to be used as threshold for the channel initiation (Fig. 4).

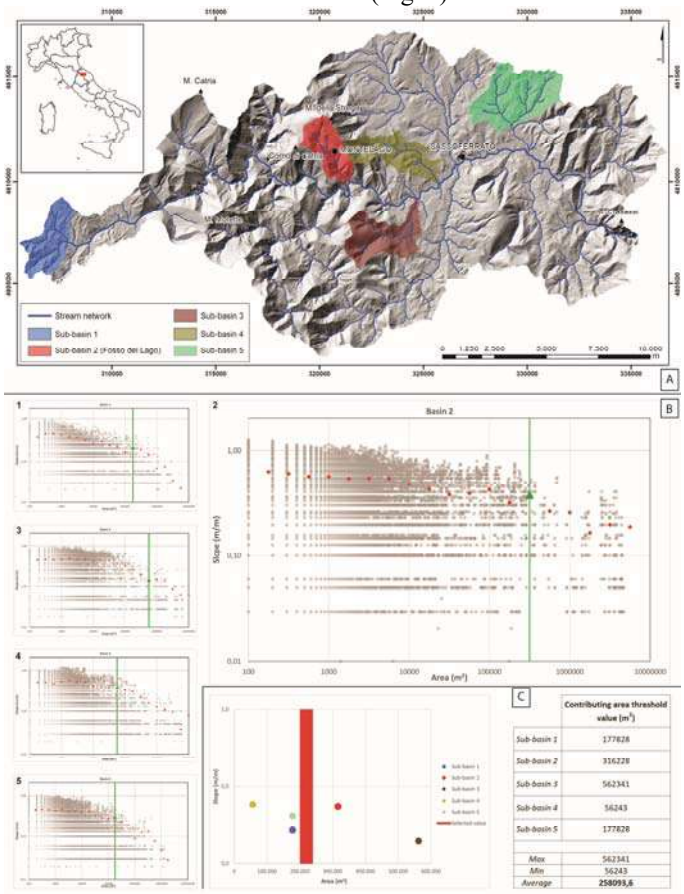

Figure 4. SA total basin analysis within five-selected tributary basins (A). The trends and forms of the SA function provided the contributing area threshold value for the extraction of the stream network (B). The selection of the contributing area value equal to 0.25 km^2 for the channel initiation (C) allows for extracting only those streams, which are actual dominated by the fluvial process.

The value of 0.25 km^2 resulted as mean value of the SA plots computed within five selected tributary catchments, representative of the complex lithological and geomorphological settings of the Sentino River basin. This channel threshold allows the extraction of the stream network including only those channels where the fluvial process is dominant.

Along the extracted stream network, using the procedure included in the SLiX toolbox, the raster map of the location of the major SL anomalous zones has been produced [5]. This map outlines the main knickzones occurring within the Sentino River basin (i.e. SL-HCA map according to [3]) (Fig. 5).

One of the major anomalies occurs within the Fosso del Lago tributary catchment, in the western portion of the study area, along the western flank of the Mount Strega morphostructure.The left valley-side of the Fosso del Lago is characterized by the presence of a rockslide well known in literature [12]. In particular, the mass movement caused the formation of a landslide-dammed lake. This landslide-dam emplaced at the end of the Upper Pleistocene and the resulting lake existed during the Holocene until historical time [13].

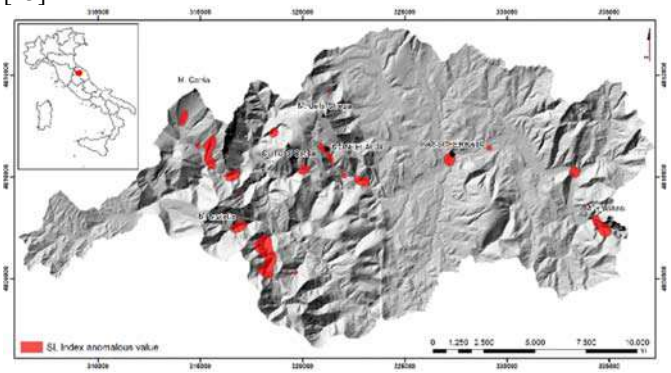

Figure 5. Distribution of the anomalous values of SL index detected by the application of the SLiX toolbox [5] within the Sentino River basin. In particular, in red are reported the knickzones identified in agreement with the Hotspot and Cluster Analysis (HCA) approach [3].

Along the main channel flowing within the Fosso del Lago tributary catchment, the SA plot has also been computed (Fig. 6). A break in the SA scaling suggests interpreting the knickzone as one of the slope-break typologies. Therefore, the present-day geometry of the Fosso del Lago long profile is the result of an upstream migrating knickzone that reached the middle portion of the catchment. Here, the augmented relief energy due to the strong stream entrenchment likely produced the morphoevolutionary context during which the slope collapsed, probably favored by the local morphostructural conditions and an intense rock mass fracturing.

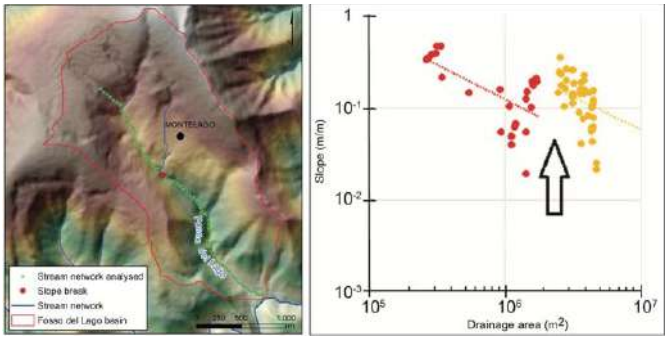

Figure 6. Location of the knickzone occurring along the Fosso del Lago tributary catchment. The break on the SA scaling along the main channel allows interpreting the knickzone as one of the slope-break typologies in agreement with Boulton et al. (2014) [4].

IV. CONCLUSIONS

In this work, we applied a coupled geomorphometric analysis of the stream network, flowing within a mountainous catchment in the central Apennines (Italy) that allowed identifying the major knickzones occurring along the stream long profiles. The results confirmed the validity of the use of the SLiX Toolbox for the computation and the spatial analysis of the SL anomalous values. Within mountainous catchments, many SL anomalies have been demonstrated to occur in correspondence of knickzones well correlated with the presence of mass movements directly interacting with the streambeds. The application to the sample area in the central Apennines confirmed this finding. Furthermore, the integration of the SL results with the analysis of the SA function allows distinguishing the possible cause-effect relationships between a major knickzone and a large landslide occurring in the sample area. The geomorphometric analysis here applied can be useful for the slope instability analysis in mountainous catchments where the slope-channel system is well-connected and the erosional behavior is dominant.

REFERENCES

[1] Troiani, F., J.P. Galve, D. Piacentini, M. Della Seta, J. Guerrero, 2014. "Spatial analysis of stream length-gradient (SL) index for detecting hillslopes processes: A case of Gállego River headwaters (Central Pyrenees, Spain)." Geomorphology 214, 183–197.

[2] Demoulin, A., A. Matherc, A. Whittaker, 2017. "Fluvial archives, a valuable record of vertical crustal deformation." Quat. Sci. Rev. 166, 10–37.

[3] Troiani, F., D. Piacentini, M. Della Seta, J.P. Galve, 2017. "Stream Length - gradient Hotspot and Cluster Analysis (SL - HCA) to fine - tune the detection and interpretation of knickzones on longitudinal profiles." Catena 156, 30‑41.

[4] Boulton, S.J., M. Stokes, A.E. Mather, 2014. "Transient fluvial incision as an indicator of active faulting and Plio-Quaternary uplift of the Moroccan High Atlas." Tectonophysics 633, 16-33.

[5] Piacentini, D., F. Troiani, T. Servizi, O. Nesci, F. Veneri, F, 2020. "SLiX: A GIS Toolbox to Support Along-Stream Knickzones Detection through the Computation and Mapping of the Stream Length-Gradient (SL) Index." ISPRS Int. J. Geo-Inf. 2020, 9, 69.

[6] Montgomery, D.R., E. Foufoula - Georgiou, 1993. "Channel Network Source Representation Using Digital Elevation Models." Water Resour. Res. 29, 3925‑3934.

[7] Vergari, F., F. Troiani, H. Faulkner, M. Del Monte, M. Della Seta, S. Ciccacci, P. Fredi, 2019. "The use of the slope - area function to analyse process domains in complex badland landscapes." Earth Surf. Process. Landf. 44, 273‑286.

[8] Hack, J. 1973. "Stream profile analysis and stream gradient index." J. Res. U.S. Geol. Surv. 1, 421–429.

[9] Dalla Fontana, G., L. Marchi, 2003. "S–A relationships and sediment dynamics in two alpine streams." Hydrological Processes 17, 73–87.

[10] Yetemen, O., E. Istanbulluoglu, E.R. Vivoni, 2010. "The implications of geology, soils, and vegetation on landscape morphology: Inferences from semi-arid basins with complex vegetation patterns in Central New Mexico, USA." Geomorphology 116(3), 246–263.

[11] Tarolli, P., G. Dalla Fontana, 2009. "Hillslope-to-valley transition morphology: new opportunities from high resolution DTMs." Geomorphology 113(1-2), 47–56.

[12] Savelli, D., O. Nesci, F. Troiani, A. Dignani, S. Teodori, 2012. "Geomorphological map of the Montelago area (North-Marche Apennines, central Italy): constrains for two relict lakes." Journal of Maps 8 (1), 113-119.

[13] Savelli, D., F. Troiani, E. Bruciapaglia, G. Calderoni, P. Cavitolo, A. Dignani, E. Ortu, S. Teodori, F. Veneri, O. Nesci, 2013. "The landslide-dammed paleolake of Montelago (North-Marche Apennines, Italy): geomorphological evolution and paleoenvironmental outlines." Geogr. Fis. Dinam. Quat. 36(2), 267-287.

GEOMORPHOMETRY 2020 PERUGIA, ITALY JUNE 22 - 26 2020

An empirical-conceptual gully evolution model using space-for-time substitution

Xiaoli Huang
College of Geographic Information and Tourism
Chuzhou University
No.1 Huifeng West Road, Chuzhou City, Anhui Province, China
xiaoliray@163.com

Guoan Tang
Key laboratory of Virtual Geographic Environment, MOE
Nanjing Normal University
No.1 Wenyuan Road, Nanjing City, Jiangsu Province, China
tangguoan@njnu.edu.cn

Abstract—**Space-for-time substitution is a concept that has been widely used in ecology and geomorphology but not strictly tested, especially in some fields of geomorphology. The objective of this study is to test whether the concept of space-for-time substitution is valid in reconstruction the evolution of a special type of gully, which called as 'Spoon-shaped Gully (SG)' in the Chinese Loess Plateau. High precision topographic data acquired by unmanned aerial vehicle (UAV) was used to analyze the morphology and morphometry of a sequence of SG ordered in terms of increasing gully length. The morphological model of gully evolution that proposed from this analysis is very similar to established models in the literature, which leads us to conclude that time can be substituted by space when reconstructing the evolution of SG of the Chinese Loess Plateau.**

I. INTRODUCTION

Due to the relatively long time scale of many geomorphic phenomena, especially some large-scale landform units, geomorphologists are generally unable to fully observe and understand landform forming processes based on existing scientific and technical conditions. Taking the loess landform as an example, although the occurrence and change of micro-topography such as rills and shallow gullies can be observed on the loess slope after heavy rainfall, the formation of the Loess Plateau takes several hundred thousand, or even millions of years. There have been various attempts to solve this problem. One approach to solve this issue has been to assume that in the modern landscape we see landforms at various stages of development and that we may therefore make inferences about changes through time based on the variety of forms we see at present. This concept is known as space-for-time substitution, which has been firstly applied in ecology to study the succession of biomes on a long time scale. The basic idea is that, in order to predict the succession process of the community, the community in the same space can be sorted according to the relative difference of the community development, under the condition that the other ecological factors, except time, are kept as stable as possible. Due to the similarity of landform evolution and community succession, this idea has been applied by some geomorphologists to the research of geomorphic evolution, such as tectonic landform, fluvial landform and estuarine and coastal landform [1], [2], [3], [4], [5], [6], [7], [8]. Despite its accepted use in the geomorphic literature, the concept of space-for-time substitution is not thoroughly tested and well proven.

We focus our study on gully system in the Chinese Loess Plateau. The landforms of the Chinese Loess Plateau have been formed through the eolian transport and accumulation of loess deposits on bedrock during the Quaternary. This unique formation mechanism and resultant landscapes attract global attention in relation to their history connected to global change, thick loess sediments, various landscape types, severe soil erosion, and the interaction between natural and human activities. Gullies caused by the water erosion are widespread in the Chinese Loess Plateau. This landform is characterized by the frequent material exchange and strong morphological changes. Among all kinds of gullies with different sizes and shapes, there exists a special type of gully, which called locally as 'Spoon-shaped Gully(SG)'. The SG is unusual because of its unique spoon like shape, unclear water confluence relationship, significant regional differences and complex erosion process.

The aims of this research are: (i) to test whether the concept of space-for-time substitution is valid in loess geomorphology, specifically in reconstructing the evolution of a special type of gully in the Chinese Loess Plateau, and (ii) to gain some new insights into the morphological evolution of gully system of the Loess Plateau.

Xiaoli Huang, Guoan Tang (2020) An empirical-conceptual gully evolution model using space-for-time substitution:
in Massimiliano Alvioli, Ivan Marchesini, Laura Melelli & Peter Guth, eds., Proceedings of the Geomorphometry 2020 Conference, doi:10.30437/GEOMORPHOMETRY2020_69.

Geomorphometry.org/2020

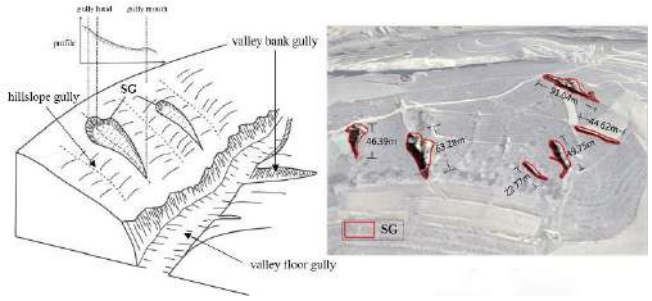

Figure 1. Sketch diagram of SG.

II. RESEARCH FOUNDATION

A. Principle of study area selection

In applications of space-for-time substitution, one should be sure that the environmental conditions are uniform across the entire study area, and there are no individual, small-scale controls (e.g. tectonics, runoff, etc.) that could affect the morphology of individual landforms. The above is fundamental to apply space-for-time substitution which is achieved by having a relative small study area or different study areas with relative same landform forming processes.

B. Regional setting

Two hillslopes situated in Xining (101°43′32″ E–101°43′39″E, 36°39′34″ N–36°39′47″N) and Yulin (108°40′23″ E–108°41′03″E, 37°23′23″ N–37°23′54″ N) of the Chinese Loess Plateau were selected as study area. Xining hillslope is located in the northwest of Xining City. The area of Xining hillslope is approximately 0.07km^2, and the difference in the elevation in this area is roughly 81m. The landform type of this area is valley plain formed by loess deposition. Yulin hillslope is located in the southwest of Jingbian County, Yulin. The area is about 0.7km^2, and the difference in the elevation in this area is roughly 98m. The area situated in the loess hilly area which are characterized by typical loess gullies and hills. Although it is likely that these 2 study areas are far away to each other which may cause other factors, such as precipitation, vegetation condition and soil texture influence SG development. However, according to previous studies [9], these 2 study areas both belong to the middle develop-ment zone (zone III) in the loess cave development density division of the Loess Plateau. The loess cave development density division comprehensively considers the geomorphological conditions, vegetation cover conditions, soil erosion modulus, rainfall and climate, etc., which affect the velopment density of loess caves. Therefore, the landform form process of these 2 areas has large similarity, which is also ma the application conditions of space-for-time substitution.

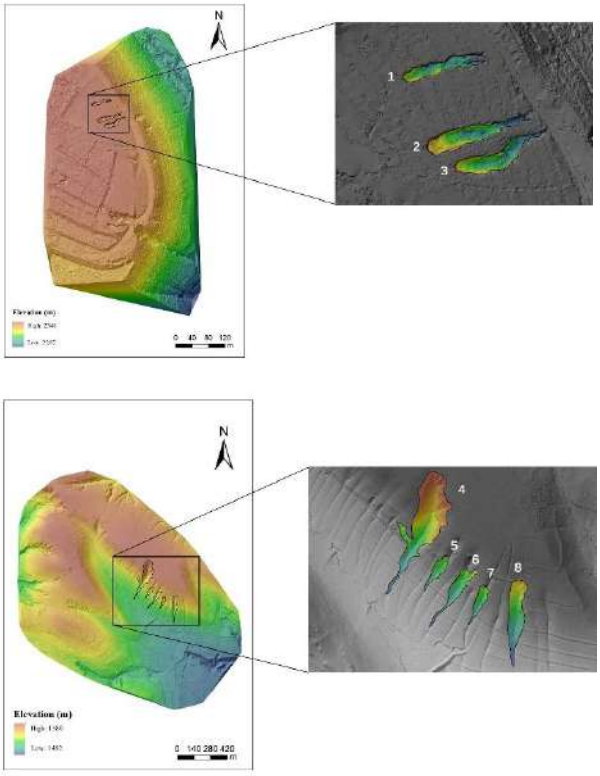

Figure 2. Distribution of SGs in study area (the upper is Xining hillslope and the lower is Yulin hillslope)

III. MATERIALS AND METHODS

A. Test data

In this study, the source data were composed of 19 color aerial photographs taken by UAV photogrammetry with a Matrice 210 (SZ DJI Technology Co., Ltd., Shenzhen, China), and digital aerial photogrammetry was used to generate a Digital Elevation Model (DEM) of 0.1m resolution. The processing flow is as follows. Forty-nine ground control points were obtained by the GPS-RTK (Global Positioning System Real - time kinematic) method. The geodetic datum, projection, and central meridian were WGS-84, Gauss-Kruger projection, and 111°, respectively. Aerial triangulation was performed inside a laboratory according to the control points obtained through field-work. The Digital Surface Model (DSM), including the vegetation and manmade features above the pure earth surface, was constructed using photogrammetric software (Pix4Dmapper). Editing is required to modify elevation and consequently eliminate the influences of the buildings and vegetation. Topographic features, such as contour lines, feature lines and feature points were also obtained. Finally,

DEM was derived from the DSM at 0.1m resolution by using Pix4Dmapper. Besides, 0.04 m digital orthophoto maps (DOMs) were also simultaneously generated by UAV photogrammetry which served as ground truth and as reference maps.

B. Ergodic indicator

Choosing the suitable terrain factor as the ergodic indicator is the key to the research of landform evolution by using space-for-time substitution. Distance, location, landform dimension and complexity are generally used as ergodic indicators of landform evolution to derive the spatial sequence. According to the previous research and the basic principle of geomorphology, the most important consideration when choosing an ergodic indicator is that its main controlling factor is time (and not other factors related to lithostratigraphy, structure, exogenic controls, etc.). Therefore, combing the characteristic of the loess landform, gully length is chosen as the ergodic indicator of this research.

C. Morphometric parameters of SGs

To test our hypothesis that space can be substituted for time to reconstruct the evolution of SG, we used gully length as an ergodic indicator of landform evolution. We organized the eight SGs dis-tribute on the hillslopes from study area, i.e. Xining and Jingbian into a sequence of increasing gully length and labelled these SGs as 'features 1-8'. For each feature we extracted a number of morphometric parameters from high-resolution DEM.

1. Gully length: The gully length includes the channel length (Lc) and straight length (Ls). Channel length is defined as the length of the gully from head to mouth along the stream channel, while the straight length is defined as the linear distance from the gully head to its mouth. For the same area, if the gully is much longer, there will be a larger drainage area and the gully will have experienced a much longer erosion process. At a given time, the length of each gully is fixed.
2. Gully width: The top width at any cross-section of the gully is called the gully width. A gully has many cross-sections, and thus there is more than one gully width. From the gully head to the mouth, the gully widths at 1/4, 1/2, and 3/4 of the way along the gully are marked as W1/4, W1/2 (also called middle width, Wh), and W3/4, respectively. The value obtained by dividing erosional area (A) by Lc is called the average width (Wa) or equivalent width (El Maaoui et al., 2012). The changes of gully widths along the gully and the length–width ratios can effectively describe the plane form of the gully.
3. Gully depth: The gully depth is the difference between the average elevation before the gul-ly erosion and the average elevation after the gully erosion within the gully area. The gully depth calculated in SG is the main gully depth. The change in gully depth reflects the undercut process of the valley.
4. Erosion area: The erosional area (A) refers to the area of the closed curve zone enclosed by the shoulder line, namely the area eroded away under gully erosion.
5. Erosion volume: The erosion volume refers to the change of soil volume caused by gully erosion. The calculation method is the product of the projected area of the channel and the average gully depth. The greater the amount of gully erosion per unit time, the stronger the gully erosion.
6. Opening degree: The opening degree is defined as the ratio of the average width and the av-erage depth of the gully. For deep erosion gully, the opening degree is relatively small, which is characterized by steep gully slop. For the relatively open gully, the corresponding opening degree is larger, reflecting that the gully slope is gentle, and the site conditions and land use potential are better. There are three types of gully opening degree including semi-open (1.32~2.61), open (>2.61) and deep open (<1.32).

IV. RESULTS AND DISCUSSION

A. Gully morphometric characteristics

The statistical results of gully morphometric parameters show below.

Table 1. Morphometric parameters of SG from Xining hillslope

Xining	1	2	3
Gully length(m)	25.78	34.17	32.07
Gully width(m)	2.94	3.84	3.52
Gully depth(m)	0.81	1.60	1.44
Erosion volume(m^3)	63.89	481.84	379.28
Opening degree	3.63	2.40	2.44

Table 2. Morphometric parameters of SG from Yulin hillslope

Yulin	4	5	6	7	8
Gully length(m)	179.65	91.04	116.29	76.76	124.45
Gully width(m)	25.69	10.40	14.98	7.16	11.22
Gully depth(m)	23.47	17.81	18.18	15.83	20,15
Erosion volume(m^3)	92574.36	14743.47	25082.76	7267.87	24638.01
Opening degree	1.09	0.58	0.82	0.45	0.56

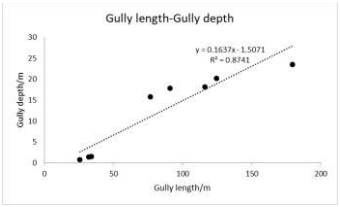

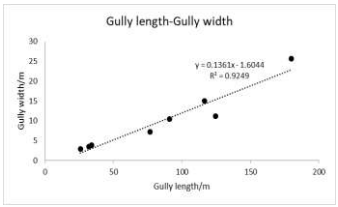

Geomorphometry.org/2020

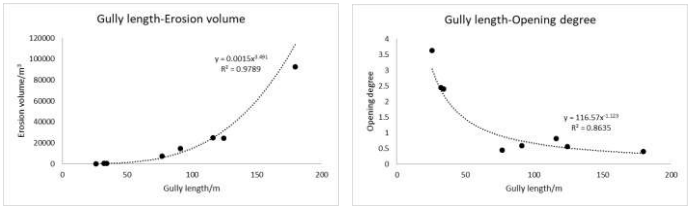

Figure 3. The variation of morphometric parameters of SG

B. Validity of space-for-time substitution model

The inferred model for the morphological evolution of SGs shows many parallels with established gully evolution models in the literature.

In terms of gully evolution in the Loess Plateau, the most distinguishing characteristics is that as the gully length increases, the width and depth of the gully are increasing simultaneously due to the lateral erosion and vertical erosion by fluviation [10]. The above process is consistent with the results obtained above.

Besides, there was a very prominent relationship of power function between erosion volume and gully length and gully area and thus the gully length and the gully area can be used to estimate the gully erosion rate at the large spatial scales because they can be easily determined from very high-resolution satellite images and DEMs [11], [12], [13]. These also show strong similarities with the results obtained.

C. SG development and tunnel erosion

4407 SGs (incomplete statistics) were marked in the Loess Plateau by visual interpretation based on Google Earth image. By using Kernel Density tool of ArcGIS 10.0, kernel density plot of SGs in the Chinese Loess Plateau was obtained. It can be seen from the plot that most of the SGs are distributed in the northwestern margin of the Loess Plateau and the Lanzhou-Dingxi area. According to previous studies [9], these areas are short of precipitation, and the loess particle is dominated by sandy loess, which has strong collapsibility and is prone to loess piping and tunnel erosion, forming a large number of loess cave systems.

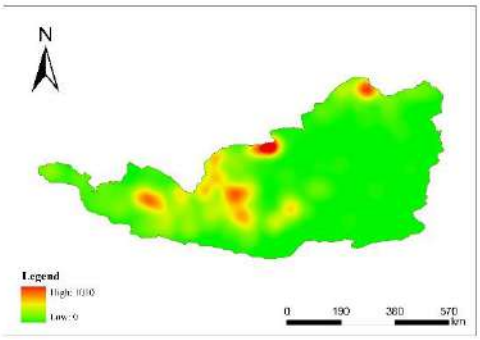

Figure 4. The kernel density plot of SG

Detailed field studies were carried out to investigate the interactions between SG development and tunnel formation processes in the selected 8 gullies. Smoke tracer method was used to investigate the SG and the associated loess cave system. The tracer method has been widely used in the fields of physics, chemistry, biology, etc. The principle is to use the radionuclide as a tracer to mark the research object to observe its trajectory and spatial distribution characteristics. Some scholars have introduced it into the study of gully erosion on the Loess Plateau, and have also obtained corresponding research results. Inspired by this, the smoke tracer method is used to roughly determine the spatial pattern of the loess cave system. The smoke generator was put into the loess cave, and blast the hole and observe the exit position of the smoke to determine the connectivity and development of the cave. The results show that the formation of SG is strongly associated with loess piping and tunnel erosion. A large number of slope surface runoff flows through the underground loess caves, resulting in the special shape of SG. The SG can be considered as a special initial form of a hillside gully widely distributed in the collapsible sandy loess area, which is dominated by piping and tunnel erosion, surface fluvial erosion and gravity erosion.

Figure 4. Tunnel outlet exploration using smoke tracer method

D. Other new insights of SG evolution in the Chinese Loess Plateau

Compared with other types of loess gullies, the amount of SG distributed in the entire Loess Plateau is small. On the one hand, because of its special development mechanism, it mostly appears in the collapsible loess area; on the other hand, because it is an intermediate form of loess gully development, its development process is sudden and accidental. The sudden collapse of the loess cave will cause SG to continue to develop in the next stage, causing SG to occupy only a short period of time throughout the development of the loess gully. Therefore, under natural conditions, it is difficult to observe a large number of SGs compared to other gullies.

REFERENCES

[1] Paine A D M. 'Ergodic' reasoning in geomorphology: time for a review of the term. Progress in Physical Geography, 1985, 9(1):1-15.

[2] Kirkbride M, Matthews D. The Role of Fluvial and Glacial Erosion in Landscape Evolution: The Ben Ohau Range, New Zealand. Earth Surface Processes & Landforms, 2015, 22(3):317-327.

[3] Stolar D B, Willett S D, Montgomery D R. Characterization of topographic steady state in Taiwan. Earth & Planetary Science Letters, 2007, 261(3–4):421-431.

[4] Leyland J, Darby S E. An empirical–conceptual gully evolution model for channelled sea cliffs. Geomorphology, 2008, 102(3–4):419-434.

[5] Hilley G E, Ramón Arrowsmith J. Geomorphic response to uplift along the Dragon's Back pressure ridge, Carrizo Plain, California. Geology, 2008, 36(5):367-370.

[6] Fryirs K, Brierley G J, Erskine W D. Use of ergodic reasoning to reconstruct the historical range of variability and evolutionary trajectory of rivers. Earth Surface Processes & Landforms, 2012, 37(7):763–773.

[7] Micallef A, Ribó M, Canals M, et al. Space-for-time substitution and the evolution of a submarine canyon–channel system in a passive progradational margin. Geomorphology, 2014, 221(11):34-50.

[8] Ely J C, Clark C D, Spagnolo M, et al. Using the size and position of drumlins to understand how they grow, interact and evolve. Earth Surface Processes & Landforms, 2017, 43(5):1073-1087.

[9] Peng J B. Loess cave disaster. Science Press, Beijing, 2009.

[10] Liu D S. Loess and Environment. Science Press, Beijing, 1985.

[11] Li Z, Zhang Y, Zhu Q K, et al. A gully erosion assessment model for the Chinese Loess Plateau based on changes in gully length and area. Catena, 2017, 148: 195－203.

[12] Dong Y F, Xiong D H, Su Z A, et al. Critical topographic threshold of gully erosion in Yuanmou Dry-hot Valley in Southwestern Southwestern China. Physical Geography, 2013, 34(1): 50－59.

[13] Zhang T Y, Liu G, Duan X W, et al. Spatial distribution and morphologic characteristics of gullies in the Black Soil Region of Northeast China: Hebei watershed. Physical Geography, 2016, 37(3-4): 228－250.

GEOMORPHOMETRY 2020
PERUGIA, ITALY
JUNE 22 - 26 2020
PARTNERS SPONSORS

Probabilistic behavior modeling of morphometric parameters for thermokarst plains with fluvial erosion in Cryolithozone

Alexey Victorov[§], Olga Trapeznikova, Timofey Orlov
Sergeev Institute of Environmental Geoscience
Russian Academy of Science
Ulanskii pereulok 13, b.2 Moscow, Russia, 101000
[§] vic_as@mail.ru

Abstract—**This work aims to study the patterns of changing morphometric characteristics of thermokarst plains with fluvial erosion for different variants of their development. The research involved a series of essential morphometric parameters of the thermokarst plains with fluvial erosion, such as the number of lakes at a trial plot, a number of khasyreis at a trial plot, and areas of thermokarst lakes. The developed a probabilistic model is suitable for a homogenous area with a continuous generation of new thermokarst depressions ("asynchronous start") under a stable climate. The mathematical analysis of the model shows that after a long time of development with uneven occurrence and vanishing (drainage) of lakes, we get the stable share of the area covered by water and a particular distribution for the lakes' area – an integral exponential distribution. We chose 17 key sites in different regions of Western and Eastern Siberia and Canada for empirical testing of the model. The examination includes checking the conformity of the area samples to different types of distributions by the Pearson criterion. The test used aerial and satellite imagery of the two survey dates, including Corona archival photographs. The research revealed that at a majority of the key sites, the areas of the thermokarst lakes obey the integral-exponential distribution within homogeneous sections of the thermokarst plains with fluvial erosion in different natural environments. Moreover, the morphological pattern of the thermokarst plains with fluvial erosion is in a state of dynamic balance, and forecasting development and assessing natural risks should take it into account.**

I. Introduction

Many researchers deal with the cryolithozone landforms [1,2,3,4], but only a few of them analyze the behavior of morphometric parameters. The goal of this work is to study the patterns of changing morphometric characteristics of thermokarst plains with fluvial erosion.

Landscapes of thermokarst plains with fluvial erosion also include slight wavy subhorizontal areas covered by tundra vegetation, interspersed with lakes, and khasyreis (a khasyrei is a drained thermokarst lake), and crossed by a rare enough fluvial erosion network. The lakes of isometric often roundish shape are randomly scattered across the plain. Khasyreis are also isometric flat-bottomed and flattened peaty depressions covered with meadow or bog vegetation; like the lakes, they are randomly distributed across the plain (Fig.1).

The research involved a series of essential morphometric parameters of the thermokarst plains with fluvial erosion, such as a number of lakes at a trial plot, a number of khasyreis at a trial plot, and areas of thermokarst lakes. Thermokarst, thermoabrasion, and thermoerosion have a complex interrelation affect the area. As a result, new primary thermokarst depressions appear; different thermokarst depressions grow independently on each other as lakes (ponds) due to thermoabrasion; at a random moment, a lake can be drained by fluvial erosion and transforms into a khasyrei. At that, its growth stops because of the absence of water. These processes change the mentioned above morphometric parameters raising the following questions:

- What are the laws ruling the analyzed parameters?
- What are the dynamics of the analyzed parameters for a long time of development?
- Does the up-to-date climatic change influence the laws ruling the analyzed parameters?

II. Methods

We developed a probabilistic analytical model suitable for a homogenous area with a continuous generation of new thermokarst depressions ("asynchronous start") under a stable climate. The model belongs to the recent scientific branch called "the mathematical morphology of landscapes"[4].

Alexey Victorov, Olga Trapeznikova and Timofey Orlov (2020) Probabilistic behavior modeling of morphometric parameters for thermokarst plains with fluvial erosion in Cryolithozone: in Massimiliano Alvioli, Ivan Marchesini, Laura Melelli & Peter Guth, eds., Proceedings of the Geomorphometry 2020 Conference, doi:10.30437/GEOMORPHOMETRY2020_70.

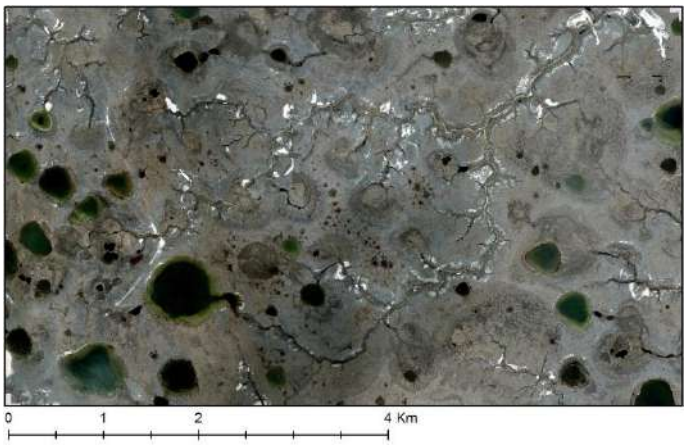

Figure 1. A typical image of a thermokarst plain with fluvial erosion on the remote sensing data.

The base of the model 1.0 includes the following underlying assumptions:

1. Thermokarst depressions (germs of thermokarst lakes) were appearing within a relatively short period independently across the different non-adjacent sites. At that, for small plots and time intervals, the probability of several depressions to occur is much less than that of a single depression.

2. The change of the radius of an appeared thermokarst depression is a random variable; it is independent of other lakes, and the growth rate is directly proportional to heat losses through the side surface of the lake basin.

3. In the course of its growth, a lake can transform into a khasyrei after draining by the erosion network; the probability of this does not depend on the development of other lakes; if it happens, the depression stops growing.

4. The appearances of new sources of fluvial erosion within a randomly selected area are random and independent events. At that, the probability of occurrence of more than one source is an infinitesimal of a higher-order than the probability of the appearance of one source.

5. The primary thermokarst depressions do not occur within already existing thermokarst lakes.

The following primary dependencies obtained earlier in the frames of the mathematical morphology of landscapes are valid [1,4]:

- The radius distribution for free growing thermokarst lakes since time t after lake emergence (lognormal distribution):

$$f_0(x,t) = \frac{1}{\sqrt{2\pi}\sigma x\sqrt{t}} e^{-\frac{(\ln x - at)^2}{2\sigma^2 t}} \quad (1)$$

where a, σ are distribution parameters, t is the time since the process has started.

- The distance distribution from the center of the growing lake to the nearest sources of erosion structure (stream) which stops the lake growth and transform it into a khasyrei, obeys the Rayleigh distribution

$$F(x) = 1 - e^{-\pi\gamma x^2} \quad (2)$$

where γ is an average density of the stream sources.

- The number of primary depressions on a free surface without lakes corresponds to the Poisson distribution.

The most uncomplicated characteristics include a number of lakes and a number of khasyreis within a random plot. Since the probability for a lake to transform into a khasyrei does not depend on its location, it is easy to show that the distributions of lakes and khasyreis within a test plot are Poisson at any moment.

The behavior of lakes' areas is more complicated. The density distribution of the lake radii at time t is equal to the ratio of the number of lakes of a given radius to the total number of lakes, taking into account the different times of their appearance and the probability not to transform to a khasyrei. The assumption of the model that primary depressions appear only outside the lakes means that a variable density of generation of initial depressions is equal to

$$\lambda_1(t) = \lambda[1 - P_l(t)] \quad (3)$$

where $P_l(t)$ is a share of water covered area, λ is a generation density of initial depressions within the free of lakes territory.

The function $P_l(t)$ is a fraction of the whole area occupied by lakes at time t and, as shown earlier [4], is related to the process parameters by the dependence

$$P_l(t) = 1 - e^{-\tau(t)\bar{s}(t)} \quad (4)$$

where $\bar{s}(t)$ is an average lake area at time *t*, $\tau(t)$ is an average number of lakes per unit area at time *t.*

The probability of a lake to remain the lake without transforming into a khasyrei depends on the lake radius distribution in the case of free growth if the distance to a fluvial source is more significant than the lake radius. The distance to the

source fits the Rayleigh distribution (2). Thus, after simplification, the distribution density for the thermokarst lakes at time t is equal to

$$f(x,t)=\frac{e^{-\pi\lambda x^2}\int_0^t[1-P_l(u)]\,f_0(x,t-u)du}{\int_0^t[1-P_l(u)]\int_0^{+\infty}e^{-\pi\lambda x^2}\,f_0(x,t-u)dxdu} \qquad (5)$$

Let us examine the area distribution of the thermokarst lakes after a long time of development, which we observe now. First, our model gives us an expression of the dynamics of a share of the area covered with water. If we take the average lake area from the above formula for the lake radius distribution, then involving equations (4) and (1) after simplifying and taking the logarithm we get the integral equation [5]

$$ln[1-P_l(u)]= -\pi\lambda\int_0^t[1-P_l(u)]\int_0^{+\infty}x^2e^{-\pi\lambda x^2}\,f_0(x,t-u)dxdu \qquad (6)$$

The function $P_l(t)$ is the solution of this equation. Using this integral equation, we can show that if the integral converges

$$I=\int_0^{+\infty}\int_0^{+\infty}x^2e^{-\pi\lambda x^2}\,f_0(x,u)dxdu \qquad (7)$$

and the solution of the equation (8) (at that, we can prove that this equation has a solution and the only one)does not exceed $(1-e^{-1})$ that is 0.63; then, there is a limit of function $P_l(t)$ if $t\to+\infty$. It is equal to the solution of the equation (P_l^*). The proof needs the construction of a pair of step functions that bound a function $P_l(t)$ from above and below [4,5].

$$\ln[1-P_l^*]=-\lambda\pi[1-P_l^*]I \qquad (8)$$

Under these conditions, ensuring the existence of a limiting value of the lake area percentage, there is also a limiting distribution of the radii of lakes if $t\to+\infty$

$$f(x,\infty)=\frac{e^{-\pi\lambda x^2}\int_0^{+\infty}f_0(x,u)du}{\int_0^{+\infty}\int_0^{+\infty}e^{-\pi\lambda x^2}\,f_0(x,u)dxdu} \qquad (9)$$

Using expression (1) for the density distribution of the lake radii in the case of free growth and calculating the upper integral as the Laplace transform, we obtain the area distribution (with ε area for the primary depressions)

$$f_{sl}(x,\infty)=-\frac{2}{xEi(-\gamma\varepsilon)}e^{-\gamma x},\ x\ge\varepsilon \qquad (10)$$

where

$$Ei(-x)=\int_{-\infty}^{x}\frac{e^{-u}}{u}du \qquad (11)$$

is an integral exponential function, and thus, this distribution can be called the integral exponential distribution.

Thus, our model shows that after a long time of development, we obtain the stabilization of the total lake area and the integral exponential distribution of lake areas. The empirical testing of these analytical results involved 17 key sites within the thermokarst plains with fluvial erosion in different natural environments (Fig. 2).

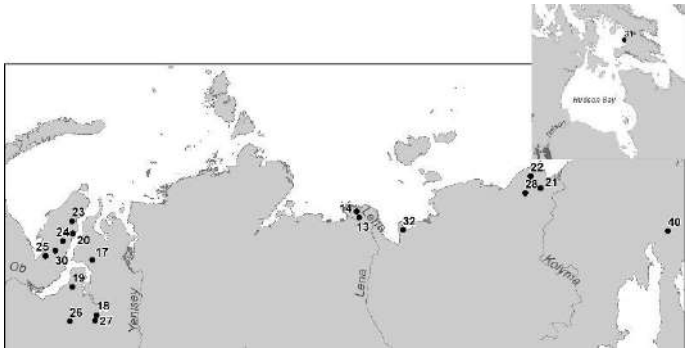

Figure 2. A location scheme of the key sites of the thermokarst plains with fluvial erosion.

We used repeated remote sensing data. The first date of the survey comes from the archive Corona imagery (3-7 m/pix, 1965-1976) for eleven key sites. The recent imagery includes Sentinel 2A 2017-2018, Resurs-P, ICONOS, QuickBird, Worldview 2, Geoeye-1, 2008-2014 for the whole set of 17 key sites.

We found the Pearson criterion for the common distributions using the STATISTICA package, while we have to make a special software for the integral exponential distribution. Parameter ε is the minimal value of the sample, while γ resulted from the numerical solving the equations in the frame of this software package.

$$-\frac{1}{\gamma Ei(-\gamma\varepsilon)}e^{-\gamma\varepsilon}=\bar{s} \qquad (12)$$

where $\bar{s}$ is an average lake area.

III. DISCUSSION

The empirical data of the thermokarst lakes from the key sites include samples from 49 to 2108 lakes. The empirical distributions fit the integral exponential distribution (fig. 3 as an example) for ten key sites from 17 key sites (59%) of the second date and five key sites of 11 (45%) of the first date.

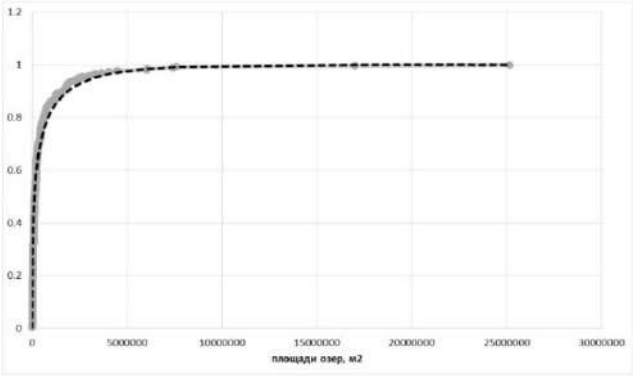

Figure 3. A graph demonstrating closeness between an empirical distribution and the integral exponential distribution (key site 28).

At the same time, the lognormal distribution characterizes area distribution of the thermokarst lakes at eight key sites of 17 of the second date. For three key sites of these 17, the empirical distributions of the thermokarst lakes' areas obey both the gamma and lognormal distributions. This situation corresponds to the synchronous start model [4] and can be explained by two reasons:

- At the first stage, the thermokarst plains with fluvial erosion are just lacustrine thermokarst plains since the probability of lake drainage was small due to their little size; this causes the lognormal distribution of the lakes' areas.
- The integral exponential distribution is a limit distribution at $t \to \infty$, while the time since the start of the thermokarst process is long but finite.

Interestingly, typical lacustrine thermokarst plains fit generally the lognormal distribution only [4].

We can explain the fact that the distribution of the lake areas fits neither the integral exponential nor the lognormal distribution for several key sites by the beginning change of these sections under the influence of climate change. Four of these key sites demonstrate a significant (by the Smirnov's criterion) difference in the distribution of lake areas for the two periods.

IV. CONCLUSIONS

The model fitting the asynchronous start and the lake growth rate proportional to heat losses through the side surface is relevant for most of the homogenous sections of thermokarst plains with fluvial erosion in different natural environments.

These sections have mostly integral exponential distribution of the thermokarst lake areas.

The morphological pattern of the thermokarst plains with fluvial erosion can be in the state of the dynamic balance; natural risk assessment and prognosis studies should take it into account.

There are the signs of a shift of the dynamic balance apparently due to climate change.

ACKNOWLEDGEMENTS

The research was done with the support of RSF project 18-17-00226.

REFERENCES

[1] **Burn C.R., Smith M. W.** Development of Thermokarst Lakes During the Holocene at Sites Near Mayo, Yukon Territory. Permafrost and Periglacial Processes, v. 1, 1990, pp. 161-176.

[2] **Grosse G., Jones B. M., Nitze I., Lindgren P. R., Walter Anthony K. M., & Romanovsky V. E.** Massive thermokarst lake area loss in continuous ice-rich permafrost of the northern Seward Peninsula, Northwestern Alaska, 1949-2015 // XI. International Conference on Permafrost – Book of Abstracts, 20 – 24 June 2016, Potsdam, Germany. Bibliothek Wissenschaftspark Albert Einstein, 2016, pp 739-740.

[3] **Smith L.C., Sheng Y., Macdonald G.M., Hinzman L.D.** Disappearing Arctic Lakes // Science. V. 308. № 3, 2005, p. 14.

[4] **Viktorov A.S., Kapralova V.N., Orlov T.V., Trapeznikova O.N., Arkhipova M.V., Berezin P.V., Zverev A.V., Sadkov S.A., Panchenko E.G**. Mathematical morphology of cryolithozone landscapes. Moscow RUDN, 2016. 232 p. (in Russian)

[5] **Victorov A.S.** Mathematical Models of Thermokarst Erosion Plains // GIS and Spatial Analysis. Proc. of IAMG, Toronto, Canada, 2005, V. 1, pp.. 62-67.